R-05-12

Regional hydrogeological simulations – Numerical modelling using ConnectFlow

Preliminary site description Simpevarp sub area – version 1.2

Lee Hartley, Andrew Hoch, Fiona Hunter, Peter Jackson
Serco Assurance

Niko Marsic
Kemakta Konsult

February 2005

Svensk Kärnbränslehantering AB
Swedish Nuclear Fuel
and Waste Management Co
Box 5864
SE-102 40 Stockholm Sweden
Tel 08-459 84 00
+46 8 459 84 00
Fax 08-661 57 19
+46 8 661 57 19

ISSN 1402-3091
SKB Rapport R-05-12

Regional hydrogeological simulations – Numerical modelling using ConnectFlow

Preliminary site description Simpevarp sub area – version 1.2

Lee Hartley, Andrew Hoch, Fiona Hunter, Peter Jackson
Serco Assurance

Niko Marsic
Kemakta Konsult

February 2005

Summary

The Swedish Nuclear Fuel and Waste Management Company (SKB) carries out site investigations in two different candidate areas in Sweden with the objective of describing the in situ conditions for a bedrock repository for spent nuclear fuel. The two candidate areas are named Forsmark and Simpevarp. The site characterisation work is divided into two phases, an initial site investigation phase (IPLU) and a complete site investigation phase (KPLU). The results of IPLU are used as a basis for deciding on a subsequent KPLU phase. On the basis of the KPLU investigations a decision is made as to whether detailed characterisation will be performed (including sinking of a shaft).

An integrated component in the site characterisation work is the development of site descriptive models. These comprise basic models in three dimensions with an accompanying text description. Central in the modelling work is the geological model which provides the geometrical context in terms of a model of deformation zones and the rock mass between the zones. Using the geological and geometrical description models as a basis, descriptive models for other geo-disciplines (hydrogeology, hydro-geochemistry, rock mechanics, thermal properties and transport properties) will be developed. Great care is taken to arrive at a general consistency in the description of the various models and assessment of uncertainty and possible needs of alternative models.

Here, a numerical model is developed on a regional-scale (hundreds of square kilometres) to understand the zone of influence for groundwater flow that effects the Simpevarp area. Transport calculations are then performed by particle tracking from a local-scale release area (tens of square kilometres) to identify potential discharge areas for the site. The transport from the two site-scale release areas (a few square kilometres) at the Simpevarp site and the Laxemar site are also considered more specifically and using greater grid resolution.

The main objective of this study is to support the development of a preliminary Site Description of the Simpevarp area on a regional-scale based on the available data of August 2004 (Data Freeze S1.2) and the previous Site Description. A more specific objective of this study is to assess the role of known and unknown hydrogeological conditions for the present-day distribution of saline groundwater in the Simpevarp area on a regional-scale. An improved understanding of the paleo-hydrogeology is necessary in order to gain credibility for the Site Description in general and the hydrogeological description in particular. This is to serve as a basis for describing the present hydrogeological conditions on a local-scale as well as predictions of future hydrogeological conditions. Other key objectives were to identify the model domain required to simulate regional flow and solute transport at the Simpevarp area and to incorporate a new geological model of the deformation zones produced for Version S1.2.

Another difference with Version S1.1 is the increased effort invested in conditioning the hydrogeological property models to the fracture boremap and hydraulic data. A new methodology was developed for interpreting the discrete fracture network (DFN) by integrating the geological description of the DFN (GeoDFN) with the hydraulic test data from Posiva Flow-Log and Pipe-String System double-packer techniques to produce a conditioned Hydro-DFN model. This was done in a systematic way that addressed uncertainties associated with the assumptions made in interpreting the data, such as the relationship between fracture transmissivity and length. Consistent hydraulic data was only available for three boreholes, and therefore only relatively simplistic models were proposed as there isn't sufficient data to justify extrapolating the DFN away from the boreholes based on rock domain, for example.

Significantly, a far greater quantity of hydro-geochemical data was available for calibration in the Version S1.2 data freeze for Simpevarp. This was provided for boreholes KLX01, KLX02, KSH01A, KSH02, KSH03A, KAV01 and the KAS series of boreholes. Further, the data was provided in terms of interpreted mixing fractions for reference waters, stable isotope ratios in addition to the salinity data that had been supplied previously. This motivated a more widespread and comprehensive calibration of the groundwater flow models than was possible previously. However, data at elevations below –700 m was still sparse, and hence there remains uncertainty in interpreting and modelling the deep groundwaters.

The numerical modelling was performed by two separate modelling teams. The work presented in this report was conducted by The *CONNECTFLOW Team* involving modelling experts from Serco Assurance, Kemakta Konsult and Golder Associates.

The main conclusions from the groundwater modelling are:

- A new methodology has been developed for integrating the PFL and PSS hydraulic data with the geological fracture interpretation to produce a conditioned Hydro-DFN model and to quantify the uncertainties to various assumptions. This methodology uses flow simulations in DFN models to calibrate several alternative relationships between fracture transmissivity and length. This demonstrates it is possible to calibrate several possible models for fracture transmissivity, although the direct correlation between transmissivity and length is perhaps easier to match to the borehole flow data.
- The GeoDFN model as delivered had several ambiguities that were hard to understand and hence required additional work to reproduce a DFN model that reflected the fracture statistics seen in the boreholes. These include: the threshold for splitting the sub-vertical and sub-horizontal sets; how the borehole and outcrop data has been combined; the basis for choosing the length distribution, especially for the sub-horizontal set; whether the length distributions chosen are continuous with the HCD model; how the Terzaghi correction has been implemented for calculating corrected fracture intensities.
- Using the PSS data to further calibrate the Hydro-DFN model beyond just the PFL anomaly actually helped narrow some uncertainties. This is primarily because it has a lower detection limit, so it was possible to eliminate some possibilities such as there being many small conductive fractures with transmissivities around 10^{-9} m^2/s that may effect the background flow and transport properties such as flow-wetted surface. The additional calibration helped narrow the range of uncertainties in the both $P32_c$ for open connected fractures and the transmissivity distribution.
- Considering three alternative fracture length versus transmissivity relations gave: for a 100 m block the median $Log(K_{eff})$ is –8.2 for the correlated case, –8.9 for the uncorrelated case and –8.6 for the semi-correlated case. There is localised horizontal anisotropy of Khmax/Khmin about 2–3 within a block for all cases due to the discrete nature of the DFN. For the uncorrelated model there is no regional trend to the anisotropy. Whereas for the correlated and semi-correlated case there is a clear trend toward higher Khmax in the direction with strike about 90°–130°. This is consistent with the orientations of PFL flow anomalies seen in KSH01A and KSH02. These block-scale hydraulic conductivities based on calibration of a Hydro-DFN on hydraulic data were also found to be of the correct order of magnitude to predict hydro-geochemistry.
- The minimum domain size is about ~14 km (E-W) by 7 km (N-S) based simulation of the hydro-geochemistry in the boreholes for site areas. This is larger than model domain suggested by sensitivity analysis of groundwater pathways by the DarcyTools Team in the Version S1.1 modelling. It is thought this is due to the much greater emphasis of the sub-horizontal fracture set in the Version S1.2 Hydro-DFN giving rise to longer horizontal flow paths.

- Considering the necessary initial and boundary conditions: Glacial water was probably injected under high pressures down to about 700 m–1.5 km during early post-glacial period, and there was a large Glacial water composition in early freshwater in the Baltic Lake, Yoldia Sea and Ancylus Lake periods.
- Small, low confidence deformation zones have limited effect on regional-scale flows, but do affect hydro-geochemistry local to individual boreholes. This suggests one can use hydro-geochemistry to confirm extent and properties of individual zones locally.
- A large number of variant cases were considered, but all were based on the properties that had been calibrated on the boremap, hydraulic data and hydro-geochemistry data. As such it was generally found the model is not very sensitive to the changes considered. The distributions of the four reference waters and the vertical Darcy velocity are affected little in the different cases compared to the Base Case. The only cases that appeared sensitive were: a shallower initial profile for Brine; an uncorrelated transmissivity; and having a gradual reduction in hydraulic conductivity with depth. The seeming lack of sensitivity is partly a result of the conditioning of the models against both hydraulic and hydro-geochemical information that appears to give a range of parameter uncertainties that do not impact the regional flow results significantly.
- The use of data for tritium has the potential to help constrain and check a groundwater flow model. However, in order for the data to provide useful information, it is necessary to have a fair number of good quality measurements down a number of boreholes. The measurements need to have low detection levels, and small errors relative to the expected levels (of order a few TU). Care needs to be taken to ensure uncontaminated samples. Measurements need to be taken down to depths of as much as a kilometre or more, particularly in the vicinity of transmissive features. A sensitivity analysis on the flow-wetted surface suggests that a lower value of $a_r = 0.5$ m^2/m^3 may give an improved match than the value used in the Base Case (2.0 m^2/m^3).

A series of transport calculations were performed for each of the varaints considered to provide guidance for the Preliminary Safety Evaluation (PSE). Based on these results the following conclusions are drawn:

- The transport pathway studies suggest discharge areas are strongly linked to the HCD structures including the eastern end of ZSMEW007A in the centre of the local-scale area, ZSMEW004A in the south around the shore, and ZSMEW013A just north of Simpevarp. The F-quotient for most of the local-scale area is of order 10^6 yr/m, with lower values (10^4 to 10^5 yr/m) around the zone ZSMNE040A.
- The Simpevarp and Laxemar release areas show quite different statistics. The medians of both t_w and F are about one order of magnitude higher for the Simpevarp release area than for Laxemar release area. Correspondingly the median of q_c is about one order of magnitude lower in Simpevarp. This indicates the effects of differences in the local structural model (i.e. stochastic and deterministic fracture zones); and the positions relative to the regional hydrogeology with Laxemar being largely freshwater at 500 m depth, and Simpevarp having reduced flows due to the presence of salinity at 500 m depth.
- The variations in the performance measures between the variants considered is generally low, around 10%. This perhaps should not be a surprise since all the cases considered have been calibrated against the same hydraulic data in the case of the Hydro-DFN variants, and against the same hydro-geochemistry data in the case of regional flow and solute transport.

Important issues that should be addressed in future studies include:

- Performing more detailed DFN flow simulations of the PSS tests to consider the transient response and flow geometry more explicitly.
- Modelling the transport of the major ions explicitly rather than interpreted mixing fractions and calibrating these against the measured ion concentrations from the boreholes. This will quantify the uncertainties associated with calibrating the model against the raw hydro-geochemistry data as opposed to the interpreted M3 mixing fractions.
- Oxygen and hydrogen stable-isotope ratios have been considered in this study since they can reasonably be assumed to be conservative tracers, and hence are straightforward to model. One only needs to know their values in the reference waters and the mixing fractions of the reference waters at any point to predict their value at that point. Tritium is more complicated since it is non-conservative due to radioactive decay. However, the decay has been accounted for in this study to allow the "Bomb-test" tritium pulse to be used as tracer. Carbon-14 could also be considered as additional tracer as it may indicate flows on different time-scales, although radioactive decay and rock interactions would have to be represented.
- A number of issues relating to the HCD model are outstanding. Firstly, the geometric properties (dips and thickness), and hydraulic properties (transmissivities) should be sampled stochastically. Secondly, there should be a more consistent spatial distribution of DZs to avoid the problem of having more DZs in the site area simply because of higher detection confidence. Away from the site area, stochastic DZs should be generated to supplement the regional HCD model.
- Simulations with a flux based boundary condition should be used to calibrate the near surface hydrology and quantify the uncertainty to the top surface flow boundary condition. This is non-trivial for a transient situation with land-rise and marine transgressions on the regional-scale since the areas of recharge and discharge will evolve.

This study has suggested some issues on which to focus further acquisition of site data:

- The PSS data helped reduce uncertainty in the intensity of flowing features and the low end of the transmissivity distribution. This may be particularly useful for understanding flows on the canister-scale in safety assessment calculations.
- The hydro-geochemistry data in the Simpevarp sub-area shows indicates each reference water type is present above 600–700 m elevation, and hence this depth of data samples is probably adequate in the near coastal area. However, in the Laxemar sub-area the mixing zone is deeper and probably requires data down to 1 km to capture the reference water mixing and hence aid the calibration of groundwater models.
- The models of the reference water transport suggest some pockets of Glacial inland and Marine near the coast. This motivates an integration of the borehole location selection and the groundwater modelling to confirm some of model predictions.
- The groundwater model calibration has suggested that groundwater chemistry in the fracture system should be similar to that in the matrix. This is useful information since it suggests groundwater infiltrates a network of small but connected fractures that give access to significant matrix diffusion, and hence potential retardation of radionuclides in the host rock. Experiments would be useful to verify this finding.

Contents

1 Introduction

1.1 Background

The Swedish Nuclear Fuel and Waste Management Company (SKB) carries out site investigations in two different candidate areas in Sweden with the objective of describing the in situ conditions for a bedrock repository for spent nuclear fuel. The two candidate areas are named Forsmark and Simpevarp. The site characterisation work is divided into two phases, an initial site investigation phase (IPLU) and a complete site investigation phase (KPLU) /1/. The results of IPLU are used as a basis for deciding on a subsequent KPLU phase. On the basis of the KPLU investigations a decision is made as to whether detailed characterisation will be performed (including sinking of a shaft).

An integrated component in the site characterisation work is the development of site descriptive models. These comprise basic models in three dimensions with an accompanying text description. Central in the modelling work is the geological model which provides the geometrical context in terms of a model of deformation zones and the rock mass between the zones. Using the geological and geometrical description models as a basis, descriptive models for other geo-disciplines (hydrogeology, hydro-geochemistry, rock mechanics, thermal properties and transport properties) will be developed /2/. In addition, a description is provided of the surface ecological system, the latter which partly constitutes the interface between the geosphere and the biosphere. Great care is taken to arrive at a general consistency in the description of the various models and assessment of uncertainty and possible needs of alternative models /3/.

A numerical model is developed on a regional-scale (hundreds of square kilometres) to understand the zone of influence for groundwater flow that effects the Simpevarp area. Transport calculations are then performed by particle tracking from a local-scale release area (tens of square kilometres) to identify potential discharge areas for the site. The transport from the two site-scale release areas (a few square kilometres) at the Simpevarp site and the Laxemar site are also considered more specifically and using greater grid resolution.

Descriptive model versions are produced at specified times which are adapted to the needs of the primary users, i.e. repository design and safety assessment. These specified times define a “data freeze” which singles out the database which should inform the model version in question. The results of the descriptive modelling also serve to produce feedback to, and setting the priorities for the ongoing site characterisation.

1.2 Scope and objectives

The main objective of this study is to support the development of a preliminary Site Description of the Simpevarp area on a regional-scale based on the available data of August 2004 (Data Freeze S1.2) and the previous Site Description /4/.

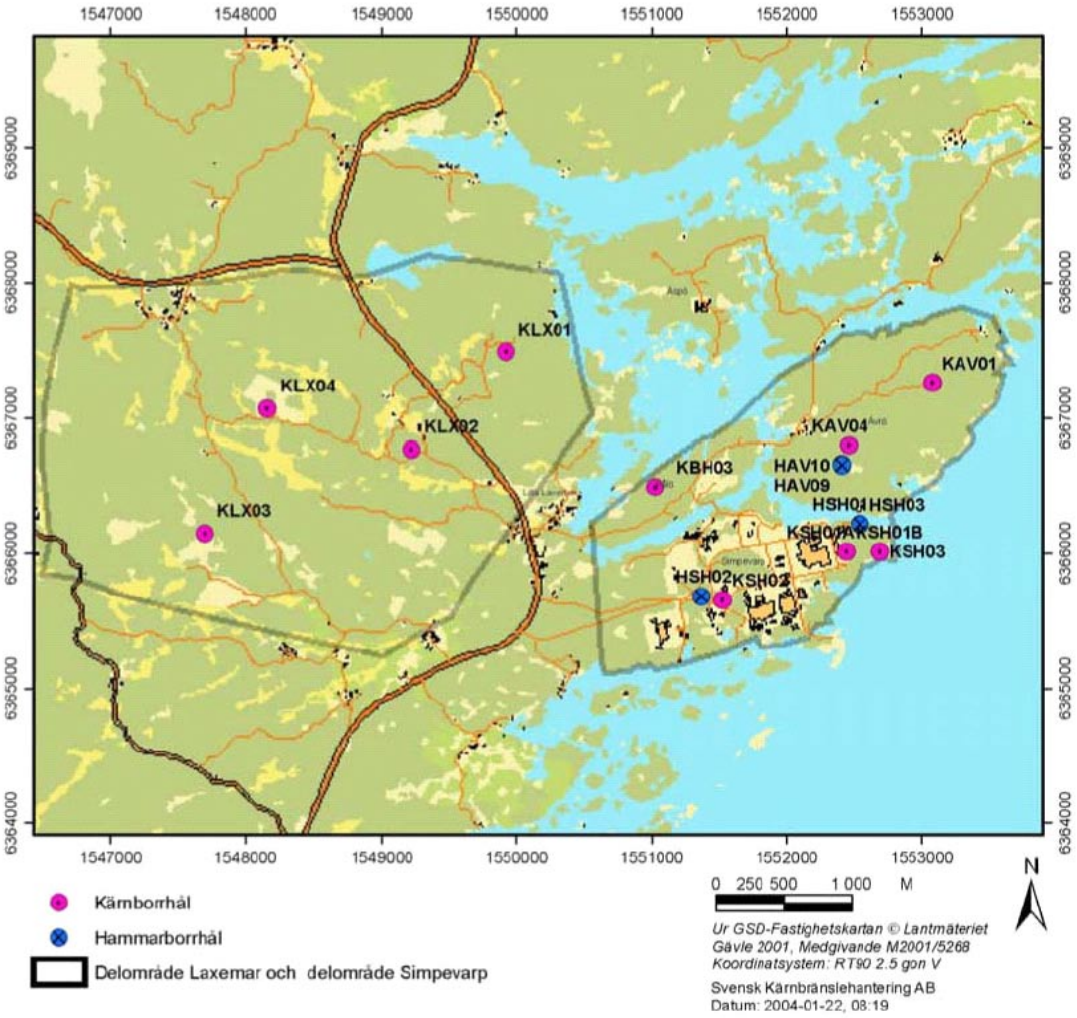

Figure 1-1. *The Simpevarp investigation area (within the grey boundary centre-right), and the Laxemar area (within the grey boundary centre-left). The positions of cored and percussions boreholes is shown although not all these are included in the S1.2 data freeze.*

A more specific objective of this study is to assess the role of known and unknown hydrogeological conditions for the present-day distribution of saline groundwater in the Simpevarp area on a regional-scale. An improved understanding of the paleo-hydrogeology is necessary in order to gain credibility for the Site Description in general and the hydrogeological description in particular. This is to serve as a basis for describing the present hydrogeological conditions on a local-scale as well as predictions of future hydrogeological conditions.

1.3 Setting and limitations

One key objective was to identify the model domain required to simulate regional flow and solute transport at the Simpevarp area. The starting point for identifying this area was the region used in the Version S1.1 modelling, the dimensions of which are 21 km , 13 km and 2.3 km in the Easting (x), Northing (y), and Elevation (z) directions. A new geological model of the deformation zones was produced for Version S1.2, and this was included along with newly interpreted hydraulic properties in this study. The dimensions of the local-scale release area for transport calculations was a model domain 7.8 km and 3.2 km in the x,y-directions.

Significantly, a far greater quantity of hydro-geochemical data was available for calibration in the Version S1.2 data freeze for Simpevarp. This was provided for boreholes KLX01, KLX02, KSH01A, KSH02, KSH03A, KAV01 and the KAS series of boreholes. Further, the data was provided in terms of interpreted mixing fractions for reference waters, stable isotope ratios in addition to the salinity data that had been supplied previously. This motivated a more widespread and comprehensive calibration of the groundwater flow models than was possible previously. However, data at elevations below –700 m was still sparse, and hence there remains uncertainty in interpreting and modelling the deep groundwaters.

Another difference with Version S1.1 is the increased effort invested in conditioning the hydrogeological property models to the fracture boremap and hydraulic data. A new methodology was developed for interpreting the discrete fracture network (DFN) by integrating the geological description of the DFN (GeoDFN) with the hydraulic test data from Posiva Flow-Log and Pipe-String System double-packer techniques to produce a conditioned Hydro-DFN model. This was done in a systematic way that addressed uncertainties associated with the assumptions made in interpreting the data, such as the relationship between fracture transmissivity and length. Consistent hydraulic data was only available for three boreholes, and therefore only relatively simplistic models were proposed as there isn't sufficient data to justify extrapolating the DFN away from the boreholes based on rock domain, for example.

1.4 Organisation of work and layout of report

The numerical modelling was performed by two separate modelling teams. The work presented in this report was conducted by The *CONNECTFLOW Team* involving modelling experts from Serco Assurance, Kemakta Konsult and Golder Associates. The CONNECTFLOW code is developed by Serco Assurance /5, 6 and 7/.

This report presents the development of a HydroDFN for Simpevarp, simulations of regional-scale variable-density groundwater flow, and transport calculations. Many variants were considered for the regional-scale groundwater flow to investigate the influence of conceptual and parameter uncertainties relating to initial and boundary conditions, DFN data interpretation, and background rock properties including some of the properties known to affect the rock matrix diffusion. Section 2 presents the overall modelling methodology, the model specifications and the deliverables on groundwater flow and particle tracking. Section 3 describes the methodology for deriving the Hydro-DFN parameters and its application to Simpevarp. In Section 4 these parameters are used to study block-scale hydraulic properties required by Design and the regional-scale modelling. Section 5 gives more specific information on the overall approach to modelling groundwater flow at Simpevarp and the various assumptions and uncertainties. The methods and data available for calibrating the regional flow models are detailed in Section 6. Section 7 presents the results for the calibration of the regional flow model and variants against the hydro-geochemistry and hydraulic data in boreholes. The results for the simulations of reference waters at the present-day are illustrated in Section 8. Further results for the groundwater flow patterns, discharge areas and reference water distributions for each variant considered is included in Section 9. Finally, Section 10 concludes the study.

A glossary of abbreviations used in the report is included in Appendix A. A series of transport calculations for particles released in the local-scale and site-scale release areas were performed for each of the variants considered to provide guidance for the Preliminary Safety Evaluation (PSE) and are presented in Appendix B.

2 Model setup and specifications

2.1 Modelling methodology

Sections 2.1.1 to 2.1.6 describe the main concepts and assumptions used in the Simpevarp 1.2 modelling study.

2.1.1 DFN model representation

The Discrete Fracture Network (DFN) concept assumes flow though a fractured rock is predominantly through an inter-connected network of flow conductive fractures with groundwater moving from one fracture to another at the intersections between them. The properties of the network are usually characterized in terms of:

- Spatial distribution (e.g. Poisson, fractal, clustered around points or lineaments).
- Fracture intensity (and it's spatial variation).
- Number of fracture orientation sets.

The properties of individual fractures are primarily:

- Either deterministic or stochastic.
- Length.
- Orientation (Strike and dip).
- Transmissivity (and possibly spatial variability within the plane).
- Transport aperture.
- Storativity.

In CONNECTFLOW fractures are rectangular, or may be right-angle triangles where a complex surface has been triangulated into many pieces. For stochastic fractures the properties are sampled from probability distribution functions (PDF) specified for each fracture set. The properties may be sampled independently or correlated.

The purposes of the Hydro-DFN modelling exercise were:

- Checking the fracture distributions in the boreholes based on the GeoDFN.
- Deriving transmissivity distributions to match the observed flows in the Posiva Flow-Log (PFL) and Pipe-String System (PSS) data.
- Deriving the statistical distributions of Equivalent Porous Medium (EPM) properties on specified block scales for addressing designs issues using flux-based upscaling.
- Creating realisations of the regional-scale EPM model based on upscaling regional-scale DFN models.

The DFN concept is very useful since it naturally reflects the individual flow conduits in fractured rock, and the available field data. However, to understand flow and transport on the regional-scale it is often necessary to consider larger scale bulk properties in the context of an EPM continuum concept. This requires methods to convert a network of discrete fractures of lengths less than the continuum blocks, known as upscaling, and to

represent larger scale features such as fracture zones by appropriate properties in a series of continuum blocks, i.e. a downscaling method. The implementation of upscaling and downscaling in CONNECTFLOW is described in sections 2.1.2 and 2.1.3, respectively.

2.1.2 Fracture representation as equivalent EPM flow properties

In order to assess the implications of the DFN model on flow and transport on the regional-scale it is often necessary for practical reasons to convert the DFN model to an EPM model with appropriate properties. The result is a directional hydraulic conductivity tensor, fracture porosity (and other transport properties such as the fracture surface area per unit volume). In CONNECTFLOW a flux-based upscaling method is used that requires several flow calculations through a DFN model in different directions.

Figure 2-1 shows an illustration of how flow is calculated in a DFN model (A 2D network is shown for simplicity). To calculate equivalent hydraulic conductivity for the block shown, the flux through the network is calculated for a linear head gradient in each of the axial directions. Due to the variety of connections across the network, several flow paths are possible, and may result in cross-flows non-parallel to the head gradient. Cross-flows

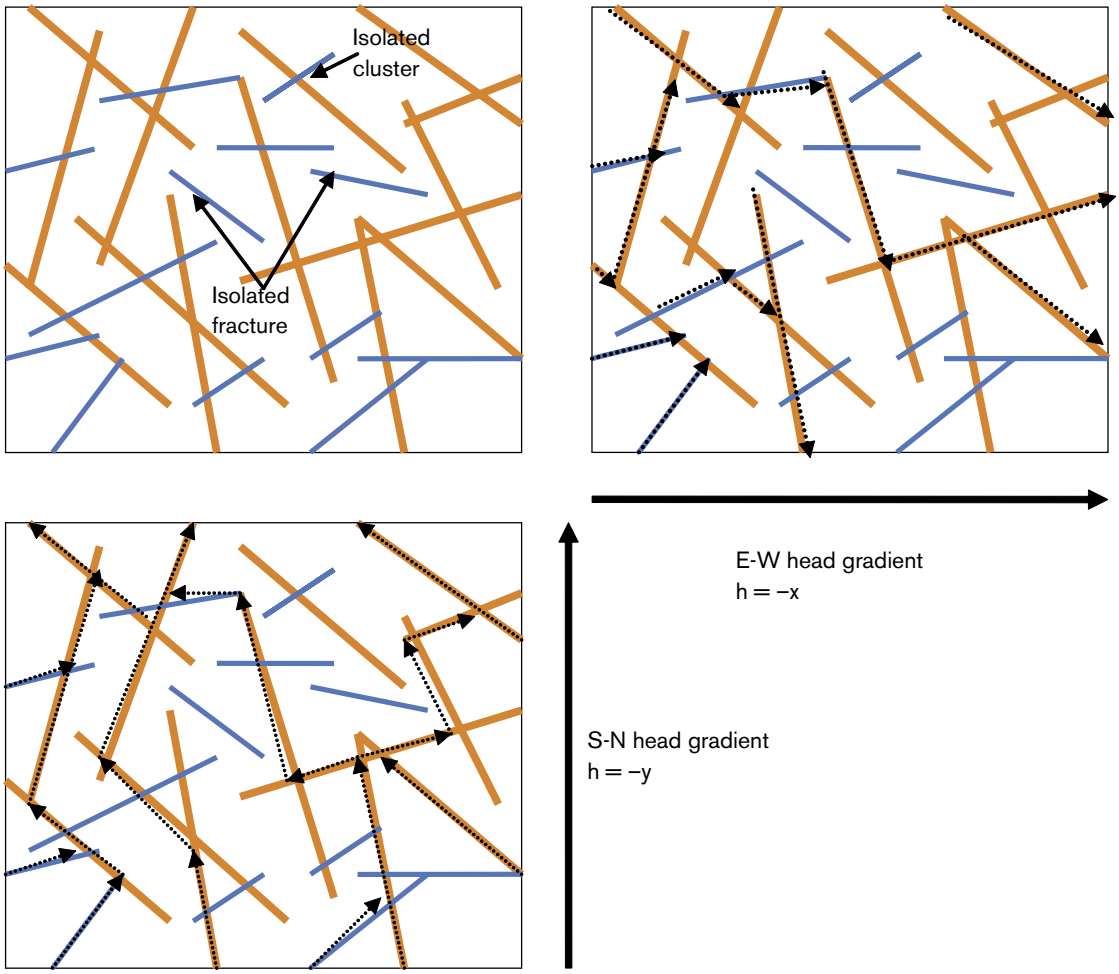

Figure 2-1. *2D illustration of flow through a network of fractures. A random network of fractures with variable length and transmissivity is shown top left (orange fractures are large transmissivity, blue are low). Top right: flow paths for a linear head gradient E-W decreasing along the x-axis. Bottom left: flow paths through the network for a linear head gradient S-N decreasing along the y-axis.*

are a common characteristic of DFN models and can be approximated in an EPM by an anisotropic hydraulic conductivity. In 3D, CONNECTFLOW uses a six component symmetric hydraulic conductivity tensor. Using the DFN flow simulations, the fluxes through each face of the block are calculated for each head gradient direction. The hydraulic conductivity tensor is then derived by a least-squares fit to these flux responses for the fixed head gradients. Other authors /8/ have only considered the components of the equivalent hydraulic conductivity parallel to the coordinate axes using a head difference between opposite faces and no-flow on the other faces. This leads to a very poor representation of blocks in which the network connections, and hence flow, are mostly between adjacent faces rather than between opposite faces. The effective permeability assigned to such blocks may be essentially zero, even though the flow paths through the block may contribute significantly to the overall flow through the network.

In the 3D, the blocks have to be hexahedra (cuboids), but the upscaling method can be applied to an array of sub-blocks within a much larger DFN domain by performing the upscaling on each sub-block in sequence. The upscaling method is typically used in one of two ways:

1. To obtain the statistical distribution of hydraulic conductivity on a given block scale a DFN model is generated for a much larger domain, and then EPM properties are calculated for an array of sub-blocks of equal size and shape to give an ensemble of properties.
2. To obtain an EPM model for local- or regional-scale grid a DFN model is generated within the grid domain, and the upscaling is performed within each grid element to derive the EPM properties element by element.

A detailed description of the upscaling method to calculate the EPM hydraulic conductivity tensor is given in /9/. Briefly, the method can be summarised by the following steps:

- Define a sub-block within a DFN model.
- Identify the fractures that are either inside or cut the block.
- Calculate the connections between these fractures and their connection to the faces of the block.
- Specify a linear head gradient parallel to each coordinate axis on all the faces of the block.
- Calculate the flow through the network and the flux through each face of the block and for each axial head gradient.
- Fit a symmetric anisotropic hydraulic conductivity tensor that best fits (least-squares) the flux response of the network.
- Fracture porosity is calculated as the sum (over all fractures that are connected on the scale of the block) of fracture area within the block multiplied by the transport aperture of the fracture.

Hence, to calculate the EPM properties for a finite-element grid with 1 million elements, say, involves 3 times 1 million DFN flow calculations. One important aspect of this approach is the properties are calculated on a particular scale, that of the blocks, and that a connectivity analysis of the network is performed only on the scale of the block. Bulk flows across many blocks will depend on the correlation and variability of properties between blocks.

One refinement of the upscaling methodology is to simulate flow through a slightly larger domain than the block size require for the EPM properties, but then calculate the flux responses through the correct block size. The reason is to avoid over-prediction of hydraulic conductivity from flows through fractures that just clip the corner of the block that are unrepresentative of flows through the fracture network in-situ. This is illustrated in Figure 2-2. The area around the block is known as a 'guard-zone', and an appropriate choice for its thickness is about half a fracture length. The problem is most significant in sparse heterogeneous networks such that the flux through the network of fractures is affected by 'bottlenecks' through low transmissivity fractures, and quite different flux through single fractures.

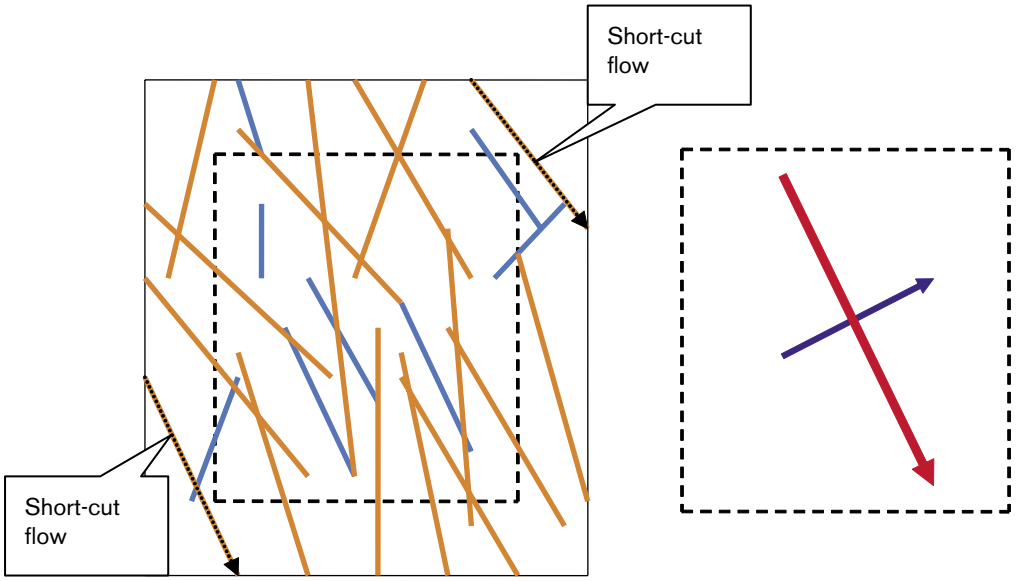

Figure 2-2. *2D sketch of how block-scale hydraulic conductivity can be over-estimated using a linear head gradient by high transmissivity fractures that cut across a corner of the block. By simulating flow through a larger domain, but only calculating the flux through the required block size (dashed block) then fluxes more consistent with flow through a network in-situ are obtained. The EPM hydraulic conductivities are then calculated for the dashed block to give principal components (right). The red arrow is the maximum component, blue is minimum.*

2.1.3 Implicit representation of fracture zones (the 'IFZ' method)

For Simpevarp 1.2 the basic concept is that fractures exist on a continuous range of length scales which motivates a methodology to generate sub-lineament scale fractures stochastically on scales between tens of metres and about 1 km , and then combine this DFN by superposition with the larger scale deterministic deformation zones. In CONNECTFLOW the approach taken was to create one or more realisation of the stochastic network on the regional-scale and then using the upscaling methods described above to convert this to a realisation of the EPM model, minus the deformation zones. That is, at this point the EPM model is only an equivalent representation of the stochastic network. The EPM model was then modified to incorporate the structural model in terms of the geometry and properties of a set of large-scale deformation zones using the Implicit Fracture Zone (IFZ) method in CONNECTFLOW as described in /10/. The reason for this approach was that it was then relatively quick to combine different scenarios for the deformation zones with the stochastic DFN model without having to repeat the computationally expensive upscaling step.

The IFZ downscaling method identifies which elements are crossed by a fracture zone and combines a hydraulic conductivity tensor associated with the fracture zone with a hydraulic conductivity tensor for the background fractured rock. For each element crossed by the fracture zone the following steps are performed:

- The volume of intersection between the fracture zone and the element is determined.
- The effective hydraulic conductivity tensor that includes the effect of the fracture zone is determined in the coordinate system aligned with the fracture zone.
- The effective hydraulic conductivity tensor is transform to the original coordinate system.

The methodology is sketched in Figure 2-3. In 3D, the resultant hydraulic conductivity is a 6 component symmetric tensor in the Cartesian coordinate system. The tensor can be diaganolised to give the principal components and directions of anisotropy.

Similarly, a combined scalar block-sale porosity is calculated for the element based on combining the fracture zone porosity and the background block-sale porosity using a weighting either based simply on either the relative volume or on relative transmissibility (total channel flow capacity, transmissivity times flow length (m3/s)). The latter weighting can be suitable for transport since it weights the combined porosity toward the fracture zone porosity if this is of a relatively high hydraulic conductivity. The result of this step is to produce a spatial distribution of CPM element properties (hydraulic conductivity tensor and porosity) that represent the combined influence of both the deterministic fractures zones and background stochastic fractures.

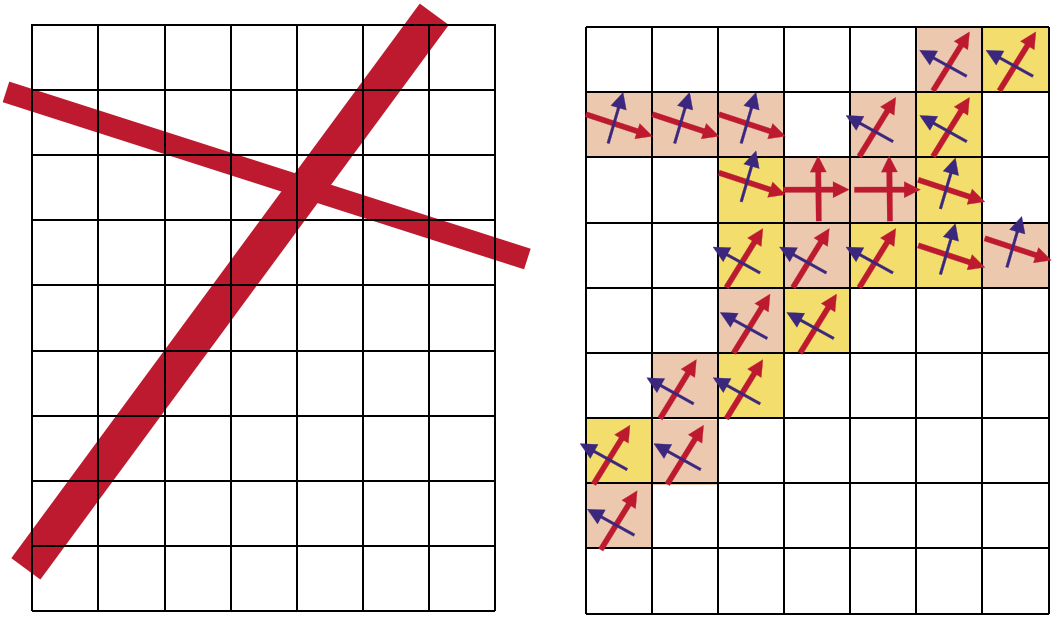

Figure 2-3. *Schematic illustration of the modification of the hydraulic conductivity tensor by the IFZ method. A finite-element grid crossed obliquely by two fracture zones of different thickness (left). The effect on the equivalent porous medium hydraulic conductivity (right). Elements with a large IFZ effect are coloured pink. Ones with a lesser effect where the fracture zone only cross one corner are coloured orange. The principal directions of the resultant anisotropic hydraulic conductivity tensor are shown by arrows (red for major component, blue for minor).*

2.1.4 Variable density groundwater flow and salt transport

An option has been added to CONNECTFLOW in time for the Version S1.2 modelling to model flow in a porous medium for groundwater of variable salinity, where the salinity arises from a number of groundwater constituents. This can be modelled either in terms of transport of mass fractions of the basic groundwater constituents (such as chloride, sodium, oxygen isotope ratio), which are taken to be conservative, or in terms of transport of fractions of selected reference waters (end-member waters). The transport equations are coupled with the overall mass conservation equation for groundwater.

The option for transport of reference water fractions is of more practical use since the boundary conditions for the flow modelling are most naturally expressed in the terms of the reference waters. The option also provides a very user-friendly way of presenting the results of multi-component groundwater flow calculations, which are given directly in terms of the selected reference waters. The results can also be post-processed to provide the concentrations of the basic groundwater constituents for direct comparison with measurements of groundwater chemistry. This option has been used in the EPM regional-scale model. A simplified representation in terms of four reference waters (Rain 1960, Marine, Glacial, and Brine) was used (see Section 5.3)

Transport of fractions of reference waters can be modelled using the same equations used to model transport of groundwater constituents (the various ionic species, oxygen and hydrogen isotope ratios) provided that it is assumed that the constituents have the same dispersion, matrix diffusion and sorption properties. This may be a good approximation for dispersion, which may be largely determined by the variations in groundwater velocity within and between pores. However, the self-diffusion coefficients for the various constituents differ by about a factor of about two, and so the effective (or intrinsic) diffusion coefficients would be expected to differ by a similar extent, or even more, if anion exclusion is significant. If differences of this order are considered important, then the standard transport equations can only be used to model the transport of constituents. For this work it has been assumed that these factor differences in diffusion rates are relatively unimportant, and hence we can work in terms of mixing fractions.

However, the following point should be noted. Because of the linearity of the transport equations (in the assumed absence of reactions), linear combinations of the constituents also satisfy transport equations. Transport equations for the fractions of reference waters can still be written down, therefore, even if the diffusion coefficients for the different constituents are different. However, the key point is that each equation no longer involves only a single reference water, but the equations are coupled. In this case, it would probably be best to carry out the transport calculations in terms of constituents, translating between reference waters and constituents before and after the calculations if necessary.

It should also be noted that if the constituents have different transport properties, it is also necessary to account for the constraint of electro-neutrality.

It is also possible to model diffusion of the reference waters, or constituents, between groundwater flowing in fractures and immobile water in the rock matrix between in the fractures (rock-matrix diffusion or RMD). The numerical approach used /11/ is based on a method developed by Carrera et al. /12/ enhanced to enable potentially larger time-steps to be taken. The approach combines an approximation that is accurate for small times with one that is accurate for long times to give a representation of the diffusion into the rock matrix that is accurate for all times. At early times, the diffusion represented in terms of the inverse of the square root of time, and at long times it is represented as a series of decaying exponentials. The approach is very efficient computationally, although it is necessary to make the assumption that the groundwater density does not vary in the rock matrix at each location.

2.1.5 Boundary condition concepts

Simulating the Paleo-hydrogeology for Simpevarp 1.2 requires modelling of the evolution of groundwater flow and solute transport during the post-glacial period up to the present day. A key issue in this exercise is how to represent the time-varying boundary conditions for both flow and solutes or reference waters.

For flow, there are two main possibilities onshore: either specified head, or a flux type boundary condition. For specified head, the model is assumed to be fully saturated, and hence head is equal to the height of the topographic surface at that time according to the sea-level transgression. Offshore it is most natural to use a specified head type boundary condition. Here, the head is equal to the depth of the sea multiplied by the relative salinity of the Baltic Sea, and both the salinity of the Baltic and sea depth alter in time.

Specified head boundary conditions are straightforward to implement numerically by setting the value at nodes on the surface to the required head at each time-step. For the flux type boundary condition is more complicated because in reality the flux through the top surface will vary spatially both in magnitude and direction since in some areas groundwater is recharging and other it is discharging. This distribution of flux varies according to the amount of potential infiltration and the hydraulic properties it is also going to change in time as the shoreline retreats. The approach taken in CONNECTFLOW is to define the recharge flux, R, into or out of the model as a function of the current head, h, in the model, the topographic surface height, z, and the potential infiltration, I. Appropriate functions for the flux, R, must have certain characteristics. For recharge areas the head, or watertable, is below groundsurface and so the recharge must be equal to the full infiltration, I. In discharge areas, the watertable is just above groundsurface so head is just above groundsurface, which can be achieved by having a taking a suitably large flux out of the model, i.e. negative value of R, whenever the head goes above groundsurface. The standard function used in CONNECTFLOW is:

$$R = \begin{cases} I & h \le z - \varepsilon \\ -I(h-z)/\varepsilon & h > z - \varepsilon \end{cases},$$

where ε is a small number. This function implies that if the water table is more than ε below the topographic surface then recharge equals the full potential infiltration. Above that, the recharge reduces until the water table is at the surface. If the water table is above the topographic surface, then recharge becomes negative, i.e. discharge, and an appropriate flux of groundwater is taken from the model to reduce the head until the water table is restored to the topographic height. Hence, this boundary condition is a non-linear equation (the flux depends on the free-variable head) that ensures a specified flux if the water table is low and a specified head where the water table is at or above ground surface. The non-linearity requires that multiple iterations of the groundwater flow equations be performed at each time-step to reach convergence which implies longer run times for this boundary condition. The topographic surface is not constant in time due to post-glacial rebound and marine transgressions, and hence z = z(t). Newton-Raphson iteration was used to achieve convergence of the the non-linear equations at each time-step. This technique works best for systems with smooth gradients. The standard function given above for flux has a discontinuous derivative at h = z–ε and this led to a slow rate of convergence; typically 3–5 Newton-Raphson iterations were required at each timestep. Hence, an alternative smooth function for recharge was tried:

$$R = I \times \left(\exp\left(\frac{h-z}{0.5} \right) - 1 \right).$$

This has similar characteristics to the standard function, but has smooth derivatives around h = z. It was found to always converge in 2 Newton-Raphson iterations for the time-step used, and hence gave quicker and more robust solutions. There are other candidates for this function such as a modification to the standard function but using a hyperbola to give a smooth transition around h = z.

For solutes, the boundary conditions are generally a specified value where there is an advective flow into the model (recharge area), or an outflow condition where there is flow out (discharge). Because the flows are transient, the areas of recharge and discharge evolve in time, and hence it is important to have an automatic way of determining the recharge and discharge areas automatically. The problems in achieving this are that it requires mixing a Neumann, or flux, type boundary on outflow with a Dirichlet, or value, type boundary condition on inflow; and since the recharge/discharge areas change in time, then the type of boundary condition has be changed in time. Hence, we use a trick to specify a flux of solute over the top surface that changes depending on the direction of low across the model boundary with the Dirichlet condition on inflow being achieved as a penalty weight function of the difference between solute concentration in the model and the required input concentration. The flux of solute out of the model, F_c, is then given by the equation:

$$F_c = \begin{cases} (q \cdot n)c & q \cdot n \geq 0 \\ (c - c_0)/\delta & q \cdot n < 0 \end{cases},$$

where q·n is the advective flux out of the model, i.e. the groundwater flow, q, in the direction parallel to the outward normal to the surface, n, c is the solute concentration or mixing fraction, and δ is a small number. For $q \cdot n \geq 0$ the flux corresponds an outflow condition, for $q \cdot n < 0$ a specified value condition, $c = c_0$, is implemented as a penalty function such that solute is removed if $c > c_0$, and injected if $c < c_0$ this effectively ensures that $c \approx c_0$.

2.1.6 Transport performance measures: canister flux (q), travel time (t_w), Pathlength (L), and F-quotient (F)

One objective of the site descriptive modelling is to understand groundwater pathways from local-scale area to the surface. The approach taken is track particles moving with the advective flow velocity from a range of release points until they reach the top surface. Although it would be possible in CONNECTFLOW to track particles as they move through a velocity field that evolves in time, it is preferred here to only use the velocity field from the present day. This is mainly because particle tracks released in a transient velocity field would be sensitive to the release time and the kinematic porosity, making it more difficult to interpret the results due to the added uncertainties. One uncertainty that is important to address here is the effect of the stochastic DFN on regional-scale pathways. Hence, several realizations of the DFN model, and hence the EPM model, will be considered here to quantify the sensitivity of transport performance measures to particular realizations. The four performance measures required are:

- Travel time, $t_w = \sum_l \frac{\phi \delta l}{q}$, where δl is a step in distance along the path, for example through one finite-element, φ is the kinematic porosity, and q the Darcy velocity.
- Canister flux, $q = q_0$, the initial Darcy velocity at the release point.
- Pathlength, $L = \sum_l \delta l$.
- F-quotient, $F = \sum_l \frac{a_r \delta l}{q}$, where a_r is the fracture surface area per unit volume.

The approach to calculating the performance measures is to release a large number of particles distributed evenly, fixed spacing, over the local-scale area and use these to produce ensemble statistics for the performance measures, as well as locating the discharge areas. No attempt is made to avoid starting particles in either deterministic fracture zones or high transmissivity stochastic fractures in order to get the full range of possible values.

3 Assessment of hydraulic DFN model

The current site characterisation of Simpevarp, S1.2, has provided a GeoDFN model of fracture geometrical data (orientation and intensities) based on outcrop and borehole data. However, for the hydrogeological modelling it is necessary to integrate the hydraulic data, principally the Posiva flow log (PFL) data, but also the double packer injection test data, known as Pipe-String System (PSS) data. In doing so it may be necessary to make some practical simplifications to derive a complete Hydro-DFN fit for modelling. Having derived a Hydro-DFN, block-scale properties on a 100 m and 20 m scale are required for regional groundwater flow (GWF) property assignment, and also for repository design issues.

Task descriptions POM_1–2_HydroDFN_1.0.doc and POM_1–2_Block_K_v1.0.doc have been issued to specify these tasks. The work reported here on the Hydro DFN includes:

- Simulating the DFN model(s) based on delivery by Geology (GeoDFN) and testing different relationships between transmissivity models, fracture (feature) size and fracture (feature) intensities. Then comparing with borehole fracture statistics and hydraulic data from borehole tests and evaluating the transmissivies and comparing with measured transmissivities (Posiva Flow Log (PFL) primarily, but preferably to PSS data as well). This was achieved by performing flow simulations based on drawdowns during PFL measurements and comparison to flow distribution during PFL measurements.
- For each borehole (KSH01, KSH02, KSH03, KAV01, KLX02), the fracture analysis and DFN parameterisation based on core logs is summarised. In the case of KSH01A, KSH02 and KAV01, DFN simulations of the Posiva Flow Log (PFL) tests were carried out for various transmissivity models to compare modelled flow-rates with the flow anomalies. The flow simulations considered alternative transmissivity models and are used to identify parameter ranges that can reproduce the observed flows.
- Based on a collation of the information from the group of Simpevarp boreholes, recommendations are made for the DFN definition to be applied in the regional and site-scale groundwater flow (GWF) modelling.
- A further check on the Hydro-DFN definition is performed based on the double packer injection test (PSS) data for KSH01A and KSH02 to try to reduce uncertainties in the model parameterisation.
- As an alternative model, a set of parameters are derived based solely on the packer-test data for KLX01.

The work reported here on the block properties in the Simpevarp sub-area includes:

- Estimate anisotropy in horizontal and vertical directions.
- Calculate the statistics of the hydraulic conductivity of 100 m and 20 m blocks for Sub-area Simpevarp.
- Evaluate effects of size-truncation of stochastic features and cell-background properties for the forthcoming Regional Scale GWF modelling.
- Calculate fracture porosity based on aperture = function(Transmissivity) relationship from Äspö Task Force 6c /15/.
- Calculate the block properties for an alternative Hydro-DFN model based on KLX01.
- Compare block properties derived from by the DT Team and the CF Team to quantify uncertainties.

3.1 Methodology

A methodology was developed and tested during the Pre-S1.2 modelling exercises based on borehole KSH01A /13/. The methodology has been further refined in the S1.2 using the available data. The current workflow used in S1.2 can be summarised by the following steps:

1. Group fractures using the borehole core log according to inside or outside of deformation zones (DZ), and into rock domains for fractures outside of a DZ.
2. Generate stereonets for each deformation zone that are Terzaghi corrected for borehole and fracture orientation. Identify major orientation set/sets (focus on brittle deformation zones). Calculate fracture intensity in each zone.
3. Within a borehole compare the mean poles of dominant fracture sets within each deformation zone, and fracture intensity.
4. Calculate P10, P10corrected (and range of values according to confidence indicator /certain/probable/possible/) for rock domains outside of DZs, and identify orientation sets. Use GeoDFN classification as a guide to choosing sets. In the GeoDFN, the sets are split into two classes: three lineament related sets (EW-WNW, NW-NNW and NNE-NE), and four background related sets (BGNW, BGNE, BGNS and BGHZ). Use Terzaghi correction for borehole data to compare P10corrected with that obtained in GeoDFN.
5. Fit orientation statistics for sets in rock domains outside of DZs.
6. Derive modified GeoDFN set statistics (mean azimuth, mean dip, Fisher concentration, open P10corrected) for each of the 7 GeoDFN sets. Note: here fracture intensity is based on both confidence indicators ‘open’ and ‘partly-open’, although for simplicity, this is denoted as open P10corrected in this text.
7. Use length distribution from GeoDFN.
8. However, need to modify BGHZ to be a power-law length distribution. This is mainly to capture the deformation zones as stochastic sub-horizontal features of significant length (certainly > 10 m, and probably of the order of 100 m). Choose slope of power-law to be consistent with P10 for deformation zones as stochastic features > 100 m in length. Use $K_r = 2.6$ for sub-horizontal features, derived from the average over each of the GeoDFN sets when fitting a power-law to the lognormal length distributions defined in the GeoDFN.
9. Assume L_0 for the P10corrected model (either borehole diameter (76 mm) or outcrop min (0.5 m).
10. Generate five realisations of the DFN model around the borehole and check the modelled P10open in the borehole against that in the field-data. Adjust P10corrected if necessary. (Note: the actual number of open fractures is not known. We only have an estimated range based on the confidence indicator P10corrected, open/certain to P10corrected, open).
11. Cross check P21 distribution qualitatively with outcrop maps.
12. Define alternative transmissivity concepts (uncorrelated: log-normal, correlated: direct T vs L correlation, semi-correlated: correlated but with log-normal perturbation).
13. For each T concept, use DFN flow simulations to match the Qcorrected distribution from PFL (remember that Q is measured, not T; $Q_{corrected} = Q * \Delta h_{model}/\Delta h_{observed}$). Group Qs in deformation zones as a single Q value since conceptual it is a single feature. Parameters to be varied/considered are open P10corrected, and T distribution parameters.

14. For each T concept, identify possible ranges of parameters i.e. uncertainties.
15. Analyse PFL data for orientations of flow anomalies. Compare with regional stress.
16. Analyse fracture intensity for depth trend.
17. Analysis of PSS data fitting for flow.
18. For each T concept, calculate block-scale directional permeability.

The ambition of this modelling was to demonstrate one or more matches to the observations in the boreholes in a statistical sense based on distributions of quantities such as flow-rates rather than to reproduce very specific and perhaps localised characteristics seen in each borehole. The rationale behind this approach is that we are aiming to make conclusions that can applied over the whole Simpevarp sub-area and also for the regional-scale GWF models, and hence it is most important to understand the DFN characteristics in a broad sense and their uncertainties.

3.2 Modelling assumptions and input data

The available data that has been used in this study included:

- The borehole core logs that record all the fractures identified in the cores (and cross-checked with the BIPS borehole image logs) along with a comprehensive set of fracture classifications (KSH01A, KSH02, KSH03A, KAV01, KLX02);
- The PFL flow anomalies including the flow rates and head changes for each feature (KSH01A, KSH02 and KAV01).
- Rock domain data in boreholes including deformation zones for KSH01A; KSH02.
- The outcrop maps (ASM000025, ASM000026, ASM000205 and ASM000206).
- The preliminary GeoDFN fracture characterisation based on all outcrops and boreholes.
- Double packer injection test data for 5 m intervals in KSH01A and KSH02 and known as Pipe-String System (PSS) data.
- Double packer injection test data for 3 m intervals in KLX01 and analysed using either transient or steady-state flow assumptions.

The following assumptions have been made:

- L_0 for open fractures is either the borehole diameter (0.076 m) or minimum measured length in outcrop (~0.5 m).
- Deformation zones represent a swarm of fractures, but these are modelled and characterised as a single large stochastic feature.
- Fractures exist on all scales with stochastic fractures ranging in lengths from L_0 to 1 km.
- Fracture sets can be categorised based on orientation and length groupings (based on GeoDFN).
- Fracture dip $\geq 60°$ for sub-vertical sets. Fractures with dips $< 60°$ are assigned to the 'sub-horizontal' set.

3.3 Conceptual models with potential alternatives

Few characteristics of the DFN can be determined uniquely and directly, so it is necessary to assume a framework of conceptual models, and then derive parameters that best match observed data.

3.3.1 Continuous power-law length distribution

One of the most difficult fracture characteristics of fractures to measure directly in the sub-surface is fracture length. Fracture lengths can be measured on outcrops for fractures on the scale of metres to tens of metres, and data is available for lineaments on the scale of 500 m to several kilometres, but this leaves a gap between the scales. A widely used assumption is one of a continuous scale of fracturing that spans all scales in a continuous manner that can be described by a power-law relationship between fracture intensity and length. A schematic illustration of such a relationship is shown in Figure 3-1 and is compared with a lognormal distribution that is another commonly used model for fracture length. The key parameters for the power-law distribution are the slope and reference length L_0. The distribution is often defined only in a truncated range, $L_{min} < L < L_{max}$.

In the groundwater flow modelling for Simpevarp 1.2 it will be assumed that fracture of length greater than 1 km will be modelled deterministically having been detected as lineaments or fracture zones, while fractures less than 1,000 m length will have to be modelled stochastically based on the Hydro-DFN model developed here.

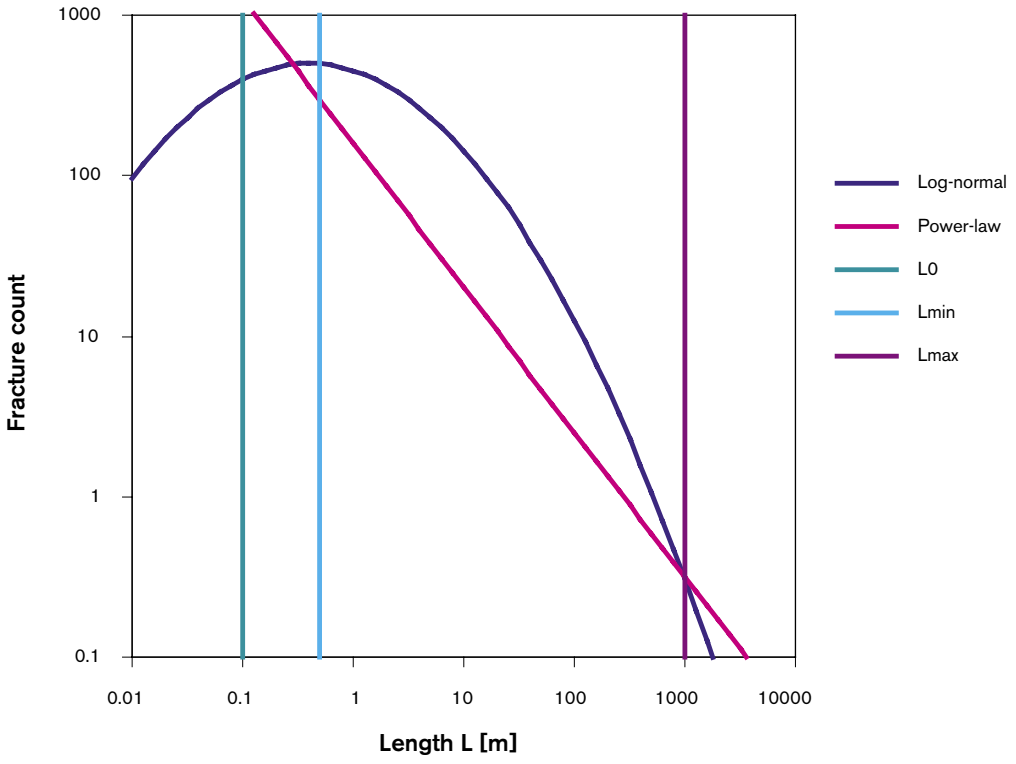

Figure 3-1. *Example of a power-law and lognormal model of fracture length distribution. Also shown is an example of the minimum length, L_0, which depends on the resolution of the fracture observation technique. When a fracture network is simulated it is often necessary for practical reasons to truncate the power-law distribution and these parameters will be referred to as Lmin and Lmax.*

3.3.2 Stochastic lineament swarms represented as planar features

Large fractures of lengths on the order of 100 m may exist as single breaks. However, it is more common that discontinuities of lengths greater than about 50 m exist as deformation zones or 'lineament swarms'. A number of deformation zones are observed in the boreholes, and hence it is useful to characterise these features to get some indication of the width and fracture intensities within these zones. However, at this stage deformation zones will be approximated as large stochastic fracture planes as a continuous range of fracture sizes as shown in Figure 3-2. It is important that data such as fracture intensity and the PFL flow anomalies are handled consistent with this concept. Also, transport parameters such as fracture porosity and flow-wetted surface may have to be enhanced in the larger fractures to reflect their zone characteristic.

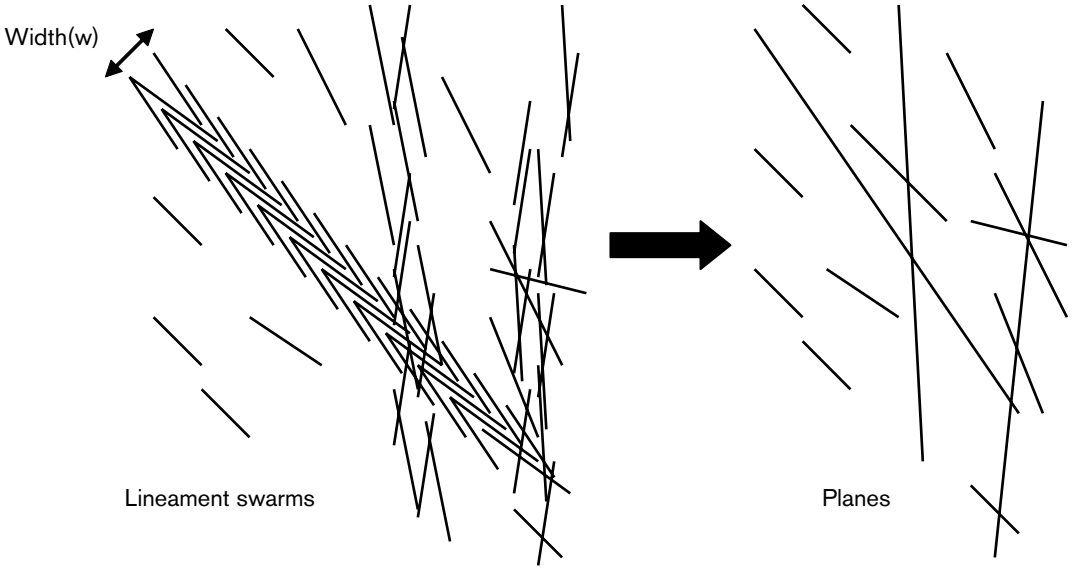

Figure 3-2. *Representation of lineament swarms as stochastic planar features using the power-law distribution.*

3.3.3 Fracture intensity and Terzaghi correction

The potential bias arising from observing fractures cutting boreholes of varying trajectory was removed by correcting for the orientation of fractures relative to the trajectory of the borehole in which they were observed. The sketch in Figure 3-3 illustrates the issue in an idealised case. For sub-vertical fractures, a vertical borehole will cut fractures at an average separation of s that is much larger than the true separation t. The ratio of $s/t = 1/\cos(\vartheta)$, where ϑ is the angle between the fracture pole and the borehole trajectory. For an inclined borehole near orthogonal to the fractures the angle is much smaller and so s/t is close to 1. However, for a horizontal borehole parallel to the fracture strike s/t would again be large. The implication is that care has to be used when combining fracture statistics e.g. fracture intensities or counts from boreholes of varying orientation. In this illustration P10 is 1/s, while $P10_{corrected}$ is 1/t. In reality, each fracture has a different orientation and the borehole trajectory may vary downhole. Hence, a correction $1/\cos(\vartheta)$ is calculated for every fracture and this correction is used as a weighting when calculating statistics such as mean fracture poles, $P10_{corrected}$, and when plotting density contours on stereonets. In addition, the orientation correction was used when calculating the percentage of fractures in each orientation set. Rather than just counting the number of fractures in each set, a weighted percentage was calculated by weighting each fracture by $1/\cos(\vartheta)$ (but using a maximum weight of 5 where ϑ is near to 90°.

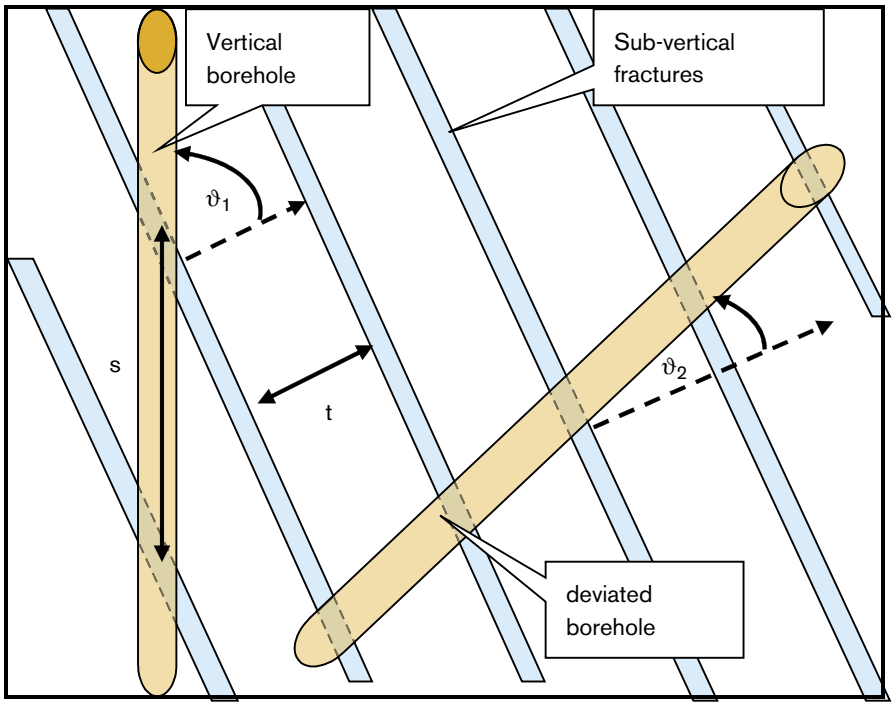

Figure 3-3. *Example of Terzaghi correction for different borehole orientations. The angles ϑ_1 and ϑ_2 are shown between the fracture pole (dotted arrow) and two different borehole orientations. The Terzaghi correction is proportional to 1/cos(ϑ).*

An alternative correction factor is proposed by Darcel et al. /14/ for the case where the fractures encountered in the borehole are dominated by small ones whose length is comparable to the borehole diameter. Based on power-law length model they propose a correction factor around $1/(\cos(\vartheta))^3$ for Simpevarp which emphasises the sub-vertical fractures more, and perhaps gives more consistency when comparing the relative intensity of fracture sets when measured in boreholes against outcrops.

3.3.4 Fracture transmissivity models

In the Version S1.1 modelling a direct correlation between fracture transmissivity and length was assumed. In order to illustrate the implications of this assumption, three alternative transmissivity concepts were considered (as shown in Figure 3-4):

1. Uncorrelated T versus L using a log-normal distribution (mean, μ, and spread, σ).
2. Directly correlated T versus L (factor, a, and exponent, b).
3. Semi-correlated T versus L: random log-normal spread about a mean based on a correlated function (factor, a, exponent, b, and spread, σ).

Each of these concepts has an associated set of parameters, as given in the brackets above, and it is the objective of Hydro-DFN to explore what ranges of parameters required in the DFN simulations to give a match to hydrogeological data.

The second relationship was proposed in /15/. One argument for it is that, at least for deformation zones, the zone width often increases with length, and thus generally the number of individual conductive fractures associated with zone. If the transmissivity distribution for individual fracture is the same, then based on the above assumption it follows that the effective transmissivity for the fracture zone should increase with the length of the fracture zone.

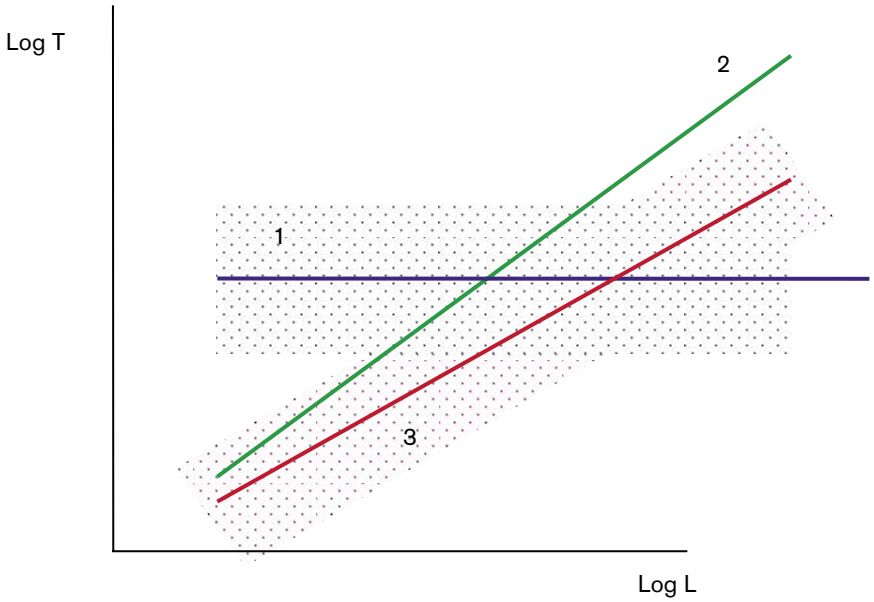

Figure 3-4. *Schematic of transmissivity models: 1) Uncorrelated, 2) Correlated, and 3) Semi-correlated. The dotted areas indicate a random variation.*

3.3.5 Fracture porosity models

As part of the modelling, it is intended to derive a fracture porosity as part of the block properties as these will be needed in the regional GWF modelling. There is no new data such as tracer test to try to interpret, so the model for the porosity of an individual fracture will be based on Äspö Task Force 6c results /15/. This approximates a direct correlation between the transport aperture e_t, and the transmissivity, such that:

$e_t = aT^b$.

The values suggested from Äspö Task Force 6c are a = 0.46, b = 0.5.

3.4 Analysis of geological data and Geo-DFN model

The first step is to group the fractures according to whether they are inside/outside a DZ and divide them for each DZ. The purpose is to see whether each DZ has a clearly dominant set. If such a set exists, then it may be expected that this will coincide with the general orientation of the DZ, although there isn't any clear way to validate this hypothesis based on geophysical data, for example. KSH01A is a sub-vertical borehole, about 70° incline, and so it will tend to have a bias toward intersecting sub-horizontal fractures. To mitigate against under-predicting the intensity of sub-vertical fractures, the Terzaghi correction was used. This was done by calculating a weighting factor, f_T, for each fracture based on the angle, θ, between the pole to the fracture plane and the borehole trajectory:

$f_T = \max(1/\cos(\vartheta),5)$.

A maximum factor of 5 was used. This weighting was used when calculating density contours on stereonets, and also for estimating $P10_{corrected}$. That is, P10 is calculated as number of fractures in an interval divided by the interval length, whereas $P10_{corrected}$ is estimated as the sum of weight factors divided by the interval length. It is our experience that this gives an accurate prediction of the $P10_{corrected}$ that can be used as a guess for P32 (fracture area per unit volume) in a DFN model to simulate the correct P10.

3.4.1 KSH01A: Deformation zone orientations and fracture intensities

Examples of fracture orientations in deformations zones in KSH01A are shown as Terzaghi weighted lower-hemisphere equal-area stereonets are shown in Figure 3-5, Figure 3-6, Figure 3-7 and Figure 3-8. Only open and partly-open fractures are included.

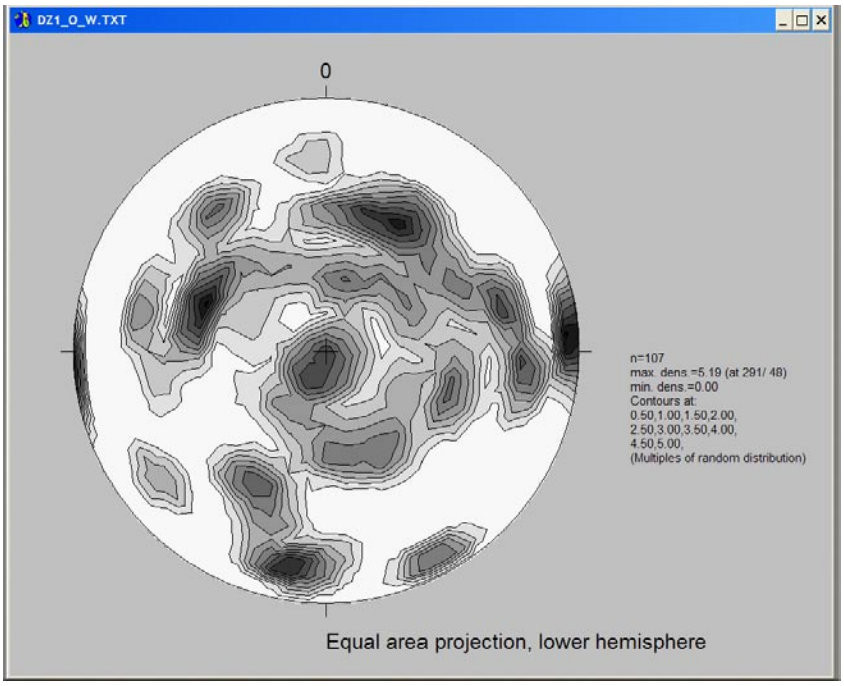

Figure 3-5. *Terzaghi corrected density contours for poles to DZ1 open and partly-open fractures, KSH01A (irrespective of confidence indicator).*

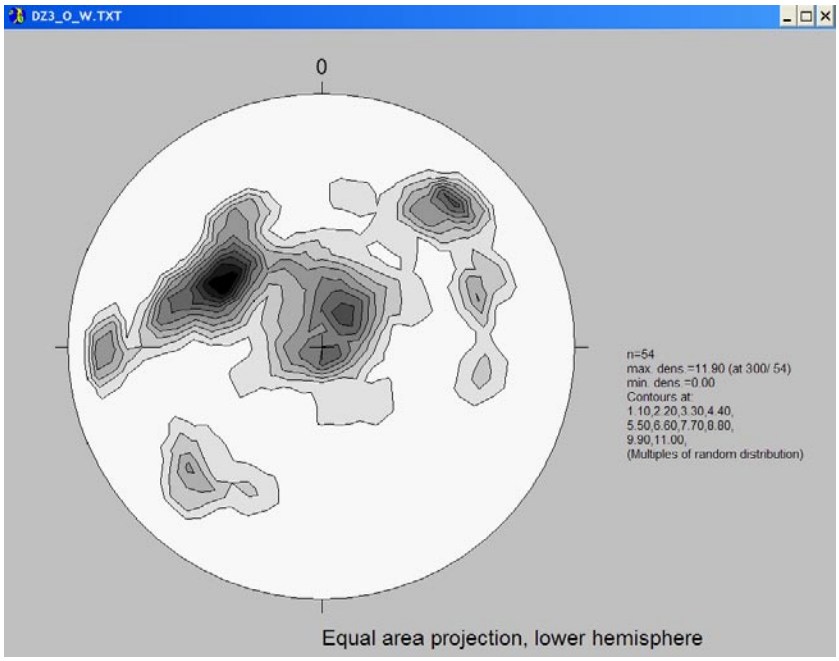

Figure 3-6. *Terzaghi corrected density contours for poles to DZ3 open and partly-open fractures, KSH01A (irrespective of confidence indicator).*

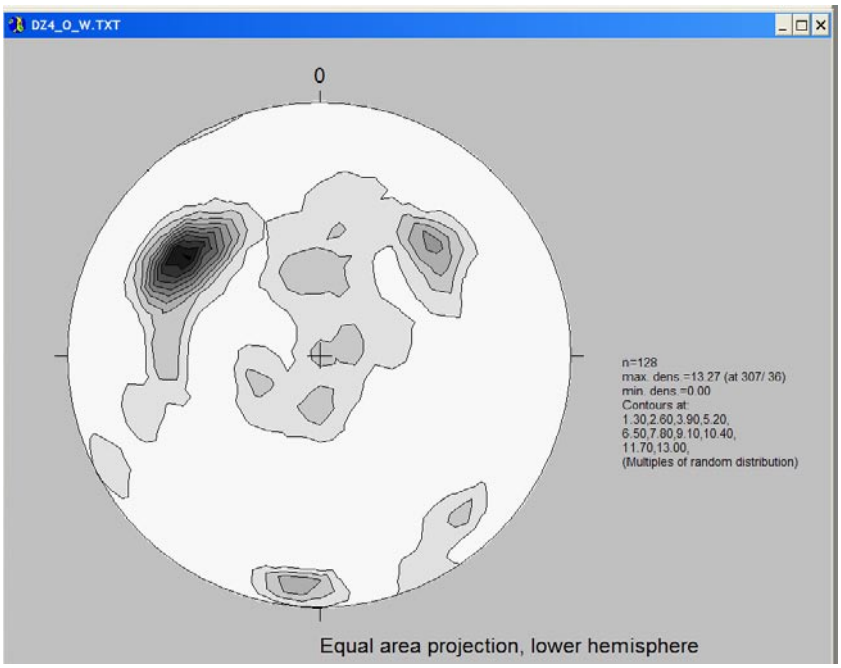

Figure 3-7. *Terzaghi corrected density contours for poles to DZ4 open and partly-open fractures, KSH01A (irrespective of confidence indicator).*

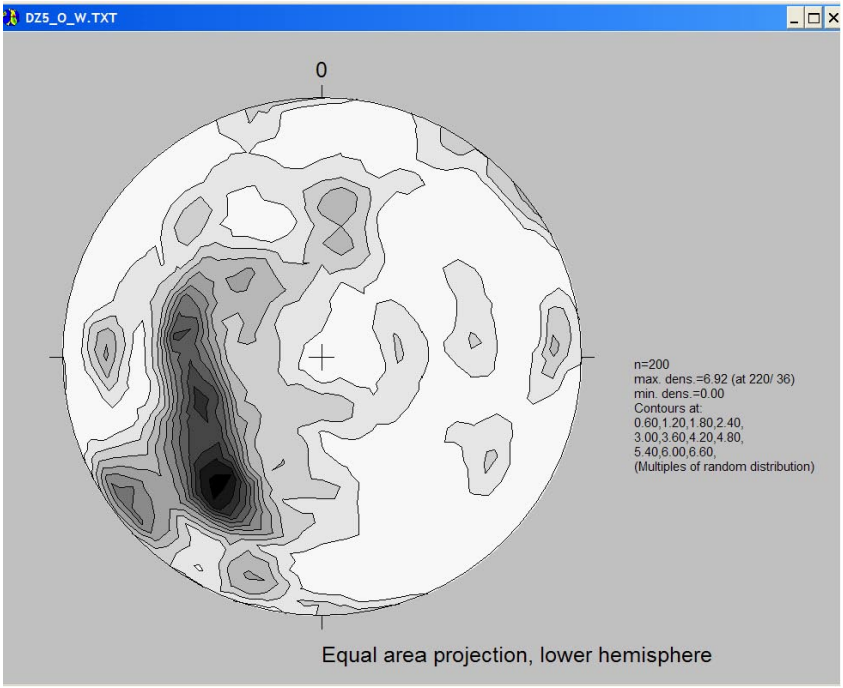

Figure 3-8. *Terzaghi corrected density contours for poles to DZ5 open and partly-open fractures, KSH01A (irrespective of confidence indicator).*

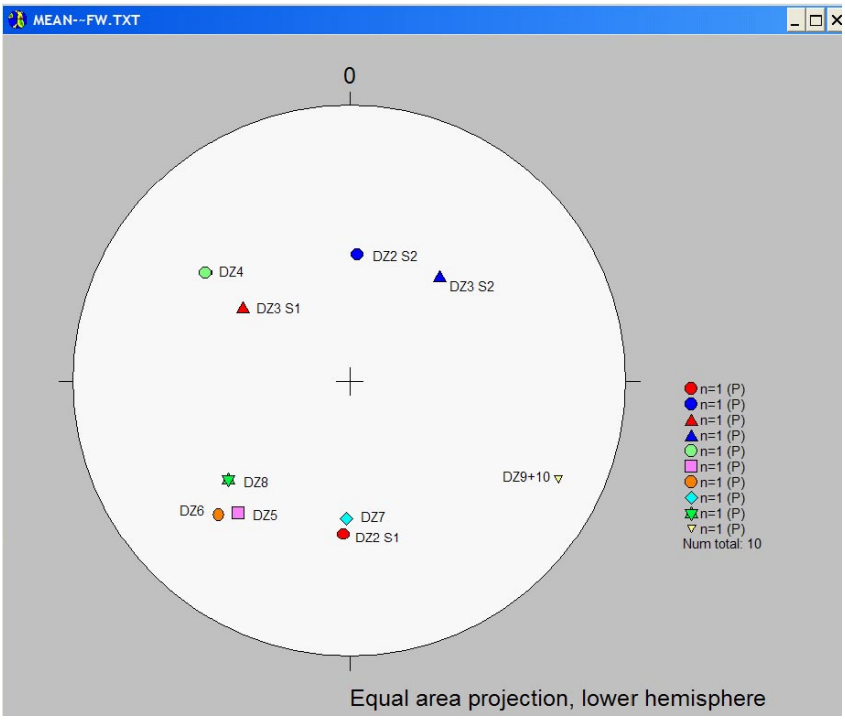

Figure 3-9. *Summary of deformation zone orientations as given by mean fracture pole, KSH01A.*

Apart from DZ1, the other DZs tend to be dominated by one or two major orientations. To illustrate how these compare between DZs, the mean pole of the dominant sets were identified and plotted on a stereonet (Figure 3-9). Two sets were identified for DZ2 and DZ3, while only a single set was chosen for the others. From this it can be seen that there are a large range of azimuths, and dip angles vary from about 38° to 72°. Also the pole azimuth tends to move anticlockwise as the DZs become deeper. For DZ2 and DZ3 the strike is about EW, DZ4 it is NE-SW, DZ5, DZ6 and DZ8 it is NW-SE, and DZ9-10 it is NE-SW.

Table 3-1. Summary of deformation zone statistics for KSH01A.

DZ	Mean Depth	BH Interval length	$P10_{all}$	$P10_{open}$	$P10_{corrected}$	Open $P10_{corrected}$	Mean azimuth/dip	Fisher Conc
DZ1	148	23.5	12.5	4.6	21.6	7.2	4–5 sets	
DZ2	245	12	16.2	4.5	28.8	6.6	2.4/46.4 183.4/37.6	15.4 19.9
DZ3	255	7.5	19.1	7.2	26.8	9.8	124.3/38.6 220.7/41.1	29.3 12.4
DZ4	273	28	12.3	4.6	19.0	7.2	126.8/54.7	40.1
DZ5	437	35	15.7	5.7	28.2	9.7	40.2/52.5	10.4
DZ6	574	68.5	17.6	3.9	30.9	7.0	44.4/57.3	8.9
DZ7	611	5.5	9.5	6.4	13.2	8.4	1.4/41.3	10.9
DZ8	623	17	13.2	7.5	20.2	11.3	50.8/47.4	11.1
DZ9	679	14.5	9.7	4.5	21.3	10.9	295.3/72.2	43.6
DZ10	689	6	10	4.5	25.3	11.5	295.3/72.2	43.6
DZ11	692	0.5	14	0	28.1	–		
DZ12	766	1	5	2	14.4	6.0		
DZ13	833	1	9	1	15.1	6.9		

Statistics for each deformation zone including fracture intensities and the dominant orientations in each zone is given in Table 3-1. Fracture intensities for open $P10_{corrected}$ vary between 6.0 and 11.5 with a mean over all zones of 7.7. This is about twice that for the fractures outside of deformation zones.

3.4.2 KSH02: Deformation zone orientations and fracture intensities

Borehole KSH02 is vertical and contains four Deformation Zones (DZ1, DZ2, DZ3, and DZ4). The orientations for sets associated with these zones are shown in Figure 3-10, Figure 3-11, Figure 3-12 and Figure 3-13.

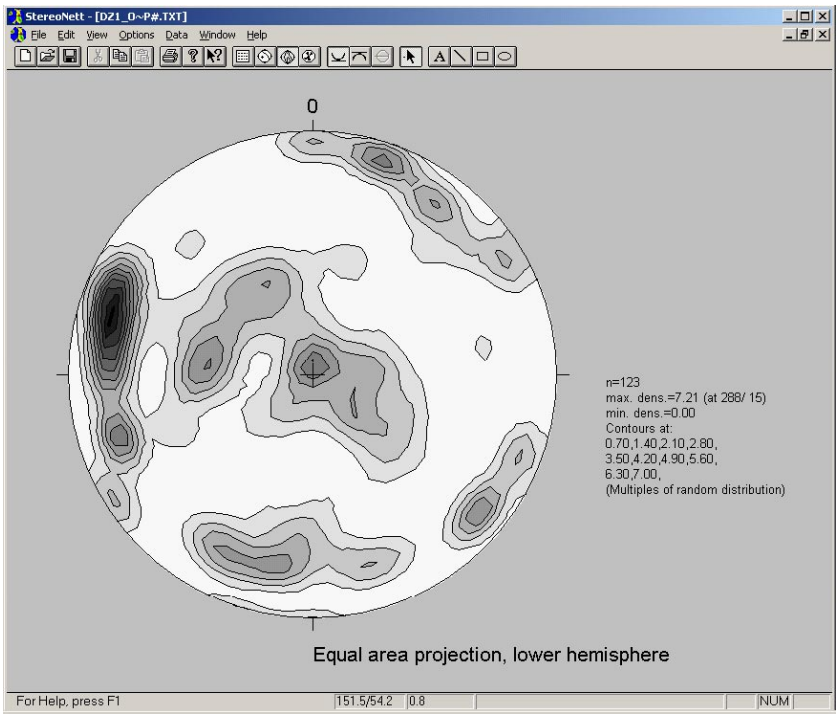

Figure 3-10. *Terzaghi corrected density contours for the poles to DZ1 open and partly-open fractures, KSH02.*

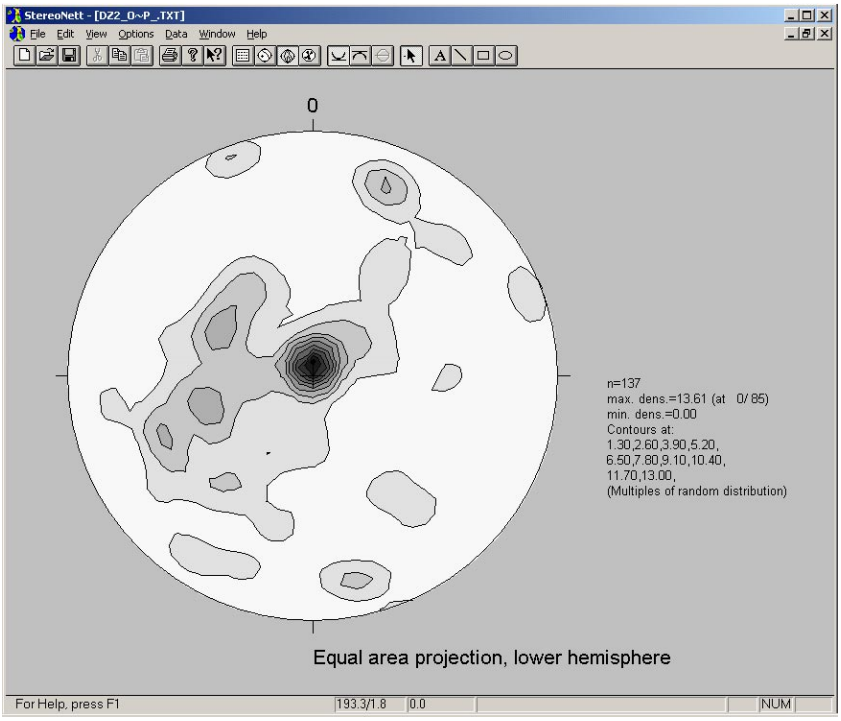

Figure 3-11. *Terzaghi corrected density contours for the poles to DZ2 open and partly-open fractures, KSH02.*

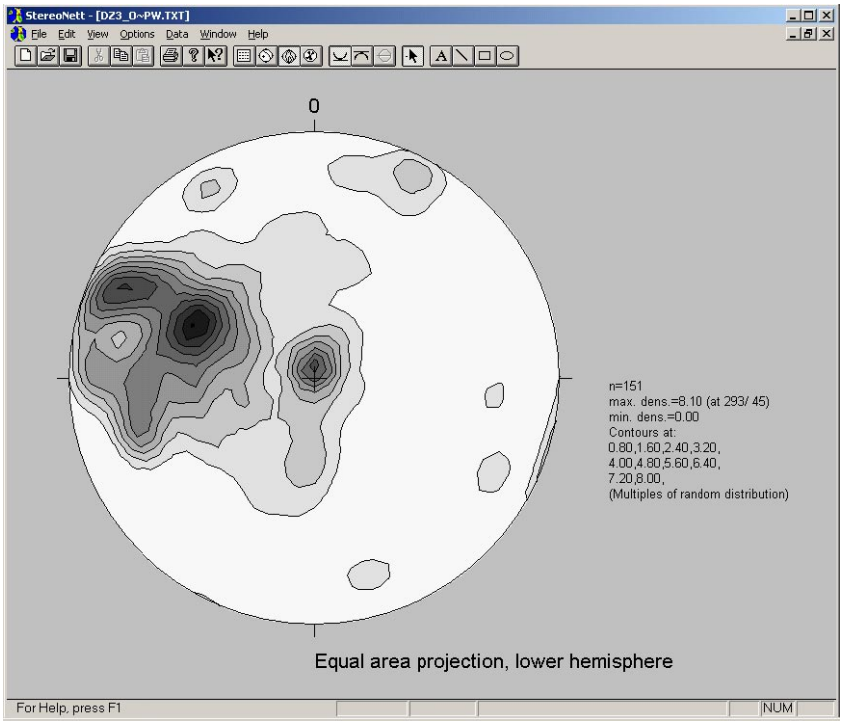

Figure 3-12. *Terzaghi corrected density contours for the poles to DZ3 open and partly-open fractures, KSH02.*

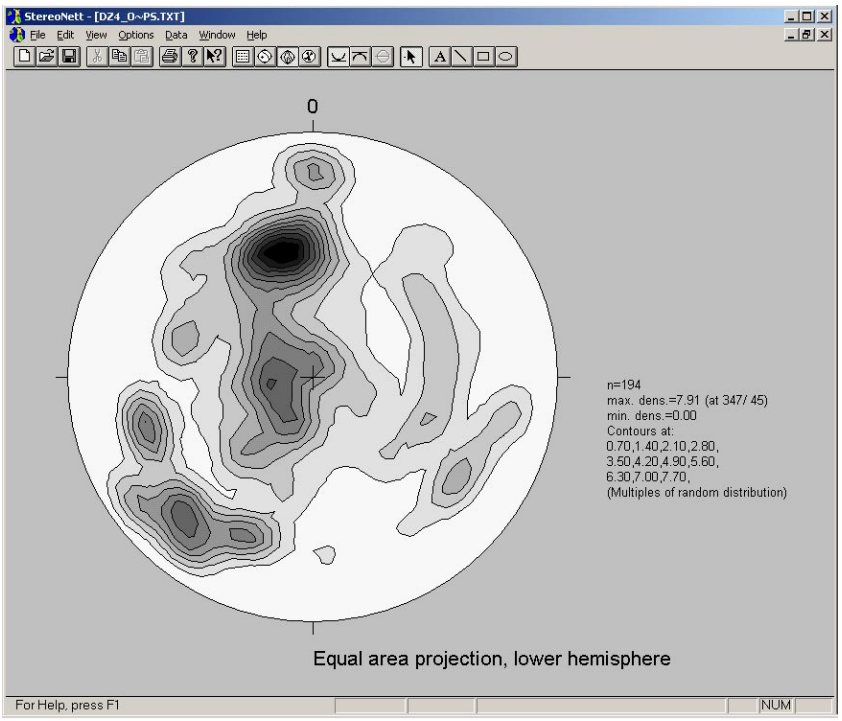

Figure 3-13. *Terzaghi corrected density contours for poles to DZ4 open and partly-open fractures, KSH02.*

To aid interpretation, the mean fracture pole for each Deformation Zone has been has been estimated by eye and plotted in Figure 3-14. The four deformation zones seem to be dominated by north-west dip azimuth, however, the dip angle varies widely. DZ3 is near-horizontal, while DZ2 and DZ4 have around a 45° dip angle, and DZ1 is near-vertical. The near-horizontal and near-vertical dips found in DZ3 and DZ1 are not seen in KSH01A.

Quantitative information for each DZ, P10, $P10_{open}$ and open $P10_{corrected}$ together with mean azimuth and dip angle are given in Table 3-2. The open $P10_{corrected}$ value varies between 4.9 and 11.8, with a mean of 9 taken over all DZ's. Similar to KSH01A, this is a high fracture intensity showing DZ's correspond to swarms of relatively high fracture occurrence. In comparison, Rock Domain B shows a value of open $P10_{corrected}$ of 5.1. That is, the fracture intensity in deformation zones is again about twice that for fractures outside of deformation zones. This is greater than that calculated for Rock Domain B in KSH01A (Open $P10_{corrected}$ = 3.8). Fractures outside the DZ's show a much wider variety of orientations, as discussed in the next sections.

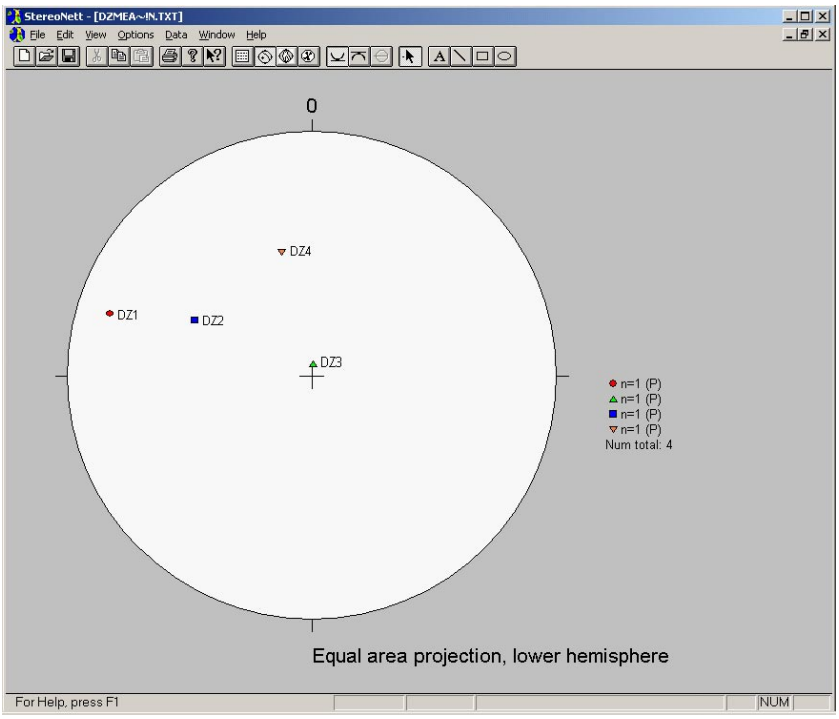

Figure 3-14. *Summary of deformation zone orientations as given by mean fracture pole.*

Table 3-2. Summary of deformation zone for KSH02. The orientation of the Deformation Zones (not Terzaghi corrected) has been estimated, by eye, from the stereonet data.

	Mean Depth	Interval length in borehole	$P10_{all}$	$P10_{open}$	Open $P10_{corrected}$	Mean azimuth/dip
DZ1	257	47	15.9	2.6	4.9	107.0/75.0
DZ2	292	23	11.4	6.0	8.7	185.0/4.0
DZ3	521.5	21	13.5	7.2	11.8	115.0/44.0
DZ4	667.5	27	16.7	7.2	10.6	166.0/43.0

3.4.3 KAV01: Deformation zone orientations and fracture intensities

Borehole KAV01is vertical and contains three Deformation Zones (DZ1, DZ2, DZ3). The fracture intensities and orientations for fractures within the deformations zones in KAV01 are given in Table 3-3.

Table 3-3. Summary of deformation zone statistics for KAV01. The orientation of the Deformation Zones are Terzaghi corrected.

	Mean Depth	Interval length in borehole	$P10_{all}$	$P10_{open}$	Open $P10_{corrected}$	Mean azimuth/ dip
DZ1	431	10	11.8	6.9	12.7	276/8.9
DZ2	452	26	12.6	7.9	12.9	30.7/12.3
DZ3	512	101	9.9	5.82	11.1	358.6/22.1

3.4.4 KSH01A: Background orientations and fracture intensities

In a similar way, Terzaghi corrected density contoured stereonets were produced for the fractures poles in each of the rock domains (B and C) seen in KSH01A outside of a DZ. The trajectory of KSH01A has a dip of about 70° toward South. Again, only the open or partly-open fractures were considered. The results for rock domain B are shown in Figure 3-15 and for rock domain C in Figure 3-16. Visually, these suggest up to 3 shallow dipping sets with dip angles less than about 60°, and about 3 sub-vertical sets. The classification provided by the GeoDFN interpretation gave a sub-horizontal set with a dip up to 25°, and a sub-vertical set with a dip 60° to 90°. This presents difficulties for incorporation into the Hydro-DFN modelling since this would not account for a large proportion of fractures falling outside of these two limits. Instead, a decision was taken to consider both the borehole data and the GeoDFN, but create a new classification for use in the Hydro-DFN modelling.

The next step was to integrate the orientation sets identified in the GeoDFN, based primarily on outcrop data, and the sets identified here. The problem with the borehole data is that it tends to have limited resolution of sub-vertical fractures, whereas the outcrop data does not capture the sub-horizontal fractures because of the relative orientation of the sampling direction to the fractures. The approach taken was to split the stereonet into 5 areas in a simplified way taking in to account both the sets identified in both the GeoDFN and in KSH01A and KSH02 as shown in Figure 3-17. The division of sets is tabulated Table 3-4 and the relationship to the GeoDFN sets is included.

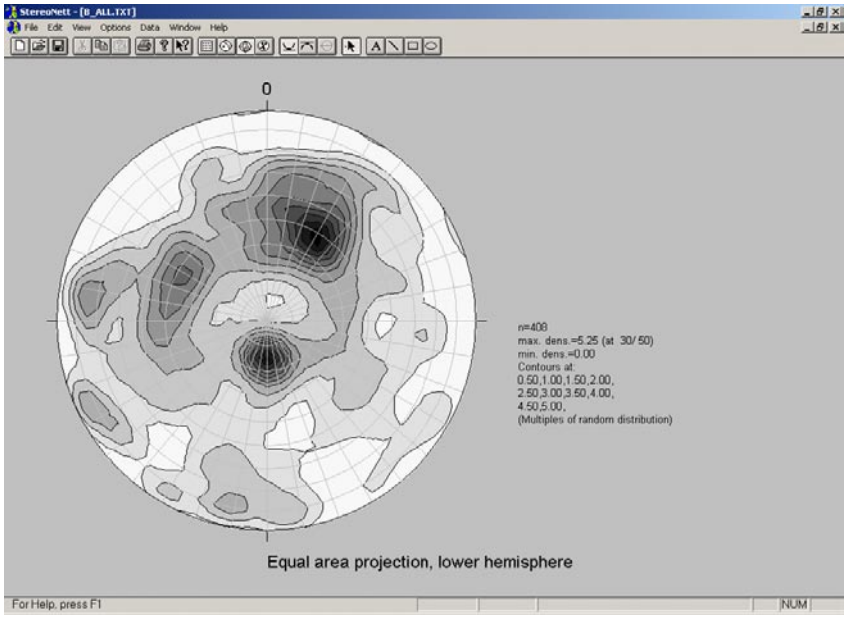

Figure 3-15. *Terzaghi corrected density contours for Rock domain B (outside DZs) non-sealed fractures, KSH01A.*

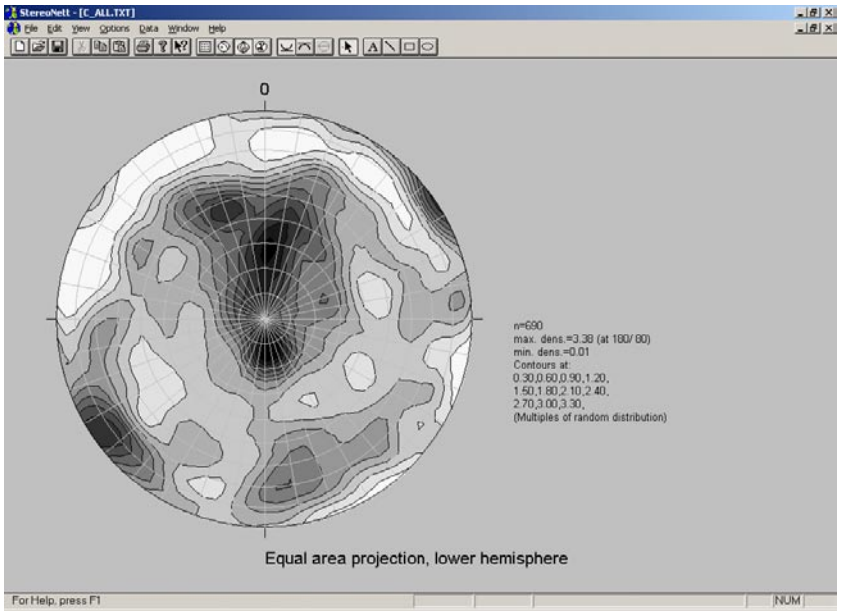

Figure 3-16. *Terzaghi corrected density contours for Rock domain C (outside DZs) non-sealed fractures, KSH01A.*

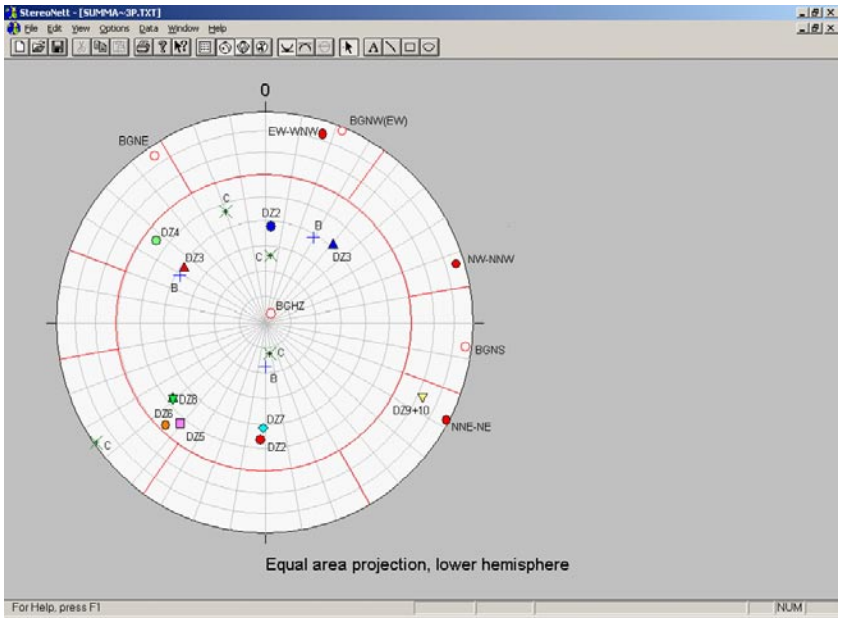

Figure 3-17. *Division of fractures into 5 orientation sets for analysis of KSH01A data. GeoDFN lineament sets are shown as (●), GeoDFN background sets are shown as (○). (Note that the GeoDFN set BGNW is orientated in an E – W direction, hence has been denoted BGNW(EW).) Major fracture sets in Rock Domain B and C are shown as (+) and (×) respectively (outside of Deformation Zones; identified by eye from Figure 3-15 and Figure 3-16). Deformation Zones are identified in varying colours and symbols, as marked on the stereonet.*

Table 3-4. Simplified classification of orientation sets and comparison to GeoDFN classification. *The set number given to the GeoDFN classification is indicated in brackets.

Orientation set	GeoDFN (outcrop) relationship *	Azimuth range	Dip range (degrees)
NE	NNE-NE (1), BGNE (4)	108–150, 288–330	60 to 90
EW	EW-WNW (2), BGNW (6)	330–35, 150–215	60 to 90
NW	NW-NNW (3)	35–80, 215–260	60 to 90
NS	BGNS (5)	80–108, 260–288	60 to 90
HZ	BGHZ (7)	0–360	0 to < 60

In order to demonstrate how the sub-vertical sets were identified, stereonets for fractures with dips greater than 60° are shown for rock domains B and C in Figure 3-18 and Figure 3-19, respectively. Using this classification, the open and partly-open fractures in KSH01A were split into 5 orientation sets to quantify the mean azimuth, dip angle and Fisher concentration as well as the open $P10_{corrected}$ for each set and each rock domain (see Table 3-5). The distribution between sets is similar between both rock domains with the sub-horizontal set HZ and sub-vertical set EW having the largest magnitudes, and the combined open $P10_{corrected}$ for the sub-vertical sets being less than that of HZ. Again, $P10_{corrected}$ has been derived using the Terzaghi correction to compensate for the bias associated with the borehole trajectory.

Table 3-5. Orientations and fracture intensity for each orientation set and each rock domain in KSH01A.

Set	Open/partly-open fracs	Mean azimuth	Mean dip	Fisher concentration	$P10_{open}$	Open $10_{corrected}$
Rock B NE	12	303.8	89.7	12.9	0.07	0.19
Rock B EW	31	188.8	88.3	75.9	0.17	0.46
Rock B NW	137	59.7	85.1	15.5	0.12	0.37
Rock B NS	13	94.2	87.7	14.0	0.07	0.02
Rock B HZ	330	173.7	10.5	4.5	1.81	2.54
Rock C NE	30	307.5	79.5	16.5	0.06	0.14
Rock C EW	61	2.3	83.4	10.3	0.12	0.31
Rock C NW	43	57.0	84.4	23.3	0.09	0.30
Rock C NS	20	267.7	88.4	16.1	0.04	0.12
Rock C HZ	535	180.5	8.5	4.8	1.07	1.43

To consider how this division of sets compares with the GeoDFN, Table 3-6 compares the percentage of fractures in the sub-vertical sets and the open $P10_{corrected}$ for rock domain C in each set. The main difference is that EW and NE are swapped around in their relative importance. For KSH01A, EW is the dominant sub-vertical set, whereas for the GeoDFN it is the NNE-NE set. Overall though, the $P10_{corrected}$ for the sub-vertical sets is consistent with the GeoDFN. This builds confidence that using the Terzaghi correction for the borehole can compensate reasonably for the sub-vertical fractures. However, the outcrop data used in the GeoDFN completely under-samples the sub-horizontal fractures that constitute about 62% of fractures in KSH01A.

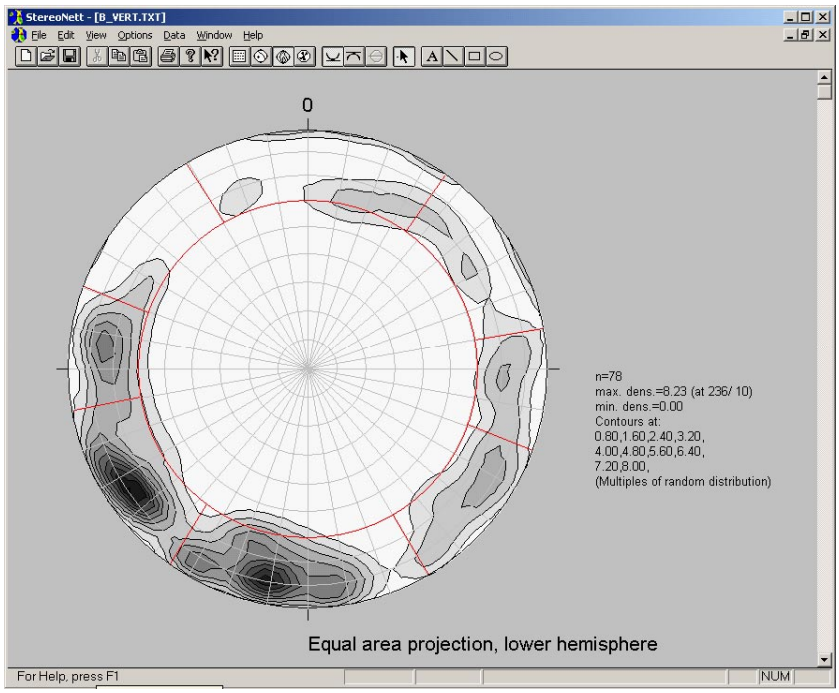

Figure 3-18. *Terzaghi corrected density contours for poles of sub-vertical fractures from Rock Domain B, KSH01A. The classification into different fracture sets is overprinted in red.*

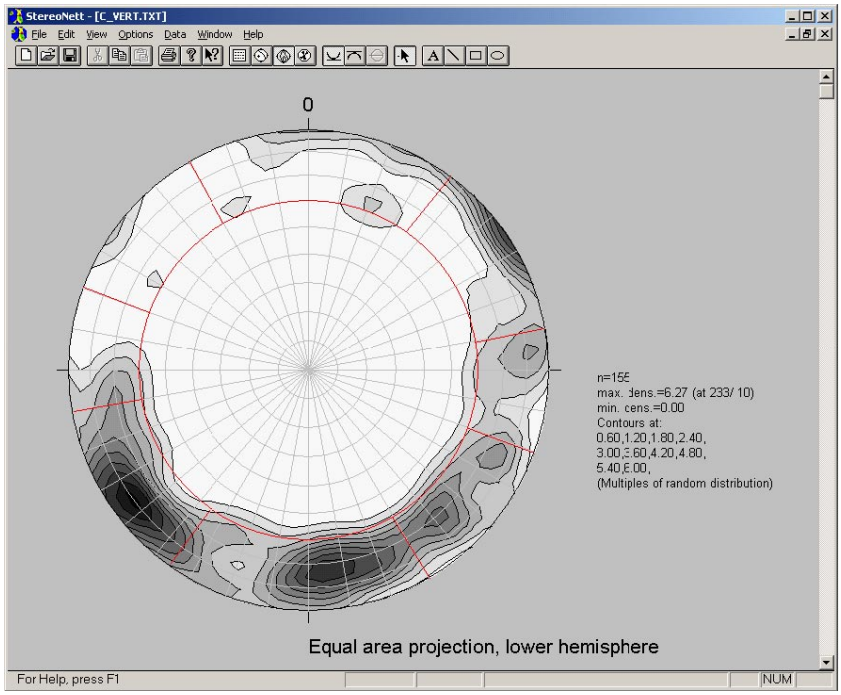

Figure 3-19. *Terzaghi corrected density contours for poles of sub-vertical fractures from Rock Domain C, KSH01A. The classification into different fracture sets is overprinted in red.*

Table 3-6. Comparison of set distribution for Rock C between KSH01A and GeoDFN from outcrop data. (*) denotes % of all fractures for the sub-horizontal fractures.

KSH01A Set	GeoDFN Set	KSH01A % vertical	GeoDFN % vertical	KSH01A Open $P10_{corrected}$	GeoDFN (Outcrop) Open $P10_{corrected}$
Rock C NE	NNE-NE, BGNE	16.1	37.6	0.18	0.30
Rock C EW	EW-WNW, BGNW	35.6	24.4	0.40	0.19
Rock C NW	NW-NNW	34.6	22.5	0.34	0.18
Rock C NS	BGNS	13.7	15.4	0.13	0.12
Rock C HZ	BGHZ	62.3*	6.7*	1.37	0.05

Another important issue is the confidence in the interpretation of open or partly-open fractures. Each open fracture is assigned a confidence indicator: certain, probable or possible. This gives some indication of the uncertainty in the intensity of open fractures. Table 3-7 gives the percentages and corresponding open $P10_{corrected}$ values for each rock domain based on the various confidence indicators. From this, it is seen there is actually a large uncertainty in the numbers of open fractures in KSH01A. Only 9–14% of open fractures are certain, and 21–29% of open fractures are either certain or probable. This suggests that it is important that the uncertainty in open $P10_{corrected}$ is assessed in the Hydro-DFN modelling by sensitivity studies.

Table 3-7. $P10_{corrected}$ for open fractures based on confidence indicators for the rock outside of deformation zones, KSH01A.

Rock domain	$P10_{corrected}$ (open)	$P10_{corrected}$ (open/certain)	$P10_{corrected}$ (open/certain or probable)
B (not DZ)	3.8 (100%)	0.34 (9%)	0.80 (21%)
C (not DZ)	2.43 (100%)	0.33 (14%)	0.72 (29%)

Based on Table 3-6 it is clear that set HZ has to be modified from that specified in the GeoDFN model. One modification is to increase open $P10_{corrected}$ for the set by use of the borehole data. However, the fact that there is about 10 large moderately dipping deformation zones intersecting the borehole would suggest that the HZ (dip < 60°) is not limited to small background fractures. In the GeoDFN the mean length of the subHZ set was about 0.6 m. Therefore, the length distribution was changed to power-law. This then raises the issue of how to select an exponent in the power-law for the modified HZ set. It was decided to choose an exponent such that the open $P10_{corrected}$ for stochastic fractures of length greater than 100 m should be approximately the number of deformation zones observed in KSH01A, i.e. about 10. Considering the case where 29% of open or partly-open fractures are conductive (i.e. taking all certain and probable open fractures) gives an open $P10_{corrected}$ of 0.415 for HZ fractures in rock C, then about 21 large fractures will be observed in KSH01A if $k_r = 2.4$. There are about 9 large fractures if $k_r = 2.6$, and there are about 3 if $k_r = 2.8$. This would suggest an exponent of about 2.6 is correct, although large values of k_r would be required for cases with a higher percentage of open fractures. For this study, an exponent of 2.6 was used for HZ throughout. This is consistent with the study performed by the DarcyTools Team.

The cumulative $P10_{corrected}$ (open and partly-open) has been plotted against depth (Figure 3-21). KSH01A shows a fairly constant $P10_{corrected}$ down to about 700 m depth, then there is a sharp decrease in open fracture intensity.

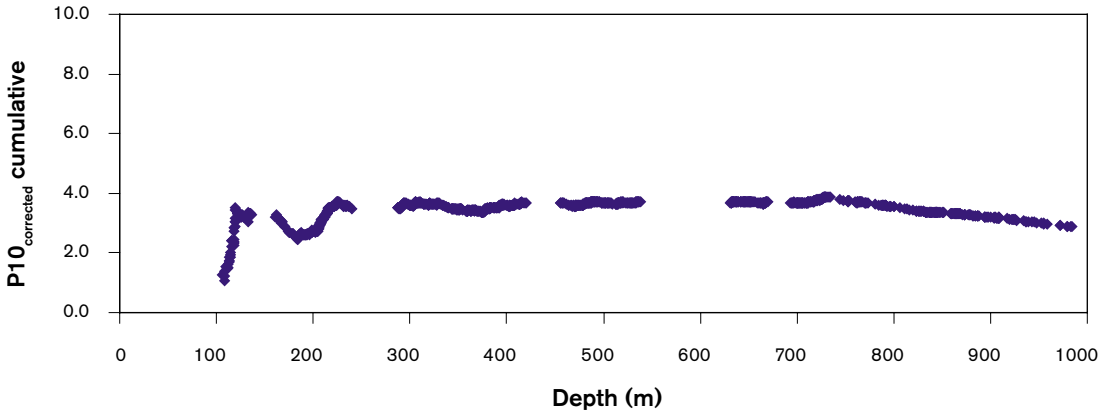

Figure 3-20. *Cumulative P10corrected for open and partly-open fractures in KSH01A for the rock outside of deformation zones. The apparent 'gaps' in the data correspond to Deformation Zones.*

3.4.5 KSH02: Background orientations and fracture intensities

Density contoured stereonets were produced for the open and partly-open fractures outside Deformation Zones. Only Rock Domain B is found in KSH02 (Figure 3-21). KSH02 is a vertical borehole. Figure 3-21 shows that the mean pole of the RD_B fractures is near horizontal with no overall azimuth direction. As a summary, the mean poles from each of the DZ's along with the mean pole for RD_B, and the outcrop sets are compared in Figure 3-22. The simplified classification of five orientation sets that was adopted for KSH01A has been added and is also shown.

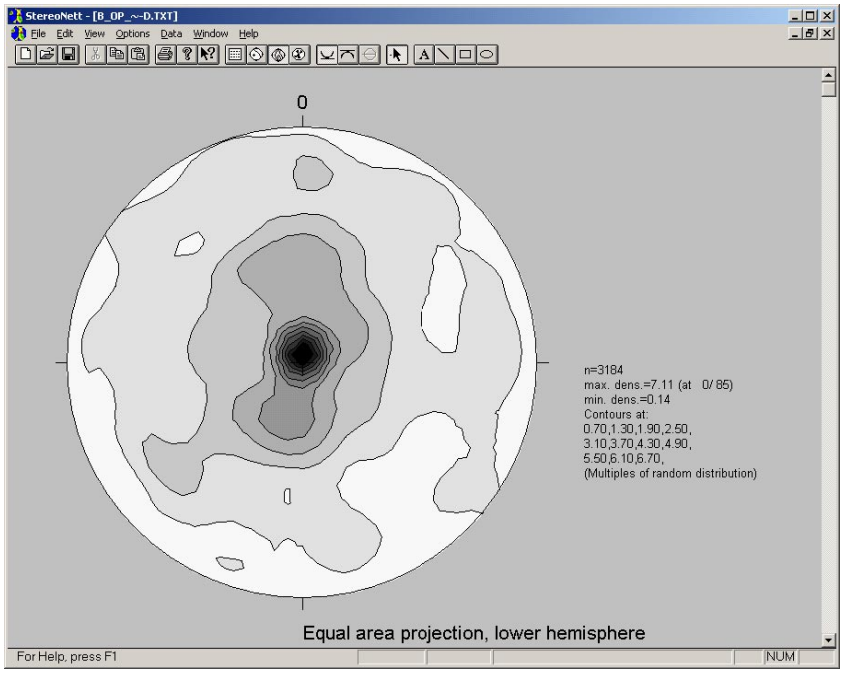

Figure 3-21. *Terzaghi corrected density contours for all poles to Rock domain B (outside DZs) open fractures. This includes the (dominating) sub-horizontal fractures, and the sub-vertical fractures.*

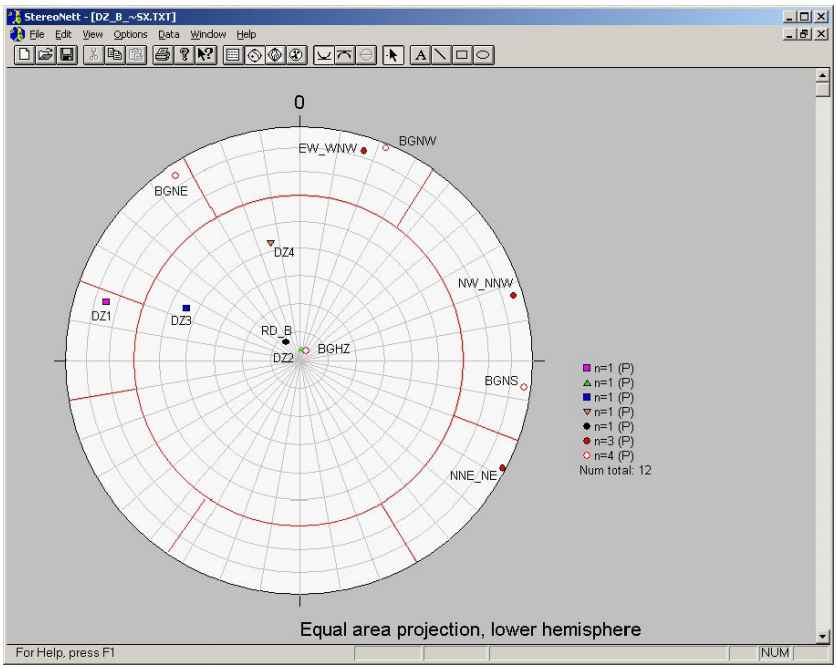

Figure 3-22. *Summary of mean poles of DZs, Rock Domain B (●) and outcrop sets (●) and background outcrop sets (○). Each mean pole is labelled on the stereonet. The red line denotes the fracture set classification used for the Hydro-DFN.*

To aid interpretation of the borehole data, which is dominated by the horizontal fracture sets (83%), a density weighted plot of the fractures with dip greater than 60 ° has been plotted (Figure 3-23). Most of the sub-vertical fractures in KSH02 can be consistently grouped according to the classification used for KSH01A, although the EW set falls across more than one class. The mean azimuth, dip angle, Fisher concentration and open $P10_{corrected}$ for the fractures (outside a DZ) within each of these orientation sets are shown in Table 3-8.

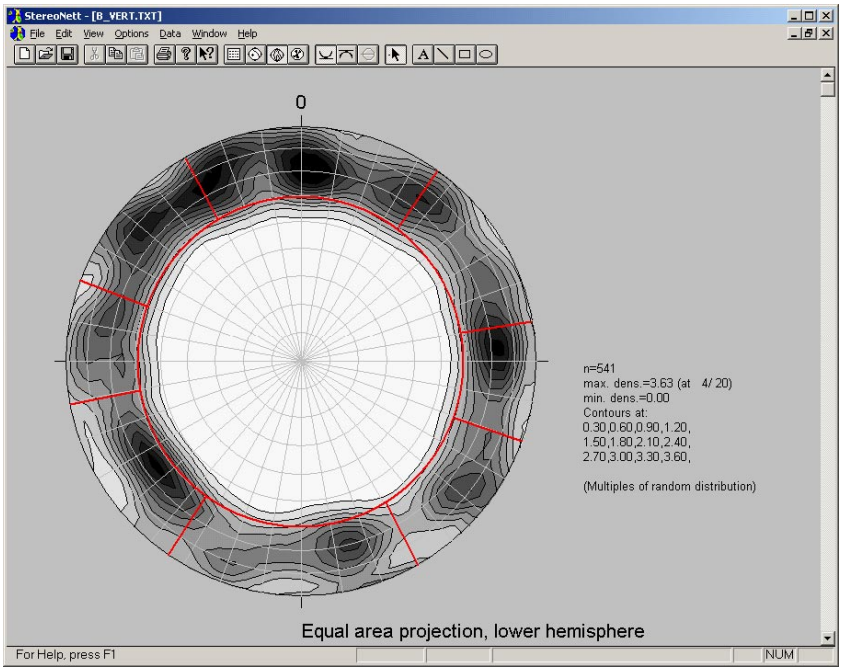

Figure 3-23. *Terzaghi corrected density contours for all poles to sub-vertical fractures in Rock Domain B, KSH02 (dip angle > 60°). The red lines indicate the simplified set classification used for the Hydro-DFN.*

Table 3-8. Summary of Rock Domain B fracture sets for KSH02 (length of cored borehole = 863 m). $P10_{corrected}$ is Terzaghi corrected for borehole orientation. The mean fracture azimuth, dip and Fisher concentration are similarly Terzaghi corrected.

Set	N (total fractures)	N (Open fractures)	P10 open	Open $P10_{corrected}$	Mean fracture azimuth	Mean fracture dip	Fisher conc
B_NE	473	111	0.129	0.440	128.16	87.80	16.03
B_EW	787	205	0.237	0.766	180.40	86.02	10.12
B_NW	571	135	0.156	0.473	55.44	87.19	11.99
B_NS	347	94	0.109	0.335	92.42	89.71	14.88
B_HZ	7,950	2,639	3.057	3.744	134.70	4.40	5.52

Table 3-9 shows a comparison of the division of sets for the GeoDFN and KSH02. As seen in KSH01A, the borehole data shows the EW set to be of greatest importance, with 36% of the sub-vertical fractures, while the NE fracture set dominates the sub-vertical fractures for the GeoDFN. The open $P10_{corrected}$ gives much higher values for RD_B for KSH02 than the outcrop data. However, the outcrop data, as seen for KSH01A, completely under-samples the sub-horizontal fractures that constitute 83% of the fractures recorded.

Table 3-9. Comparison of set distribution for Rock B between KSH02 and GeoDFN from outcrop data. (*) denotes % of all fractures for the sub-horizontal fractures.

KSH02 set	GeoDFN set	KSH02 % vertical fractures	GeoDFN % vertical fractures	KSH02 open $P10_{corrected}$	GeoDFN (outcrop) open $P10_{corrected,}$
B_NE	NNE_NE, BGNE	20.4	37.6	0.39	0.35
B_EW	EW_WNW, BGNW	37.6	24.4	0.67	0.17
B_NW	NW_NNW	24.8	22.5	0.42	0.26
B_NS	BGNS	17.2	15.4	0.30	0.14
B_HZ	BGHZ*	82.9	6.7*	3.29	0.04

To help assess the sensitivity of open $P10_{corrected}$ to variations in confidence indicator, Table 3-10 gives the percentages of each class of confidence and the corresponding open $P10_{corrected}$ values. Borehole KSH02 has a large percentage of open fractures with a confidence indicator classified as ’possible’ (88%), which means that any scaling of open $P10_{corrected}$ by confidence indicators greatly reduces the remaining open $P10_{corrected}$. The cumulative $P10_{corrected}$ (open and partly-open) has been plotted against depth (Figure 3-23). KSH02 is composed of only one Rock Domain (RD_B), and shows fairly constant $P10_{corrected}$ for the most part of the borehole, with a lower open $P10_{corrected}$ between about 400 m to 500 m depth, and below 800 m.

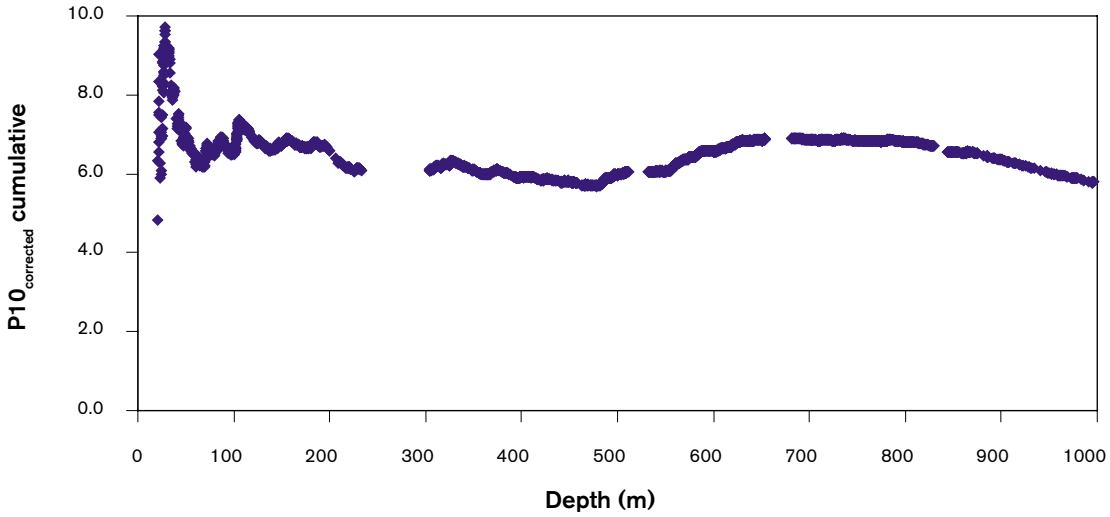

Figure 3-24. *Cumulative P10corrected for open and partly-open fractures in KSH02 for the rock outside of deformation zones. The apparent 'gaps' in the data correspond to Deformation Zones.*

Table 3-10. $P10_{corrected}$ for open and partly-open fractures based on confidence indicators for the rock outside of deformation zones in KSH02.

Rock domain	$P10_{corrected}$ (open)	$P10_{corrected}$ (open/certain)	$P10_{corrected}$ (open/ certain or probable))
B (not DZ)	5.1 (100%)	0.2 (5%)	0.6 (12%)

3.4.5 KSH03A: Background orientations and fracture intensities

Borehole KSH03A is composed of Rock Domain C (169 m) towards the shallower depths (up to ~270 m) underlain by Rock Domain A (731 m). It contains no identified Deformation Zones. However, there are two deterministic fracture zones that cut the borehole in the S1.2 geological model at depths around 200 m–300 m. The borehole has been drilled at an inclined angle. The bearing of the borehole KSH03A varies from 123° to 180°, while the inclination remains fairly constant at around 56.8°. All fracture orientations have been Terzaghi corrected to prevent underestimation of fractures parallel to the inclined borehole.

Density contoured stereonets were produced for the open and partly-open fractures outside Deformation Zones, for each of the Rock Domains A and C (Figure 3-25 and Figure 3-26). These show that the sub-horizontal set dominates. Therefore the sub-vertical fractures with a dip > 60° are shown in Figure 3-27 and Figure 3-28. The sub-vertical fractures are predominantly in the NE and EW orientation sets.

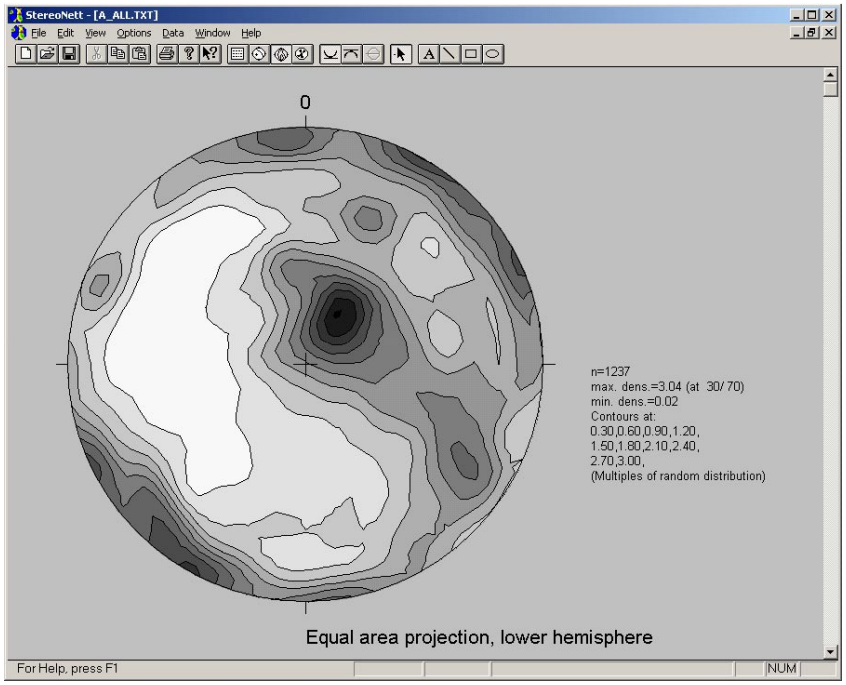

Figure 3-25. *Terzaghi corrected density contours for all poles to open and partly-open fractures in Rock domain A (outside DZs), KSH03A. This includes the (dominating) sub-horizontal fractures, and the sub-vertical fractures.*

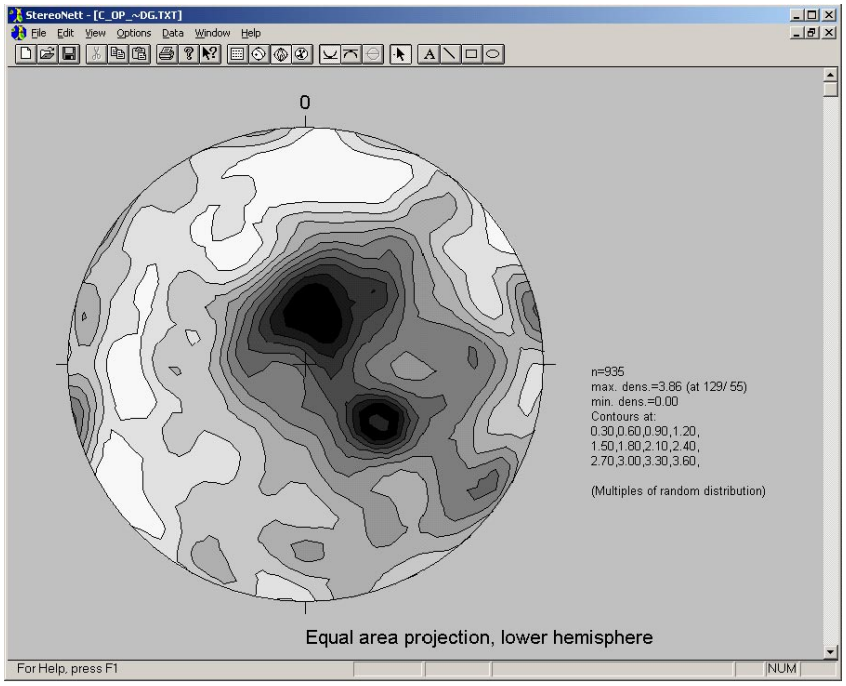

Figure 3-26. *Terzaghi corrected density contours for all poles to open and partly-open fractures in Rock domain C (outside DZs), KSH03A. This includes the (dominating) sub-horizontal fractures, and the sub-vertical fractures.*

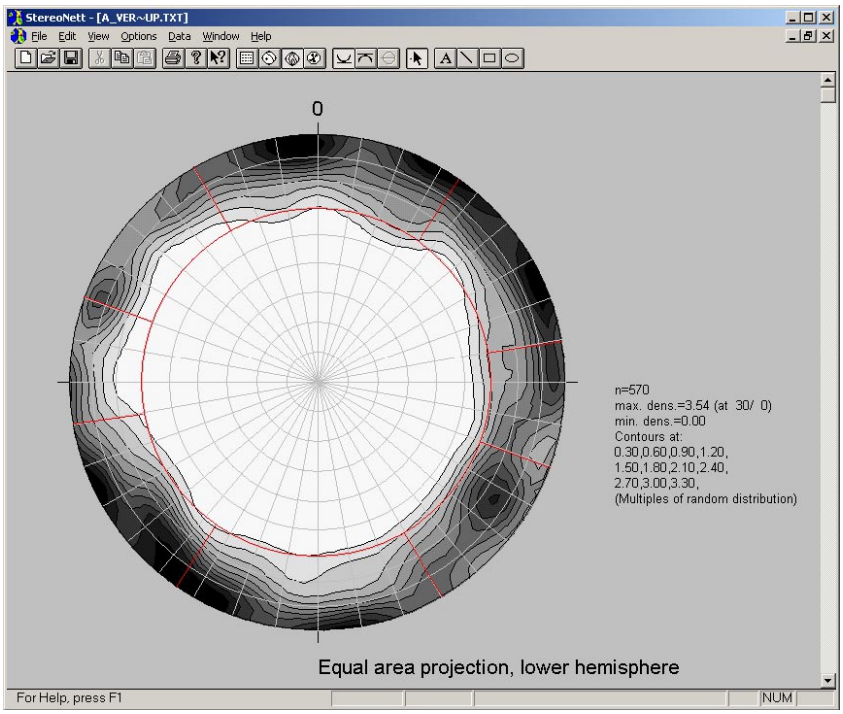

Figure 3-27. *Terzaghi corrected density contours for all poles of sub-vertical open and partly-open fractures in Rock Domain A, KSH03A (dip angle > 60°). The red lines indicate the simplified set classification used.*

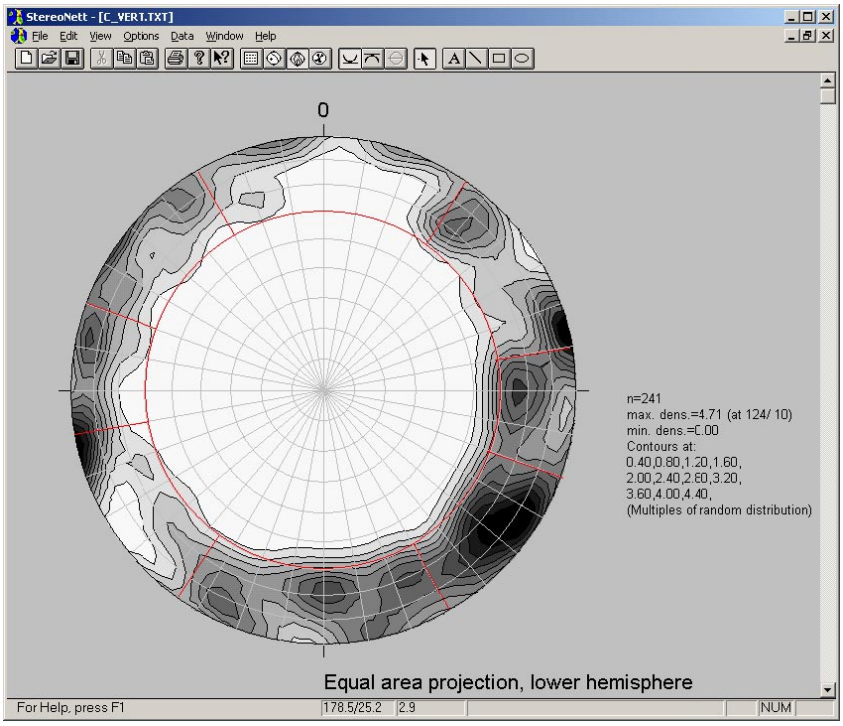

Figure 3-28. *Terzaghi corrected density contours for all poles of sub-vertical open and partly-open fractures in Rock Domain C, KSH03A (dip angle > 60°). The red lines indicate the simplified set classification used.*

The mean azimuth, dip angle, Fisher concentration and open $P10_{corrected}$ for the fractures (outside a DZ) within each of the orientation sets are shown in Table 3-11 as subdivided by rock domain.

Table 3-11. Orientations and fracture intensity for each orientation set and each rock domain in KSH03A.

Set	Open/partly-open fracs	Mean azimuth	Mean dip	Fisher concentration	$P10_{open}$	Open $P10_{corrected}$
Rock A NE	144	307.2	82.1	19.7	0.20	0.36
Rock A EW	227	185.5	88.1	12.1	0.31	0.63
Rock A NW	137	56.9	89.7	19.6	0.19	0.54
Rock A NS	64	272.3	80.2	30.9	0.09	0.19
Rock A HZ	667	248.0	17.1	5.6	1.69	1.33
Rock C NE	93	308.2	82.2	21.4	0.55	0.90
Rock C EW	68	358.5	77.0	14.2	0.40	0.81
Rock C NW	32	238.5	85.3	14.2	0.19	0.59
Rock C NS	695	273.0	81.7	20.9	0.28	0.55
Rock C HZ	935	261.2	10.2	5.4	4.11	5.67

Table 3-12 gives the percentages of each class of confidence and corresponding open $P10_{corrected}$ values for each rock domain based on the various confidence indicators. From this, it is seen there is actually a large uncertainty in the numbers of open fractures. The percentage of open and certain fractures varies a lot from 22% in rock domain C, around the two deterministic zones, to only 8% for the majority of the rock in rock domain A. For certain or probable these numbers become 27% and 10%. Taken overall, the percentage of certain is 14%, and certain or probable is 18%.

Table 3-12. $P10_{corrected}$ for open fractures based on confidence indicators for the rock outside of deformation zones, KSH03A.

Rock domain	$P10_{corrected}$ (open)	$P10_{corrected}$ (open/certain)	$P10_{corrected}$ (open/certain or probable)
A	3.05 (100%)	0.23 (7.6%)	0.31 (10.3%)
C	8.44 (100%)	1.84 (21.8%)	2.26 (26.8%)

3.4.6 KAV01: Background orientations and fracture intensities

All of Borehole KAV01 is within Rock Domain A (602 m outside of DZs). It contains 3 Deformation Zones around 430–510 m. A SW-NE shallowly dipping (toward SE) deterministic fracture zone included in the S1.2 geological model also cuts the borehole at about 500 m depth. The borehole is vertical. The mean azimuth, dip angle, Fisher concentration and open $P10_{corrected}$ for the fractures (outside a DZ) within each of the orientation sets are shown in Table 3-13.

Table 3-14 gives the percentages of each class of confidence and the corresponding open $P10_{corrected}$ values. Borehole KAV01 has a large percentage of open fractures with a confidence indicator classified as 'certain' (77%), which is far higher than any of the

KSH boreholes. This may be an issue related to the consistency in the classifications used in the older boreholes, or a genuine result due to the effects of the large regional-scale fracture zone cutting the borehole. It is also in contradiction of the observation that the frequency of mineral filled fractures is much higher at Ävrö and Laxemar than at Simpevarp /16/.

Table 3-13. Orientations and fracture intensity for each orientation set and each rock domain in KAV01.

Set	Open/partly-open fracs	Mean azimuth	Mean dip	Fisher concentration	$P10_{open}$	Open $P10_{corrected}$
Rock A NE	166	306.3	78.5	18.7	0.28	0.87
Rock A EW	141	355.8	85.4	8.9	0.23	0.82
Rock A NW	84	229.4	89.5	18.3	0.14	0.51
Rock A NS	30	276.8	85.4	16.3	0.05	0.15
Rock A HZ	1,191	311.4	15.8	5.3	1.98	2.54

Table 3-14. $P10_{corrected}$ for open and partly-open fractures based on confidence indicators for the rock outside of deformation zones in KAV01.

Rock domain	$P10_{corrected}$ (open)	$P10_{corrected}$ (open/certain)	$P10_{corrected}$ (open/certain or probable))
A (not DZ)	4.9 (100%)	3.75 (76.6%)	3.75 (76.6%)

3.4.7 KLX02: Background orientations and fracture intensities

Borehole KLX02 is completely within Rock Domain A (1,006 m outside of DZs). The borehole is vertical. The mean azimuth, dip angle, Fisher concentration and open $P10_{corrected}$ for the fractures (outside a DZ) within each of the orientation sets are shown in Table 3-15.

Table 3-15. Orientations and fracture intensity for each orientation set and each rock domain in KLX02.

Set	Open/partly-open fracs	Mean azimuth	Mean dip	Fisher concentration	$P10_{open}$	Open $P10_{corrected}$
Rock A NE	141	125.6	79.9	20.2	0.14	0.47
Rock A EW	197	182.2	88.4	10.7	0.20	0.64
Rock A NW	134	234.3	85.7	16.7	0.13	0.45
Rock A NS	81	95.7	76.3	1.6	0.08	0.30
Rock A HZ	1,654	87.5	2.1	4.2	1.65	2.16

Table 3-16 gives the percentages of each class of confidence and the corresponding open $P10_{corrected}$ values. Borehole KLX02 has a large percentage of open fractures with a confidence indicator classified as ’certain’ (73%), which is far higher than any of the KSH boreholes and again questions the consistency in the classifications used in the older boreholes.

Table 3-16. $P10_{corrected}$ for open and partly-open fractures based on confidence indicators for the rock outside of deformation zones in KLX02.

Rock domain	$P10_{corrected}$ (open)	$P10_{corrected}$ (open/certain)	$P10_{corrected}$ (open/certain or probable))
A (not DZ)	4.02 (100%)	2.93 (72.8%)	2.93 (73.0%)

3.4.8 Summary of fracture intensities

A summary of the fracture intensities $P10_{corrected}$ for the various confidence classes of open and partly-open fractures is given in

Table 3-17 for all boreholes, and split into rock domains and inside or outside of deformation zones. A row for KLX01 is included based on rock fracture engineering data, although this lacks information on orientation and confidence indicators. From this summary some observations can be made:

- Fracture intensity of open fractures in deformation zones is about twice that in the surrounding rock based on all open, and nearly three times for open and certain.
- Fracture intensity for all open fractures in the background varies between about 2.5 to 5 m^{-1} (ignoring rock C in KSH03A where are 2 large deterministic zones).
- There is a marked difference in the confidence indicator percentage between the newer Simpevarp boreholes and the boreholes in Ävrö and Laxemar.
- $P10_{corrected}$ for open/certain or probable is only 0.3 to 0.8 m^{-1}; and very similar for Rock Domains B and C in KSH01A and KSH02, although higher than in Rock Domain A in KSH03A.
- Hence, it is not possible to conclude with confidence any distinct difference in conductive fracture intensity between the rock domains.

Table 3-17. A summary of $P10_{corrected}$ for open and partly-open fractures based on confidence indicators for the rock outside of deformation zones in all boreholes. The percentiles indicate the percentage of all open or partly-open fractures. KLX01† based on rock fracture engineering data from Laxemar.

Borehole	Rock domain	P10 (all)	P10 (open)	$P10_{corrected}$ (open)	$P10_{corrected}$ (open/certain)	$P10_{corrected}$ (open/certain or probable))
KSH01A	B (not DZ)	22.4	2.24	3.8	0.34 (8.8%)	0.80 (21.1%)
	C (not DZ)	5.9	1.38	2.43	0.33 (14%)	0.72 (29%)
	DZ	14.7	4.85	7.7	1.06 (13.8%)	2.16 (28.0%)
KSH02	B (not DZ)	11.7	3.69	5.75	0.2 (5%)	0.6 (12%)
	DZ	14.8	5.13	8.2	0.57 (6.9%)	1.44 (17.7%)
KSH03A	A	4.0	1.69	3.05	0.23 (7.6%)	0.31 (10.3%)
	C	17.0	5.49	8.44	1.84 (21.8%)	2.26 (26.8%)
KAV01	A (not DZ)	4.7	2.68	4.9	3.75 (76.6%)	3.75 (76.6%)
	DZ	10.5	6.31	11.54	10.04 (87.0%)	10.05 (87.1%)
KLX02	A (not DZ)	3.1	2.20	4.02	2.93 (72.8%)	2.93 (73.0%)
KLX01†	A (not DZ)		4.51	NA	NA	NA

Further, a summary of the percentage of fractures in each orientation set is given in Table 3-14 for all boreholes. This demonstrates a reasonable level of consistency between the boreholes and rock domains with the HZ set (dip < 60°) dominant having 44–67% of the open fracture intensity. The EW and NW sets are the next most frequent, followed by NE and NS being the least frequent.

Table 3-18. A summary of the percentage of $P10_{corrected}$ of each orientation sets for all open and partly-open fractures for the rock outside of deformation zones in all the boreholes.

Borehole	Rock domain	NE	EW	NW	NS	HZ
KSH01A	B (not DZ)	5.8%	15.1%	11.1%	6.4%	61.7%
	C (not DZ)	7.5%	16.6%	14.1%	5.2%	56.6%
KSH02	B (not DZ)	7.6%	13.3%	8.2%	5.8%	65.0%
KSH03A	A	11.7%	20.6%	17.9%	6.3%	43.6%
	C	10.6%	9.51%	6.9%	6.4%	66.6%
KAV01	A (not DZ)	17.9%	16.7%	10.5%	3.1%	51.8%
KLX02	A (not DZ)	11.7%	16.0%	11.3%	7.3%	53.7%

3.5 Analysis of hydrogeological data

To help interpret the flow data measured by the Posiva Flow Log (PFL), borehole fractures that correspond most closely to flow anomalies identified in the PFL tests have been selected. The orientations of poles to these fractures seen are then plotted on a stereonet as an indication of preferred orientations for high flow features. For each anomaly the fracture (or fractures) most ‘consistent’ with the anomaly is (are) selected. Consistency is judged primarily on the distance between the depth of the fracture and the depth of the anomaly. However, a fracture slightly further away may be preferred if it is has a higher open confidence indicator. If there is no unique fracture associated with an anomaly, then the poles of all the fractures are used. Mostly there is one consistent fracture, but sometimes there are 2–4 equally consistent fractures. The fractures are coloured on the stereonet according to the magnitude of the transmissivity associated with the anomaly.

3.5.1 KSH01A, Orientation of flowing fractures

KSH01A has a strong signature for fractures with strikes between EW and NW, or sub-horizontal (Figure 3-29).

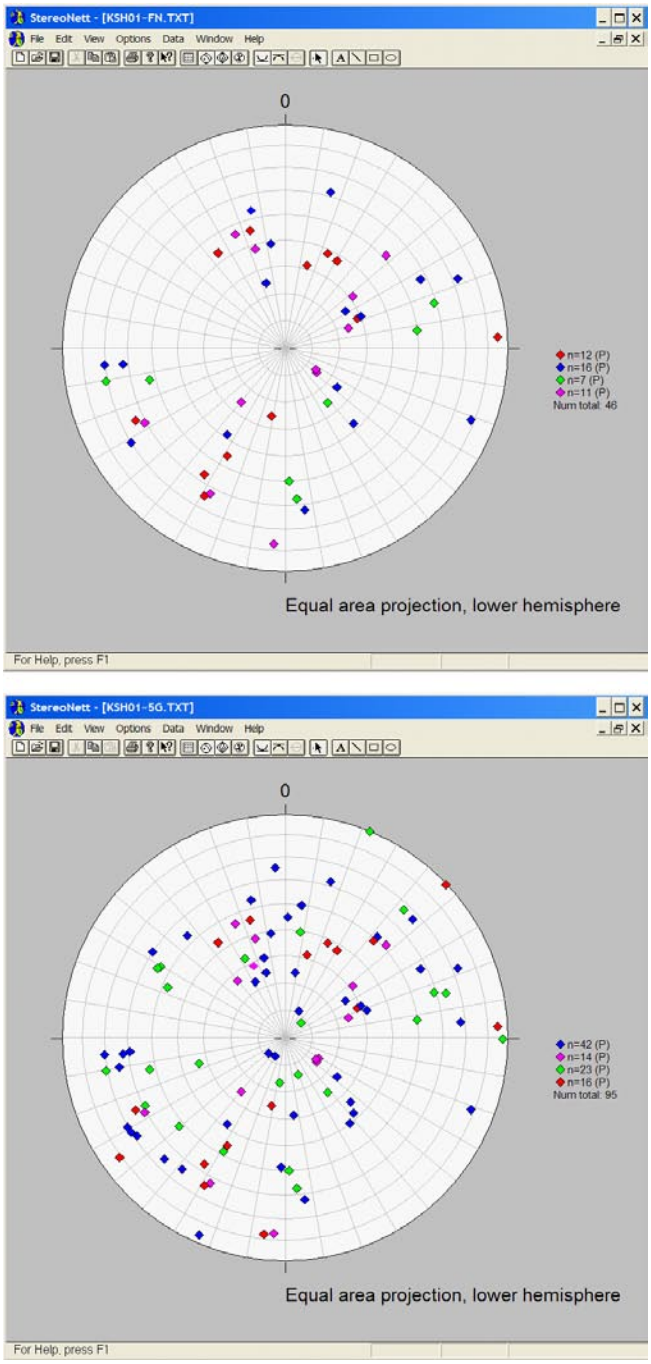

Figure 3-29. *Orientations of the pole to fractures associated with PFL anomalies in KSH01A for all fractures outside of DZs (top), and all fractures (bottom). Fractures are coloured by the PFL anomaly transmissivity magnitude: $T > 10^{-7}$ m/s (♦), $10^{-7} > T > 10^{-8}$ m/s (♦), $10^{-8} > T > 10^{-9}$ m/s (♦), $10^{-9} > T > 10^{-10}$ m/s (♦).*

3.5.2 KSH02, Orientation of flowing fractures

KSH02 shows a majority of fractures with a strike in the NW quadrant or sub-horizontal (Figure 3-30).

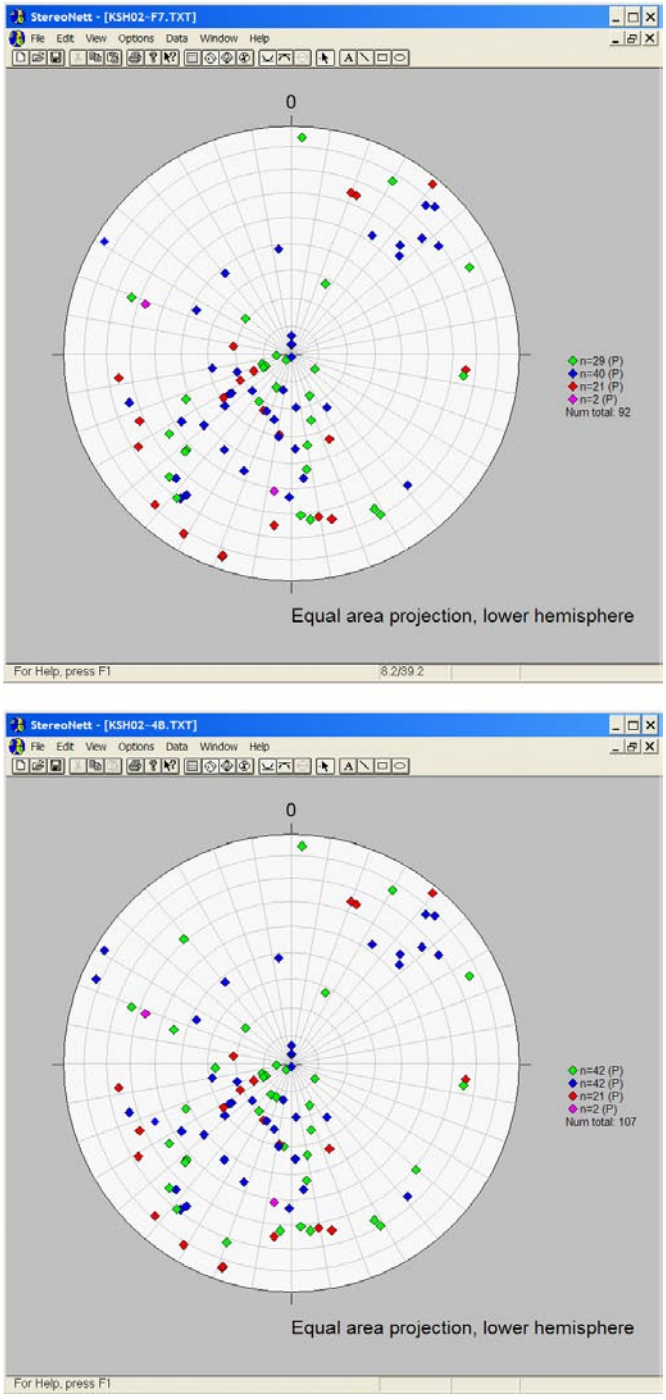

Figure 3-30. *Orientations of the pole to fractures associated with PFL anomalies in KSH02 for all fractures outside of DZs (top), and all fractures (bottom). Fractures are coloured by the PFL anomaly transmissivity magnitude: $T > 10^{-7}$ m/s (♦), $10^{-7} > T > 10^{-8}$ m/s (♦), $10^{-8} > T > 10^{-9}$ m/s (♦), $10^{-9} > T > 10^{-10}$ m/s (♦).*

3.5.3 KAV01, Orientation of flowing fractures

KAV01 shows almost the opposite picture, with many fractures showing a strike to the NE. Even if sealed fractures are removed from KAV01, as well as those fractures with measured 'uncertain' PFL data, this NE strike of the fractures is still apparent. Noting the principal stress in the area is NW-SE /4, pg. 200, for example/, then one possible interpretation is that KSH01A and KSH02 see the effect of the regional stress whereas KAV01, which cuts through an ENE extensive regional zone (see Figure 3-33) which may modify the stress locally so that the maximum stress is sub-parallel to the zone. Boreholes KSH03A and KLX02 have no measured PFL data.

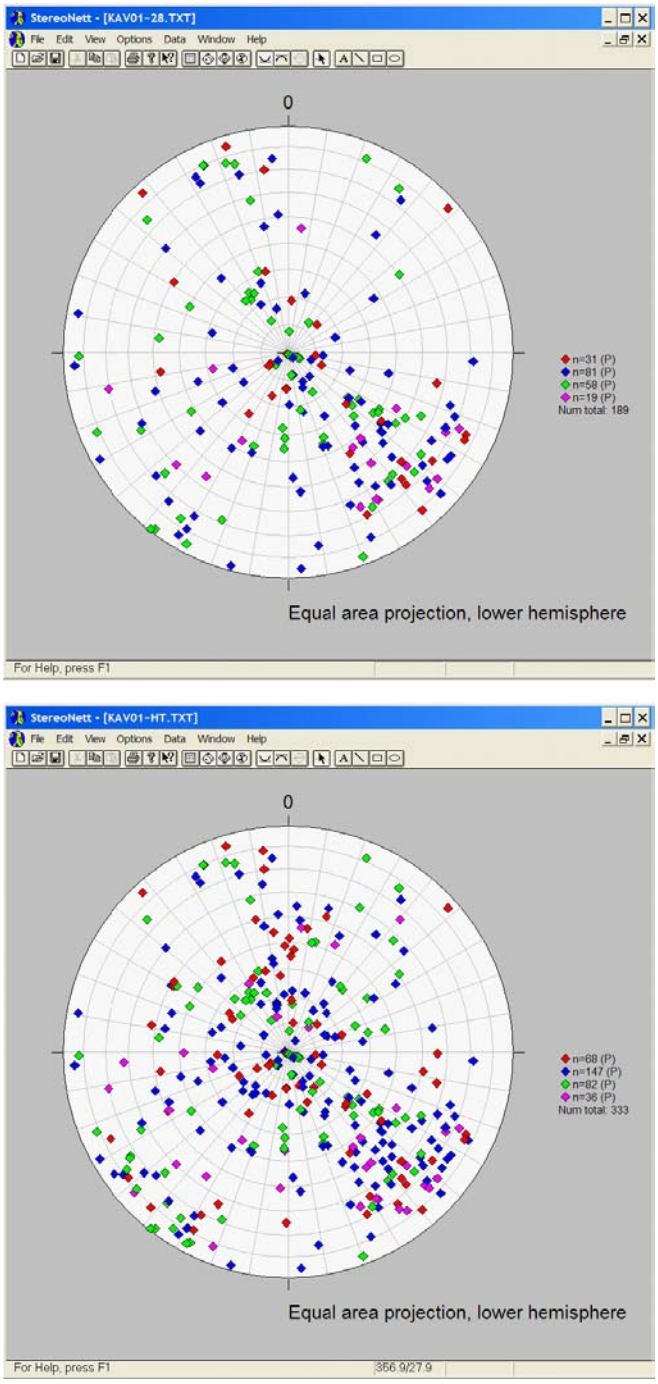

Figure 3-31. *Orientations of the pole to fractures associated with PFL anomalies in KAV01 for all fractures outside of DZs (top), and all fractures (bottom). Fractures are coloured by the PFL anomaly transmissivity magnitude: $T > 10^{-7}$ m/s (♦), $10^{-7} > T > 10^{-8}$ m/s (♦), $10^{-8} > T > 10^{-9}$ m/s (♦), $10^{-9} > T > 10^{-10}$ m/s (♦).*

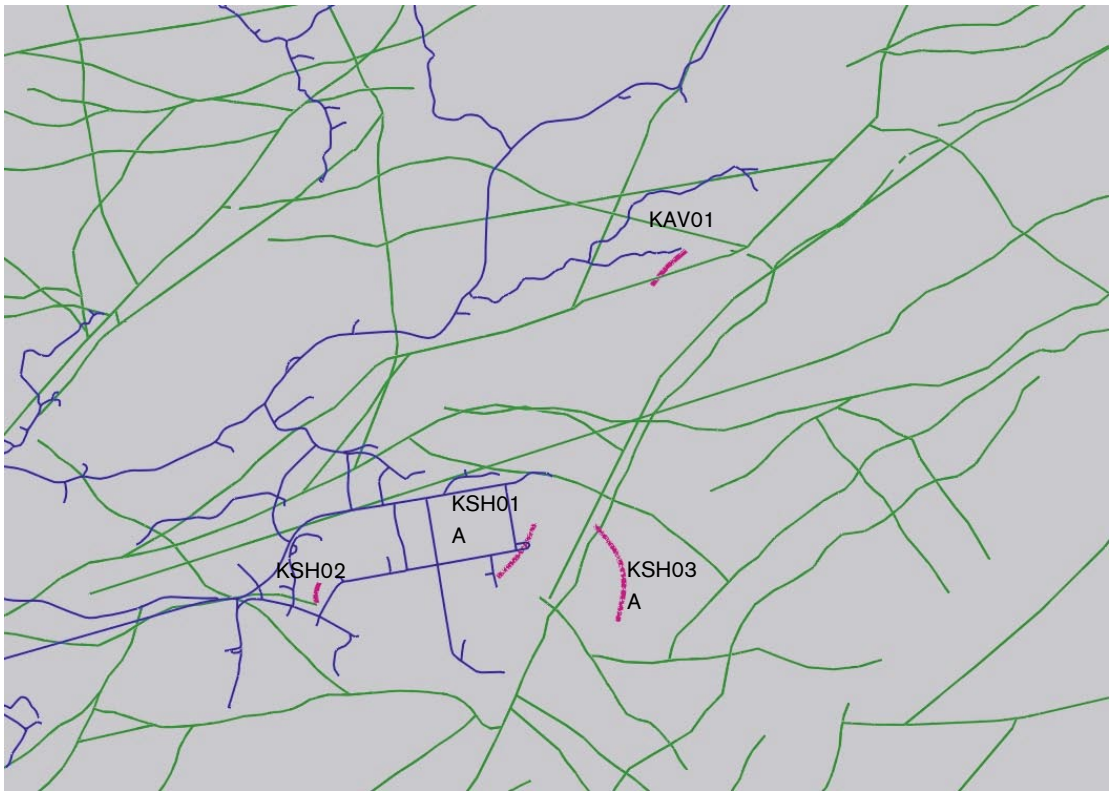

Figure 3-32. *Locations of boreholes (pink) relative to the deterministic fractures zones (green) identified in the regional geological model (sliced at a depth of 500 m), and road system in the Simpevarp sub-area.*

3.6 Simulations for assessment of DFN properties

The next steps are firstly to generate several realisations of the Hydro-DFN model of all the open fractures around KSH01A and check the predicted frequency of open fractures with the observation to check whether open $P10_{corrected}$ is an accurate estimate of P32; secondly to simulate the PFL data to investigate alternative transmissivity distributions.

3.6.1 DFN simulations, KSH01A

A model of 800 m vertical extent was used in the simulations as the approximate length of borehole for which there is PFL data is 700 m and a 50 m extension above and below the borehole is added to have a gap between the borehole and boundary conditions. Appropriate vertical boundaries are uncertain since it is not clear what the zone of influence is for the PFL test. The duration of pumping lasts several days, so the zone of influence is likely to be substantial. A 100 m radius region was used.

Using the GeoDFN as a basis, seven sets of fractures were generated: BGNE, BGNW, BGNS are all small-scale fractures with log-normal length distribution; NE, EW, NW and HZ are on a range of scales having a power-law length distribution. N.B. the orientation of the background fracture set, BGNW, has been updated in the final S1.2 GeoDFN and it now falls within the classification of EW, hence it is denoted BGNW (EW) in this report. Small-scale fractures (0.5 m to 10 m) were only generated with centres with a 10 m diameter region around the borehole. Larger fractures (> 10 m) were generated such

that they would span the whole model of 100 m radius. For simplicity, the whole borehole was assumed to be of the most prevalent rock domain, i.e. Rock Domain C. The open $P10_{corrected}$ for the various sets was taken from Table 3-6 with some sets being split between small (log-normal) sets and larger (power-law) sets according to the relative percentages reported in the GeoDFN. A detailed description of the DFN parameters used is given in Table 3-19.

Table 3-19. Description of DFN parameters used for simulation of fractures in KSH01A. Orientation set are numbered: 1 = NE, 2 = EW, 3 = NW, 4 = BGNE, 5 = BGNS, 6 = BGNW (EW), 7 = HZ.

Rock domain	Fracture set name	Orientation set pole: (trend, plunge), concentration	Length model, Constants: lognormal (μ, σ), power-law (L_0, k_r) (m)	Intensity, (P_{32}), valid length interval: L_0, L_{max} (m^2/m^3)	Relative intensity of P32	Transmissivity model Eq no, constants $T(m^2/s)$
C	NE	1: (128, 11)16.5	1: (L_0, k_r) (0.5,2.58)	2.43, (0.5, 1,000)	1: 0.031	N/A
	EW	2: (182, 7) 10.3	2: (L_0, k_r) (0.5,2.80)		2: 0.097	
	NW	3: (237, 6) 23.3	3: (L_0, k_r) (0.5,2.87)		3: 0.052	
	BGNE	4: (128, 11)16.5	4: (μ, σ) (–0.58,0.6)		4: 0.030	
	BGNS	5: (88, 2) 16.1	5: (μ, σ) (–0.58,0.88)		5: 0.052	
	BGNW(EW)	6: (182, 7) 10.3	6: (μ, σ) (–0.58,0.63)		6: 0.037	
	HZ	7: (0, 81) 4.8	7: (L_0, k_r) (0.5,2.6)		7: 0.624	

Table 3-20. Comparison of predicted open fractures in 721 m (700 m vertically) section of KSH01A for 5 realisations.

Case	Number of open fractures	P10
L_0 = 0.076 m realisation 1	1,006	1.39
L_0 = 0.5 m realisation 1	956	1.33
L_0 = 0.5 m realisation 1	969	1.34
L_0 = 0.5 m realisation 1	952	1.33
L_0 = 0.5 m realisation 1	935	1.30
L_0 = 0.5 m realisation 1	956	1.33
Average L_0 = 0.5 m	927	1.32
Observation	994	1.38

In order to check the interpreted open $P10_{corrected}$, 5 realisations of the DFN were calculated for the full 100% of open and partly-open fractures with L_0 in the power-law distributions set to 0.5 m. A single realisation was computed with L_0 = 0.076 m to demonstrate the relative insensitivity in the predicted P10 to the choice of L_0. Note $L_{min} = L_0$ in these cases, so there is no truncation of the power-law distribution when L_0 = 0.5 m. If a length truncation of L_{min} = 0.5 m is applied in the case with L_0 = 0.076 m then the P10 is reduced by a factor of about one third. The results are shown in Table 3-20. The predicted open P10 in the DFN simulations is about 96% of that observed, and considered sufficiently good as to not require adjustment to match exactly.

One realisation of the DFN model is shown in Figure 3-33. The minimum length used here was 0.5 m for all sets, and gave about 145,000 fractures in total. The smaller scale fractures of lengths 0.5 m to 10 m generated in a 10 m diameter region around KSH01A is shown in Figure 3-34. In Figure 3-35 (close-up) only the fractures intersecting the borehole are shown. This demonstrates how much the large stochastic fractures dominate what is seen in the borehole, since although they are of low intensity, volumetrically, their extent means they are preferentially sampled by an orthogonal borehole.

A further check was to compare the percentage of fractures intersecting the borehole belonging to each set between the core data and each of five realisations, see Table 3-21. The agreement between the simulations and the observation is clearly good, and confirms that the general approach to estimating P32 based on the Terzaghi corrected P10 and the fitted Fisher distributions captures the core data.

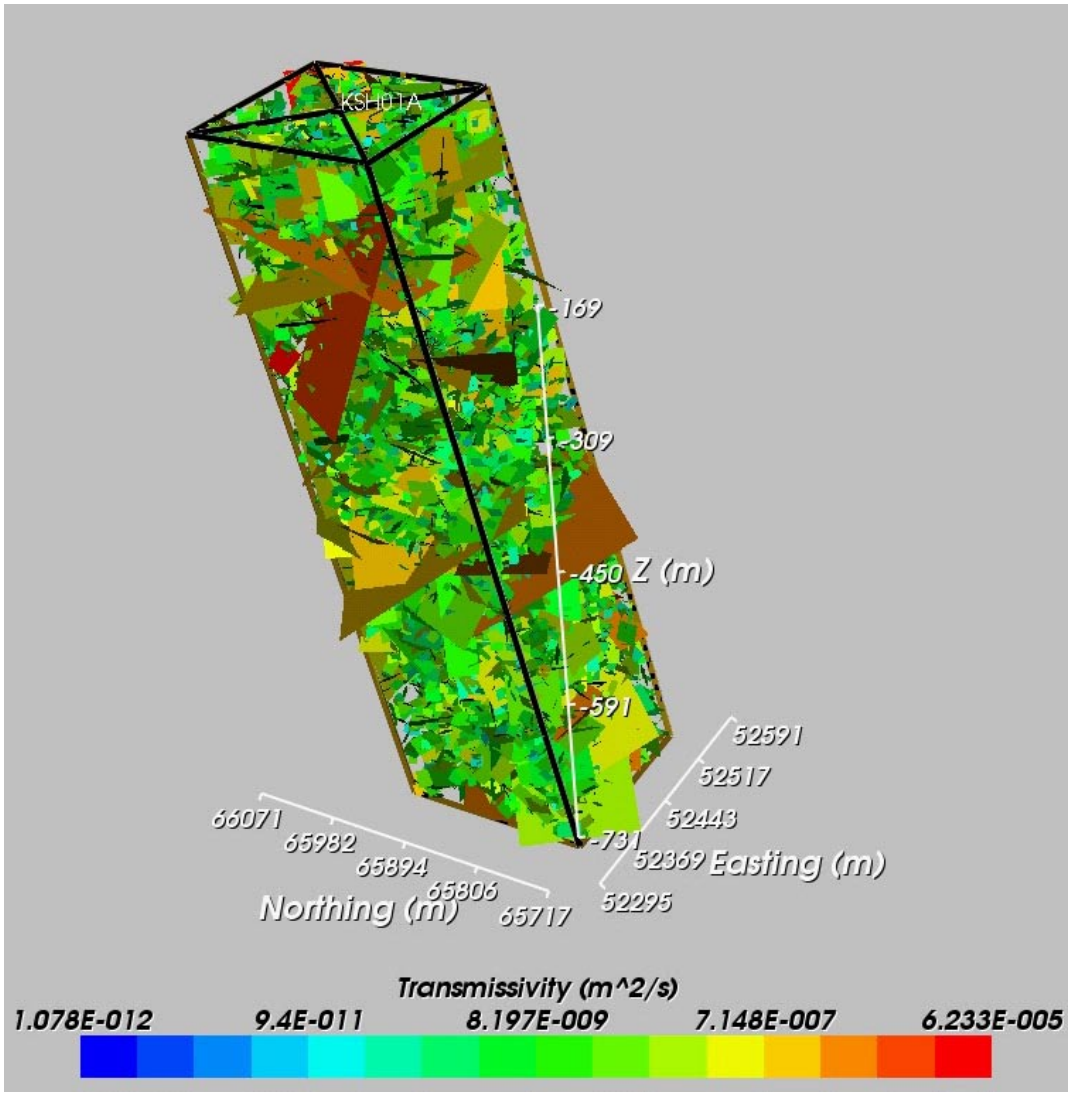

Figure 3-33. *DFN realisation for a 100 m radius region around the inclined borehole KSH01A. All fractures (145,000) are shown and coloured by log (T) (in this case T is lognormally distributed and not correlated to L).*

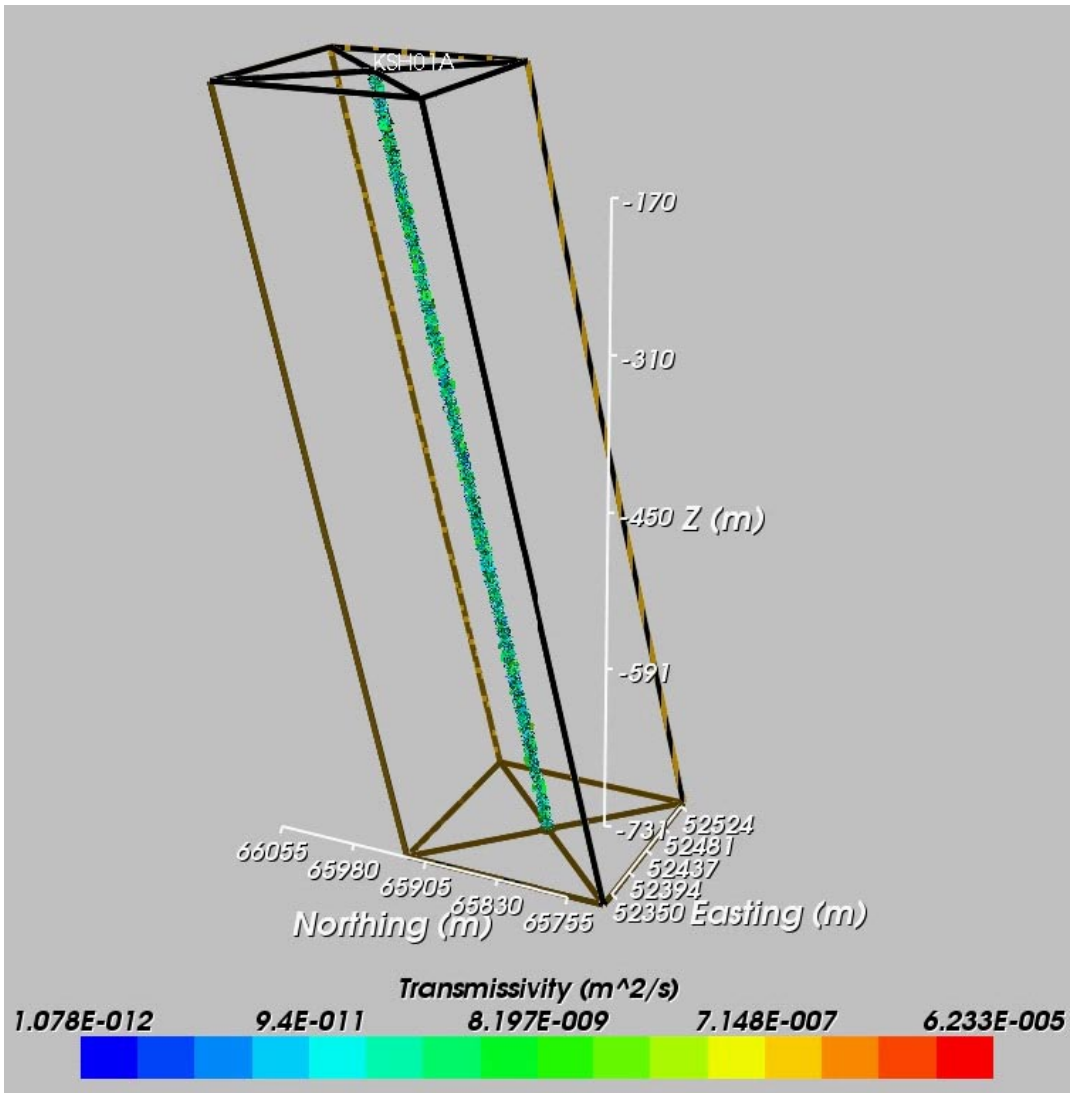

Figure 3-34. *Small-scale fractures intersected by borehole KSH01A within a 10 m diameter region around the borehole. Fractures are coloured by log (T) (in this case T is lognormally distributed and not correlated to L).*

Figure 3-35. *Close-up of fractures intersected by borehole KSH01A to show different scales of fractures seen in borehole. Fractures are coloured by log (T) (in this case T is lognormally distributed and not correlated to L).*

Table 3-21. Comparison of relative $P10_{corrected}$ density in borehole KSH01A between that observed in Rock Domain C and in the 5 realisations.

Set	Boremap data	Realisation 1% P10	Realisation 2% P10	Realisation 3% P10	Realisation 4% P10	Realisation 5% P10
NE	4.2%	3.4%	3.1%	3.2%	2.6%	3.5%
EW	8.9%	8.6%	8.3%	9.6%	7.8%	8.7%
NW	6.3%	6.3%	6.2%	5.7%	5.6%	6.3%
NS	2.9%	2.6%	2.5%	3.0%	1.3%	2.0%
HZ	77.8%	79.7%	81.3%	79.2%	83.3%	82.2%

The final comparison with field data was to simulate trace maps on a horizontal section with the outcrops. The model was sliced horizontally and the fracture intensity calculated for the plane to obtain P21 (total fracture length per unit area). Fracture traces were calculated on a horizontal square of side 20 m, a similar area to that of the outcrops. Three different scenarios were considered:

- L_0 equal to the borehole diameter (0.076 m).
- Fractures distributed with L_0 of 0.076 m, but all fractures less than L_{min} = 0.5 m discarded.
- L_0 equal to that measured in the outcrop (0.5 m).

The P32 used in these simulations is based on the $P10_{corrected}$ for open and partly-open fractures. Unfortunately, it is difficult to distinguish between open and sealed fractures on an outcrop, or at least in a way consistent with the boreholes due to alteration at the surface. Hence, it is difficult to make a quantitative calibration of the model against the outcrop, and so the comparison is only made in a qualitative approach. Table 3-17 suggests a ratio of around 2–3 between all fractures and open fractures in the boreholes. Hence, as an approximation we might expect the P21 (open) predicted by the model to be around one third to one half that seen on the outcrops. The figures for the simulations can be seen in Figure 3-36 to Figure 3-38. The outcrops that are nearest to the location of KSH01A are: ASM000206 (P21 = 3.2 m/m^2), and ASM000205 (P21 = 5.0 m/m^2) (Figure 3-39 and Figure 3-40). A minimum fracture length around 0.5 m was used in the outcrop mapping, and hence it is assumed that the P21 values quoted are based on a length truncation of L_{min} = 0.5 m.

It can be seen that using the borehole diameter for L_0 gives many small fractures when compared to the outcrop data (Figure 3-36). The simulated P21 (open) for L_0 = 0.076 m (borehole) is 1.78 m/m^2, but about 66% of this is distributed in fractures with traces less than the outcrop minimum length of 0.5 m as seen in Figure 3-37. The P21 (open) for fractures with length greater than 0.5 m, i.e. L_{min} = 0.5 m, is only 0.60 m/m^2, or about one third of the total, and so using L_0 = 0.076 m gives a P21 in the model about 5–10 less than seen in the outcrop. However, using L_0 = 0.5 m gives a much more realistic simulation of the outcrop data (Figure 3-38; P21 (open) for L_0 = 0.5 m is 1.66 m/m^2). The outcrop P21 (all) is indeed around 2–3 times that for the simulated P21 (open) with L_0 = 0.5 m, and the length distributions shown on the cross-section are qualitatively similar.

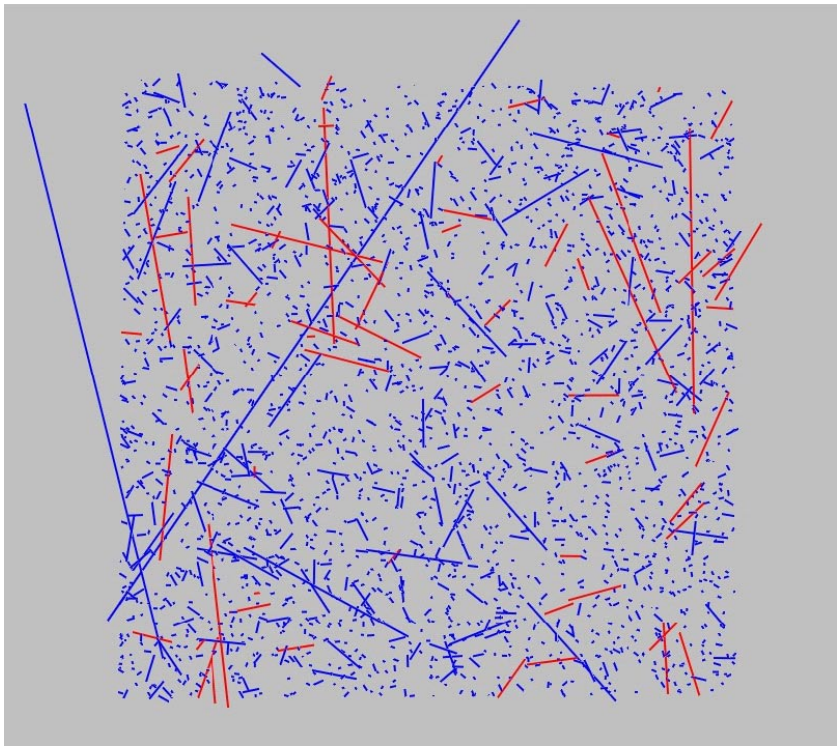

Figure 3-36. *A horizontal slice through the simulation based on data from KSH01A, using a fracture distribution with L_0 = 0.076 m, the borehole diameter.*

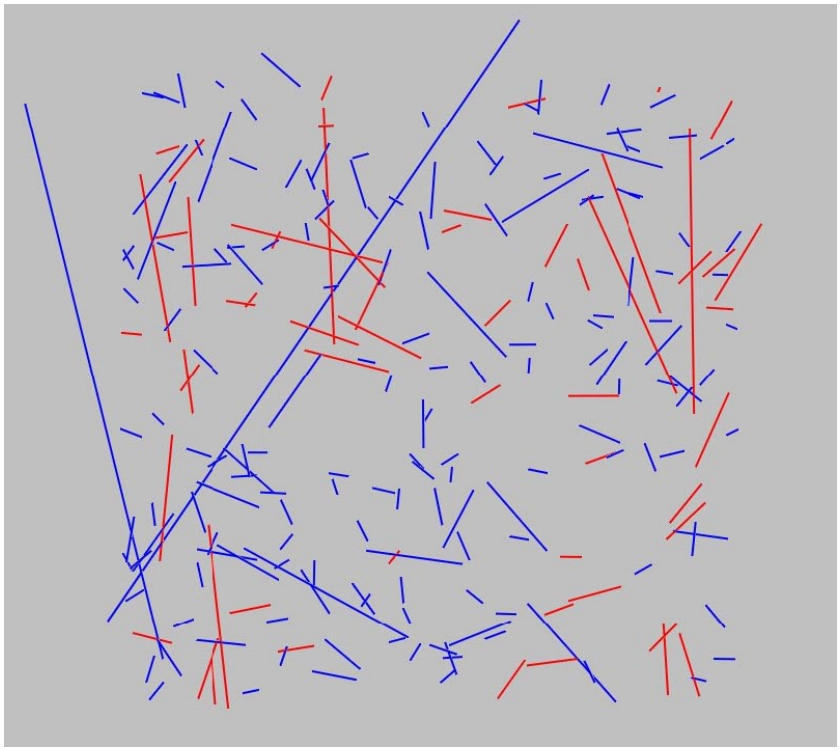

Figure 3-37. *A horizontal slice through the simulation based on data from KSH01A, using a fracture distribution with L_0 = 0.076 m, the borehole diameter, but discarding small fractures L_{min} = 0.5 m.*

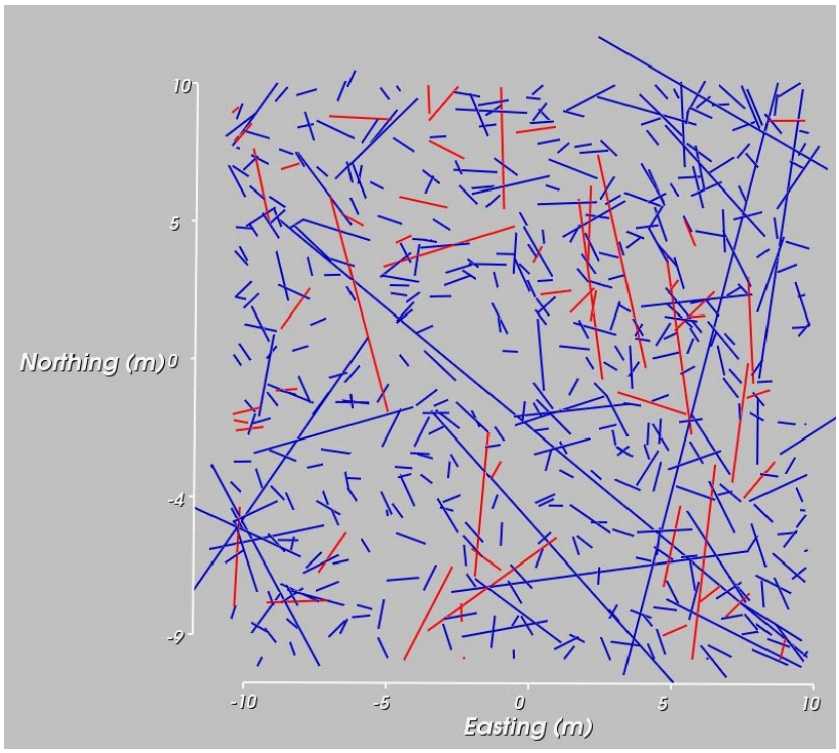

Figure 3-38. *A horizontal slice through the simulation based on data from KSH01A, using L_0 = 0.5 m, approximately the minimum fracture length measured in the outcrop.*

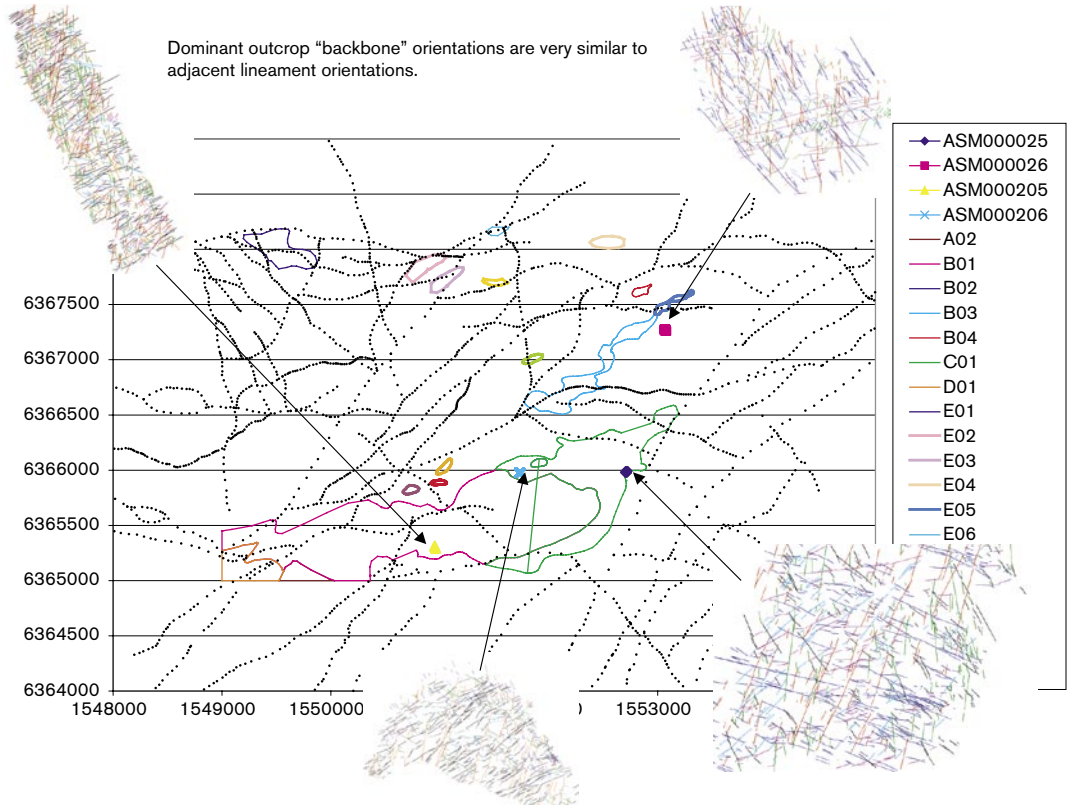

Figure 3-39. *Locations of fracture outcrop maps (from Simpevarp 1.1 /4/).*

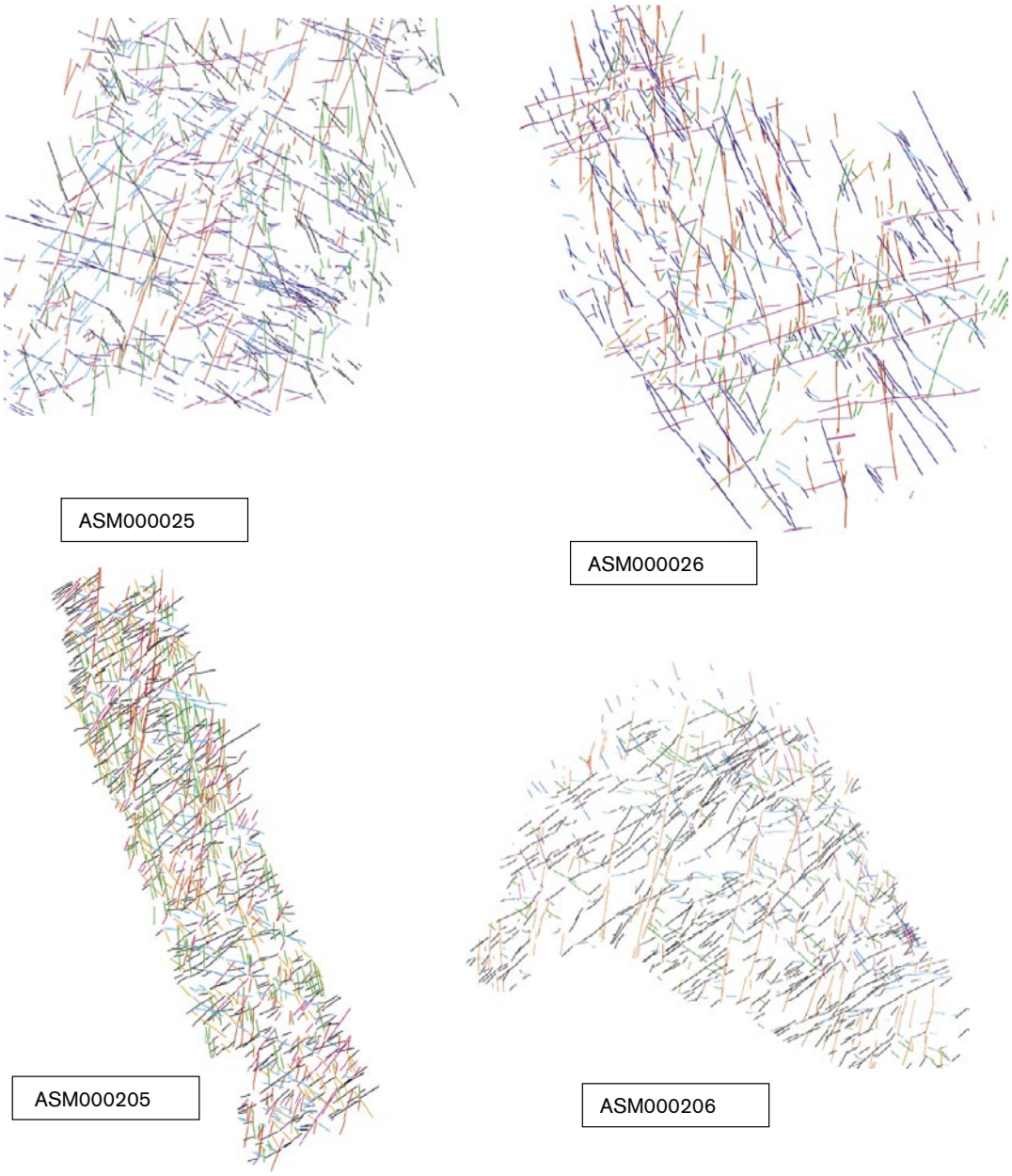

Figure 3-40. *Distribution of fracture traces measured in the outcrop (from Simpevarp 1.1 /4/).*

3.6.2 DFN simulations, KSH02

A 900 m length of vertical borehole was used in the simulation since this is approximately the length of KSH02 for which there is measured PFL data. The model domain is 1,000 m high, therefore extending 50 m above and below the vertical borehole. The model region has a 100 m radius.

Based on the GeoDFN classification, the same seven classes of fracture sets as that derived for KSH01A were used. The main fracture sets were generated on a range of scales with a power-law length distribution. The small scale fractures (0.5 to 10 m) were generated with fracture centres with a 10 m diameter around the modelled borehole. Larger scale fractures (10 to 1,000 m) were generated such that they would span the whole model (100 m radius). The input data to the DFN simulations are tabulated in Table 3-22.

Table 3-22. Description of DFN parameters used for simulation of fractures in KSH02. Orientation set are numbered: 1 = NE, 2 = EW, 3 = NW, 4 = BGNE, 5 = BGNS, 6 = BGNW (EW), 7 = HZ.

Rock domain	Fracture set name	Orientation set pole: (trend, plunge), concentration	Length model, Constants: lognormal (μ, σ), power-law (L_0, k_r) (m)	Intensity, (P_{32}), valid length interval: L_0, L_{max} (m^2/m^3)	Relative intensity of P32	Transmissivity model Eq no, constants $T(m^2/s)$
B	NE	1: (308, 3)13.5	1: (L_0, k_r) (0.5,2.58)	5.75, (0.5, 1,000)	1: 0.024	N/A
	EW	2: (1, 4) 9.0	2: (L_0, k_r) (0.5,2.80)		2: 0.056	
	NW	3: (236, 5) 10.8	3: (L_0, k_r) (0.5,2.87)		3: 0.056	
	BGNE	4: (308, 3)13.5	4: (μ, σ) (–0.58,0.6)		4: 0.023	
	BGNS	5: (273, 1) 12.2	5: (μ, σ) (–0.58,0.88)		5: 0.034	
	BGNW(EW)	6: (1, 4) 9.0	6: (μ, σ) (–0.58,0.63)		6: 0.021	
	HZ	7: (326, 85) 4.1	7: (L_0, k_r) (0.5,2.6)		7: 0.785	

Initially, the model was verified to check that the correct number of open and partly-open fractures intersecting the borehole had been generated (Table 3-23). The modelled P10 for each of the five realisations slightly overestimates the $P10_{measured}$, but all $P10_{modelled}$ values are within 7.5% of the expected value.

Table 3-23. Comparison of five realisations of $P10_{modelled}$ with $P10_{measured}$ for KSH02 ($P10_{measured}$ is 3.69).

Realisation	$P10_{model}$	$P10_{model}$ as a percentage of $P10_{boremap}$
1	3.72	100.83%
2	3.90	105.63%
3	3.84	104.04%
4	3.83	103.77%
5	3.96	107.34%
Mean	3.85	104.32%

A trace map for a horizontal section of side 20 m based on KSH02 and for the case with L_0 = 0.5 m is shown in Figure 3-41. For L_0 = 0.5 m the simulated P21 (open) is 3.31 m/m^2. For a case with L_{min} = 0.076 m (borehole) simulated P21 (open) is 3.87 m/m^2. The outcrop nearest to the location of KSH02 is ASM000205 (P21 = 5.0 m/m^2) (Figure 3-39 and Figure 3-40). Hence, again the simulated P21 (open) is about one half the outcrop P21 (all) suggesting a reasonable agreement with the field-data.

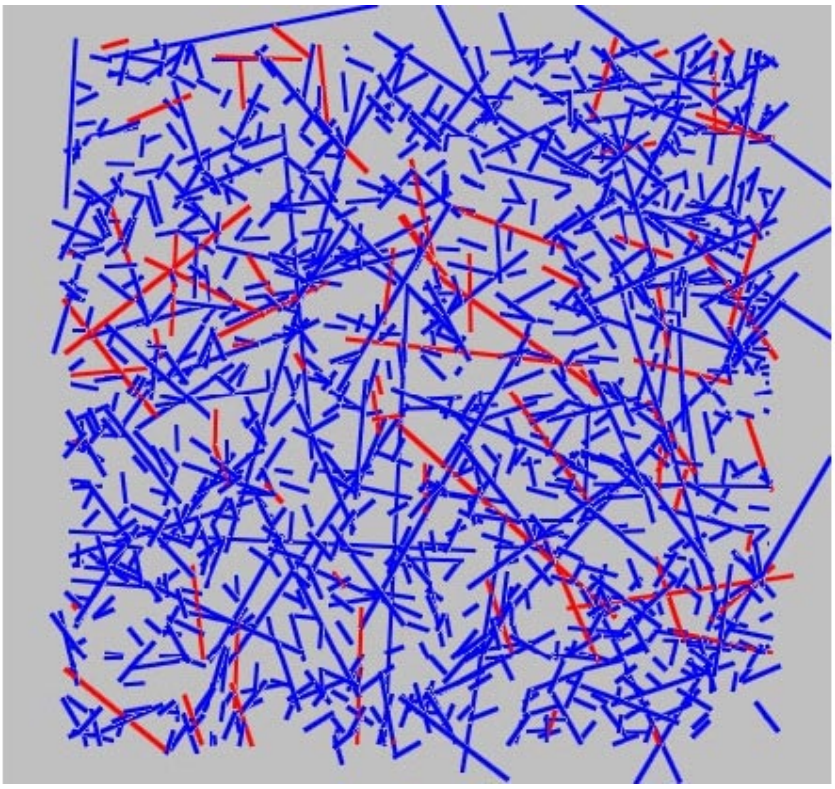

Figure 3-41. *A horizontal slice through the simulation based on KSH02, using L_0 = 0.5 m, approximately the minimum fracture length measured in the outcrop.*

3.7 Conditioning transmissivity against PFL data

Clearly the choice of statistical distribution used for transmissivity is a key assumption in interpreting the flow test-data. Three alternative transmissivity concepts were considered (as shown in Figure 3-4). For each of these concepts an associated set of parameters are required in the DFN simulations to give a match to the distribution of flow-rates, Q, seen in the PFL data. The reasons for matching Q rather T from the PFL data are firstly that it is Q that is measured not T (T is inferred from Q), and secondly a fracture intersecting the borehole may have a substantial T value, but zero Q because it is not connected to the network. Matching Q necessitates performing flow calculations for flow to the borehole. Matching T would be more straightforward, since all that is required is to generate a DFN model and get the T values for the fractures that intersect the borehole.

The flow simulations of the PFL tests were performed using the following assumptions:

- Zero head on the vertical and top boundary. The vertical boundaries were 100 m away from the borehole. The top boundary was 50 m above the top of the borehole. A no-flow boundary was used on the base of the model, 50 m below the base of the borehole.
- A uniform drawdown of 10 m was specified throughout the length of the borehole.
- Fractures smaller than 1 m were discarded to make the flow calculations tractable.
- Small fractures less than 10 m in length were generated only with a 10 m diameter region surrounding the borehole.
- The flow-rate Q (m^3/s) into the borehole was calculated and compared with Q from the PFL differencing.
- Possible skin effects are neglected.

Further, in matching Q the objective is only to match statistically the distribution of Q and not the actual positions where the flows occur or reproduce any clustering of flow anomalies as may arise around DZs, for example. Also, the minimum flow-rate associated with a PFL flow anomaly is about 4 10^{-9} m^3/s, which is a function of the detection limit, but it is assumed that there may exist smaller fractures flows not detected by this equipment. Indeed, the PSS tests indicate fractures with smaller flow-rates as these tests generally have a lower detection limit. Hence, we will aim to match the part of the Q distribution that has been measured, but not worry about the distribution of Q below the detection limit, apart from noting that PSS data indicates there should be one.

One important uncertainty that needs to be considered in matching the flow-tests is the percentage of open and partly-open fractures that contribute to flow given the uncertainties in their characterisation from core. Hence, as well as varying the T parameters, we also vary the percentage of open $P10_{corrected}$ that is used.

Prior to matching the hydraulic simulations to the PFL anomaly data, the PFL data must be processed in two important ways:

1. Firstly, the actual drawdown in the boreholes is of the order of 10 m but varies considerably down the borehole, generally decreasing down the hole. Hence, the effective drawdown associated with the flow-rate measured from each anomaly is not constant, and so there is some bias. Since, we want to match Q as a distribution, it is important to remove this bias by renormalizing Q: $Q_{unbiased} = Q \times 10/\Delta h$, where Δh is the measured drawdown, and 10 m is the drawdown used in the simulations.
2. Secondly, for self-consistency if several PFL anomalies are associated with a deformation zone, then the Q values for the anomalies is amalgamated into a single data point since the DFN model conceptualises the deformation zones as single large stochastic fractures.

3.7.1 KSH01A transmissivity

The approach taken in the simulations was to perform flow simulations in a DFN model using NAPSAC. In NAPSAC, the connectivity between fractures, boreholes and boundaries is established and then flow is calculated through each fracture connected to the network using the finite-element method and applying Darcy's law. The flow rate into the borehole from each connected fracture intersecting the borehole is then derived. The steady-state head distribution was calculated using a Pre-Conditioned Conjugate Gradient (PCCG) iterative solver with a low convergence criterion due to the large heterogeneity in the DFN models. This gave a relative mass balance of around 10^{-7}. About quarter of a million nodes were used in the largest flow model. Figure 3-42 gives an example of the head distribution in a flow model. This is a case based on a correlated T distribution and with 30% of the open fractures that was found to give a good match to the PFL data. Here, fractures are coloured by the average head on the fracture. Most are red since we only see the fractures on the outside of the model and these are connected to the high head, 0 m, on the external boundaries. Fractures coloured grey show the fractures which do not carry flow since they are isolated from the network or dead-ends. They are coloured grey since there is no water in them, and hence no head can be calculated in them. The fractures connected to the borehole see the greatest drawdown, and Figure 3-43 shows only the fractures connected to the borehole or have a significant drawdown.

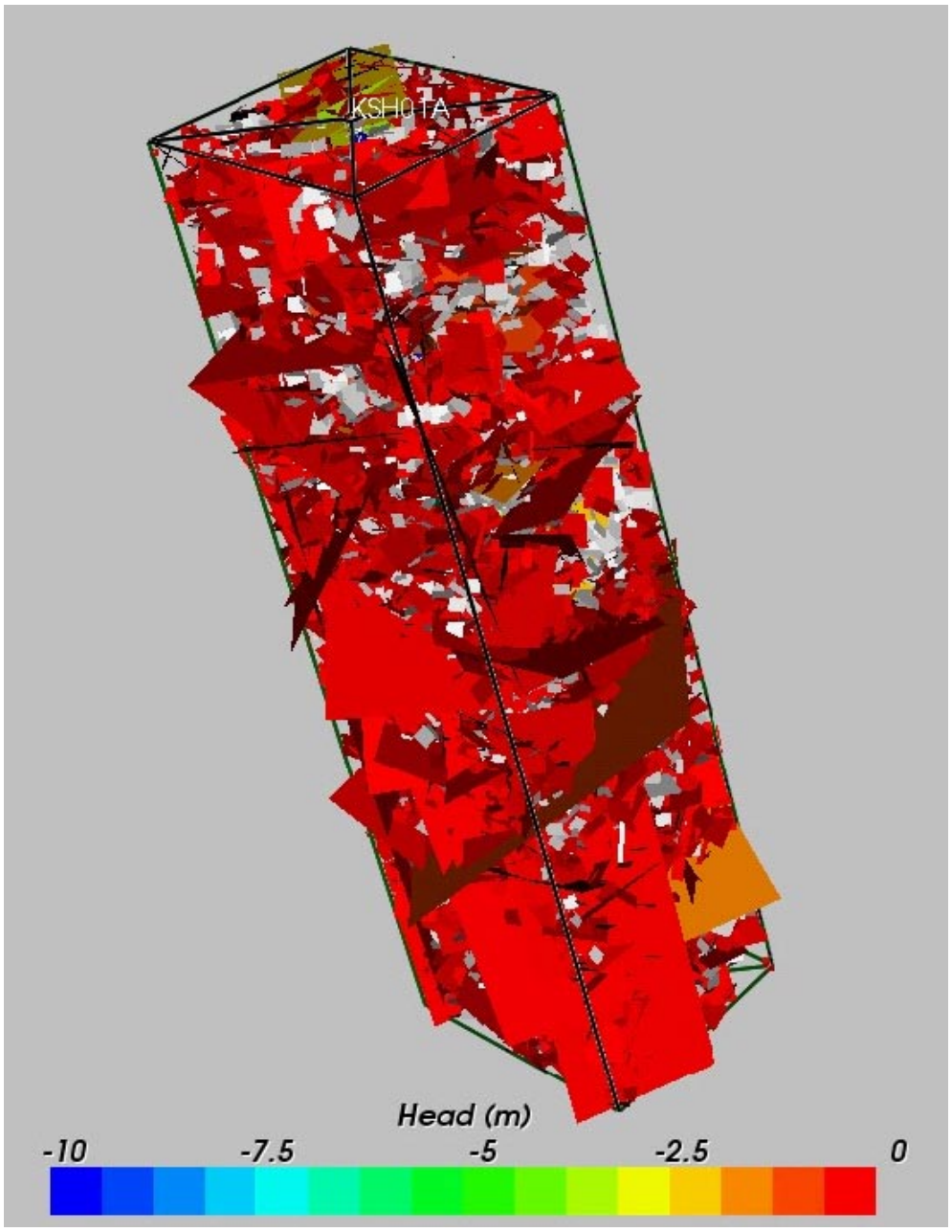

Figure 3-42. *DFN realisation for a 100 m radius region around KSH01A used in the PFL simulation. For the case shown here, it is assumed that only 30% of open and partly-open fractures are actually open. Also, only fractures with length greater than 1 m are used. Fractures are coloured by the average head on the fracture or grey where they are either isolated or dead-ends.*

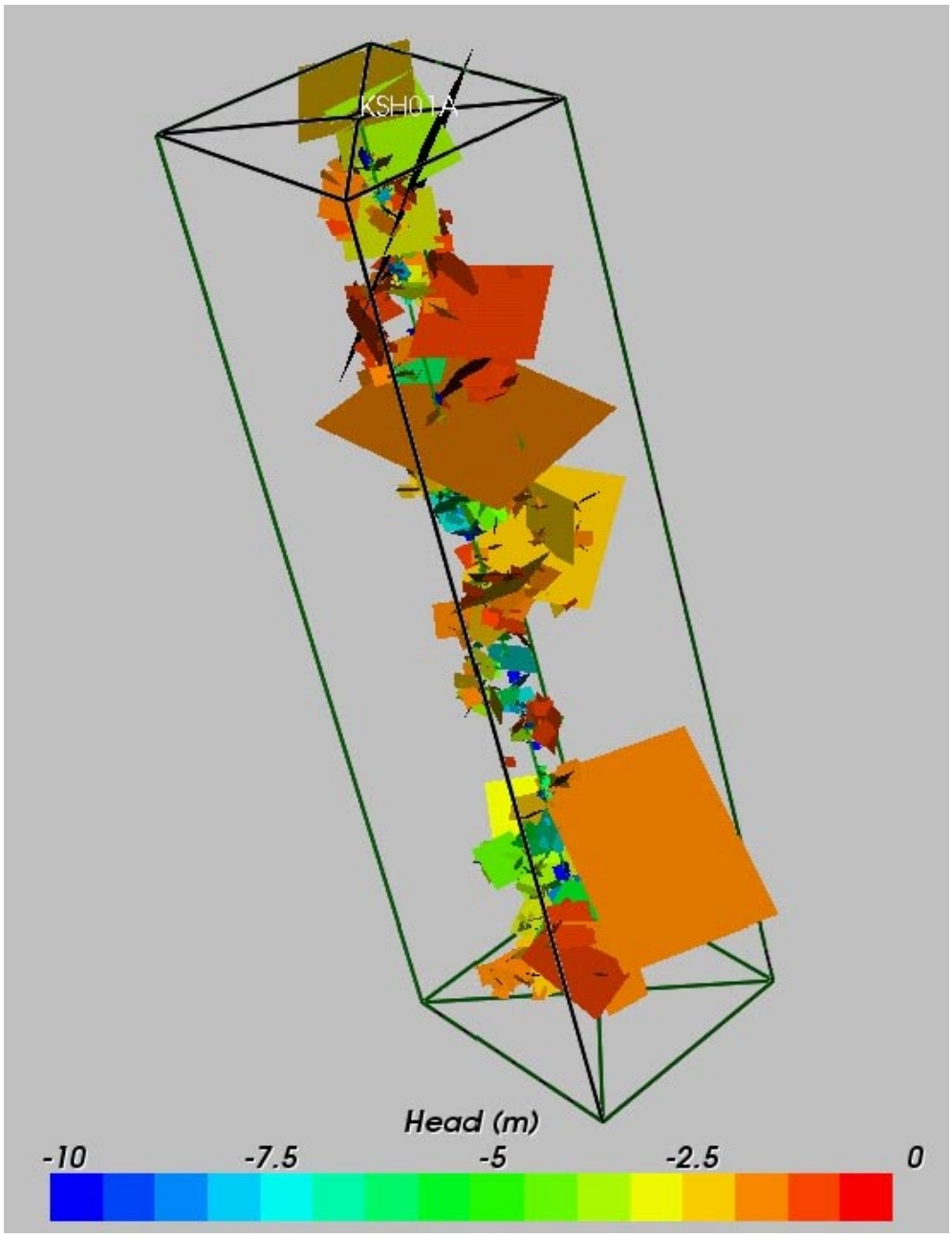

Figure 3-43. *DFN realisation as for Figure 3-42, but only showing the fractures around the borehole with a significant drawdown.*

The approach taken for fitting the parameters of the various T models was a trial and error process to try and match both the total flux (adjusted for drawdown variations) to the borehole and the histogram of Q values in the range above the detection limit. The total flux adjusted flux for KSH01A was 5.05×10^{-5} m^3 s^{-1}. These comparisons were performed in a stochastic manner by comparing 3 realisations (Monte Carlo simulation) with the observed PFL data. The issue of uncertainty in how many of the fractures identified as open or partly-open in the boremap actually contribute to flow was addressed by adjusting the overall P32 based on three cases:

1. Only certain open or partly-open fractures (14% for rock domain C).
2. Either certain or probable open or partly-open fractures (30% for rock domain C).

3. The majority of open or partly-open fractures based on the highest percentage of open/certain fractures seen in any borehole (77% in KAV01).

The values of P32 appropriate to these cases were based on the open $P10_{corrected}$ values given in Table 3-17. The results of the simulations are displayed as histograms of Q with a comparison of each case against the adjusted PFL Q data. The uncorrelated T model cases are shown in Figure 3-44 and Figure 3-45 for the cases based on taking either 30% (certain or probable) and 14% (certain) of open fractures, respectively. As can be seen the match is good for 30% of open fractures. The modelled distribution varies significantly between realisations, but the overall consistency is good for the range of Qs for which there is data. The model suggests quite a long tail to the distribution for small flow-rates below the detection limit. N.B. the histogram bin interval between Log (Q) = –8 to –7.5 is uncertain since it spans the detection limit. For 14% of open fractures, the connectivity of the network is poor and the flows occur only where the occasional large fractures spans the model domain. Hence, there is a clear lower limit on the percentage of open fractures that can be used to match the data. This lower limit is around 25% for KSH01A. For the uncorrelated T distribution it becomes hard to match the data for a greater percentage of open fractures, since the network become well connected and flows to the borehole become more homogeneous. The only way to get any sort of match is to have a very high variability in the fracture transmissivity (a standard deviation of perhaps 2 or 3 orders of magnitude).

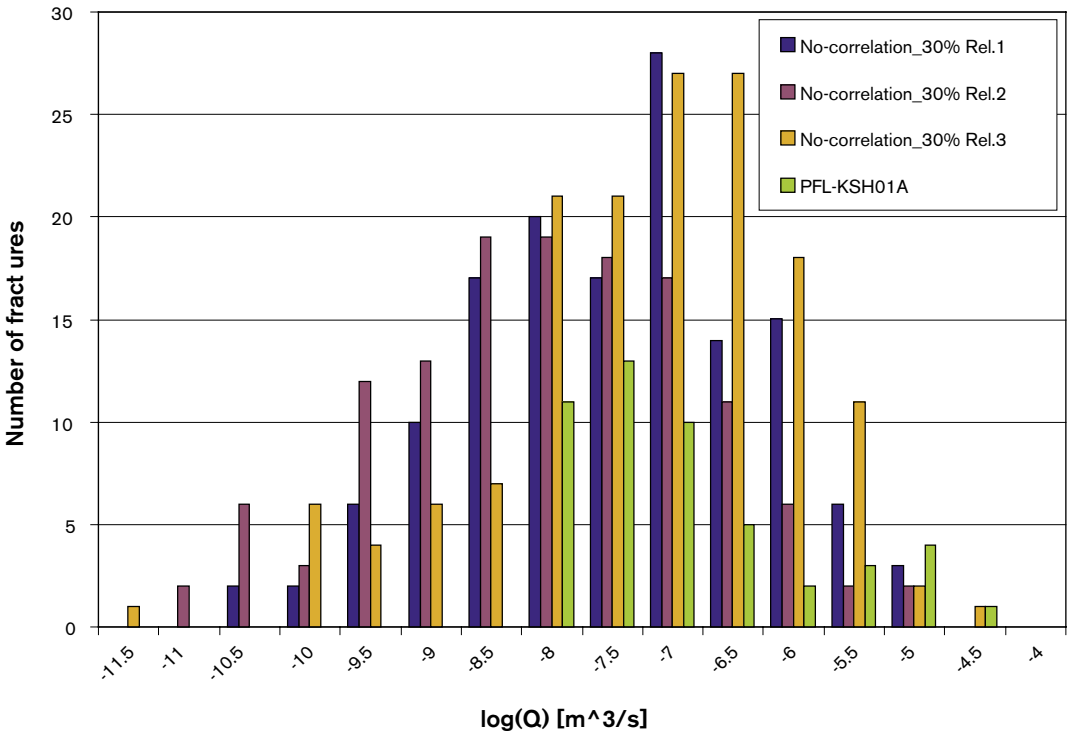

Figure 3-44. *Histogram of Log (Q), flow-rate to borehole, for 3 realisations of the uncorrelated T distribution compared to the PFL anomaly data for KSH01A. This case is based on both certain and probable open or partly-open fractures, 30% open.*

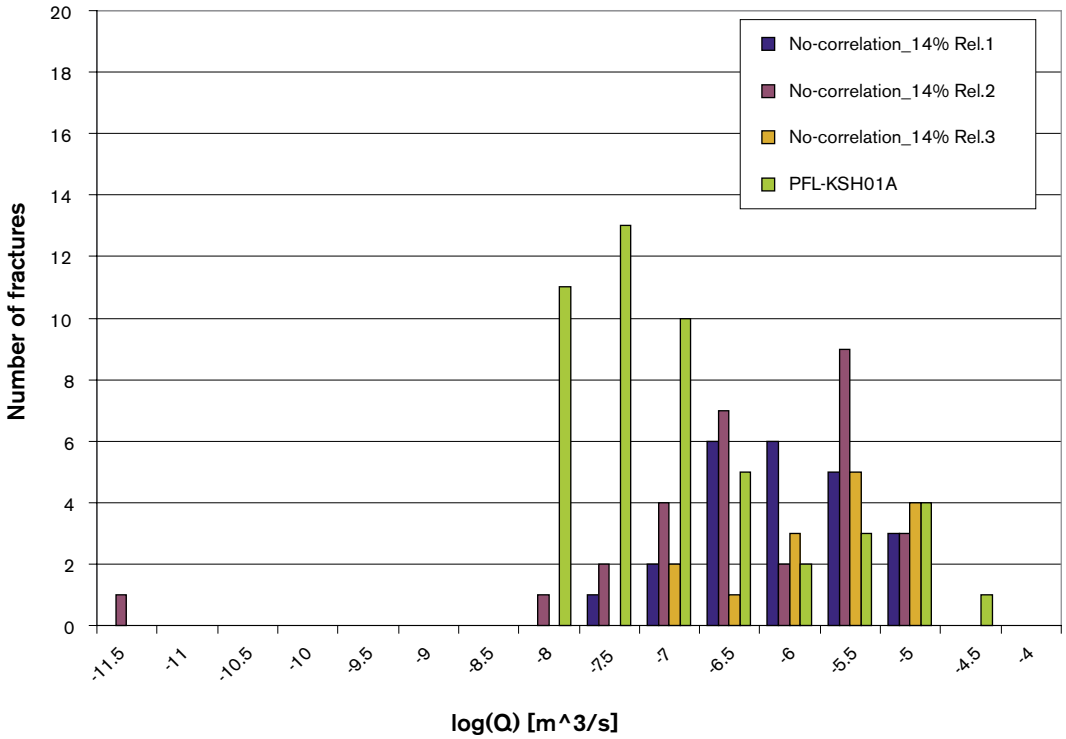

Figure 3-45. *Histogram of Log (Q), flow-rate to borehole, for 3 realisations of the uncorrelated T distribution compared to the PFL anomaly data for KSH01A. This case is based on only certain open or partly-open fractures, 30% of open.*

The results for the correlated cases are shown in Figure 3-46 and Figure 3-47 based on the certain or probable fractures, 30%, and a pessimistic case using the certain percentage from KAV01, 77%, respectively. Again, a good match is obtained for the case with 30% of open fractures and there is less variation between realisations. A match can also be obtained for the case with 77% of open fractures by using a much higher slope in the correlation function. However, since the network is very connected in this case, then there is a long tail to the distribution corresponding to flows from small fractures. It is not possible based on the PFL data alone to determine which of these cases is more realistic. This motivates using other forms of hydraulic data such as the double-packer test (PSS) data, which has a lower detection limit, to try and narrow the range of uncertainty.

Finally, a case is included for the semi-correlated transmissivity. This is implemented as a log-normal distribution with mean based on the correlation and a specified constant spread independent of L. Also, to avoid extreme T values the log-normal distribution is truncated at $\pm 2*\sigma$. For this realisation, the standard deviation in $\log_{10}$ was set as 1.0. The result is shown in Figure 3-48. Here, 5 realisations were used since there was more variation between realisations. Only the case with 30% of open fractures was considered. Some of the realisations, 4 and 5, reproduce the observed data very well. The DFN model parameters used for each of the cases is given in Table 3-24. For the uncorrelated case, the mean has to be decreased and the standard deviation increased as P32 is increased. For the correlated case, the coefficient, a, has to decreased and the exponent, b, has to be increased as P32 is increased.

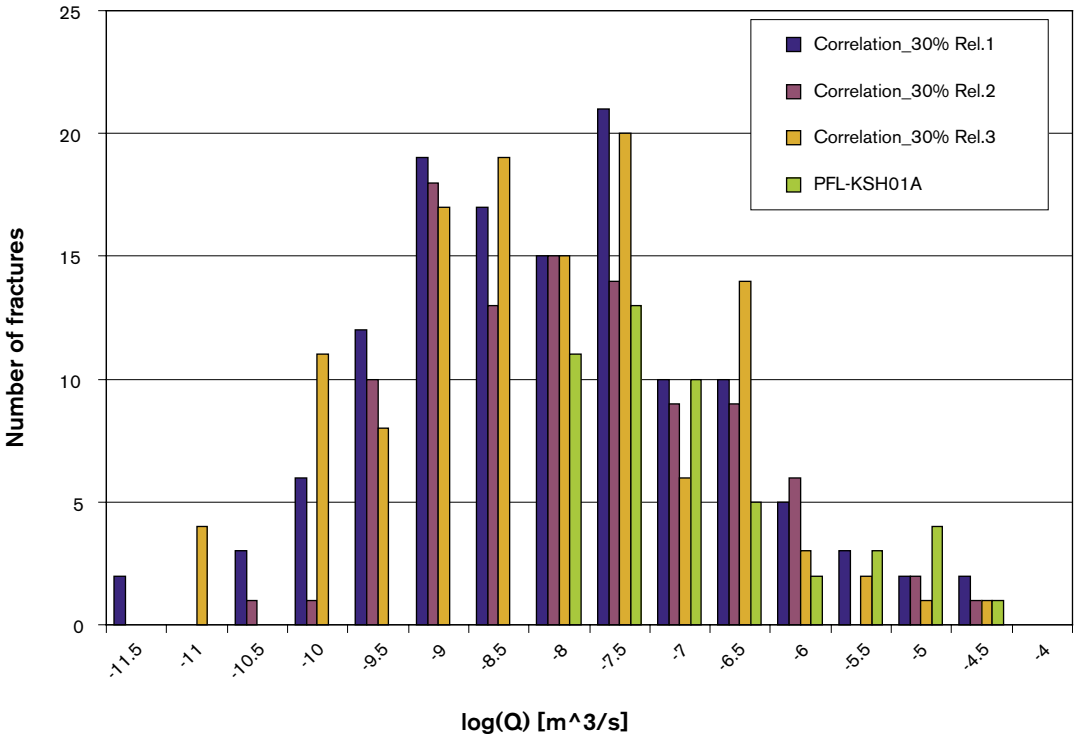

Figure 3-46. *Histogram of Log (Q), flow-rate to borehole, for 3 realisations of the correlated T distribution compared to the PFL anomaly data for KSH01A. This case is based on certain or probable (30%) of open or partly-open fractures.*

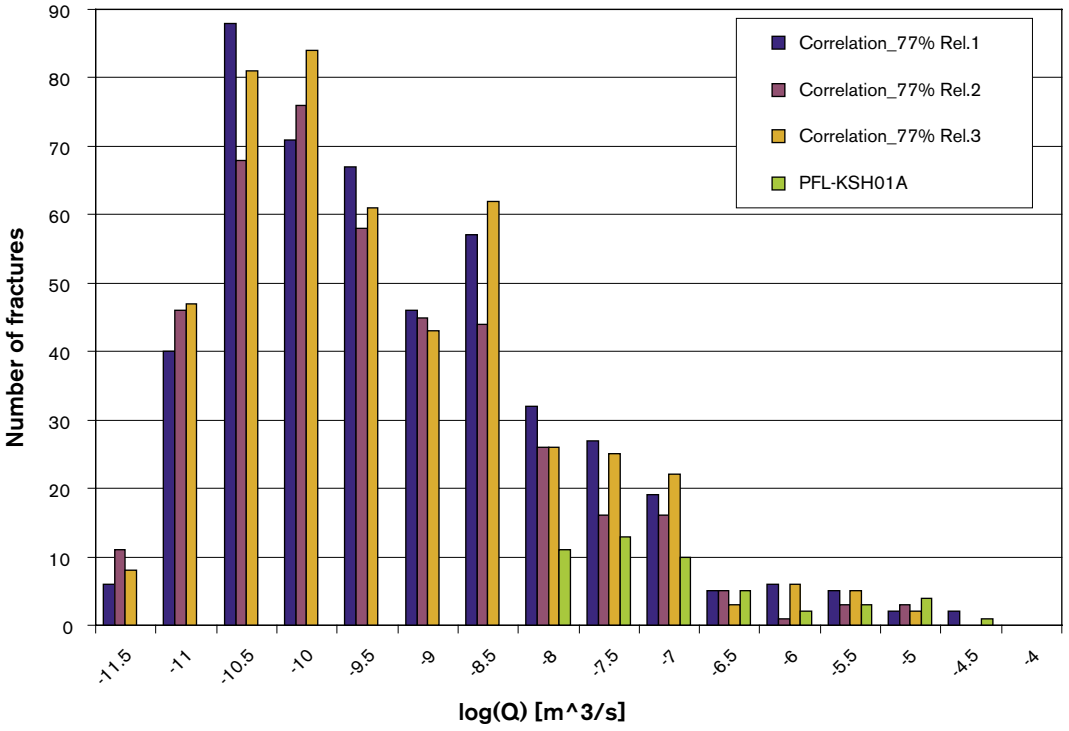

Figure 3-47. *Histogram of Log (Q), flow-rate to borehole, for 3 realisations of the correlated T distribution compared to the PFL anomaly data for KSH01A. This case is based on the percentage of certain fractures seen in KAV01, 77% of open.*

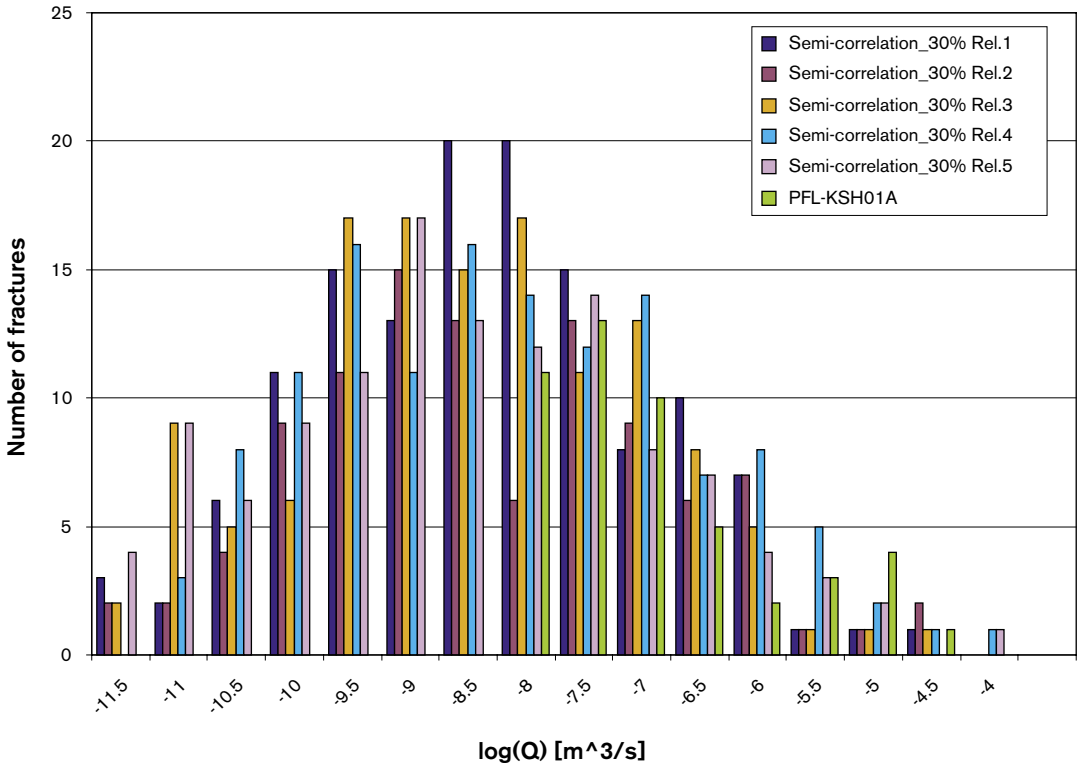

Figure 3-48. *Histogram of Log (Q), flow-rate to borehole, for 5 realisations of the semi-correlated T distribution compared to the PFL anomaly data for KSH01A. This case is based on certain or probable (30%) of open or partly-open fractures.*

Table 3-24. Description of DFN parameters used for simulation of fractures in of the PFL anomalies for KSH01A. Orientation sets are numbered: 1 = NE, 2 = EW, 3 = NW, 4 = BGNE, 5 = BGNS, 6 = BGNW (EW), 7 = HZ. P32 and the transmissivity model parameters are given for each of the cases, denoted in italics.

Rock domain	Fracture set name	Orientation, Set pole: (trend, plunge), conc	Length model, Constants: lognormal (μ, σ), power-law (L_0, k_r) (m)	Intensity, (P_{32}), valid length interval: L_0, L_{max} (m^2/m^3)	Relative intensity of P32	Transmissivity model Eq no, constants $T(m^2/s)$
C	NE	1: (308, 3)13.5	1: (L_0, k_r) (0.5,2.58)	*Uncorrelated 30%:* 0.73, (0.5, 1,000)	1: 0.024	*Uncorrelated 30%:* (μ, σ) (–6.7,1.3)
	EW	2: (1, 4) 9.0	2: (L_0, k_r) (0.5,2.80)		2: 0.056	
	NW	3: (236, 5) 10.8	3: (L_0, k_r) (0.5,2.87)	*Uncorrelated 14%:* 0.34, (0.5, 1,000)	3: 0.056	*Uncorrelated 14%:* (μ, σ) (–5.9,0.9)
	BGNE	4: (308, 3)13.5	4: (μ, σ) (–0.58,0.6)	*Correlated 30%:* 0.73, (0.5, 1,000)	4: 0.023	*Correlated 30%:* (a,b) (1.5 10^{-10}, 1.5)
	BGNS	5: (273, 1) 12.2	5: (μ, σ) (–0.58,0.88)		5: 0.034	
	BGNW (EW)	6: (1, 4) 9.0	6: (μ, σ) (–0.58,0.63)	*Correlated 77%:* 1.87, (0.5, 1,000)	6: 0.021	*Correlated 77%:* (a,b) (1.0 10^{-12}, 2.2)
	HZ	7: (326, 85) 4.1	7: (L_0, k_r) (0.5,2.6)	*Semi-correlated 30%:* 0.73, (0.5, 1,000)	7: 0.785	*Semi-correlated 30%:* (a,b,σ) (2.0 10^{-10}, 1.5, 1.0)

3.7.2 KSH02 transmissivity

The approach used was to start with the best-fit parameters used for borehole KSH01A. The total flux was monitored for each test case to match the measured value; the flux measured by PFL for KSH02 is equals 7.08×10^{-5} m^3 s^{-1}. The number of open fractures was reduced to 12% of the total to correspond with the number of certain and probable open or partly-open fractures seen in KSH02. Three realisations were carried out; the parameters used in the log-normal distribution are tabulated in Table 3-25. The uncorrelated T model was simulated for three cases with the results shown in Figure 3-49, Figure 3-50 and Figure 3-51:

1. Only certain open or partly-open fractures (5% for rock domain B).
2. Either certain or probable open or partly-open fractures (12% for rock domain B).
3. A more pessimistic case for the number of open or partly-open fractures based on the percentage of open/certain or probable fractures seen in KSH01A (30%).

The best match is obtained for the case with 12% of open fractures based on the certain and probable open or partly-open fractures in the KSH02 boremap data. For 5% of open (certain only) the network is too sparse, while for 30% open there are too many flowing features even with a standard deviation of 3 orders of magnitude. N.B. the histogram bin interval between Log (Q) = –8.0 to –7.5 (and possibly –7.5 to 7.0 as the detection limit varies even within the borehole) is uncertain since it spans the detection limit. For the correlated T distribution, the best fit case for the uncorrelated case (i.e. 12% of open fractures) was used as the basis. The match is shown in Figure 3-52 and again demonstrates a good fit for the correlated model. The parameters used in matching the PFL are given in Table 3-25.

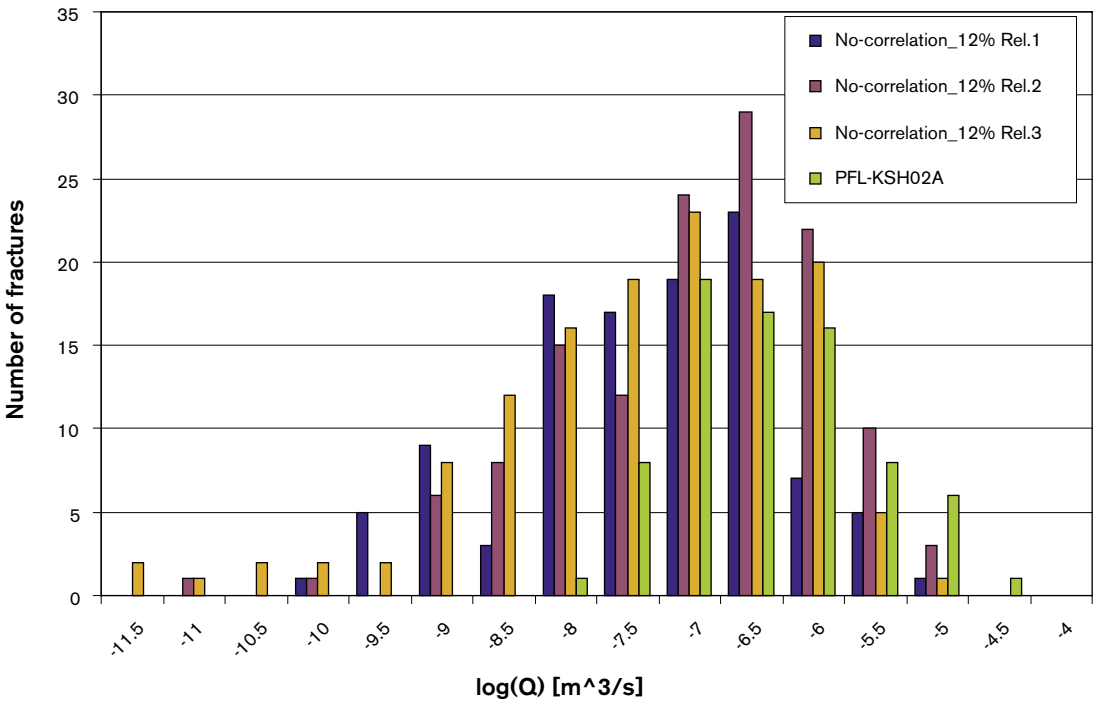

Figure 3-49. *Histogram of Log (Q), flow-rate to borehole, for 3 realisations of the uncorrelated T distribution compared to the PFL anomaly data for KSH02. This case is based on both certain and probable open or partly-open fractures, 12% open.*

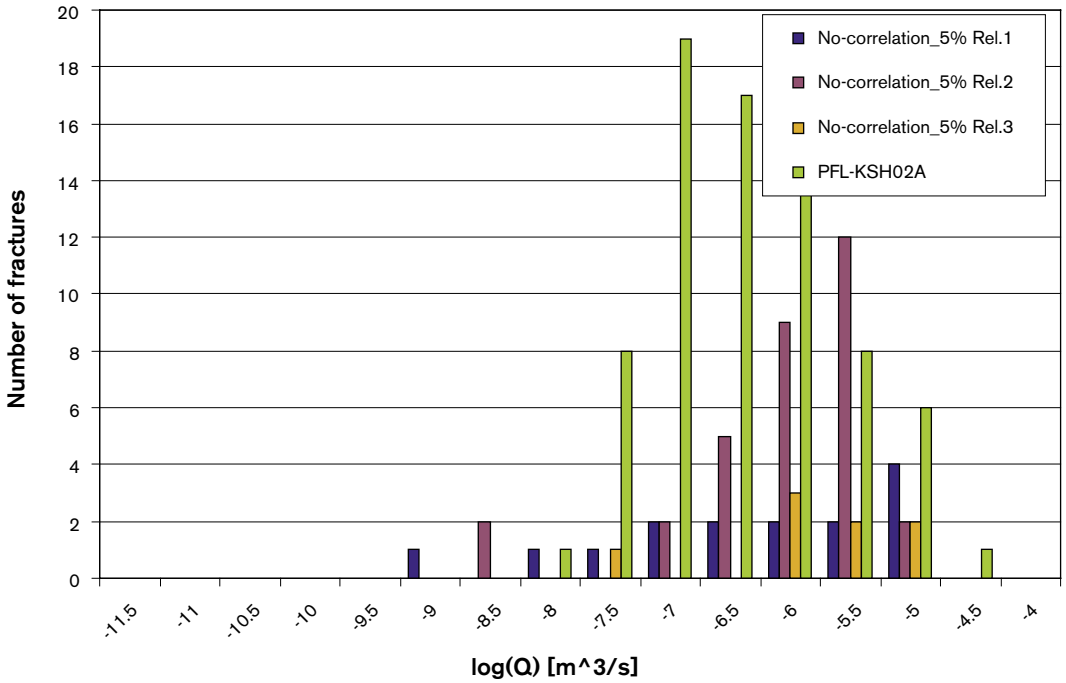

Figure 3-50. *Histogram of Log (Q), flow-rate to borehole, for 3 realisations of the uncorrelated T distribution compared to the PFL anomaly data for KSH02. This case is based on only certain open or partly-open fractures, 5% of open.*

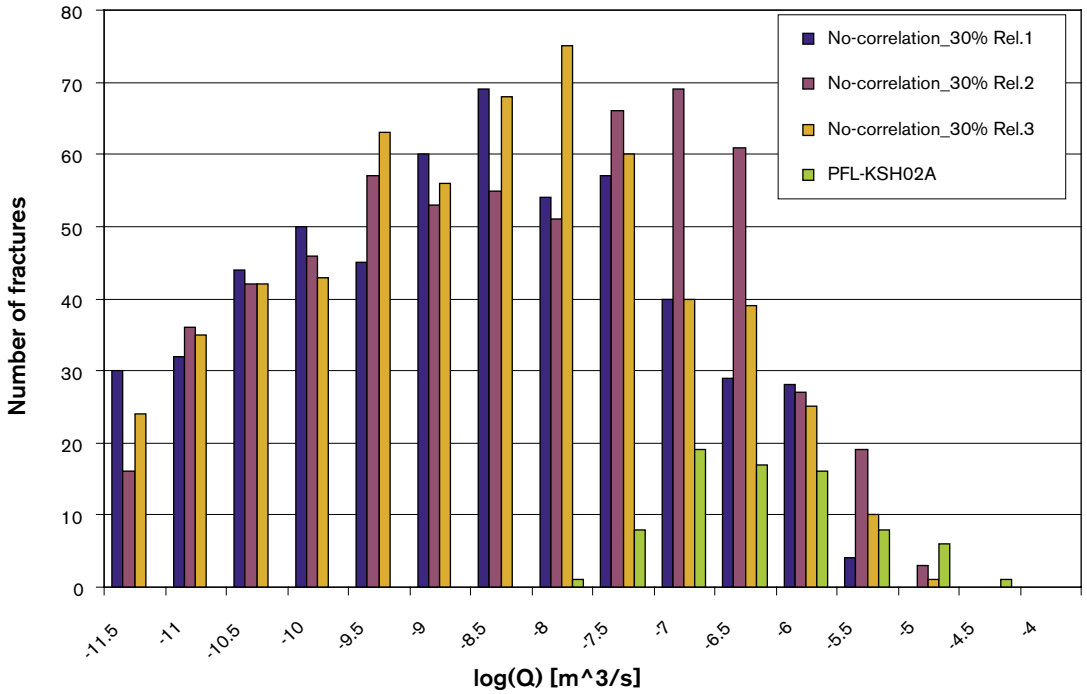

Figure 3-51. *Histogram of Log (Q), flow-rate to borehole, for 3 realisations of the correlated T distribution compared to the PFL anomaly data for KSH02. This case is based on the percentage of certain or probable (30%) of fractures seen in KSH01A.*

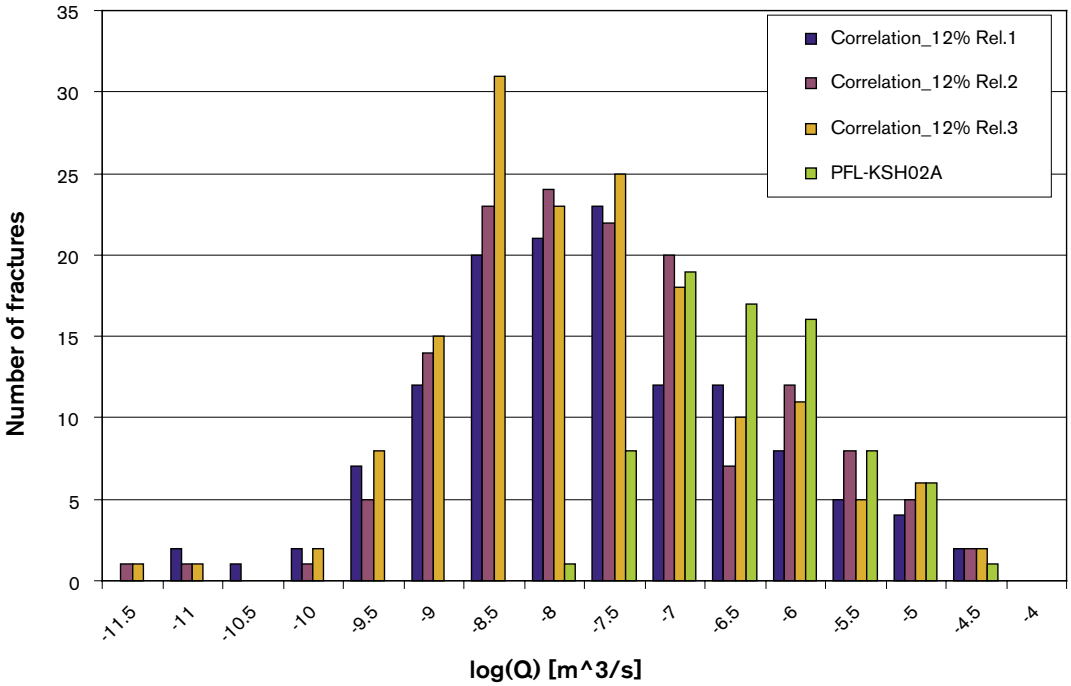

Figure 3-52. *Histogram of Log(Q), flow-rate to borehole, for 3 realisations of the correlated T distribution compared to the PFL anomaly data for KSH02. This case is based on both the certain or probable open or partly-open fractures, 30% of open.*

Table 3-25. Description of DFN parameters used for simulation of fractures in of the PFL anomalies for KSH02. Orientation sets are numbered: 1 = NE, 2 = EW, 3 = NW, 4 = BGNE, 5 = BGNS, 6 = BGNW (EW), 7 = HZ. P32 and the transmissivity model parameters are given for each of the cases, denoted in italics.

Rock domain	Fracture set name	Orientation, Set pole: (trend, plunge), conc	Length model, Constants: lognormal (μ, σ), power-law (L_0, k_r) (m)	Intensity, (P_{32}), valid length interval: L_0, L_{max} (m^2/m^3)	Relative intensity of P32	Transmissivity model Eq no, constants $T(m^2/s)$
C	NE	1: (308, 3)13.5	1: (L_0, k_r) (0.5,2.58)	*Uncorrelated 5%:* 0.29, (0.5, 1,000)	1: 0.024	*Uncorrelated 5%:* (μ, σ) (–4.9,1.1)
	EW	2: (1, 4) 9.0	2: (L_0, k_r) (0.5,2.80)	*Uncorrelated 12%:* 0.69, (0.5, 1,000)	2: 0.056	*Uncorrelated 12%:* (μ, σ) (–6.7,1.3)
	NW	3: (236, 5) 10.8	3: (L_0, k_r) (0.5,2.87)		3: 0.056	
	BGNE	4: (308, 3)13.5	4: (μ, σ) (–0.58,0.6)	*Uncorrelated 30%:* 1.73, (0.5, 1,000)	4: 0.023	*Uncorrelated 30%:* (μ, σ) (–7.3,3.0)
	BGNS	5: (273, 1) 12.2	5: (μ, σ) (–0.58,0.88)	*Correlated 30%:* 0.69, (0.5, 1,000)	5: 0.034	*Correlated 77%:* (a,b) (1.5 10^{-10}, 1.5)
	BGNW (EW)	6: (1, 4) 9.0	6: (μ, σ) (–0.58,0.63)		6: 0.021	
	HZ	7: (326, 85) 4.1	7: (L_0, k_r) (0.5,2.6)	*Semi-correlated 30%:* 0.73, (0.5, 1,000)	7: 0.785	*Semi-correlated 30%:* (a,b,σ) (2.0 10^{-10}, 1.5, 1.0)

3.8 Conditioning of transmissivity against PSS data

Further conditioning of the transmissivity models is possible by considering the packer-test data (PSS) data. The main motivation for using the PSS data was to address the uncertainty about how many fractures there are with low transmissivity below the detection limit for the PFL data. The detection limit for the PSS data is about 1–1.5 orders of magnitude lower.

This makes it possible to say more about realistic values for the P32 of open fractures that contribute to flow. For example, In Section 3.7.1 it was shown that a match to the PFL data could be obtained for a range of P32 values for the correlated case, although the transmissivity model parameters had to be varied to maintain a match. Using the PSS data it is possible to identify a narrower range of P32 values that are consistent with the hydraulic data. For KSH01A and KSH02 the PSS was available for 5 m, 20 m and 100 m intervals. In order to compare with the PFL data only the finest scale data, 5 m intervals, was used. This was available between depths of about 300 m and 700 m. Unfortunately, this is a shorter length than for the PFL data, which is about 600 m for KSH01A and 900 m for KSH02.

To incorporate the PSS data, the first step was to try to cross-validate the PSS data with the PFL data. This was done by grouping PFL anomalies into the same 5 m intervals as measured in the PSS logs, and there cross-plotting the transmissivity for the intervals.

The next step was to compare use the distribution of flow-rates simulated in the DFN models described in Section 3.7 to give a distribution of fitted transmissivities for 5 m intervals for comparison with the PSS data. This is a very simplified approach since it relies on a number of assumptions, but nonetheless yields a useful comparison of simulated and observed transmssivities in the boreholes. The assumptions include:

- the measured and simulated transmissivities can be compared as simple distributions without concern for spatial bias,
- using the above assumption it is possible to compare the PSS transmssivity distribution from 400 m borehole with the modelled transmissivity distribution for 700–800 m of borehole by simply renormalizing according the ratio of lengths,
- the transmissivity of the modelled fractures can be derived from a simulated radial flow system, and compared with the measured transmissivity derived from a spherical flow system.

3.8.1 KSH01A transmissivity

Figure 3-53 shows the cross-plot of interval transmissivity for the PFL and PSS transient test (TT) data for the same 5 m intervals. Ideally all points should lie on the 1:1 line to show a direct correlation between the two techniques. About half the flowing intervals lie near to this line, but the other half correspond to high transmissivity in the PSS data, but are close to the detection limit in the PFL data. Hence, there is some uncertainty in the PFL transmissivity acquisition for KSH01A.

Figure 3-54 and Figure 3-55 show a comparison of the transmissivity distribution for 3 model simulations with the PSS and PFL data for the cases with a correlated and uncorrelated transmissivity model, respectively. In these case 30% of open and partly-open fractures were used. The distribution of transmissivity for PFL anomalies was grouped into 5 m intervals, and compared with the PSS data by renormalizing the PSS data for the relative lengths of borehole for which data was available. The match to the PSS distribution is good for the range of Log (transmissivity) values measured, although it is perhaps slightly under-predicted in the range 10^{-10} to 10^{-9} m^2/s. Perhaps more interesting is to see the comparison for the case with 77% open and a correlated tranmissivity model in Figure 3-56. This shows a reasonable match for transmissivities above about 10^{-8} m^2/s, but a large over-prediction for smaller values. Hence, the PSS data suggests an upper limit for the percentage of open fractures; say 40% even for the correlated transmissivity model. Figure 3-57 shows the semi-correlated case.

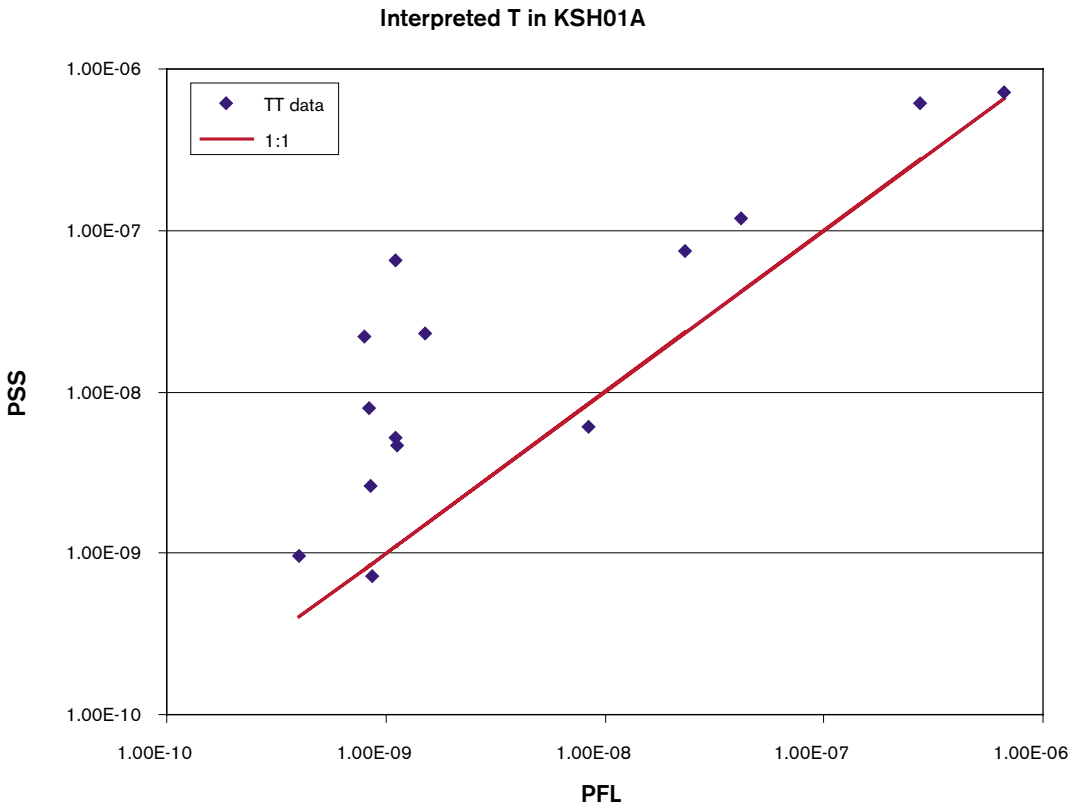

Figure 3-53. *Consistency check between PFL and PSS data for KSH01A.*

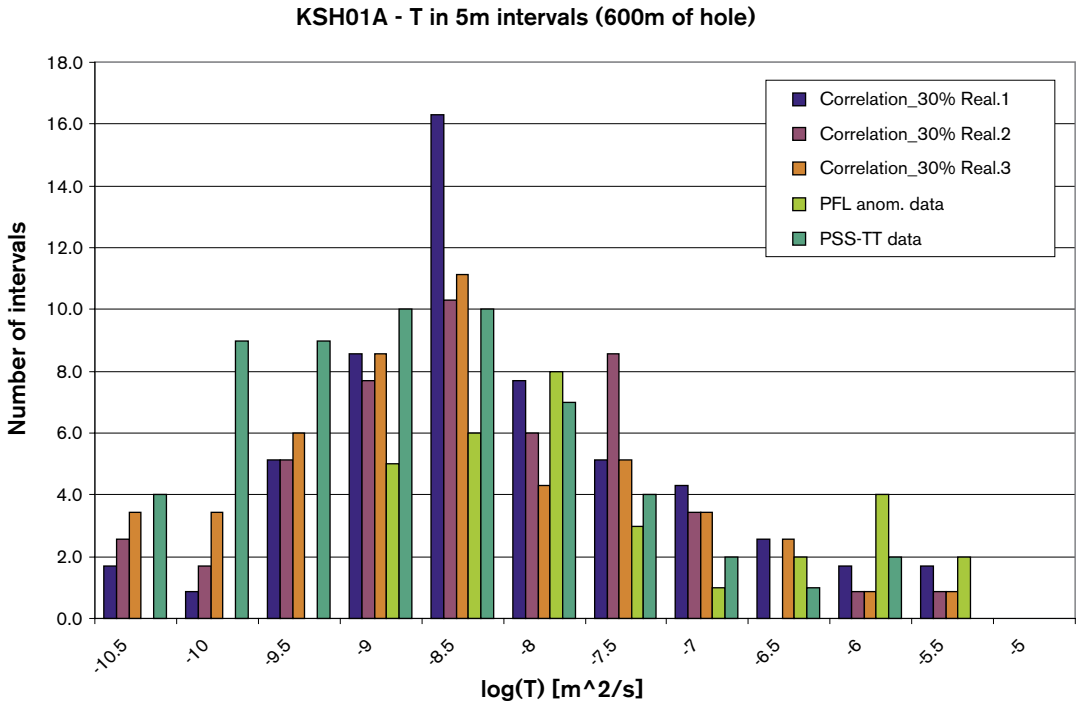

Figure 3-54. *Histogram of Log (T), for 3 realisations of the correlated T model compared to the PSS data for KSH01A. This case is based on 30% of open fractures.*

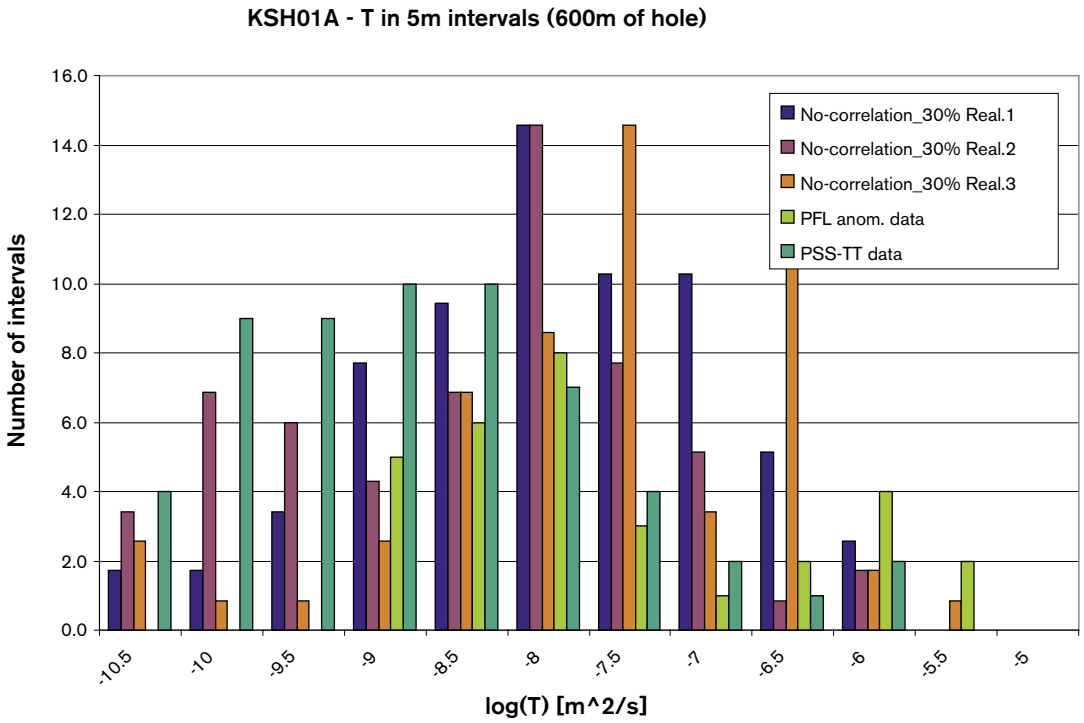

Figure 3-55. *Histogram of Log (T), for 3 realisations of the uncorrelated T model compared to the PSS data for KSH01A. This case is based on the 30% of open fractures.*

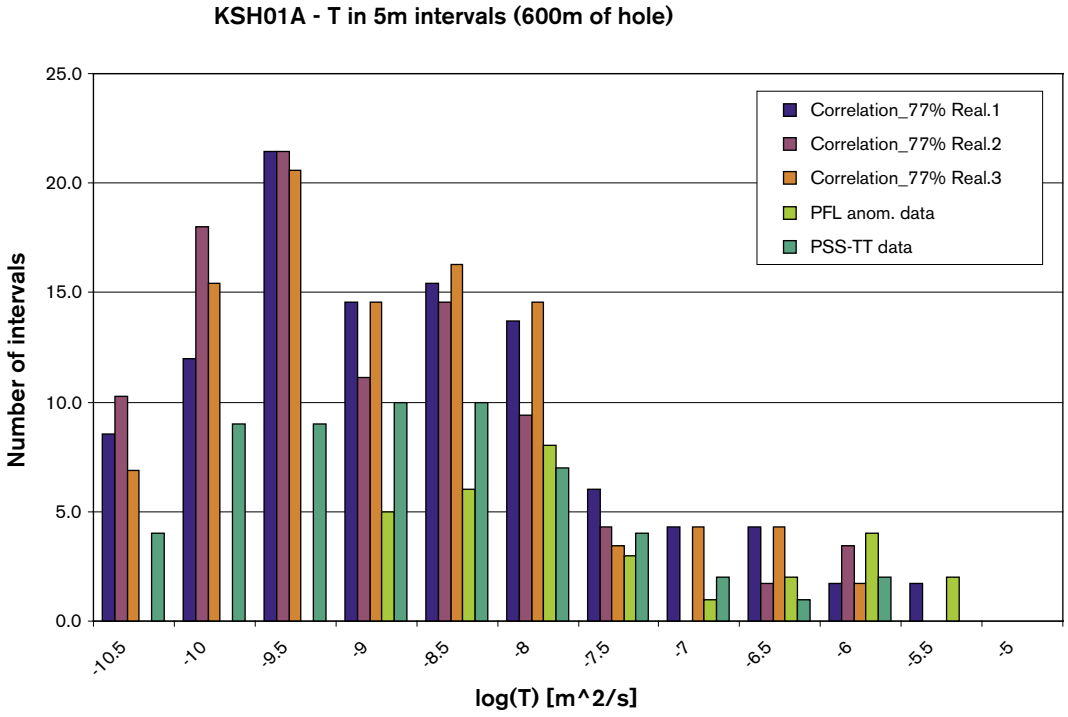

Figure 3-56. *Histogram of Log (T), for 3 realisations of the correlated T model compared to the PSS data for KSH01A. This case is based on the 77% of open fractures.*

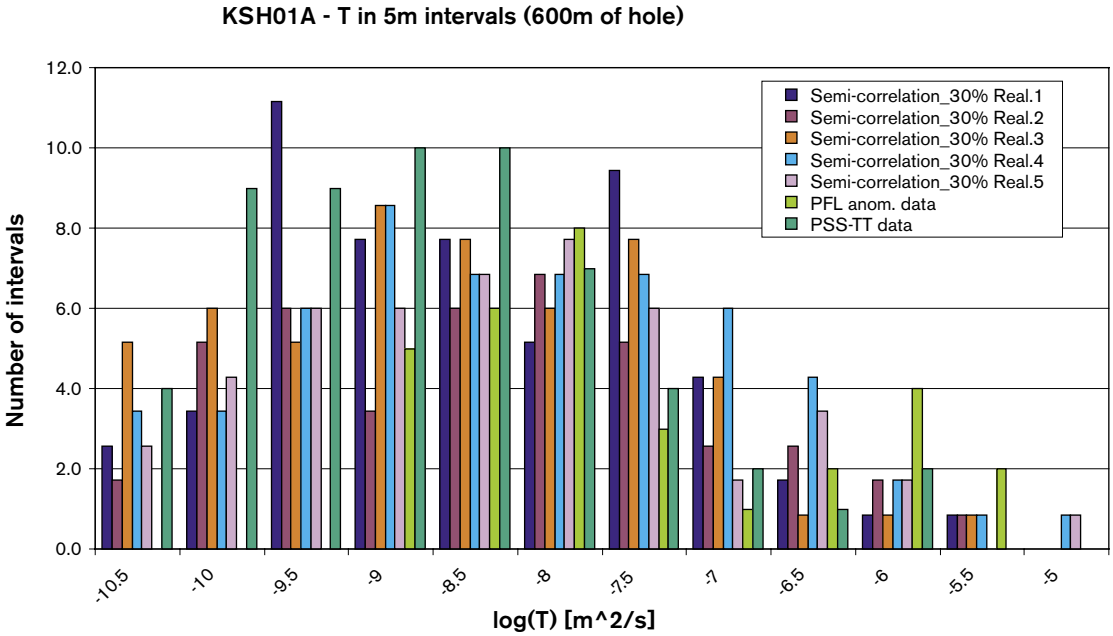

Figure 3-57. *Histogram of Log (T), for 5 realisations of the semi-correlated T model compared to the PSS data for KSH01A. This case is based on 30% of open fractures.*

3.8.2 KSH02 transmissivity

The PFL/PSS cross-plot for KSH02 shown in Figure 3-58 demonstrates more consistency between the two measurement techniques, although there seems a slight tendency toward higher values of transmissivity in the PFL data.

Figure 3-59 and Figure 3-60 show the comparison of the simulated and measured (PSS and PFL data) transmissivity for the cases with 12% of open fractures (based on certain or probable open fractures in KSH02) and either correlated or un-correlated transmissivity models, respectively. Again, the match between the distributions appears to be good, although the anomalous spike in the PSS distribution at 10^{-9} m^2/s can not be reproduced. A case with 30% open fractures is shown in Figure 3-61 for comparison of a case with higher P32, which demonstrates an over-prediction of conductive fractures. Hence, again an upper limit can be put on the P32 of open conductive fractures, and using the percentage of certain or probable open fractures seems to give an estimate of this limit. The actual upper limit for which a match can be obtained is probably around 15% of open fractures. Three realisations of the semi-correlated case are shown in Figure 3-62. The extra variability between realisations in this case gives perhaps a more realistic picture where some realisations may look more similar to the actual data.

Hence, PSS data can provide a valuable tool for reducing the uncertainties in deriving a Hydro-DFN model since its lower detection limit lead to be reduced range of possible interpretations for open fracture intensity and the transmissivity model parameters. Also, in both KSH01A and KSH02 the correlated model matched slightly better than the un-correlated model, giving some indication that perhaps the correlated model is model like reality. The lower detection limit could be particularly important for characterising the flows that might be seen in fractures cutting or in the vicinity of deposition holes, and hence be important for Safety Assessment.

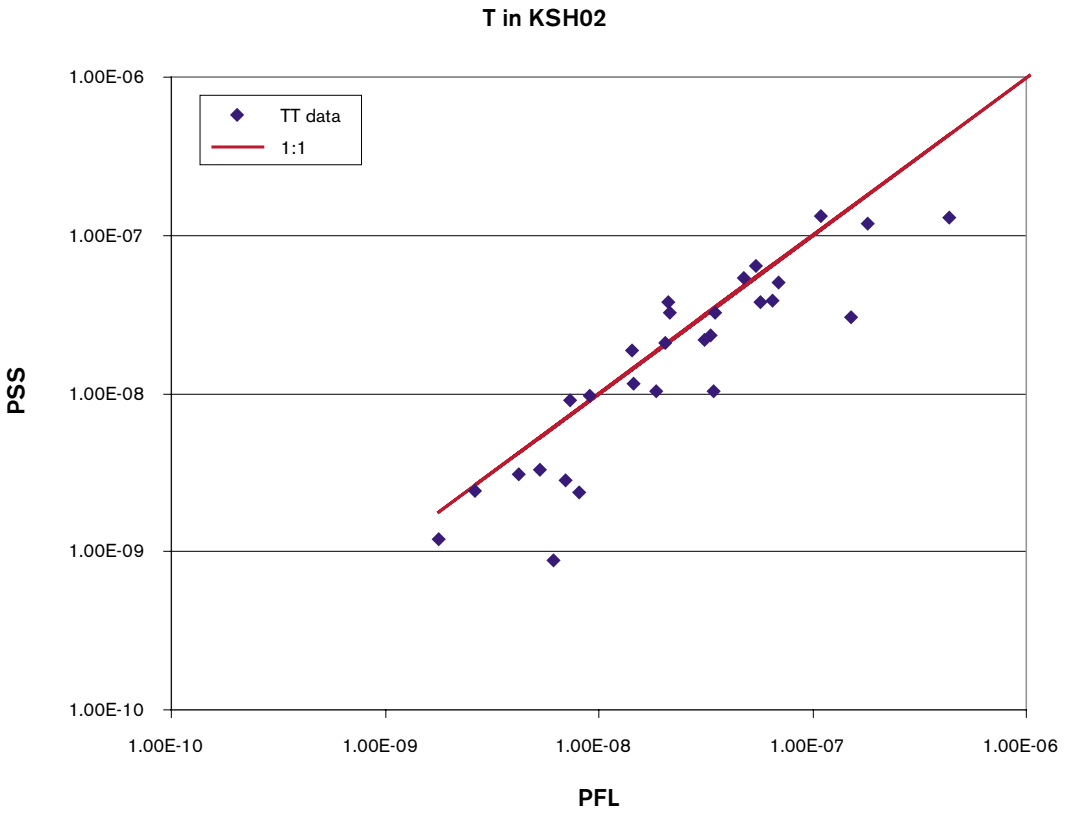

Figure 3-58. *Consistency check between PFL and PSS data for KSH02.*

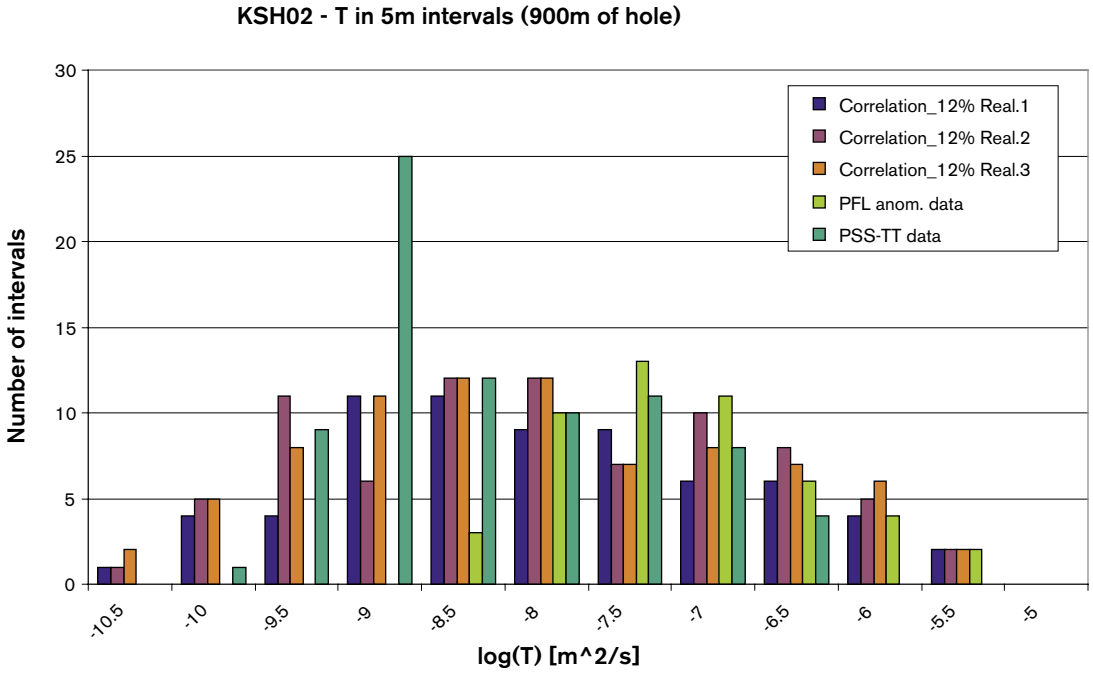

Figure 3-59. *Histogram of Log (T), for 3 realisations of the correlated T model compared to the PSS data for KSH02. This case is based on 12% of open fractures.*

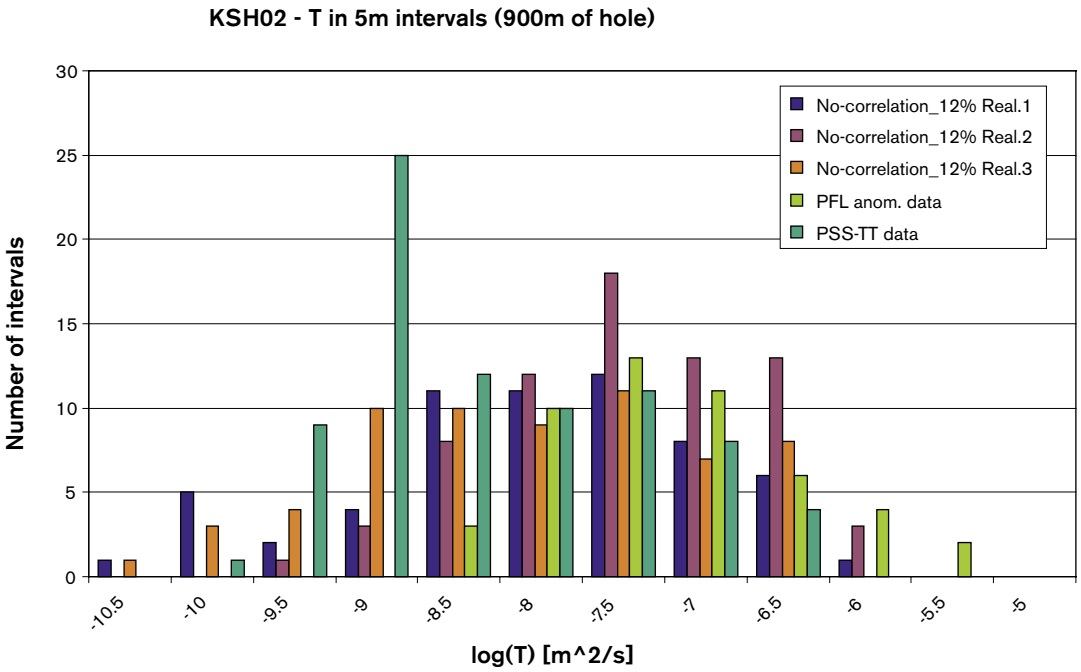

Figure 3-60. *Histogram of Log (T), for 3 realisations of the uncorrelated T model compared to the PSS data for KSH02. This case is based on 12% of open fractures.*

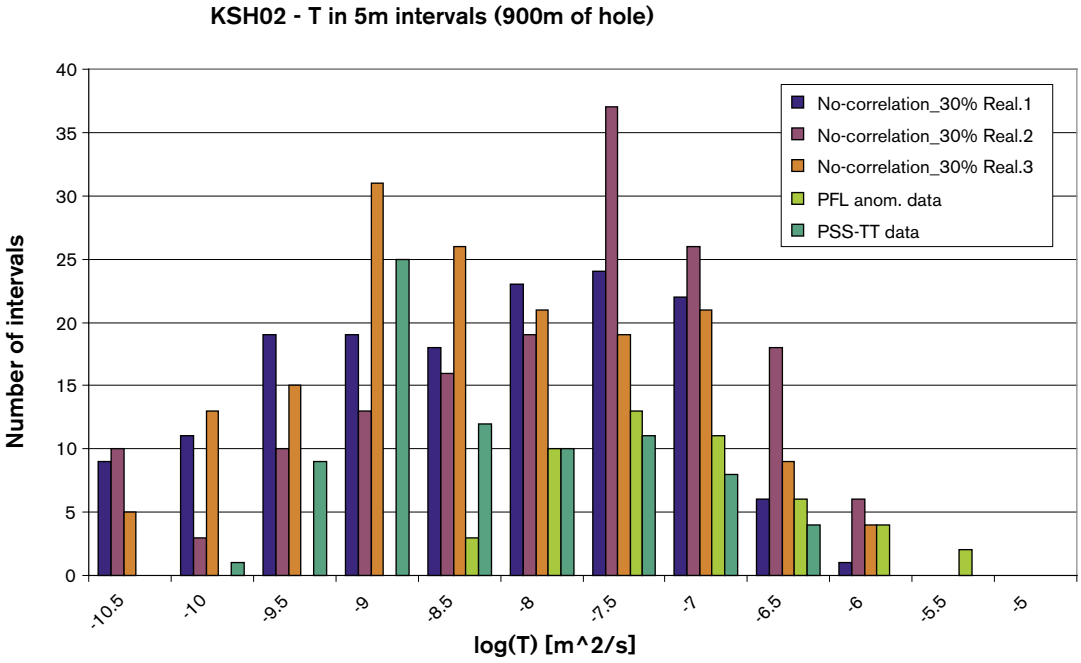

Figure 3-61. *Histogram of Log (T), for 3 realisations of the uncorrelated T model compared to the PSS data for KSH02. This case is based on 30% of open fractures.*

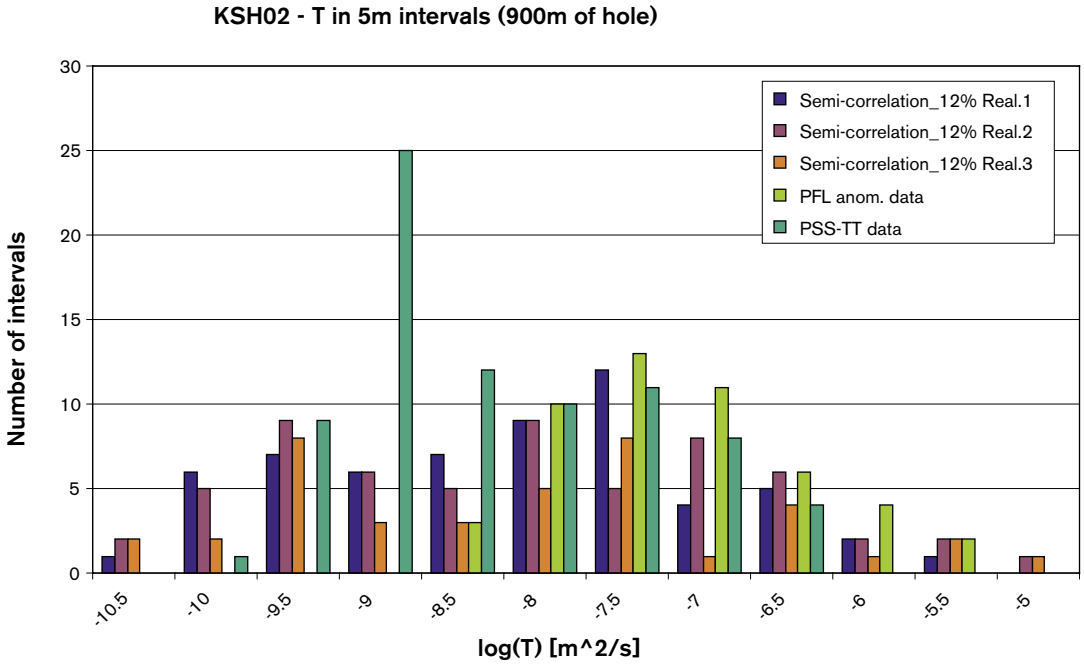

Figure 3-62. *Histogram of Log (T), for 3 realisations of the semi-correlated T model compared to the PSS data for KSH02. This case is based on 12% of open fractures.*

3.9 Model parameters of the Hydro-DFN models with uncertainties

To aid design issues, calculations of block properties such as hydraulic conductivity are required over the whole Simpevarp sub-area. Hence, a Hydro-DFN model needs to be derived that captures the broad features of the whole area, but not necessarily all the localised characteristics of particular boreholes. To this aim the following pragmatic assumptions were made in producing a Hydro-DFN for the Simpevarp sub-area that combines the data from KSH01A, KSH02 and KSH03A:

1. The fracture intensity of flowing fractures is not controlled significantly by rock domain.
2. The best estimate of the average fracture intensity for flowing features is given by the certain or probable open fractures, and these fractures from KSH01A, KSH02 and KSH03A can be grouped together to approximate statistics for the Hydro-DFN over the whole Simpevarp sub-area.
3. The three proposed transmissivity models can be used as alternative cases with the parameterisation derived for the analysis of the PFL data for KSH01A and KSH02.
4. Localised effects associated with large deterministic deformation zones will be captured by the geological model and definition of hydraulic conductor domains.

The basis for Assumption 1 is based on the data in Table 3-17. The $P10_{corrected}$ for certain or probable open fractures varies between 0.6 and 0.8 in KSH01A and KSH02 for rocks B and C. There is a greater variation in KSH03A between A and C, but this is probably due to the presence of two large deterministic zones in the upper part of the borehole.

Assumption 2 is based on the PFL flow simulation of KSH01A and KSH02 where it was found that approximating P32 by $P10_{corrected}$ for certain or probable open fractures gave the best match to the flow data. This gave similar P32 values for the open conductive fractures.

It should be made clear that in making this assumption we are not proposing that all individual certain or probable open fractures picked in the boremap logs correspond to large conductive features (something like only a half of the PFL anomalies correspond to high confidence open fractures), but on average this confidence indicator gives about the right intensity of open conductive fractures.

Assumption 3 is based on the fact that the PFL anomaly data for both KSH01A and KSH02 could be matched with the same parameter values for each transmissivity model.

Assumption 4 is based on the observation that large localised effects seen in the boreholes seem to correspond to the presence of large deformation zones that have been identified in the regional-scale geological model.

3.9.1 Model parameters

Hence, parameters for the Hydro-DFN were derived by combining the boremap data from KSH01A, KSH02 and KSH03A using only the certain or probable open fractures from these boreholes. This combined class of fractures was used to recalculate the orientation statistics, percentage of fractures in each set and the $P10_{corrected}$ as an estimate of P32 for open conductive fractures. Each of the three transmisisvity models were propagated, but based only on the parameters used for KSH01A with 30% open fractures. A summary of the parameters used is given in Table 3-26. All seven sets are used with two types of length distribution: log-normal and power-law. One interesting result of this analysis of only the high confidence open fractures is that it has promoted the importance of the EW and NW sub-vertical sets which are sub-parallel to the maximum horizontal stress direction, NW-SE /4, pg. 200, for example/.

Table 3-26. Description of DFN parameters used for simulation of fractures in the Simpevarp sub-area for calculating block properties. Orientation sets are numbered: 1 = NE, 2 = EW, 3 = NW, 4 = BGNE, 5 = BGNS, 6 = BGNW (EW), 7 = HZ. Transmissivity model parameters are given for each of the cases, denoted in italics. $P32_t$ is the total fracture intensity m^2/m^3, $P32_c$ is the connected fracture intensity m^2/m^3.

Rock domain	Fracture set name	Orientation set pole: (trend, plunge), concentration	Length model, Constants: lognormal (μ, σ), power-law (L_0, k_r) (m)	Intensity, ($P32_t$, $P32_c$), valid length interval: L_0, L_{max} (m^2/m^3)	Relative intensity of P32	Transmissivity model Eq no, constants T (m^2/s)
All	NE	1: (128, 4) 19.1	1: (L_0, k_r) (0.5,2.58)	(0.71, 0.29) (0.5, 1,000)	1: 0.036	*Uncorrelated:* (μ, σ) (–6.7,1.3)
	EW,	2: (182, 2) 11.0	2: (L_0, k_r) (0.5,2.80)		2: 0.079	*Correlated:* (a,b) (1.5 10^{-10}, 1.5)
	NW	3: (237, 1) 18.5	3: (L_0, k_r) (0.5,2.87)		3: 0.096	
	BGNE,	4: (128, 4) 19.1	4: (μ, σ) (–0.58,0.6)		4: 0.035	*Semi-correlated:* (a,b,σ) (2.0 10^{-10}, 1.5, 1.0)
	BGNS	5: (271, 0) 18.1	5: (μ, σ) (–0.58,0.88)		5: 0.055	
	BGNW(EW)	6: (182, 2) 11.0	6: (μ, σ) (–0.58,0.63)		6: 0.030	
	HZ	7: (30, 81) 4.5	7: (L_0, k_r) (0.5,2.6)		7: 0.669	

3.9.2 Evaluation of uncertainties

The key uncertainties in the Hydro-DFN model and how they might be addressed can be summarised as follows:

- The correlation between transmissivity and length. This will be addressed here by considering three alternative transmissivity models. Use of the double-packer (PSS) data has suggested that the correlated case perhaps gives a more realistic distribution of flow below the PFL detection.
- For the correlated transmissivity model it was possible to get a match for a higher P32, but with lower coefficient and higher slope. This uncertainty has again been addressed by using the PSS data. A sensitivity variant model for the block properties with a higher P32 could be performed if necessary.
- It is possible there is a higher fracture intensity of conductive fractures outside of the Simpevarp area. This is addressed in Section 3.9.3 using the packer-test data from KLX01.

3.9.3 Laxemar packer-test data

One issue for the regional groundwater flow modelling is whether the DFN derived for the Simpevarp sub-area can be extrapolated over a larger area that encompasses the Laxemar sub-area also. Unfortunately, the data available for Laxemar is currently more limited and dates from an earlier data acquisition programme. There is boremap data for KLX02 and PFL data, but this does not include flow anomaly data consistent with that used for KSH01A and KSH02. KLX01 has rock engineering data that gives a record of fracture count and an indicator for whether fractures are natural and open, but no orientation data, so only open P10 can be calculated not open $P10_{corrected}$. However, KLX01 does have packer-test data for 3 m intervals over 582 m of the borehole. Hence, it was decide to use the KLX01 packer-test data as means for validating whether the Hydro-DFN model fro m Simpevarp could be applied also at Laxemar.

The approach used was to perform DFN flow simulations in the same way as for the PFL analysis described in Section 3.7 to derive a distribution of transmissivity in 3 m intervals for a vertical borehole of length 582 m. Since there is no orientation data for KLX01, the DFN was based on the parameterisation given in Table 3-26. Using the open P32 specified in Table 3-26 would represent just slightly less than 9% of the fractures judged to open in the rock engineering data to actually correspond to open conductive fractures. Hence, this would be similar to KSH02 which had about 12% of open. The result of this comparison for the correlated transmissivity model is shown in Figure 3-63 with the Simpevarp model coloured in blue and denoted as ‘Correlation – 9% P10’. The packer-test data is shown using two alternative interpretation methods: steady-state, or Jacob. Clearly there are too few borehole intervals with measurable flow to match the data using the Simpevarp model. This suggests that the fracture system around KLX01 is better connected and gives a more homogeneous flow distribution. This motivated using a higher P32 for KLX01 to improve the match. By doubling the P32 to 1.4 m^2/m^3, which would correspond to about 17% of the open the rock engineering data, a much better match was achieved. The red data series in Figure 3-63 denoted ‘Correlation – 17% P10’ shows this modified model with a higher P32, but the same correlated transmissivity model. This model has a peak in transmissivity greater than the data and the distribution generally over-predicts the number of high transmissivity intervals. Hence, the transmissivity parameters were also modified ($a = 2\ 10^{-11}$ and $b = 1.7$) to improve the match as shown by the orange data series. To illustrate the statistical uncertainty in matching the PSS distribution, 3 realisations of the KLX01 alternative DFN were generated as shown in Figure 3-64.

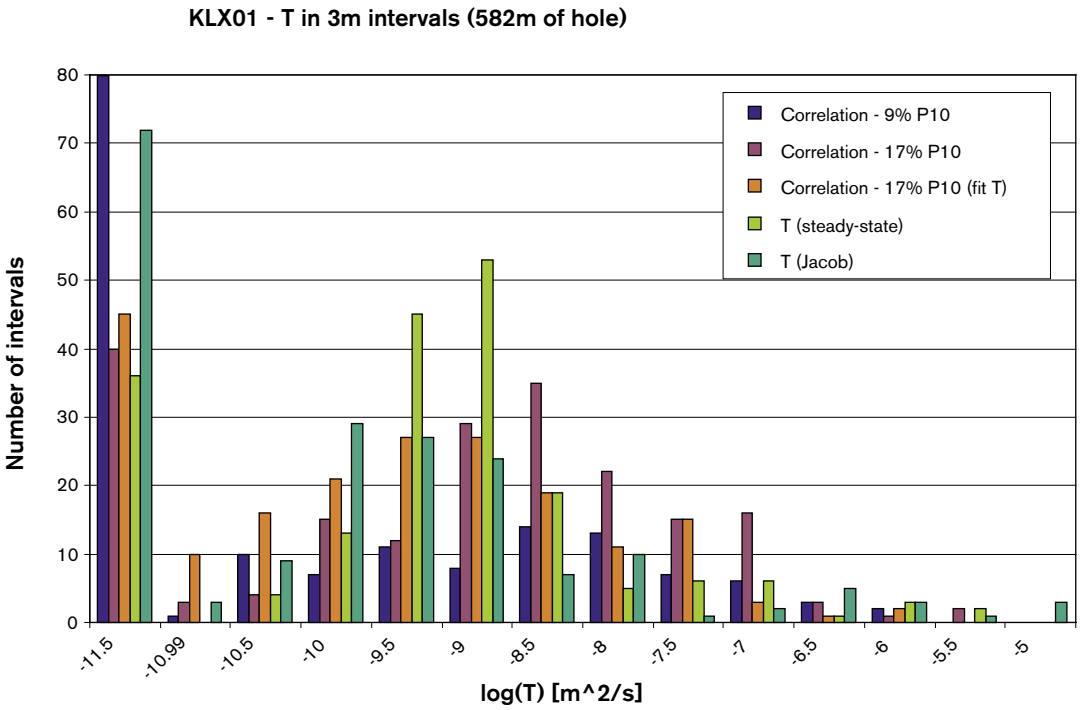

Figure 3-63. *Histogram of Log (T), for 3 cases based on the correlated T model compared to the PSS data for KLX01. These cases are based on the combined Simpevarp DFN, but consider the same or twice the P32 value, and modified T parameters.*

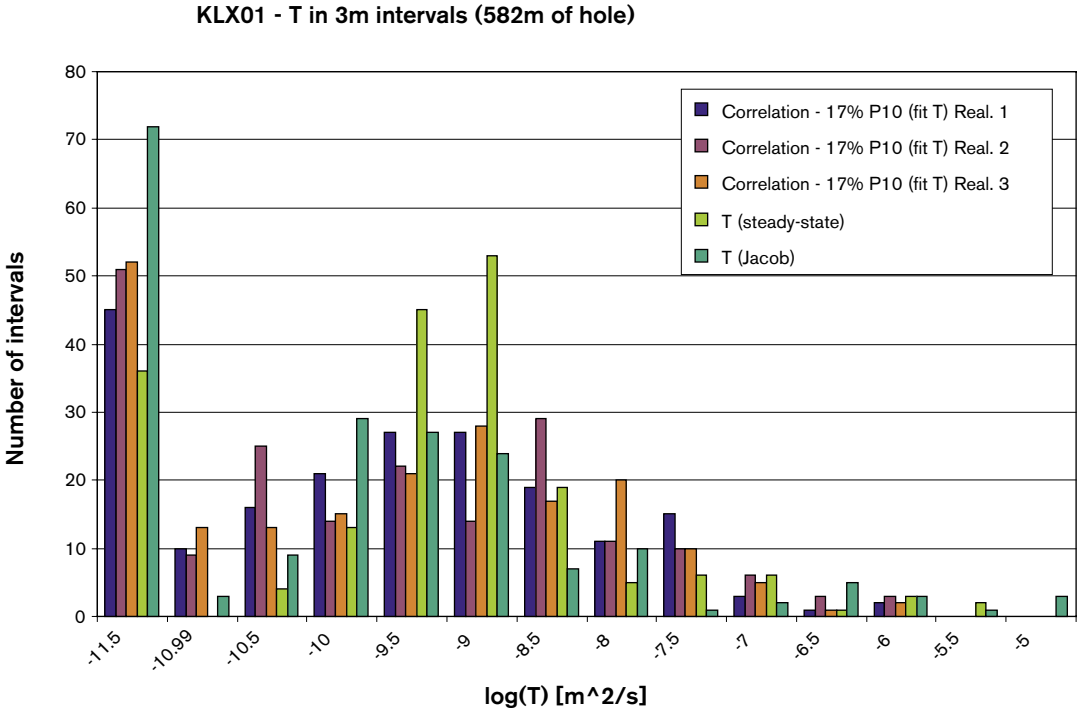

Figure 3-64. *Histogram of Log(T), for 3 realisations of correlated T model compared to the PSS data for KLX01 using the best fit for KLX01.*

The conclusion is that it is not possible to apply the Simpevarp model directly at KLX01 since there is higher fracture connectivity and more homogeneous flow distribution. Hence, a modified DFN model is suggested based on KLX01, and is parameterised in Table 3-27. Obviously, since this is based on only one borehole at Laxemar, there is no way of cross-checking the model. However, it provides an alternative model that should be assessed to quantify uncertainties in the assumptions used.

Table 3-27. Description of DFN parameters for an alternative model based on KLX01. Orientation sets are numbered: 1 = NE, 2 = EW, 3 = NW, 4 = BGNE, 5 = BGNS, 6 = BGNW (EW), 7 = HZ.

Rock domain	Fracture set name	Orientation set pole: (trend, plunge), concentration	Length model, Constants: lognormal (μ, σ), power-law (L_0, k_r) (m)	Intensity, ($P32_t$, $P32_c$), valid length interval: L_0, L_{max} (m^2/m^3)	Relative intensity of P32	Transmissivity model Eq no, constants T (m^2/s)
All	NE	1: (128, 4) 19.1	1: (L_0, k_r) (0.5,2.58)	(1.42, 0.95) (0.5, 1,000)	1: 0.036	*Correlated:* (a,b) (2.0 10^{-11}, 1.7)
	EW,	2: (182, 2) 11.0	2: (L_0, k_r) (0.5,2.80)		2: 0.079	
	NW	3: (237, 1) 18.5	3: (L_0, k_r) (0.5,2.87)		3: 0.096	
	BGNE,	4: (128, 4) 19.1	4: (μ, σ) (–0.58,0.6)		4: 0.035	
	BGNS	5: (271, 0) 18.1	5: (μ, σ) (–0.58,0.88)		5: 0.055	
	BGNW(EW)	6: (182, 2) 11.0	6: (μ, σ) (–0.58,0.63)		6: 0.030	
	HZ	7: (30, 81) 4.5	7: (L_0, k_r) (0.5,2.6)		7: 0.669	

3.9.4 DarcyTools alternative DFN interpretation

The DarcyTools Team also interpreted the fracture boremap and PFL data for Simpevarp independently. Their DFN parameterisation is included in Table 3-28 since block-scale properties and regional DFN models were calculated for this alternative model were calculated in the study reported here to quantify sensitivities to the DFN interpretation. The main differences from the CONNECTFLOW DFN are that it uses the same power-law length distribution for all sets, has a slightly higher $P32_t$, and a different correlated transmissivity model with a higher slope.

Table 3-28. Description of DFN parameters for the DarcyTools alternative DFN model interpretation. Orientation sets are numbered: 1 = NE, 2 = EW, 3 = NW, 4 = BGNE, 5 = BGNS, 6 = BGNW (EW), 7 = HZ. $P32_t$ is the total fracture intensity m^2/m^3, $P32_c$ is the connected fracture intensity m^2/m^3.

Rock domain	Fracture set name	Orientation set pole: (trend, plunge), concentration	Length model, Constants: lognormal (μ, σ), power-law (L_0, k_r) (m)	Intensity, ($P32_t$, $P32_c$), valid length interval: L_0, L_{max} (m^2/m^3)	Relative intensity of P32	Transmissivity model Eq no constants T (m^2/s)
All	NE	1: (118, 2) 17.3	(L_0, k_r) (0.5,2.6)	(1.1, 0.41) (0.5, 1,000)	1: 0.07	*Correlated:* (a,b) (5.0 10^{-12}, 2.0)
	EW,	2: (17, 7) 11.2			2: 0.20	
	NW	3: (73, 5) 13.7			3: 0.11	
	BGNE,	4: (316, 6) 17.9			4: 0.12	
	BGNS	5: (97, 4) 20.3			5: 0.01	
	BGNW(EW)	6: (22, 2) 6.0			6: 0.07	
	HZ	7: (125, 75) 5.0			7: 0.43	

4 Assessment of hydraulic block properties

The objectives for the hydraulic block property are defined in the Task Description TD_ID17_Block_K_v1.0.doc and can be summarised as:

- Calculate the statistics of the hydraulic conductivity of 100 m and 20 m blocks for Sub-area Simpevarp.
- Estimate anisotropy for Sub-area Simpevarp.
- Evaluate effects of size-truncation of stochastic features and cell-background properties for the forthcoming Regional Scale GWF modelling.
- Compute fracture porosity based on aperture = function (Transmissivity) relationship from Äspö Task 6c /22/.

4.1 Methodology

To calculate equivalent CPM block properties (directional hydraulic conductivity and porosity) based on an underlying DFN model the following modelling steps are performed:

1. A fracture network is calculated stochastically by generating fractures within some domain much larger than the required block size (1,000 m for a 100 m block and 200 m for a 20 m block was used here).
2. Split the fracture domain into sub-blocks of a selected scale.
3. Perform flow simulations through the DFN model in each of the axial directions. For the flow simulations a linear pressure gradient is specified parallel to each of the axial directions and imposed on all six faces of a cube to allow a general symmetric hydraulic conductivity tensor (6 components) to be calculated.
4. For each set of the three axial pressure gradients, compute the flux through each of the six faces of the block. Based on these 18 flux responses for the 3 pressure gradients a full symmetric 3D hydraulic conductivity tensor is fitted based a least-squares optimisation.
5. An enhancement to this methodology is to divide the domain of fractures into blocks larger than the size on which the properties are required, simulate flow through the larger block, but then only calculate the flux through the central cube of the required size. This has the advantage that flows are calculated through the fractures ‘in-situ’ i.e. within a network, and avoids overestimating hydraulic conductivity due to flows through fractures that cut across edges or corners of the block and do not represent flows within a network.
6. The hydraulic conductivity was calculated for 100 m and 20 m blocks and different fracture length truncations were considered. For the 100 m block K, fractures were generated in a 1,000 m cube which was split into an array of 9×9×9 (729 blocks in total) overlapping cubes of side 200 m for use in the flow simulations. The hydraulic conductivity was then calculated based on the flux through the central 100 m block, so as to avoid problems with high flows through the corner or edge of a cube unrepresentative of flow in a network.

7. Hydraulic conductivities were then calculated as a CDF of the values for an ensemble of 729 blocks.
8. For a 20 m block, fractures were generated in a 200 m cube and an array of 9×9×9 (729 blocks in total) cubes of side 40 m.
9. Anisotropy was studied in several ways. The overall hydraulic conductivity was calculated as the geometric mean of the axial components. A principal component analysis was used to derive the minimum and maximum horizontal hydraulic conductivities together with the strike of the maximum hydraulic conductivity for each of the 729 blocks. In this way it seen whether there is anisotropy in any given block and if there is a general trend toward certain directions over all blocks. The directions of anisotropy in the horizontal plane is requested from design as one factor for guiding the preliminary orientation of tunnels.
10. Fracture porosity was calculated by summing the fracture area multiplied by transport aperture for each connected fracture within each block and dividing by the block volume.

4.2 Modelling assumptions and input data

The remit for this study was specified by SKB's Design Team to calculate the statistics of the hydraulic conductivity tensor of 20 m and 100 m blocks using the results of the TD ID16 – Hydro-DFN as described in Section 3.

The main modelling assumptions in the study performed here are:

1. The hydraulic conductivity in the host rock is completely dominated by the connected fracture system and hence can be modelled by the DFN concept.
2. Flow within fractures can be approximated by Darcy's law.
3. The heterogeneity between blocks on a specified scale can be modelled by calculating the hydraulic conductivity of an array of sub-blocks within a domain much larger (as big as the largest stochastic fracture, and ten times the block size) and use this as an ensemble.
4. The whole Simpevarp sub-area can be represented by average DFN properties based on combining KSH01A, KSH02 and KSH03A.
5. Fracture transmissivity can be described by one of three alternative models.
6. Fracture porosity (transport aperture) is correlated to fracture transmissivity.

4.3 Simulations for assessment of hydraulic block properties

Simulations of the hydraulic properties are based on the combined DFN model as described by the parameters in Table 3-26. An example of the DFN model used to calculate hydraulic properties for a 100 m block for the case with a correlated transmissivity is shown in Figure 4-1. Here, the DFN is created within a 1,000 m domain and then sub-divided into 200 m blocks for flow simulations. Clearly blocks cut by a large fracture, coloured red here, will have a high hydraulic conductivity. A corresponding example of the DFN used for the 20 m block properties is shown in Figure 4-2.

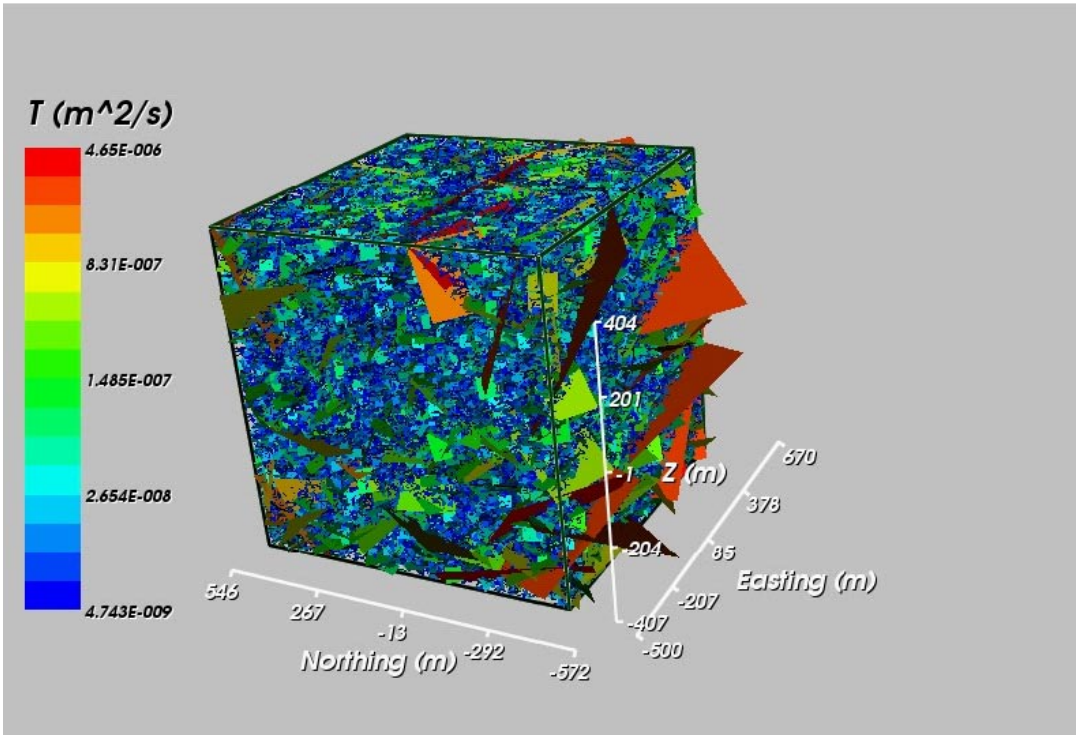

Figure 4-1. *Combined Simpevarp DFN model simulation for a 1,000 m domain used to calculate hydraulic block properties for 100 m blocks and the correlated T model.*

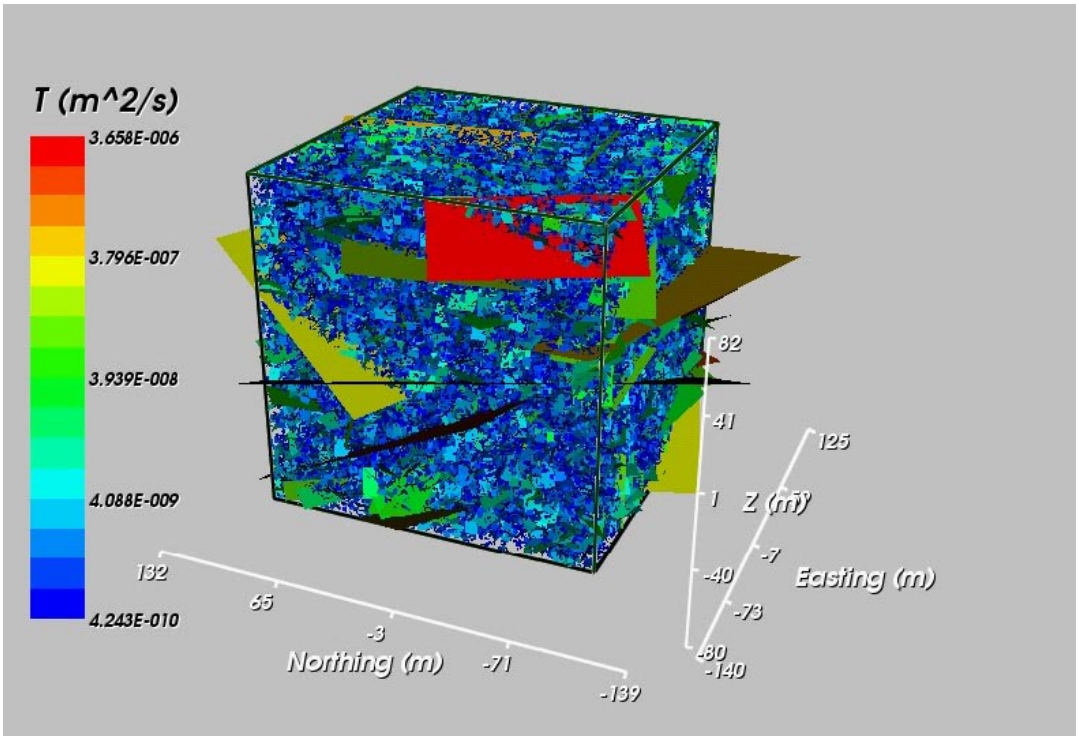

Figure 4-2. *Combined Simpevarp DFN model simulation for a 200 m domain used to calculate hydraulic block properties for 20 m blocks and the correlated T model.*

4.4 Model parameters for block properties with uncertainties

Using the combined DFN model as described by the parameters in Table 3-26, simulations were performed for the 100 m and 20 m block sizes and for the three different transmissivity models. All three transmissivity models were propagated to the block scale modelling in order to quantify the sensitivity to the assumption of a relationship between fracture transmissivity and length, and see if there are any distinct differences between the models that may point toward one model being more realistic. An additional case was included based on the alternative DFN model based on the packer-test data from KLX01, as detailed in Table 3-27.

Another modelling issue is what range of fracture lengths needs to be included to get an accurate prediction of block properties on a given scale. That is, in the regional GWF we have applied an L_{min} truncation when the DFN model is generated on a regional scale for practical reasons, and the choice of this truncation needs to be made at a value where we can be confident that it will not bias the results. Hence, a range of different L_{min} values are considered in the study to establish where we can make a defensible choice for L_{min} for the regional modelling and defend the values that have been used here for deriving hydraulic block properties.

4.4.1 Model parameters

Some examples of the calculations of the resultant model parameters for the hydraulic block properties are shown in Figure 4-3 to Figure 4-6 for the 100 m block. Figure 4-3 shows the x (East-West) hydraulic conductivity for the uncorrelated T model case. Figure 4-4 shows the same properties, but with the most transmissive fractures superimposed. This case demonstrates some characteristic features particular to the uncorrelated model. There is considerable heterogeneity, and there is little correlation between adjacent blocks. This stems from the fact that high transmissivity fractures can be any length, and because of the power-law length distribution for the larger sets, then many of the high T fractures are relatively small, and so only affect 1 or 2 blocks. It is rare that a large fracture is generated with a high T, so there are few, if any, continuous lineaments of high hydraulic conductivity.

Figure 4-5 and Figure 4-6 show the corresponding plots for the case with a correlated T model. A clear difference here is the much greater correlation between blocks due to the effect of large fractures with high transmissivity. Figure 4-6 shows clearly the strong correlation between streaks of high hydraulic conductivity and large fractures.

Statistics for 20 m and 100 m blocks for each T model and various L_{min} truncations are included in Table 4-1. The results are given in terms of percentiles (10, 25, 50, 75 and 90) to capture the distribution of K_{eff}, the geometric mean of the axial components of the hydraulic conductivity tensor. For a 20 m block the median (50-percentile) for each case is very similar, around Log (K_{eff}) = –8.5. For a 100 m block the median Log (K_{eff}) is –8.2 for the correlated case, –8.9 for the uncorrelated case, and –8.2 for the semi-correlated case. For the alternative model based on KLX01, it is –8.1. Using the DarcyTools DFN parameters it is –8.3. The results for these cases are also presented in Table 4-2 in terms of the individual axial components of hydraulic conductivity (Kx, Ky and Kz); the median ratios of maximum horizontal and minimum horizontal conductivities; the median ratios

of maximum horizontal and vertical conductivities; and the strike of any general trend in the maximum horizontal conductivity. The ratios of anisotropy are calculated block-by-block and then the median is computed over the ensemble of 729 blocks. The ratio of Khmax to Khmin is generally around 2, and the ratio between Khmax to Kz is around 3. Interestingly, the DarcyTools model is more isotropic with a Khmax to Kz ration of only 1.5. This presumably is due to low percentage of fractures in the sub-horizontal set. For the correlated and semi-correlated cases there is a distinct trend towards horizontal anisotropy with strike between about 80° to 140° which is parallel to the maximum in-situ stress. In contrast, there is no general trend in the uncorrelated case.

The corresponding fracture porosity percentiles (10, 25, 50, 75 and 90) are given in Table 4-3. The median Log (porosity) for the is between –4.7 to –4.8 in a 100 m block for all cases. L_{min} has little effect in the correlated case, but a significant one for the uncorrelated case.

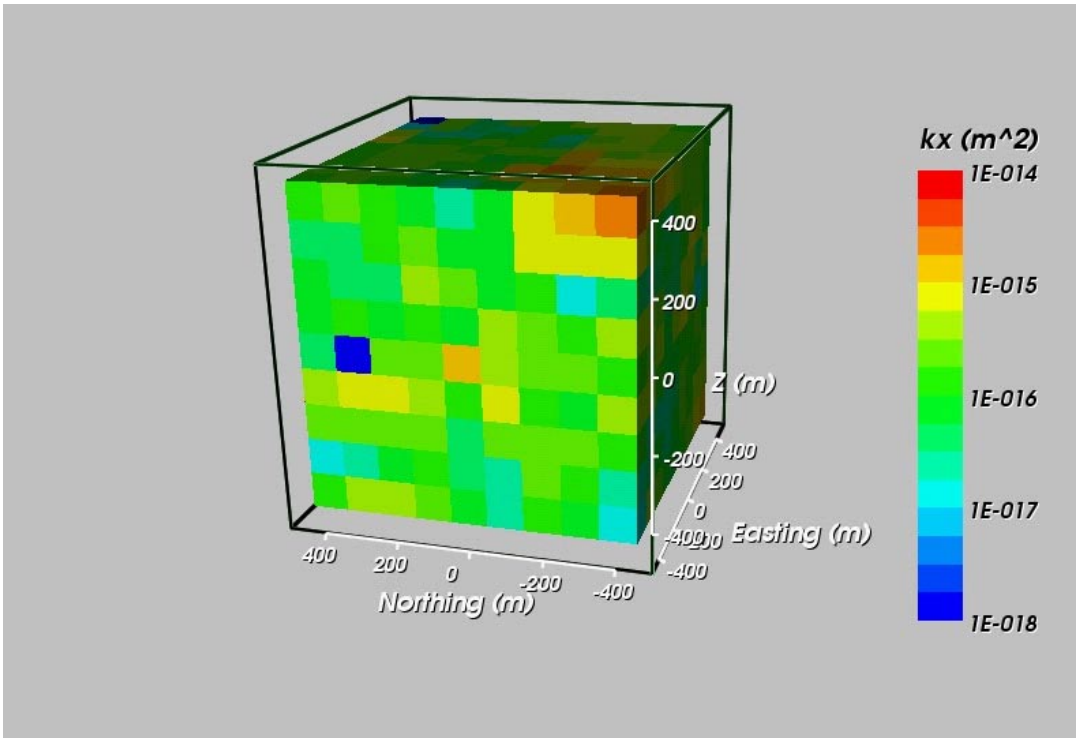

Figure 4-3. *Calculated hydraulic conductivity in the East-West direction for a 9×9×9 array of 100 m blocks for the combined Simpevarp DFN with an uncorrelated T model.*

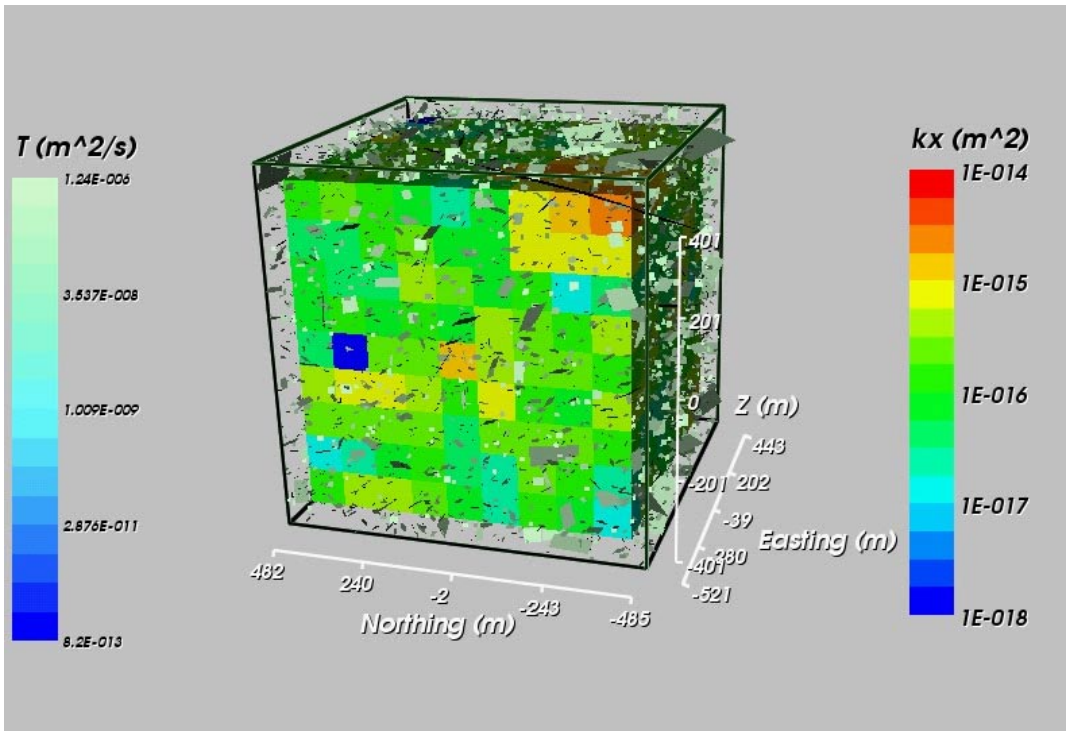

Figure 4-4. *Calculated hydraulic conductivity in the East-West direction for a 9×9×9 array of 100 m blocks for the combined Simpevarp DFN with an uncorrelated T model. Fractures with large transmissivity are superimposed.*

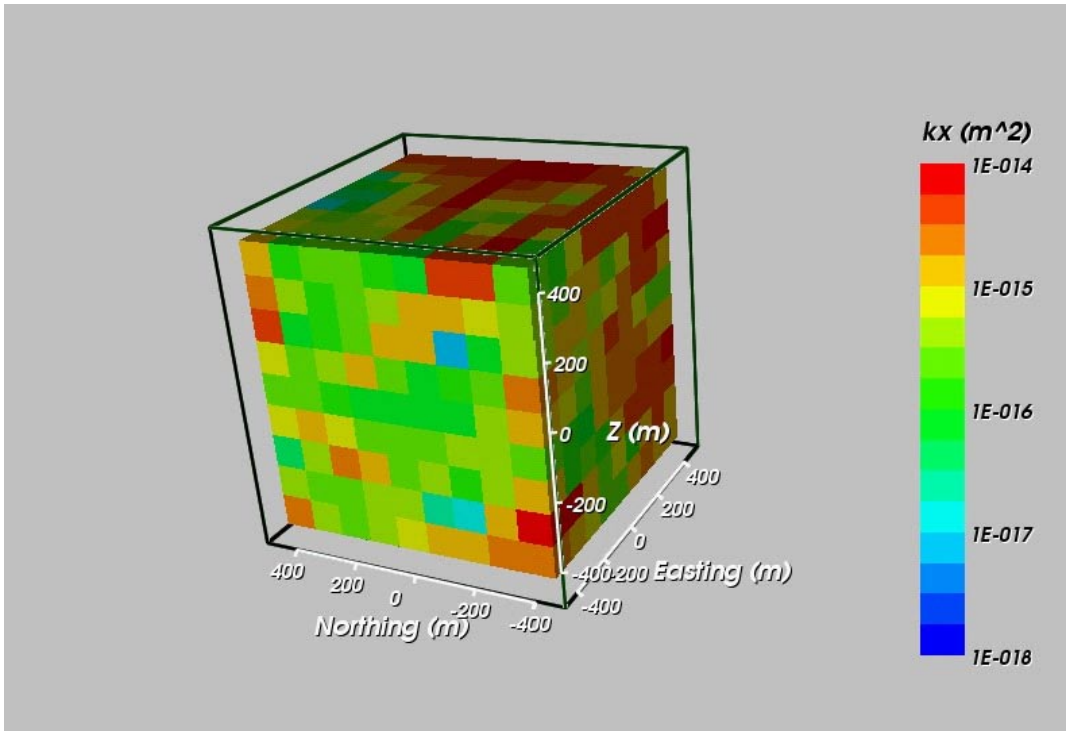

Figure 4-5. *Calculated hydraulic conductivity in the East-West direction for a 9×9×9 array of 100 m blocks for the combined Simpevarp DFN with a correlated T model.*

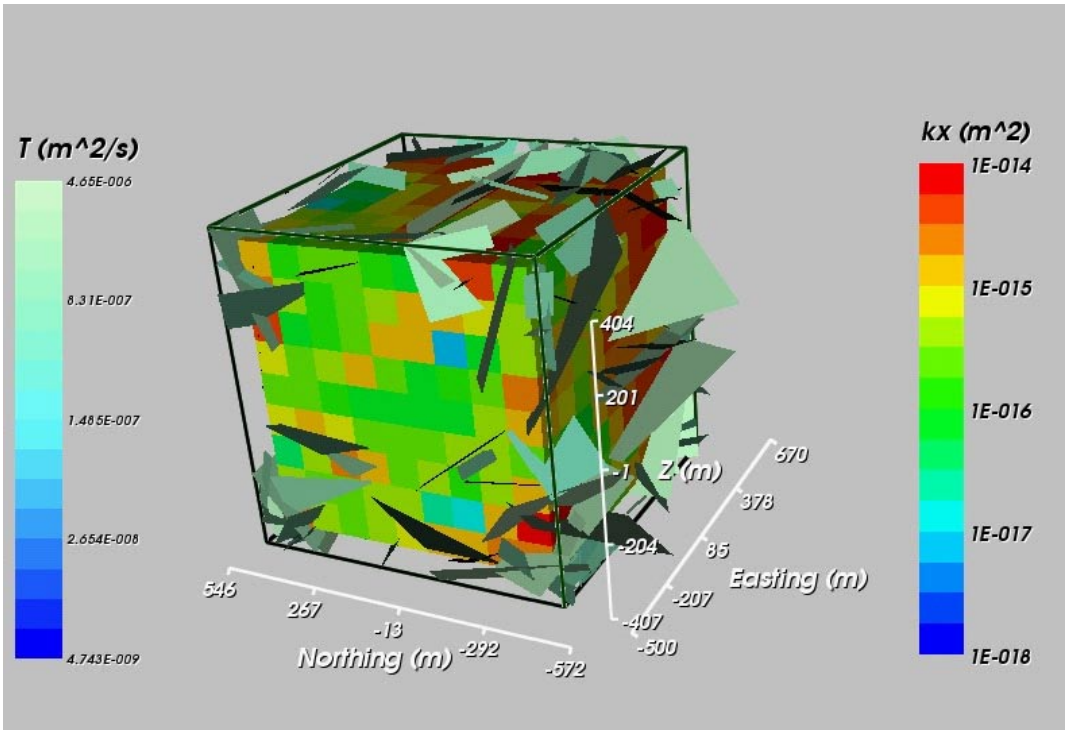

Figure 4-6. *Calculated hydraulic conductivity in the East-West direction for a 9×9×9 array of 100 m blocks for the combined Simpevarp DFN with a correlated T model. Fractures with large transmissivity are superimposed.*

Table 4-1. Effective hydraulic conductivity for correlated, uncorrelated and semi-correlated Transmissivity concepts. Scale (cell size) and L_{min} are recorded in metres. Two alternative models based on PSS data from KLX01, and the Darcy Tools (DT) model is included.

T model	Scale	L_{min}	Log10 (K_{eff}) (m/s)					
			10–percentile	25–percentile	50–percentile	75–percentile	90–percentile	StDev
Correlated	20	0.5	–9.94	–9.20	–8.46	–7.54	–7.04	1.09
	100	10	–9.07	–9.60	–8.15	–7.73	–7.49	0.59
	100	50	–9.45	–8.82	–8.24	–7.74	–7.46	0.77
Uncorrelated	20	0.5	–9.65	–9.06	–8.57	–8.23	–7.95	0.69
	100	10	–9.47	–9.19	–8.91	–8.66	–8.45	0.39
	100	50	–10.55	–9.84	–9.32	–8.91	–8.62	0.66
Semi-correlated	20	0.5	–10.16	–9.37	–8.57	–7.86	–7.43	1.09
	100	10	–9.24	–8.80	–8.23	–7.76	–7.36	0.74
Correlated based on KLX01	20	0.5	–9.79	–9.28	–8.73	–8.18	–7.69	0.75
	100	10	–8.68	–8.42	–8.09	–7.83	–7.65	0.40
Correlated based on DT DFN	100	10	–8.97	–8.62	–8.25	–7.87	–7.69	0.50

Table 4-2. Comparison of anisotropy for correlated, uncorrelated and semi-correlated Transmissivity concepts. Scale (cell size) and L_{min} are recorded in metres. Two alternative models based on PSS data from KLX01, and the Darcy Tools (DT) model is included.

T model	Block scale	L_{min}	Mean (Log10 (K_x)) /m/s]	Ky	Kz	Median ratio Khmax/Khmin	Median ratio Khmax/Kz	Strike of Khmax
Correlated	20	0.5	–8.31	–8.32	–8.87	2.21	3.81	100–140
	100	10	–8.07	–8.14	–8.42	1.96	2.43	90–130
	100	50	–8.44	–8.53	–8.82	2.56	2.59	80–130
Un-correlated	20	0.5	–8.71	–8.68	–9.01	2.56	2.54	No trend
	100	10	–8.92	–8.95	–9.26	2.00	2.62	No trend
	100	50	–9.82	–9.84	–10.18	3.24	2.94	No trend
Semi-correlated	20	0.5	–8.59	–8.60	–8.94	3.17	2.55	120–160
	100	10	–8.16	–8.18	–8.48	2.95	2.59	120–150
Correlated based on KLX01	20	0.5	–8.66	–8.67	–8.92	2.15	2.15	80–110
	100	10	–8.01	–8.07	–8.32	1.60	2.15	80–110
Correlated based on DT DFN	100	10	–8.24	–8.30	–8.31	2.50	1.48	90–140

Table 4-3. Porosity for correlated, uncorrelated and semi-correlated Transmissivity concepts. Scale (cell size) and L_{min} are recorded in metres.

T model	Scale	L_{min}	Log10 (porosity) (–)					
			10–percentile	25–percentile	50–percentile	75–percentile	90–percentile	StDev
Correlated	20	0.5	–4.95	–4.84	–4.68	–4.39	–4.19	0.28
	100	10	–5.00	–4.92	–4.82	–4.71	–4.61	0.15
	100	50	–5.20	–5.08	–4.94	–4.79	–4.69	0.19
Uncorrelated	20	0.5	–4.32	–4.29	–4.26	–4.22	–4.19	0.05
	100	10	–4.83	–4.81	–4.78	–4.75	–4.73	0.04
	100	50	–5.40	–5.34	–5.26	–5.19	–5.11	0.10
Semi-correlated	20	0.5	–4.89	–4.79	–4.63	–4.44	–4.28	0.22
	100	10	–4.91	–4.84	–4.75	–4.65	–4.54	0.15
Correlated based on KLX01	20	0.5	–5.03	–4.90	–4.77	–4.64	–4.57	0.18
	100	10	–4.90	–4.82	–4.74	–4.66	–4.58	0.12
Correlated based on DT DFN	100	10	–5.08	–4.99	–4.90	–4.81	–4.74	0.13

These block-scale hydraulic conductivities are also presented as CDF distributions in Figure 4-7 for the uncorrelated case, Figure 4-8 for the correlated case, and Figure 4-9 for the semi-correlated case. For the uncorrelated case, the mean is higher for the 20 m blocks and has larger spread than the 100 m blocks since properties are averaged over a greater volume in the 100 m blocks. For the correlated case the median is about the same for 20 m and 100 m blocks, but there is greater spread for the 20 m blocks. Both cases show Kx and

Ky very similar, but kz about a factor 3 less. The semi-correlated case lies between the two other cases. Figure 4-10 shows the distribution of the strike Khmax for the 20 m and 100 m blocks in the uncorrelated case. This exhibits no clear trend. In contrast, the correlated case shown in Figure 4-11 has a distinct peak in the range 100° to 140° for 20 m blocks, and between 90° to 130° for 100 m blocks. It noted that although this is a clear bias toward a horizontal maximum between E-W to NW-SE, it is relatively subtle compared to the horizontal/vertical anisotropy, and other directions may dominate locally.

The next issue to be addressed is how sensitive are calculated block properties to the fracture length truncation L_{min}. Block-scale hydraulic properties were calculated for values of L_{min} = 10 m, 50 m and 100 m for 100 m blocks. An example is shown in Figure 4-12 for the uncorrelated case. For a truncation at 100 m there are about 25% of blocks without a connected network. Below 50 m truncation all cells have some hydraulic conductivity, and going down to 10 m increases the hydraulic conductivity by a factor of about 2. Hence, L_{min} needs to be about 10–20 m for the uncorrelated case. For the correlated case an L_{min} of 50 m is sufficient as shown in Figure 4-13. As a general rule of thumb, fractures down to a length at least as small as half the block-size need to be included.

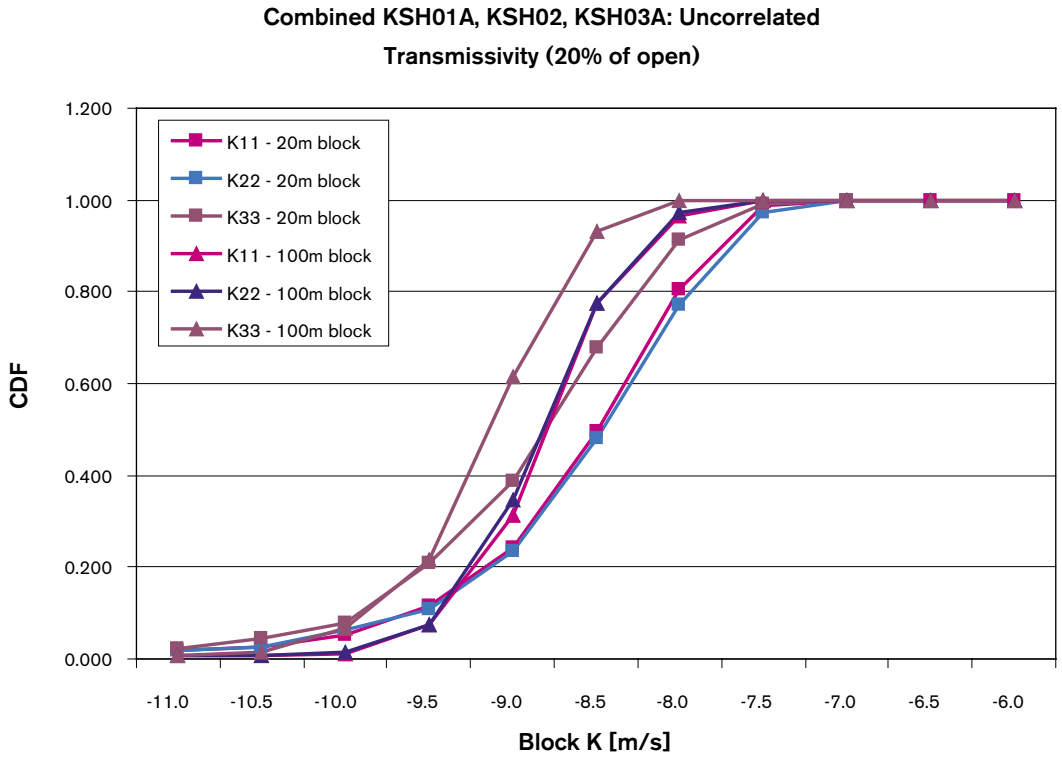

Figure 4-7. *Hydraulic conductivity distribution for an uncorrelated transmissivity, for the combined DFN model of Simpevarp. K11, K22, K33 correspond to Kx (Easting), Ky (Northing) and Kz (vertical), respectively.*

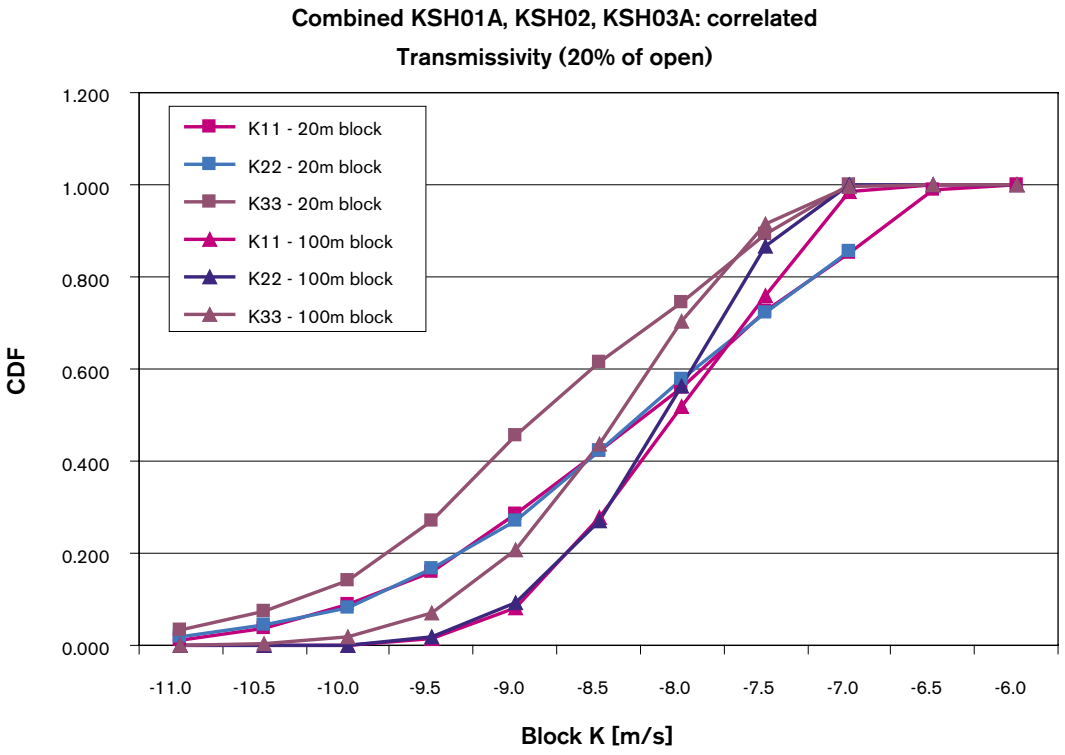

Figure 4-8. *Hydraulic conductivity distribution for a correlated transmissivity, for the combined DFN model of Simpevarp. K11, K22, K33 correspond to Kx (Easting), Ky (Northing) and Kz (vertical), respectively.*

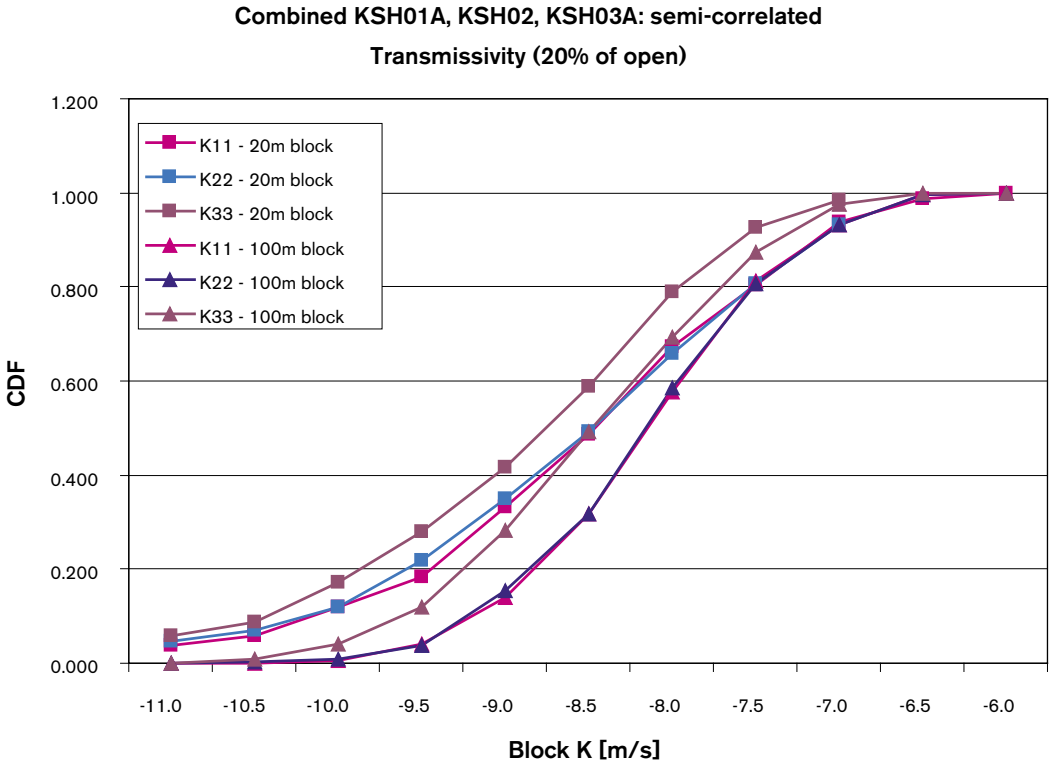

Figure 4-9. *Hydraulic conductivity distribution for a semi-correlated transmissivity, for the combined DFN model of Simpevarp. K11, K22, K33 correspond to Kx (Easting), Ky (Northing) and Kz (vertical), respectively.*

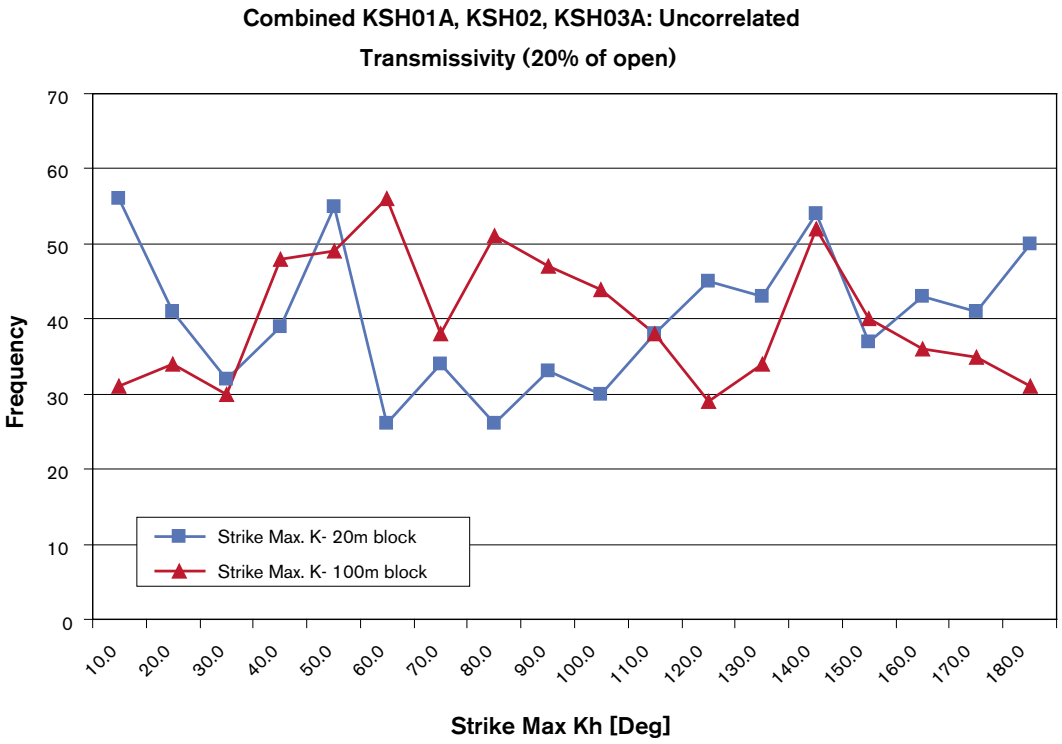

Figure 4-10. *Distribution of the strike of the maximum horizontal hydraulic conductivity for an uncorrelated transmissivity, for the combined DFN model of Simpevarp.*

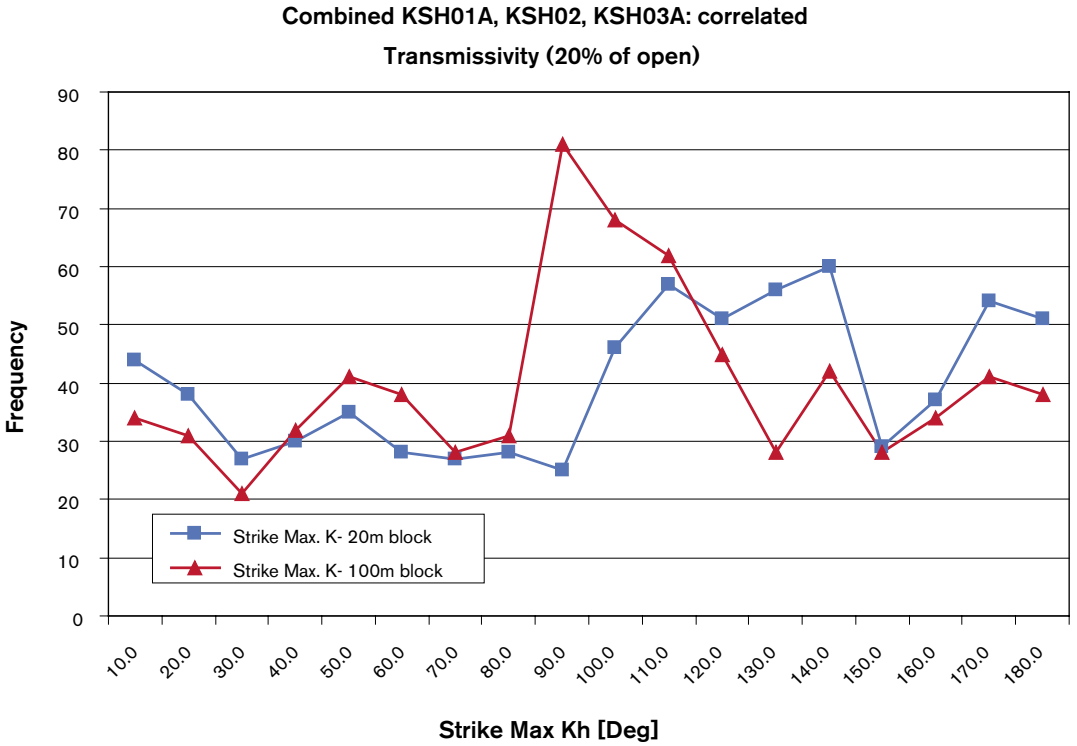

Figure 4-11. *Distribution of the strike of the maximum horizontal hydraulic conductivity for a correlated transmissivity, for the combined DFN model of Simpevarp.*

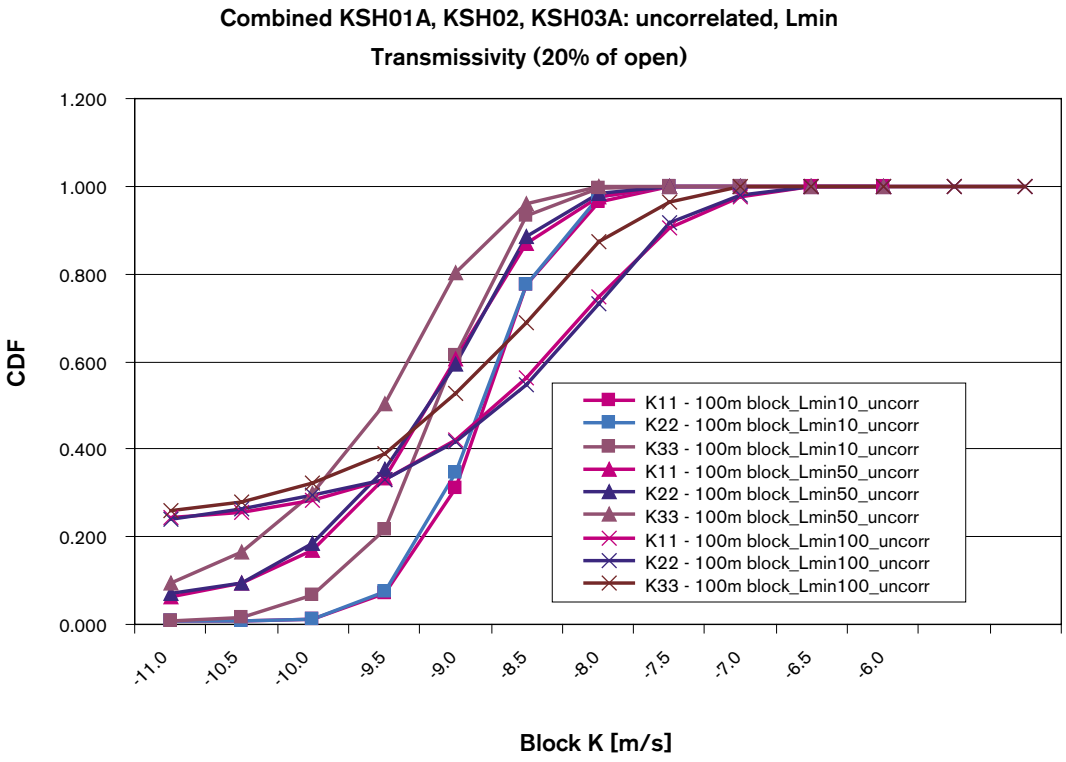

Figure 4-12. *Hydraulic conductivity distribution for an uncorrelated transmissivity, for the combined DFN model of Simpevarp. Different L_{min} are used for the 100 m block. K11, K22, K33 correspond to Kx (Easting), Ky (Northing) and Kz (vertical), respectively.*

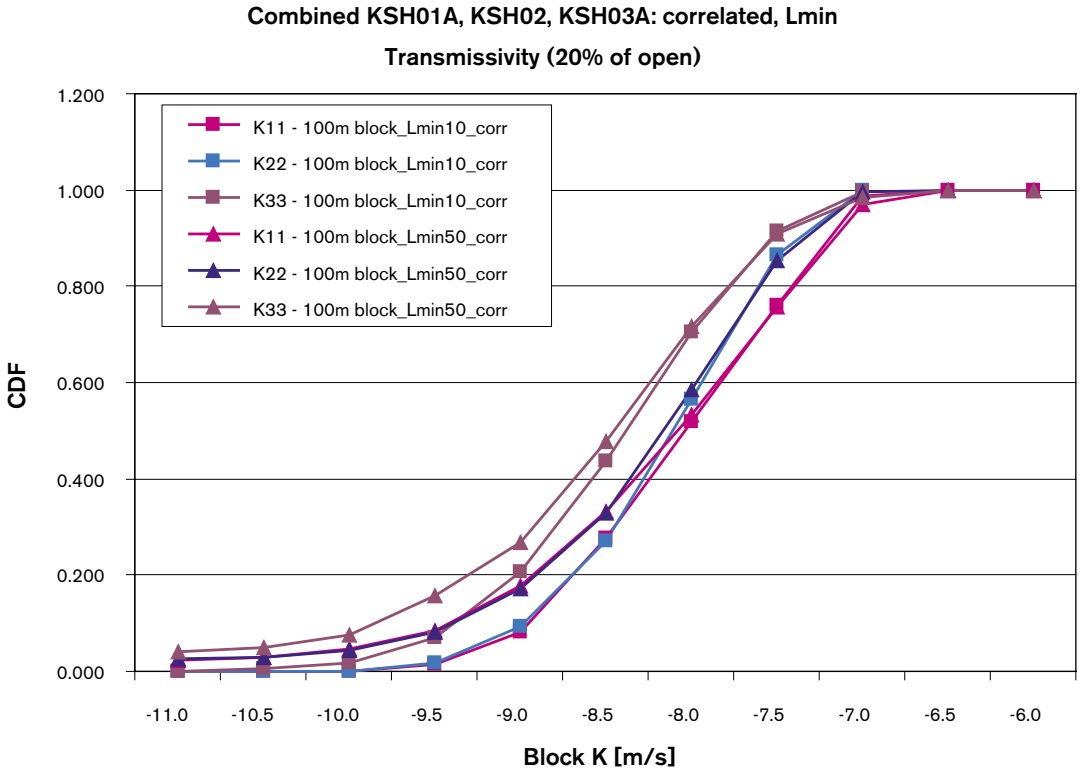

Figure 4-13. *Hydraulic conductivity distribution for correlated transmissivity, for the combined DFN model of Simpevarp. Different L_{min} are used for the 100 m block. K11, K22, K33 correspond to Kx (Easting), Ky (Northing) and Kz (vertical), respectively.*

4.4.2 Evaluation of uncertainties

The sensitivity of the block-scale properties with regard to all the assumptions listed in Section 4.2 was not considered exhaustively. However, two important alternative models were considered explicitly to see how the block-scale properties might be affected:

1. The Hydro-DFN variant based on the PSS data from KLX01 as described in Table 3-27.
2. The Hydro-DFN model derived by the Darcy Tools (DT) Team as described in Table 4-4.

The first of these alternatives gives an indication of the sensitivity to extrapolating the hydraulic properties fro the regional modelling from the Laxemar sub-area rather than the Simpevarp sub-area. The second alternative illustrates how sensitive the block-scale properties are to assumptions made in interpreting the fracture data. The Darcy Tools Team used a lower value, 45°, for separating the sub-vertical and sub-horizontal sets, and derived a different correlated transmissivity model. However, they arrived at a very similar value for total open fracture intensity of 0.77 compared to 0.71 from Table 3-26, and the connected open fracture intensity is identical 0.29. This suggests constraining the models to the hydraulic data has lead to equivalent Hydro-DFN models, and hence narrowed uncertainties.

Table 4-4. Description of DFN parameters derived for the Darcy Tools (DT) model. Orientation sets are numbered: 1 = NE, 2 = EW, 3 = NW, 4 = BGNE, 5 = BGNS, 6 = BGNW (EW), 7 = HZ. Transmissivity model parameters are given for each of the cases, denoted in italics.

Rock domain	Fracture set name	Orientation, Set pole: (trend, plunge), concentration	Length model, Constants: lognormal (μ, σ), power-law (L_0, k_r) (m)	Intensity, (P_{32t}, P_{32c}), valid length interval: (L_0, L_{max}) (m^2/m^3)	Relative intensity of P32	Transmissivity model Eq no constants $T(m^2/s)$
All	1. NE	(118, 1.9) 17.3	(L_0, k_r) (0.5,2.6)	(0.77,0.29) (0.5, 1,000)	0.07	*Correlated:* (a,b)
	2. EW,	(17.1, 7.3) 11.2			0.20	($5 \cdot 10^{-12}$, 2.0)
	3. NW	(73.1, 4.7) 13.7			0.11	
	4. BGNE,	(316.3, 5.5) 17.9			0.12	
	5. BGNS	(96.8, 3.8) 20.3			0.01	
	6. BGNW(EW)	(22.1, 2.4) 6.0			0.07	
	7. HZ	(125, 75) 5.0			0.43	

The distribution of hydraulic conductivity components for 20 m and 100 m blocks are shown in Figure 4-14, and tabulated in Table 4-1, Table 4-2 and Table 4-3. The median values are vary similar, slightly lower for 20 m blocks with KLX01, but the variability at KLX01 is lower due to a more connected network. Overall, the differences in the 100 m block properties would not be expected to impact the regional flow greatly.

The block-scale properties for the DT model were only calculated for 100 m block and are tabulated in Table 4-1, Table 4-2 and Table 4-3. Again, the results are very consistent with those reported here. In Figure 4-15 the distributions of the components of hydraulic conductivity of 100 m blocks for the DT and CONNECTFLOW (CF) models are compared. The distributions agree very closely with the DT model being more isotropic as the only significant difference. Looking at anisotropy as the direction of maximum horizontal conductivity, the DT model shows a consistent picture of a slight bias toward angles between 90°–130° as shown in Figure 4-16.

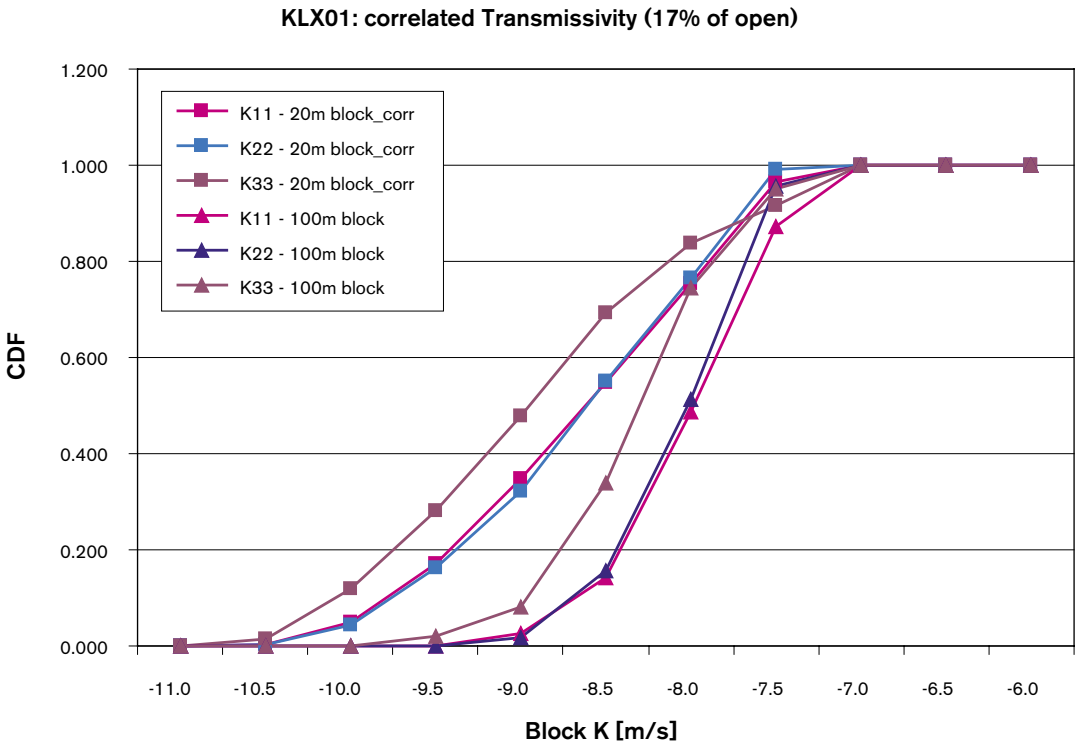

Figure 4-14. *Hydraulic conductivity distribution for correlated transmissivitybased on the PSS data from KLX01. K11, K22, K33 correspond to Kx (Easting), Ky (Northing) and Kz (vertical), respectively.*

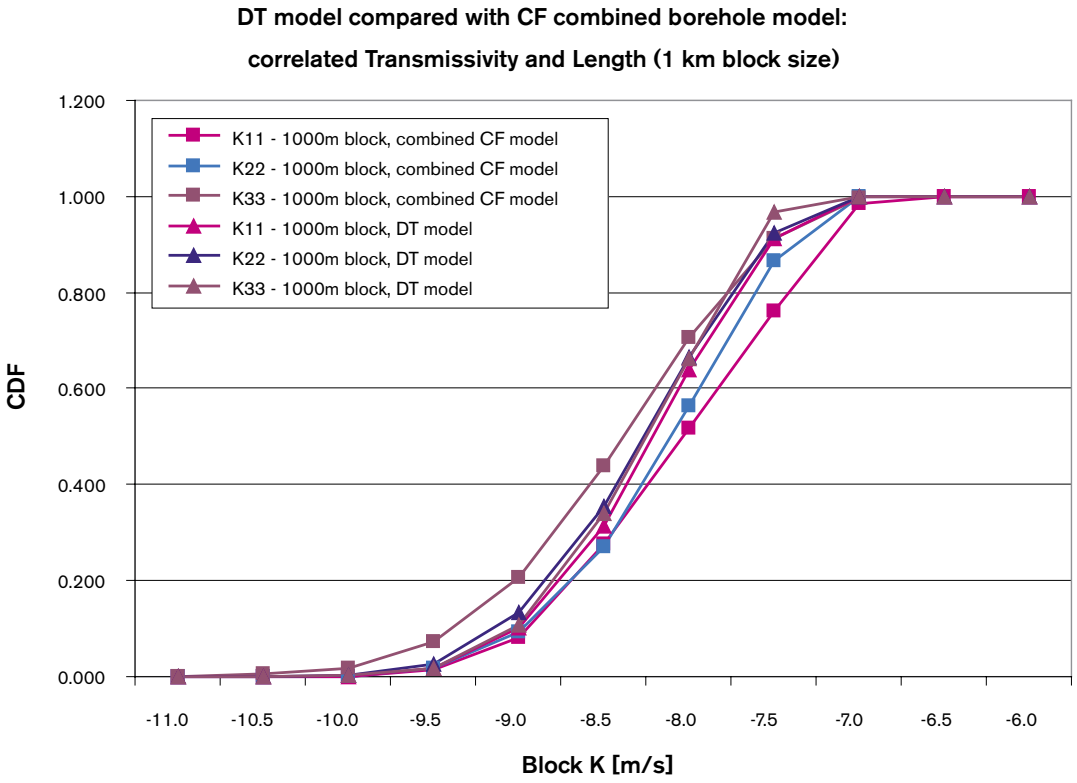

Figure 4-15. *A comparison of the 100 m block-scale hydraulic conductivity for the CF Hydro-DFN model given in Table 3-26 and DT model given in Table 4-4.*

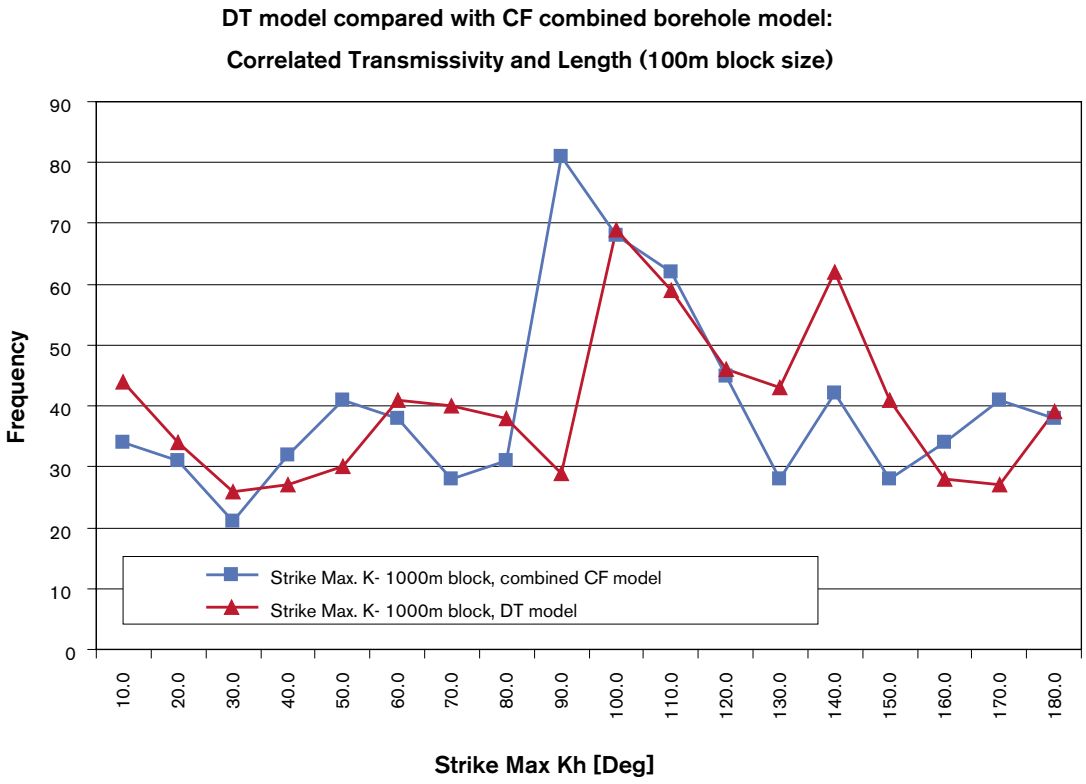

Figure 4-16. *Comparison of the distribution of the strike of the maximum horizontal hydraulic conductivity for a correlated transmissivity between the CF and DT Hydro-DFN models each with a correlated transmissivity model.*

4.5 Conclusions from block property study

- For a 20 m block the median for all transmissivity models is very similar, around Log (K_{eff}) = –8.5.
- For a 100 m block the median Log (K_{eff}) is –8.2 for the correlated case, –8.9 for the uncorrelated case and –8.6 for the semi-correlated case.
- The correlated model gives greater heterogeneity of the hydraulic conductivity, but also a greater spatial correlation between blocks associated with large stochastic deformation zones.
- There is localised horizontal anisotropy within a block for all cases due to the discrete nature of the DFN. The median horizontal anisotropy Khmax/Khmin is about 2–3. For the uncorrelated model there is no regional trend to the anisotropy. Whereas for the correlated and semi-correlated case there is a clear trend toward higher Khmax in the direction with strike about 90°–130°. This is consistent with the orientations of PFL flow anomalies seen in KSH01A and KSH02 (see Section 3.5). The fact that the direction of flow in the correlated case is more consistent with the PFL anomaly data compared to the uncorrelated case may add credence to the existence of a correlation between transmissivity and length. It is perhaps interesting to note that the anisotropy in the correlated case is parallel with the WNW direction of maximum regional stress.
- There is a regional anisotropy between the horizontal and vertical hydraulic conductivity with median ratio Khmax/Kz of about 2.5 to 3.

- Fracture porosity has a median of Log (phi) = –4.8 for a 100 m block. For the correlated case it does not have a strong dependence on L_{min}, but does for the uncorrelated case.
- A L_{min} of not more than 50 m has to be used for a 100 m for the correlated T model, but must be less than 50 m for the uncorrelated T model. As a general rule of thumb, fractures down to a length at least as small as half the block-size need to be included.
- Little bias is introduced whether the models is based on the PSS data from KLX01 or the combined PFL/PSS data from the Simpevarp boreholes KSH01A, KSH2 and KSH03A. The median hydraulic conductivities are very similar, but there is less variability for the KLX01 case, i.e. it is more homogeneous.
- The block-scale properties based on the Darcy Tools Team (DT) and CONNECTFLOW Team (CF) are consistent in terms of median value and variability, although the DT properties are more isotropic.

5 Regional model – general conditions

Regional modelling of groundwater flow and transport is required to assess the uncertainties of the hydrogeological properties and conditions at Simpevarp. The primary objective is to assess the role of known and unknown hydrogeological conditions for the present-day distribution of saline groundwater at the Simpevarp site. An improved understanding of the paleo-hydrogeology is necessary in order to gain credibility for the Site Descriptive Model in general and the Site Hydrogeological Description in particular. The numerical models developed are then to serve as a basis for describing the present hydrogeological conditions as well as predictions of future hydrogeological conditions and transport pathways.

The main objective implies a testing of following modelling components:

- Structural geology with geometrical alternatives.
- Bedrock fracturing.
- Initial and boundary conditions variants.
- Parameter uncertainties (i.e, uncertainties in the hydraulic property assignment).

Another specific objective is to assess the flow-paths from the local-scale model domain, based on the present-day flow conditions, to assess the distribution of discharge and recharge areas associated with the flow at approximate repository depth. (The subsequent Safety Assessment calculation, not part of this study, under future flow conditions and more detailed selection of particle release points may of course show different results). This aspect is necessary in order to evaluate the impact on the groundwater flow-field of the specified components and to promote proposals of further investigations of the hydrogeological conditions at the site.

5.1 Model assumptions and input data

The simulations of how flow and reference waters have evolved in the post-glacial period up to the present day is modelled in using a EPM model with fixed hydraulic properties, but with boundary conditions that change with time. In the base case, the head on the top surface was set to the topographic height that evolves in time due to post-glacial rebound. Offshore, the head was equal to the depth of the sea multiplied by the relative salinity of the Baltic Sea, and here both the salinity of the Baltic and sea depth altered in time. Simulations were started at 10,000 BC, approximately when the glaciers in the area melted, with an assumed initial distribution of the reference water fractions and run until the present-day.

The key assumptions in the modelling and the possible alternatives are:

- The deformation zone model provided by Geology represents hydraulically active features. Where no direct observation has been made of a deformation zone’s properties, then it is assumed vertical and the transmissivity is taken from a characteristic mean. Alternatives include neglecting relatively small lineaments, neglect zones with a low confidence, or sample the unknown parameters stochastically.

- The Hydro-DFN developed for the Simpevarp boreholes can be extrapolated over the whole region-scale model. Based on the Hydro-DFN for Version S1.2 there is no clear evidence for either a dependence on the rock domains (as provide by Geology) or a depth-trend in the hydraulic properties. Alternatives include several different Hydro-DFN models based on different assumptions about a transmissivity dependence on length, the Hydro-DFN models developed by the two modeling teams, or a depth dependency in the hydraulic properties.
- The hydro-geochemistry measurements are best represented in terms of 4 reference water types (Rain 1960, Brine, Marine and Glacial) with fractions computed based on the M3 analysis /17/. Alternatives are to use more reference waters or use individual ions and isotope ratios as calibration targets.
- An appropriate time to start the simulations is 10,000BC and the groundwater is a mixture of Glacial and Brine reference waters with specified mixing fraction spatial distributions. Variants include different distributions for initial mixing fractions.
- Surface groundwaters waters are appropriate mixtures of Glacial and Marine waters during the early Baltic Ice Lake, Yoldia Sea, and Ancylus Lake periods. The surface groundwaters then switch to a mixture of Rain 1960 and Marine during the Littorina Sea and current Baltic Sea phases. The history of sea-water salinity has been provided and this is used to determine the relative fractions of Marine and Rain 1960 reference waters at the top surface of the model offshore. The surface water composition is implemented as boundary conditions on the reference water transport equations. Alternatives are to include some dilution by the Rain 1960 reference water during the early pre-Littorina phases.
- The surface flow condition is that onshore the head equals the evolving topographic surface as provided by ice-sheet modelling. Alternatively, a specified flux type boundary condition can be used using a potential infiltration based on surface hydrology.

5.2 Conceptual model

The primary concepts used in the regional-scale groundwater flow modelling are:

- The current hydrogeological and hydro-geochemical situation at Simpevarp has arisen to due to natural transient processes that have evolved over post-glacial period.
- The hydro-geochemistry can be modelled in terms of four reference water (Rain 1960, Brine, Marine and Glacial) using the reference water fractions as conservative tracers.
- The natural transient processes (land-rise, marine transgressions, dilution/mixing of sea water) can be modelled by appropriate choice of flow and refrence water boundary conditions.
- The spatial variability of hydraulic properties can be represented in an EPM model by appropriate upscaling of bedrock fracturing and downscaling of deformation zones on a suitable grid resolution.
- The properties of the hydraulic rock domain (HRD) is represented as EPM under-pinned by a regional-scale stochastic DFN model. The HRD properties (hydraulic conductivity tensor, and porosity) are calculated explicitly for each element in the EPM model by an upscaling method.
- For the hydraulic conductor domains (HCD) the properties (transmissivity, thickness, and porosity) are constant over each deformation zone.
- For the hydraulic surface domains (HSD) the properties (hydraulic conductivity, thickness, and porosity) are constant over the whole top surface of the model.

Sections 5.3–5.9 give details of the actual concepts, parameters values, and variants considered in the regional-scale groundwater flow modelling.

5.3 Concepts for reference water transport

Based on the analysis of Hydro-geochemistry /17/, groundwater compositions were described using a simplified system of four reference waters, which have been previously used in M3 geochemical modelling:

- **Brine water:** Represents the sampled deep brine type (Cl = 47,000 mg/L) of water found in KLX02. An old age for the Brine is suggested by the measured 36Cl values indicating a minimum residence time of 1.5 Ma for the Cl component.
- **Glacial water:** Represents a possible melt-water composition from the last glaciation > 13,000 BP. Modern sampled glacial melt water from Norway was used for the major elements and the $\delta^{18}O$ isotope value (−21 ‰ SMOW) was based on measured values of $\delta^{18}O$ in calcite surface deposits. The δD value (−158 ‰ SMOW) is a calculated value based on the equation ($\delta D = 8\times\delta^{18}O+10$) for the global meteoric water line.
- **Marine** is a composite of **Littorina Sea** and a modified sea water (Sea sediment). Littorina represents old marine water. This water is used for modelling purposes to represent past Baltic Sea water composition. The Modified Sea water (Sea sediment): represents sea water affected by microbial sulphate reduction.
- **Rain 1960:** Corresponds to infiltration of meteoric water (the origin can be rain or snow) from 1960. Sampled modern meteoric water with modelled high tritium content was used to represent precipitation fro m that period.

The major ion components and stable isotope composition for the selected reference waters are given in Table 5-1.

Table 5-1. Groundwater analytical or modelled data used as reference waters for Simpevarp /18/.

	Cl (g/L)	Na (g/L)	K (g/L)	Ca (g/L)	Mg (g/L)	HCO_3 (g/L)	SO_4 (g/L)	δD (‰)	$\delta^{18}O$ (‰)
Brine	47.2	8.5	0.045	19.3	0.002	0.014	0.906	–44.9	–8.9
Marine	6.5	3.674	0.134	0.151	0.448	0.093	0.89	–38	–4.7
Rain 1960	0	0	0	0	0	0.012	0.001	–80	–10.5
Glacial	0.001	0	0	0	0	0	0.001	–158	–21

In the modelling, the groundwater density and viscosity are taken to be functions of the total groundwater salinity (and pressure and temperature). The salinity for a given water composition is just the sum of the products of each reference water fraction with the salinity of that reference water. The salinities for the reference waters were calculated from the Total Dissolved Solids (TDS, g L^{-1}) using

Salinity = TDS / density,

where density is a function of salinity (and temperature, pressure). It was assumed that the data given in Table 5-1 were obtained under laboratory conditions. Therefore, it was assumed that the data correspond to a temperature of 20°C and pressure of one atmosphere.

The density and viscosity were obtained using empirical correlations for NaCl brines (See /19/ and /20/). This corresponds to representing transport of equivalent NaCl for each water. The approximation made is reasonable, but it will lead to the density and salinity being slightly under-estimated for a Ca-rich solution such as the Brine reference water.

Assuming a pressure profile down-core (surface ~1atm to ~25 MPa at depth), a salinity profile (surface 0‰ to 72.3‰ (brine) at depth), and a temperature range (surface 6 °C; geothermal gradient 0.01°C m–1; i.e.~30°C at bottom of model), the groundwater density (ρ) can be calculated from the equation of state. At the surface, the density is around 1,000 kg m^{-3}; and at depth the density is around 1,056 kg m^{-3} (the greatest model depth is 2,300 m). The groundwater viscosity (μ) can be similarly calculated. At the surface, the viscosity is around 1.3×10^{-3} Pa s^{-1} and at depth, the viscosity at depth is around 0.9×10^{-3} Pa s^{-1}.

The equations used to represent the transport of fractions of reference waters, with rock-matrix diffusion, are:

$$\frac{\partial(\phi_f \rho)}{\partial t} + \nabla \cdot (\rho \mathbf{q}) = 0 \qquad \text{(Mass conservation for groundwater)}$$

$$\frac{\partial(\phi_f \rho \sigma_i)}{\partial t} + \nabla \cdot (\rho \sigma_i \mathbf{q}) = \nabla \cdot (\phi_f \rho D \nabla \sigma_i) + \zeta \rho D_{\text{int}} \left.\frac{\partial \sigma'_i}{\partial w}\right|_{w=0} \qquad \text{(Transport of reference waters)}$$

$$\alpha_i \frac{\partial \sigma_i}{\partial t} = D_{\text{int}} \frac{\partial^2 \sigma'_i}{\partial w^2} \qquad \text{(Rock-matrix diffusion)}$$

where σ_i is the mass fraction of reference water i in the water in the fracture system (mobile water); σ'_i is the mass fraction of reference water i in the water in the matrix (immobile water); $\boldsymbol{q}$ is the Darcy velocity:

$$q = -\frac{k}{\mu}(\nabla p + \rho g);$$

$\boldsymbol{D}$ is the dispersion tensor; ϕ_f is the fracture porosity, ρ is the groundwater density, ζ is the specific surface area of the fractures D_{int} is the intrinsic (or effective) diffusion coefficient, α_i is the capacity factor for the rock matrix (which allows for sorption), w is a coordinate into the rock matrix, k is the permeability, μ is the fluid viscosity, p is residual pressure, t is time, and g is gravitational acceleration. All parameters use SI units.

In fact, the transport equations for the fractions of reference waters are not all independent. Since the sum of the reference water fractions must add to one, then it is not necessary to solve explicitly the transport equation for the final reference water. It can simply be evaluated as the remaining water fraction once the other reference water fractions have been computed at each time-step.

In the above equations, the groundwater density and viscosity are taken to be functions of the salinity (and the temperature and pressure). The salinity is just the sum of the products of each reference water fraction and the salinity of that reference water. The density and viscosity were calculated from the salinity using empirical correlations for NaCl brines /20/.

5.4 Topography and model domain

Topographic data was supplied on two scales, 50 m and 10 m. Since the refined 10 m data covered the entire regional-scale model area defined in the TD, this fine-scale data was used both to define the model area and to set boundary conditions on the top surface. In addition, a number of regional and local water divides had been identified. In CONNECTFLOW it is possible to construct unstructured meshes with irregular boundaries, and hence it is possible to choose boundaries that follow water divides. Figure 5-1 shows the extent of the topographic data and water divides along with the regional model domain as proposed in the TD.

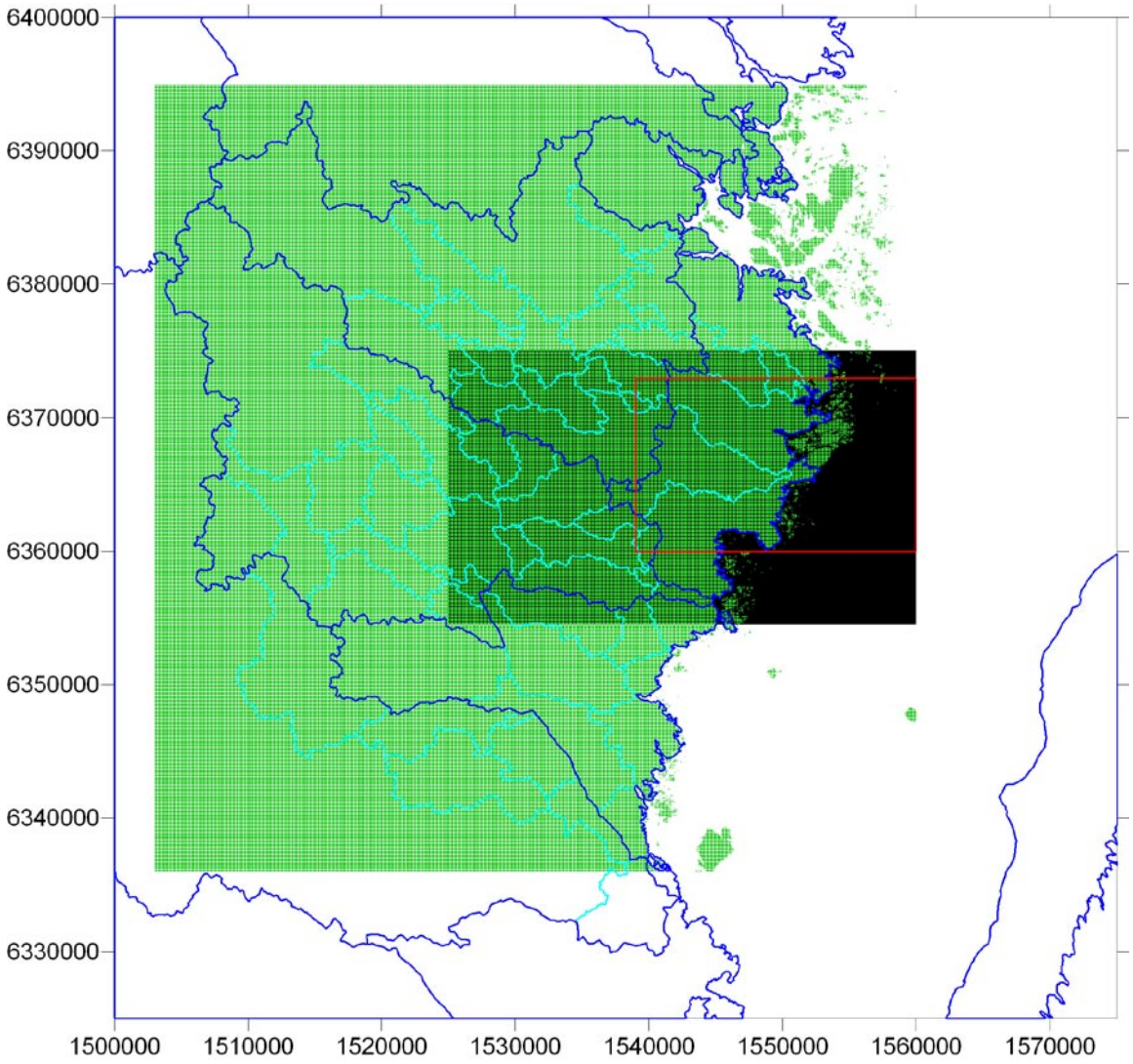

Figure 5-1. *Overview of available data 10 m topographic data (dark green), 50 m topographic data (light green), regional water divides (dark blue), local water divides (light blue), and the suggested regional scale area (red).*

Modelling transient flow coupled to transport of four reference waters created significant computational demands, and hence it became important to establish a minimum sized model domain for calibrating the model using many realisations and variants. Hence, part of the study concentrated on quantifying the sensitivity of the calibration targets to domain size with the aim of finding a minimum size for the regional model for which stable calibration results could be obtained. The primary calibration targets used were the profiles of salinity down the boreholes KLX01, KLX02, KSH01A, KSH02 and KSH03A. The salinity was also considered at KAV01 and a hypothetical borehole at the centre of Äspö. The starting domain was based on Simpevarp 1.1 /21/. This model domain covered the whole regional-scale area although some areas outside of regional or local water divides were removed and assumed as no-flow boundaries (See Figure 5-2).

A series of different size domains were considered (see Figure 5-3) starting from the local-scale area (shown in red); one extending west (grey) to capture some hills and a valley, one extending north (yellow) to capture the Mederhult zone; one extending in all directions (orange) to capture some hills to the west and to valleys north and south as well as out into the Baltic; and finally a much larger region similar to the Simpevarp 1.1 model. In all cases, a no-flow condition was used for the vertical and bottom boundary. For all domain size variants the same spatial distribution of HRD properties were used, but the property model was just trimmed to the specified EPM model domain.

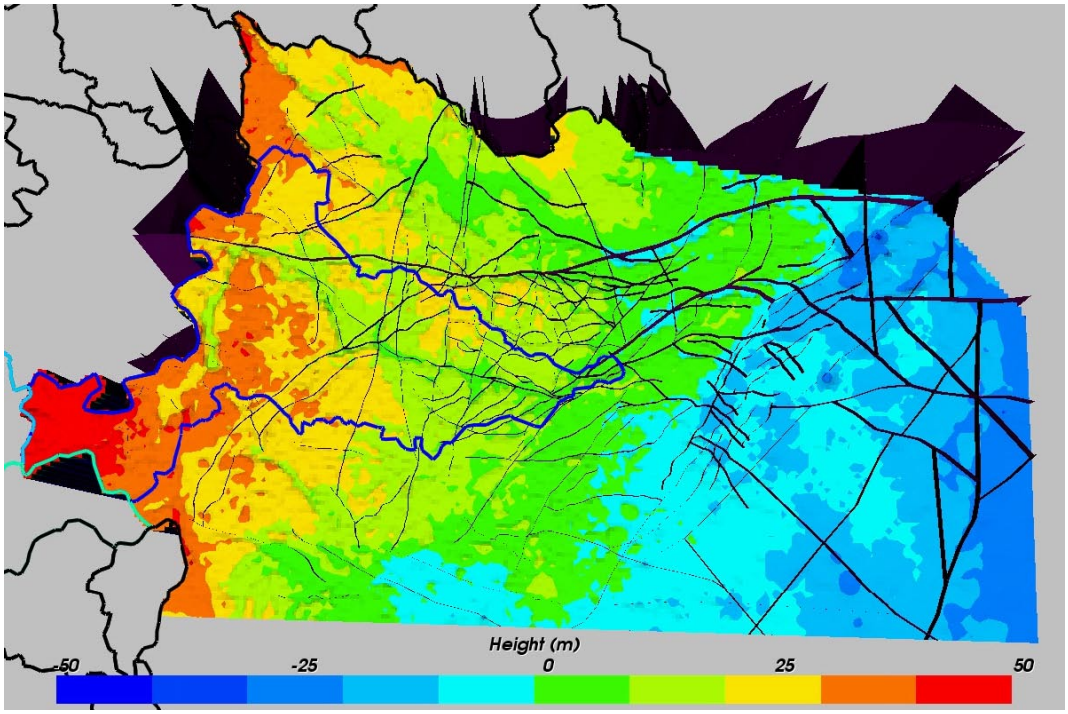

Figure 5-2. *Topographic height for the Simpevarp 1.1 model domain. The water divides are drawn in Figure 5-1 are superimposed, as is the HCD model.*

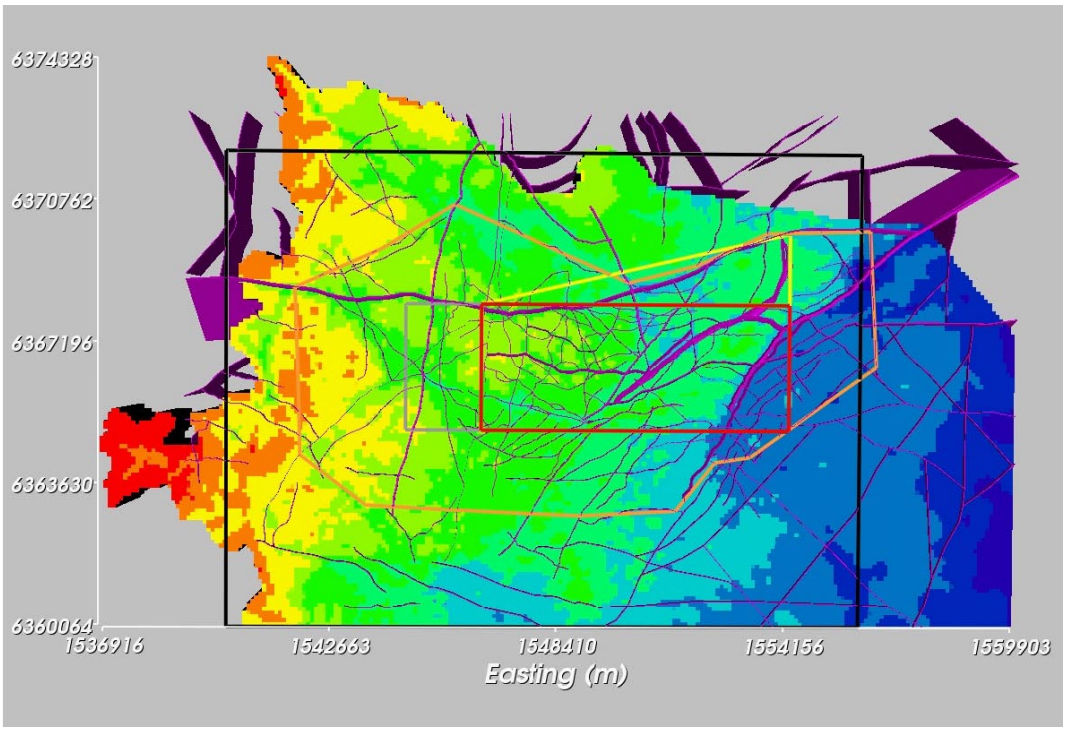

Figure 5-3. *The alternative regional model domains considered for Simpevarp 1.2 superimposed on the Simpevarp 1.1 coloured by topographic height.*

5.5 Selection of grid resolution

Based on the requirements of Design, hydraulic properties were calculated on a 20 m and 100 m block-scale. The task description for the regional-scale modelling specified a 100 m grid resolution. For practical reasons of model size, greater resolution would be prohibitive for transient multi-component reference water transport problems. Figure 5-4 shows the resolution of the hydraulic conductivity of both stochastic HRD and deterministic HCD features using a 100 m element-size over approximately the local-scale area. Figure 5-5 is the same plot with the HCD deformations zones superimposed as semi-transparent volumes. It can be seen that representation of the deformation zones is quite coarse and there is a potential for zones to be smeared out sufficiently to create artificial connections between zones (The downscaling method for mapping the deformation zone properties onto a grid is described in Section 2.1.3). For this reason it was decided to add additional refinement down to 50 m locally within the two site-scale release area s to a depth of 1,100 m. The resultant embedded grid is shown in Figure 5-4. At the interface between the two levels of refinement internal boundary conditions are imposed to ensure continuity of variables (pressure, and reference water fractions) and conservation of mass and reference water flux /10/. The improved refinement clearly gives a better representation of both the deformation zones and the heterogeneity of the HRD between them albeit only in the site-scale areas.

Some sensitivity studies using transport statistics as a performance measure suggested that the finer 50 m grid would reveal a bi-modal type behaviour caused by a better distinction between particles starting in a deformation zone and the surrounding rock that is not apparent for uniform 100 m grid.

It is important to note that different length truncations L_{min} were used in the regional-scale DFN model for 100 m and 50 m blocks based on the finding of Section 4 that L_{min} should be no greater than half the block size.

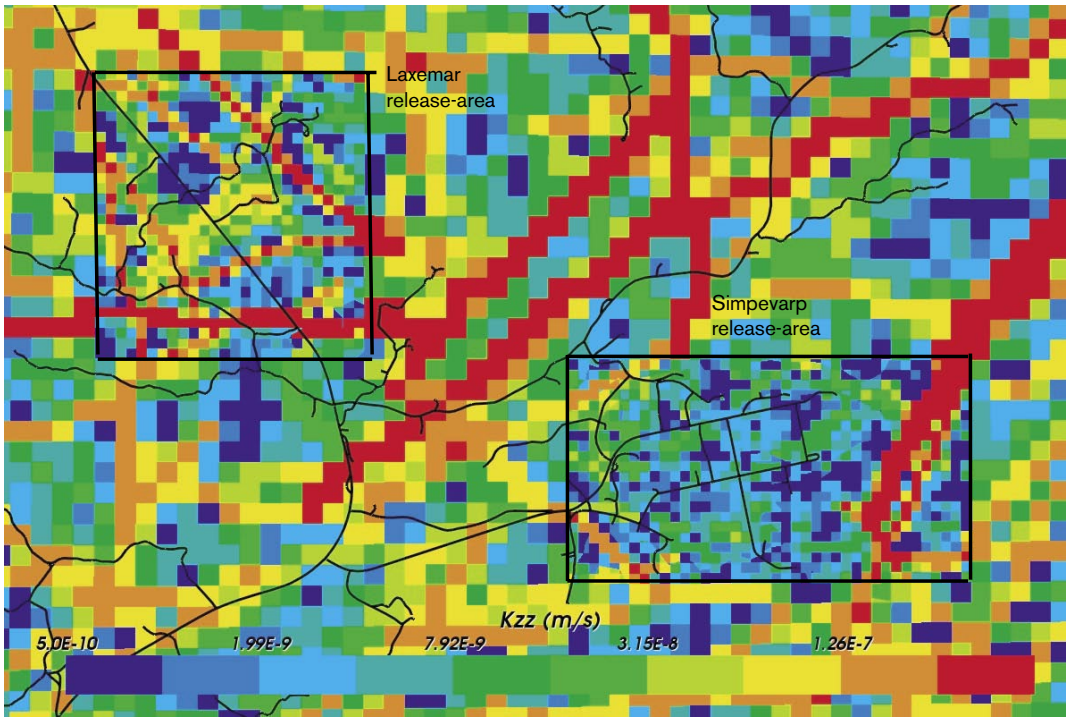

Figure 5-4. *Vertical hydraulic conductivity Kzz (m/s) on a horizontal slice at z = –50 m showing the representation of the HRD and HCD on the regional- and site-scales using an embedded grid.*

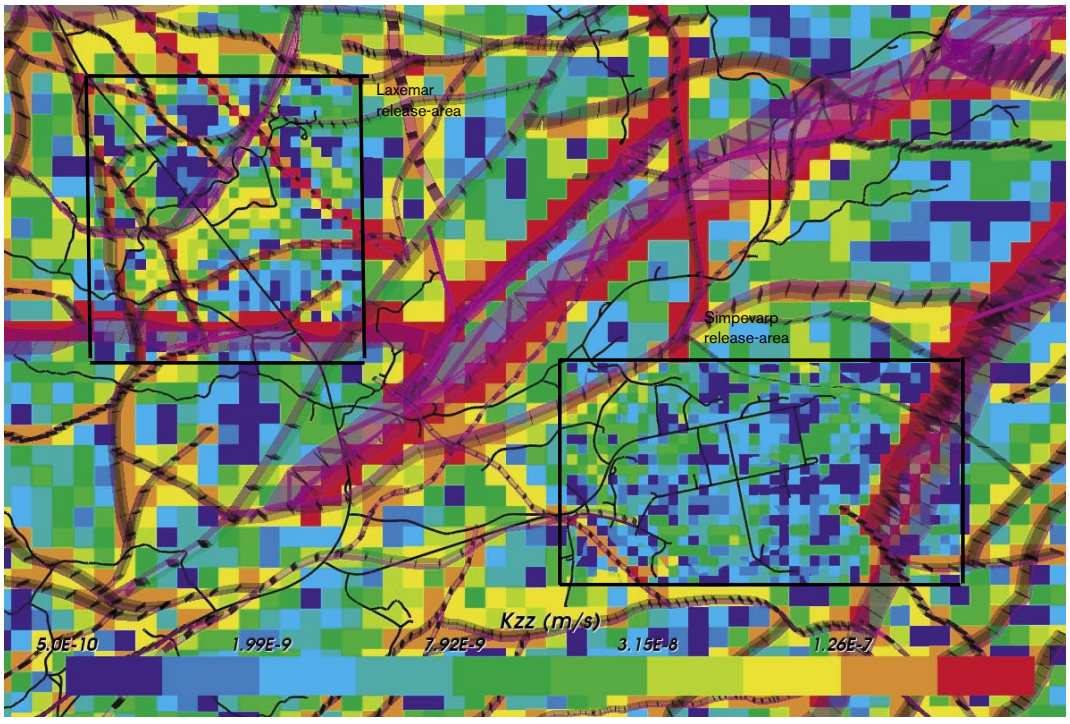

Figure 5-5. *Vertical hydraulic conductivity Kzz (m/s) on a horizontal slice at z = –50 m showing the representation of the HRD and HCD on the regional- and site-scales using an embedded grid with the deformation zones superimposed and shown semi-transparent (purple).*

5.6 Initial and boundary conditions

The boundary conditions used have to represent the transient processes of shore displacement due to post-glacial rebound and the variations in the salinity of the Baltic Sea. The evolutions of these two quantities are shown over the post-glacial period are shown in Figure 5-6 and Figure 5-7. The general modelling approach was to hold the model domain fixed (i.e. same x, y and z coordinates), but modify the head and salinity on the top surface in time. One clear feature of the land-rise scenario is the very sharp change in shoreline of about 40 m corresponding to rapid melting of the glacier occurs around –9,700 BC. This may have implications for the numerics during the early part of the simulations.

The evolution of salinity in the Baltic informs of how the mixtures of the Glacial, Marine and Rain 1960 references waters have mixed in differing fractions over time. It is also important to have a more general hypothesis of the evolution of surface and sub-surface reference waters. The current understanding is illustrated in Figure 5-8.

For flow, the head on the top surface was set to the topographic height that evolves in time due to changes in the height relative to the shoreline (see Figure 5-6). Offshore, the head was equal to the depth of the sea multiplied by the relative density of the Baltic Sea to freshwater. A variant considered was to use a flux type boundary condition as defined in Section 2.1.5 with a potential infiltration of 165 mm/year (as specified in the Task Description).

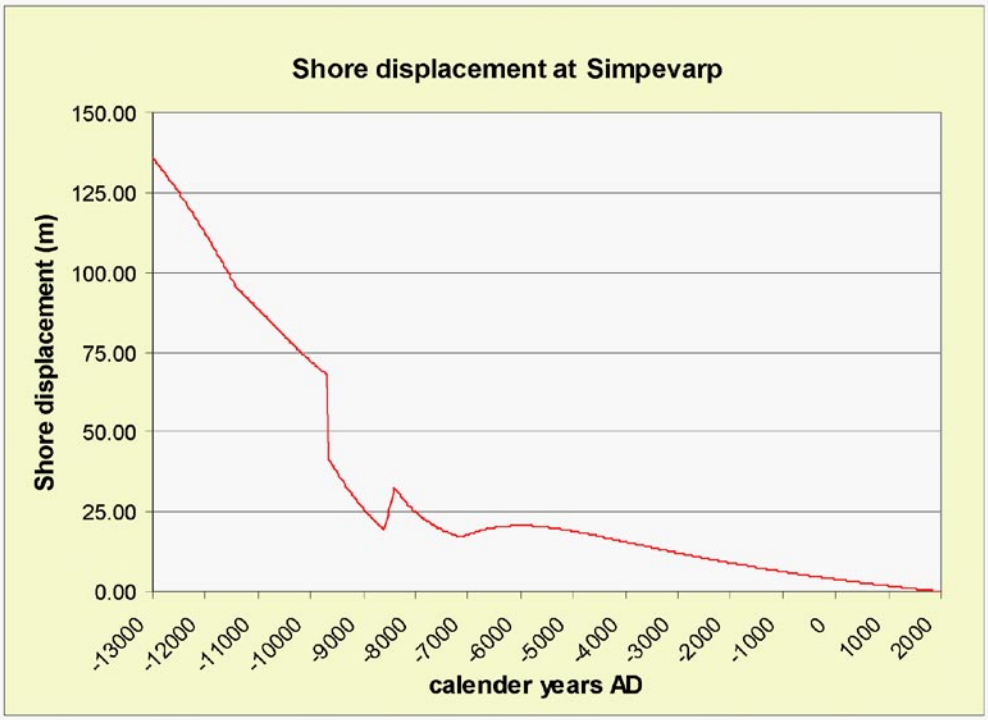

Figure 5-6. *The shore line displacement at Simpevarp.*

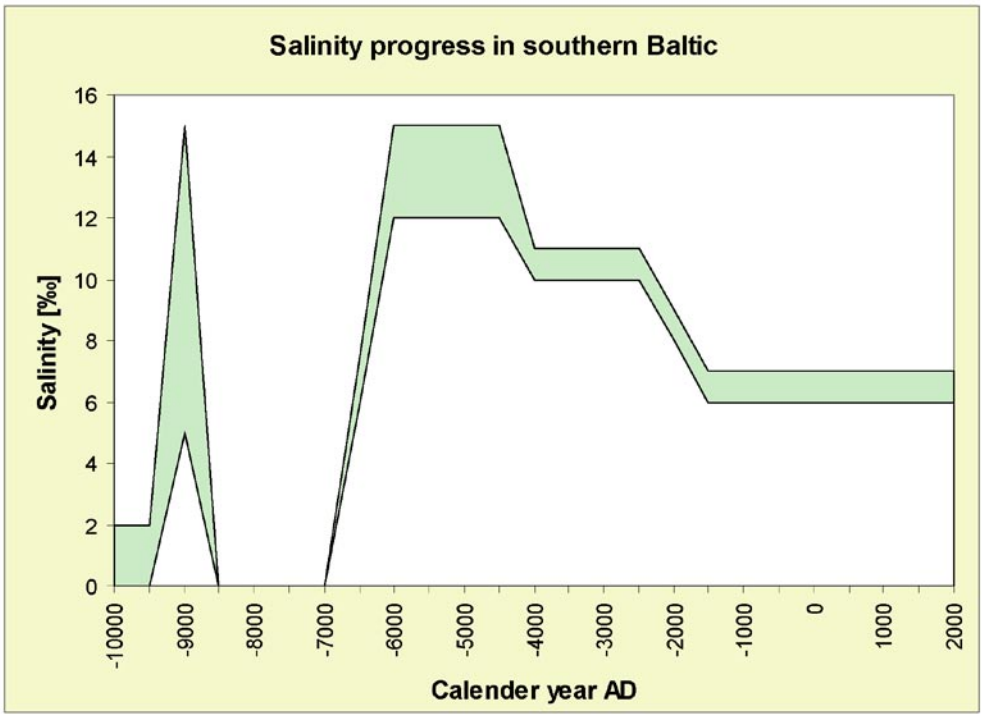

Figure 5-7. *The salinity progress in southern Baltic Sea. Two possible scenarios are shown (The uncertainty shown in green). Only the lower scenario was used here.*

Based on the surface hydro-chemistry concept shown in Figure 5-8, the definition of reference water boundary conditions was specified according to the following stages:

- Baltic Ice Lake: Full Rain 1960 onshore; Full Glacial offshore.
- Yoldia Sea: Full Rain 1960 onshore; Offshore a mixture of Marine and Glacial reference waters according to the ratio of TDS shown in Figure 5-7 to the TDS of the Marine reference water.
- Ancylus Ice Lake: Full Rain 1960 onshore; Full Glacial Offshore.
- Littorina Sea to present-day: Full Rain 1960 onshore; Offshore a mixture of Marine and Rain 1960 reference waters according to the ratio of TDS shown in Figure 5-7 to the TDS of the Marine reference water.

An earlier prescription of the reference water boundary condition used Rain 1960 reference water rather than Glacial water for the surface freshwater for all stages. However, this was found to lead to the Glacial water being flushed out too early, and so this alternative reference water boundary condition was rejected since it was felt to be both unlikely and not to give good predictions of present-day groundwater composition.

The boundary conditions on the sides are no-flow and zero flux of reference waters. On the bottom of the model at z = –2,300 m, there is a no-flow condition and groundwater is set to pure Brine, i.e Brine fraction = 1.0, all other fractions = 0.

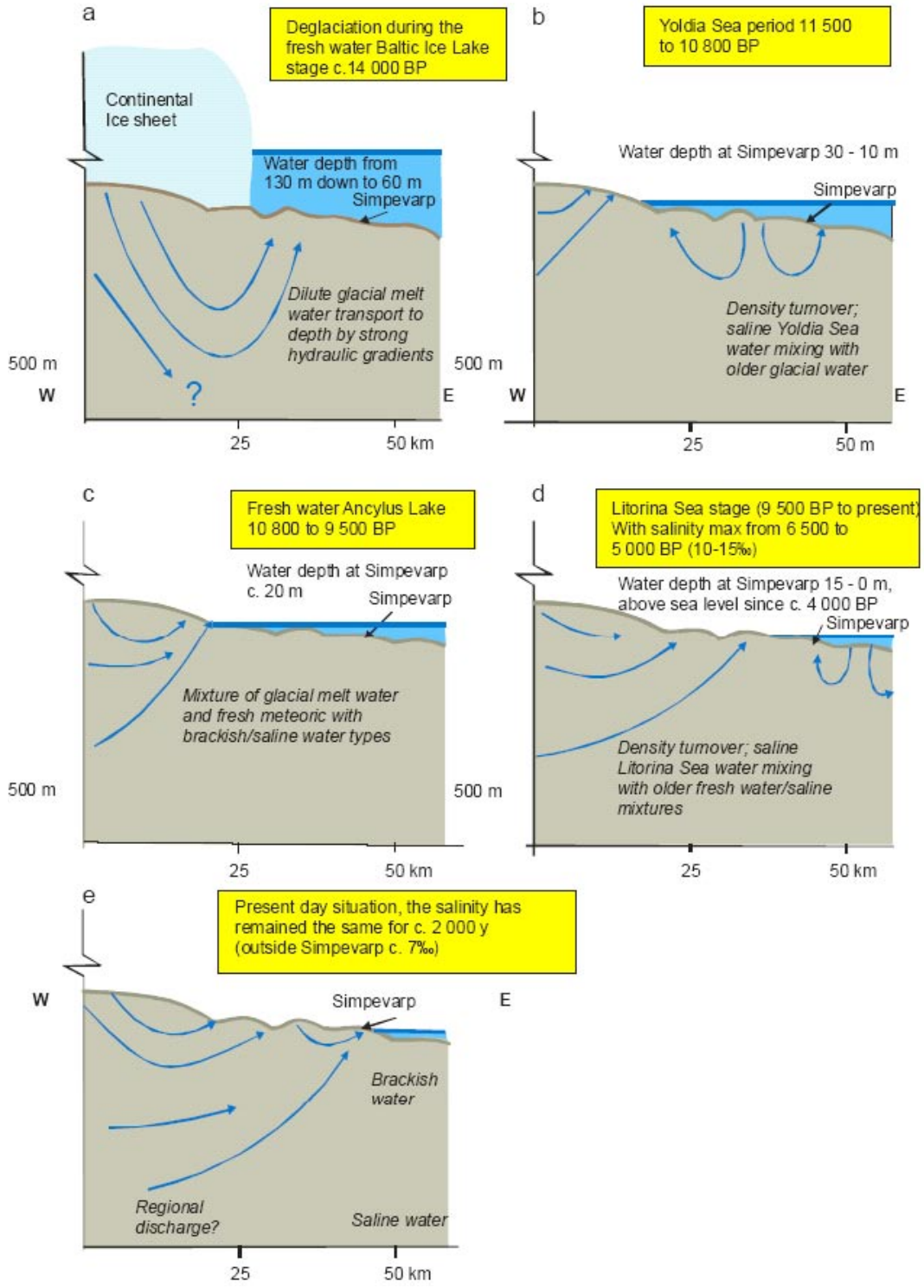

Figure 5-8. *Hydro-chemistry scenario for evolution of reference water transport from 14,000 BP to present-day showing 5 distinct stages /17/.*

The initial condition for the reference waters assumes a profile of Brine at depth and Glacial water at the surface, with a start time of 12 000 BP. Based on the present-day profile of Brine and Glacial water in KLX02, the only borehole deep enough to measure the full Brine reference water, a piecewise linear initial condition was chosen with full Glacial to 700 m depth, then a gradual rise in Brine to full Brine at 1,500 m depth. This profile is illustrated in Figure 5-9. An alternative initial condition was tried with full Glacial to 500 m depth increasing to full Brine at 1,000 m depth as a sensitivity test to shallower initial Brine. The initial condition for flow is calculated by holding the reference water fractions fixed, and calculating the flow field that is hydrostatic equilibrium at the initial time of 12,000 BP.

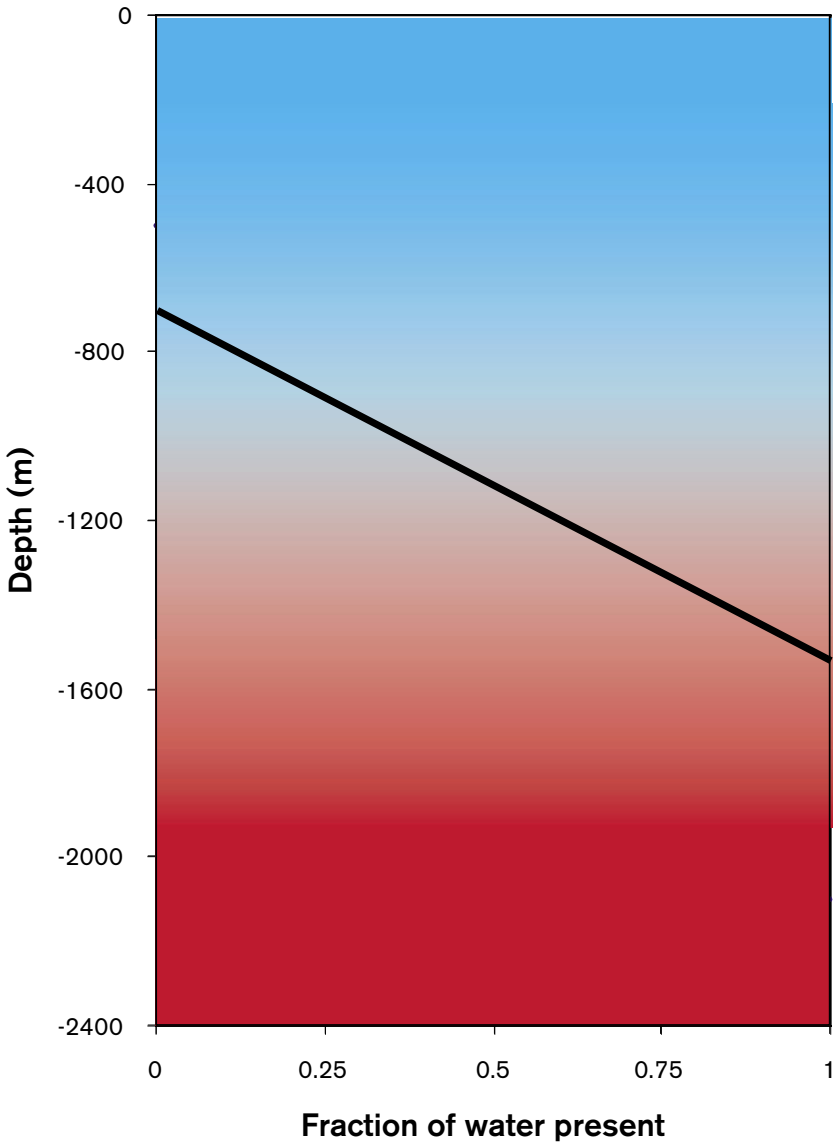

Figure 5-9. *Initial condition for reference water transport, at 12 000 BP. Above 700 m the water is pure Glacial (coloured cyan). There is then a linear transition between Glacial and Brine (coloured red) toward pure Brine below 1,500 m.*

5.7 HCD model

The updated deformation zone geometries were supplied by Geology. The model contains around twenty zones that have been verified, and is supplemented by a much large number of lineaments that are more uncertain (See Figure 5-10). Some of the high confidence zones have been represented in detail in 3D with varying dip, although all are sub-vertical. The lineaments are all assumed to be vertical. Hydraulic thickness is based on geological estimates of the width of the Deformation Zone (DZ). If no value is given by the geologist the thickness is approximated with default value of 20 m. The resulting 3D HCD model is shown in Figure 5-11.

For 18 of the zones an explicit transmissivity was estimated based on the hydraulic tests in the HCDs. The remaining zones have a transmissivity of $1.26\ 10^{-5}$ m^2/s. It is also stipulated that all HCD should be in hydraulic contact with the overburden (the modelled HSD).

Due to the uncertainties in the HCD model are a number of alternative cases were proposed. The ones considered here are:

- **Base Case** – Constant values on each DZ according to Table 5-2 for HCD-Properties. 18 HCDs have properties based on hydraulic tests in the HCDs.
- **Case 2** – Model only HCD with high confidence of existence and with Length Class 2 and 3 (L > 1,500 m). Properties as for the base case.
- **Case 3** – Model only HCD with high confidence of existence and with Length Class 3 (L > 3,000 m). Properties as for the base case.

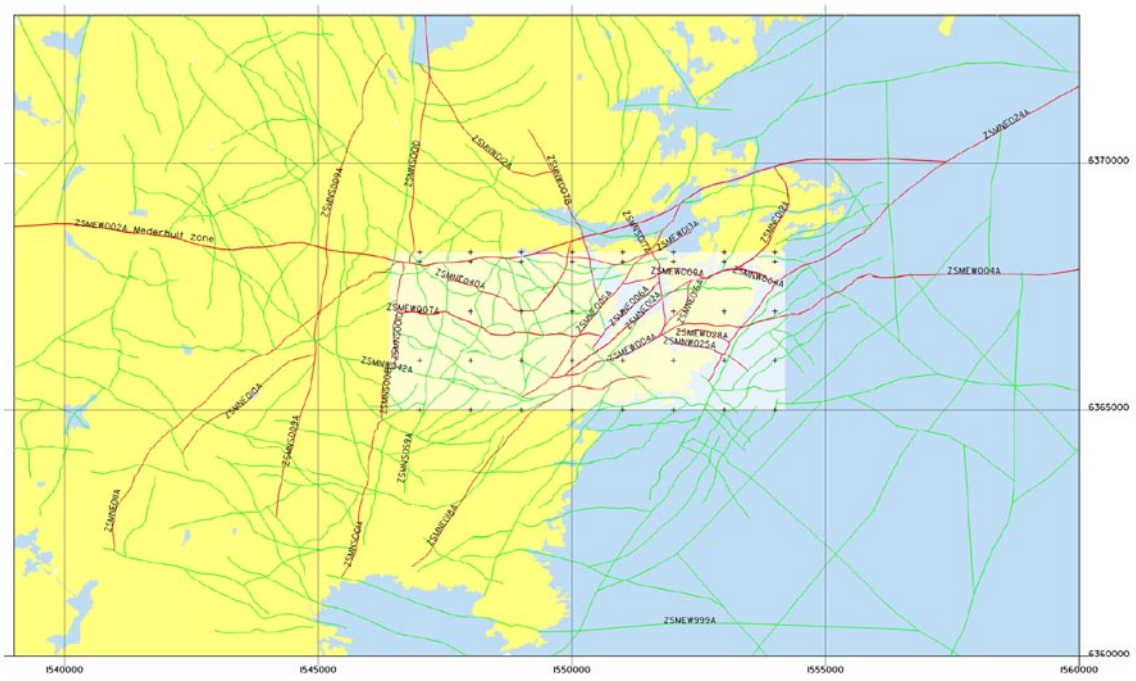

Figure 5-10. *HCD for regional-scale modelling. The white area in the middle is the local-scale area. Deformation zones coloured red have been verified and are high confidence. Lineaments are coloured green and have low confidence.*

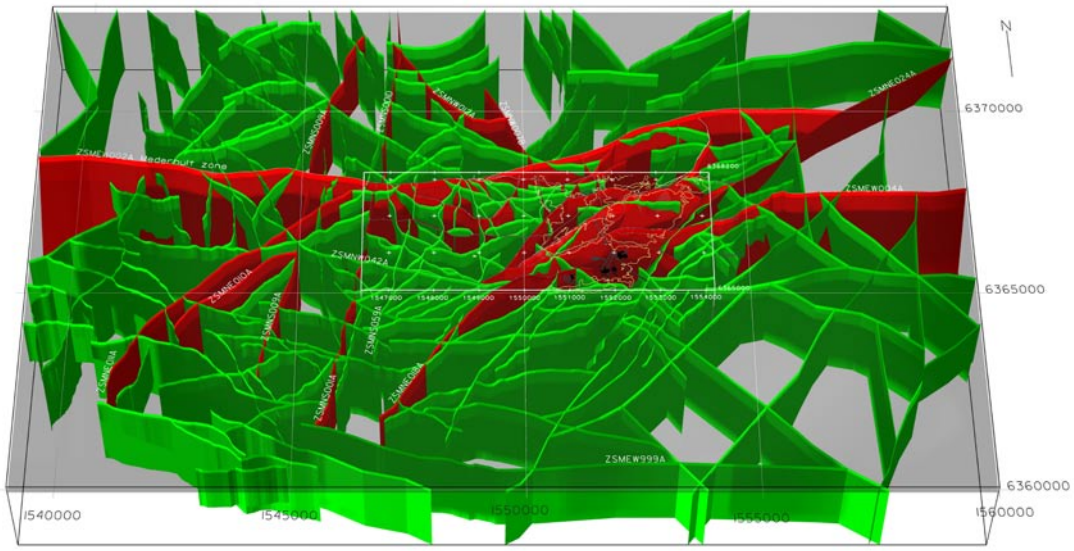

Figure 5-11. *HCD for regional-scale modelling in 3D. The white line in the middle shows the extent of the local-scale area. Deformation zones coloured red have been verified and are high confidence. Lineaments are coloured green and have low confidence.*

Table 5-2. Hydraulic properties for high confidence zones based on hydraulic tests in the HCDs.

DZ-ID	Hydraulic thickness th (m)	Transmissivity T (m^2/s)
ZSMEW028A	10	8.45E–08
ZSMNW025A	5	2.60E–07
ZSMEW013A	20	4.00E–07
ZSMEW039A	20	5.70E–07
ZSMNE005A	40	6.63E–07
ZSMEW038A	20	1.10E–06
ZSMNE018A	30	2.94E–06
ZSMNE040A	15	3.74E–06
ZSMEW002A	45	1.00E–05
ZSMEW013C	20	1.13E–05
ZSMEW009A	12	1.70E–05
ZSMNE031A	20	2.58E–05
ZSMNW048A	20	3.00E–05
ZSMNS017A	20	6.50E–05
ZSMNE012A	41	1.06E–04
ZSMNE006A	28	2.20E–04
ZSMEW007A	2	2.29E–04
ZSMNE024A	80	3.64E–04

Additional alternatives were proposed based on an approach to keep the transmissivity constant within each DZ, but to sample the transmissivity from a lognormal distribution using mean and standard deviations give in /22/. These alternatives were not implemented in this study due to a lack of sufficient time to develop the necessary tools. The Base Case and Case 2 models are shown in 3D in Figure 5-12 by colouring the DZs omitted in Case 2 in green. These are the lower confidence or short DZs. Case 3 is shown in Figure 5-15. These are the high confidence or longest DZs.

Transport aperture for was prescribed for each DZ as the kinematic porosity multiplied with the thickness of a hydraulic feature – in this case a HCD. It is considered as a calibration parameter but the base case should be $e_t = aT^b$, a = 0.5, b = 0.5, based on /15/. In CONNECTFLOW the kinematic porosity, φ_k, is defined for each DZ rather than transport aperture, e_t, so the formula $\varphi_k = e_t/th$ was used.

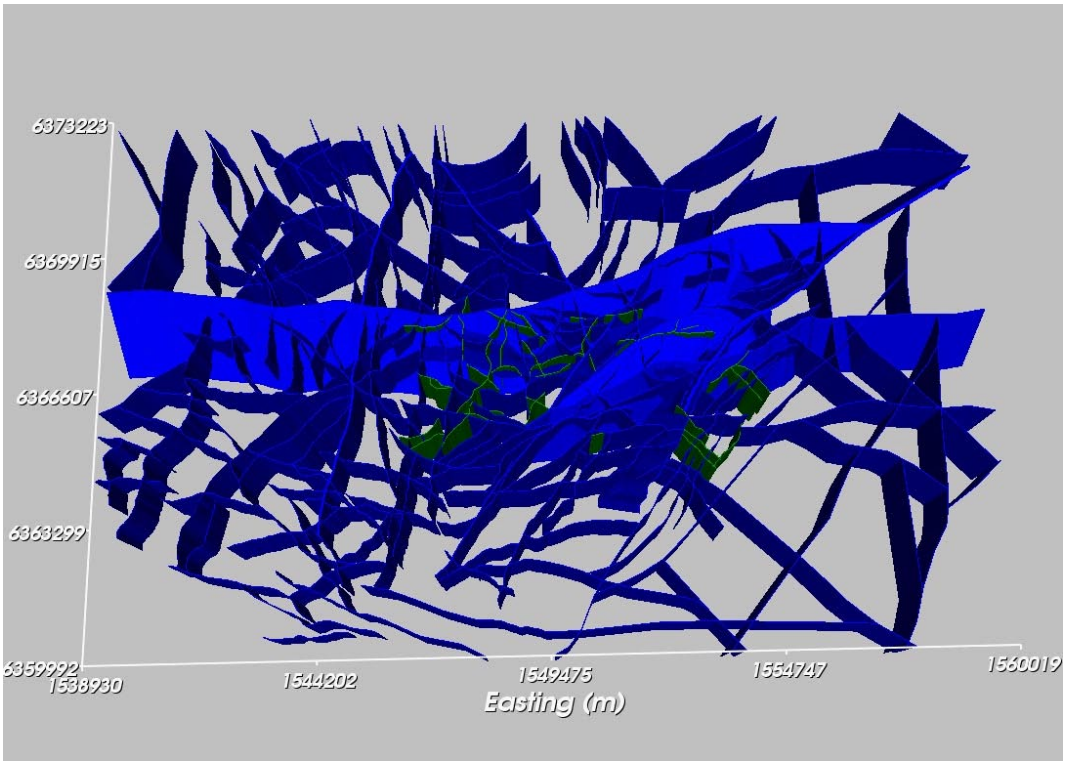

Figure 5-12. *HCD Base Case model (blue and green DZs), and Case 2 model (high confidence zones with Length Class 2 or 3 – blue DZs only).*

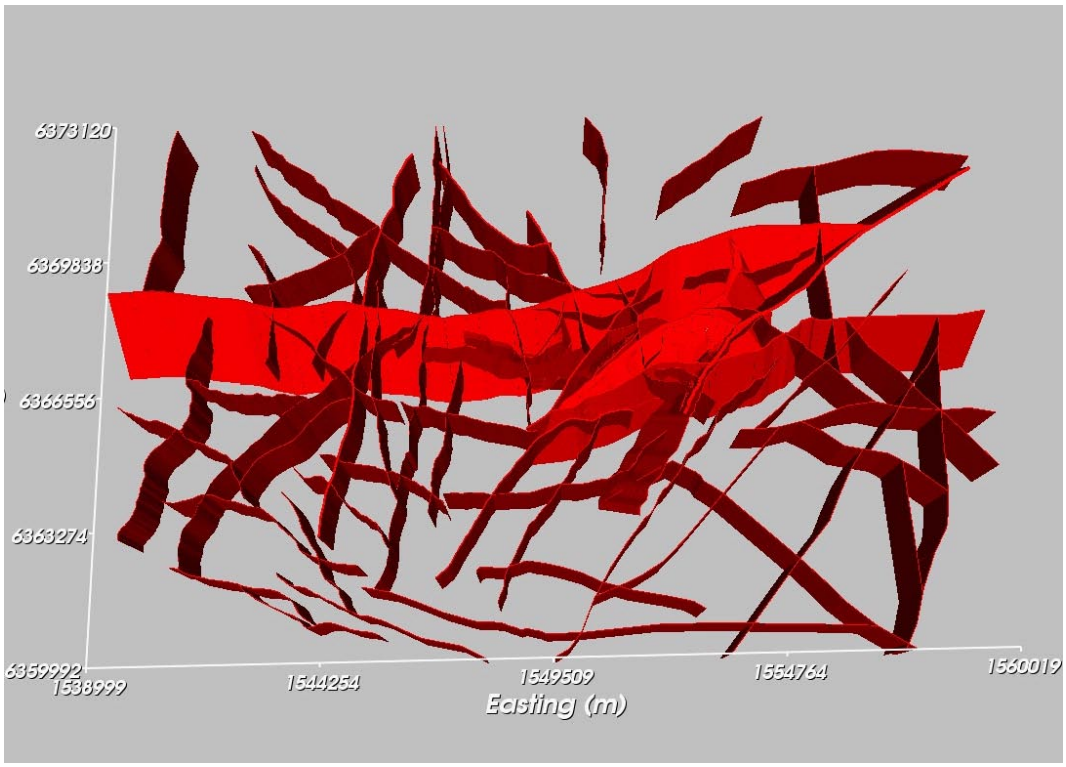

Figure 5-13. *HCD Case 3 model – high confidence zones with Length Class 3.*

5.8 HRD and DFN model

The concept for the HRD was to generate stochastic realisations of DFN model on the regional-scale based on the Hydro-DFN described in Section 3.9, with variants parameterised in Section 3.9.2, and using the upscaling method defined in Section 2.1.2 to obtain EPM properties. The regional-scale DFN model was assumed to have uniform statistics over the whole the model, and hence spatial variations of EPM properties only occurs due to the stochastic nature of the DFN parameters. The spatial difference in the DFN input was introduced to take account of the different grid size used for the site-scale embedded grid. Here, the element-size was 50 m compared to 100 m everywhere else. Based on the findings of block-scale upscaling in Section 4.5, L_{min} (the minimum fracture length sampled) should be no less than half the element size. Hence, L_{min} = 25 m in the site-scale area and 50 m elsewhere. The different DFN generation regions are shown in Figure 5-14. The extent of the regional-scale DFN was based on the domain used in Simpevarp 1.1. One realisation of the regional-scale DFN model is shown in Figure 5-15 as the full 3D model in map view, and as a horizontal cross-section at z = –500 m (i.e. a trace map) in Figure 5-16. The equivalent plot with the deterministic HCD model superimposed is shown in Figure 5-17.

As an illustration of how the DFN fits onto the EPM grid, Figure 5-18 shows a close-up map view of a slice through the DFN and finite-element grid. The finite-elements are cubes, but the visualisation tool draws a slice through them as 2 triangles. It can be seen that some elements are not cut by a fracture (at least in this 2D view), some have several fractures and some larger stochastic fractures cut many elements. This is all due to the stochastic nature of the DFN model.

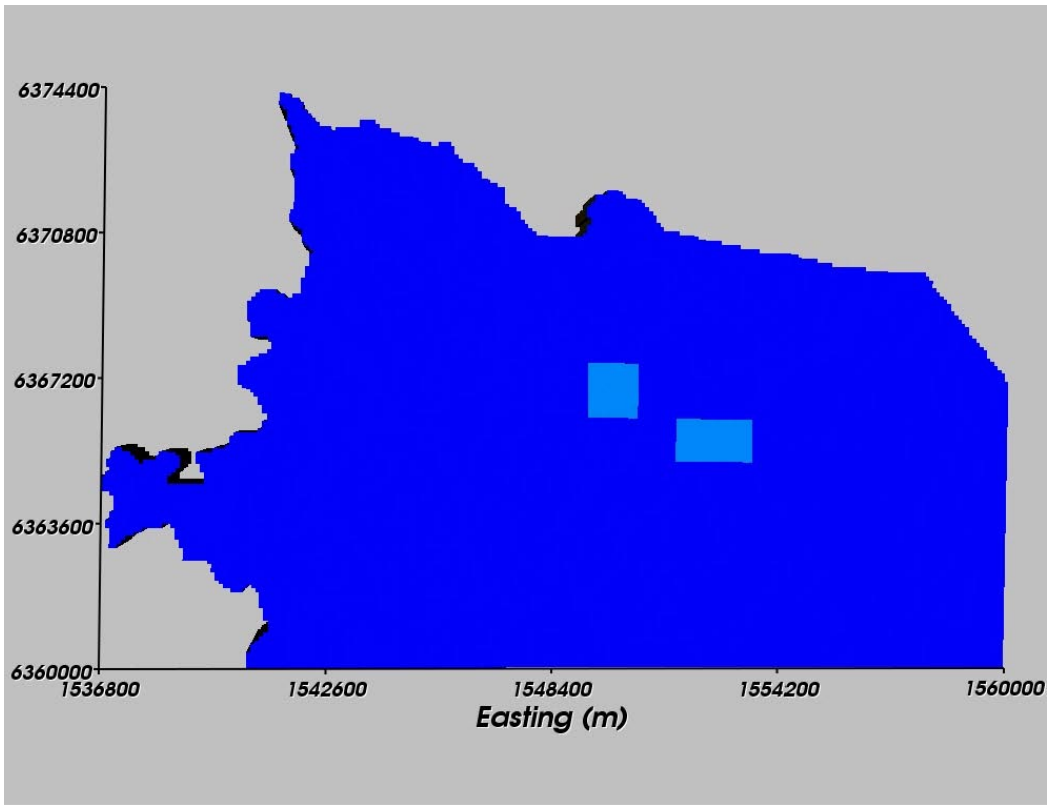

Figure 5-14. *Model areas in regional-scale DFN model. L_{min} was set to 25 m in the site-scale areas (coloured light blue), and 50 m in the regional-scale area (dark blue) due to a different grid resolution.*

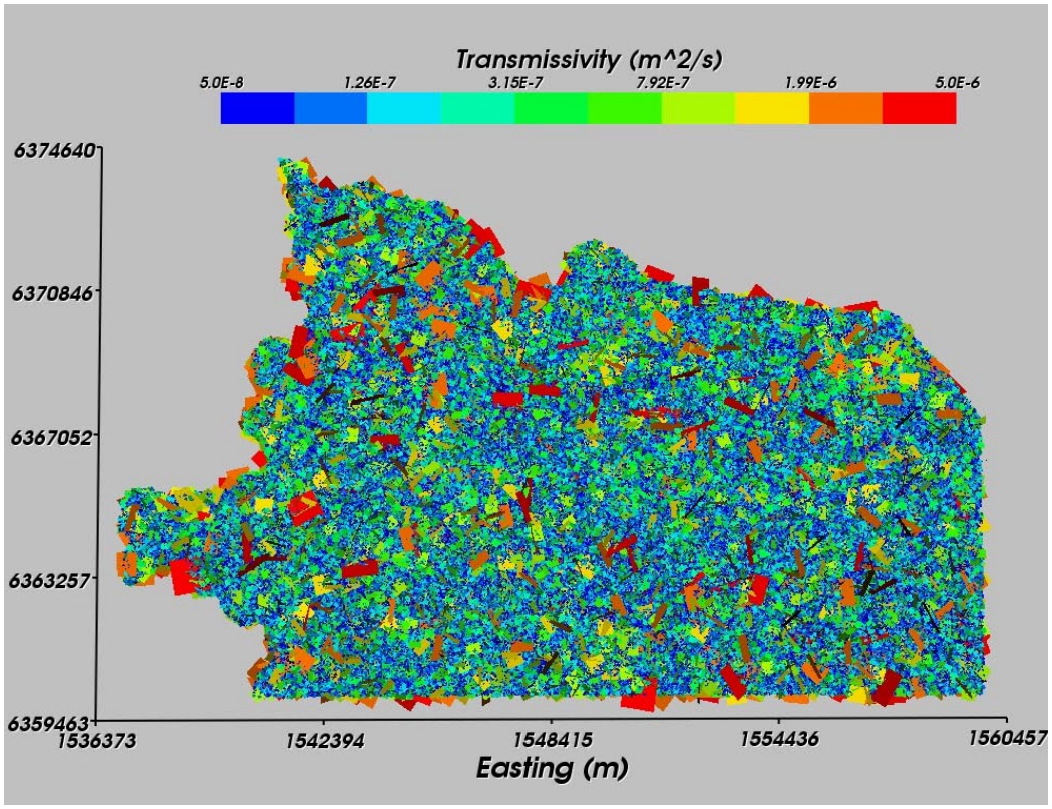

Figure 5-15. *Regional-scale DFN model showing all stochastic fractures (in 3D) coloured by Log (transmissivity).*

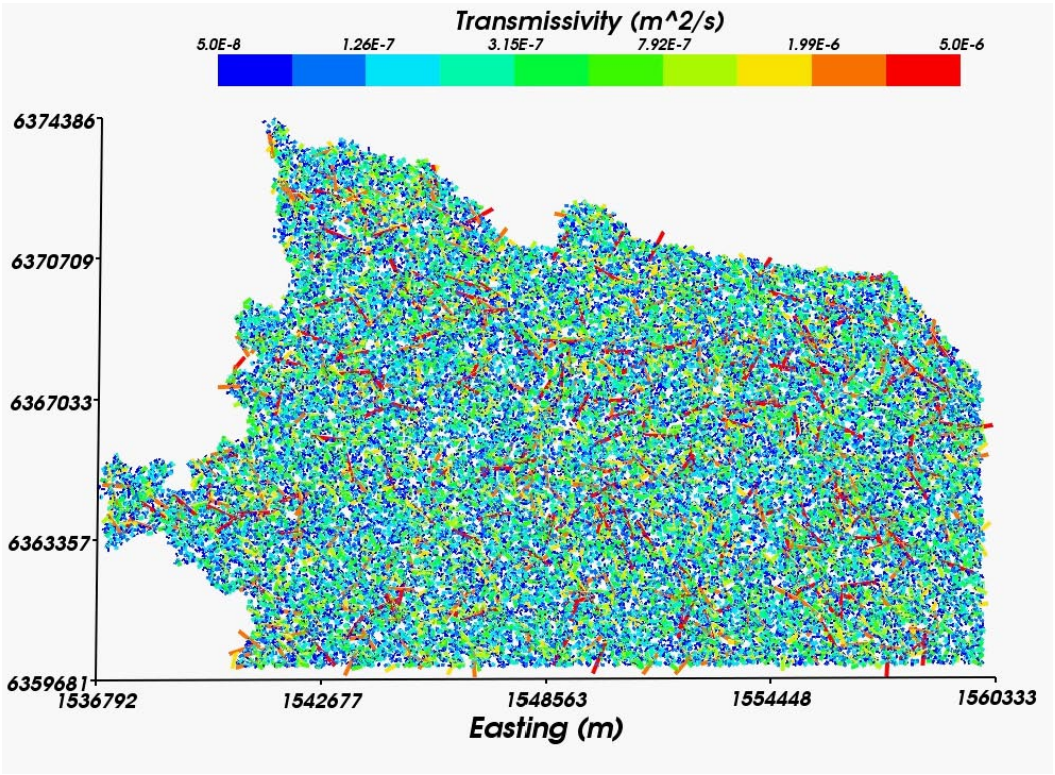

Figure 5-16. *Regional-scale DFN model showing stochastic fractures cutting a horizontal slice at z = –500 m coloured by Log (transmissivity).*

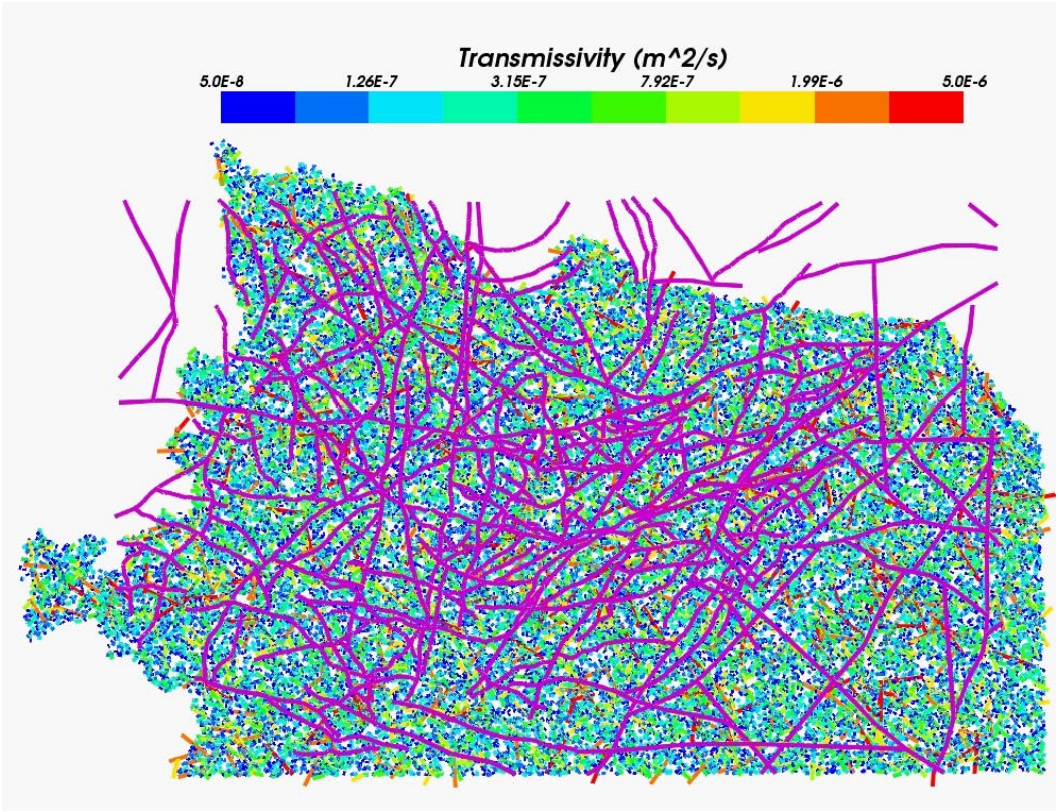

Figure 5-17. *Regional-scale DFN model showing stochastic fractures cutting a horizontal slice at z = –500 m coloured by Log (transmissivity) and the HCD model superimposed (purple).*

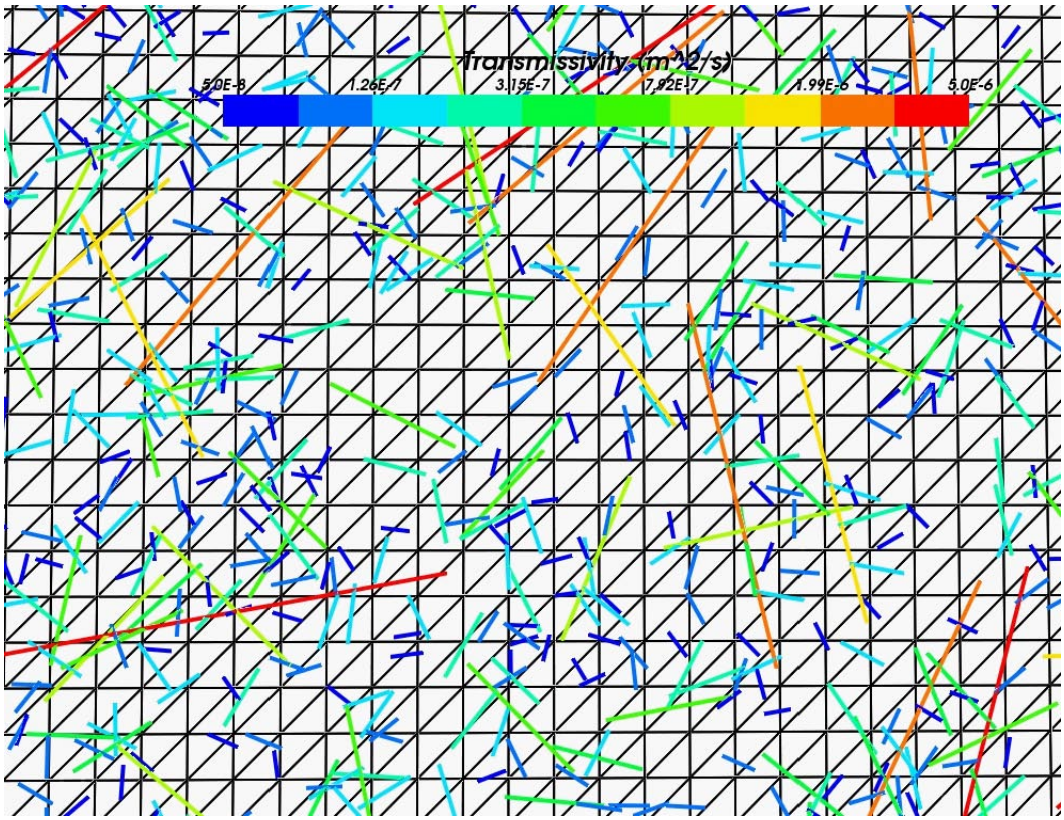

Figure 5-18. *A part of the DFN model as shown on a slice through the fractures coloured by Log (transmissivity) and the 100 m finite-element grid (coloured black and each element drawn as 2 triangles).*

In order to perform sensitivity tests on the DFN input, several DFN models were created. These are listed in Table 5-3 with names that denote the size and resolution of the model, the interpretation used in deriving the DFN, the transmissivity model used, and the realisation number. The L_{min} values given are firstly in the outer elements, and then in the refined embedded area. In the local-scale area, a refined model was considered with 25 m elements in the site-scale areas and 50 m elsewhere. Although it was computationally feasible to run this fine resolution EPM model on the local-scale, it was practically impossible to use this refinement on the regional-scale.

In all cases, the transport aperture was calculated using $e_t = aT^b$, a = 0.5, b = 0.5, based on /15/. The kinematic porosity, n_{etb}, for a block was then calculated as the sum of products of fracture area within the block and the transport aperture, and then divided by the volume of the block.

Due to the use of a relatively high L_{min} of 50 m for practical reasons, a few elements will have no fractures and hence have zero hydraulic conductivity and porosity. This is potentially non-conservative and so a background hydraulic conductivity needs to be specified that has equivalent properties of the fracture network of fractures shorter than L_{min}. We have some handle on appropriate properties for the background from the block-scale modelling of Section 4.5 where block-scale properties were calculated for 100 m for different values of L_{min} down to L_{min} = 10 m. Based on the 10-percentile for L_{min} = 10 m a minimum hydraulic conductivity for a block was estimated as 5 10^{-10} m/s, and a minimum porosity of 10^{-5}. In CONNECTFLOW the background properties were implemented such that if the EPM properties based on the stochastic DFN for an element fell below these minimum values, then the EPM values were reset to the minimum.

Table 5-3. DFN variants created and their parameters.

DFN Case	Grid	Seed	Fracture model	L_{min}
LReg_CF_Corr_1	Large-regional embedded	101	CONNECTFLOW interpretation – T/L correlated	50 m/25 m
LReg_CF_Corr_2	Large-regional embedded	201	CONNECTFLOW interpretation – T/L correlated	50 m/25 m
LReg_CF_Corr_3	Large-regional embedded	301	CONNECTFLOW interpretation – T/L correlated	50 m/25 m
LReg_CF_UnCorr_1	Large-regional embedded	101	CONNECTFLOW interpretation – T/L uncorrelated	50 m/25 m
LReg_CF_SemiCorr_1	Large-regional embedded	101	CONNECTFLOW interpretation – T/L semi-correlated	50 m/25 m
LReg_DT_Corr_1	Large-regional embedded	101	DarcyTools interpretation – T/L correlated	50 m/25 m
LReg_KLX01_Corr_1	Large-regional embedded	101	Interpretation based on KLX01– T/L correlated	50 m/25 m
Local_Fine_CF_Corr_1	Refined Local embedded	101	CONNECTFLOW interpretation – T/L correlated	25 m/12.5 m
Local _CF_Corr_1	Local embedded	101	CONNECTFLOW interpretation – T/L correlated	50 m/25 m

5.9 HSD model

The overburden in the Simpevarp area is dominated by silty till but in several valleys the till is overlayed by clay deposits and on top of hills the thickness of the till is small or the rock is out-cropping. In minor parts of the area eskers with coarse grained material is found. It is assumed in this Simpevarp 1.2 modelling that the entire area is covered by 3 m thick silty till with the upper 1 m more conductive due to soil forming processes. The definition of the HSD model is summarised in Table 5-4. This was represented explicitly in the model as two very thin layers of finite-elements at the top surface of the model with uniform properties. A third layer of 10 m thick was also added beneath these in which it was required that the hydraulic conductivity be no less than 10^{-9} m/s. This is only twice the minimum background hydraulic conductivity, so it was felt that this extra requirement need not be implemented directly in the modelling.

Table 5-4. Surface hydraulic domains, properties and reference sources (in brackets).

HSD-ID	Geological description	Hydraulic Thickness (m)	Hydraulic conductivity (m/s)	Kinematic porosity
HSD1 /23/	Sandy till, near surface	1	10^{-5}	$5\ 10^{-2}$
HSD2 /24/	Sandy till, below HSD1	2	10^{-7}	$5\ 10^{-2}$

5.10 Tritium migration model

The calculations of tritium migration were carried out by extending the models developed for simulating groundwater flow and reference water transport.

5.10.1 Period modelled

Tritium is formed naturally by cosmic rays in the upper atmosphere. The atomic bomb tests in the 1950's, 60's and 70's also produced large amounts of tritium, leading to much higher atmospheric concentrations than the natural background. There is a detailed record of atmospheric concentrations measured at Ottawa (see Figure 5-19). From this plot it appears that background levels of tritium are around 15 Tritium Units (TU). The bomb tests led to tritium levels that at their peak were about 100 times greater than this. Records for other locations are less detailed. However, the available measurements for locations in Sweden appear to be consistent with the measurements at Ottawa /17/, although some variation between locations might be expected, particularly for the bomb-test tritium.

Tritium is removed from the atmosphere in precipitation, and then enters the groundwater flow system. Tritium has a very short half-life (12.43 years), and hence tritium that entered the groundwater flow system more than fifty years ago will have been reduced in level by more than an order of magnitude (about a factor 16), and tritium that entered the groundwater flow system in precipitation more than a hundred years ago would have been reduced in level by more than two orders of magnitude (about a factor 256). Given the atmospheric concentrations shown in Figure 5-19, it is therefore really only necessary to consider migration of tritium since the 1950's. The natural background of tritium in precipitation prior to the bomb tests will now contribute less than 1 TU to the current groundwater concentrations, and so can be neglected. However, in order to facilitate a comparison of the levels of tritium in groundwater due to the bomb-test tritium with the levels due to the natural background, the calculations of tritium migration were carried out for a period of 120 years (about ten tritium half lives) starting from 1,890 AD.

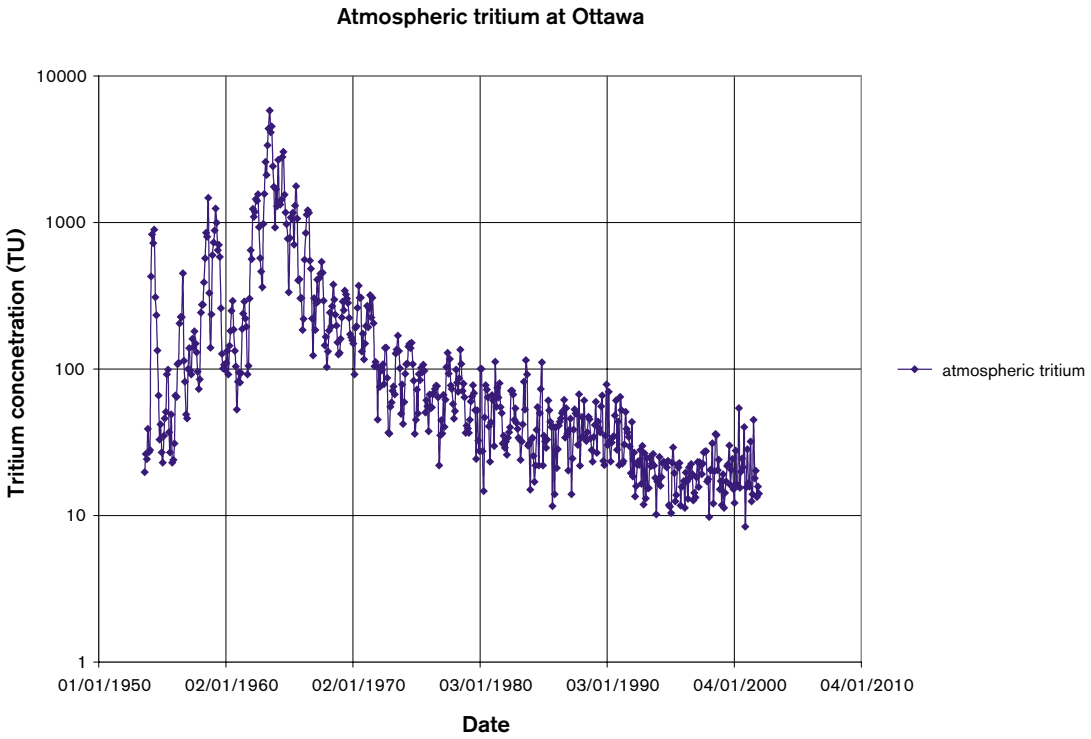

Figure 5-19. *Atmospheric concentrations of tritium measured at Ottawa.*

The results of the calculations therefore effectively provide results for an initial 60 year period with natural background levels of tritium in precipitation, and a 60 year period with the bomb-test tritium as well. (Carrying out the calculations in this way also ensured that the initial conditions for the calculations with the bomb-test tritium included are realistic, although this is not strictly necessary, for the reason discussed above.) It should be noted that the final time for the calculations is 2,005 AD, due to practical reasons relating to the range of time-steps considered. The final concentrations in the model will therefore be slightly lower than those for the present day, because the bomb-test tritium has had another 5 years of decay, which corresponds to a reduction to about 75% of the current contribution.

The time period modelled is short relative to the time-scale of natural evolutions of the regional groundwater flow such as sea-level and sea-water salinity changes that occur on time scales of thousands of years, and the results of the regional groundwater flow calculations were only saved every 1,000 years. Therefore, the flow and distributions of reference waters at the end of the transient regional groundwater flow calculation from 10,000BC to the present day were used as the initial conditions for the calculations of tritium migration. This introduced a small error, in that the change in the flow since 1,890 AD and the present-day was effectively neglected. However, this change is small.

Using the conditions at the end of the transient regional groundwater flow as the initial conditions effectively takes the conditions in the rock matrix to be in equilibrium at the start of the tritium migration calculations. Provided that the distributions of the reference waters were not changing rapidly towards the end of the regional groundwater flow calculations, this will be a reasonable approximation.

5.10.2 Boundary conditions

As indicated, calculations of tritium migration were carried out for the period since 1,890 AD. The calculations used multi-component groundwater flow, with rock-matrix diffusion. Tritium enters the model through the top surface, where the boundary condition was effectively specified such that the flux of tritium was equal to the recharge flux of groundwater multiplied by the concentration of tritium in precipitation, which was obtained from the data shown in Figure 5-19.

The option for modelling multi-component flow allows for modelling of tracers (e.g. $\delta^{18}O$, δD) as well as the main groundwater constituents (e.g. Na, Cl), but it does not currently allow for decay. All tracers are modelled as conservative, in the same way as the main groundwater constituents. However, it is straightforward to deal with this.

Since tritium must be transported as a non-decaying (i.e. conservative) tracer, then the 'undecayed' value of tritium is calculated, to give the required value of tritium in precipitation, at time, t. This 'undecayed' tritium is transported conservatively within the groundwater flow model. The value of tritium after transport must then be decayed to give the final tritium result. For instance, the background value of tritium in 1,890 AD (the reference time, t_{1890}) is given as 15 TU. Hence the 'undecayed' input concentration for CONNECTFLOW (C_{input}) would be calculated as:

$$C_{input} = C_{ottawa}(t_{input}) \times exp\,(\lambda\,[t_{input} - t_{1890}]),$$

where t_{input} is the time in years AD at the time under consideration, λ is ln (2)/12.43 years, C_{ottawa} is the atmospheric concentration of tritium at time, t. This example would give an 'undecayed' input concentration to CONNECTFLOW of 15 TU at 1,890 AD. Similarly, if at 1,950 AD the atmospheric tritium concentration is 2,000 TU, then the 'undecayed' input

to CONNECTFLOW is 56,769 TU. After solute transport, the output tritium concentration from CONNECTFLOW must be decayed to give the final tritium result, C_{final}, using the formula:

$$C_{final} = C_{model}(t_{output}) \times exp(-\lambda\,[t_{output} - t_{1890}]),$$

where C_{model} is the output tritium value from CONNECTFLOW, t_{output} is the time in years AD of the results, (generally 2,005 AD is used as the final time). For instance, a CONNECTFLOW, C_{model}, tritium value of 7,000 TU at 2,005 AD would be decayed to give a final tritium result of 11.5 TU at 2005.

Figure 5-20 shows the corrected tritium concentration in precipitation, given monthly, together with two simplified piecewise-constant approximations to this that were used in the modelling. In calculations with small time-steps, the finer temporal discretisation was used, taking the value corresponding to the end of a time-step. However, some calculations with carried out with a relatively long time-step of 20 years, and it was considered that using the value at the end of the time-step would not properly take into account the peak due to bomb tritium. For these calculations, the integrated value over the 20 year time-steps was used. Although a time-step of 20 years is very large for modelling the tritium migration, particularly in view of the tritium half life (12.43 years), this time-step was used for the initial tritium migration calculations since it was the time-step used for the groundwater flow calculations, and it was desired to avoid possible complications resulting from changing the time-step for the groundwater flow calculations.

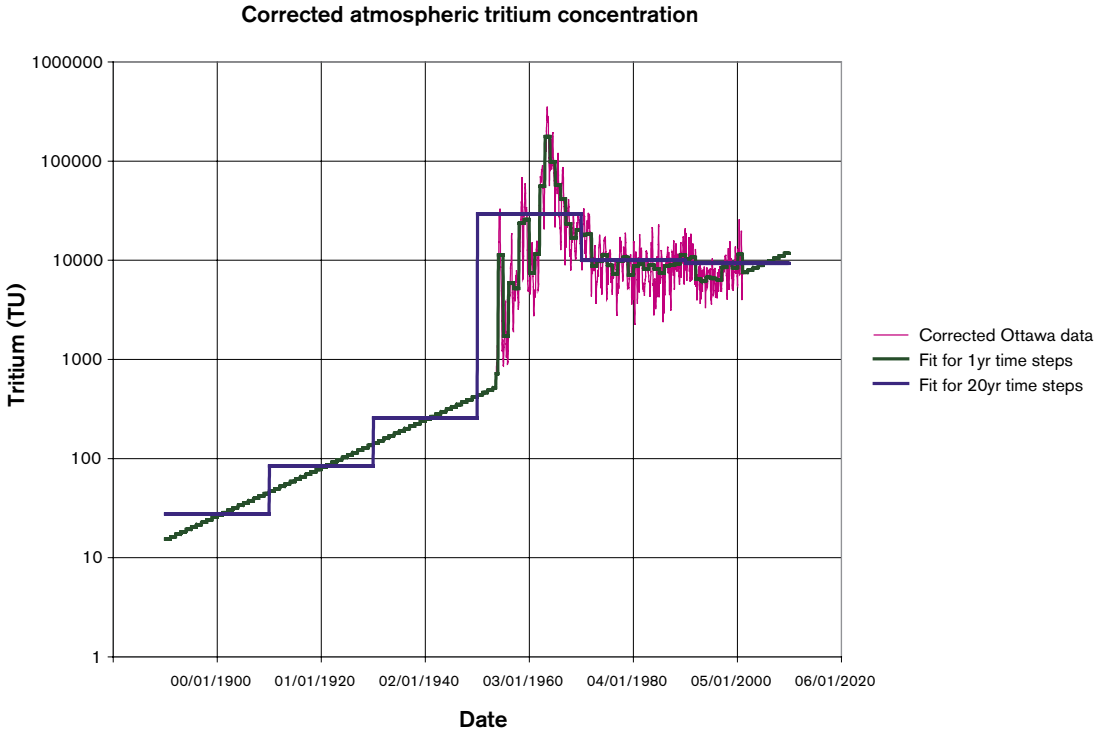

Figure 5-20. *The 'undecayed' input concentration for precipitation for CONNECTFLOW, shown between the 2,010 AD and the reference time of 1,890 AD.*

6 Regional model – Calibration targets

The primary data used for calibration of the hydrogeological model concepts and parameters was the hydro-geochemistry data available from boreholes in the regional model area. More precisely, this includes the salinity profiles and mixing ratios along the trend and plunge of KAV01, KAV04A, KLX01, KLX02, KSH01A, KSH02, KSH03 and vertically at the centre of Äspö, under present-day conditions. It also includes mixing fractions of the reference waters and ratios of environmental isotopes (Oxygen-18 and Deuterium). In addition, the S1.2 Task Description requested visualisation of the evolution of reference water fractions on a series of vertical sections through the model as a more qualitative calibration of the overall evolution of the hydrogeological situation. The new reference water transport modelling facility in CONNECTFLOW when used in conjunction with RMD calculates a mixing fraction for both the fracture system and the matrix. Hence, in theory it would be possible to calibrate the model against hydro-geochemistry data from both the flowing features (as is acquired currently) and that from the much tighter matrix. However, due to the obvious from problems of sampling water from the rock matrix there is no such data currently.

Another possible calibration test is to compare the hydraulic conductivity along the boreholes in the model with the long interval PSS data. The grid resolution is either 50 m or 100 m, and hence it is most appropriate to compare with the 100 m interval PSS data. However, it has to be pointed out that the model is a uniform stochastic model that has not been locally conditioned to the borehole data, and therefore this comparison should only be done in a qualitative sense by comparing the overall magnitude of hydraulic conductivity, for example.

6.1 Salinity profiles in boreholes

6.1.1 Data

The list of boreholes for which data is available is given in Table 6-1, and includes their positions and amount of data available. Figure 6-1 shows the relative location of these boreholes in 3D with reference to the road network.

Table 6-1. Coordinates of the boreholes used as calibration targets. The amount and coverage of hydro-geochemistry data is also indicated.

Name	Easting	Northing	Number of data points	Highest elevation of data (m)	Lowest elevation of data (m)
KLX01	1549923	6367485	4	–257	–673
KLX02	1549224	6366769	24	–87	–1,527
KSH01A	1552449	6365980	3	–96	–536
KSH02	1551521	6365677	4	–110	–571
KSH03A	1552732	6366003	1	–39	–39
KAV01	1553090	6367246	1	–546	–546
KAS series	1551259	6367993	15	–43	–914

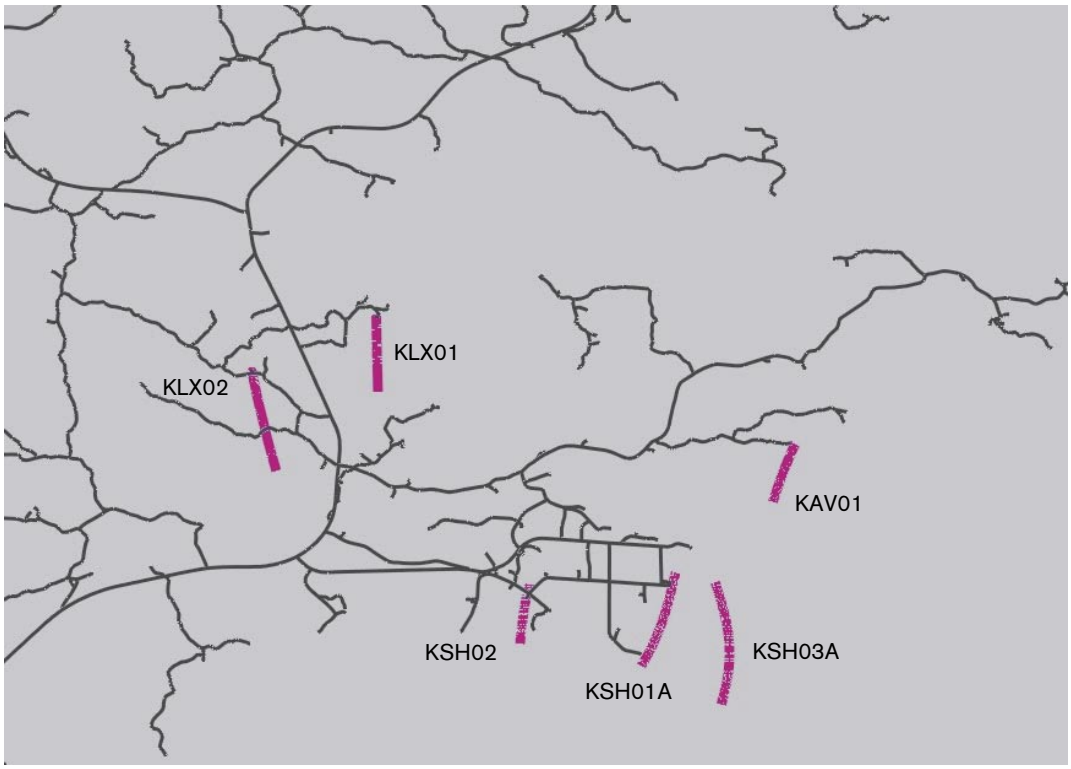

Figure 6-1. *Locations of the calibration boreholes (purple) relative to the surface road network (black).*

6.1.2 Calibration targets

For Simpevarp 1.1, the calibration target used was only the salinity in KLX01 and KLX02. Salinity gives an indication of the balance in driving forces between hydraulic gradients at the surface and buoyancy effects of the dense brine, and how this balance has changed over time due to land-rise. Hence, it acts as a natural tracer for transient variable-density flow. However, by including the mixing fractions of reference waters a more stringent calibration of the hydrogeological properties and boundary conditions is possible since it introduces freshwater tracers of varying age, such as the Glacial and Rain 1960, and the less dense Marine waters. In the Simpevarp 1.1 CONNECTFLOW modelling /21/ the salinity was found to be relatively insensitive to the initial condition for salinity. Hence, it is interesting to see if the uncertainties in initial conditions can be reduced by considering the individual reference waters.

The salinity for a given water composition in the model is calculated as the sum of the products of each reference water fraction with the salinity of that reference water. The salinities for the reference waters were calculated from the TDS based on Table 5-1.

6.1.3 Uncertainties in data

A much greater amount of data is available for calibration in Version S1.2. In particular, the 3 Simpevarp boreholes are used as well as data from Ävrö and Äspö. However, the data at Simpevarp and Ävrö is quite limited in quantity and depth (See Table 6-1) only going down to –571 m. Data from below 1 km is still only available for KLX02, the next deepest is –914 m in KAS03, and since Brine is not seen in significant proportion until

about –900 m, then the data on the dense saline water is quite sparse. Thus, there is a risk of bias if we base the calibration of salinity on just the one or two deep boreholes. In addition, most of the boreholes are near to the coast in very low topographic areas, and so there is additional risk of bias due to sampling essentially a single hydrogeological environment. This is one motivation for visualisation of regional-scale salinity pattern using cross-sections. The Task Description asks for:

- The transient salinity (g/L) and mixing ratios evolution (driven by advection) in **4 E-W profiles** (one through KLX01 and all parallel to the regional model boundaries. Northing: 6370000, 6367520 (KLX01), 6366000, 6364000).
- **One N-S profile** through KLX01 (Easting: 1549915).
- Visualised at 5,000 BC, 0 BC, 2,000 AD.

In terms of the salinity data itself, it is a direct measurement without much interpretation.

6.2 Water types in boreholes

The reference water mixing fractions gives us several different tracers that have entered the groundwater system at different times and with different densities. As such, they give the possibility to quantify sensitivities to initial conditions, boundary conditions and hydraulic properties not possible with salinity data alone.

6.2.1 Data

Each of the groundwater samples described in Table 6-1 has been interpreted using the M3 method (see /18/, for example) to compute the mixing fractions of reference waters. The original M3 analysis was performed using 5 reference waters, by splitting the Marine reference water into the Littorina and Sea Sediment reference waters. However, for calibration purposes it was decided by Hydro-geochemistry to simplify the data and group these two reference waters into a single Marine reference water by simply summing the mixing fractions. This was done rather redefining or limiting the reference waters and re-interpreting the groundwater samples using M3. However, for the reference water transport modelling the ion and isotope composition of each reference water is needed, and so the composition of the combined Marine reference water was assumed equal to the Littorina reference water (see Table 5-1).

The environmental isotopes are assumed to be conservative tracers and are used as additional calibration targets. Both δD and $\delta^{18}O$ help to differentiate between Glacial and Rain 1960 reference fresh waters, and to some extent $\delta^{18}O$ can be used to distinguish the saline reference waters (Brine from Marine).

6.2.2 Calibration targets

The main calibration target of coupled groundwater flow and reference water transport then is to compare the mixing fractions along the boreholes. The comparison is done in a visual way by comparing the trend for mixing fractions along the whole length of borehole, and below, with the interpreted field-data. It is done this way, rather than some sort of error norm only at the data points, to gain an understanding of the broader mixing pattern at a variety of depths.

6.2.3 Uncertainties in data

The same comments apply as for the salinity data with the addition of some extra uncertainty associated with interpretation of the mixing fractions using the M3 approach. The mixing fractions interpreted by M3 are not unique, especially when a large number of reference waters are used, and in particular when the actual mixture of groundwater is not dominated by any one reference water. The uncertainty in deriving the water type fractions from M3 is about ±0.1. Thus, some caution needs to be exercised in not reading too much into matching the mixing fractions. They should be viewed more as a guide. It should be emphasised that the reference waters are a very useful concept for the modelling though, as they provide a natural conceptual framework for defining initial and boundary conditions.

Some of the uncertainties associated with using the M3 interpretation could be reduced by matching the 'raw' data in terms of compositions of individual ions and isotopes which are less prone to interpretation errors. Some of this was possible using the δD and $\delta^{18}O$ isotopes, although groundwater compositions of individual ions were not supplied. Hence, using ion compositions and other environmental isotopes such as $\delta^{14}C$ and $\delta^{3}H$ have scope for enhancing the calibration process in the future. Ultimately though, any extra understanding gained would have to be back-interpreted in the context of reference waters in order to aid the hydrogeological modelling.

The measurement error on $\delta^{18}O$ is approximately ±0.2ppt, and ±1ppt on δD.

6.3 Hydraulic conductivity in boreholes

In developing the Hydro-DFN, the DFN hydraulic properties were matched against relatively small scale measurements, i.e. individual flow anomalies from PFL or 5 m test intervals for PSS. A further testing of the models is possible by considering the EPM hydraulic properties on larger scales.

6.3.1 Data

PSS data gives interpreted hydraulic conductivity measurements generally on 5 m, 20 m and 100 m scales. This is provided for KLX01, KLX02, KSH01A, KSH02, KSH03A and KAV01. Since the regional-scale model has an element-size of either 50 m or 100 m, then it is most appropriate to compare the hydraulic conductivity in the model simulations to the 100 m PSS intervals. Where 100 m intervals are not available, then the hydraulic conductivity from several shorter intervals has been averaged (i.e. assuming radial flow) to give an equivalent 100 m interval. For each borehole the PSS data typically covers from –100 m to either –600 m or –1,000 m, i.e. about 6–10 intervals.

6.3.2 Calibration targets

The calibration against the hydraulic conductivities is done by plotting the distribution in the model compared with PSS data with axes of elevation and Log (K_{eff}). It is expected that the hydraulic conductivities should be of comparable magnitude and in particular high values corresponding to large deterministic DZs should match closely as they have been conditioned in the HCD data interpretation.

6.3.3 Uncertainties in data

There are several uncertainties associated with the PSS data. Firstly, these are single-hole measurements, so there are issues relating to borehole skin or other localised effects like the test only evaluates part of the zone adjacent to the borehole. There are then interpretation uncertainties, for example two alternative methods used in the PSS interpretation are based on either the Moye or 2D radial transient flow assumptions have been used. For the PSS data, the transient evaluation is considered to "filter out" the effect of the skin factor. There are also some intervals in which there have been problems in making the single-hole test, and here a small hydraulic conductivity is given, so it is not always clear if this is a realistic value. Hence, in doing the comparison we might expect the overall magnitude of hydraulic conductivity to agree, with perhaps the high values to be in closer agreement, and lower values may indicate tighter areas although these are more uncertain.

6.4 Tritium in boreholes

Tritium provides a potential tracer for recent precipitation, because it only enters the groundwater flow system in precipitation and has a short half life (12.43 years).

6.4.1 Data

Only in three boreholes (KLX02, KSH01A and KSH02) are there more than a few measurements of tritium. Hence, the calibration was performed mainly based on these three boreholes, although KSH03A was also included.

6.4.2 Calibration targets

The calibration against tritium was carried out by visually comparing the calculated concentrations of tritium down boreholes with measurements.

6.4.3 Uncertainties in data

The samples have been labelled as 'representative' or 'unrepresentative' by the geochemists. For instance, 'representative' samples was based on several criteria including that the sample had a charge balance of ± 5% and less than 1% drilling fluid /1/. The tritium measurements were carried out at different times (for example, samples from Simpevarp are from 2003, while those in KLX02 are predominantly from 1993, with a few representative samples from 1997 and a few 'unrepresentative' samples from 1999). For KSH01A and KSH03A, the unrepresentative samples have much higher contamination from drilling water (generally > 10%). For KSH02, the unrepresentative samples have a drilling water contents up to ~ 10%. However, for KLX02 the fraction of drilling water contamination is not reported. Some of the earlier measurements from KLX02 have a detection limit of 8 TU, whereas the more recent measurements (KSH01A, KSH02 and KSH03A) have a detection limit of 0.02 TU.

KLX02 should be considered with care since these samples were collected after the borehole had been cased and pumped at 1,000 m depth for around one month. Hence it is likely that the tritium results from KLX02 above 1,000 m depth are an artefact of this process, representing a mixture of modern surface water and water from depth.

7 Regional model – flow simulations

The Task Description required that modelling be performed in two main phases:

1. Model the groundwater flow from the last glaciation up to present-day with different boundary conditions and hydraulic properties, and compare with measured TDS and interpreted mixing fractions.
   a. Part of the purpose is to motivate the size of the model and applied boundary conditions.
   b. Also, the effects of discretisation should be tested and be a part of the motivation for grid size and assigned grid properties.
2. Select representative cases from Part 1 and perform flow-path calculations based on the present boundary conditions. Calculate Darcy velocities and hydraulic conductivity for selected areas.

Both CONNECTFLOW and DarcyTools modelling teams followed this sequence but a difference emphasis was put on Part 1a. The CONNECTFLOW team sought a smaller regional model (compared to Version S1.1) based on potential natural boundaries that could give stable results for the site-scale mixing fractions and groundwater paths. The DarcyTools team considered extending the regional model approximately 10 km to the west and to 3 km depth to illustrate the effects of significant increases in model size. Both modelling teams considered what hydraulic properties, initial conditions and boundary conditions that could give consistent simulations of the present-day salinity and mixing fractions.

This section describes the sensitivity analysis performed with CONNECTFLOW in matching the salinity and mixing fractions. The predictions of transient flow and groundwater flow-paths for some calibrated cases are given in Sections 8 and 9.

7.1 Methodology

Figure 7-1 shows a schematic overview of the modelling workflow used in the project. The startig point is the Hydro-DFN conceptual model and the associated fracture properties. This can be used to obtain the statistics of block-scale properties or to construct a regional-scale DFN that is upscaled to produce an EPM model that has HRD hydraulic properties consistent with a realisation of the underlying DFN data. Within EPM regional-model, the HCD and HSD properties are then combined with HRD. Finally, simulations of transient groundwater flow and reference water transport provide the calibration targets and required transport performance measures.

The calibration is performed by plotting profiles of each of the 4 reference water fractions, salinity and isotope ratios down each borehole. The transport performance measures are processed as statistics over an ensemble of particles released from many points in the local-scale or site-scale areas to give histograms and tables. Several model variants were created to quantify the sensitivities to a number of key issues such as hydraulic properties, initial and boundary conditions.

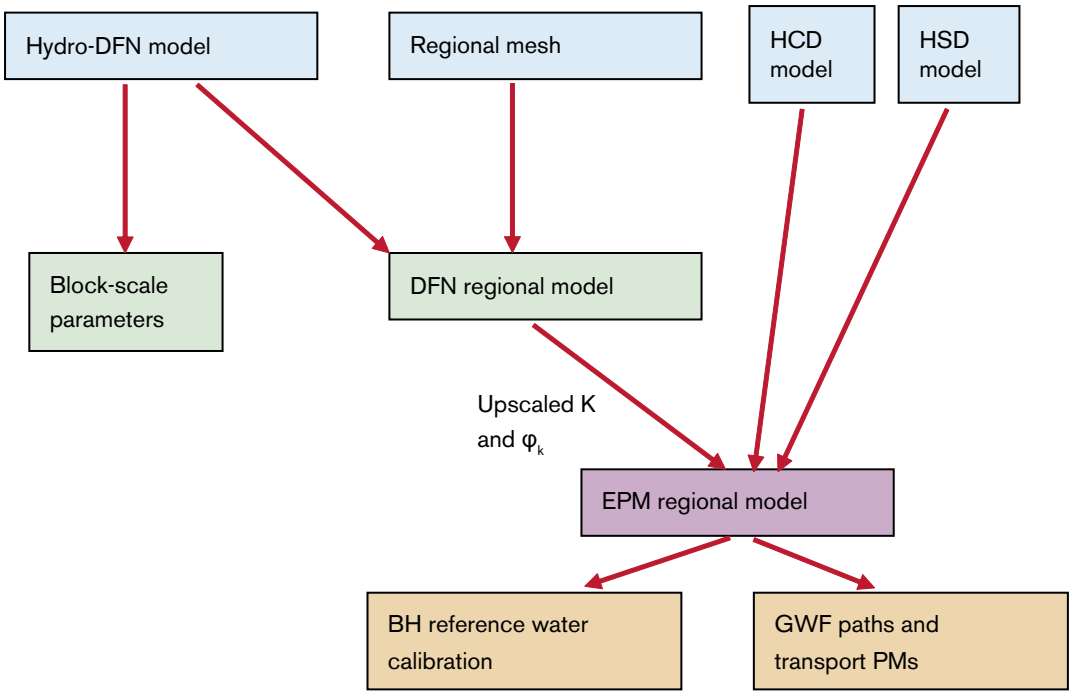

Figure 7-1. *A schematic workflow for the CONNECTFLOW modelling.*

7.2 Summary of applied regional model cases

The key issues simulated by CONNECTFLOW modelling were:

- Model domain size.
- Initial and boundary conditions for flow and reference water transport.
- Hydro-DFN parameters.
- Hydraulic properties of HRD and HCD.
- Transport parameters for RMD and safety assessment calculations.

Several model cases were constructed to quantify the effects of and illustrate each of issues. During the initial stages of the modelling a significant number of other cases were created on route to gaining an understanding of how individual model parameters affected the calibration, and ultimately to what ranges of parameters gave a reasonable match to the field-data. Not all these steps are reported here since they are of limited interest. Instead, the approach was to define a base case that gives a reasonable match, and then consider variants about this to illustrate the sensitivity to the various issues. The variants considered are grouped by these key issues to give structure to the discussions.

The final base case properties and conditions arrived at were:

- Small regional model (about 14×7 km) with 50 m element-size embedded grid in Laxemar and Simpevarp release area s and 100 m element-size elsewhere.
- Initial Condition (IC2) set to full Glacial 0–700 m; then linear gradient to no Glacial, full Brine at 1,500 m; full Brine below 1,500 m.
- Top-surface head equals topography.

- Top surface waters = Baltic Ice Lake (Glacial), Yoldia Sea (Marine/Glacial), Ancylus Ice Lake (Glacial), Littorina Sea (Marine), Baltic Sea/Precipitation with land rise (Marine diluting with Rain 1960).
- Hydro-DFN model from CONNECTFLOW model of Simpevarp with Correlated T vs L (LReg_CF_Corr_1, Table 5-3). This had block-scale properties of $K_{50\%}$ ~ 5 10^{-9} m/s, $K_{10\%}$ = 5 10^{-10} m/s.
- No depth dependence on hydraulic conductivity.
- Density and viscosity a function of salinity (transient), temperature (fixed), and total pressure (transient).
- HRD Kinematic porosity $n_{etb} \geq 10^{-5}$ (Based on DFN value, Section 5.8).
- Matrix porosity n_m = 5 10^{-3}.
- HCD Base Case with transport aperture, e_t, increased by factor 10.
- Flow-wetted-surface (FWS) per unit volume for RMD a_r = 2.0 m^2/m^3.
- Matrix diffusion length into matrix blocks L_D = 0.5 m.
- Intrinsic diffusion coefficient into matrix D_e = 5 10^{-13} m^2/s.

A list of the variants considered about this base case is given in Table 7-1 with a colour coding to highlight the key issue they were designed to address. The names of the variants were chosen to denote the size of model; type of reference water calculation; realisation number; Hydro-DFN case; hydraulic, boundary or transport property; and initial condition. SReg_4Component_IC2 is the overall base case.

Each of the key issues and associated variants are discussed in terms of the calibration results in the following Subsections.

Table 7-1. Summary of the main regional-scale model cases performed. The cases are grouped by colour coding according to the sensitivities they quantify: model size (brown); initial and boundary conditions (green); DFN parameters (blue); HRD and HCD hydraulic properties (purple); Transport properties (yellow).

EPM Case	Properties	Region (See Figure 5-3)	Purpose/Comments
SReg_2Component	CF DFN – correlated	Small Regional (orange)	Base Case for salt transport
LReg_2Component	CF DFN – correlated	Medium Regional (black)	Test model area slightly smaller than S1.1
Local_2Component	CF DFN – correlated	Local (red)	Test if local-scale area sufficient
Local_North_2Component	CF DFN – correlated	Local_North Ext. (grey)	Test sensitivity of local-scale to extension North
Local_West_2Component	CF DFN – correlated	Local_West Ext. (yellow)	Test sensitivity of local-scale to extension West
LReg_V11_ 2Component	CF DFN – correlated	Large Regional S1.1 (blue)	Test model area from S1.1
SReg_4Component_IC2	CF DFN – correlated	Small Regional (orange)	Base Case for reference water transport
SReg_4Component_IC1	CF DFN – correlated	Small Regional (orange)	Sensitivity to different I.C. – Shallower Brine
LReg_4Component_IC2	CF DFN – correlated	Medium Regional (black)	Sensitivity to B.C. on reference waters and GW paths
SReg_4Component_ Infiltration_IC2	CF DFN – correlated	Small Regional (orange)	Sensitivity to flow B.C. – specified flux/infiltration

EPM Case	Properties	Region (See Figure 5-3)	Purpose/Comments
SReg_4Component2_IC2	CF DFN – correlated Realisation 2	Small Regional (orange)	Sensitivity to stochastic DFN
SReg_4Component3_IC2	CF DFN – correlated Realisation 3	Small Regional (orange)	Sensitivity to stochastic DFN
SReg_4Component_DT_IC2	DT DFN – correlated	Small Regional (orange)	Sensitivity to DFN parameters (DarcyTools)
SReg_4Component_ UnCorr_IC2	CF DFN – uncorrelated	Small Regional (orange)	Sensitivity to DFN transmissivity model
SReg_4Component_ SemiCorr_IC2	CF DFN – semi-correlated	Small Regional (orange)	Sensitivity to DFN transmissivity model
SReg_4Component_KLX01_ IC2	CF DFN –correlated (KLX01)	Small Regional (orange)	Sensitivity to DFN parameters (data from KLX01)
SReg_4Component_IFZ2_ IC2	CF DFN – correlated HCD case 2	Small Regional (orange)	Sensitivity to HCD – Case 2
SReg_4Component_IFZ3_ IC2	CF DFN – correlated HCD case 3	Small Regional (orange)	Sensitivity to HCD – Case 3
SReg_4Component_ DepthK_IC2	CF DFN – correlated K ↓ with depth	Small Regional (orange)	Sensitivity to K decreasing with depth K/(1–0.002z)
SReg_4Component_ K100m_IC2	CF DFN – correlated K ↑ top 100 m	Small Regional (orange)	Sensitivity to K higher (10×K) in top 100 m
SReg_4Component_FWS_ IC2	CF DFN – correlated a_r = 1.0	Small Regional (orange)	Sensitivity to RMD (moderate change)
SReg_4Component_FWSt_ IC2	CF DFN – correlated a_r = 0.1	Small Regional (orange)	Sensitivity to RMD (V1.1 flow-path value)

7.3 Sensitivity to model size

Testing of the sensitivity to model size was performed early in the modelling exercise before the facility in CONNECTFLOW to model multiple reference waters had been finalised. Hence, a simpler model based on only 2 reference waters, Brine and Rain 1960 (i.e. freshwater), was used and the calibration was only to salinity in the boreholes. In this early modelling, the initial condition was a mixture of freshwater down to –500 m, then a linear increase in Brine to reach full Brine at –2,100 m. The time-dependent boundary conditions for Brine were specified to be an appropriate mixture of freshwater and Brine to match the Baltic salinity evolution specified in Figure 5-7. The model domains considered were those shown in Figure 5-3. As an example, the model predictions of present-day salinity in KLX02 are shown in Figure 7-2 with the measured data (shown by green dots) and the initial condition superimposed. These calculations were performed with slightly different hydraulic parameters than the final 4 reference water base case. Specifically, one tenth the transport aperture, e_t, for the HCD and half the matrix porosity, n_m. These differences, together with different initial and boundary conditions did not give a good calibration to the salinity data in KLX02. However, the results gave a sufficient test case of whether the results were stable to changes in the model domain. The comparison demonstrates the local-scale area is clearly inadequate for predicting the salinity in the site boreholes since it is far from the result for the Large Regional domain from Version S1.1 (Note: the LReg_11_ 2Component case uses exactly the same properties as Local_2Component; only the domain size is different). Extending the model to the West or North to the nearest potential natural boundaries made only modest improvements.

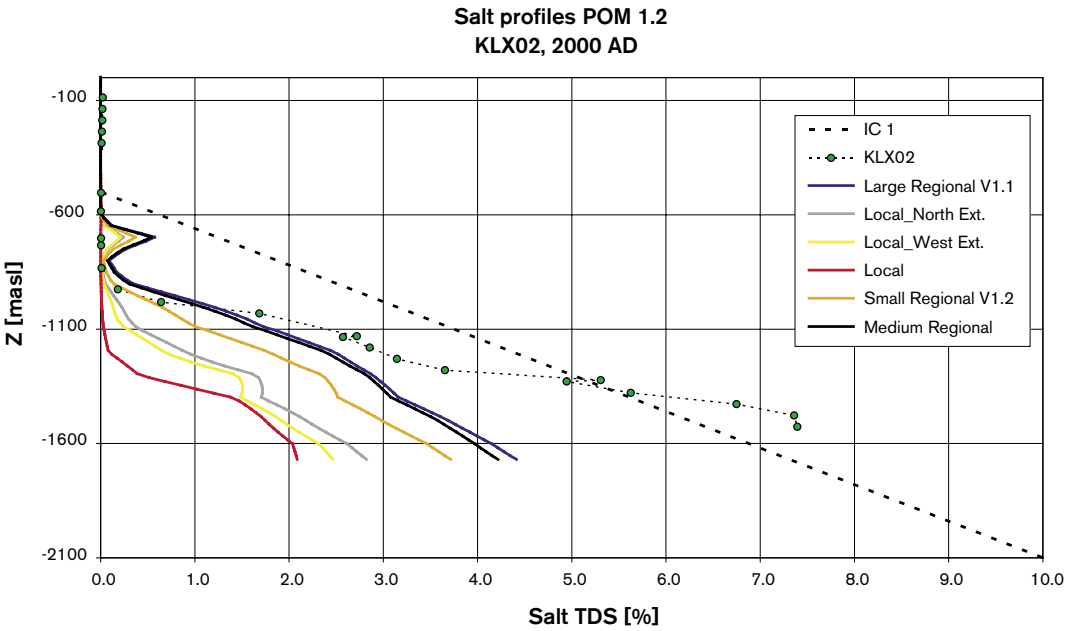

Figure 7-2. *Sensitivity to model size for salt transport modelling based on 2 reference waters (Brine and Rain 1960) in KLX02.*

It is suggested that because the dominant fracture set is sub-horizontal then groundwater recharge to the site areas is from several kilometres away giving larger flow-cells than were seen in the Version S1.1 modelling. Only when the model was extended to the Small Regional model (SReg_2Component) did the results start to converge toward the results for the Version S1.1 domain. The results are virtually identical for the Medium Regional model (LReg_2Component). Similar results were obtained for the salinity in the other boreholes.

Based on these results it was concluded that further modelling should be performed with a model no less extensive than the Small Regional model, and the Medium Regional model should also be used as a sensitivity check on model size. The Small Regional model domain was used as the base case for pragmatic reasons since it gave more manageable run times for the 4 reference water calculations, and yet the results were not so far from the larger regional models when compared to sensitivities to hydraulic properties, for example. This is confirmed in the next subsections.

7.4 Reference water mixing fractions calibration of Base Case

Using the Small Regional model domain for transient coupled groundwater flow and reference water transport a calibration process resulted in the base case properties listed in Section 7.2. The model gave a reasonable match overall to the calibration targets by changing parameters globally. A better match for individual boreholes could have been achieved by making localised changes to the hydraulic properties of specific DZs seen in or near the boreholes, but such ‘fine-tuning’ was felt to be extravagant at this early stage given we are trying to understand the regional conditions necessary to get a match. Anyway this would have taken some extra time.

7.4.1 Reference waters

Figure 7-3 to Figure 7-9 show the calibration of the Base Case against the interpreted 4 reference water profiles for the calibration boreholes. These calculations were performed with RMD, so the mixing fraction in both the fracture system and matrix are shown. The two sets of fractions are almost identical since $a_r = 2.0$ m^2/m^3 gives good communication between the fracture and matrix (Note: $a_r = 2 \times P32_c$, and hence we have set $P32_c = 1.0$ m^2/m^3 in the RMD matrix parameter). The sensitivity to this parameter is discussed in Section 7.8.

Figure 7-3 shows that in KLX01 the model predicts the mixing zone to be about 200 m too deep, suggesting the model has either too much hydraulic conductivity at depth or too little at the surface which would have the effect of focussing flow much higher. The match for KLX02 in Figure 7-4 is more interesting since the borehole has much more data and goes deeper. The transition from Brine to Rain 1960 reference water occurs at approximately the correct depth and a similar steep slope. Also, the spikes in Marine and Glacial waters are reproduced quite well. These features were difficult to match without a careful choice of both initial and boundary conditions. KSH01A is another excellent borehole match as shown in Figure 7-5. For this borehole the mixing zone is much higher, presumably because it is near the coast and there are no DZs in its vicinity. These two boreholes build confidence in the overall modelled flow conditions and properties. KSH02 is similar to KLX01 with the model predicting the mixing zone too deep in Figure 7-6. There is a vertical DZ in The HCD model near KSH02 that may either be too close or have too high a transmissivity causing this effect. KSH03A only has one data point near the surface, but nevertheless is a good match, Figure 7-7. KAV01 also has one data point at about –550 m, but again the match is reasonable in terms of the depth of the mixing zone around or below the data point, Figure 7-8. It should be noted that the embedded grid gave higher resolution, 50 m, for the Laxemar and Simpevarp boreholes, but is coarser, 100 m, around Ävrö and Äspö. Figure 7-9 groups all the data from Äspö to be used as a calibration

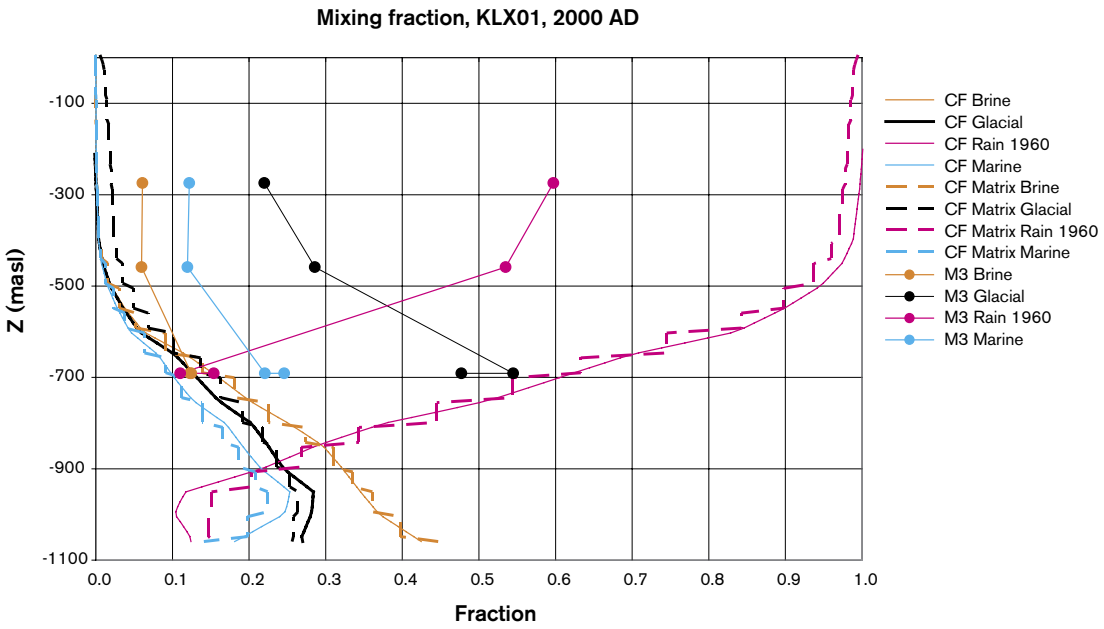

Figure 7-3. *Comparison of 4 reference water fractions in KLX01 for Base Case (SReg_4Component_IC2). The mixing fractions in the fracture system are shown by solid lines, in the matrix it is dashed, and the data by points.*

against the model profile at the centre of the island. The agreement is good with KAS02 and KAS03, which are the deeper boreholes. This might be expected since there is high certainty associated with the locations and properties of DZs in the Äspö area. Generally, it seems the model gives a good reproduction of the overall profiles for the reference waters, although some localised changes to the HCD model around KLX01 and KSH02 would probably greatly improve the match there.

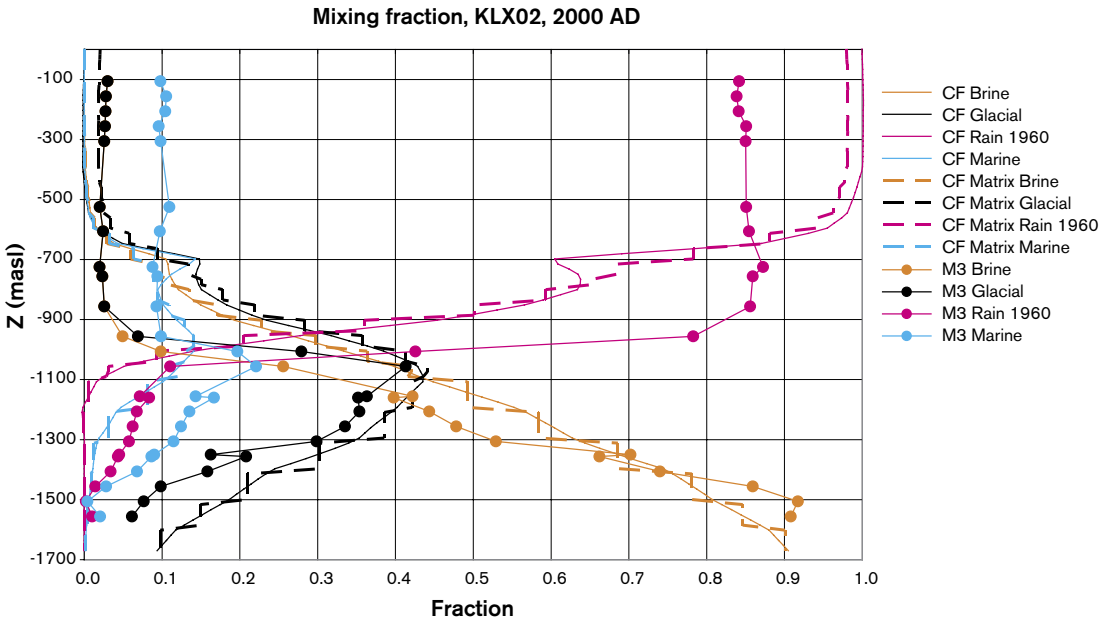

Figure 7-4. *Comparison of 4 reference water fractions in KLX02 for Base Case (SReg_4Component_IC2). The mixing fractions in the fracture system are shown by solid lines, in the matrix it is dashed, and the data by points.*

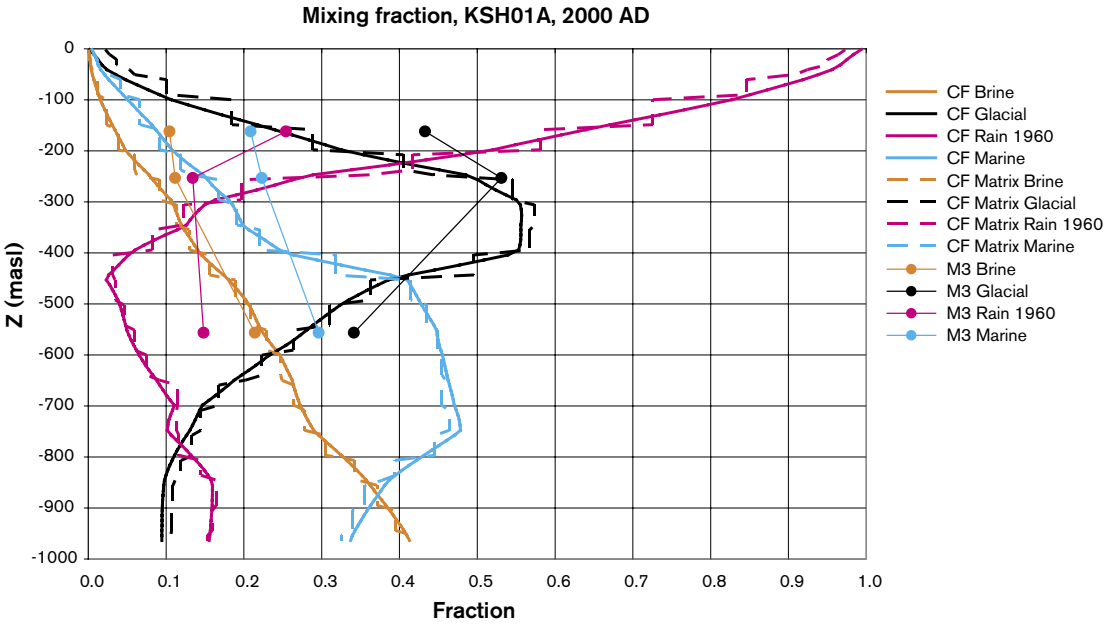

Figure 7-5. *Comparison of 4 reference water fractions in KSH01A for Base Case (SReg_4Component_IC2). The mixing fractions in the fracture system are shown by solid lines, in the matrix it is dashed, and the data by points.*

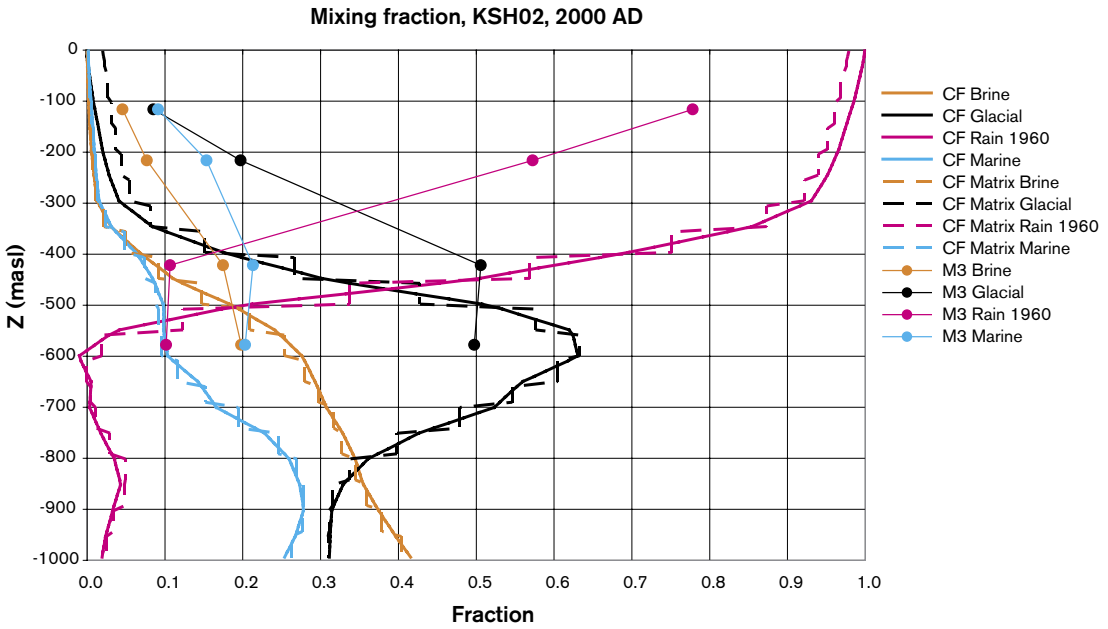

Figure 7-6. *Comparison of 4 reference water fractions in KSH02 for Base Case (SReg_4Component_IC2). The mixing fractions in the fracture system are shown by solid lines, in the matrix it is dashed, and the data by points.*

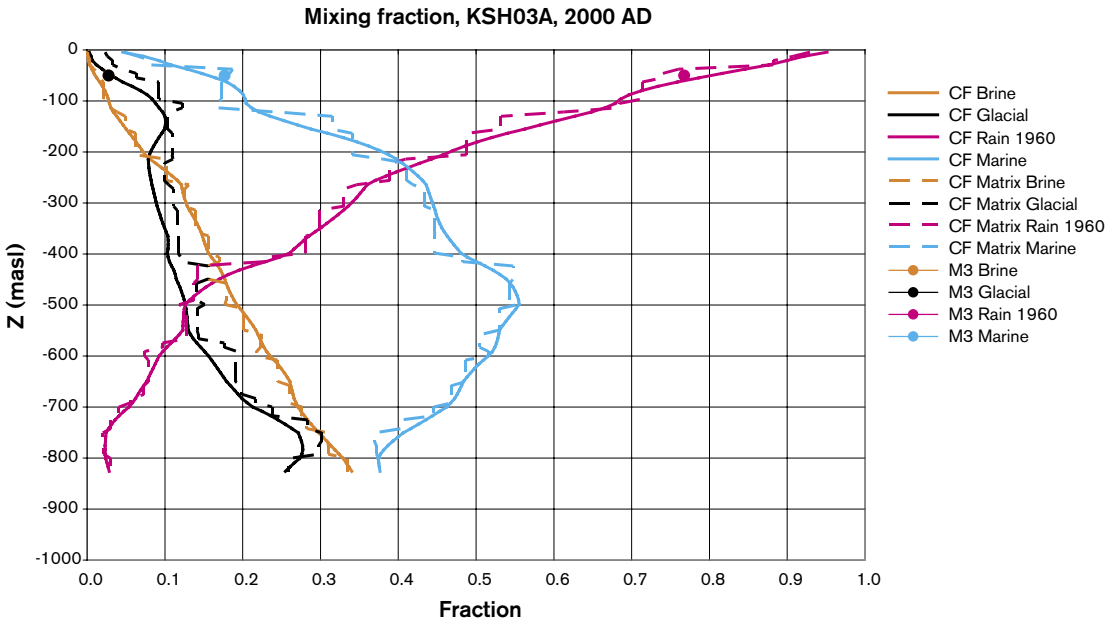

Figure 7-7. *Comparison of 4 reference water fractions in KSH03A for Base Case (SReg_4Component_IC2). The mixing fractions in the fracture system are shown by solid lines, in the matrix it is dashed, and the data by points.*

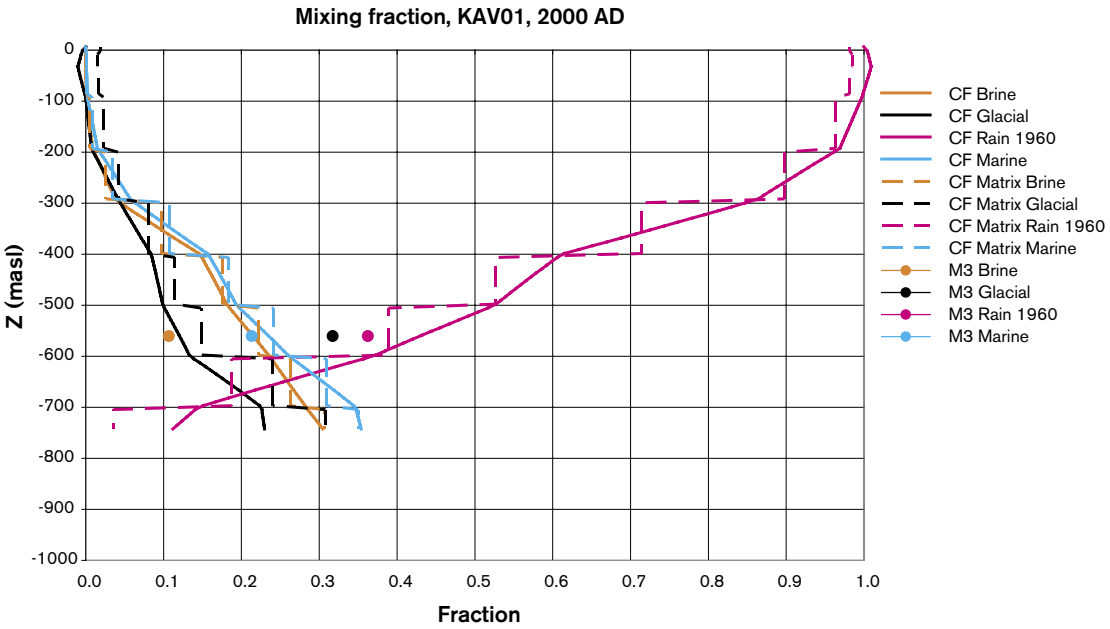

Figure 7-8. *Comparison of 4 reference water fractions in KAV01 for Base Case (SReg_4Component_IC2). The mixing fractions in the fracture system are shown by solid lines, in the matrix it is dashed, and the data by points.*

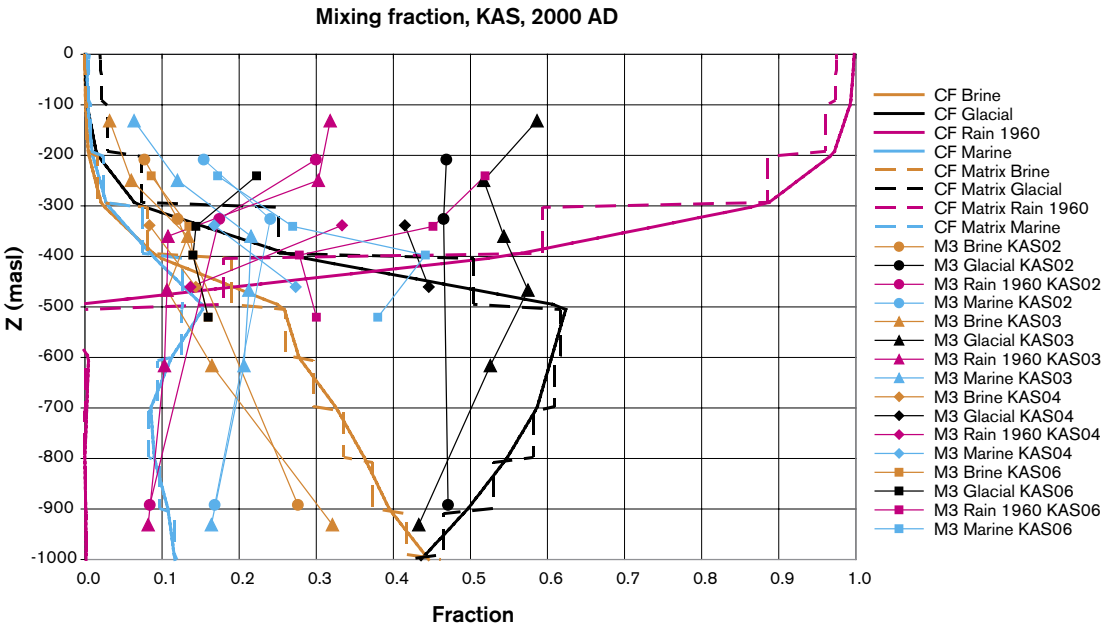

Figure 7-9. *Comparison of 4 reference water fractions in KAS02-06 for Base Case (SReg_4Component_IC2). The mixing fractions in the fracture system are shown by solid lines, in the matrix it is dashed, and the data by points.*

7.4.2 Salinity

Salinity closely follows the profile of Brine, although there is also a contribution from the Marine reference water. Figure 7-10 shows the comparison for salinity between the Base Case simulation and the data for boreholes KLX01, KLX02 and KSH01A to illustrate the differences as you move from coastal (KSH01A) to inland (KLX01), and to further inland (KLX02). The relative depths of salinity for the series of boreholes are correct. They have the right sort of slopes, although KLX02 is a bit high. The lower part of KLX02 has slightly higher hydraulic conductivity, 10^{-8} m/s, at 1 km depth compared to the deeper sections of other boreholes (See Figure 7-32). Hence, some caution is appropriate in not basing too much interpretation on KLX02 as it may be an outlier.

7.4.3 Environmental isotopes

As well as comparing the interpreted hydro-geochemistry from the M3 approach, a comparison was made with the environmental isotopes, using them as conservative tracers. The Oxygen-18 isotope ratio and Deuterium isotope ratios are shown for boreholes KLX01, KLX02, KSH01A and KSH02 in Figure 7-11 and Figure 7-12, respectively. High negative values of $\delta^{18}O$ and δD are associated with Glacial water. Hence, the model at KLX02 predicts the right sort of shape of profile, but there is a little too much Glacial water, whereas the model is not predicting enough Glacial in KLX01 due to too much mixing in the model near this borehole. Still, the shapes of the profiles down the boreholes seem to generally mirror that of the data.

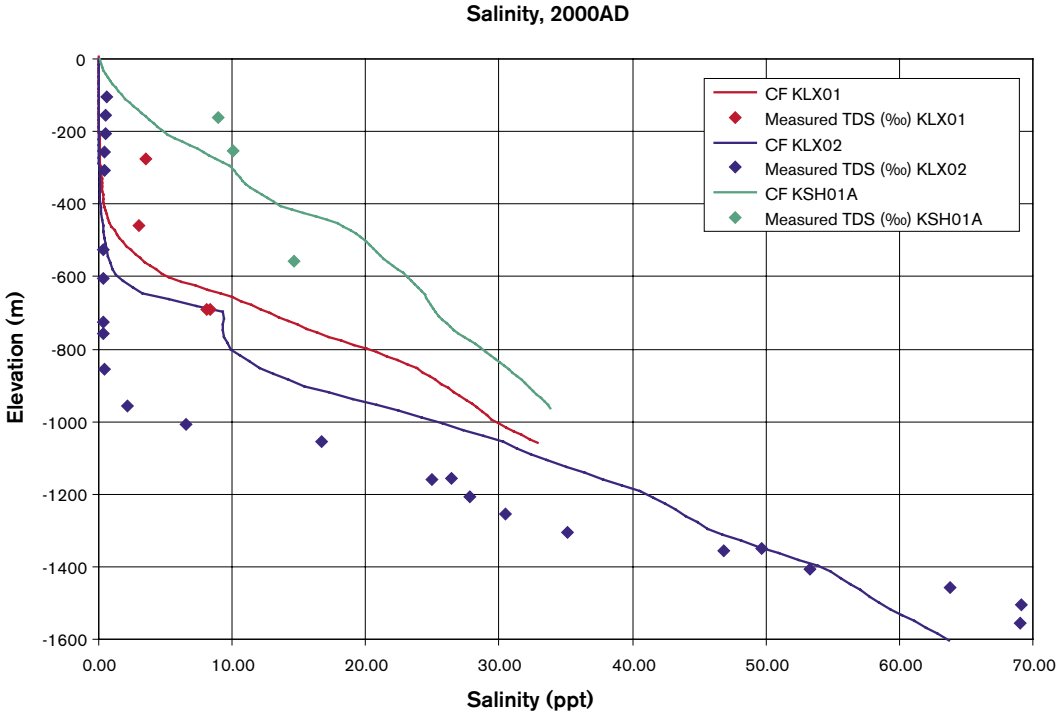

Figure 7-10. *Comparison of salinity in KLX01, KLX02 and KSH1A for Base Case (SReg_4Component_IC2). The salinity in the fracture system is shown by solid lines, and the data by points.*

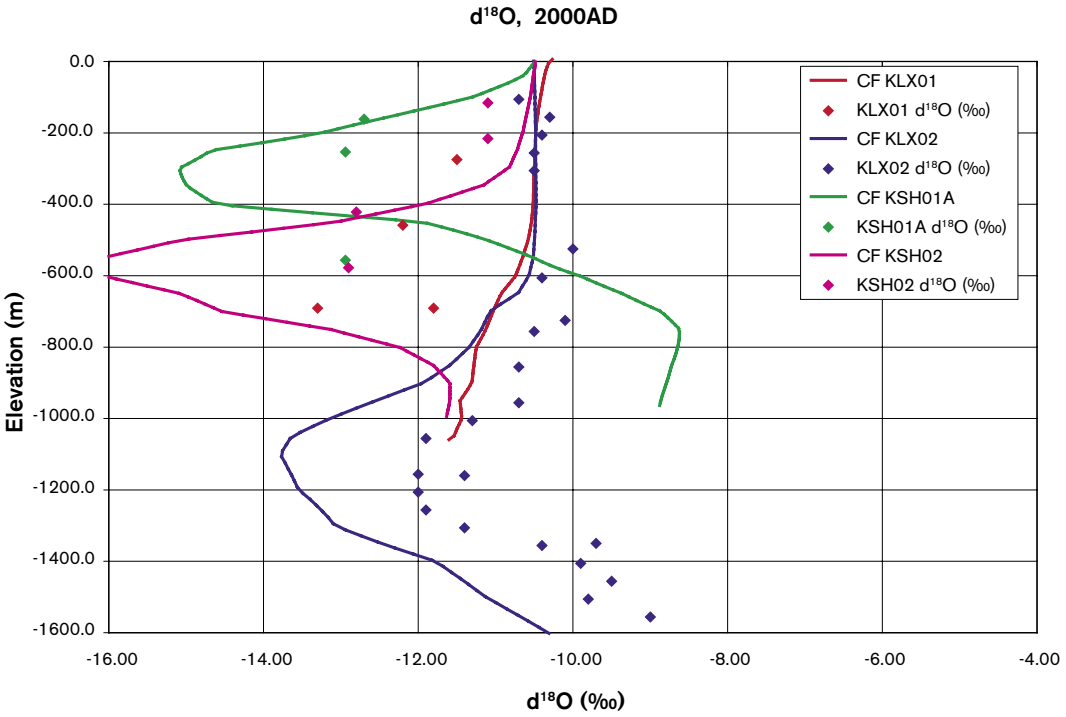

Figure 7-11. *Comparison of Oxygen isotope ratio $\delta^{18}O$ in KLX01, KLX02, KSH1A and KSH02 for Base Case (SReg_4Component_IC2). $\delta^{18}O$ in the simulated fracture system are shown by solid lines, and the data by points.*

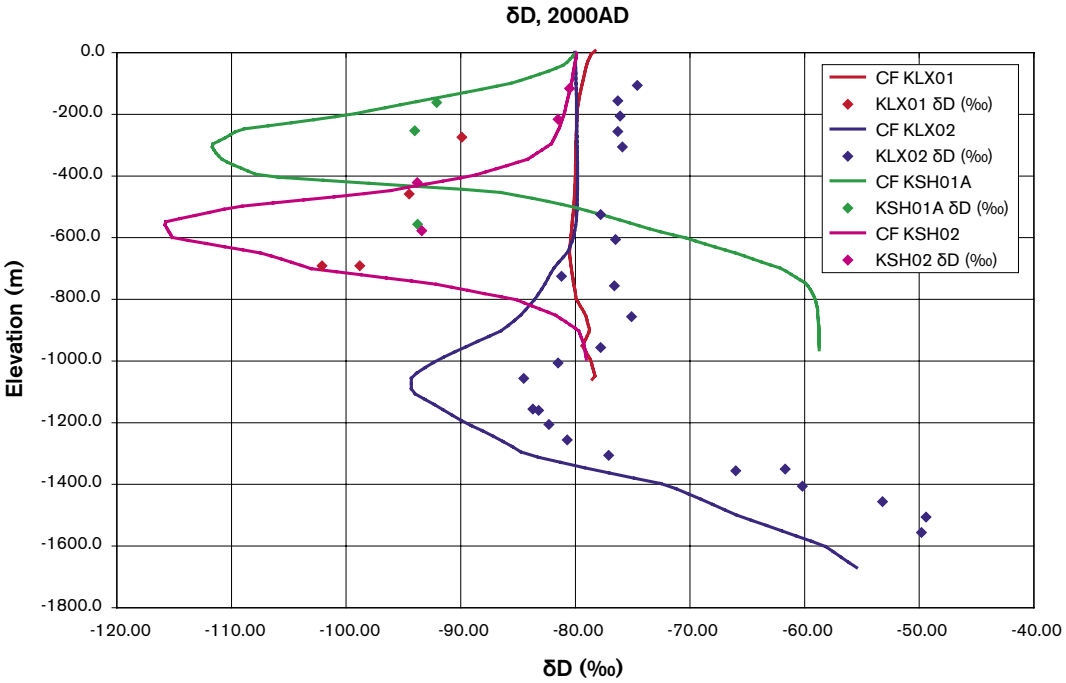

Figure 7-12. *Comparison of Deuterium ratio δD in KLX01, KLX02, KSH1A and KSH02 for Base Case (SReg_4Component_IC2). δD in the simulated fracture system are shown by solid lines, and the data by points.*

7.5 Sensitivity to initial and boundary conditions

The variants considered for initial and boundary conditions (See Table 7-1) are

- An initial linear switch from Glacial to Brine between –500 m and –1,000 m.
- A larger model domain.
- A specified flux (non-linear recharge/discharge) condition for flow onshore.

The sensitivities to these changes are discussed in the following subsections.

7.5.1 Shallower initial Brine condition (SReg_4Component_IC1)

Here, the initial condition is Glacial until 500 m depth, and then a linear increase in Brine toward full Brine at 1,000 m depth. In KLX02, the Brine becomes too shallow and the Glacial spike is much suppressed compared to the Base Case, see Figure 7-13. Similarly the Brine is too shallow at depth in KSH01A (Figure 7-14). From these results it is concluded that an initial guess with shallower Brine (around 1 km depth) is probably less likely than that used in the Base Case (about 1,500 m depth).

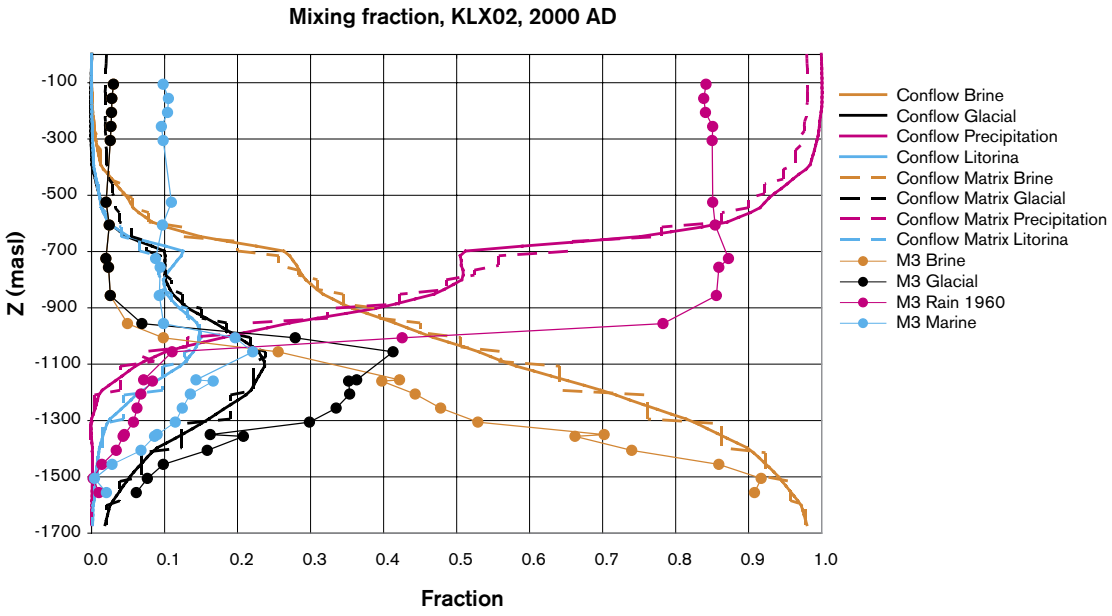

Figure 7-13. *Comparison of 4 reference water fractions in KLX02 for shallow initial Brine (SReg_4Component_IC1). The mixing fractions in the fracture system are shown by solid lines, in the matrix it is dashed, and the data by points.*

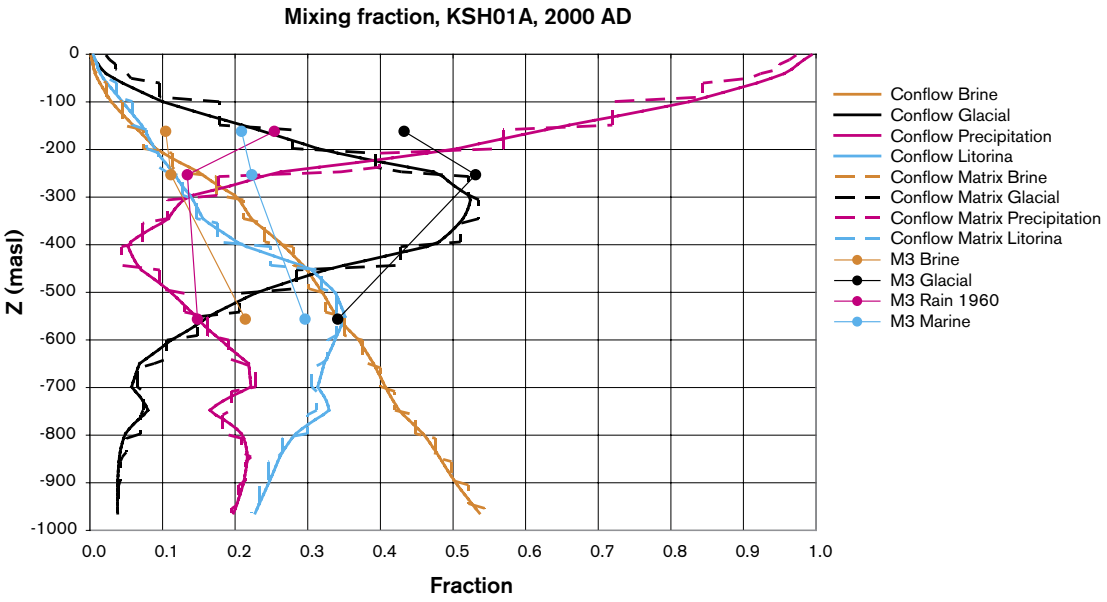

Figure 7-14. *Comparison of 4 reference water fractions in KSH01A for shallow initial Brine (SReg_4Component_IC1). The mixing fractions in the fracture system are shown by solid lines, in the matrix it is dashed, and the data by points.*

7.5.2 Larger regional model domain (LReg_4Component_IC2)

The effect of increasing the model domain to the medium regional model domain is shown in Figure 7-15 and Figure 7-16 for KLX02 and KSH01A, respectively. They show that the results differ little from the Base Case with the small regional model, and hence it confirms that the small regional model can be used for calibrating the model in terms of the reference water mixing fractions since it appears to give the same results as the larger medium regional model, but is a smaller calculation and so testing more variants is practicable.

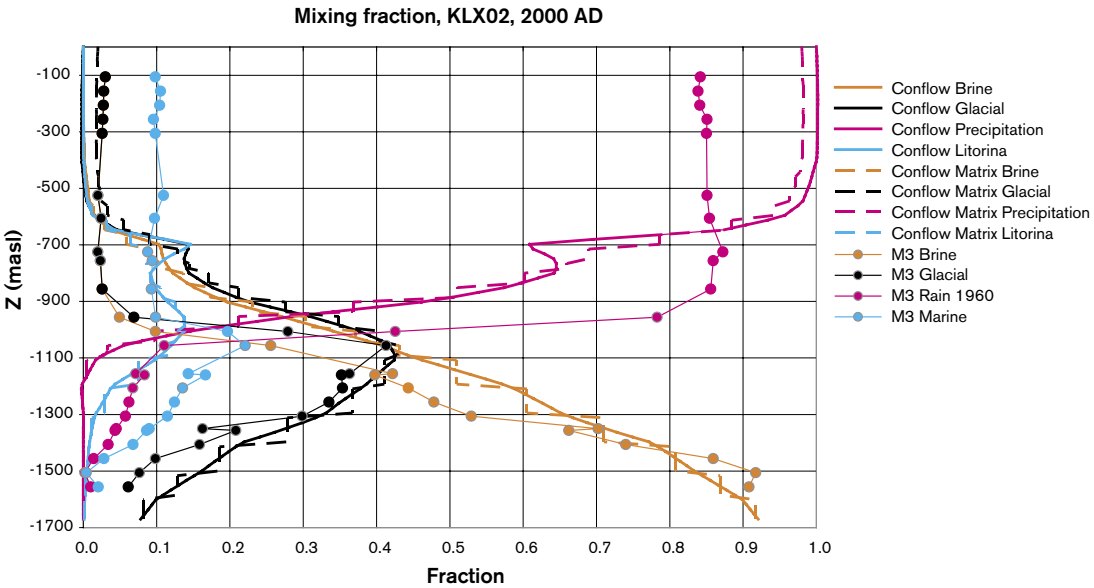

Figure 7-15*. Comparison of 4 reference water fractions in KLX02 for a larger domain (LReg_4Component_IC2). The mixing fractions in the fracture system are shown by solid lines, in the matrix it is dashed, and the data by points.*

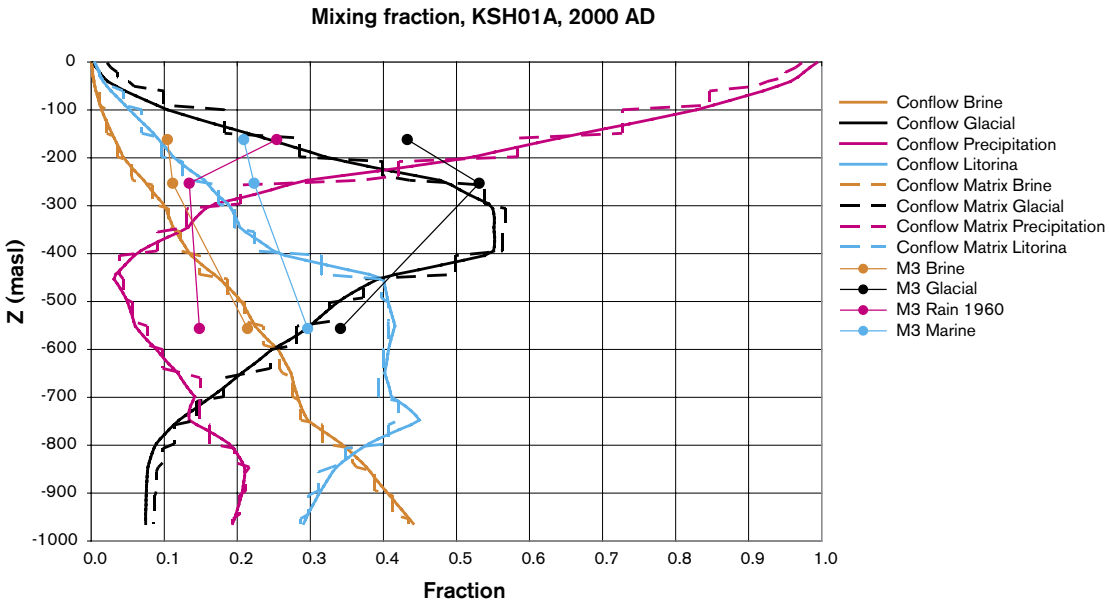

Figure 7-16. *Comparison of 4 reference water fractions in KSH01A for a larger domain (LReg_4Component_IC2). The mixing fractions in the fracture system are shown by solid lines, in the matrix it is dashed, and the data by points.*

It also suggests that the small regional model captures all the recharge areas which act as sources for surface water that affect the two site release area s. It is not necessarily true that the small regional model captures all the discharge areas for flow going through the site areas. This will be investigated later in Section 9.

7.5.3 Specified infiltration for flow (SReg_4Component_Infiltration_IC2)

Here we consider a varaint with an alternative boundary condition for the top surface based on a flux or specified infiltration type boundary condition as described in Section 2.1.5. The maximum potential infiltration on the top surface is set to 165 mm/year and all other parameters are identical to the Base Case SReg_4Component_ IC2. For the infiltration used and the hydaruilc conductivity of the HSD layers then this resulted in a phreatic surface close to groundsurface and hence the results are expected to be similar to the specified head case. Indeed, the profiles of refernce waters predicted in KLX02 and KSH01A shown in Figure 7-17 and Figure 7-18, respectively, are almost identical to the Base Case. There was insufficient time for a detailed sensitivity study to HSD properties, for example spatial variations in the cover and properties. However, it was concluded that properties of the HSD will not affect the deep conditions unless areas of very low surface hydraulic conductivity cover are included, for example clay covered areas.

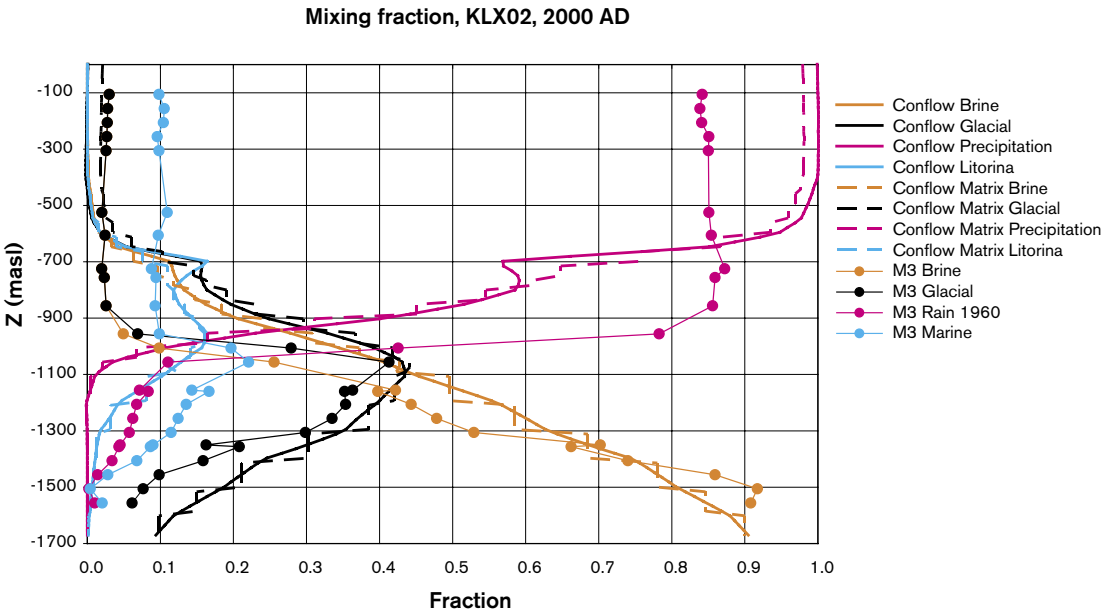

Figure 7-17. *Comparison of 4 reference water fractions in KLX02 for a specified infiltration (SReg_4Component_Infiltration_IC2). The mixing fractions in the fracture system are shown by solid lines, in the matrix it is dashed, and the data by points.*

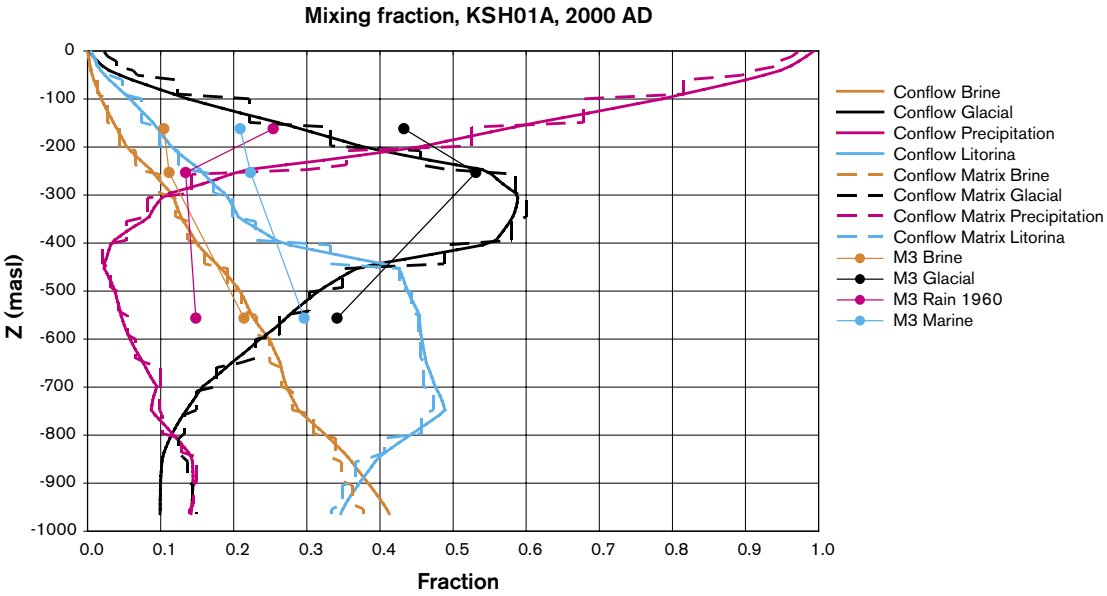

Figure 7-18. *Comparison of 4 reference water fractions in KSH01A for a specified infiltration (SReg_4Component_Infiltration_IC2). The mixing fractions in the fracture system are shown by solid lines, in the matrix dashed, and the data by points.*

7.6 Sensitivity to DFN model parameters and data interpretation

The variants for the DFN model include:

- A second realisation of the Base Case.
- A third realisation of the Base Case.
- The DarcyTools Hydro-DFN.
- An Uncorrelated transmissivity model.
- A semi-correlated transmissivity model.
- DFN interpreted from KLX01.

7.6.1 DFN Realisations 2 and 3 (SReg_4Component2_IC2 and SReg_4Component3_IC2)

These cases are intended to quantify how much affect the stochastic nature of the HRD properties has on the predicted borehole reference water profiles. The only change from the Base Case is to use a different random number seed in sampling all the DFN properties. This might be expected to give fractures in different positions in the boreholes, for example. Figure 7-19 shows the reference waters for borehole KLX02 in Realisation 2. The only significant difference is that the profile is much smoother around –700 m elevation where there was a large stochastic feature in Realisation 1. For KSH01A, the profiles are also similar in Realisation 3 apart from a slightly higher peak for the Glacial at –350 m, and Marine at –600 m (see Figure 7-20). In Realisation 3, the match for KLX02 is the best since the top of the Brine and Glacial are slightly lower, and the Rain 1960 starts slightly deeper (see Figure 7-21). However, Figure 7-22 shows that Realisation 3 gives the worst match for

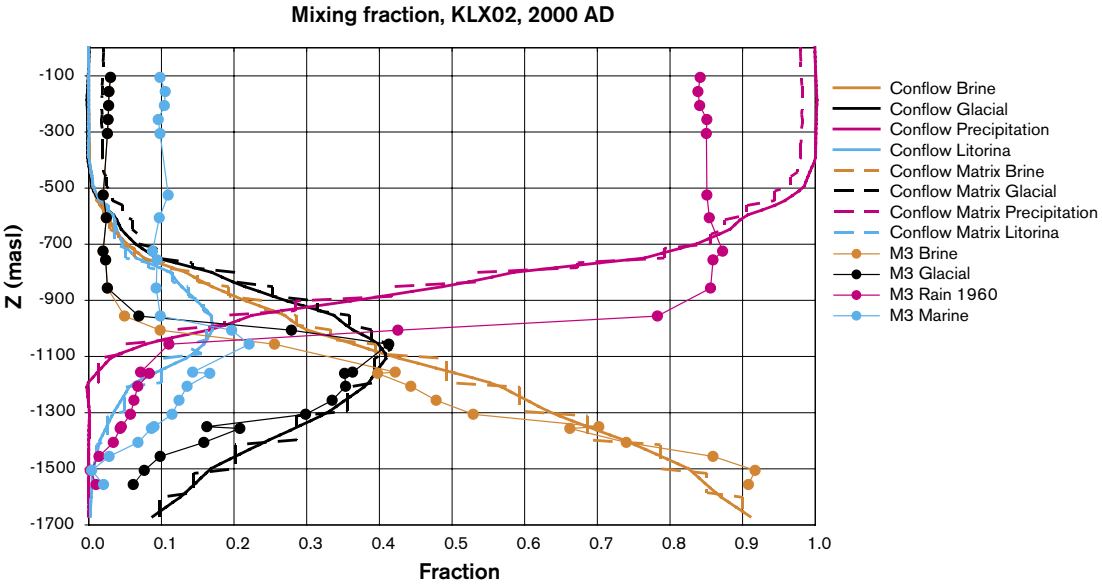

Figure 7-19. *Comparison of 4 reference water fractions in KLX02 for Realisation 2 (SReg_4Component2_IC2). The mixing fractions in the fracture system are shown by solid lines, in the matrix it is dashed, and the data by points.*

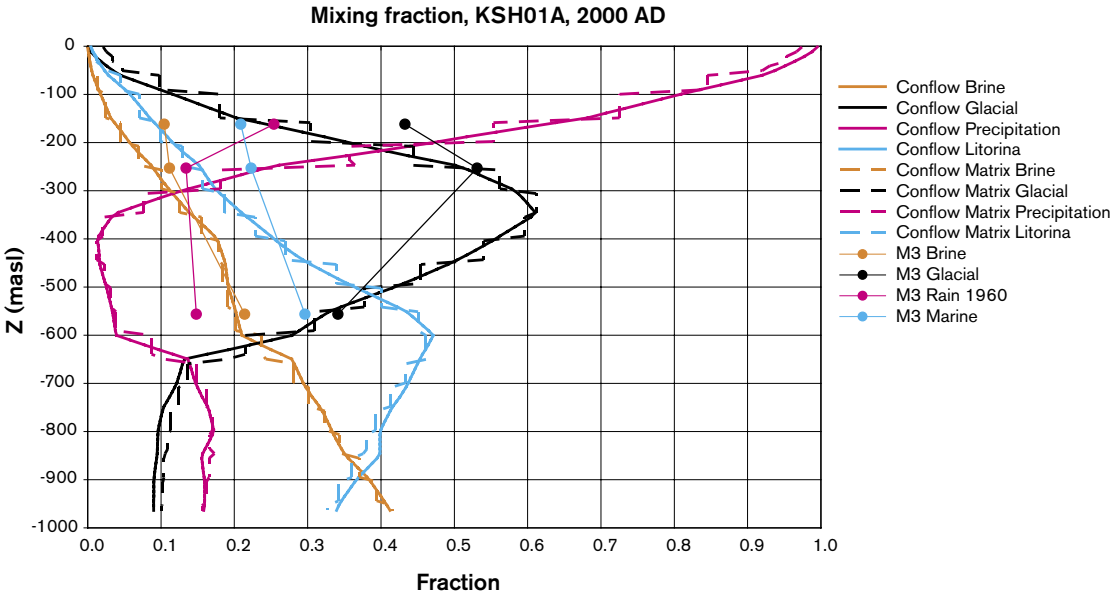

Figure 7-20. *Comparison of 4 reference water fractions in KSH01A for Realisation 2 (SReg_4Component2_IC2). The mixing fractions in the fracture system are shown by solid lines, in the matrix it is dashed, and the data by points.*

KSH01A as the Glacial and Marine about 200 m deeper than suggested by the data and in the other two realisations. It is concluded that the stochastic effect of the DFN model on the regional flow pattern is moderate and only gives rise to localised effects in the boreholes. However, there is probably sufficient difference to strictly require at least a few realisations to perform the calibration, and possibly calculation of the transport performance measures.

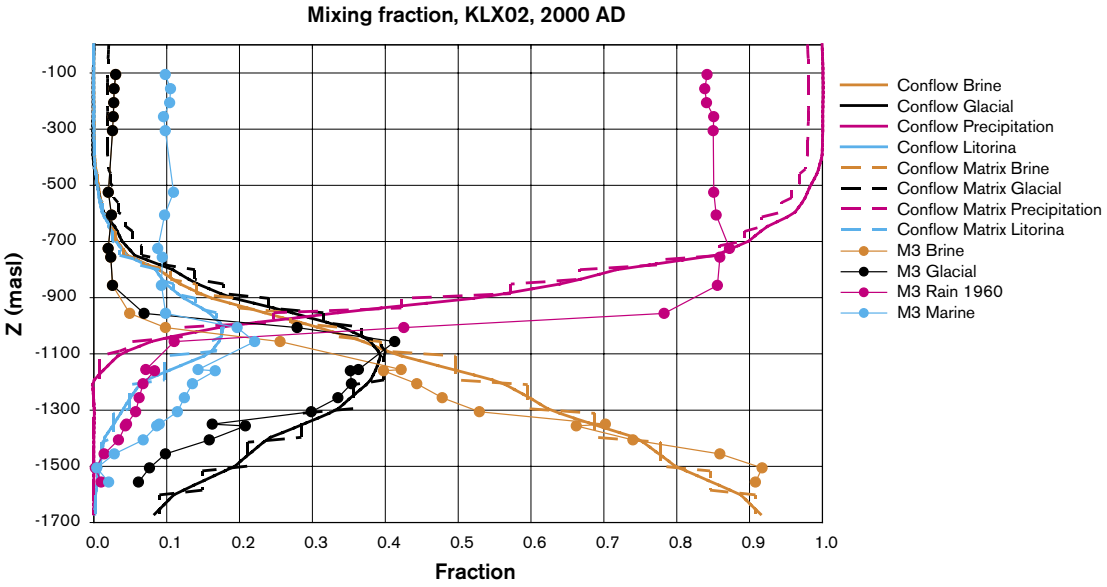

Figure 7-21. *Comparison of 4 reference water fractions in KLX02 for Realisation 3 (SReg_4Component3_IC2). The mixing fractions in the fracture system are shown by solid lines, in the matrix it is dashed, and the data by points.*

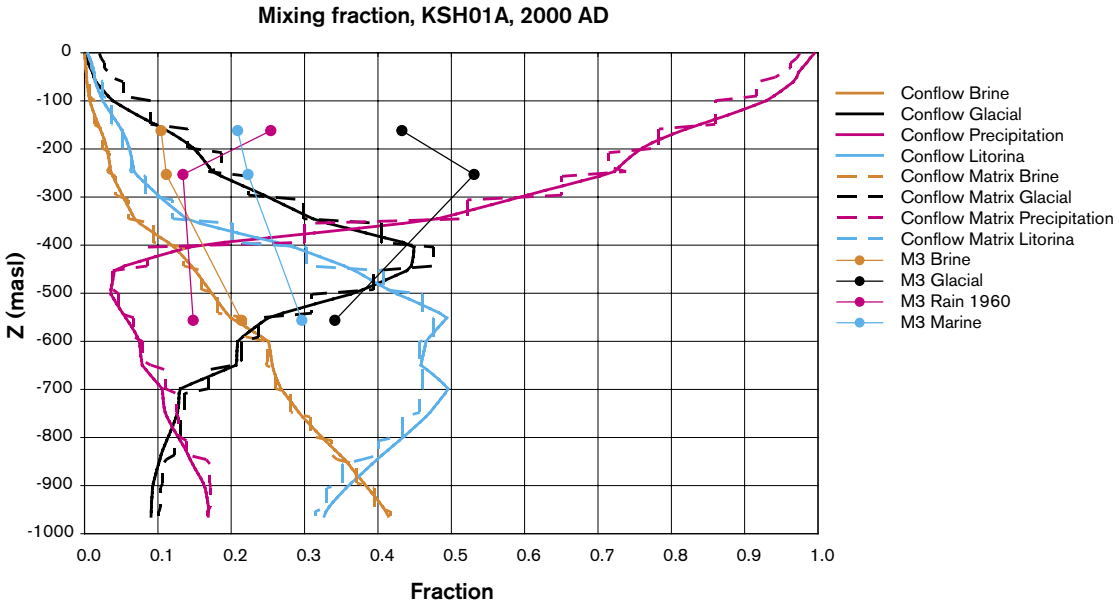

Figure 7-22. *Comparison of 4 reference water fractions in KSH01A for Realisation 3 (SReg_4Component3_IC2). The mixing fractions in the fracture system are shown by solid lines, in the matrix it is dashed, and the data by points.*

7.6.2 DarcyTools (DT) interpreted Hydro-DFN model (SReg_ 4Component_DT_IC2)

This case uses the DFN parameters derived by the DarcyTools Team given in Table 3-28. The main differences from the CONNECTFLOW DFN are that it uses the same power-law length distribution for all sets, has a slightly higher $P32_t$, and a different correlated transmissivity model with a higher slope. Hence, the case gives an indication of the uncertainty in interpreting the basic fracture data, and provides a case for comparison of the model predictions between the two codes from the same DFN input. Figure 7-23 and Figure 7-24 show the present-day reference water profiles in KLX02 and KSH01A, respectively. The profile for KLX02 is very similar to that for the CONNECTFLOW DFN. For KSH01A, the Glacial and Marine maximum are about 200 m lower than Realisations 1 and 2 of CONNECTFLOW, but more similar to Realisation 3.

Therefore, the results seem insensitive to the particular interpretation of the Hydro-DFN model. However, since both Hydro-DFN models have been derived from the same data, then it perhaps just reflects that the DFN parameters that can be deduced from the current Version S1.2 fracture data are non-unique. It also suggests that we should be able to make comparison between the results using CONNECTFLOW with those from DarcyTools.

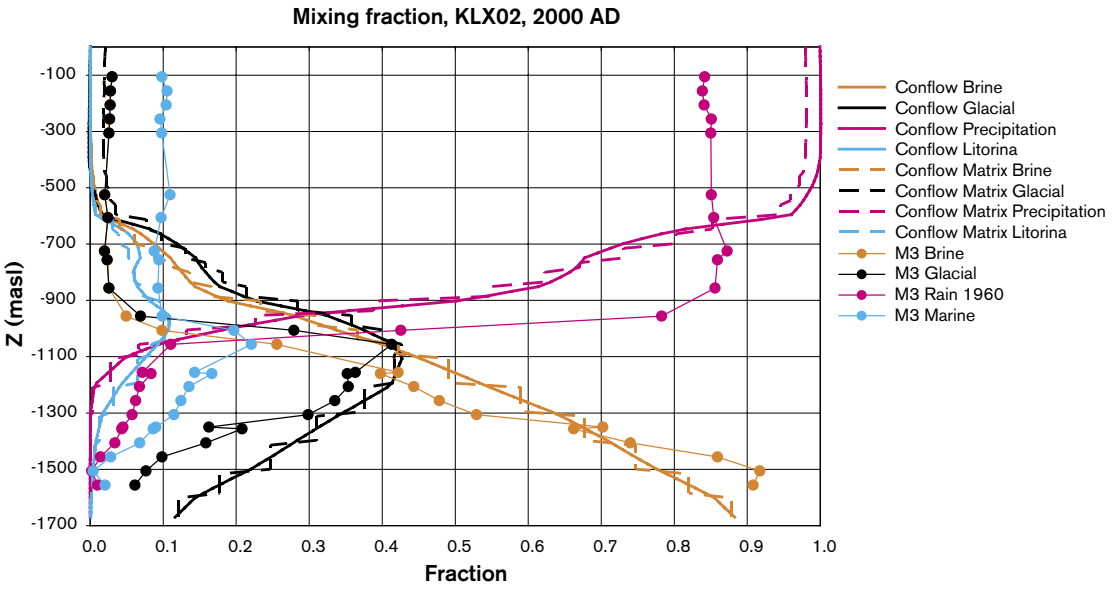

Figure 7-23. *Comparison of 4 reference water fractions in KLX02 for the DT Hydro-DFN (SReg_4Component_DT_IC2). The mixing fractions in the fracture system are shown by solid lines, in the matrix it is dashed, and the data by points.*

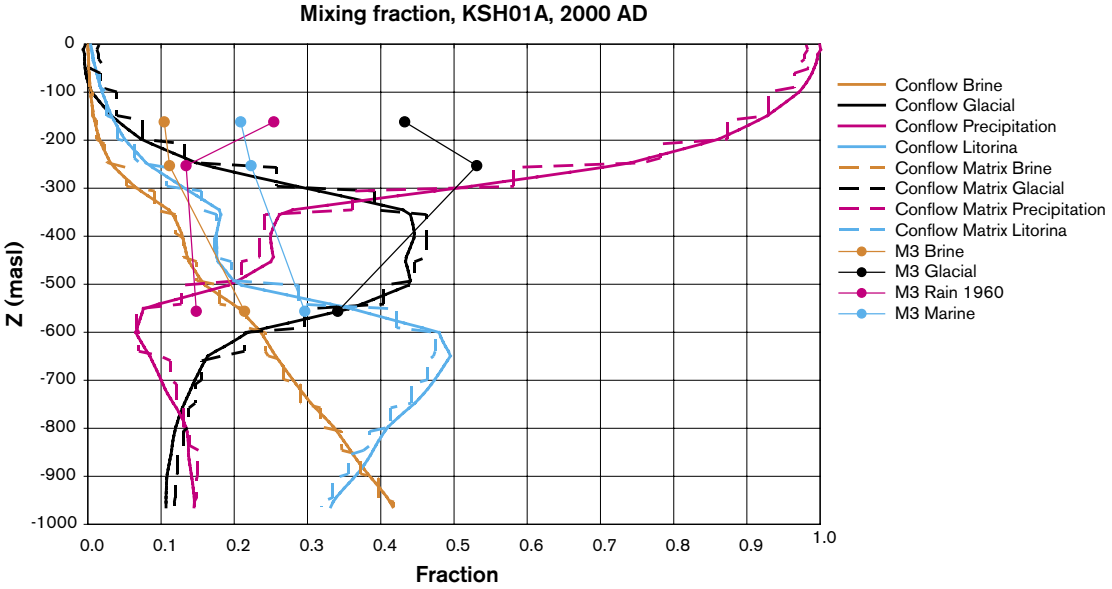

Figure 7-24. *Comparison of 4 reference water fractions in KSH01A for the DT Hydro-DFN (SReg_4Component_DT_IC2). The mixing fractions in the fracture system are shown by solid lines, in the matrix it is dashed, and the data by points.*

7.6.3 Uncorrelated and Semi-correlated transmissivity (SReg_ 4Component_UnCorr_IC2 and SReg_4Component_Semi_IC2)

One of the objectives of the Version S1.2 modelling was to consider the uncertainty to different assumptions about the fracture transmissivity model. The uncorrelated transmissivity model is based on random sampling of a lognormal distribution irrespective of fracture length; as such it is the opposite extreme to the directly correlated transmissivity/ length case. It is interesting to see if the Hydro-DFN produced for this case, tabulated in Table 3-26, will give different results and hence provide a means for discerning the more likely fracture transmissivity model. The borehole reference water fractions shown in Figure 7-25 and Figure 7-26 are in fact very similar to those for the Base Case with a correlated transmissivity model. The Brine starts higher than in the in the Base Case in KLX02 suggesting reduced mixing and not as good a match. However, it does not appear possible to dismiss this interpretation of the Hydro-DFN transmissivity model that has been calibrated to the same PFL and PSS flow data.

A single realisation of the semi-correlated transmissivity Hydro-DFN model is shown in Figure 7-27 and Figure 7-28. In this case the Glacial spike goes deeper in KLX02 than both the Base Case and the data. The Marine spike nearly disappears also in KLX02, and hence is less good a match than the Base Case Hydro-DFN. Overall the reference water profiles overall are again similar to the Base Case, and so it confirms this transmissivity model is another potential alternative Hydro-DFN model. This variant has the potential to give significant variations between realisations. Hence, it would have been interesting to consider the stochastic variability for this transmissivity model, but this was not considered within the current study.

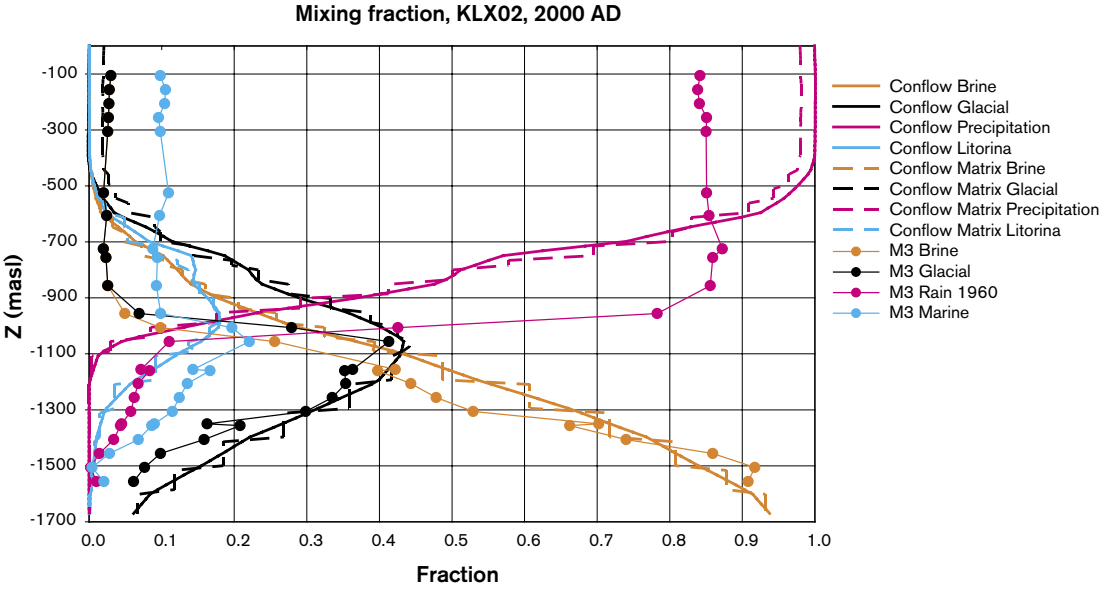

Figure 7-25. *Comparison of 4 reference water fractions in KLX02 for uncorrelated T (SReg_4Component_UnCorr_IC2). The mixing fractions in the fracture system are shown by solid lines, in the matrix it is dashed, and the data by points.*

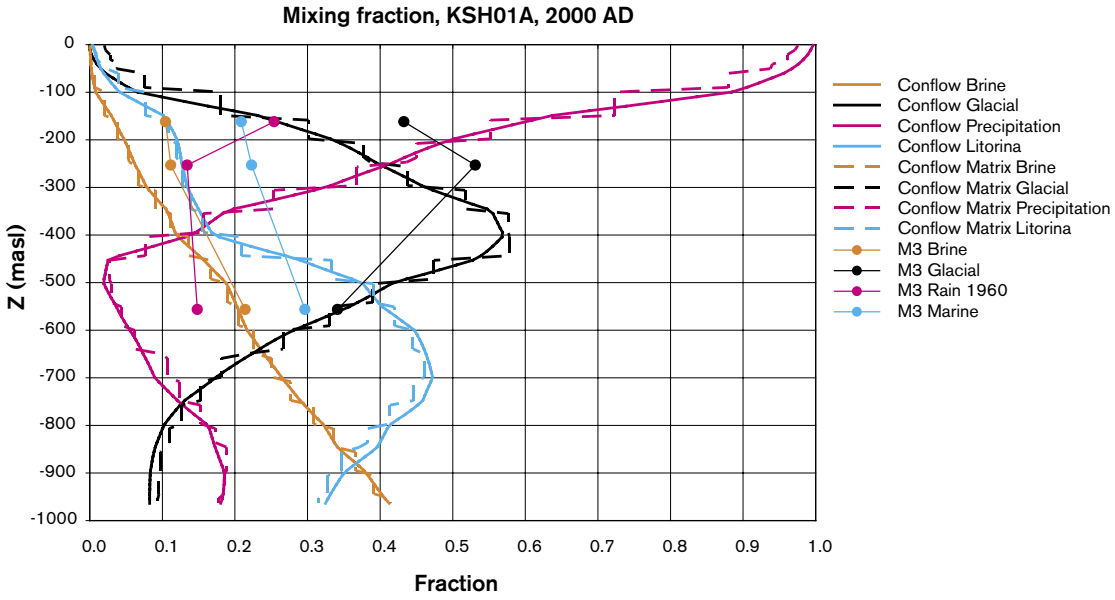

Figure 7-26. *Comparison of 4 reference water fractions in KSH01A for uncorrelated T (SReg_4Component_UnCorr_IC2). The mixing fractions in the fracture system are shown by solid lines, in the matrix it is dashed, and the data by points.*

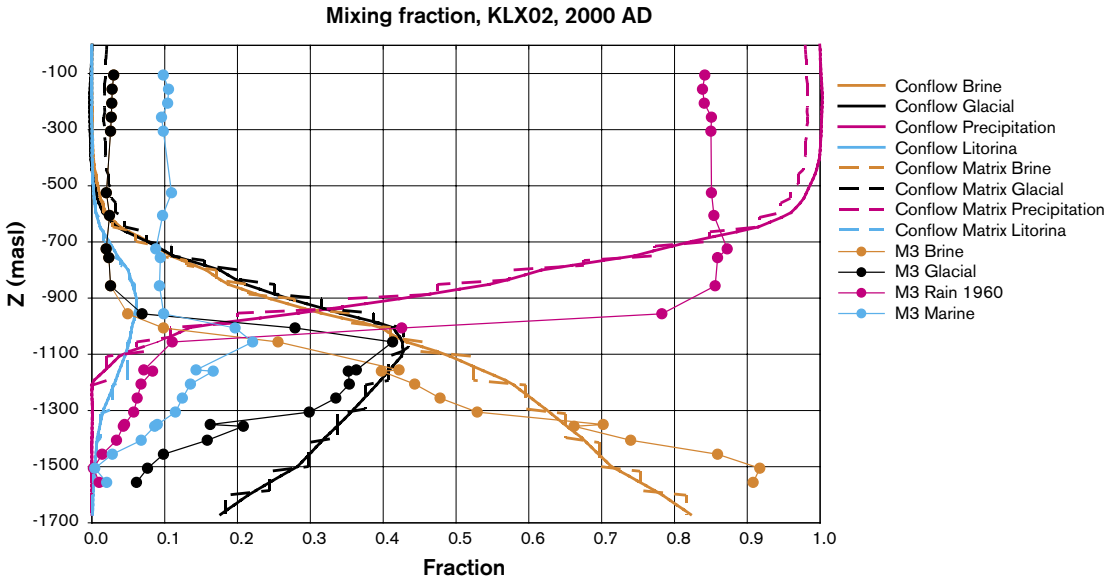

Figure 7-27. *Comparison of 4 reference water fractions in KLX02 for semi-correlated T (SReg_4Component_Semi_IC2). The mixing fractions in the fracture system are shown by solid lines, in the matrix it is dashed, and the data by points.*

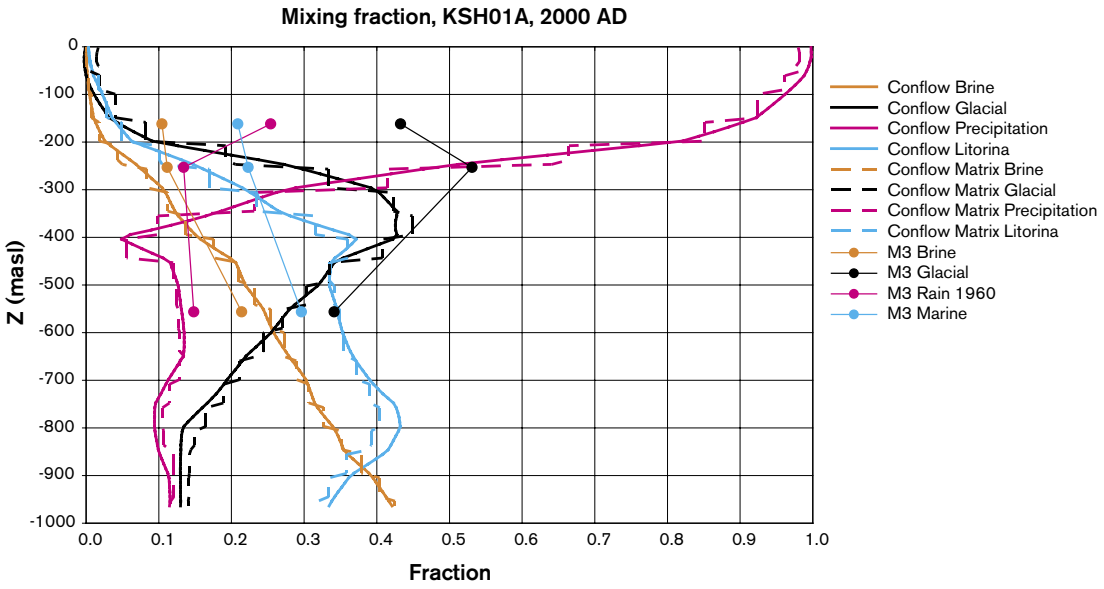

Figure 7-28. *Comparison of 4 reference water fractions in KSH01A for semi-correlated T (SReg_4Component_UnCorr_IC2). The mixing fractions in the fracture system are shown by solid lines, in the matrix it is dashed, and the data by points.*

7.6.4 DFN interpreted from KLX01 (SReg_4Component_KLX01_IC2)

The final alternative Hydro-DFN considered was that based on the interpretation of the older Borehole core and PSS data for KLX01, as described in Table 3-27. This had the same fracture sets and orientations, but a higher P32, lower transmissivity exponent and higher factor. Reference water profiles are given in Figure 7-29 and Figure 7-30. Once again the results are little changed for the alternative Hydro-DFN even though this time a different data source, that from KLX01, has been used to calibrate the Hydro-DFN. Considering the equivalent block hydraulic conductivity for a 100 m block in Table 4-1, these insensitivities to the Hydro-DFN are not unexpected since the median value, 50-percentile, varies little between the various cases apart from the uncorrelated transmissivity modedl that has a lower hydraulic conductivity.

7.6.5 Comparison of hydraulic properties for alternative DFN models in boreholes

Another comparison that can be made at the boreholes is the modelled and measured hydraulic conductivity. The Hydro-DFN as been conditioned based on short interval flow measurements, i.e. the PFL anomalies or the PSS 5 m packer interval tests, but not directly to the longer interval PSS test performed for 100 m intervals that correspond to flows from several fractures or fracture zones. The EPM models represent upscaled stochastic DFN models with hydraulic properties based on either a 50 m or 100 m scale. Hence, it is appropriate to compare the modelled hydraulic conductivity in finite-elements cut by the boreholes with the 100 m PSS intervals. The models have not been conditioned directly to this data, so the most one can expect is for the mean and spread of hydraulic conductivities in the model to be similar to the measured data, but not too reproduce any trends within individual boreholes. It is also interesting to the variability in hydraulic conductivity in the boreholes for the various Hydro-DFN models.

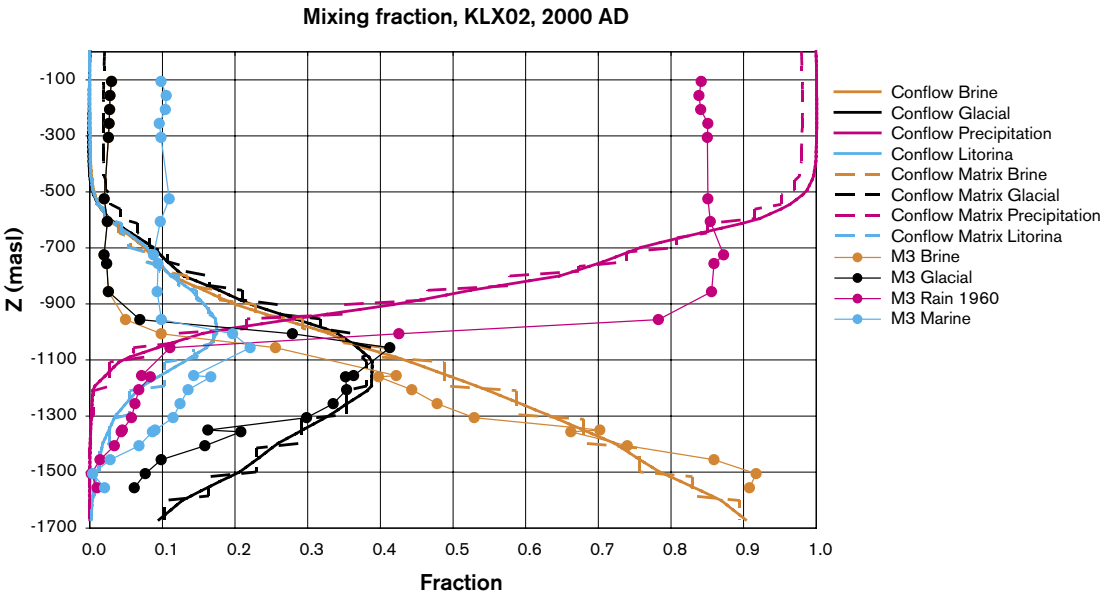

Figure 7-29. *Comparison of 4 reference water fractions in KLX02 for DFN based on KLX01 (SReg_4Component_KLX01_IC2). The mixing fractions in the fracture system are shown by solid lines, in the matrix it is dashed, and the data by points.*

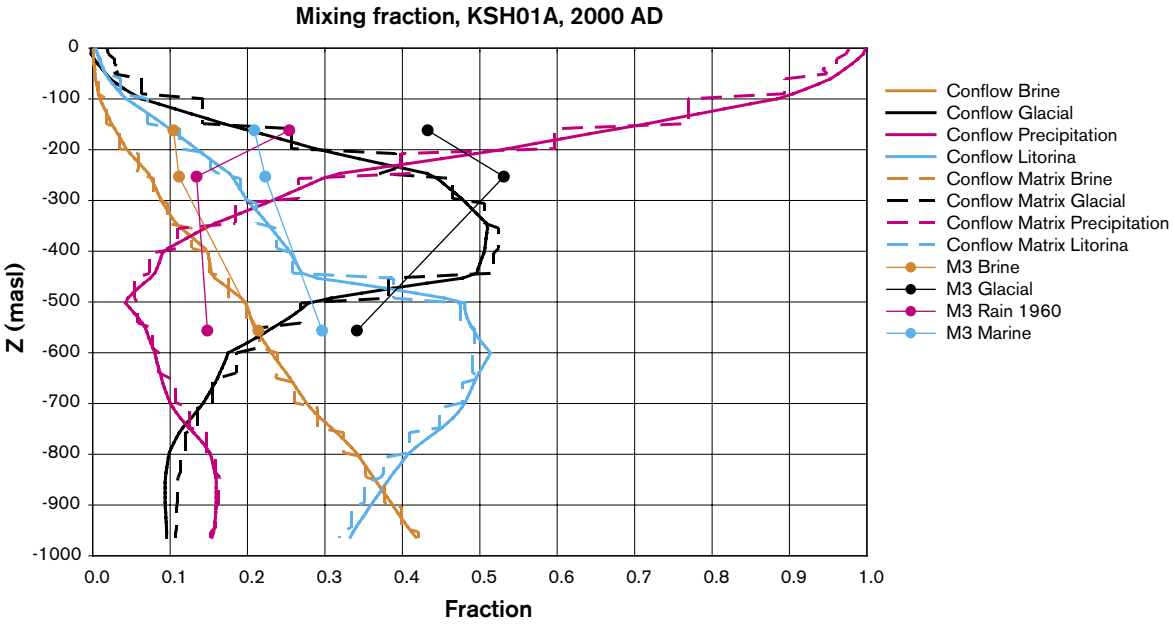

Figure 7-30. *Comparison of 4 reference water fractions in KSH01A for DFN based on KLX01 (SReg_4Component_KLX01_IC2). The mixing fractions in the fracture system are shown by solid lines, in the matrix it is dashed, and the data by points.*

Figure 7-31 to Figure 7-36 show the modelled and measured hydraulic conductivities for boreholes KLX01, KLX02, KSH01A, KSH02, KSH03A and KAV01 generally for the top 1,000 m of borehole. The geometric average hydraulic conductivity in the model, around 10^{-8} m/s, appears to be correct, but one clear feature in the comparison is that the data suggests intervals with very low hydraulic conductivity less than 10^{-10} m/s which is not reproduced in the models. This would suggest that fracture occurrence cannot be described everywhere by a uniform Poisson point process. The variation within the Hydro-DFN variants and between them is from around 10^{-9} to 10^{-6} m/s. Looking at individual boreholes: KLX01 is in reasonable agreement apart from a high measured interval at –400 m, and a very low on at –500 m; KLX02 is generally good apart from two low measured at –575 m and –625 m; KSH01A has several low conductivity intervals; KSH02 is quite well represented by Realisation 3 of the Base Case and is generally a bit lower than the model; KSH03A has high conductivity intervals near the top that are well represented in the HCD model; KAV01 is well represented by the models, especially Realisation 3 of the Base Case. These results the Hydro-DFN models give about the right overall hydraulic conductivity, but are under-predict the heterogeneity of the block properties.

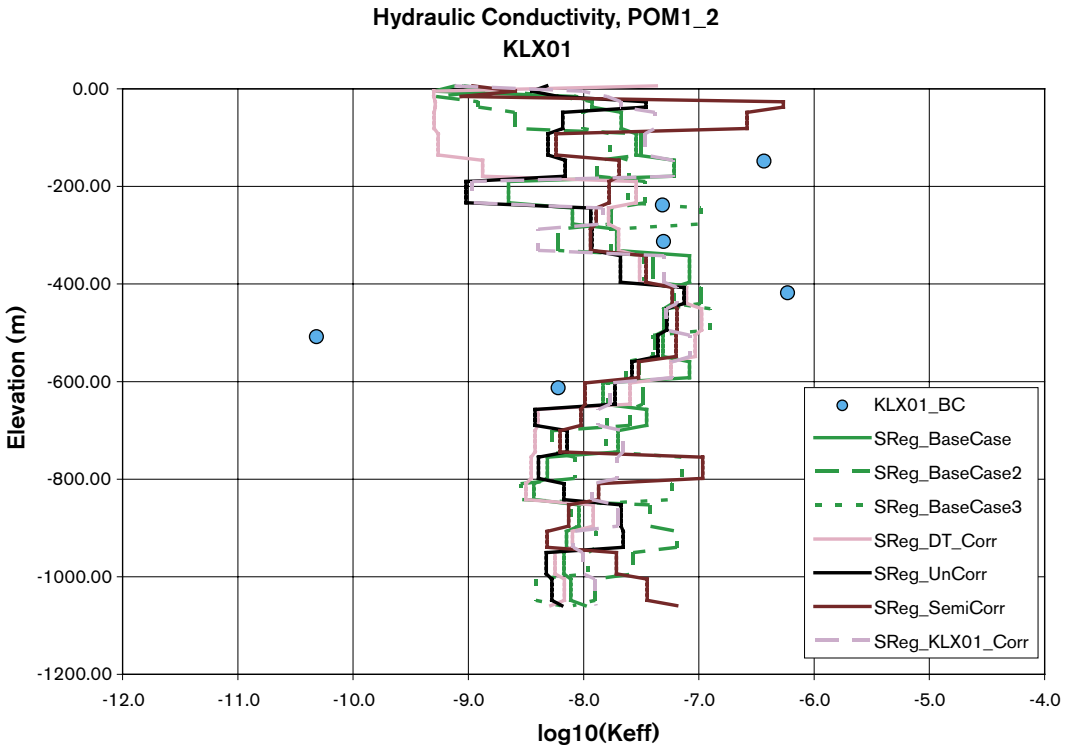

Figure 7-31. *Comparison of hydraulic conductivity along KLX01 for different HRD models with measured PSS 100 m interval data.*

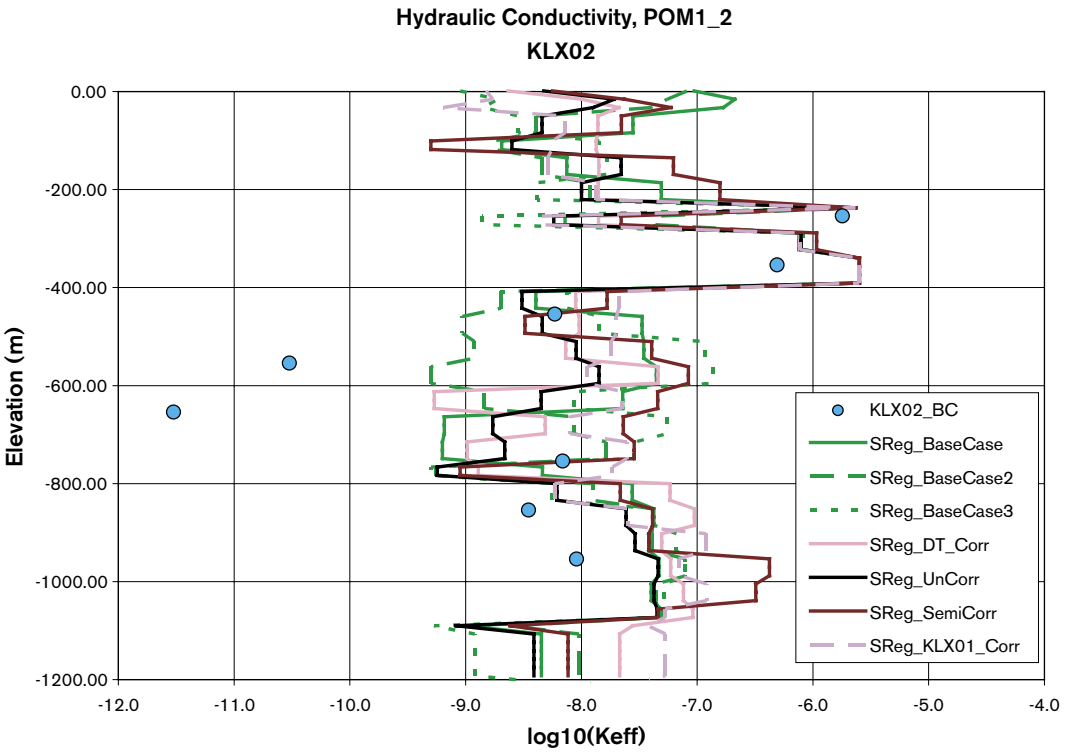

Figure 7-32. *Comparison of hydraulic conductivity along KLX02 for different HRD models with measured PSS 100 m interval data.*

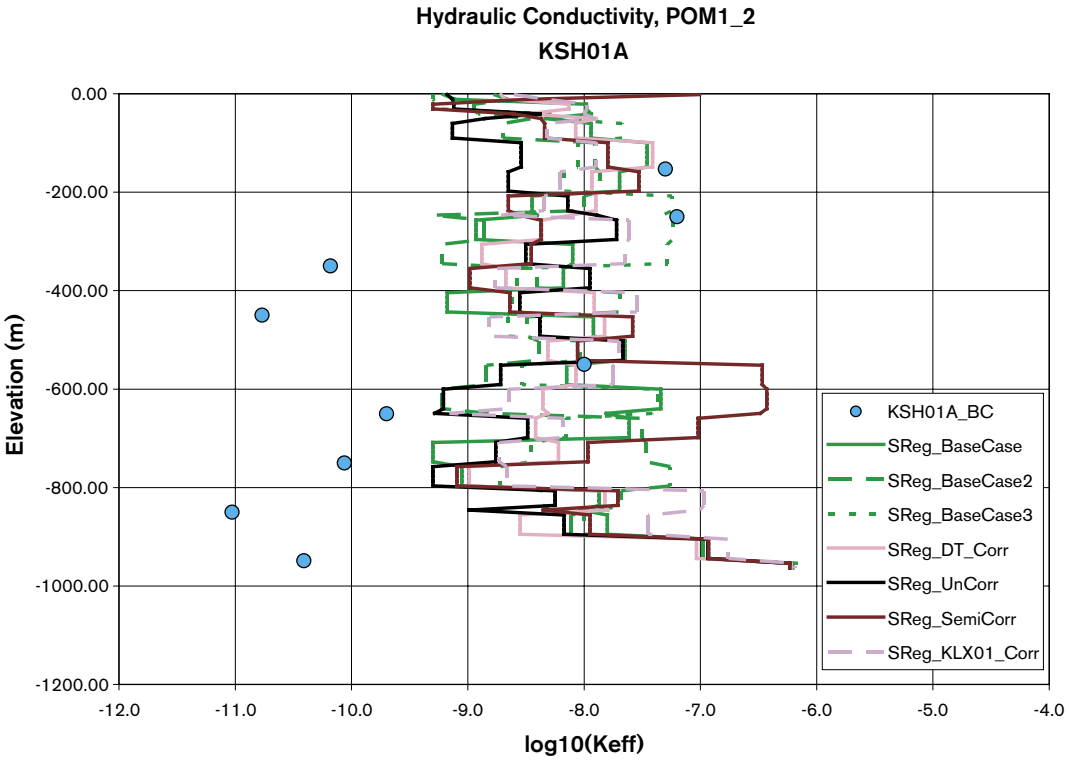

Figure 7-33. *Comparison of hydraulic conductivity along KSH01A for different HRD models with measured PSS 100 m interval data.*

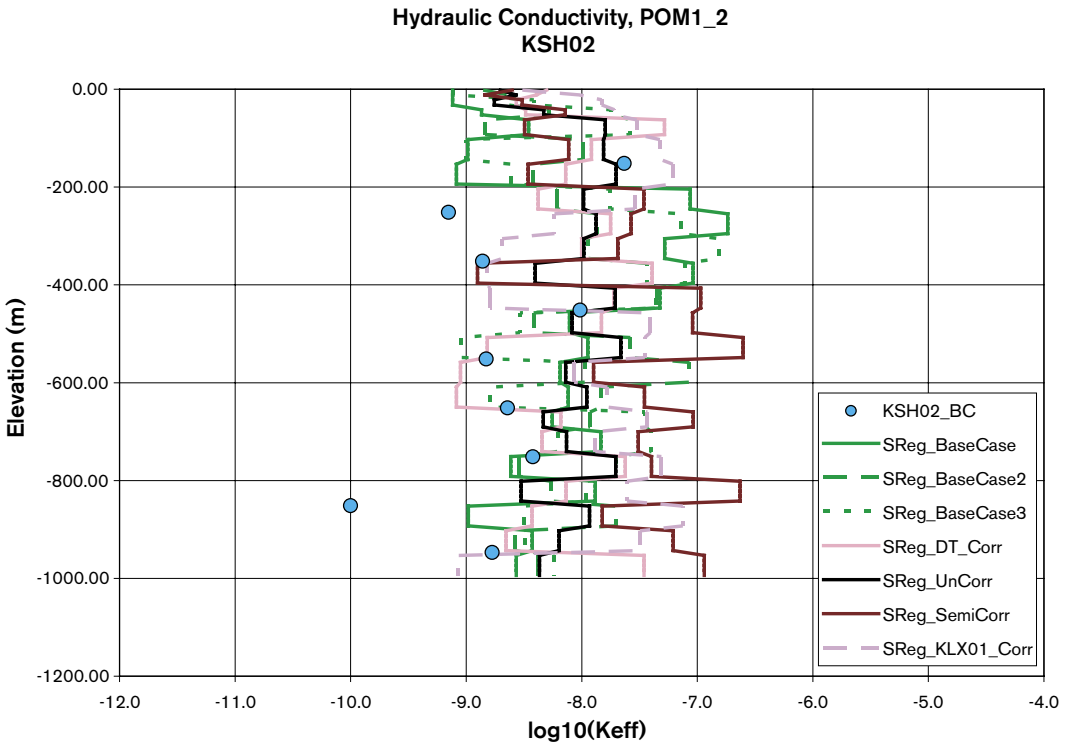

Figure 7-34. *Comparison of hydraulic conductivity along KSH02 for different HRD models with measured PSS 100 m interval data.*

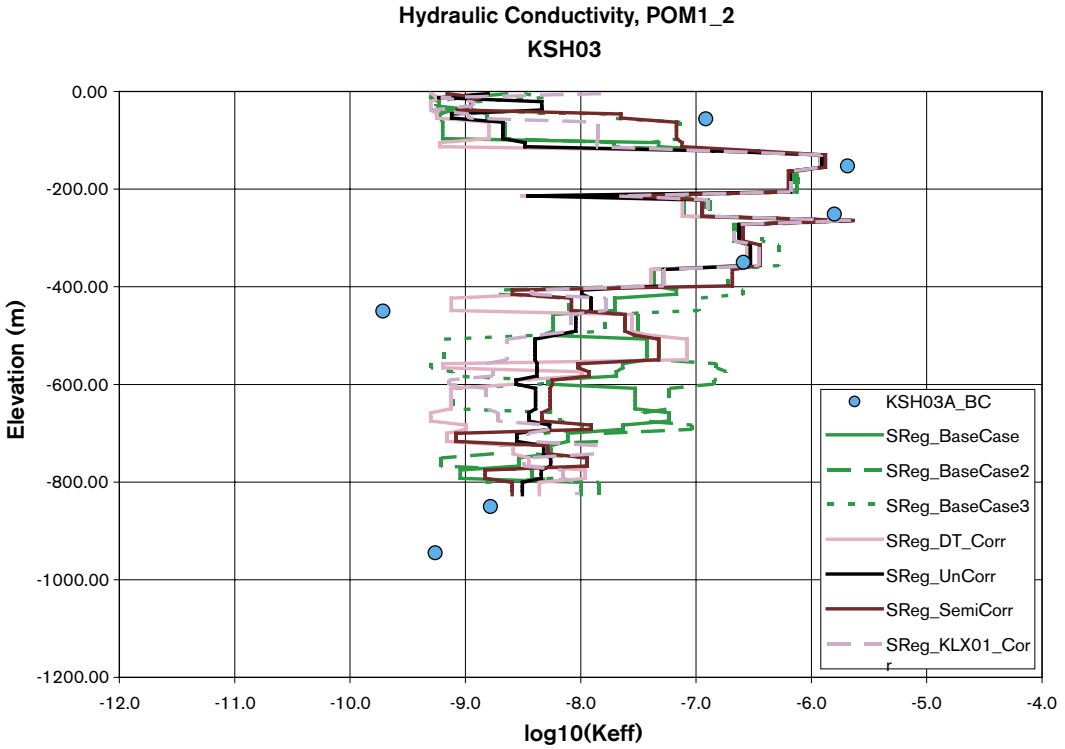

Figure 7-35. *Comparison of hydraulic conductivity along KSH03A for different HRD models with measured PSS 100 m interval data.*

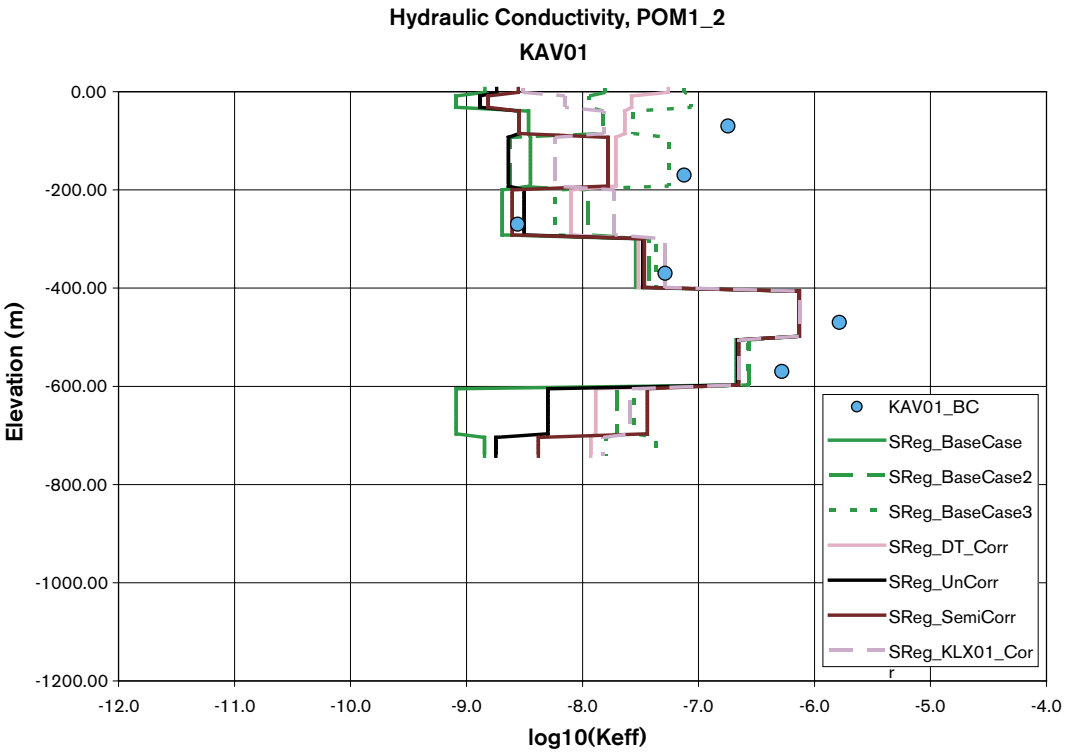

Figure 7-36. *Comparison of hydraulic conductivity along KAV01 for different HRD models with measured PSS 100 m interval data.*

7.7 Sensitivity to hydraulic properties and concepts of HCD and HRD

The variants of the hydraulic properties of the HCD and HRD include:

- HCD Case 2.
- HCD Case 3.
- A case with a depth dependency in the hydraulic conductivity, HCD and HRD, such that it decreases to one fifth at a depth of 2,000 m.
- Ten times higher hydraulic conductivity, HCD and HRD, in the top 100 m.

7.7.1 HCD Cases 2 and 3 (SReg_4Component_IFZ2_IC2 and SReg_4Component_IFZ3_IC2)

The HCD model contains 22 deterministic DZs of high confidence. The other 166 DZs have been defined with various degrees of uncertainty, and hence it is important to scope he effect of this uncertainty in the modelling. The base case included all DZs, while Case 2 includes only HCD with high confidence of existence and with Length Class 2 and 3 (L > 1,500 m), and Case 3 includes only HCD with high confidence of existence and with Length Class 3 (L > 3,000 m). Here we only consider the sensitivity of the reference water profiles in the boreholes. The profiles in KLX02 and KSH01A for HCD Case 2 are shown in Figure 7-37 and Figure 7-38. There is very little effect at these boreholes since the zones at or close to these boreholes have not been removed. For Case 3 many more DZs are removed and this has a discernible effect locally on some boreholes as shown in Figure 7-39, Figure 7-40 and Figure 7-41 for KLX01, KLX02 and KSH01A.

The difference is seen in KLX01 only where a DZ cutting the borehole has been removed. This gives a much improved match at the borehole as the Glacial water moves much higher, though still 200 m too deep, and the Rain 1960 water is also much higher and closer to the data. This suggests that removing particular zones will have a strong local effect on the reference water mixing, and hence removing or adjusting hydraulic properties of individual zones may improve the match at particular boreholes without changing the global reference water distributions. This is promising since it offers the possibility to calibrate the HCD model and hence reduce uncertainty using the hydro-geochemistry data at nearby boreholes if available.

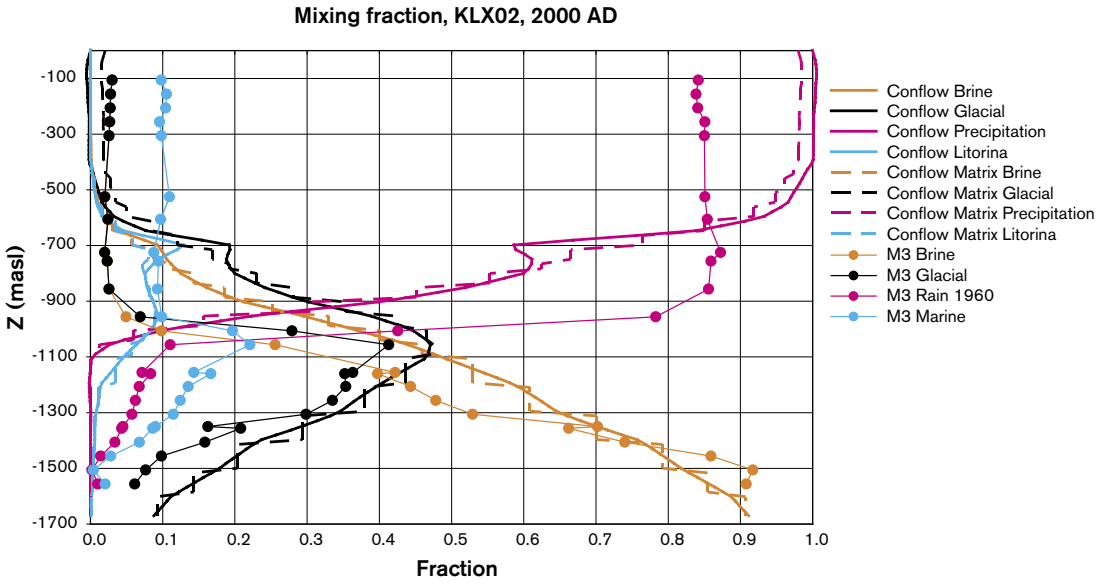

Figure 7-37. *Comparison of 4 reference water fractions in KLX02 for HCD Case 2 (SReg_4Component_IFZ2_IC2). The mixing fractions in the fracture system are shown by solid lines, in the matrix it is dashed, and the data by points.*

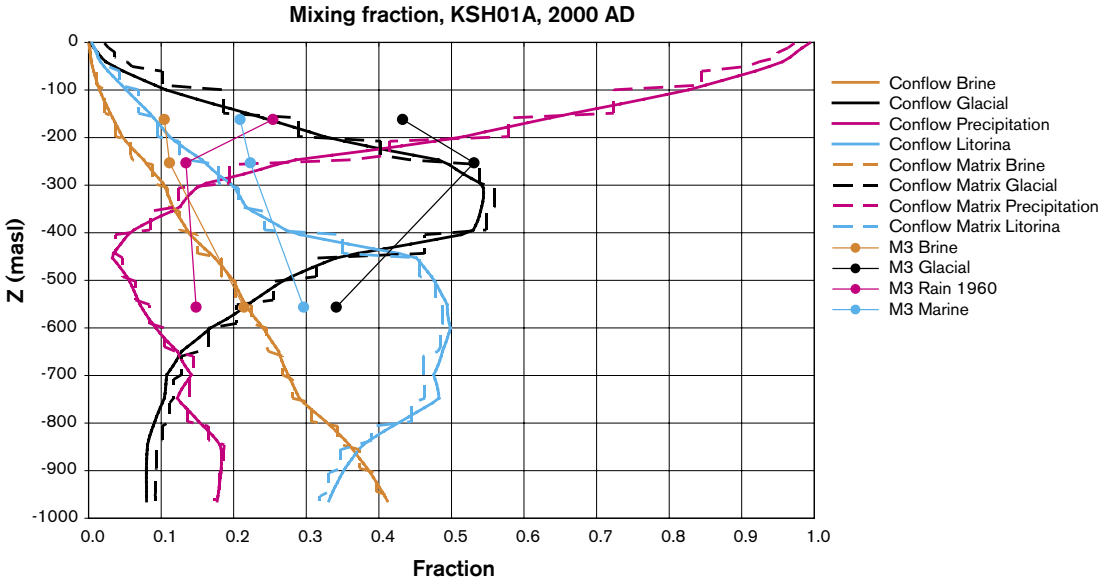

Figure 7-38. *Comparison of 4 reference water fractions in KSH01A for HCD Case 2 (SReg_4Component_IFZ2_IC2). The mixing fractions in the fracture system are shown by solid lines, in the matrix it is dashed, and the data by points.*

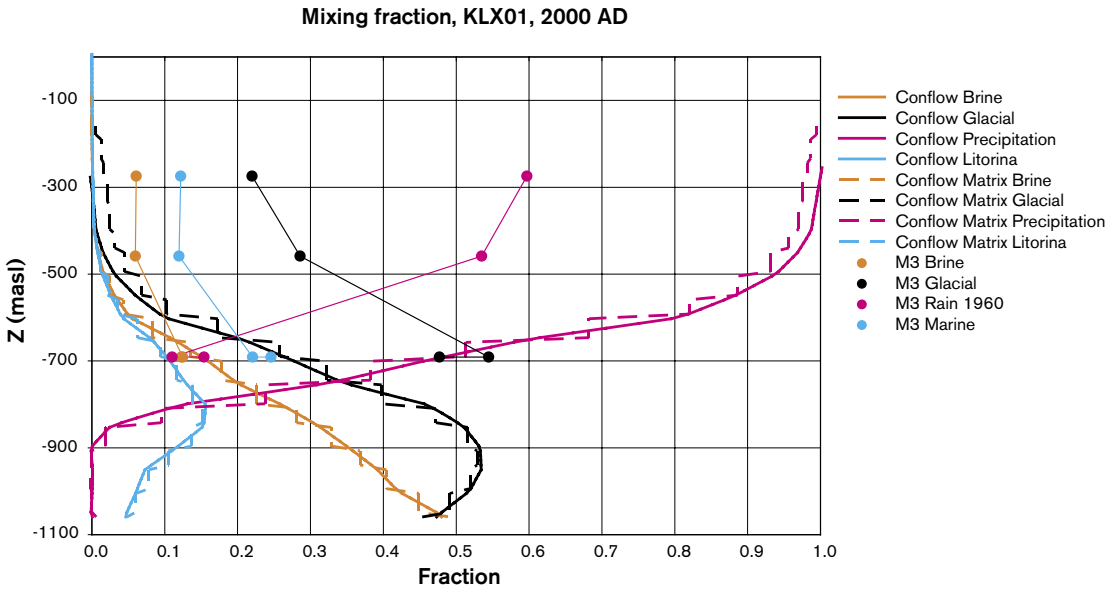

Figure 7-39. *Comparison of 4 reference water fractions in KLX01 for HCD Case 3 (SReg_4Component_IFZ3_IC2). The mixing fractions in the fracture system are shown by solid lines, in the matrix it is dashed, and the data by points.*

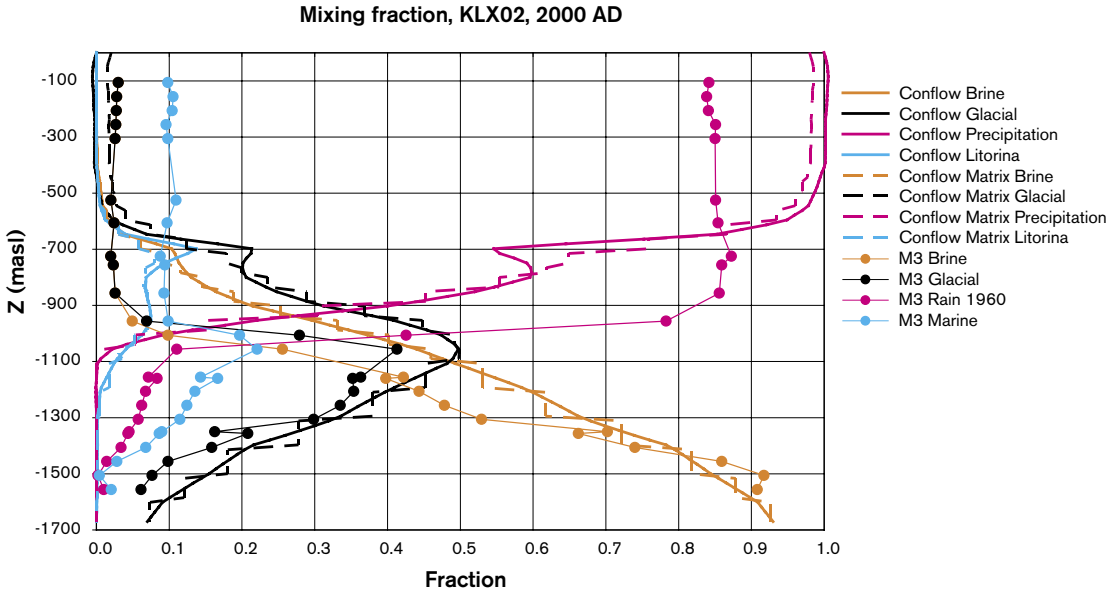

Figure 7-40. *Comparison of 4 reference water fractions in KLX02 for HCD Case 3 (SReg_4Component_IFZ3_IC2). The mixing fractions in the fracture system are shown by solid lines, in the matrix it is dashed, and the data by points.*

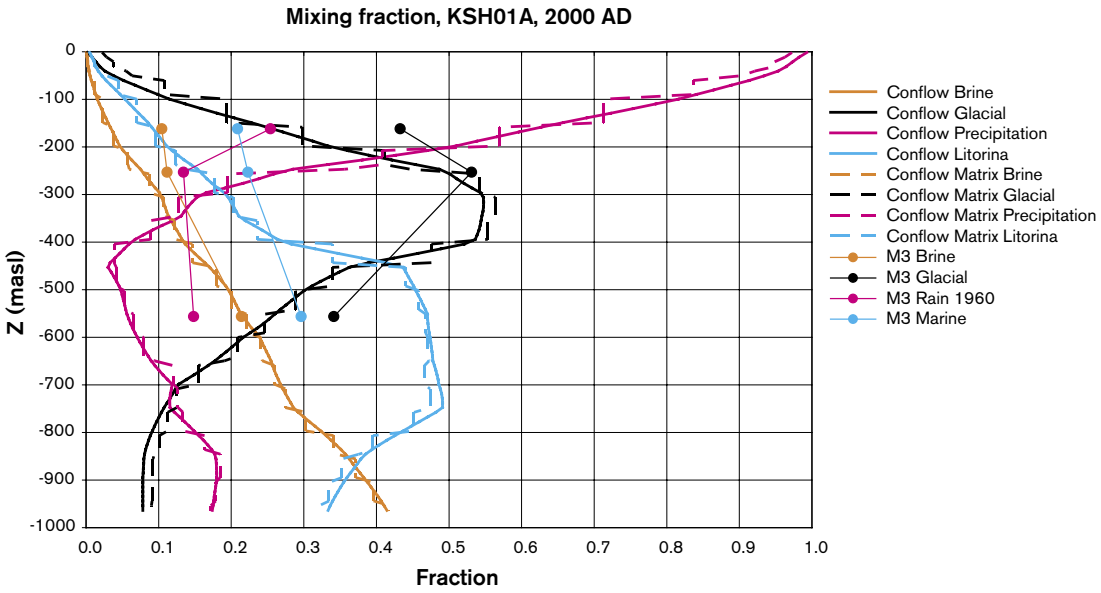

Figure 7-41. *Comparison of 4 reference water fractions in KSH01A for HCD Case 3 (SReg_4Component_IFZ3_IC2). The mixing fractions in the fracture system are shown by solid lines, in the matrix it is dashed, and the data by points.*

7.7.2 HRD with reduced K at depth (SReg_4Component_DepthK_IC2)

Considering the PSS data for 100 m intervals there appears to be an overall trend towards lower hydraulic conductivities at depth, or at least the mean hydraulic conductivity appears to decrease with depth. Hence, an illustration of what effect a reduction in hydraulic conductivity at depth would have is useful. The variant created for this case uses the same HRD ad HCD properties as for the Base Case, but has a gradual reduction in hydraulic conductivity, K´, such that $K' = K/(1+2\ 10^{-3}\times z)$, where K is the hydraulic conductivity of the Base Case. It implies that hydraulic conductivity reduces quite gradually to one fifth at –2,000 m elevation. The results for KLX02 and KSH01A are shown in Figure 7-42 and Figure 7-43. For KLX01 the reduced mixing of the reference waters is clear with the mixing zone becoming higher and coinciding with a stochastic DZ at –700 m, and the hence the match is less good. There is a more dramatic effect at KSH01A. Glacial and Rain 1960 still agree with the mixing water interpretation, but Brine is much deeper and has been replaced by Marine. This is not consistent with the data. Hence, a depth trend in hydraulic conductivity, even a relatively weak one, has a significant effect on the reference water distribution. The results from this variant may suggest a poorer match to the borehole data, but it is not clear whether better results would have been obtained if the depth trend would have been put in such the average conductivity were maintained, i.e. a slightly higher transmissivity at the top of the borehole, the same in the middle, and lower at depth. Still, the sensitivity to a depth trend suggests this issue should be pursued further in the future.

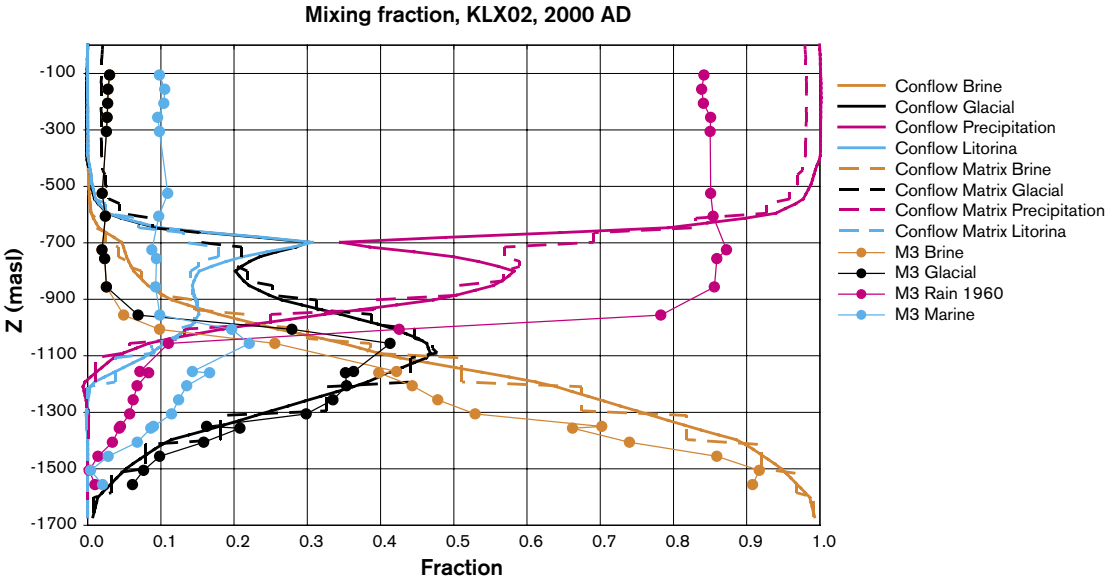

Figure 7-42. *Comparison of 4 reference water fractions in KLX02 for lower K at depth (SReg_4Component_DepthK_IC2). The mixing fractions in the fracture system are shown by solid lines, in the matrix it is dashed, and the data by points.*

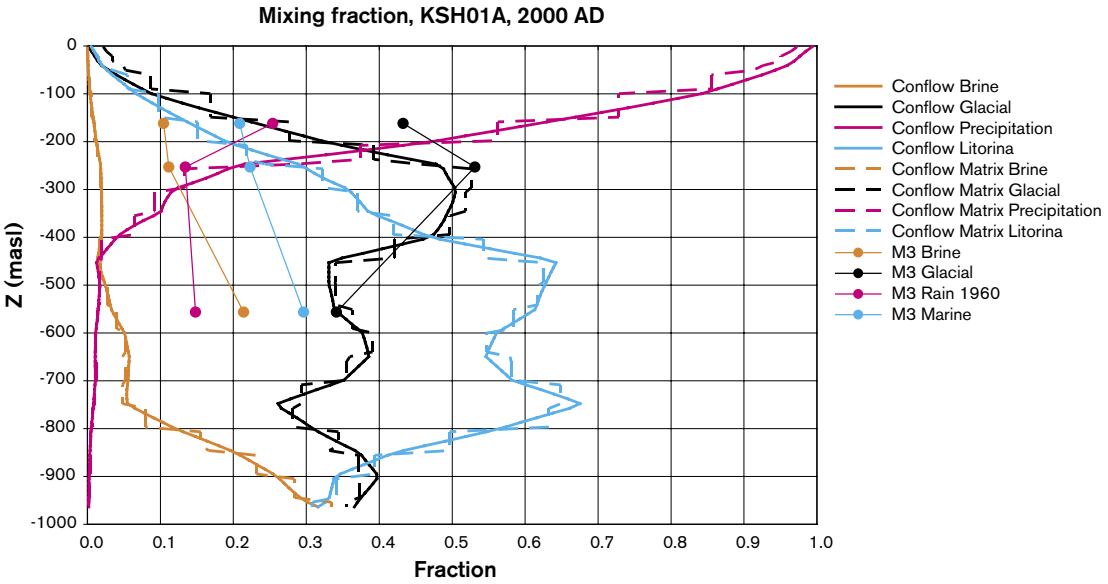

Figure 7-43. *Comparison of 4 reference water fractions in KSH01A for lower K at depth (SReg_4Component_DepthK_IC2). The mixing fractions in the fracture system are shown by solid lines, in the matrix it is dashed, and the data by points.*

7.7.3 HRD with higher K in top 100 m (SReg_4Component_K100m_IC2)

The other variant with a depth variation considered was to have a hydraulic conductivity tens time higher in the top 100 m of the model since it tends to be around 10^{-7} m/s in the upper most PSS 100 m interval (See Figure 7-31 to Figure 7-36). Reference water profiles for KLX01 and KSH01A are shown in Figure 7-44 and Figure 7-45. The profile for KLX01 is very similar to the Base Case, presumably because the mixing zone is much deeper than the top 100 m where the hydraulic conductivity has been changed. The effect is seen however in KSH01A since the mixing zone here is only about –200 m elevation. The Brine and Marine are little effected, but the Glacial/Rain 1960 mixing zone is about 100 m deeper than in the Base Case because there is presumably more flushing of Glacial water by Rain 1960 near the surface.

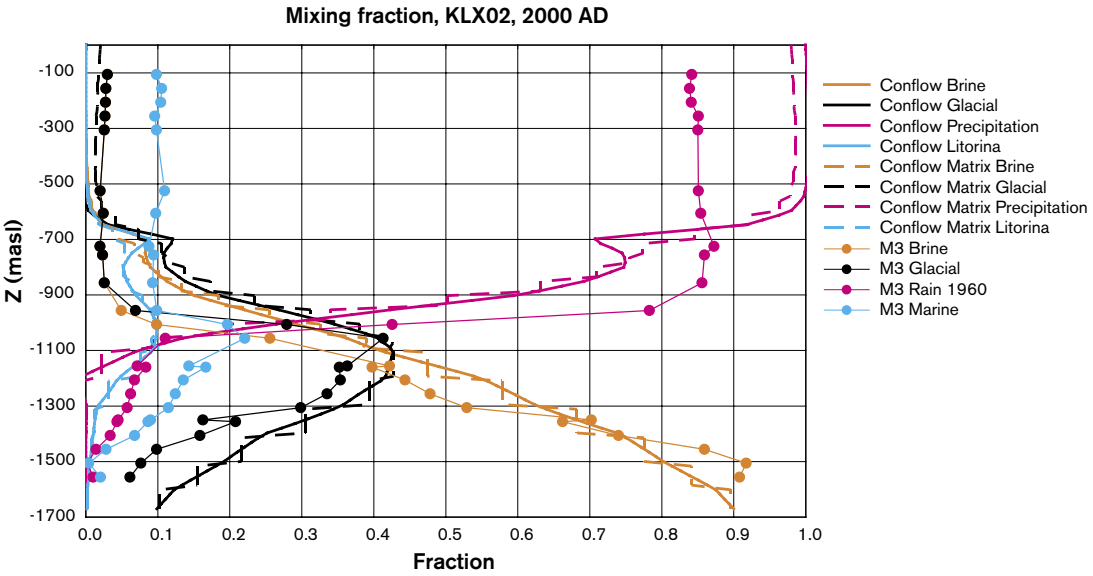

Figure 7-44. *Comparison of 4 reference water fractions in KLX02 for higher K in top 100 m (SReg_4Component_K100m_IC2). The mixing fractions in the fracture system are shown by solid lines, in the matrix it is dashed, and the data by points.*

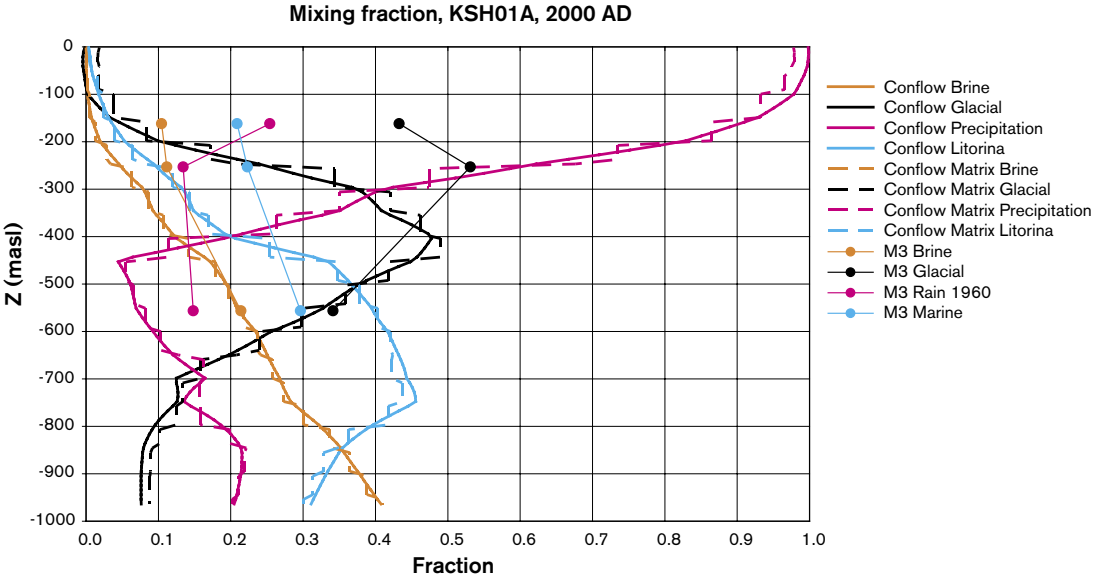

Figure 7-45. *Comparison of 4 reference water fractions in KSH01A for higher K in top 100 m (SReg_4Component_K100m_IC2). The mixing fractions in the fracture system are shown by solid lines, in the matrix it is dashed, and the data by points.*

7.8 Sensitivity to transport properties

The transport parameters of greatest interest are those that effect RMD since they effect retardation of radionuclides in groundwater flow. The timescales associated with the infiltration of surface groundwaters into the deep rock by natural transient processes are long enough, many thousands of years, to allow RMD. Hence, modelling transport and RMD of the reference waters can be a useful analogue for RMD of radionuclides. For safety assessment calculations the F-quotient is a useful concept since it allows retardation of radionuclide transport by sorption or RMD to be estimated. The formula used appropriate to an EPM is $F = \sum_l \frac{a_r \delta l}{q}$ (See Section 2.1.6), and hence the unknown hydraulic parameter is a_r, or the flow-wetted surface. Conceptually, this equates to the fracture surface area (both faces of the fracture plane) of the connected network per unit volume of rock or twice $P32_c$. Based on Table 3-26, Table 3-27 and Table 3-28 the possible range identified in the data for $P32_c$ is about 0.3 to 1.0, and hence a_r is in the range 0.6 to 2.0. In the Base Case, a value of 2.0 was chosen, i.e. the highest possible value based on the Hydro-DFN interpreted from KLX01. This high value ensures quite an efficient RMD with full access to a matrix block in a few tens of years. For $a_r = 0.6$, the timescale for full diffusion into the matrix is about ten times higher, i.e. a few hundreds of years, so one might expect more of a lag between the fracture and matrix system, but still this is shorter than the timescale on which the boundary conditions change significantly, around a thousand years. The value for a_r used in the Version S1.1 modelling was 0.1. Therefore, it is important to verify that higher values of a_r are defensible in order to get a match to the reference water distribution and this has positive implications for the predicted values of the F-quotient.

7.8.1 Lower flow-wetted-surface, $a_r = 1.0$, for RMD (SReg_4Component_FWS_IC2) and FWS based on Version S1.1, $a_r = 0.1$ (SReg_4Component_FWSt_IC2)

Several alternative values of a_r were considered, 1.0, 0.5, 0.25 and 0.1. The results shown here are for models with $a_r = 1.0$ and 0.1 for illustration. A value of 1.0 is about that based on the DarcyTools interpretation of the Hydro-DFN, and 0.1 is based on the value used in the Version S1.1 modelling. The results for KLX02 and KSH01A for $a_r = 1.0$ are shown in Figure 7-46 and Figure 7-47. There slightly more mixing of Glacial and Brine at depth in KLX02 presumably due to greater advective mixing in the fracture system. In KSH01A there is more Glacial water than marine around 400–800 m depth. Since this is a discharge area at Simpevarp, then this may relate to greater flushing of Glacial water upwards through the top surface. Hence, for $a_r = 1.0$ the results are not quite as good a match as the Base Case, but probably cannot be dismissed. Similar results were obtained for $a_r = 0.5$. However, for $a_r = 0.1$ the results are very different as shown in Figure 7-48 and Figure 7-49. In KLX02 the Brine has been flushed much deeper, Marine is almost not present and Rain 1960 reaches to 1,700 m depth. Most significantly, the reference water compositions in the fracture system and matrix are different as the time for RMD is much longer (thousands of years). The result is the fracture system mixes much more rapidly and retarded by RMD far less since little of the matrix pore volume is accessible. The results for KSH01A are equally dramatic. Based on these results it is concluded that a_r must be greater than about 0.5 m^2/m^3, which adds credence to the values derived for $P32_c$ in Section 3, and is encouraging for safety assessment transport since it suggests higher values of a_r for the HRD than were used in Version S1.1.

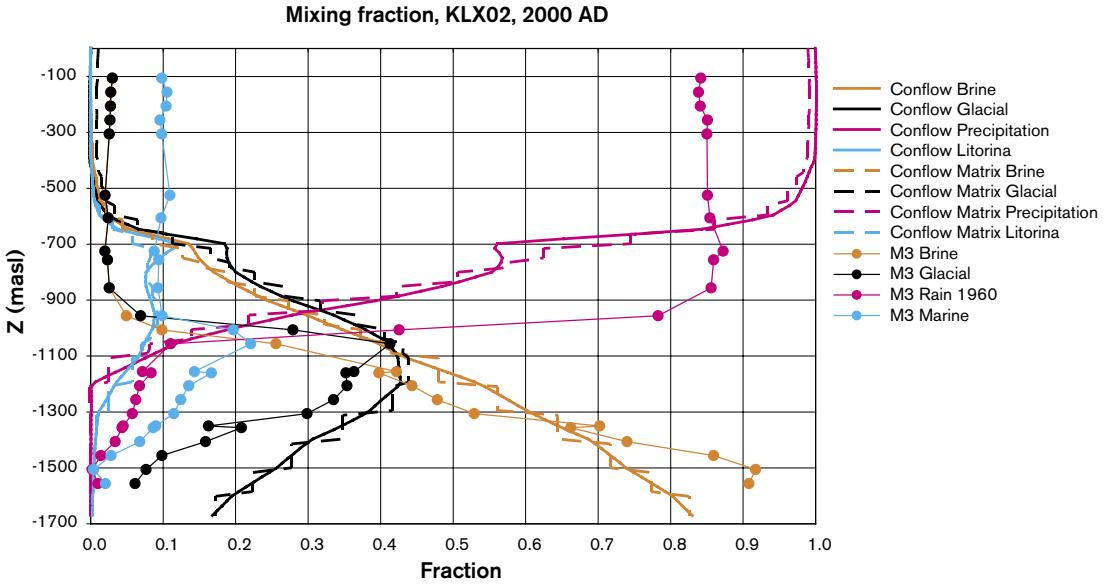

Figure 7-46. *Comparison of 4 reference water fractions in KLX02 for lower FWS, a_r = 1.0, (SReg_4Component_FWS_IC2). The mixing fractions in the fracture system are shown by solid lines, in the matrix dashed, and the data by points.*

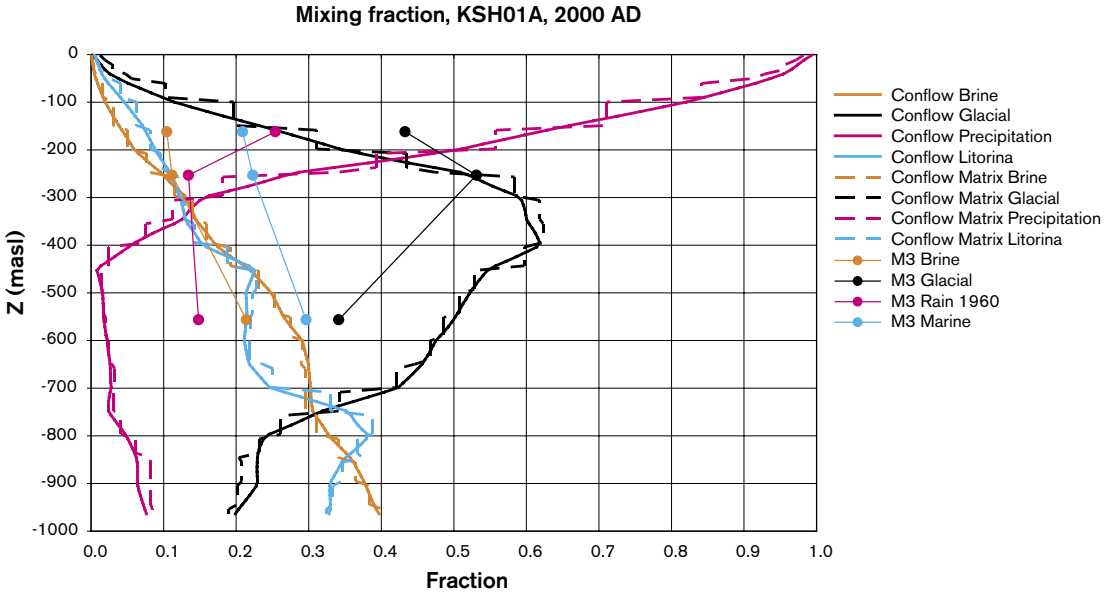

Figure 7-47. *Comparison of 4 reference water fractions in KSH01A for lower FWS, a_r = 1.0, (SReg_4Component_FWS_IC2). The mixing fractions in the fracture system are shown by solid lines, in the matrix dashed, and the data by points.*

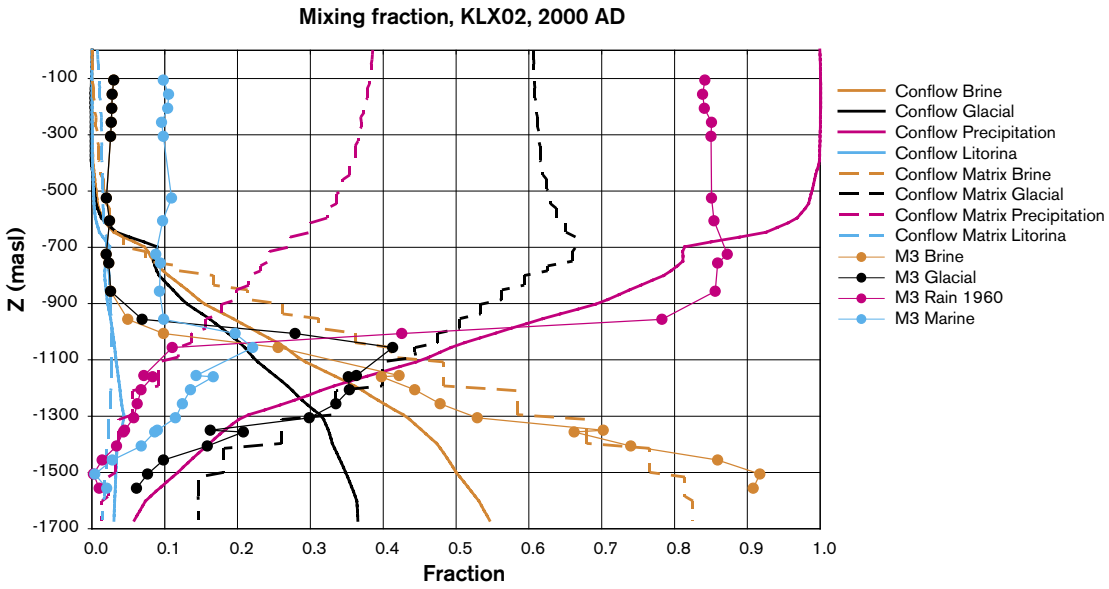

Figure 7-48. *Comparison of 4 reference water fractions in KLX02 for low FWS, a_r = 0.1, from V1.1 (SReg_4Component_FWSt_IC2). The mixing fractions in the fracture system are shown by solid lines, in the matrix dashed, and the data by points.*

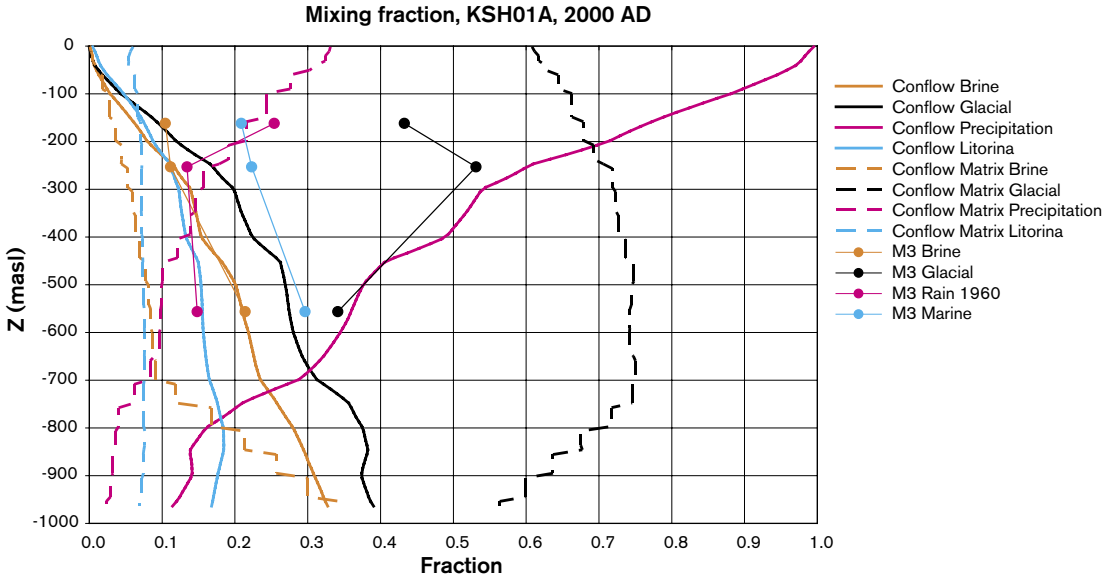

Figure 7-49. *Comparison of 4 reference water fractions in KSH01A for low FWS, a_r = 0.1, from V1.1 (SReg_4Component_FWSt_IC2). The mixing fractions in the fracture system are shown by solid lines, in the matrix dashed, and the data by points.*

7.9 Summary of modelled cases and main conclusions from each case

An overview of the main conclusions from each of the variants presented in Section 7 is given in Table 7-2.

Table 7-2. Summary of the main conclusions for model cases. The cases are grouped by colour coding according to the sensitivities they quantify: model size (brown); initial and boundary conditions (green); DFN parameters (blue); HRD and HCD hydraulic properties (purple); Transport properties (yellow).

EPM Case	Conclusions
SReg_2Component	Reasonable approximation to salinity predicted by LReg_2Component. Absolute minimum regional model domain.
LReg_2Component	Salinity results seem to stabilise for model domain about this size. Similar to Version S1.1 model domain.
Local_2Component	Model domain far too small for simulating past evolution and predicting present-day salinity in boreholes.
Local_North_2Component	Only moderate improvement on local-scale model, but more important than extending West (Local_West_2Component).
Local_West_2Component	Only moderate improvement on local-scale model.
LReg_V11_ 2Component	Almost identical prediction of salinity to domain used for Version S1.1, but can be approximated by SReg_2Component.
SReg_4Component_IC2	Base Case resulting from reference water calibration. Hydraulic parameters, initial and boundary conditions identified for reasonable match to boreholes in an global sense.
SReg_4Component_IC1	Shallower initial Brine gives a worse match. Brine is too shallow, and too little Glacial in KLX02.
LReg_4Component_IC2	Larger regional model domain gives very similar reference water profiles in boreholes to SReg_4Component_IC2. Hence, SReg_4Component_IC2 used as Base Case for calibration.
SReg_4Component_ Infiltration_IC2	In progress.
SReg_4Component2_IC2	Very similar reference water profiles to Base Case. Slightly better, no large stochastic DZ in KLX02. So small stochastic effect.
SReg_4Component3_IC2	Very similar reference water profiles to Base Case. Best realisation for KLX02, worst for KSH01A. So small stochastic effect.
SReg_4Component_DT_IC2	Very similar reference water profiles to Base Case. Slightly worse for KSH01A. Consistent hydraulic conditioning of DFN.
SReg_4Component_ UnCorr_IC2	Very similar reference water profiles to Base Case. Consistent hydraulic conditioning of DFN. Uncorrelated T model is viable.
SReg_4Component_ SemiCorr_IC2	Very similar reference water profiles to Base Case. Perhaps more mixing, and slightly less good match. Consistent hydraulic conditioning of DFN. Semi-correlated T model is viable.
SReg_4Component_KLX01_ IC2	Very similar reference water profiles to Base Case. Consistent hydraulic conditioning of DFN. Simpevarp and Laxemar have similar hydraulic properties on regional-scale.
SReg_4Component_IFZ2_ IC2	Nearly identical to Base Case. Small local-scale DZs have little effect on regional-scale reference waters.
SReg_4Component_IFZ3_ IC2	Similar to Base Case. Better in KLX01. Smaller DZs only have localised effect on regional-scale reference waters.
SReg_4Component_ DepthK_IC2	Improvement to reference waters at depth in KLX02, but worse near surface. Perhaps need higher K in top 500–1,000 m to compensate for reduction at depth (i.e. keep average constant). Relatively small depth trend has an effect.
SReg_4Component_ K100m_IC2	Very similar reference water profiles to Base Case. Worse for KSH01A.

EPM Case	Conclusions
SReg_4Component_FWS_IC2	Similar reference water profiles to Base Case. Cannot discern between a_r = 1.0 or 2.0, i.e. matrix block sizes 1 m or 2 m.
SReg_4Component_FWSt_IC2	Too much mixing of reference waters. a_r = 0.1 for HRD is too low. Hence, matrix block sizes < 20 m, confirms P32c around 1. May give high transport F-quotient than for S1.1.

7.10 Conclusions on suitable hydraulic parameter representation with uncertainties

In deriving the Base Case, the parameters selected should not be considered as the only possibility for obtaining a match to the hydro-geochemistry data. Many other combinations of parameters may give a match. Hence, in Table 7-3 a summary is given of the parameter used to obtain a global calibration to the data along with an estimate as to the range of the alternative parameters that might also result in a calibrated model. It would be useful to explore this parameter space more extensively in future modelling exercises to verify these estimates of uncertainty.

Table 7-3. Summary of hydraulic parameters and conditions used in calibration of Base Case model with an indication of the possible range of alternative parameters that may also give a match to the borehole hydro-geochemistry.

Parameter	Calibration value	Range
Model domain	Small regional model – about 14 (E-W) x 7 km (N-S) is the minimum.	This is the minimum. 16 km (E-W) x 12 km (N-S) to get good stable results.
Grid resolution	50 m necessary in site-scale.	100 m necessary on regional-scale.
Initial condition	Full Glacial 0–700 m; then linear gradient to no Glacial, full Brine at 1,500 m; full Brine below 1,500 m.	Glacial has to go to about 1 km depth then full Brine by 1,500 m.
Top surface flow BC	Topography.	Try specified infiltration to calibrate infiltration and HSD K
Top surface waters	Baltic Ice Lake (Glacial), Yoldia Sea (Marine/ Glacial), Ancylus Ice Lake (Glacial), Littorina Sea (Marine), Baltic Sea/Precipitation with land rise (Marine diluting with Rain 1960).	Onshore – Ice Lakes could be mixture of Brine and Rain 1960. Offshore, Littorina could occur at slightly different time or strength (not very sensitivite).
Hydro-DFN	CF, DT, KLX01 all calibrated.	All conditioned Hydro-DFN models calibrated, but the model is probably sensitive to changing K by a factor 5.
HRD K	This had block-scale properties of $K_{50\%}$ ~ 5 10^{-9} m/s, $K_{10\%}$ = 5 10^{-10} m/s.	
Depth dependence	None.	Weak slope (factor 5 in 2 km) may improve results, but keep mean at 1 km same.
Kinematic HRD porosity n_{etb}	Based on DFN value, Section 5.8,	Fairly insensitive.
	$t = 0.5T^{0.5}$.	Can increase by factor 10.
Matrix porosity n_m	5 10^{-3}.	2–5 10^{-3}.
Kinematic HCD porosity n_{et}	$t = 5T^{0.5}$.	a = 1–5 in $t = aT^{b}$, or could make b higher to be continuous with HRD.
FWS, a_r, for RMD	2.0 m^2/m^3.	0.5–2.0 m^2/m^3.
Maxtrix diffusion length L_D	0.5 m.	0.5 – 2 m.
Intrinisic diffusion coefficient into matrix D_e	5 10^{-13} m^2/s.	1 – 5 10^{-13} m^2/s.

7.10.1 Suitable model domain

Based on the variety of model sizes considered, it is concluded that the minimum is the Small-regional domain ~14 km (E-W) by 7 km (N-S) for reference water calculation for site areas. This is larger than model domain suggested by sensitivity analysis of groundwater pathways by the DarcyTools Team in the Version S1.1 modelling. It is thought this is due to the much greater emphasis of the sub-horizontal fracture set in the Version S1.2 Hydro-DFN giving rise to longer horizontal flow paths.

However, it is not clear if this area is sufficient for transport pathways for the whole Simpevarp release area. This is investigated check in Section 9.

7.10.2 Initial and boundary conditions

The initial and boundary conditions specified in Table 7-3 suggest the following:

- Glacial water injected under high pressures down to about 700 m–1.5 km during early post-glacial period.
- Large Glacial water composition in early freshwater in the Baltic Lake, Yoldia Sea and Ancylus Lake periods.
- Only a specified topographic head has been used. Although the approximation of a watertable at ground surface seems reasonable for this area of low topographic height, it potentially may give rise to unphysically large fluxes. Hence, a specified flux would be interesting variant to test in terms of the recharge/discharge pattern.

7.10.3 HCD, HRD, HSD properties.

Based on the variants considered and the calibration against reference water mixing the following observations are made:

- The Hydro-DFN properties give block-scale hydraulic conductivities of the correct order of magnitude to predict hydro-geochemistry.
- Smaller, low confidence zones have limited effect on regional-scale flows, but do affect hydro-geochemistry local to individual boreholes.
- This suggests one can use hydro-geochemistry to confirm extent and properties of individual zones locally.
- Reducing hydraulic conductivity at depth may give a better hydro-geochemistry match, but the average hydraulic conductivity from the Hydro-DFN needs to be conserved. However, quite moderate changes have an impact, so the depth decrease should only be a factor < 10.
- Calibrating the HSD properties requires a flux boundary condition to be considered.

7.11 Calibration against tritium measurements

An additional calibration exercise was perfomed late in the modelling using tritium measurements to assess whether this data could help address any of the outstanding uncertainties. Hence, this was only a preliminary study to motivate the value of further integration of tritium data.

7.11.1 Variants

Tritium transport simulations were carried out for a number of variants to examine the impact of different values of the flow-wetted surface per unit volume for rock-matrix diffusion. Table 7-4 lists the cases considered in the tritium modelling. The effect of varying the accessible matrix porosity was also considered using an approximate calculation. In all these calculations, the time-step was taken to be 5 years. Additional calculations were carried out to explore the sensitivity to modelling issues such as time-step size. This was felt to be appropriate because it was our first attempt to incorporate the tritium data.

Table 7-4. Variants considered in Tritium modelling.

Variant	FWS (m^2/m^3)	Comments
SReg_4Component_IC2	2.0	Used as Base Case for tritium calculations
SReg_4Component_FWS_IC2	1.0	Lower RMD
SReg_4Component_FWSh_IC2	0.5	Lower RMD
SReg_4Component_FWSt_IC2	0.1	Much lower RMD
SReg_4Component_Infiltration_IC2	2.0	recharge top surface boundary condition

The calculated distributions of tritium behaved as might be expected. Tritium concentrations are highest at the ground surface, reduce with depth and are only significant in the top few hundred metres. Tritium generally migrates deeper in the vicinity of the deformation zones. Figure 7-50 shows an example of the calculated distribution of tritium at 2,005 AD for the Base Case.

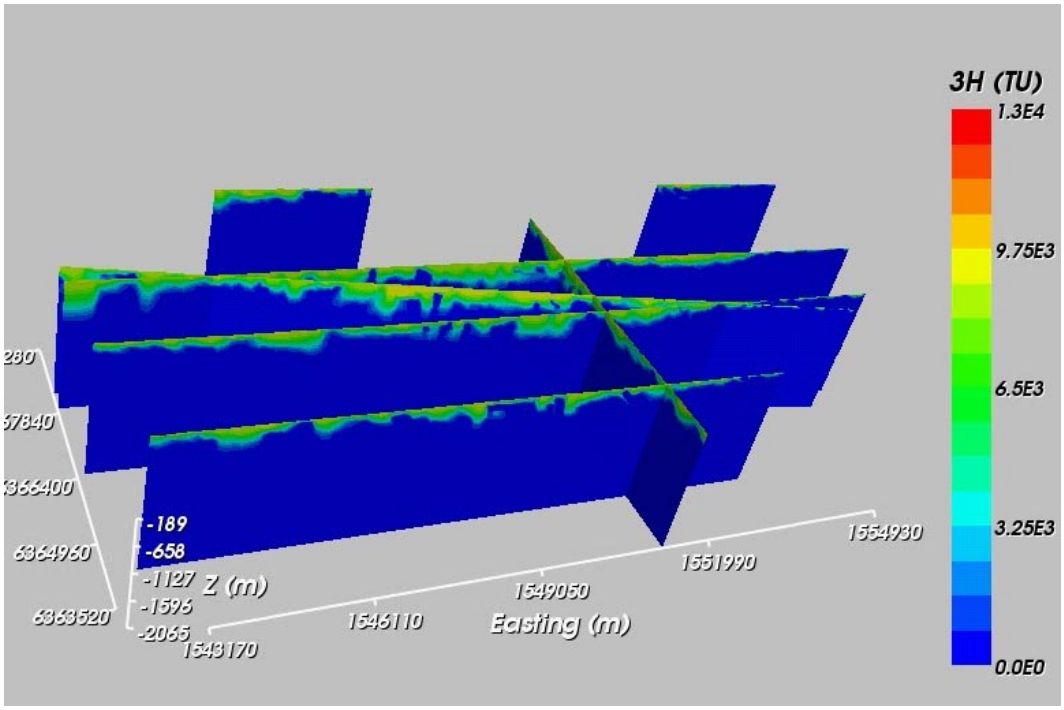

Figure 7-50. *The distribution of tritium concentration in the Base Case (SReg_4Component_IC2) at 2,005 AD. Note that these tritium values are 'undecayed' output values from connectflow (see Section 5.10.2).*

7.11.2 Tritium simulations

The results for the cases are discussed in this subsection. The calibration was performed by comparing the modelled tritium concentration, corrected for radioactive decay, with the data for the boreholes considered.

The comparison profiles of modelled and measured tritium in KLX02 for the different model cases at 2,005 AD are shown in Figure 7-51. For the base case, the calculated tritium concentrations near the ground surface are in reasonable agreement with the levels observed. At large depths greater than 1,100 m, the calculated concentrations are very small, in agreement with observation (and expectation). The measurements above 1,100 m may be a mixture of surface and deep water, as a result of the pumping procedure, and should be viewed with care (section 6.4.3). Alternatively, one possible explanation is that the hydraulic conductivity of the rocks in the vicinity of borehole KLX02 down to a depth of about 1,000 m may be underestimated in the model. In particular, deformation zone ZSMNE040A cuts KLX02 around 800 m to 1,100 m and dips sub-parallel to the borehole. This could account for the observation of tritium at depth.

The comparison of profiles of modelled and measured tritium in KSH01A for the different cases are shown in Figure 7-52. The predicted tritium concentrations for the base case are small at depths of more than 100 m. These concentrations are in agreement with the small number of measurements considered to be representative. The predicted concentrations for the lowest value of flow-wetted surface considered (0.1 m^2 m^{-3}) are significantly higher than observations.

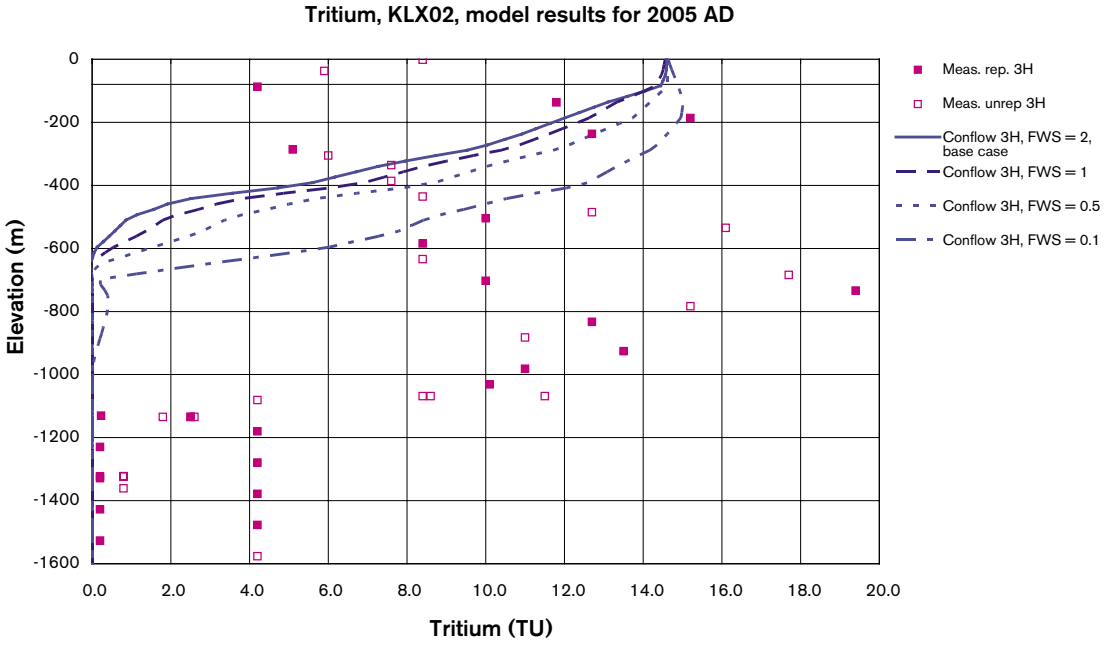

Figure 7-51. *Comparison of the calculated levels of tritium with measurements in borehole KLX02. Four model cases with varying FWS are shown for 2,005 AD. Blue lines represent the various model results. Pink data points are: representative measurements (filled), unrepresentative measurements (unfilled). The measurements below 1,100 m fall below the detection limit of 8 TU and should be viewed with care.*

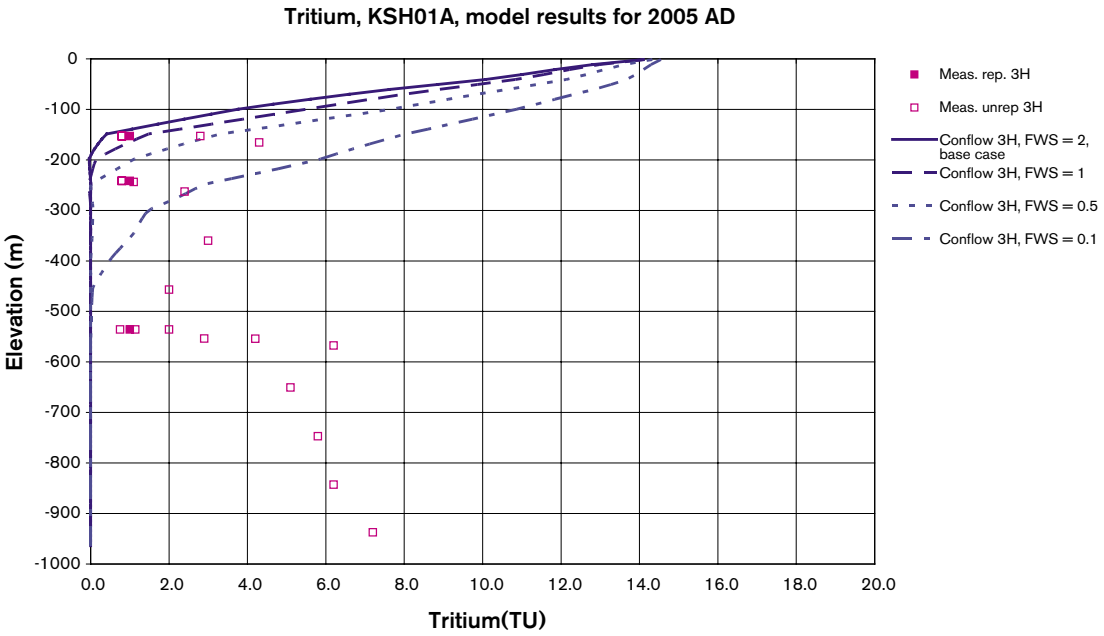

Figure 7-52. *Comparison of the calculated levels of tritium with measurements in borehole KSH01A. Four model cases with varying FWS are shown for 2,005 AD. Blue lines represent the various model results. Pink data points are: representative measurements (filled), unrepresentative measurements (unfilled).*

The comparison profiles of modelled and measured tritium in KSH02 for the different cases are shown in Figure 7-53. The predicted tritium concentrations for the base case falls from values of order 12 TU near the ground surface to near zero at a depth of about 400 m. This pattern of behaviour is in accord with observations, although the predicted tritium concentrations appear to fall off more rapidly than those measured. This may suggest that the hydraulic conductivity of the rocks in the part of the model near KSH02 has been underestimated. Alternatively the transport properties may be inaccurate. The variants with lower values of flow-wetted surface give an improved match to observations at depths of two hundred to three hundred metres. The best match is obtained for a flow wetted surface of order 0.5 to 1.0 $m^2\ m^{-3}$.

The comparison profiles of modelled and measured tritium in KSH03A for the different cases are shown in Figure 7-54. For the base case, the predicted concentrations of tritium in the upper two hundred metres of the model are of order 1 to 2 TU, whereas observed concentrations are of order 8 TU. This may suggest that the permeability of the rocks in the part of the model near borehole KSH03A has been underestimated. Alternatively the transport properties may be inaccurate. The variants with lower values of flow-wetted surface give an improved match to observations

It is worth noting that, in general, the bomb-test tritium contributes about half of the predicted current level of tritium, except near the ground surface, where concentrations are determined by the background levels in precipitation over the last few years.

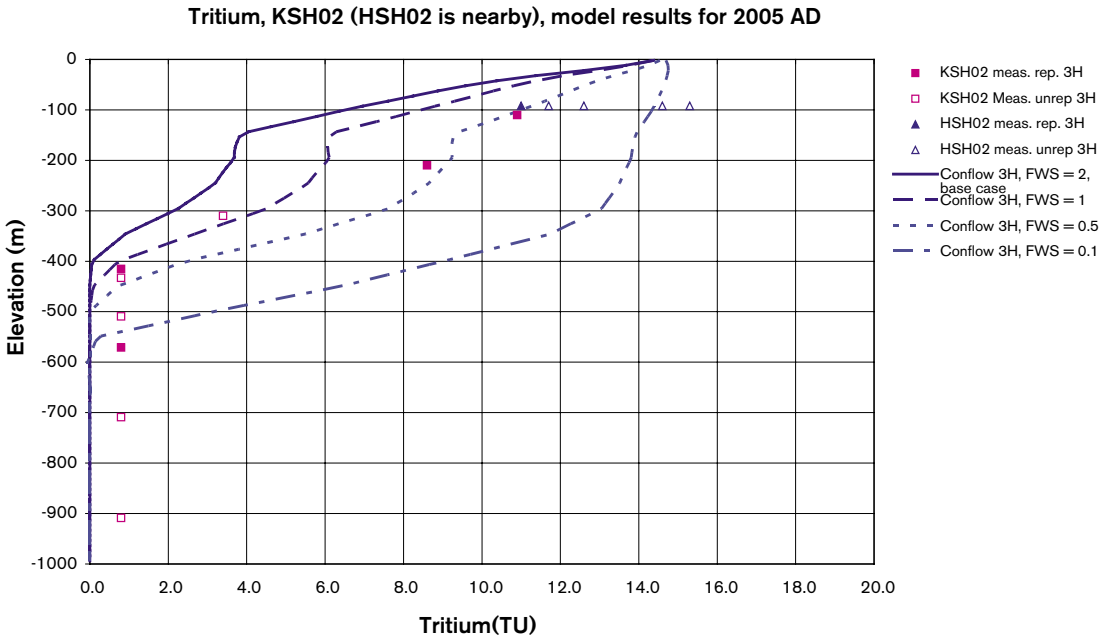

Figure 7-53. *Comparison of the calculated levels of tritium with measurements in borehole KSH02. Four model cases with varying FWS are shown for 2,005 AD. Blue lines represent the various model results. Pink data points are: representative measurements (filled), unrepresentative measurements (unfilled).*

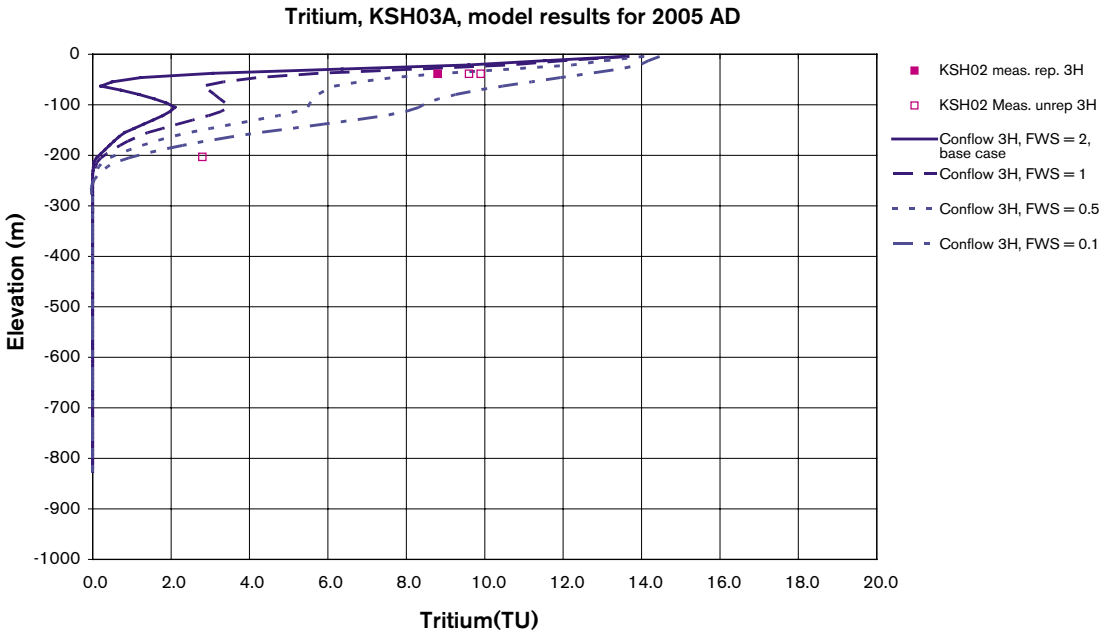

Figure 7-54. *Comparison of the calculated levels of tritium with measurements in borehole KSH03A. Four model cases with varying FWS are shown for 2,005 AD. Blue lines represent the various model results. Pink data points are: representative measurements (filled), unrepresentative measurements (unfilled).*

7.11.3 Conclusions from tritium data

The results for the different variants may suggest that the appropriate value of the flow-wetted surface is lower than the value used in the original flow calculations, with a value of about 0.5 to 1.0 perhaps being the best value. However, it must be stressed that this observation is mainly based on a comparison with few representative data points in each borehole. Therefore, it would not be advisable to place too much reliance on the observation.

Reducing the value of the accessible matrix porosity also improves the match to observations in borehole KLX02, KHS01 and KSH03A. The improved match is of similar quality to the match for the reduced value of the flow-wetted surface of 0.5. Thus, the best match to the observations may not be unique – there may be many sets of parameters that give similar matches to the observations.

The comparison with data also suggests that the permeability of the rock in the vicinity of borehole KLX02 at depths down to about 1 kilometre may have been underestimated in the model. Alternatively, the geometry of the transmisssive feature in the vicinity of KLX02 may be inaccurate.

The results of calculations with a time-step of 1 year are essentially the same as the results of the corresponding calculation with a time-step of 5 years. The results of the calculations with a time-step of 20 years show similar results to calculations with a time-step of 1 year, except close to the ground surface, where slightly lower concentrations are predicted with the longer time-step. These results suggest that for this site, a time-step of 5 years was appropriate, requiring less computational runtime, and allowing more cases to be considered. It should be emphasised that the computational cost of a calculations of tritium migration is only a small fraction of that of a groundwater flow calculation over the last ten thousand years or so. Further, it appears that reasonable results can even be obtained with a very large time-step of 20 years (large relative to the time-scale of tritium decay). This could be useful if it is necessary to use the same time-step as in the flow calculations.

The results of the calculations in which the flow field is not updated are essentially the same as those in which it is. The benefit of not updating the flow field is that it significantly reduces the computational cost of the calculations. This result also provides support for simply starting the tritium migration calculations from the flow calculations.

The calculations presented show that the use of data for tritium does indeed have the potential to help constrain and check a groundwater flow model. However, in order for the data to provide useful information, it is necessary to have a fair number of good quality measurements down a number of boreholes. The measurements need to have low detection levels, and small errors relative to the expected levels (of order a few TU). Care needs to be taken to ensure uncontaminated samples. Measurements need to be taken down to depths of as much as a kilometre or more, particularly in the vicinity of transmissive features.

8 Description of Past evolution

The simulations are started 10,000 BC and ran for 12,000 years, i.e. to 2,000 AD, corresponding to present-day conditions. At 10,000 BC, the last glaciation had ended and the modelled area is assumed to be all covered with melted ice, here referred to as Glacial water. Initially, there are only two types of water in the model. The upper part of the model is filled with Glacial water and underneath this there is an increasing fraction of Brine. As discussed previously, there are two different initial conditions used for the Brine distribution at 10,000 BC.

8.1 Base Case (SReg_4Component_ IC2)

The past evolution of the four reference waters Brine, Marine water, Rain 1960 and Glacial water, is shown in Figure 8-1 and Figure 8-2. The distributions of the different water types are presented in vertical slices at three times corresponding to: 5,000 BC, 0 BC and 2,000 AD (present day). The fraction of each water type is calculated and the sum of the fractions of the four water types equals one. The corresponding TDS distributions are presented in Figure 8-3.

As soon as the first parts of the modelled area start to rise above the sea level, the Precipitation also contributes to the fresh water load into the model. The land rise can easily be observed in Figure 8-2 as the part of the modelled area (west) where the Rain 1960 has penetrated into the model replacing the Glacial water at the top pushing it out into the sea. The Brine is slowly being moved towards the sea and up through the rock driven by the land rise and the Rain 1960. The TDS distribution is the result of mixing between Brine and Marine water, which has a time varying concentration of salt. The shape of the TDS distribution suggests that the dominant part of the salt origins from the Brine.

Some strange effects in the early stages of the simulations can be seen in the far eastern part of the modelled area. A Large amount of Marine water enters the model very rapidly and flushes the Glacial water out from the model. The reason is probably the very high transmissivity of a few moderately dipping DZs in that area allowing for water to be transported deep into the model. The large contrast in transmissivity between the fracture zones and the surrounding bed rock, about four orders of magnitude, is also likely to contribute to numerical instabilities.

The distribution of the vertical Darcy velocity, presented in Figure 8-3, shows a highly heterogeneous flow field. The general direction of the flow changes from being more directed upwards, as long as sea water dominates the top surface of the model, to being more directed downwards when land rises above the sea and Precipitation is allowed to penetrate into the model. The interface between the fresh water and the Brine is also observed as the level where the vertical flow changes direction. Some large deterministic features also appear as areas where the magnitude of flow is increased. These areas also appear in the figures presenting the reference waters.

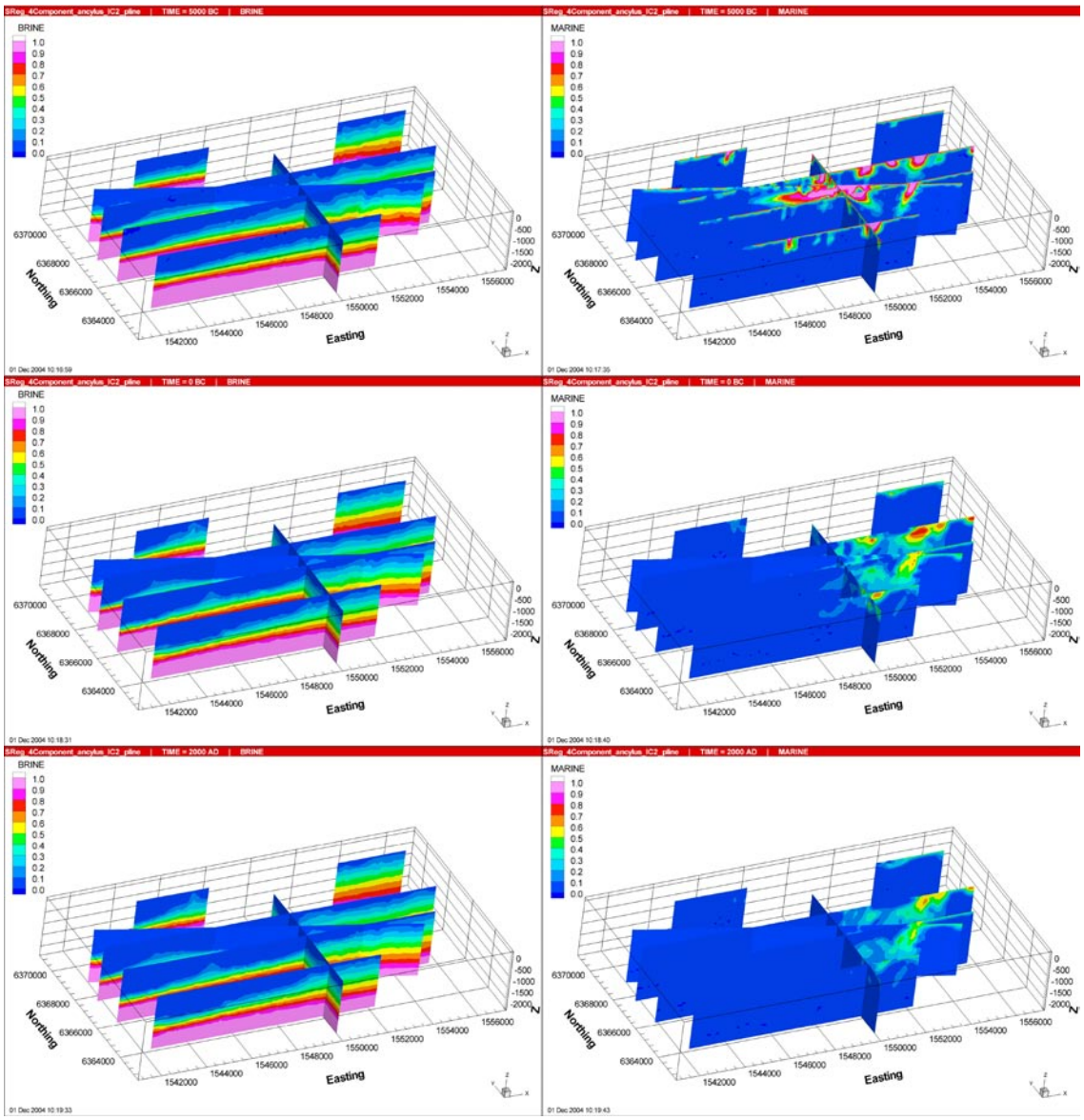

Figure 8-1. *Distribution of Brine (left) and Marine water (right) in vertical slices at times equal to (from top to bottom) 5,000 BC, 0 BC and 2,000 AD (present-day), for Base Case (SReg_4Component_IC2).*

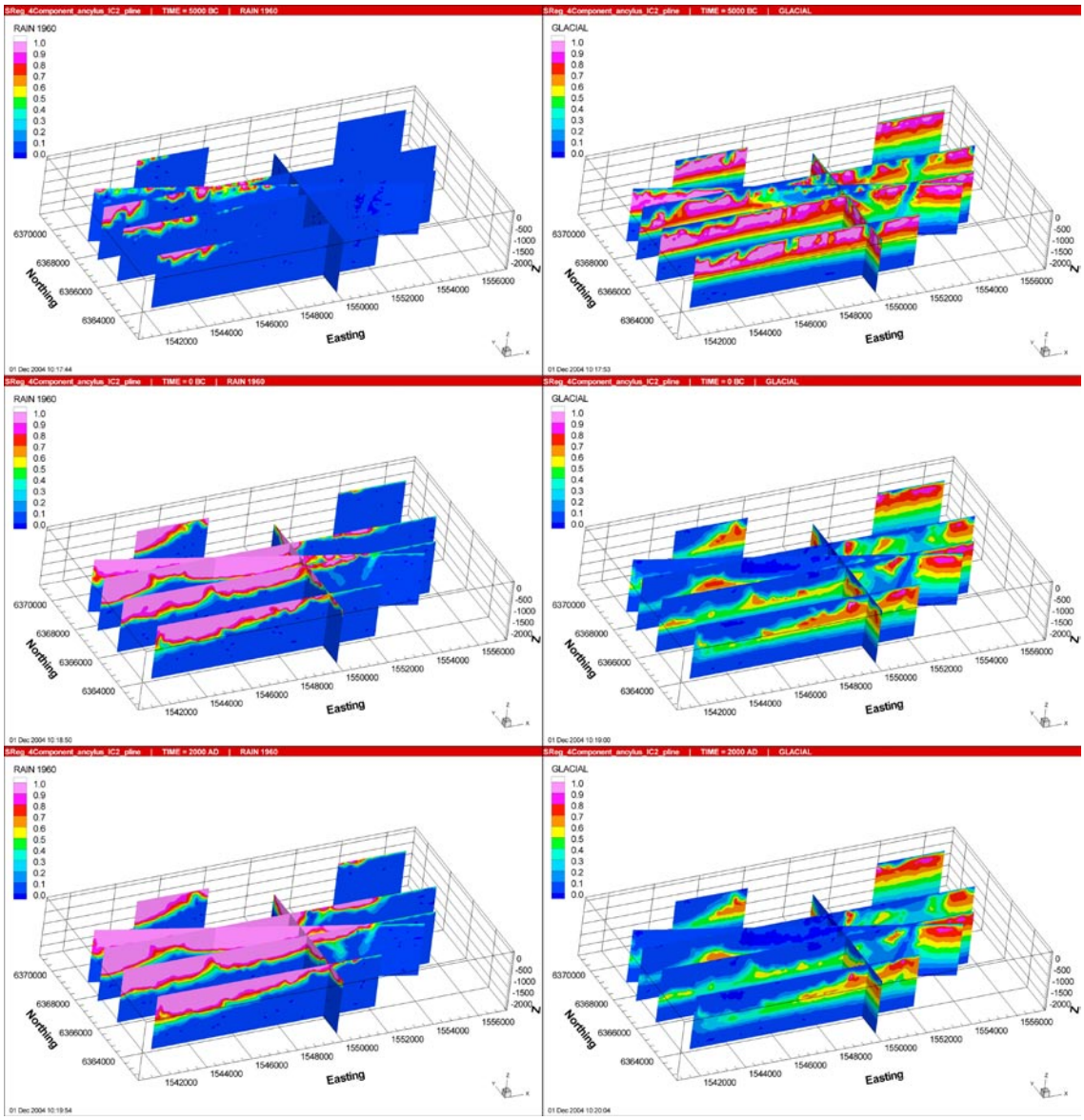

Figure 8-2. *Distribution of Rain 1960 (left) and Glacial water (right) in vertical slices at times equal to (from top to bottom) 5,000 BC, 0 BC and 2,000 AD (present-day), for Base Case (SReg_4Component_IC2).*

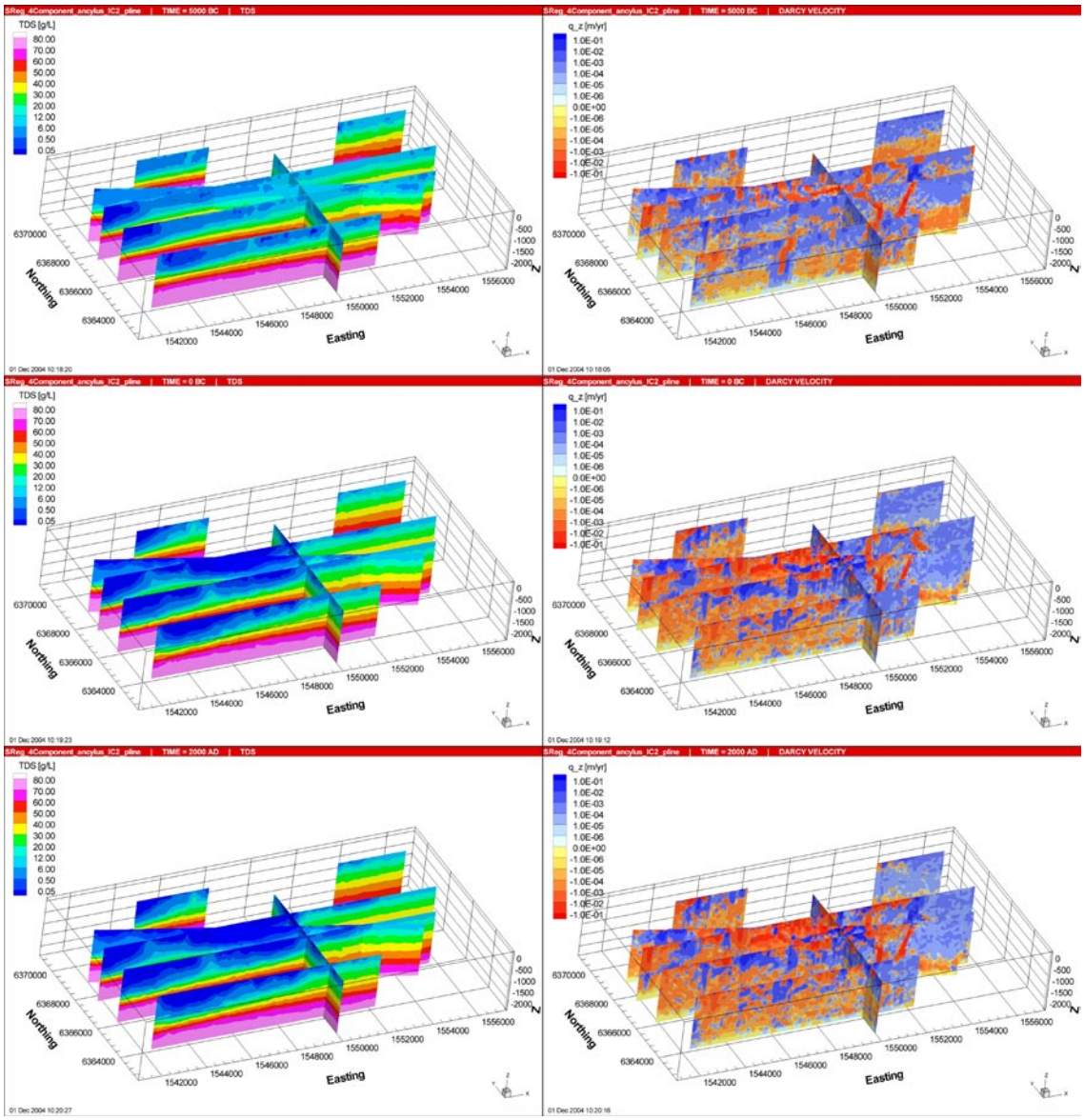

Figure 8-3. *Distribution of TDS (left) and the vertical Darcy velocity, q_z (right), in vertical slices at times equal to (from top to bottom) 5,000 BC, 0 BC and 2,000 AD (present-day), for Base Case (SReg_4Component_IC2).*

8.2 Shallower Brine initial condition (SReg_4Component_ IC1)

In Figure 8-4 and Figure 8-5, the distribution of the four reference waters is shown in vertical slices at 5,000 BC, 0 BC and 2,000 AD. This case uses the more shallow initial condition (IC1) where there is linear transition between full Glacial at –500 m and full Brine at –1,000 m. Comparing the results with the Base Case, the differences are as expected. Here, the Brine is found higher up in the rock from the start and also stays at a generally higher level up until present–day even if the Rain 1960 slowly pushes it towards the Baltic Sea. Due to the initial condition, the Glacial water is more shallow in this case and is also being flushed out faster compared to the Base Case. The Marine water does not penetrate as

deep into the rock in this case, even if the differences are not that significant. As expected the Rain 1960 acts as it did in the previous case and penetrates the rock to approximately the same degree as in the Base Case.

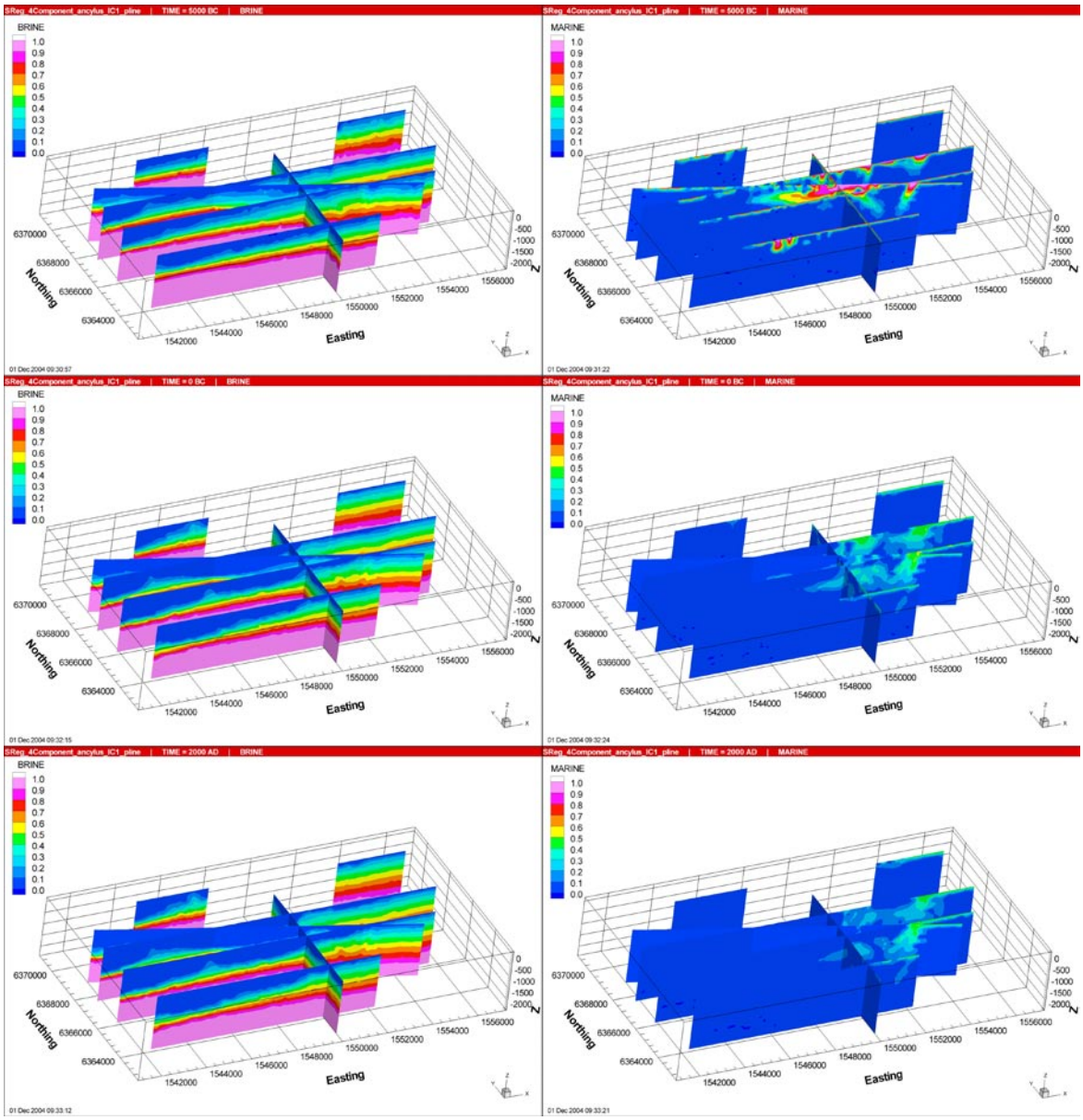

Figure 8-4. *Distribution of Brine (left) and Marine water (right) in vertical slices at times equal to (from top to bottom) 5,000 BC, 0 BC and 2,000 AD (present-day), for the shallower initial Brine (SReg_4Component_ IC1).*

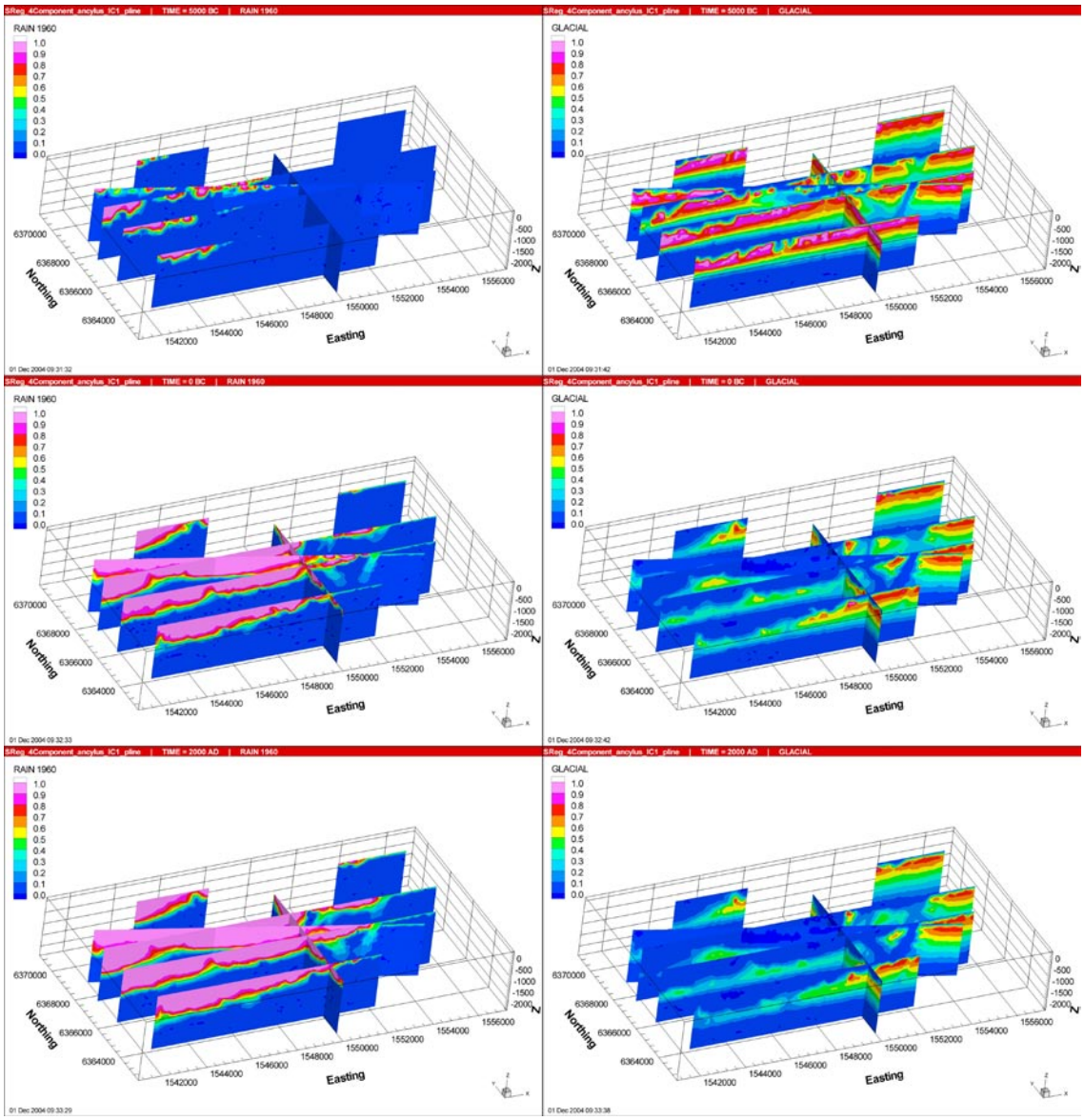

Figure 8-5. *Distribution of Rain 1960 (left) and Glacial water (right) in vertical slices at times equal to (from top to bottom) 5,000 BC, 0 BC and 2,000 AD (present-day), for the shallower initial Brine (SReg_4Component_ IC1).*

9 Description of the present-day flow conditions

9.1 Methodology

A selection of the most relevant modelled cases is presented in this section. Results representing the present-day flow conditions, i.e. 2,000 AD (the final time-step in the simulations) will be shown in terms of flow paths (particles exit locations), distributions of F-quotient, and regional distributions of reference waters and recharge and discharge rates. The purpose of the flow-path analysis is two-fold. Firstly, it provides a set of performance measures for quantifying the current groundwater flow situation that can be used to compare variants and quantify uncertainties. Secondly, the identification of discharge areas is important for the Preliminary safety Evaluation (PSE). Due to a massive amount of graphical output from the simulations, the number of figures presented in the report had to be cut down to a minimum for each case.

9.2 Base Case (SReg_4Component_IC2)

This section presents the results for the Base Case which was developed from the calibration against the reference water mixing interpreted from borehole water samples to give a reasonable match in the global sense. Hydraulic parameters, initial conditions and boundary conditions obtained for the Base Case later on formed the basis for the sensitivity study performed.

9.2.1 Flow paths

In Figure 9-1 the distribution of the $\log_{10}$(F-quotient) at particles starting locations in the local-scale release area for the Base Case is presented. Figure 9-2 shows the same information but now only for the two site-scale release area s (Simpevarp at the lower left and Laxemar at the higher right). Red colour indicates smaller F-quotient. It is clear that the characteristics of the two release area s are quite different. Simpevarp being situated closer to the Baltic Sea and intersected by less deformation zones, shows a F-quotient in the range 10^6y/ m to 10^8y/m. Laxemar however, intersected by a large deformation zone shows a F-quotient range almost two orders of magnitude lower. The effects of the topography are clearly present over the entire area. Even if the grid refinement could be better, the localised flows are present as a result of the topography and the fractured rock. These effects are even more obvious in Figure 9-4 where the F-quotient at particles exit locations in the local-scale release area for the Base Case is presented. The particles tend to exit in deformations zones present in regions with low topography (discharge areas). Some particles however find their way to exit locations further away. The major part of the released particles exit in the Baltic Sea. Quite a few particles exit through large deformation zones to the south of Laxemar and others exit in a valley to the north. An increased concentration of exit locations close to the boundary of the small-regional model indicates that the model domain may be too small for the transport calculations, i.e. some unwanted boundary effects are likely to be present.

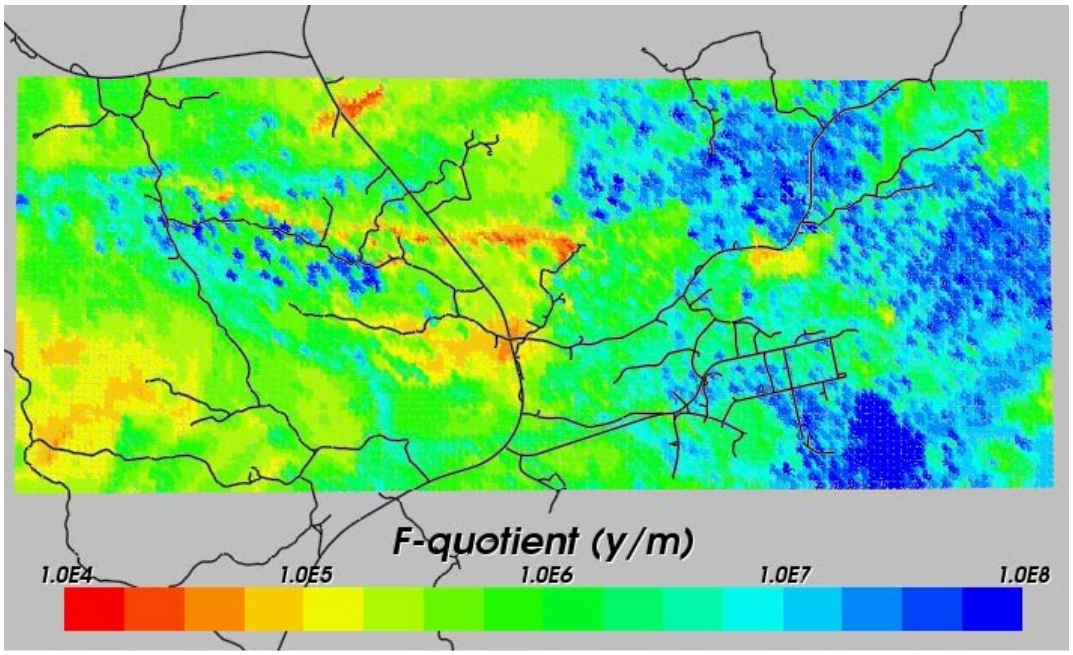

Figure 9-1. *Distribution of F-quotient (Log10) at particles starting locations in the local-scale release area for the Base Case (SReg_4Component_ IC2). Roads are shown in black for context.*

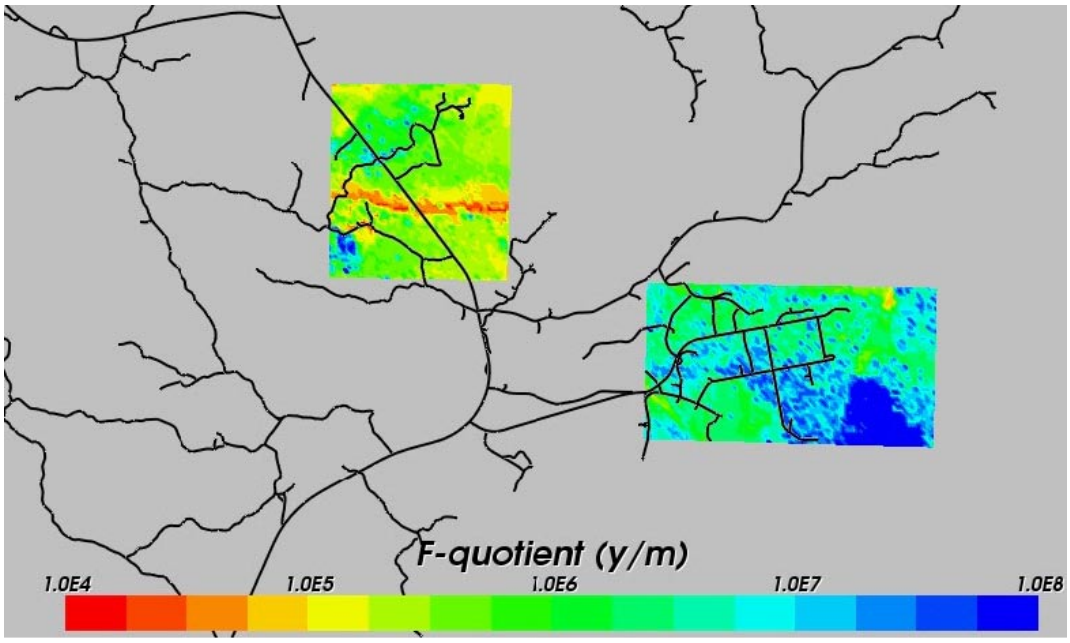

Figure 9-2. *Distribution of F-quotient (Log10) at particles starting locations in the two site-scale release areas (Simpevarp is lower left) for the Base Case (SReg_4Component_ IC2). Roads are shown in black for context.*

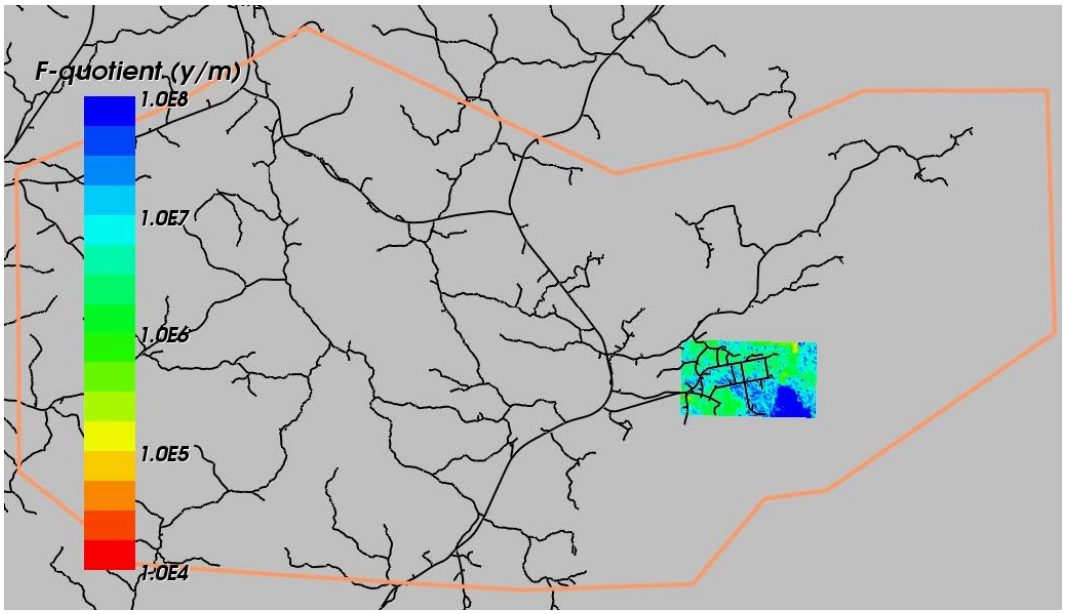

Figure 9-3. *Distribution of F-quotient (Log10) at particles starting locations in the Simpevarp release area for the Base Case (SReg_4Component_ IC2). Roads are shown in black for context.*

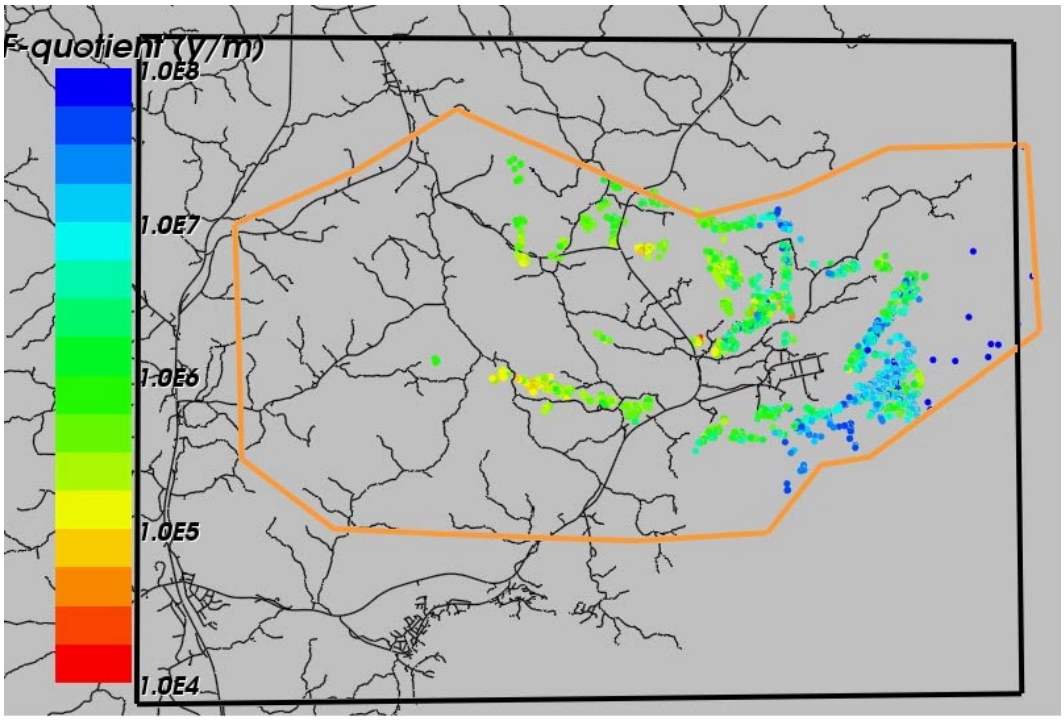

Figure 9-4. *Distribution of F-quotient (Log10) at particles exit locations in the local-scale release area (as for Figure 9-1) for the Base Case (SReg_4Component_ IC2). Roads are shown in black for context. The small-regional model domain is shown in orange, and the medium regional model domain is black.*

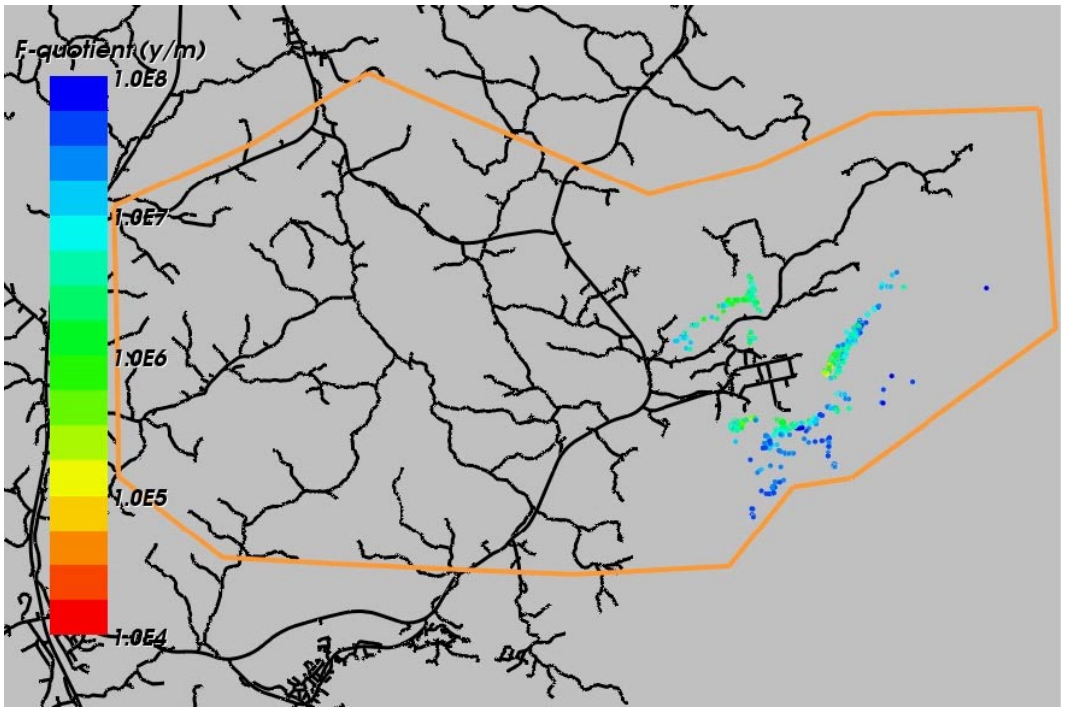

Figure 9-5. *Distribution of F-quotient (Log10) at particles exit locations for the Simpevarp release area (as for Figure 9-3) for the Base Case (SReg_4Component_ IC2). Roads are shown in black for context. The small-regional model domain is shown in orangeá.*

9.2.2 Regional distribution of reference waters

In Figure 9-6 – Figure 9-8, the present-day distributions of the four reference waters Brine, Marine water, Rain 1960 and Glacial water, are presented in vertical and horizontal slices. At –500 m no Brine is found in the western part of the modelled area. In the eastern part, however, the Brine fraction is about 20–30%, corresponding to a TDS of 14–21g/l. The Brine reaches as high up as about –200 m in the model. At a depth of –1,000 m the fraction of Brine is about 50% in the eastern part, corresponding to a TDS of about 35g/l, while the western part of the modelled area still contains freshwater originating from the Rain 1960 and Glacial water.

Marine water is only present in the eastern part of the modelled area underneath the sea. A few very transmissive deterministic DZs in this area transports Marine water deep into the rock. In the remaining rock there is little or no Marine water present at 2,000 AD.

Water originating from the Rain 1960 penetrates the rock down to about –1,500 masl in the western area where land first rose above the sea level. In the top layers the Rain 1960 covers almost the entire model domain since the dominant part of the model has risen above the sea at present-day.

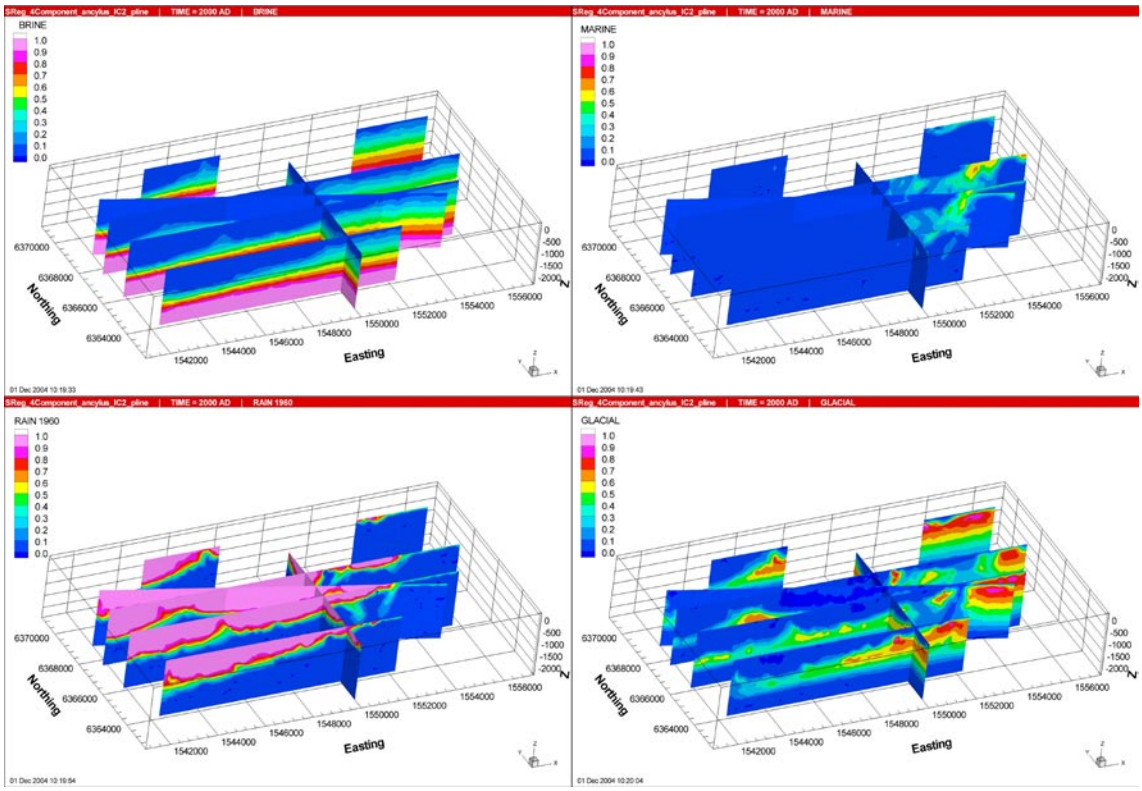

Figure 9-6. *Present-day distribution of the reference waters Brine (top left), Marine water (top right), Rain 1960 (bottom left) and Glacial water (bottom right) in vertical slices, for the Base Case (SReg_4Component_ IC2).*

The Glacial water that covered the upper part of the model at 10,000 BC has been flushed out by Rain 1960 and Marine waters down to more than –500 m. Between –500 m and –1,000 m there is however Glacial water present in the eastern part.

9.2.3 Recharge and discharge rates

In Figure 9-9 the vertical Darcy velocity distribution under present-day flow conditions is presented in horizontal slices. Close to the surface at –10 and –100 masl the flows are mainly downwards (recharge) around –0.1 to –0.001 m/year in the rock mass. The discharge is located to the Baltic Sea in the eastern part of the modelled area and around fracture zones onshore. In the fracture zones, the vertical Darcy velocity is around 0.1 m/year. The flow field near the surface is very heterogeneous indicating localised flow cells. At –500 m, the flow rates are generally around 0.01–0.0001 m/year in the recharge as well as in the discharge areas. This is an order of magnitude lower than for the flow above –100 m. The flow field also tends to be more homogeneous at this depth. At –1,000 m, the flow rates are generally less than 0.0001 m/year. Most of the flow is directed downwards at this depth.

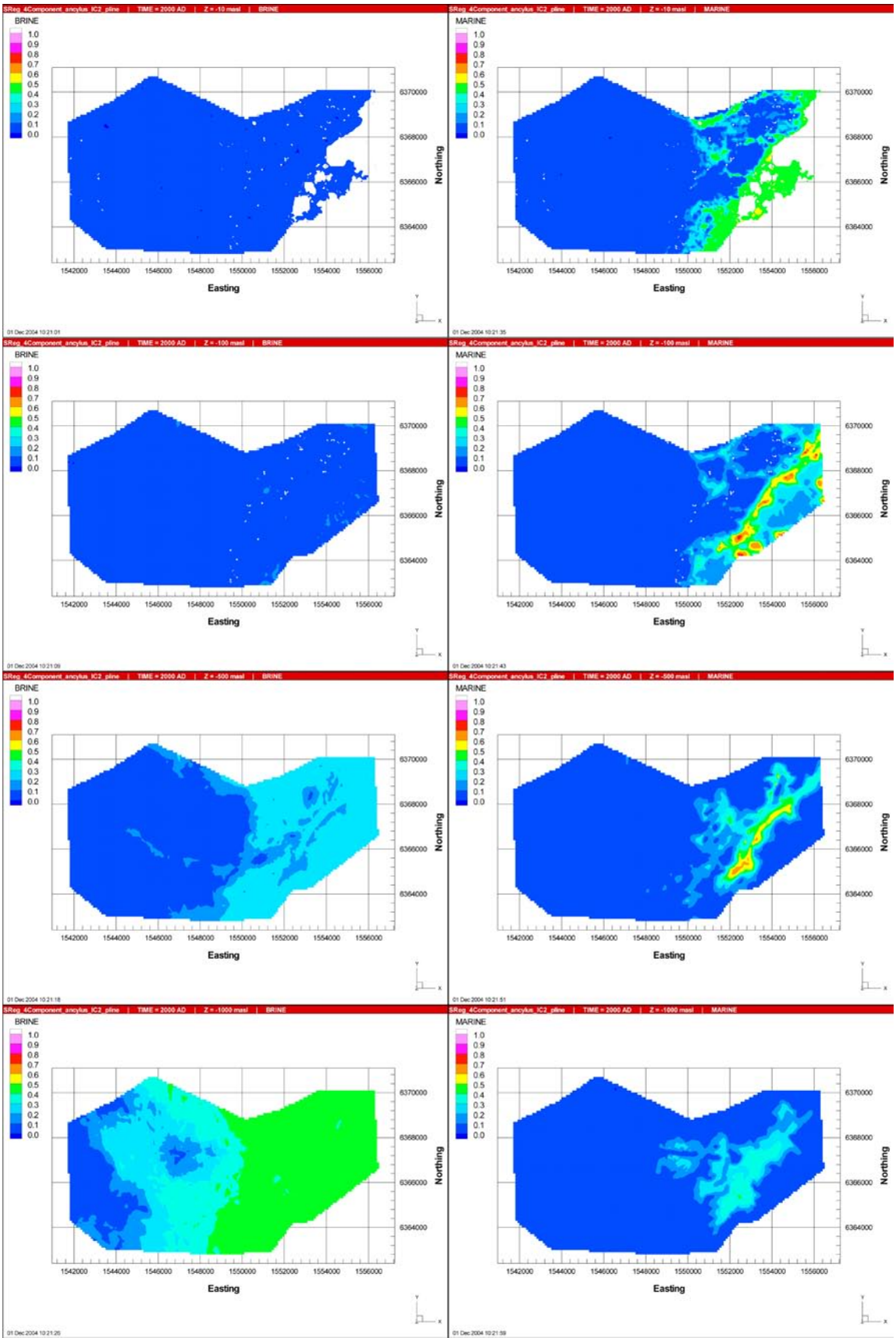

Figure 9-7. *Present-day distribution of Brine (left) and Marine water (right) in horizontal slices at elevations (from top to bottom) –10 m, –100 m, –500 m and –1,000 m, for the Base Case (SReg_4Component_ IC2).*

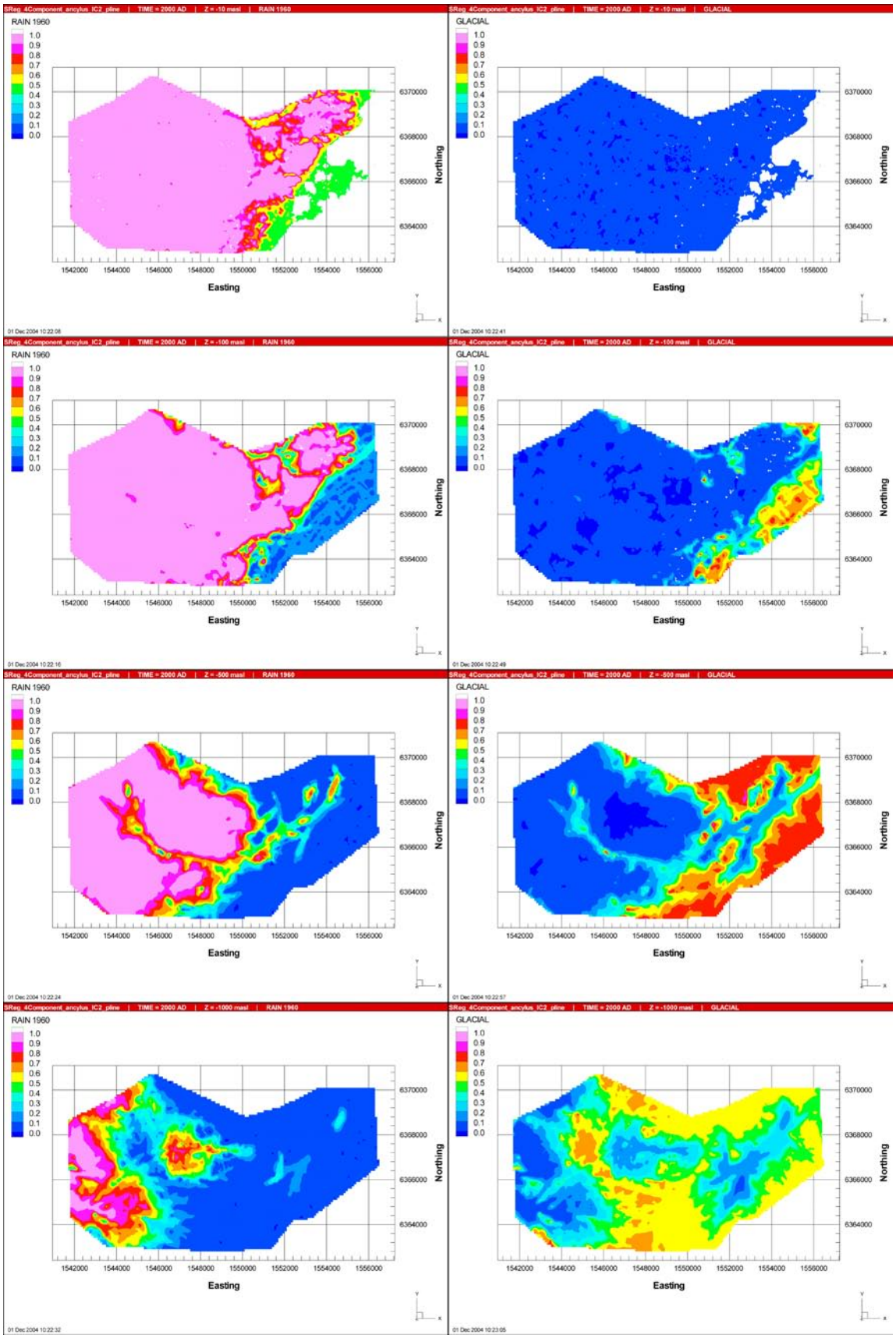

Figure 9-8. *Present-day distribution of Rain 1960 (left) and Glacial water (right) in horizontal slices at elevations (from top to bottom) –10 m, –100 m, –500 m and –1,000 m, for the Base Case (SReg_4Component_ancylus_IC2).*

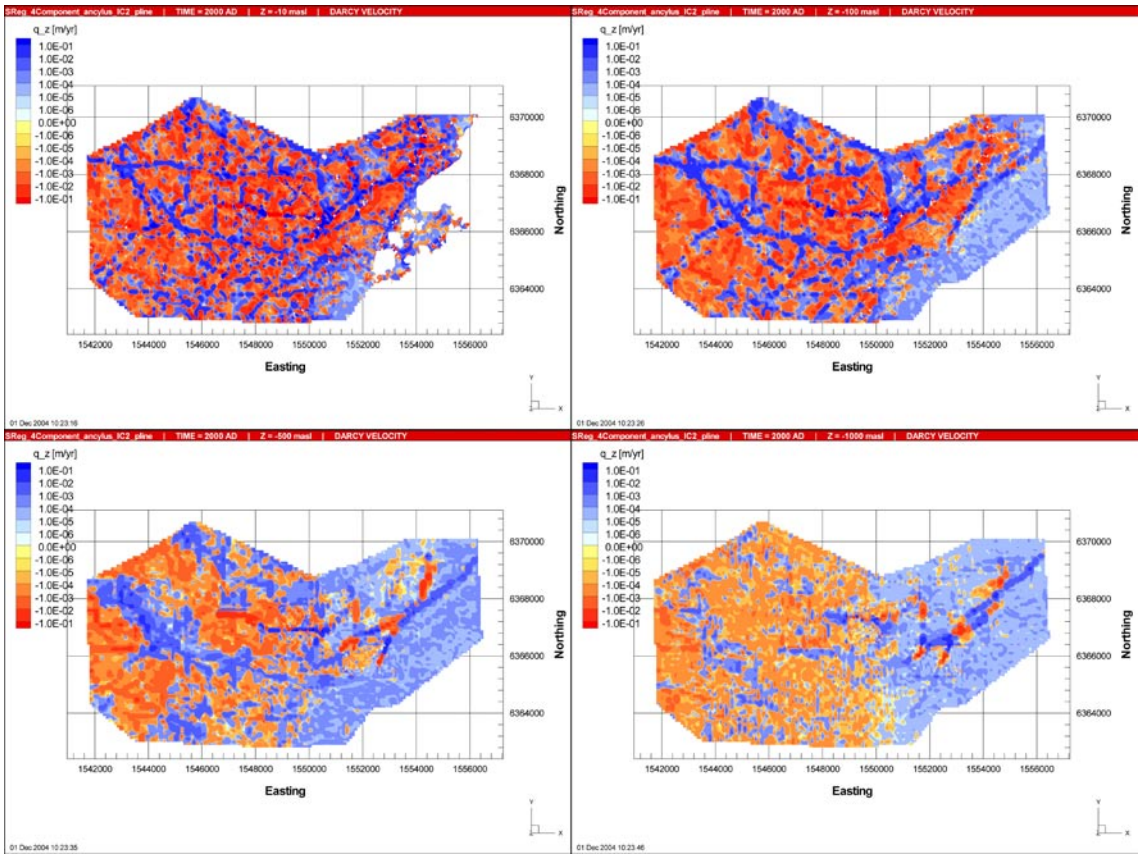

Figure 9-9. *Present-day distribution of the vertical Darcy velocity, q_z, in horizontal slices at elevations –10 m (top left), –100 m (top right), –500 m (bottom left) and –1,000 m (bottom right), for the Base Case (SReg_4Component_IC2).*

9.3 Larger regional domain (LReg_4Component_IC2)

This section presents the results for the Medium regional domain. The extension of the Larger regional model domain (black) is presented and compared to the Small regional domain (orange, Base Case) in Figure 9-11. This case showed roughly the same calibration on boreholes as for the Base Case. However, it is still of interest to study this case with respect to transport pathway calculations and possible boundary effects within the smaller regional model.

9.3.1 Flow paths

In Figure 9-10 the distribution of the $\log_{10}$(F-quotient) at particles starting locations in the local-scale release area for the Larger regional domain is presented. Red colour indicates smaller F-quotient. Figure 9-11 presents the F-quotient at particles exit locations in the local-scale area for the Larger regional domain. The results are broadly the same as for the Base Case. There are some localised differences but the main features, large deformation zones giving low F-quotients and recharge areas like valleys giving higher F-quotients, are represented in both cases. The area under the Baltic Sea has low F-quotients due to the low Darcy velocities in the rock.

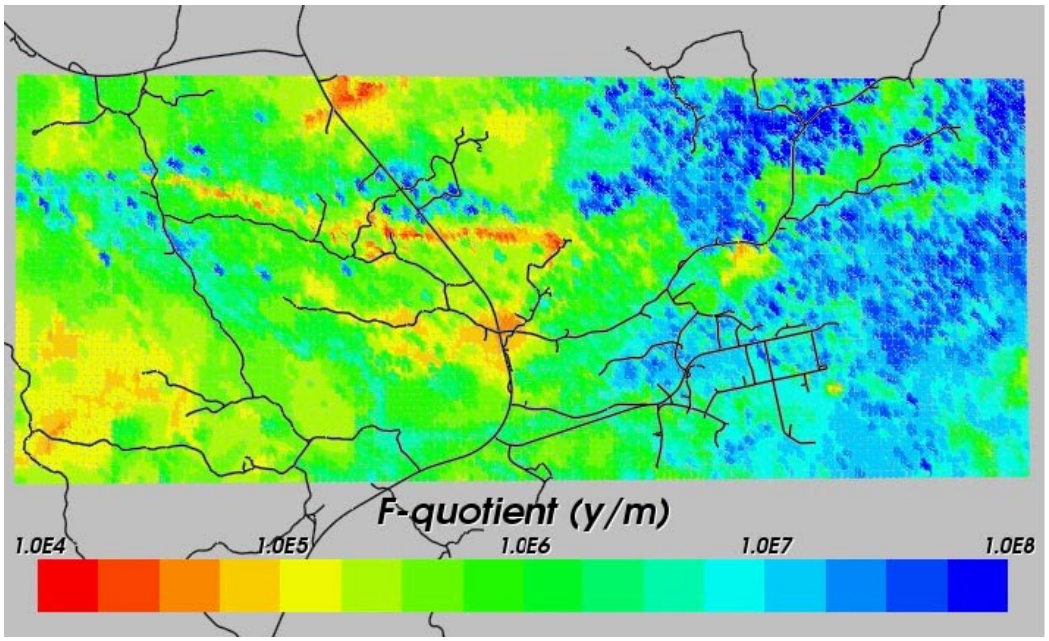

Figure 9-10. *Distribution of F-quotient (Log10) at particles starting locations in the local-scale release area for the Base Case with larger domain (LReg_4Component_ IC2). Roads are shown in black for context.*

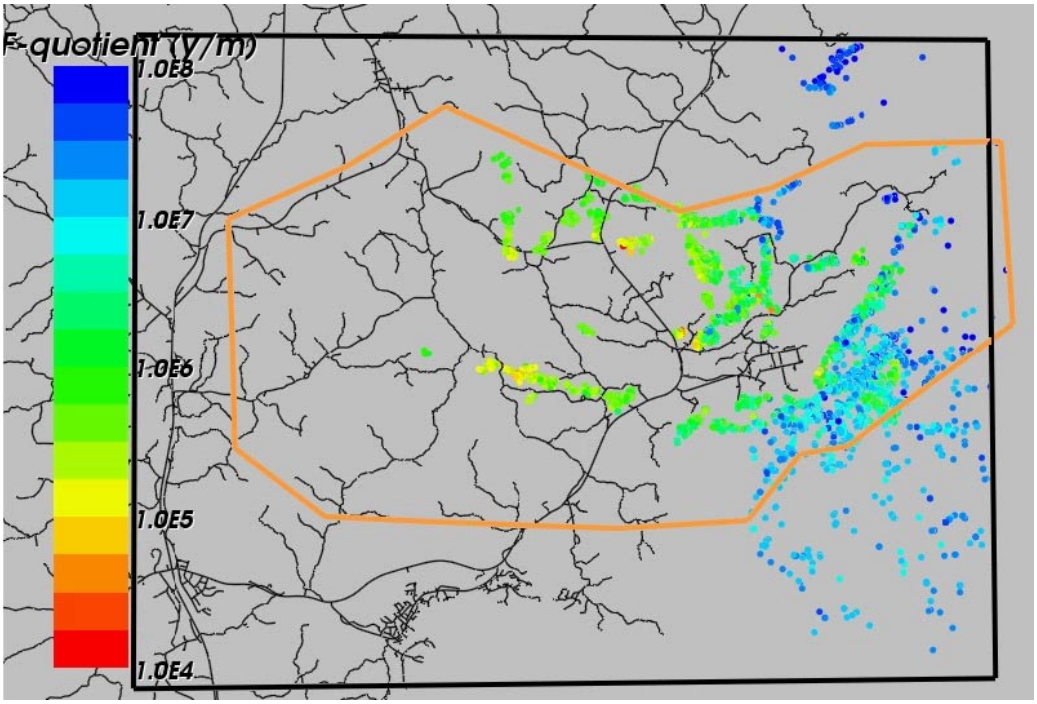

Figure 9-11. *Distribution of F-quotient (Log10) at particles exit locations in the local-scale release area for the Base Case with larger domain (LReg_4Component_ IC2). Roads are shown in black for context. The small-regional model domain is shown in orange, and the medium regional model domain is black.*

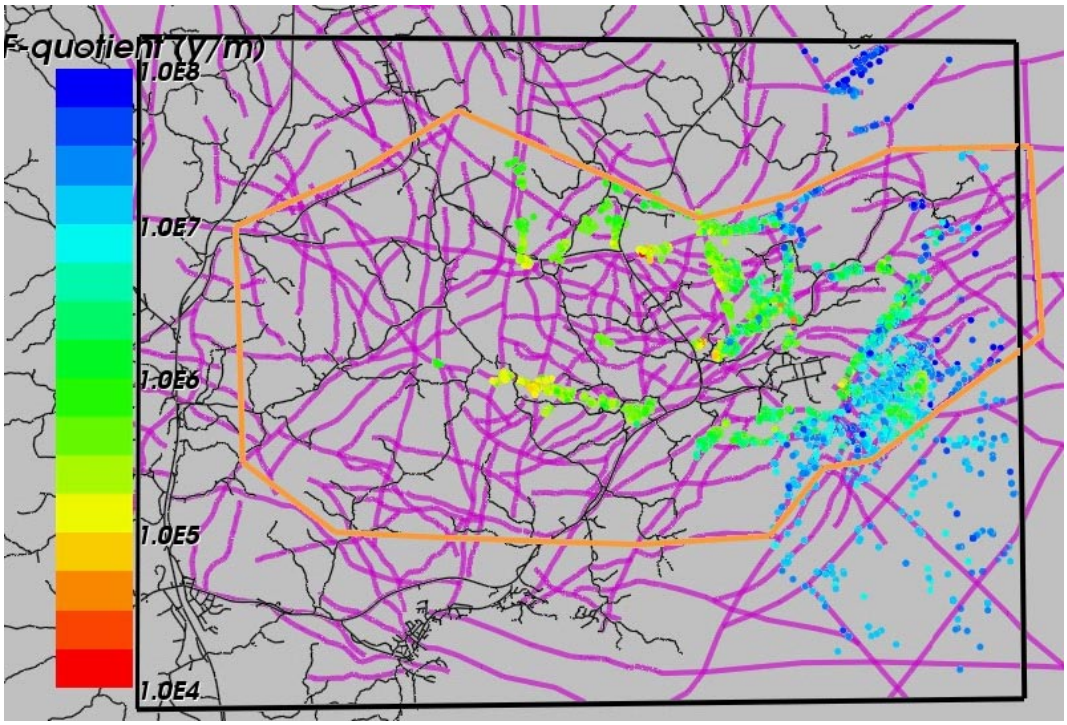

Figure 9-12. *Distribution of F-quotient (Log10) at particles exit locations in the local-scale release area for the Base Case with larger domain (LReg_4Component_ IC2). The small-regional model domain is shown in orange, and the medium regional model domain is black. A slice through the zones at surface is shown in purple.*

Considering the exit locations shown in Figure 9-11, they coincide with the smaller regional model of the Base Case. From Figure 9-12 it is clear that these areas represent DZs situated in low topography. However, it is also clear that a few particles pass the smaller regional model boundary and exit further away. It might even be a fact that the larger regional model is insufficient in terms of transport pathway calculations since some particles exit very close to the offshore boundary, but these long paths far out to sea also tend to have high F-quotients. There are two dominating directions for the particles crossing the smaller regional model boundary. One is to the north east, past the large valley and the other is to the south east out in the Baltic Sea. All particles crossing the smaller regional model boundary have high F-quotients, around 10^7y/m to 10^8y/m.

9.3.2 Regional distribution of reference waters

In Figure 9-13 – Figure 9-15, the present-day distributions of the four reference waters Brine, Marine water, Rain 1960 and Glacial water, are presented in vertical and horizontal slices. As expected the results do not differ much from the Base Case (SReg_4Component_ IC2). The only difference between the cases is the more extended boundary in this case. This is also reflected in the outer parts of the larger model where the boundary crosses the natural water divides and in places has an artificial impact on the flow field. Recharging water close to the boundary can sometimes be squeezed between natural water divides and the arbitrary placed linear boundary. An example of this can be viewed in the top left corner where the boundary is not aligned with the ridge as in the Base Case but crosses through a lower section of the topography. Some of the water entering the model in the recharge area

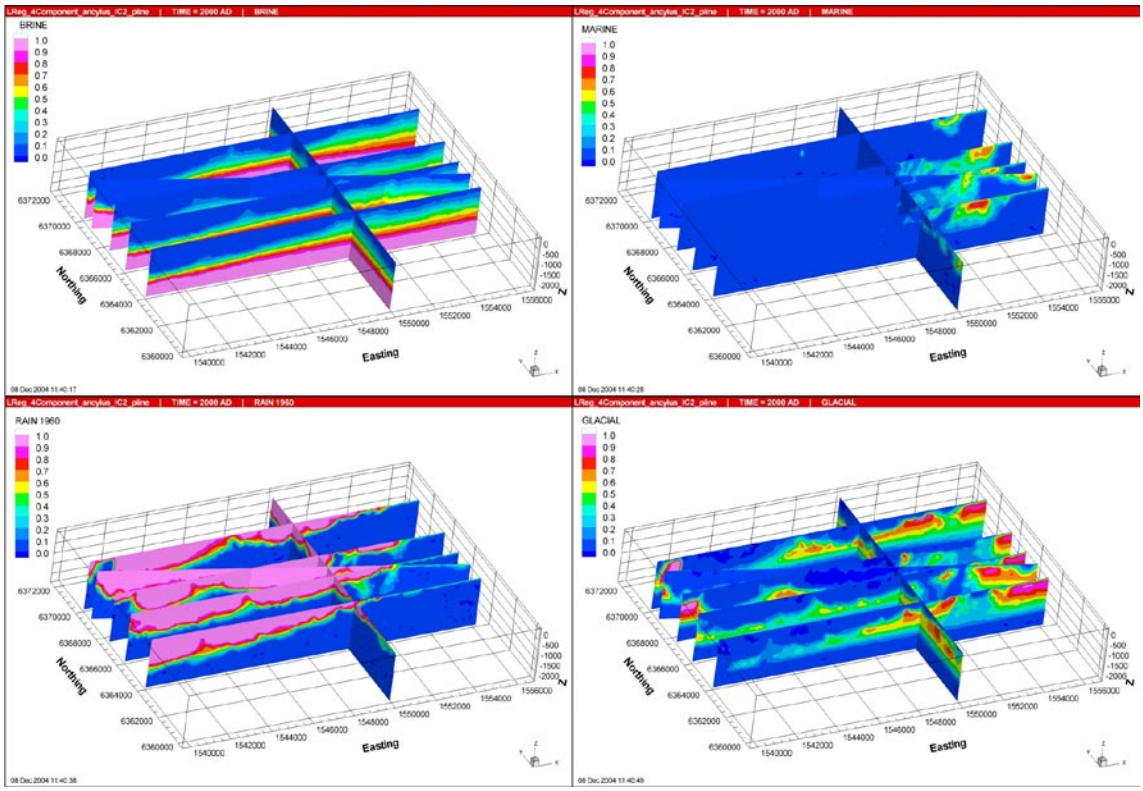

Figure 9-13. *Present-day distribution of the reference waters Brine (top left), Marine water (top right), Rain 1960 (bottom left) and Glacial water (bottom right) in vertical slices, for the Base Case with larger domain (LReg_4Component_IC2).*

(the ridge) will then flow towards the no-flow boundary and there be forced to exit through the top surface. Even if it is desirable to avoid picking boundaries without considering natural features, these effects are localised around the boundary and have little effect on the results in the middle of the model kilometres away from the boundary. As indicated, apart from the boundary effects, the results show great resemblance to the Base Case considering both distributions and magnitudes of the reference waters.

9.3.3 Recharge and discharge rates

In Figure 9-16 the vertical Darcy velocity distribution under present-day flow conditions is presented in vertical and horizontal slices. Compared to the smaller model of the Base Case, the results for the larger model are very similar. There are only small local differences but the general flow directions and flow rates are the same.

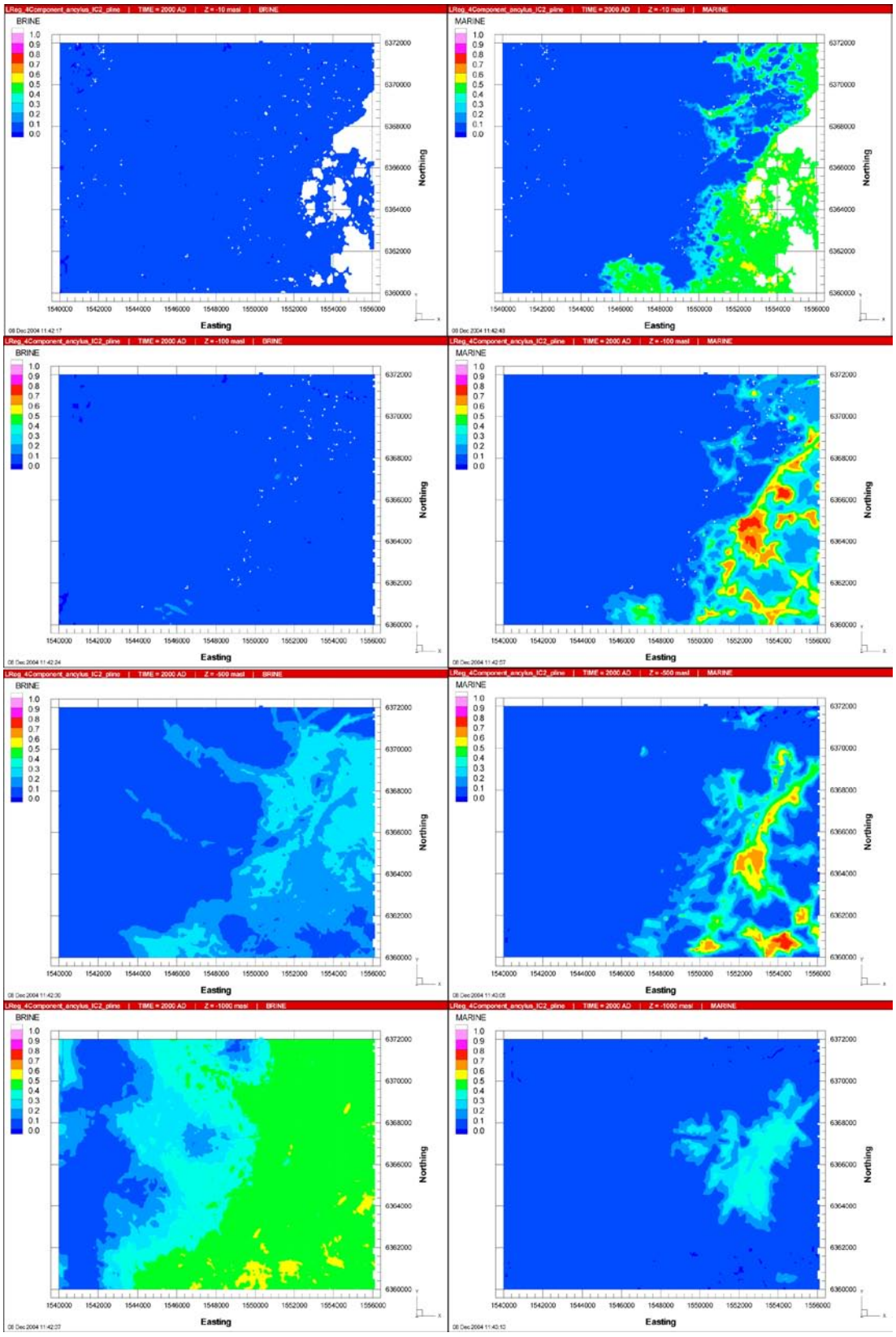

Figure 9-14. *Present-day distribution of Brine (left) and Marine water (right) in horizontal slices at elevations (from top to bottom) –10 m, –100 m, –500 m and –1,000 m, for the Base Case with larger domain (LReg_4Component_IC2).*

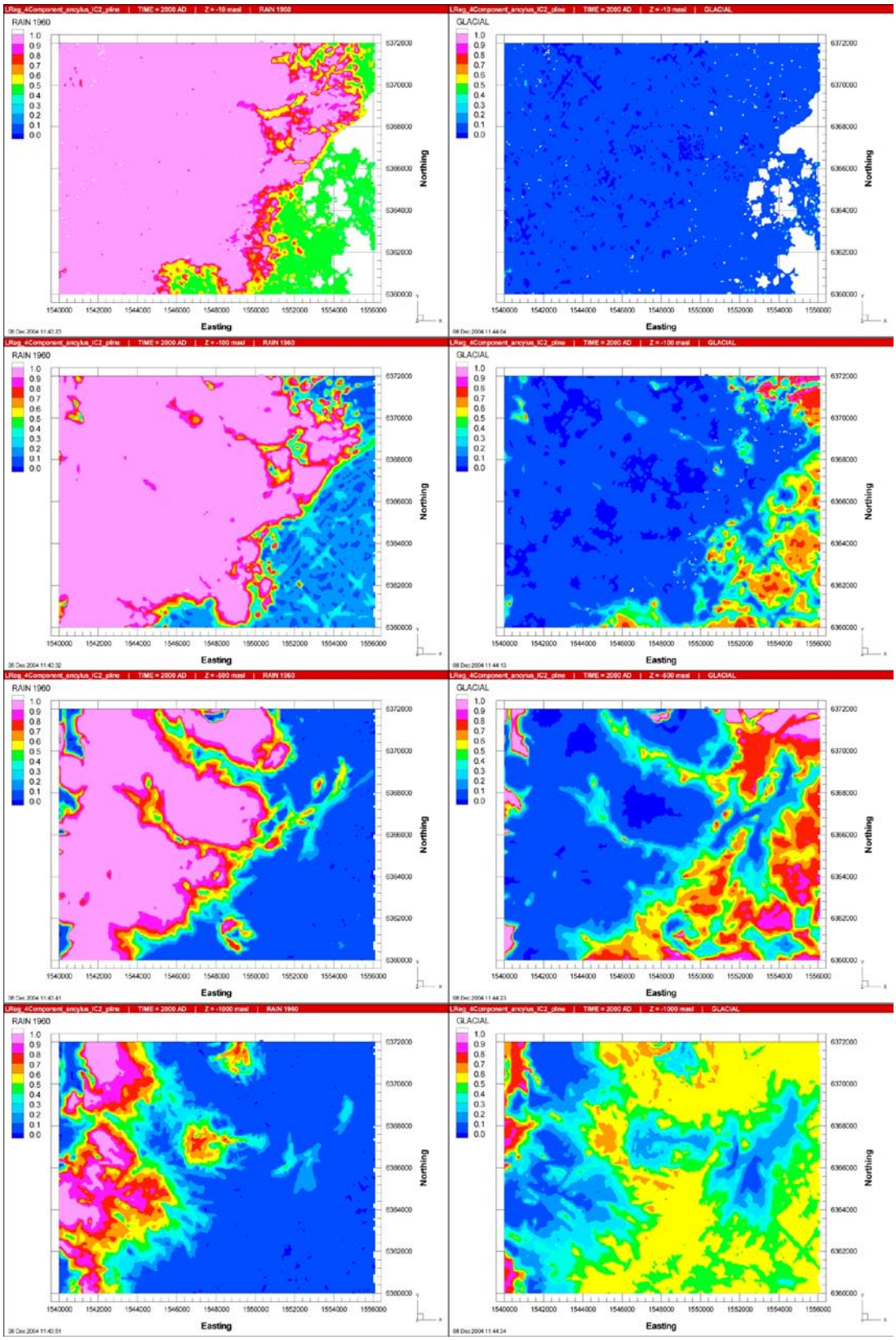

Figure 9-15. *Present-day distribution of Rain 1960 (left) and Glacial water (right) in horizontal slices at elevations (from top to bottom) –10 m, –100 m, –500 m and –1,000 m, for the Base Case with larger domain (LReg_4Component_IC2).*

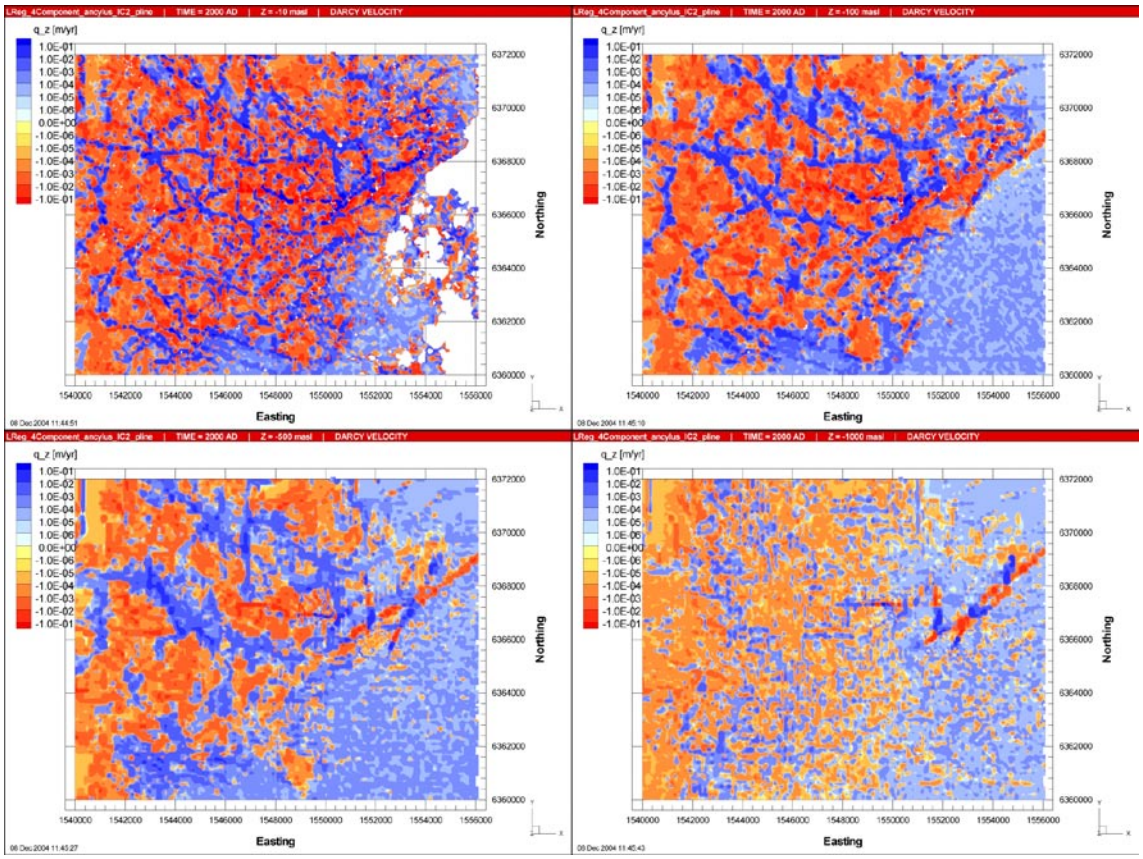

Figure 9-16. *Present-day distribution of the vertical Darcy velocity, q_z, in horizontal slices at elevations –10 m (top left), –100 m (top right), –500 m (bottom left) and –1,000 m (bottom right), for the Base Case with larger domain (LReg_4Component_IC2).*

9.4 Specified infiltration for flow (SReg_4Component_ infiltration_IC2)

This case represents a specified infiltration boundary condition for flow on the top surface as described in Sections 2.1.5 and 7.5.3.

9.4.1 Flow paths

In Figure 9-21 the distribution of the $\log_{10}$(F-quotient) at particles starting locations in the local-scale release area for the specified infiltration case is presented. Figure 9-22 presents the F-quotient at particles exit locations in the local-scale area. Red colour indicates smaller F-quotient. Looking at the distribution of the F-quotient at the starting locations the results appear almost identical to the Base Case. The red areas indicating low F-quotients in the middle of the release area are still there with similar positions and magnitudes. The exit locations presented in Figure 9-22 also show very similar results as for the Base Case.

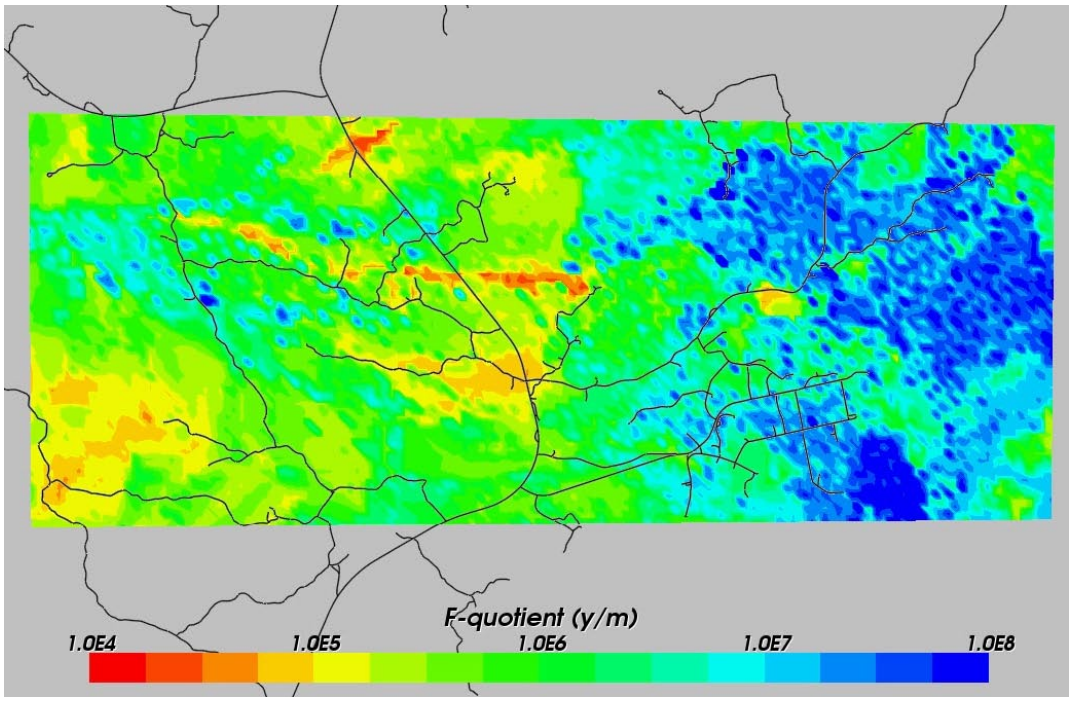

Figure 9-17. *Distribution of F-quotient (Log10) at particles starting locations in the local-scale release area (SReg_4Component_infiltration_IC2) – specified infiltration for flow. Roads are shown in black for context.*

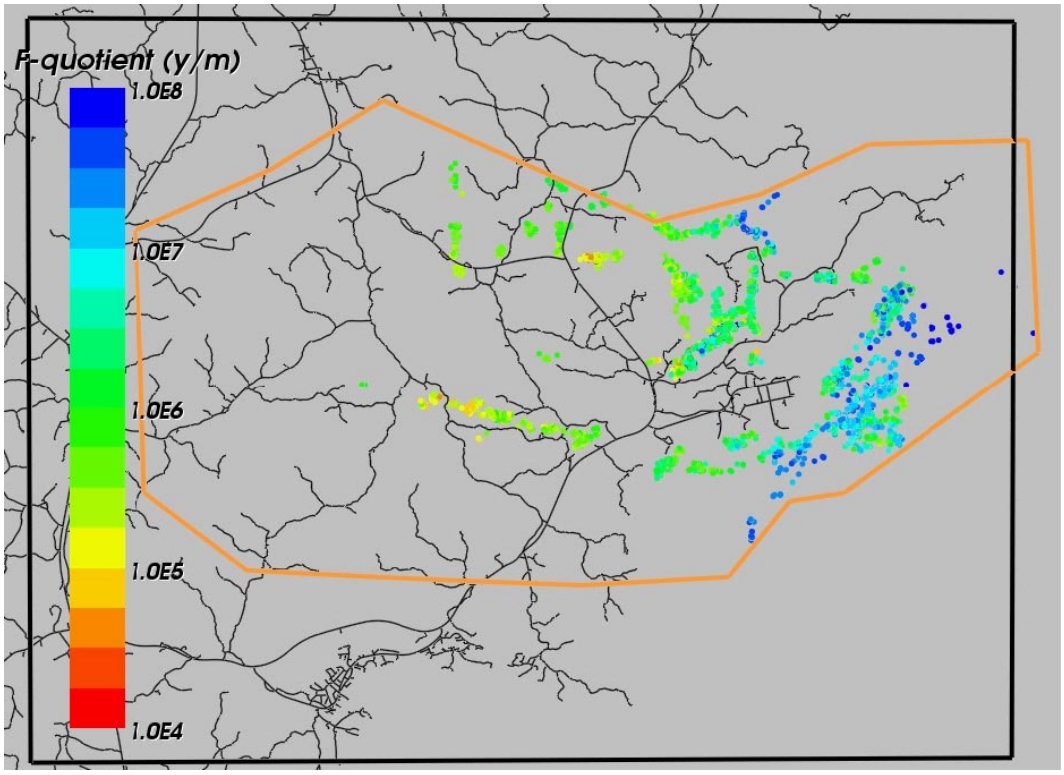

Figure 9-18. *Distribution of F-quotient (Log10) at particles exit locations in the local-scale release area for (SReg_4Component_infiltration_IC2) – specified infiltration for flow. Roads are shown in black for context. The small-regional model domain is shown in orange, and the medium regional model domain is black.*

9.4.2 Regional distribution of reference waters

In Figure 9-23 the present-day distribution of the four reference waters are presented in vertical slices. This case differs from the Base Case only in having a different boundary condition for flow on the top surface. The results show that the changes are very small. The distribution of Brine is almost the same as for the first realisation and the same is valid for the other reference waters, Marine water, Rain 1960 and Glacial water where there may be small local effects but in general the same distribution as before.

9.4.3 Recharge and discharge rates

In Figure 9-24 the vertical Darcy velocity distribution under present-day flow conditions is presented in vertical and horizontal slices for the case with specified infiltration. As already concluded, the differences between the two different realisations are generally small and local. The magnitude and direction of the Darcy velocity is unchanged.

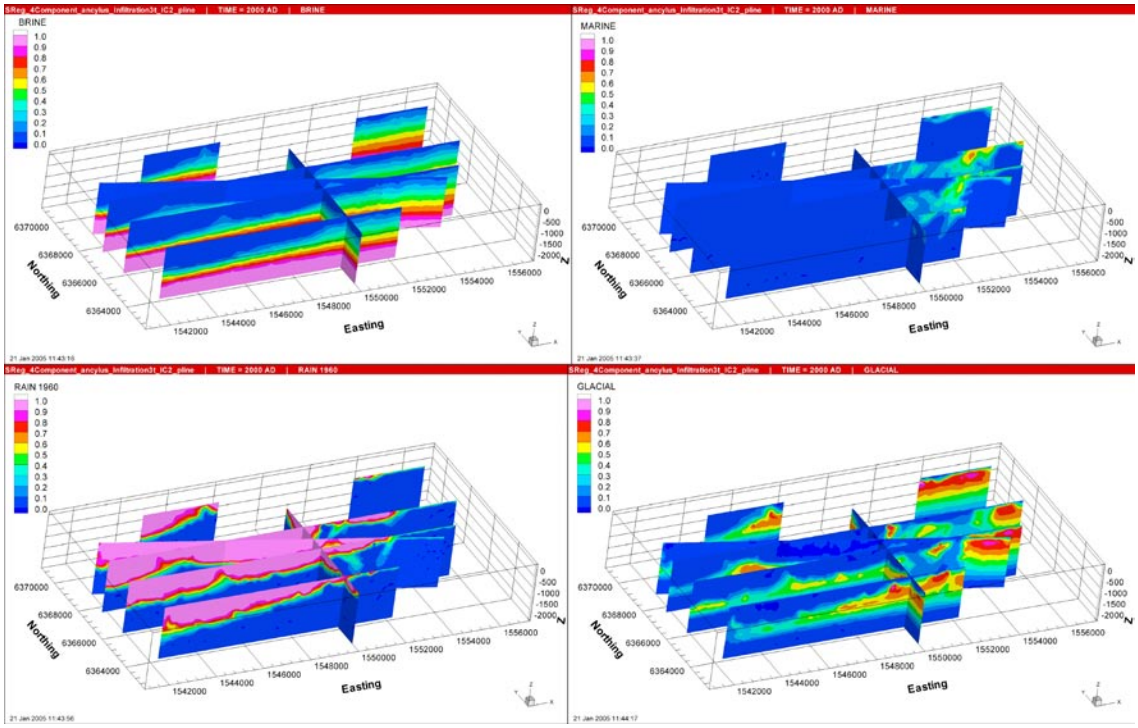

Figure 9-19. *Present-day distribution of the reference waters Brine (top left), Marine water (top right), Rain 1960 (bottom left) and Glacial water (bottom right) in vertical slices, for specified infiltration for flow (SReg_4Component_infiltration_IC2).*

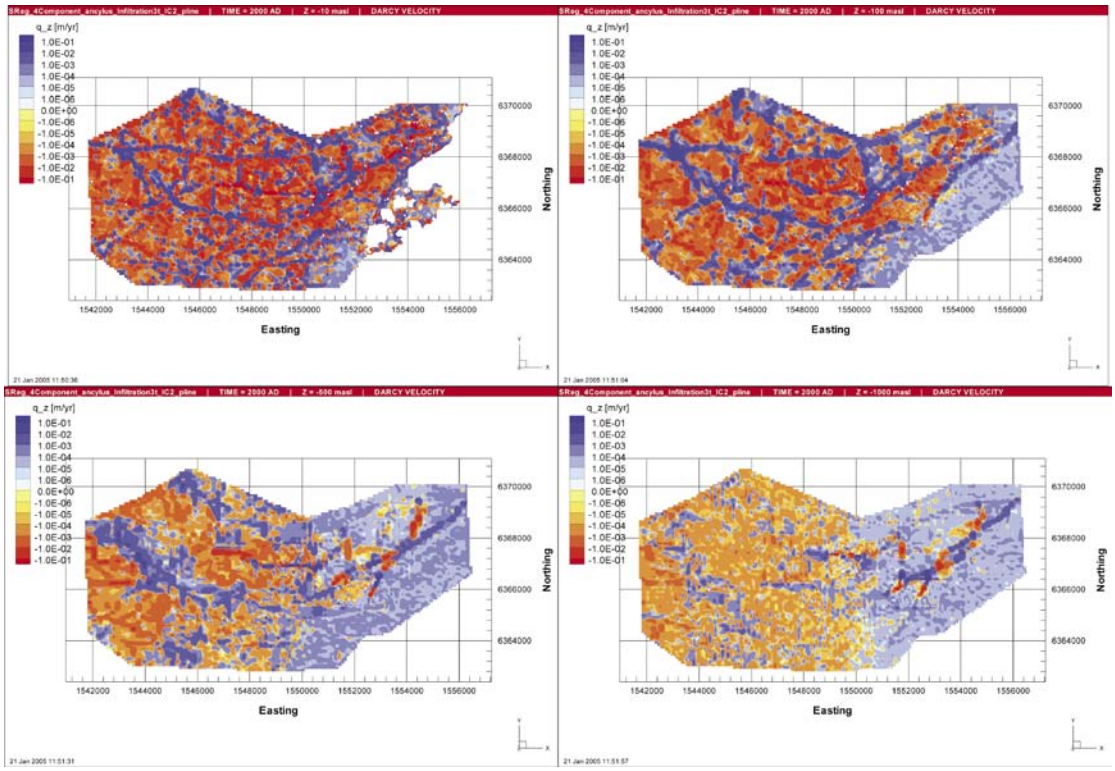

Figure 9-20. *Present-day distribution of the vertical Darcy velocity, q_z, in horizontal slices at elevations (from top to bottom) –10 m (top left), –100 m (top right), –500 m (bottom left) and –1,000 m (bottom right), for a specified infiltration for flow (SReg_4Component_infiltration_IC2).*

9.5 Base Case Realisation 2 (SReg_4Component2_IC2)

This case represents the second realisation of the Base Case.

9.5.1 Flow paths

In Figure 9-21 the distribution of the Log_{10}(F-quotient) at particles starting locations in the local-scale release area for the second realisation of the Base Case is presented. Figure 9-22 presents the F-quotient at particles exit locations in the local-scale area. Red colour indicates smaller F-quotient. Looking at the distribution of the F-quotient at the starting locations there are actually some differences compared to the first realisation of the Base Case. The red areas indicating low F-quotients in the middle of the release area are not as pronounced here in the second realisation. The exit locations presented in Figure 9-22 show broadly the same results as for the first realisation of the Base Case. There are some more particles finding their way further out into the Baltic Sea compared to the first realisation.

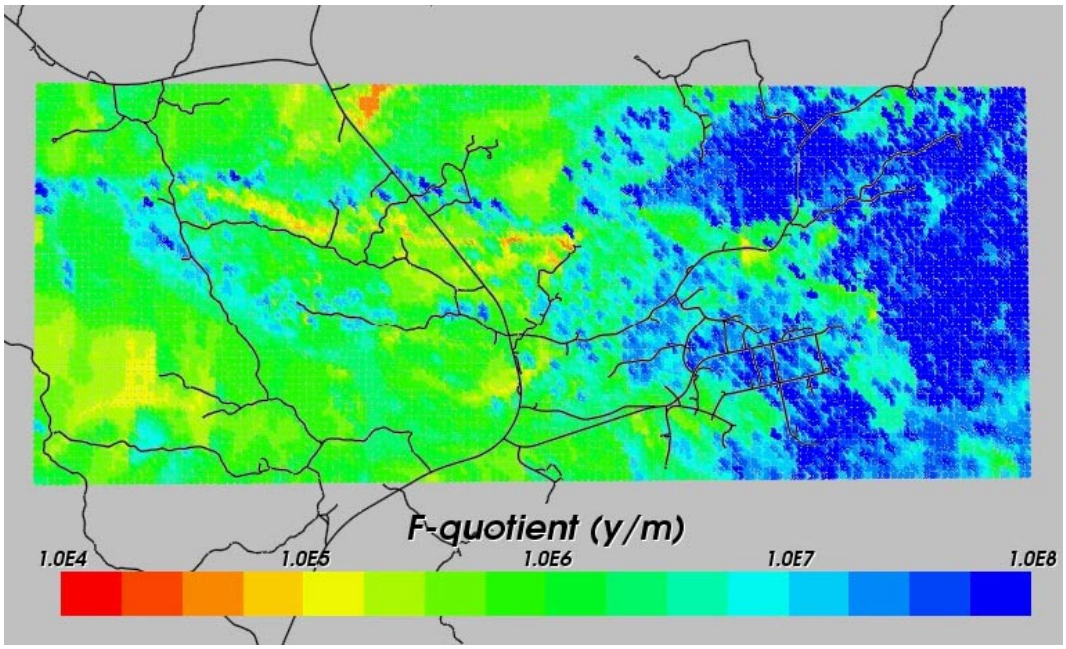

Figure 9-21. *Distribution of F-quotient (Log10) at particles starting locations in the local-scale release area for the Base Case Realisation 2 (SReg_4Component2_ IC2). Roads are shown in black for context.*

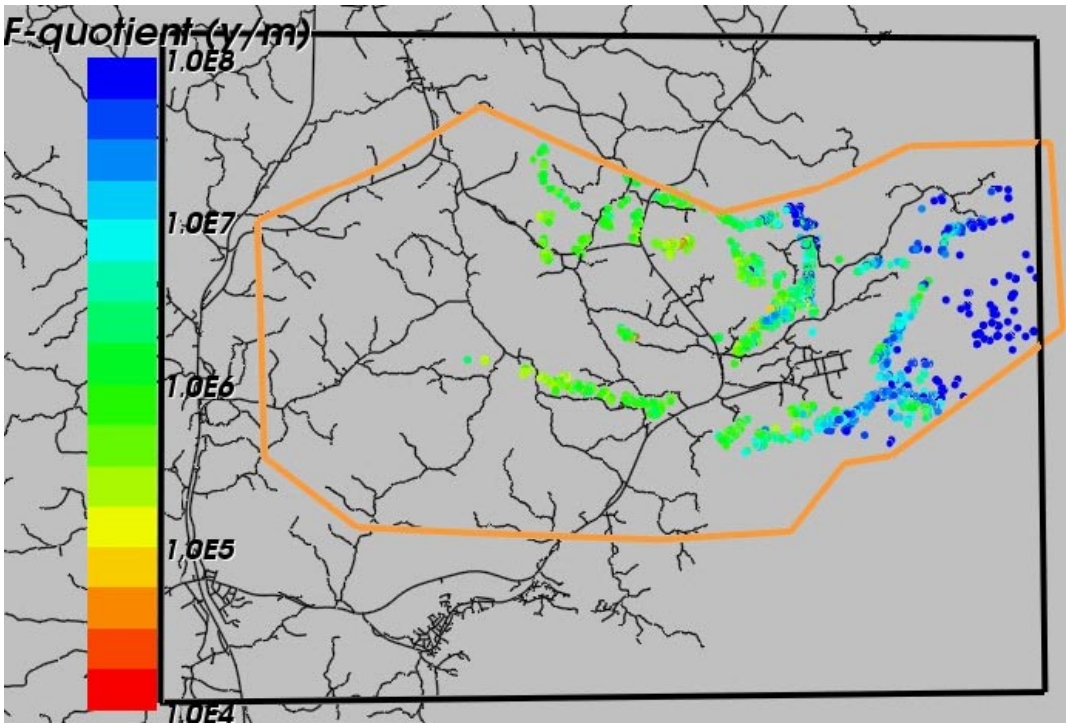

Figure 9-22. *Distribution of F-quotient (Log10) at particles exit locations in the local-scale release area for the Base Case Realisation 2 (SReg_4Component2_ IC2). Roads are shown in black for context. The small-regional model domain is shown in orange, and the medium regional model domain is black.*

9.5.2 Regional distribution of reference waters

In Figure 9-23 the present-day distribution of the four reference waters are presented in vertical slices. This case differs from the Base Case only by using a different realisation of the underlying DFN model used to generate the permeability field. The results show that the changes are very small. The distribution of Brine is almost the same as for the first realisation and the same is valid for the other reference waters, Marine water, Rain 1960 and Glacial water where there may be small local effects but in general the same distribution as before. Some effects can be seen in the area around the large deterministic fracture zones in the eastern part of the model.

9.5.3 Recharge and discharge rates

In Figure 9-24 the vertical Darcy velocity distribution under present-day flow conditions is presented in vertical and horizontal slices for the second realisation of the Base Case. As already concluded, the differences between the two different realisations are generally small and local. However, one can find places in the model where things have clearly changed, e.g. in the eastern part of the modelled area there is a fracture zone where the direction of flow has changed from being upward in the first realisation to being downward in the second realisation. The magnitude of the Darcy velocity is unchanged.

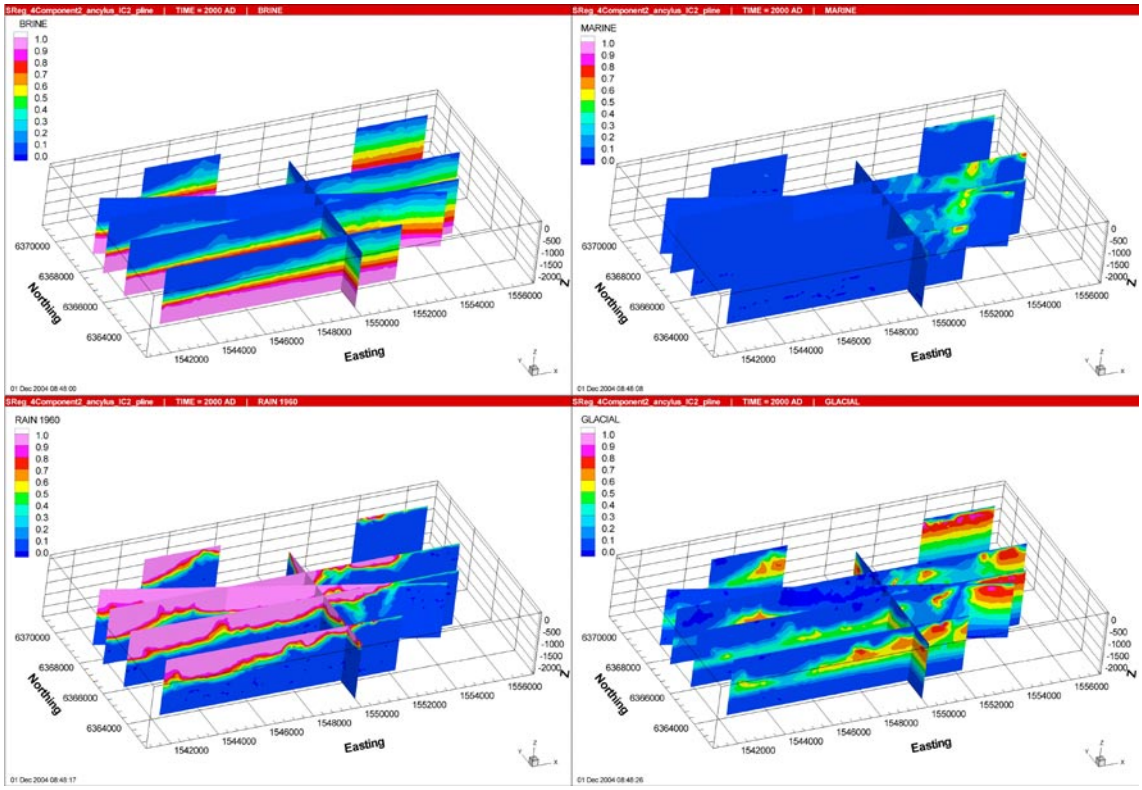

Figure 9-23. *Present-day distribution of the reference waters Brine (top left), Marine water (top right), Rain 1960 (bottom left) and Glacial water (bottom right) in vertical slices, for Realisation 2 (SReg_4Component2_ IC2).*

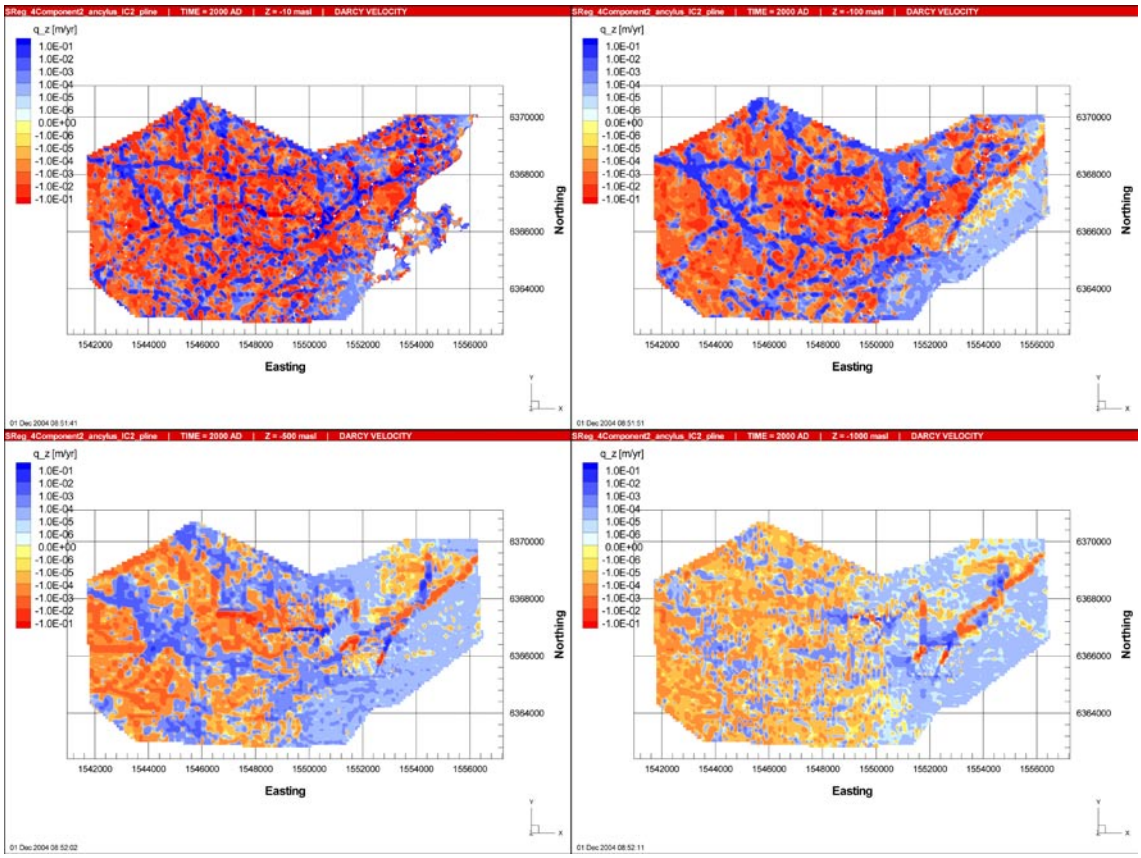

Figure 9-24. *Present-day distribution of the vertical Darcy velocity, q_z, in horizontal slices at elevations (from top to bottom) –10 m (top left), –100 m (top right), –500 m (bottom left) and –1,000 m (botto m right), for Realisation 2 (SReg_4Component2_IC2).*

9.6 Base Case Realisation 3 (SReg_4Component3_IC2)

This case represents the third realisation of the Base Case.

9.6.1 Flow paths

In Figure 9-25 the distribution of the Log_{10} (F-quotient) at particles starting locations in the local scale area for the third realisation of the Base Case is presented. Figure 9-26 presents the F-quotient at particles exit locations in the local-scale area. Red colour indicates smaller F-quotient. The results for this case are very similar to the second realisation of the Base Case. The values of the F-quotient are somewhat higher compared to the first realisation but the exit locations are near identical.

9.6.2 Regional distribution of reference waters

The case represents the third realisation of the Base Case. As was concluded for the second realisation, the changes between the realisations are generally very small with local discrepancies.

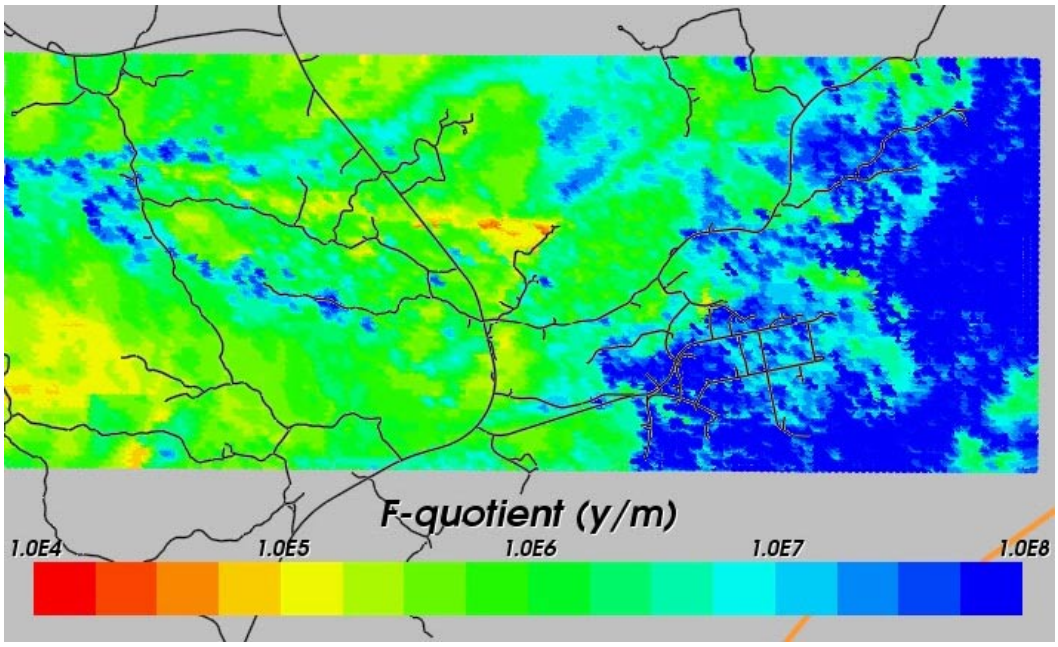

Figure 9-25. *Distribution of F-quotient (Log10) at particles starting locations in the local-scale release area for the Base Case Realisation 3 (SReg_4Component3_ IC2). Roads are shown in black for context.*

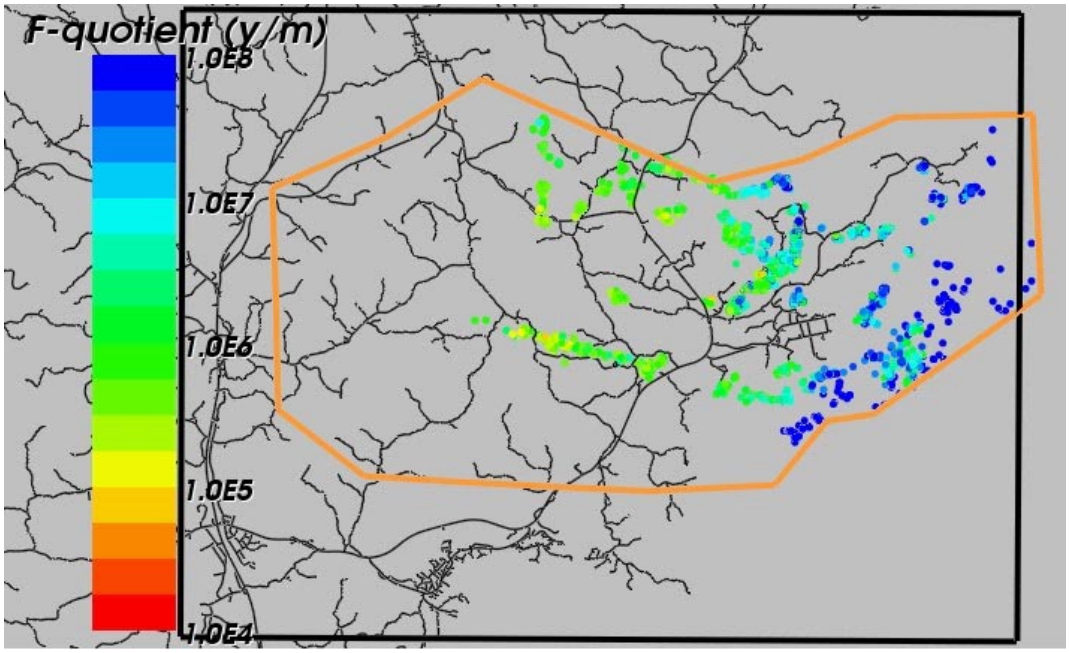

Figure 9-26. *Distribution of F-quotient (Log10) at particles exit locations in the local-scale release area for the Base Case Realisation 3 (SReg_4Component3_ IC2). Roads are shown in black for context. The small-regional model domain is shown in orange, and the mediu m regional model domain is black.*

9.6.3 Recharge and discharge rates

The changes in the vertical Darcy velocity between the three different realisations of the Base Case remains small in this third realisation (see Figure 9-27). The change of direction in the large fracture zone to the east is still present compared to the first realisation.

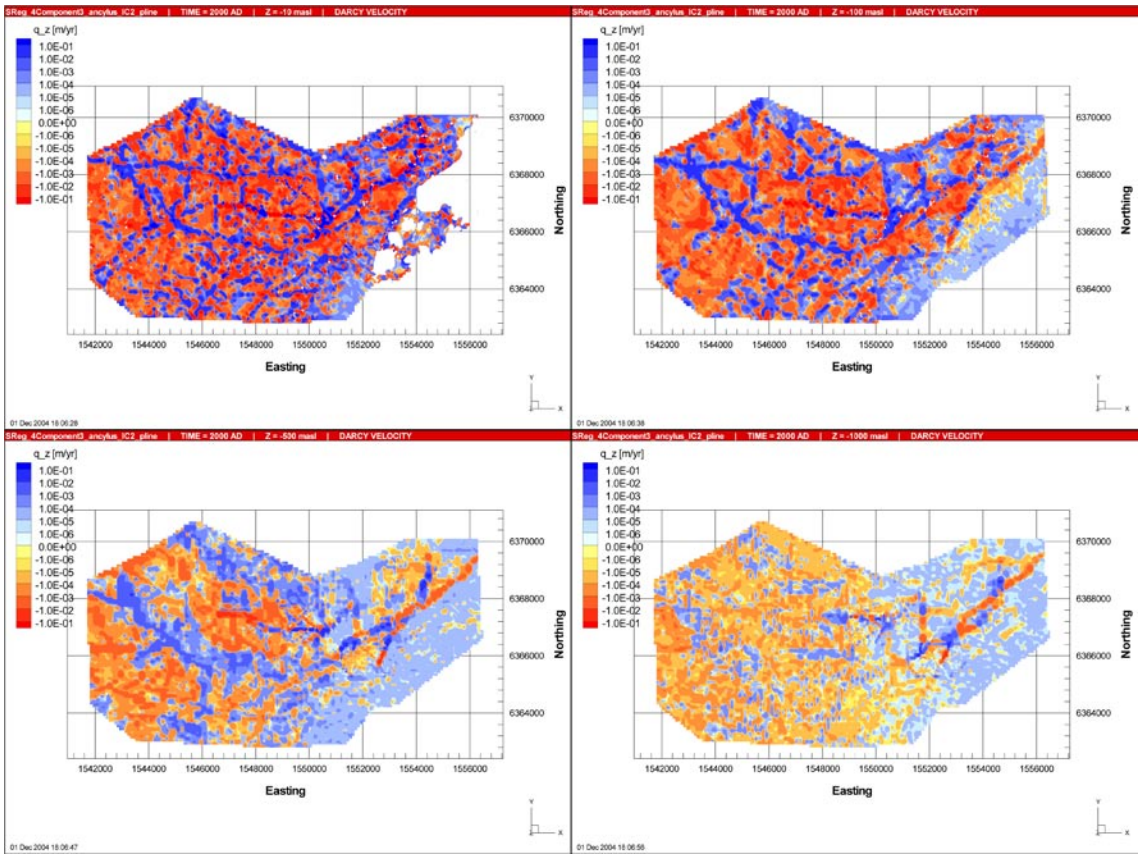

Figure 9-27. *Present-day distribution of the vertical Darcy velocity, q_z, in horizontal slices at elevations (from top to bottom) –10 m (top left), –100 m (top right), –500 m (bottom left) and –1,000 m (bottom right), for Realisation 3 (SReg_4Component3_IC2).*

9.7 Hydro-DFN based on DarcyTools interpretation (SReg_4Component_DT_IC2)

This case is a sensitivity case for the implications of the DarcyTools interpretation of the Hydro-DFN.

9.7.1 Flow paths

In Figure 9-28 the distribution of the $\log_{10}$(F-quotient) at particles starting locations in the local-scale release area for the case using a HydroDFN based on DarcyTools interpretation is presented. Figure 9-29 presents the F-quotient at particles exit locations in the local-scale area. Red colour indicates smaller F-quotient. The results are very similar to the Base Case with only minor discrepancies. In the DarcyTools case there are slightly higher values of F-quotient in the middle part of the area. On the other hand the values a bit lower in the north-west and south-west parts of the local-scale release area. The exit locations are also very similar for the two cases.

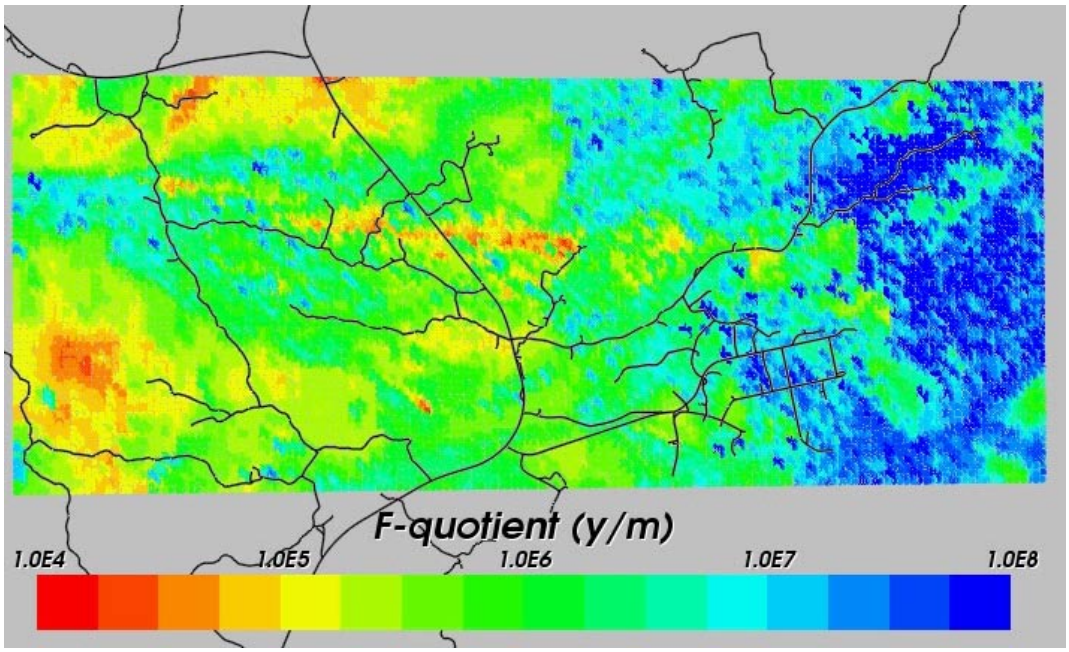

Figure 9-28. *Distribution of F-quotient (Log10) at particles starting locations in the local-scale release area for the DT DFN (SReg_4Component_DT_ IC2). Roads are shown in black for context.*

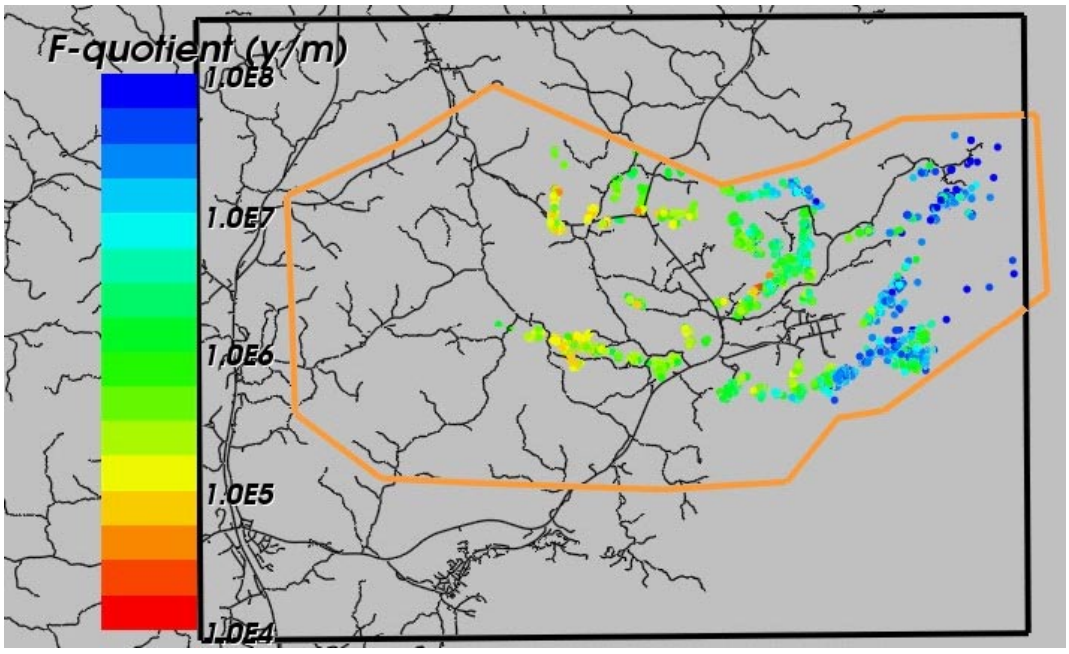

Figure 9-29. *Distribution of F-quotient (Log10) at particles exit locations in the local-scale release area for the DT DFN (SReg_4Component_DT_ IC2). Roads are shown in black for context. The small-regional model domain is shown in orange, and the medium regional model domain is black.*

9.7.2 Regional distribution of reference waters

This case is a sensitivity analysis of the implications of using the DarcyTools interpretation of the DFN model parameters. In Figure 9-30, the present-day distributions of the four reference waters Brine, Marine water, Rain 1960 and Glacial water, are presented in vertical slices. It is clear that the differences compared to the Base Case are very small. There are only small localised effects to be found and it is concluded that using the DarcyTools DFN parameters does not change the distribution of the reference waters significantly.

9.7.3 Recharge and discharge rates

In Figure 9-31 the vertical Darcy velocity distribution under present-day flow conditions is presented in horizontal slices. Again, the differences in the distribution of the vertical Darcy velocity between the Base Case and using the DarcyTools DFN parameters are very small and localised. The magnitude of the velocity is the same as for the Base Case throughout the model domain.

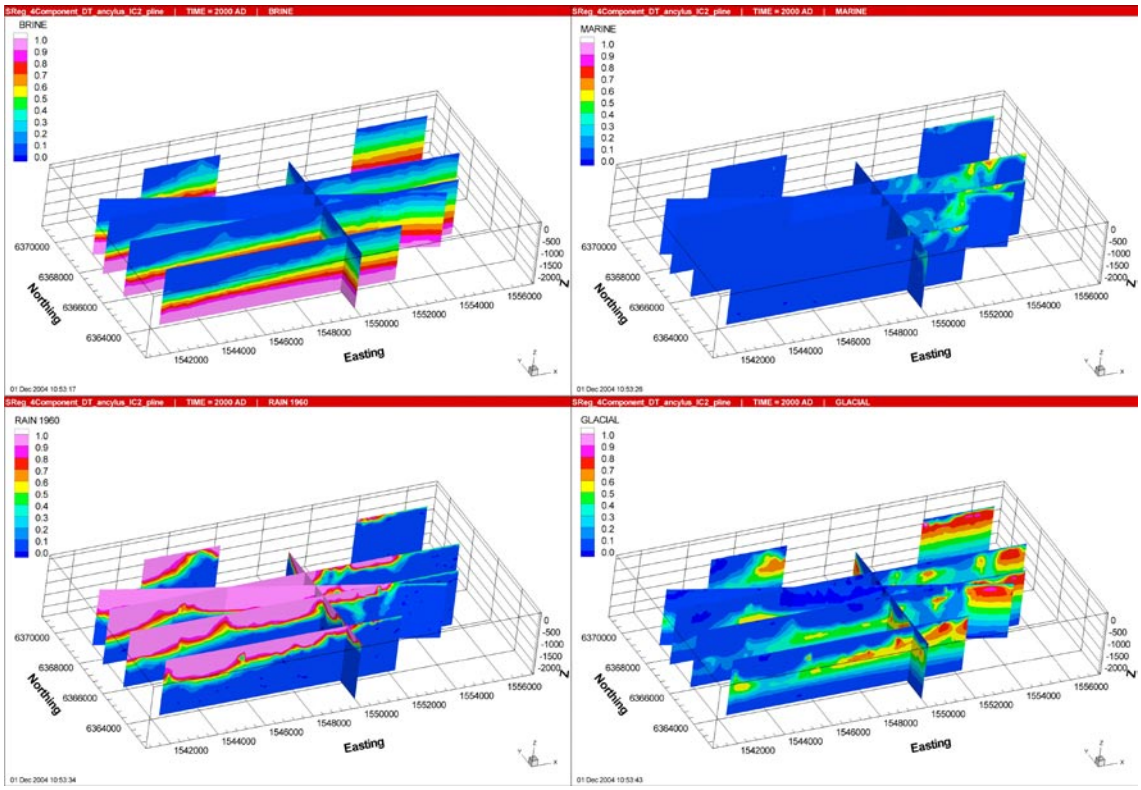

Figure 9-30. *Present-day distribution of the reference waters Brine (top left), Marine water (top right), Rain 1960 (bottom left) and Glacial water (bottom right) in vertical slices, for the DarcyTools DFN (SReg_4Component_DT_ IC2).*

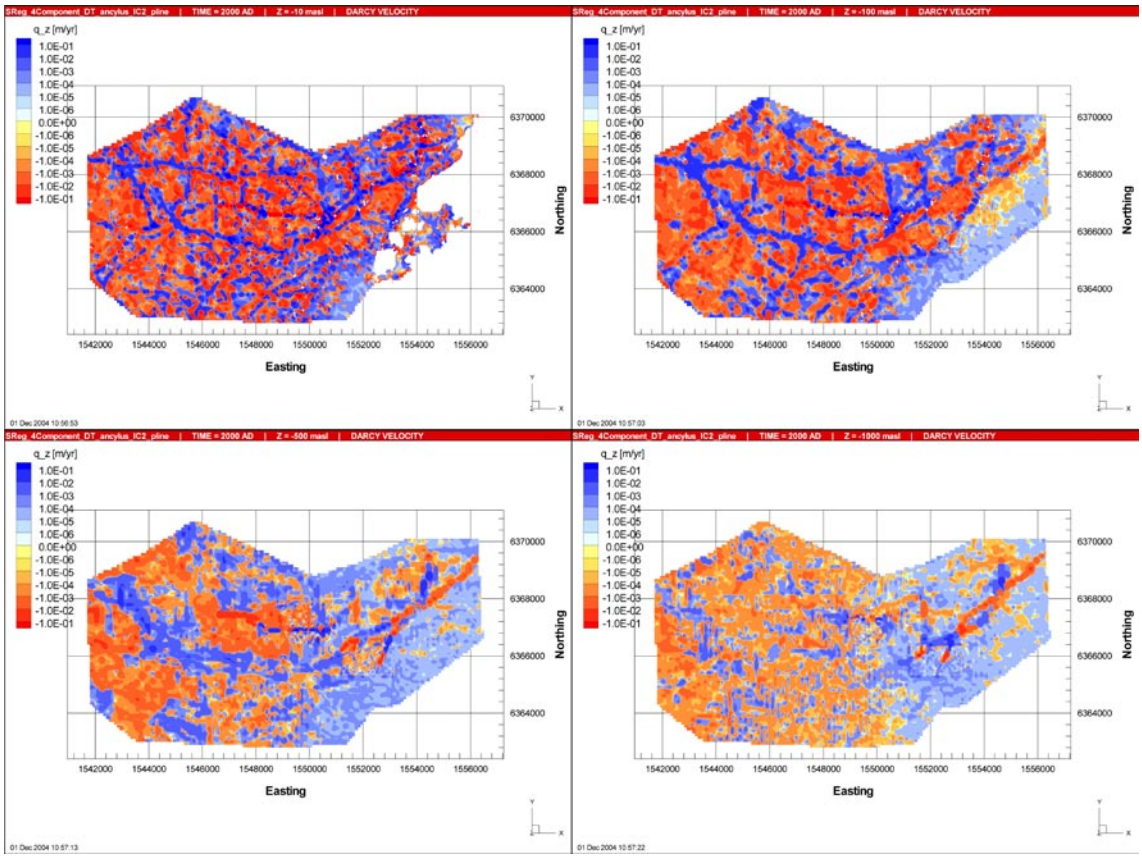

Figure 9-31. *Present-day distribution of the vertical Darcy velocity, q_z, in horizontal slices at elevations (from top to bottom) –10 m (top left), –100 m (top right), –500 m (bottom left) and –1,000 m (bottom right), for the DarcyTools DFN (SReg_4Component_DT_IC2).*

9.8 Uncorrelated transmissivity distribution (SReg_4Component_UnCorr_IC2)

This case is a variant on the Base Case DFN with an uncorrelated transmissivity distribution model.

9.8.1 Flow paths

In Figure 9-32 the distribution of the Log_{10}(F-quotient) at particles starting locations in the local scale area for the case using an uncorrelated transmissivity distribution is presented. Figure 9-33 presents the F-quotient at particles exit locations in the local-scale area. Red colour indicates smaller F-quotient. The values for the F-quotient are slightly higher compared to the Base Case presumably because the block-scale hydraulic conductivity is on average lower for this case. The exit locations are very similar for the two cases with a few more particles reaching further out in the Baltic Sea in the uncorrelated case.

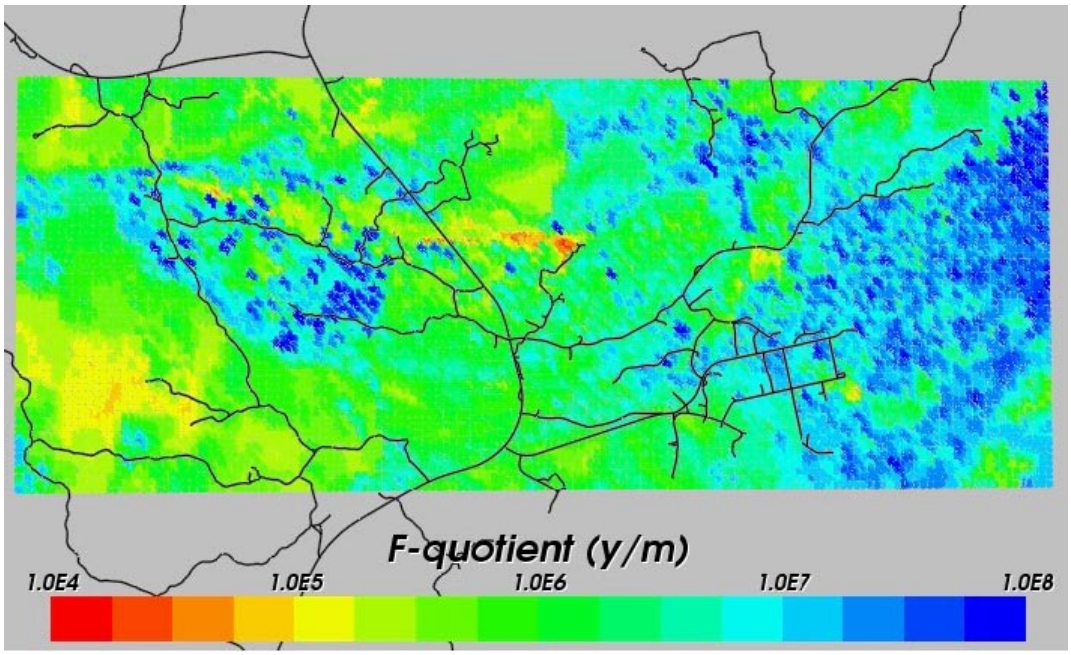

Figure 9-32. *Distribution of F-quotient (Log10) at particles starting locations in the local-scale release area for uncorrelated T model (SReg_4Component_UnCorr_ IC2). Roads are shown in black for context.*

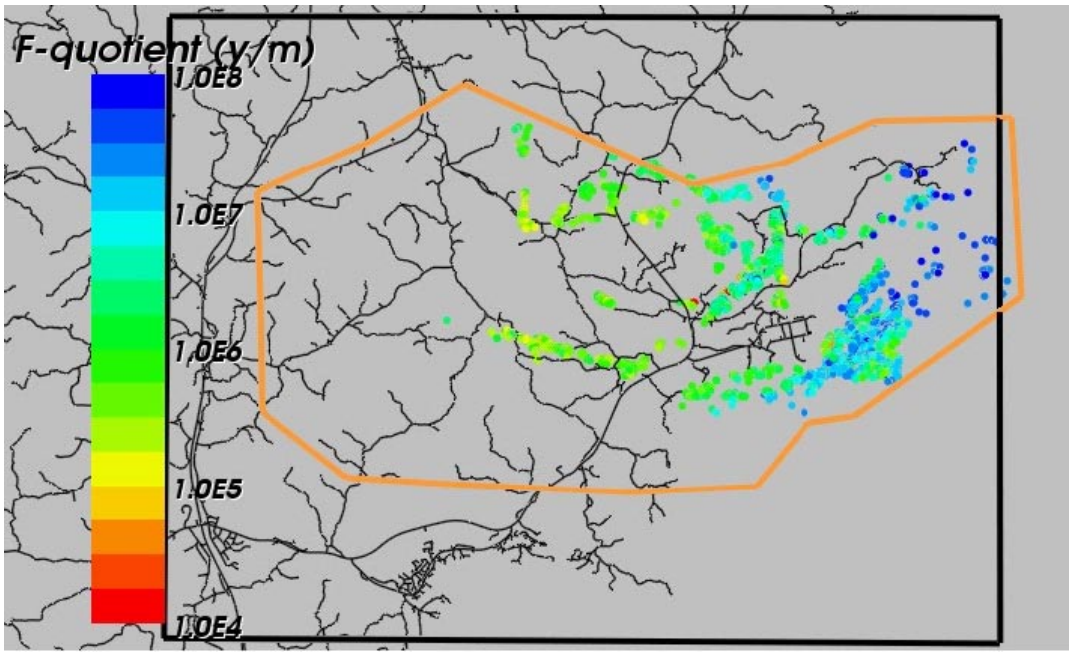

Figure 9-33. *Distribution of F-quotient (Log10) at particles exit locations in the local-scale release area for uncorrelated T model (SReg_4Component_UnCorr_ IC2). Roads are shown in black for context. The small-regional model domain is shown in orange, and the medium regional model domain is black.*

9.8.2 Regional distribution of reference waters

In this case an uncorrelated transmissivity distribution model is used instead of the correlated model used in the Base Case. In Figure 9-34, the present-day distributions of the four reference waters Brine, Marine water, Rain 1960 and Glacial water, are presented in vertical slices. Generally the differences for the distribution of reference waters compared to the Base Case are small. The Rain 1960 seems to penetrate slightly less and a bit more Glacial water can be found between –500 m and –1,000 m even if the differences are very small.

9.8.3 Recharge and discharge rates

In Figure 9-35 the vertical Darcy velocity distribution under present-day flow conditions is presented in horizontal slices. As mentioned, the differences in the distribution of the vertical Darcy velocity between the Base Case and the uncorrelated case are very small and localised. For all practical reasons the distribution of the vertical Darcy velocity is the same as in the Base Case. The differences that can be found are small and local and the magnitude of the velocity is the same as for the Base Case throughout the model domain.

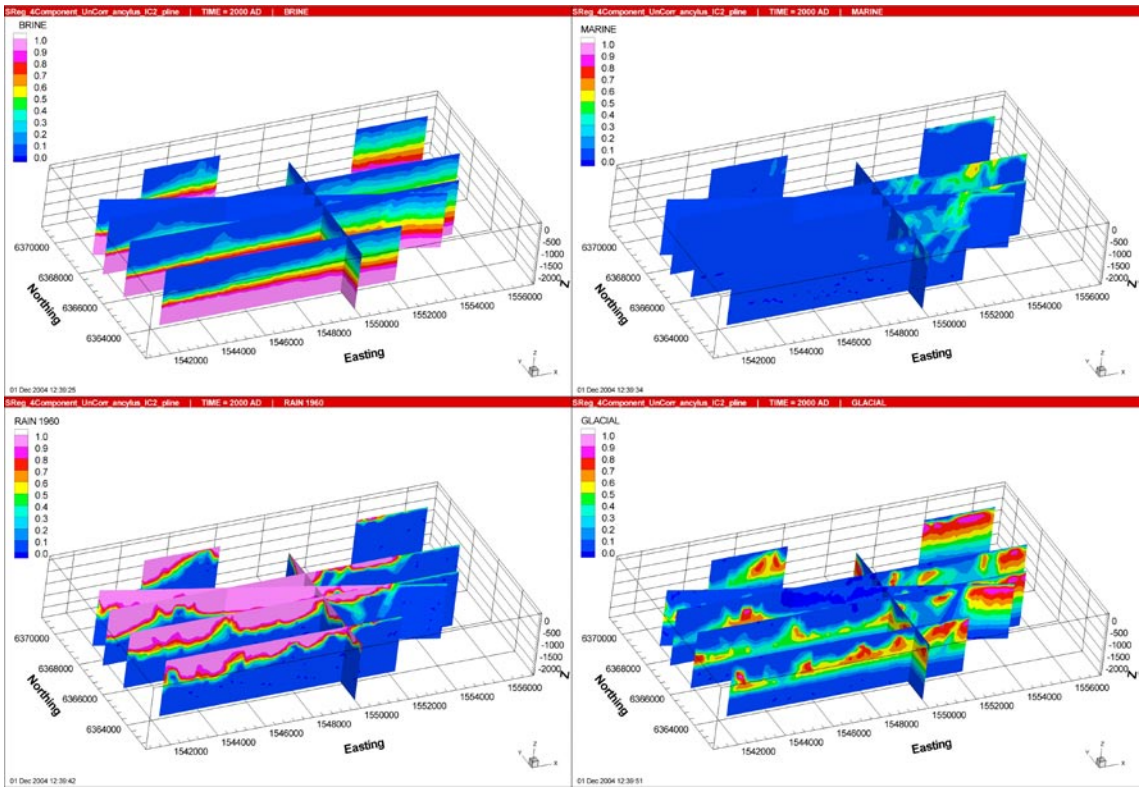

Figure 9-34. *Present-day distribution of the reference waters Brine (top left), Marine water (top right), Rain 1960 (bottom left) and Glacial water (bottom right) in vertical slices, for uncorrelated T model (SReg_4Component_UnCorr_ IC2).*

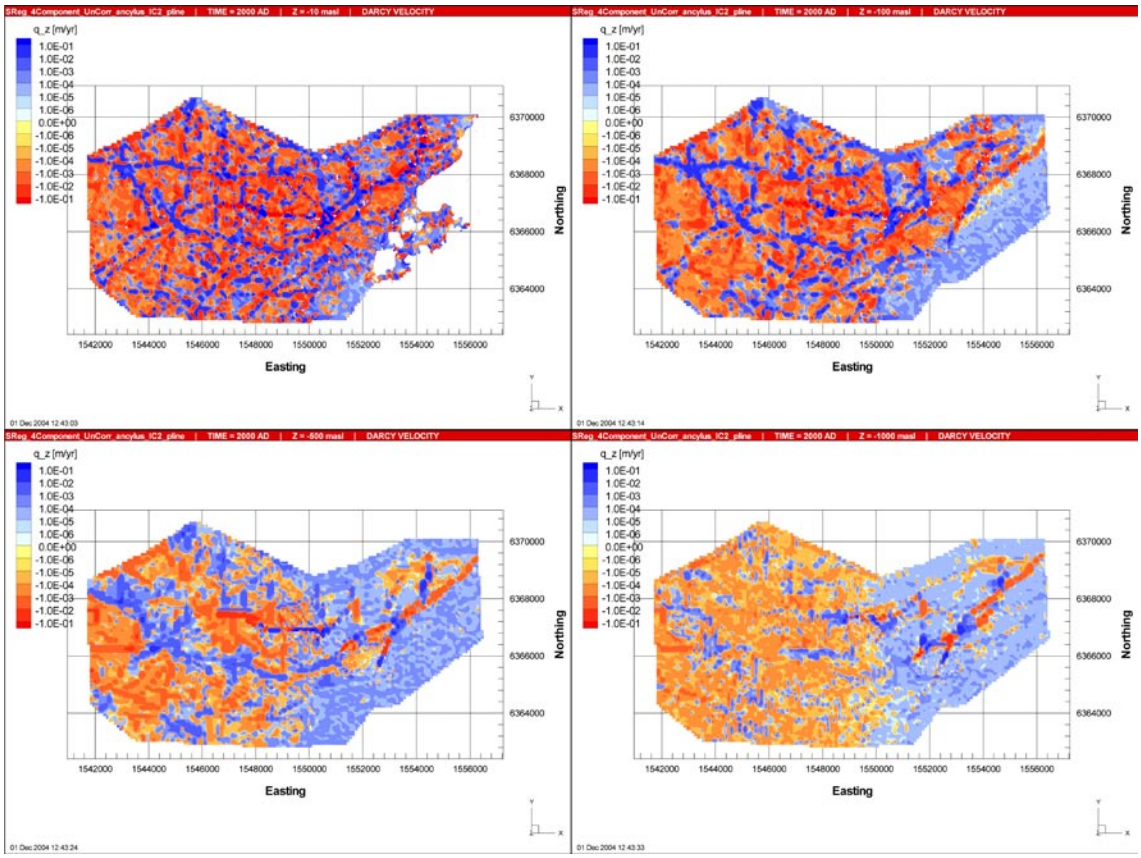

Figure 9-35. *Present-day distribution of the vertical Darcy velocity, q_z, in horizontal slices at elevations (from top to bottom) –10 m, –100 m, –500 m and –1,000 m, for uncorrelated T model (SReg_4Component_UnCorr_ IC2).*

9.9 Semi-correlated transmissivity distribution (SReg_4Component_Semi_ IC2)

This case is a variant on the Base case DFN with a semi-correlated transmissivity distribution model.

9.9.1 Flow paths

In Figure 9-36 the distribution of the Log_{10} (F-quotient) at particles starting locations in the local-scale release area for the case using a semi-correlated transmissivity distribution is presented. Figure 9-37 presents the F-quotient at particles exit locations in the local-scale area. Red colour indicates smaller F-quotient. The values for the F-quotient are similar to the Base Case, only somewhat higher in the Laxemar area. In the east the exit locations are more concentrated to a few deformation zones compared to the Base Case.

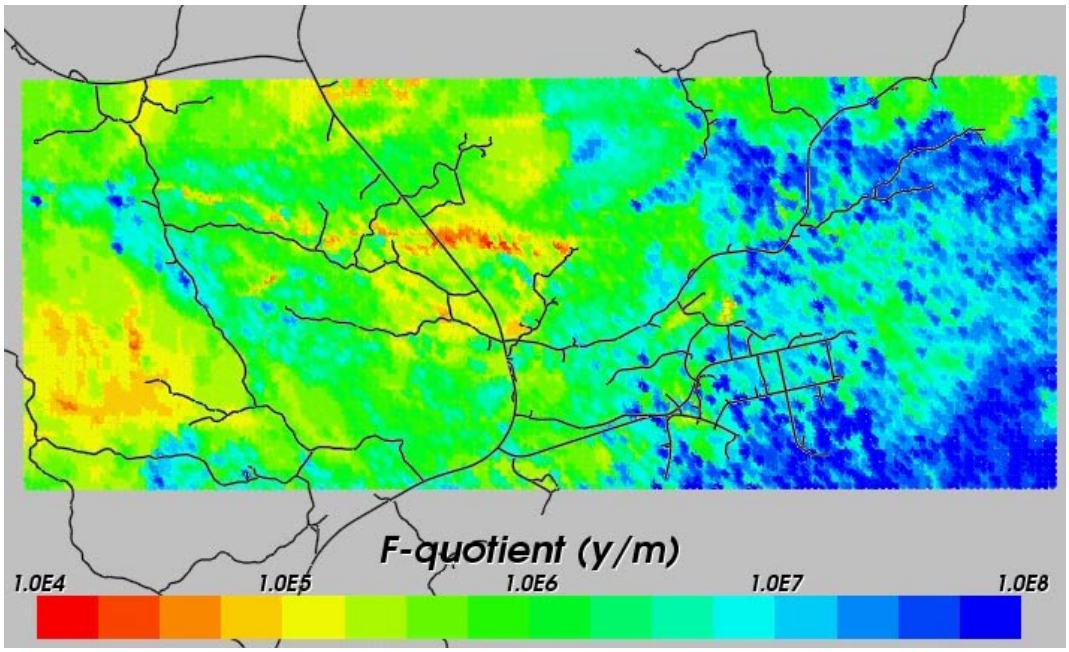

Figure 9-36. *Distribution of F-quotient (Log10) at particles starting locations in the local-scale release area for semi-correlated T model (SReg_4Component_Semi_ IC2). Roads are shown in black for context.*

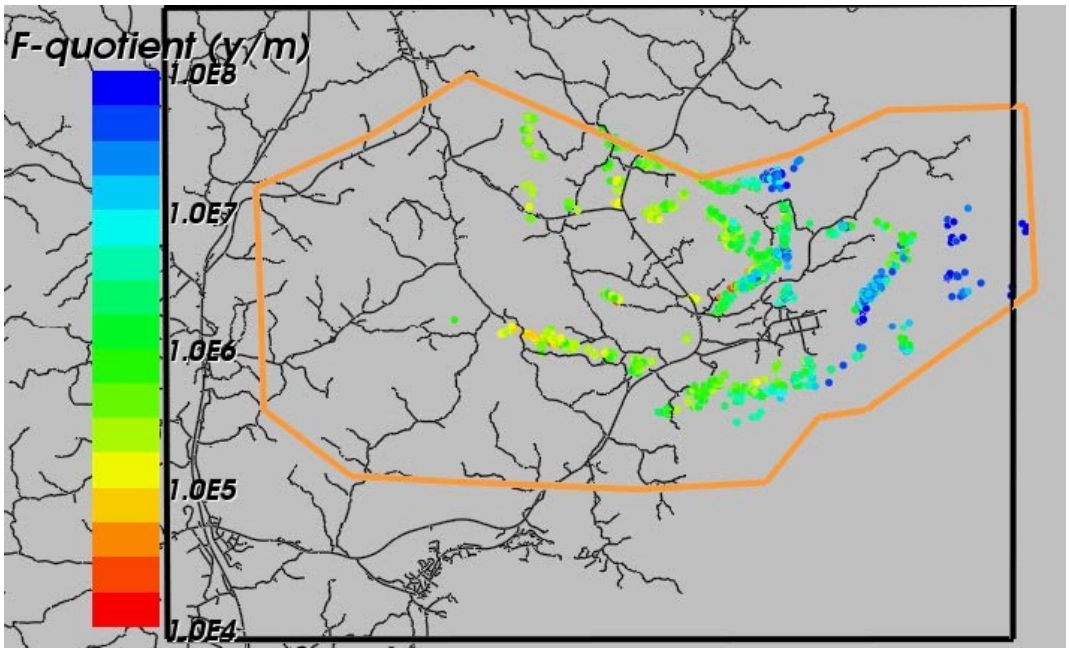

Figure 9-37. *Distribution of F-quotient (Log10) at particles exit locations in the local-scale release area for semi-correlated T model (SReg_4Component_Semi_ IC2). Roads are shown in black for context. The small-regional model domain is shown in orange, and the medium regional model domain is black.*

9.9.2 Regional distribution of reference waters

This case uses a semi-correlated T distribution model instead of the correlated model used in the Base Case. In Figure 9-38, the present-day distributions of the four reference waters Brine, Marine water, Rain 1960 and Glacial water, are presented in vertical slices. Generally the differences for the distribution of reference waters compared to the Base Case are small. The Brine is found somewhat higher up in some areas and the Glacial water has been flushed out a bit further in this case.

9.9.3 Recharge and discharge rates

In Figure 9-39 the vertical Darcy velocity distribution under present-day flow conditions is presented in horizontal slices. As before, the differences in the distribution of the vertical Darcy velocity between the Base Case and the semi-correlated case are very small and localised. There seems to be some more downward directed flow in the eastern part of the modelled area for this case at levels –500 m and below. However, the differences are small and the magnitude of the velocity is the same as for the Base Case throughout the model domain.

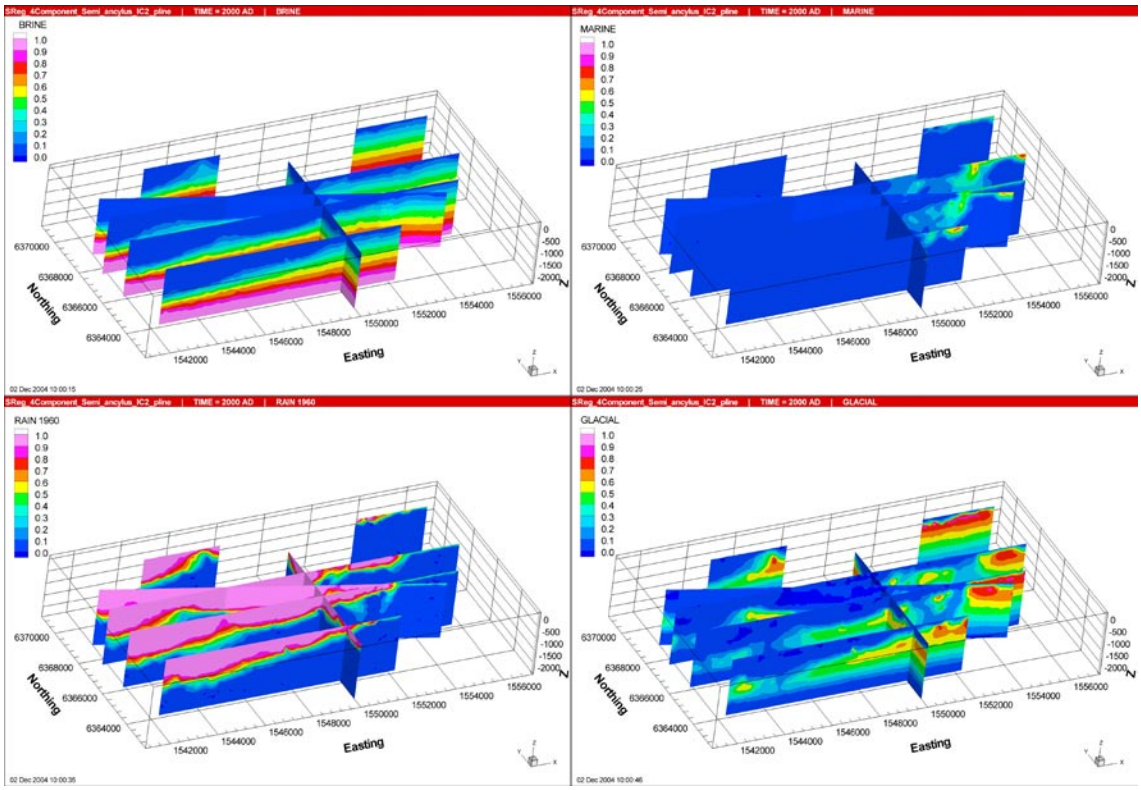

Figure 9-38. *Present-day distribution of the reference waters Brine (top left), Marine water (top right), Rain 1960 (bottom left) and Glacial water (bottom right) in vertical slices, for semi-correlated T model (SReg_4Component_Semi_ IC2).*

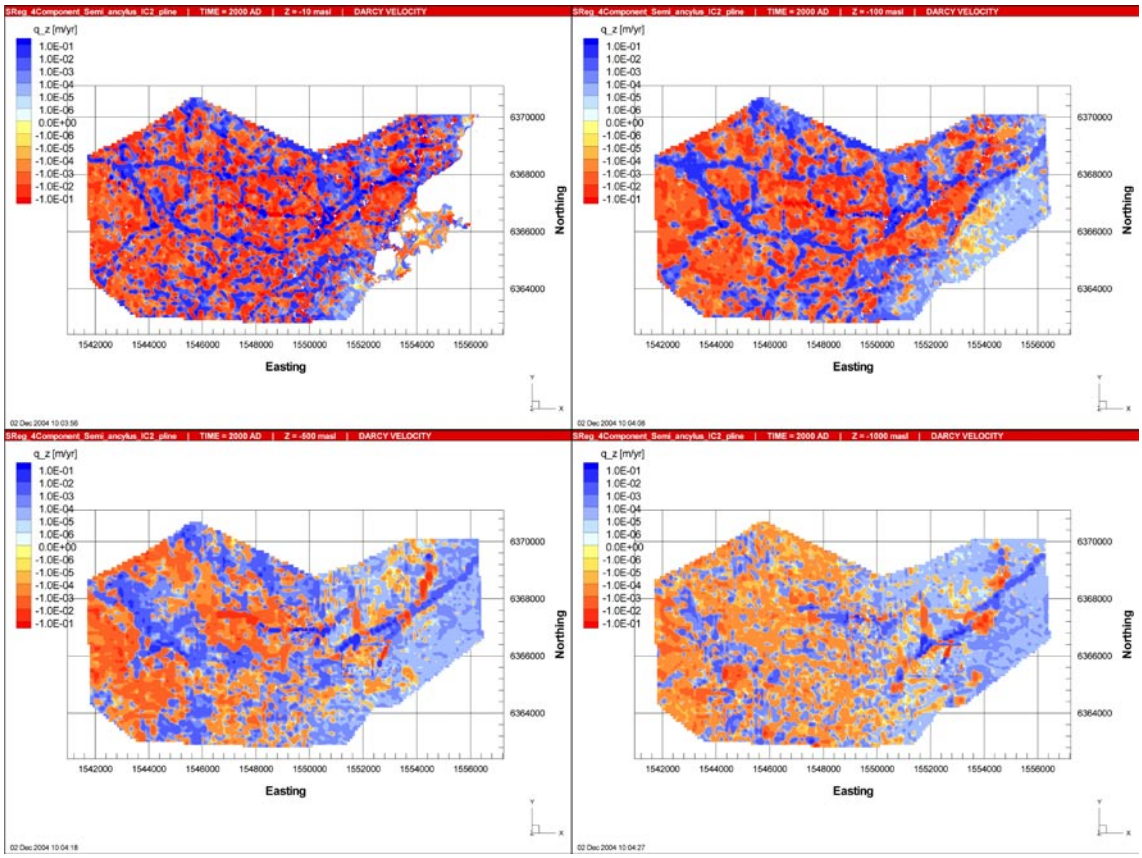

Figure 9-39. *Present-day distribution of the vertical Darcy velocity, q_z, in horizontal slices at elevations (from top to bottom) –10 m, –100 m, –500 m and –1,000 m, for semi-correlated T model (SReg_4Component_Semi_ IC2).*

9.10 HCD Case 2 (SReg_4Component_IFZ2_IC2)

In HCD Case 2 only HCDs with high confidence of existence and those with Length Class 2 and 3 (L > 1,500 m) are modelled.

9.10.1 Flow paths

In Figure 9-40 the distribution of the Log_{10}(F-quotient) at particles starting locations in the local-scale release area for HCD Case 2 is presented. Figure 9-41 presents the F-quotient at particles exit locations in the local-scale area. Red colour indicates smaller F-quotient. The values for the F-quotient are very similar to the Base Case. The same conclusion is made for the exit locations. Clearly the smaller deformation zones (L < 1,500 m) do not have an effect on the regional flow situation.

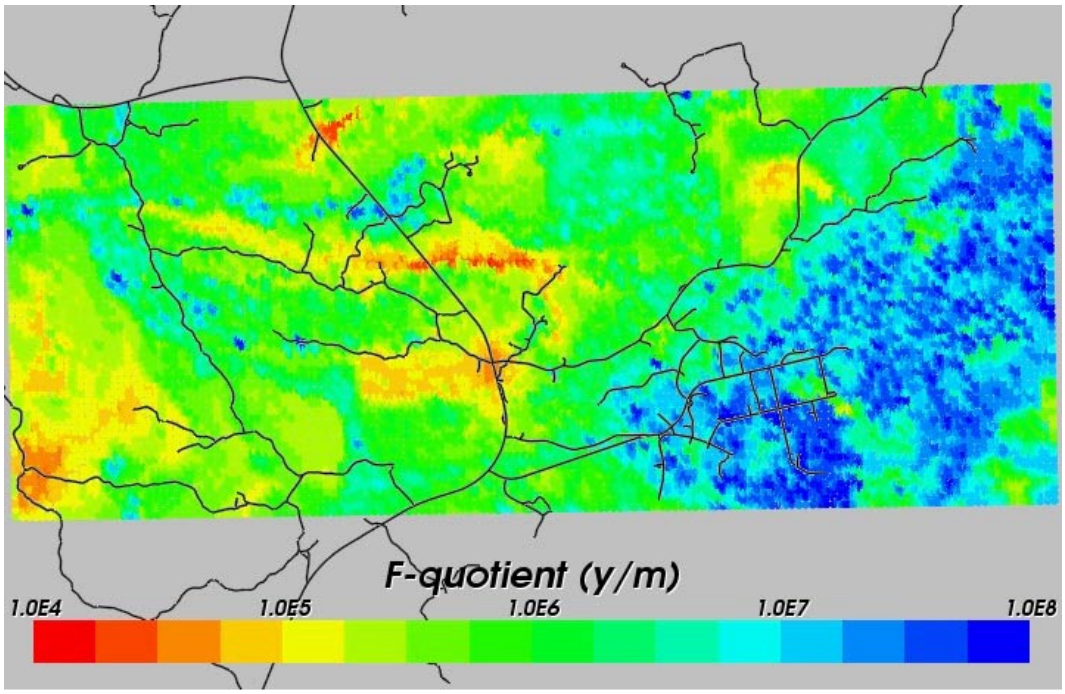

Figure 9-40. *Distribution of F-quotient (Log10) at particles starting locations in the local-scale release area for HCD Case 2 (SReg_4Component_IFZ2_ IC2). Roads are shown in black for context.*

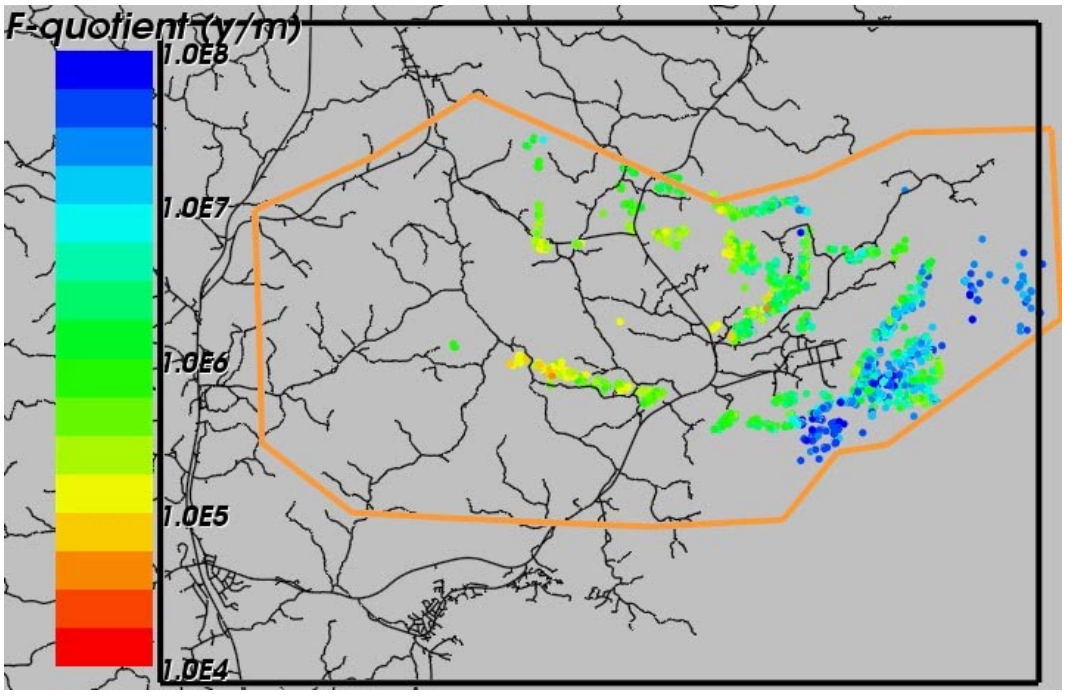

Figure 9-41. *Distribution of F-quotient (Log10) at particles exit locations in the local-scale release area for HCD Case 2 (SReg_4Component_IFZ2_ IC2). Roads are shown in black for context. The small-regional model domain is shown in orange, and the medium regional model domain is black.*

9.10.2 Regional distribution of reference waters

In HCD Case 2 only HCDs with a high confidence of existence and with Length Class 2 and 3 (L > 1,500 m) are modelled. In Figure 9-42, the present-day distributions of the four reference waters Brine, Marine water, Rain 1960 and Glacial water, are presented in vertical slices. It is clear that removing HCD Length Class 1 with lower confidence has little effect on the distribution of the reference waters compared to the Base Case.

9.10.3 Recharge and discharge rates

In Figure 9-43 the vertical Darcy velocity distribution under present-day flow conditions is presented in horizontal slices. Again, the same conclusion must be made as with the reference waters. The differences in the distribution of the vertical Darcy velocity between the Base Case and the HCD Case 2 are very small and localised.

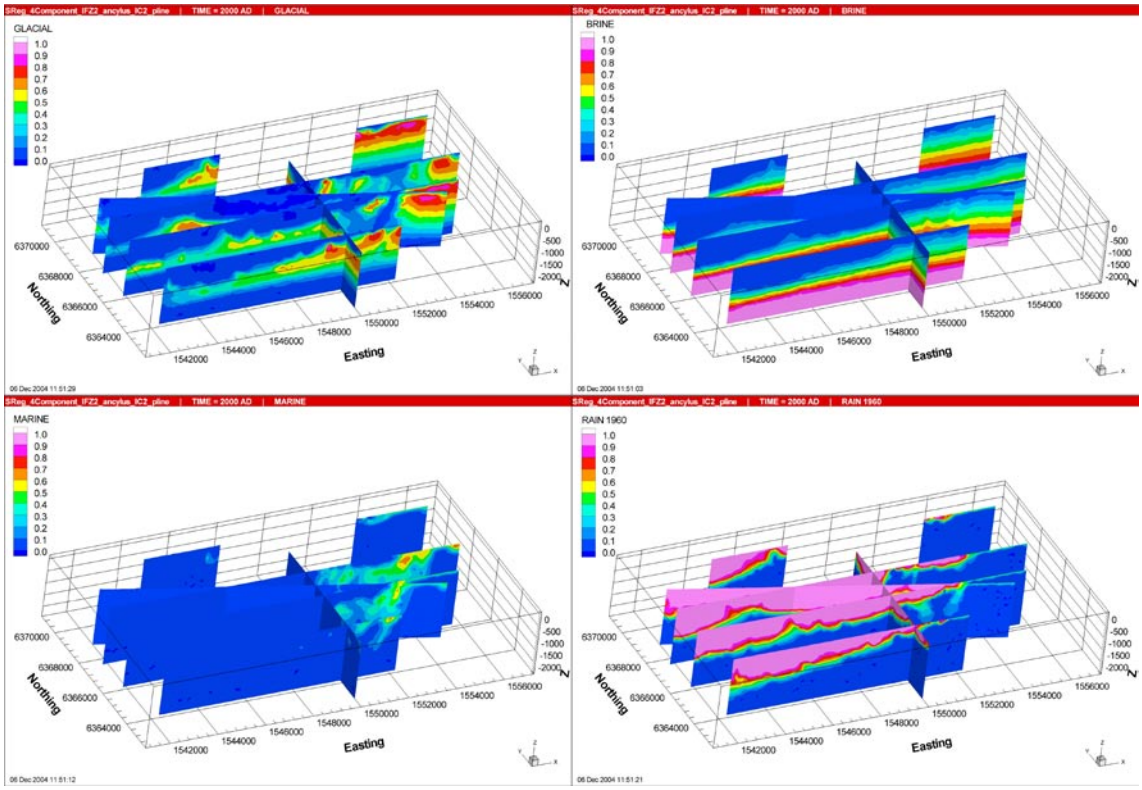

Figure 9-42. *Present-day distribution of the reference waters Brine (top left), Marine water (top right), Rain 1960 (bottom left) and Glacial water (bottom right) in vertical slices, for HCD Case 2 (SReg_4Component_IFZ2_ IC2).*

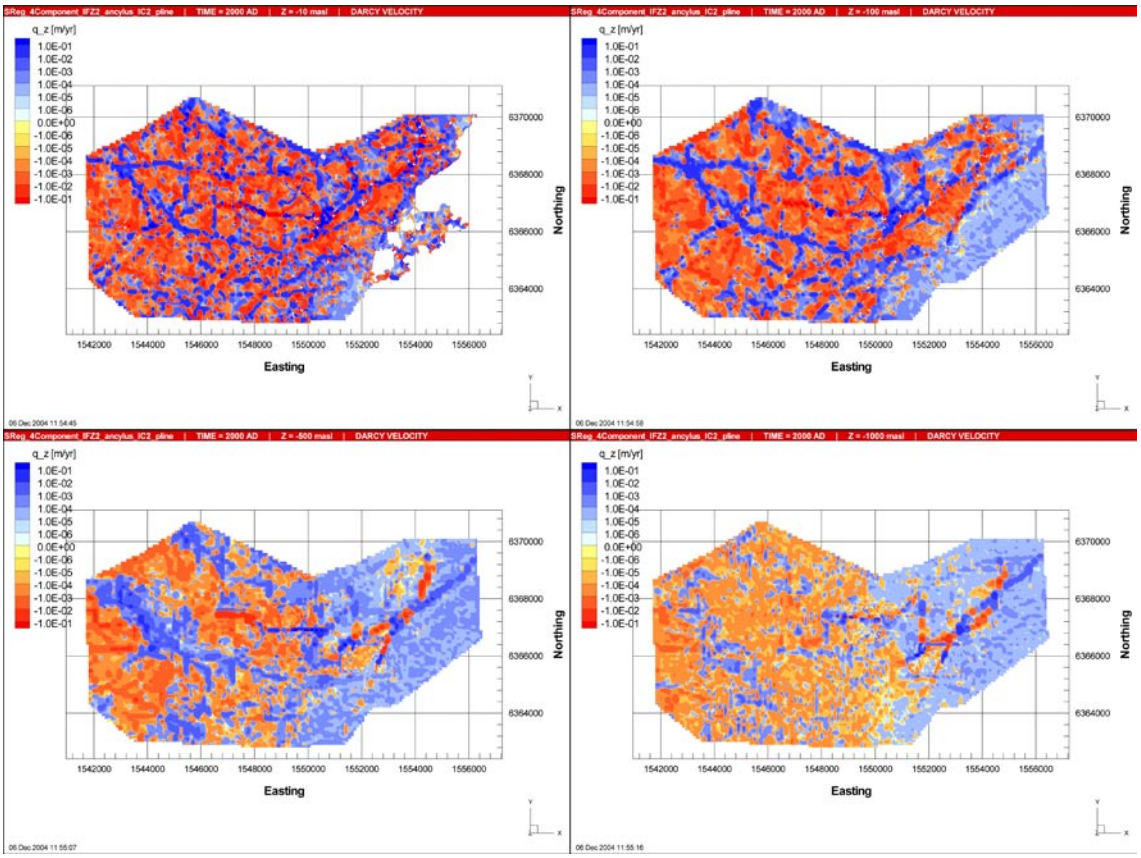

Figure 9-43. *Present-day distribution of the vertical Darcy velocity, q_z, in horizontal slices at elevations (from top to bottom) –10 m, –100 m, –500 m and –1,000 m, for HCD Case 2 (SReg_ 4Component_IFZ2_ IC2).*

9.11 HCD Case 3 (SReg_4Component_IFZ3_IC2)

In HCD Case 3 only HCDs with high confidence of existence and those with Length Class 3 (L > 3,000 m) are modelled.

9.11.1 Flow paths

In Figure 9-44 the distribution of the Log_{10}(F-quotient) at particles starting locations in the local scale area for HCD Case 2 is presented. Figure 9-45 presents the F-quotient at particles exit locations in the local-scale area. Red colour indicates smaller F-quotient. Again, the values for the F-quotient are very similar to the Base Case, with only minor localised differences. The same conclusion is made for the exit locations. Clearly deformation zones shorter than 3,000 m do not have an effect on the regional flow situation. Suggesting it is the highly transmissive large DZs that are responsible for the groundwater flow on the regional-scale.

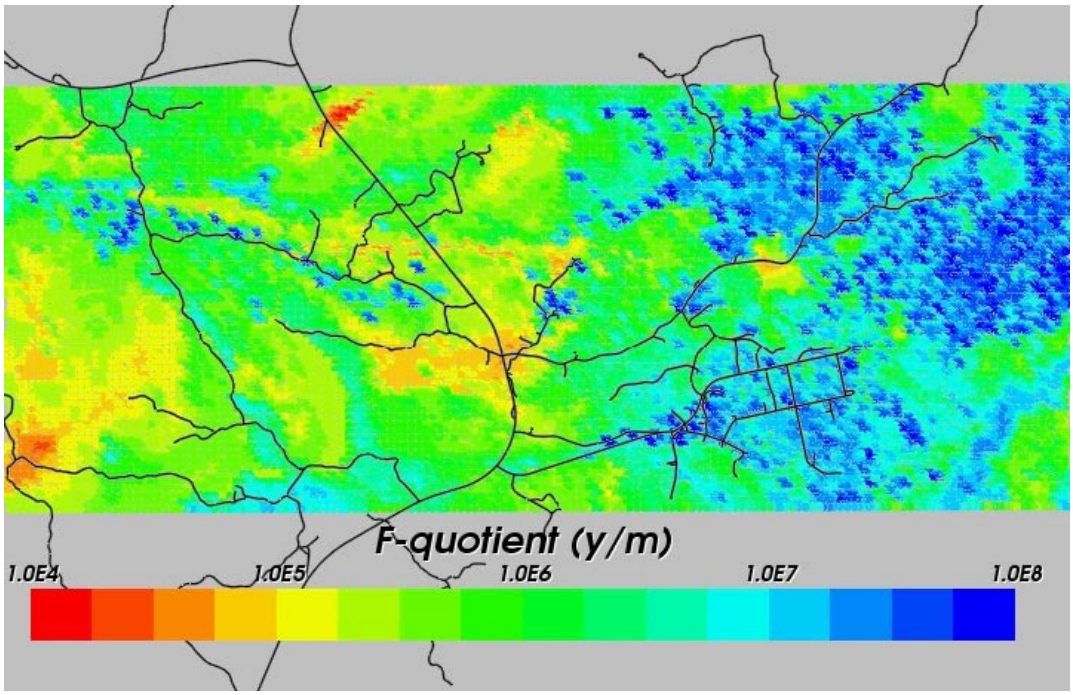

Figure 9-44. *Distribution of F-quotient (Log10) at particles starting locations in the local-scale release area for HCD Case 3 (SReg_4Component_IFZ3_ IC2). Roads are shown in black for context.*

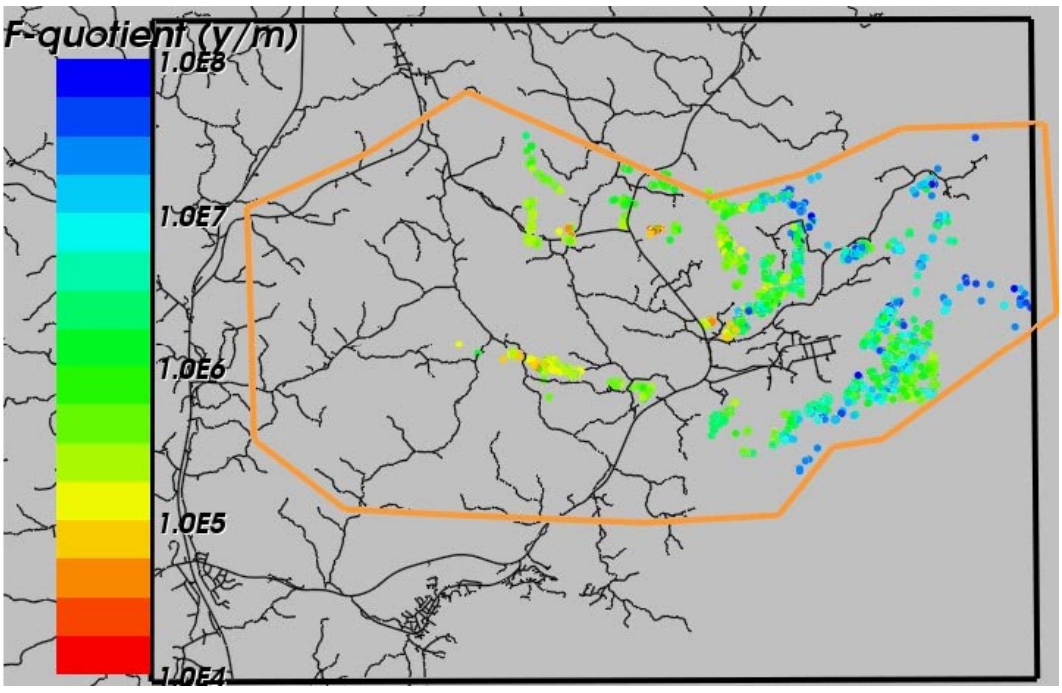

Figure 9-45. *Distribution of F-quotient (Log10) at particles exit locations in the local-scale release area for HCD Case 3 (SReg_4Component_IFZ3_ IC2). Roads are shown in black for context. The small-regional model domain is shown in orange, and the medium regional model domain is black.*

9.11.2 Regional distribution of reference waters

In HCD Case 3 only high confidence of existence HCDs and with Length Class 3 (L > 3,000 m) are modelled. In Figure 9-46, the present-day distributions of the four reference waters Brine, Marine water, Rain 1960 and Glacial water, are presented in vertical slices. Not even removing Length Class 2 from the HCD population had any great impact on the results compared to the Base Case.

9.11.3 Recharge and discharge rates

In Figure 9-47 the vertical Darcy velocity distribution under present-day flow conditions is presented in horizontal slices. Again, the same conclusion must be made as with the reference waters. The differences in the distribution of the vertical Darcy velocity between the Base Case and the HCD Case 3 are very small and localised.

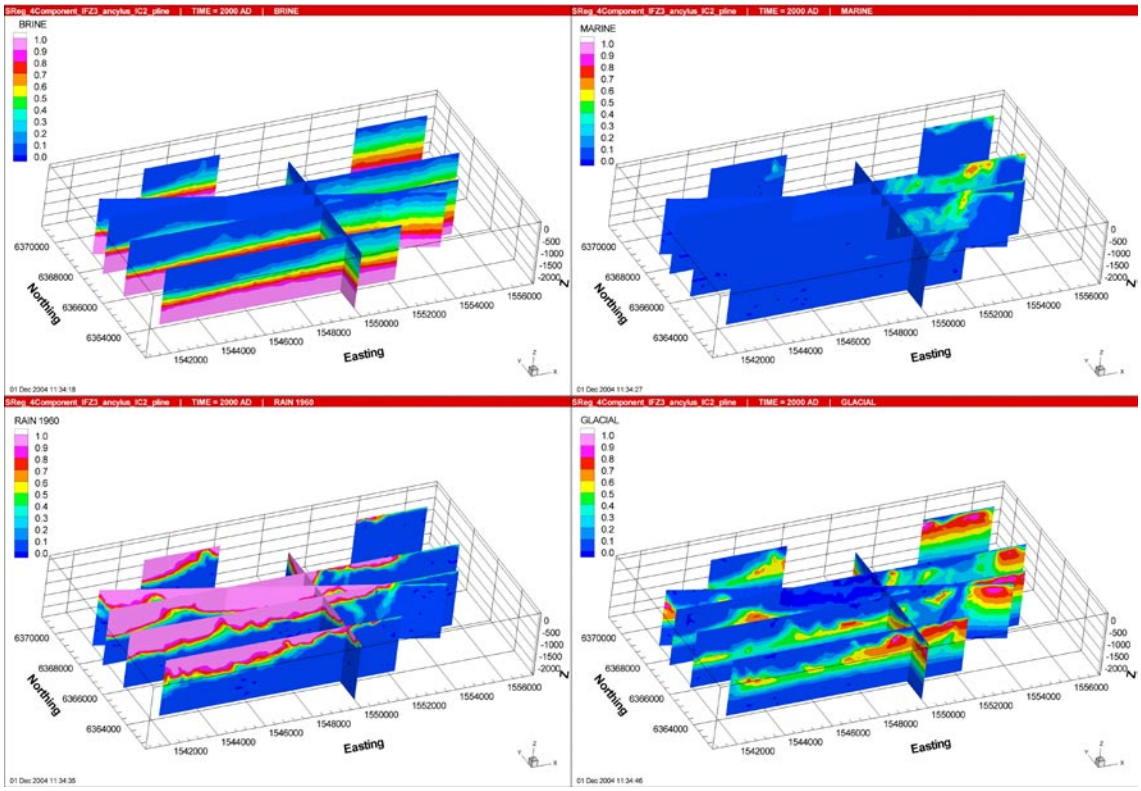

Figure 9-46. *Present-day distribution of the reference waters Brine (top left), Marine water (top right), Rain 1960 (bottom left) and Glacial water (bottom right) in vertical slices, for HCD Case 3 (SReg_4Component_IFZ3_ IC2).*

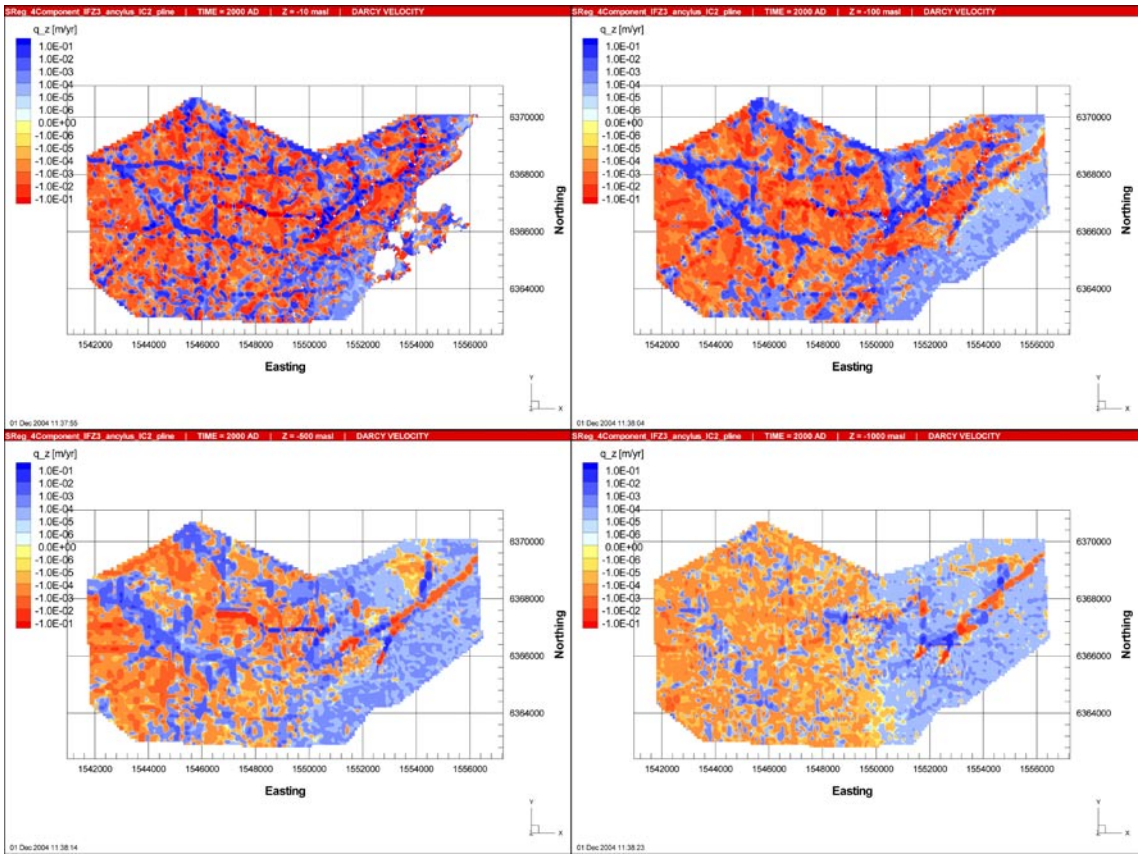

Figure 9-47. *Present-day distribution of the vertical Darcy velocity, q_z, in horizontal slices at elevations (from top to bottom) –10 m, –100 m, –500 m and –1,000 m, for HCD Case 3 (SReg_4Component_IFZ3_ IC2).*

9.12 Reduced hydraulic conductivity at depth (SReg_4Component_DepthK_IC2)

This case uses a hydraulic conductivity that reduces linearly with depth.

9.12.1 Flow paths

In Figure 9-48 the distribution of the Log_{10}(F-quotient) at particles starting locations in the local-scale release area for the case with reduced hydraulic conductivity at depth is presented. Figure 9-49 presents the F-quotient at particles exit locations in the local-scale area. Red colour indicates smaller F-quotient. The distribution of the F-quotient is slightly different from the Base Case. However, the changes are not consistent throughout the local-scale area. Under the Baltic Sea the values are a bit higher in this case whereas some parts of the onshore areas show a decrease in the F-quotient. In general, the changes are very small though. The exit locations are generally unaffected apart from the particles that discharge offshore are a bit more concentrated.

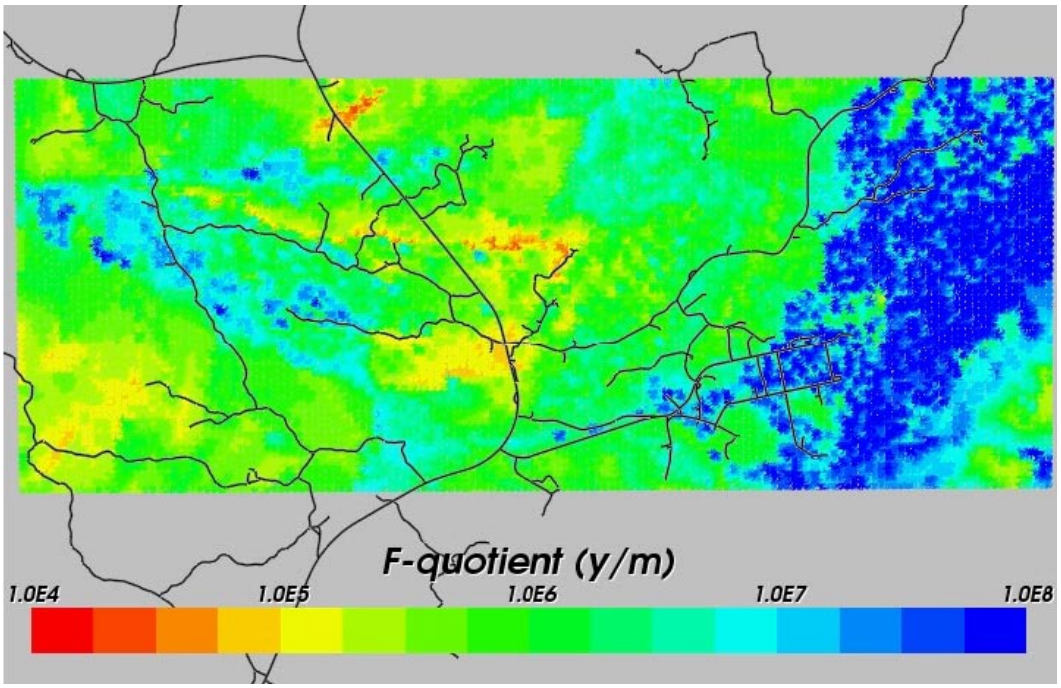

Figure 9-48. *Distribution of F-quotient (Log10) at particles starting locations in the local-scale release area for a lower K at depth (SReg_4Component_DepthK_IC2). Roads are shown in black for context.*

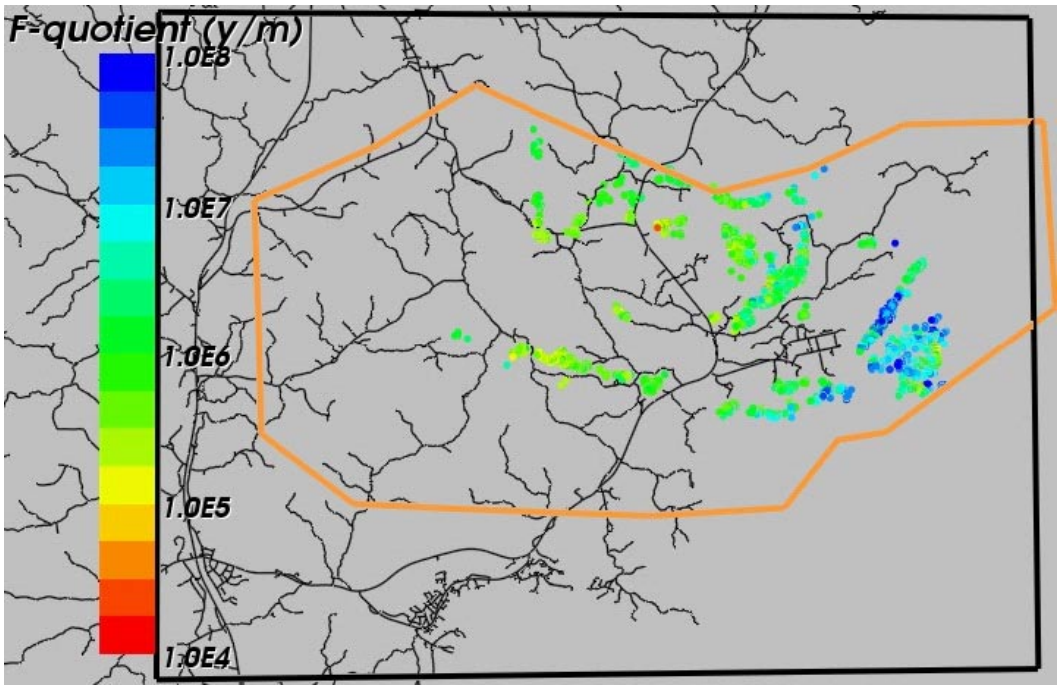

Figure 9-49. *Distribution of F-quotient (Log10) at particles exit locations in the local-scale release area for a lower K at depth (SReg_4Component_DepthK_IC2). Roads are shown in black for context. The small-regional model domain is shown in orange, and the medium regional model domain is black.*

9.12.2 Regional distribution of reference waters

In this case the hydraulic conductivity was reduced linearly at depth. This proved to have a large impact on the results compared to the Base Case. Due to the lower velocities at depth, the Brine stays shallower in the rock. From Figure 9-50 it is clear that the fraction of Brine is lower in the top 1,000 m compared to the Base Case. Correspondingly the fraction of Rain 1960 and Glacial water are higher. However, at –500 m the Glacial water is not as high as in the Base Case indicating that the flow now is shallower.

9.12.3 Recharge and discharge rates

In Figure 9-51 the vertical Darcy velocity distribution under present-day flow conditions is presented in horizontal slices. The magnitude is clearly lower now than in the Base Case. The difference is about one order of magnitude at –1,000 m. Apart from that there are no large differences.

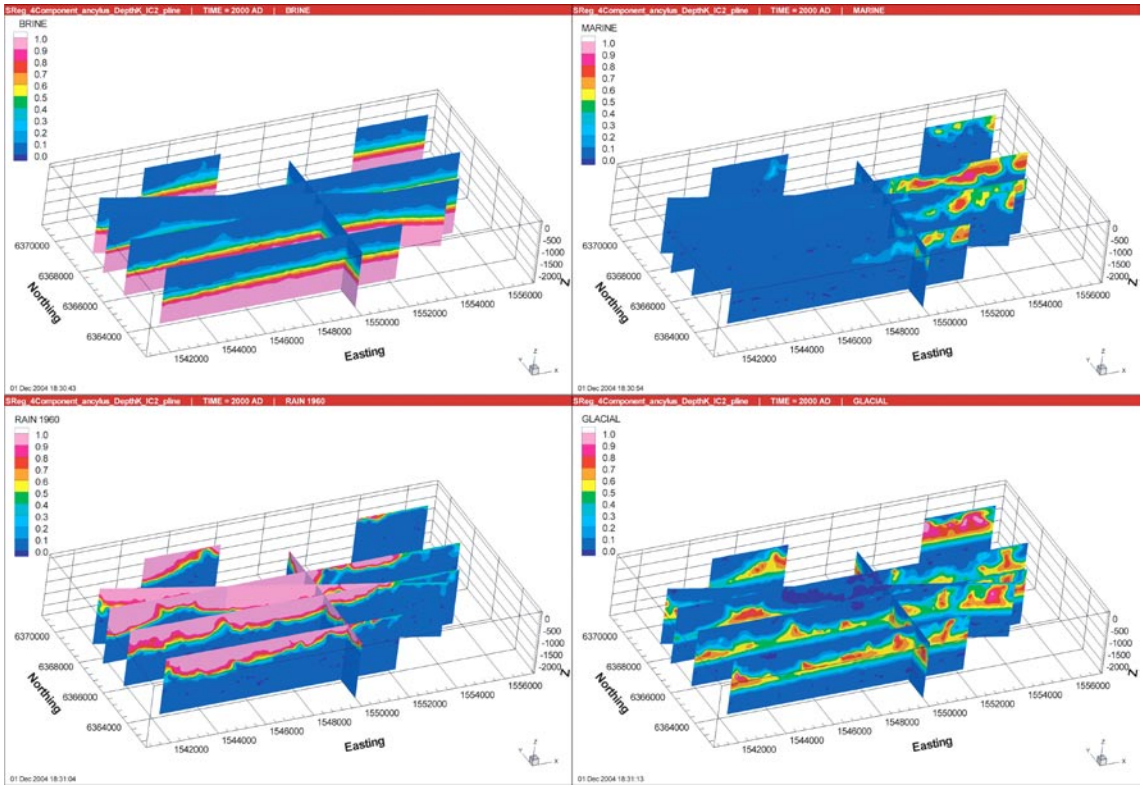

Figure 9-50. *Present-day distribution of the reference waters Brine (top left), Marine water (top right), Rain 1960 (bottom left) and Glacial water (bottom right) in vertical slices, for a lower K at depth (SReg_4Component_DepthK_IC2).*

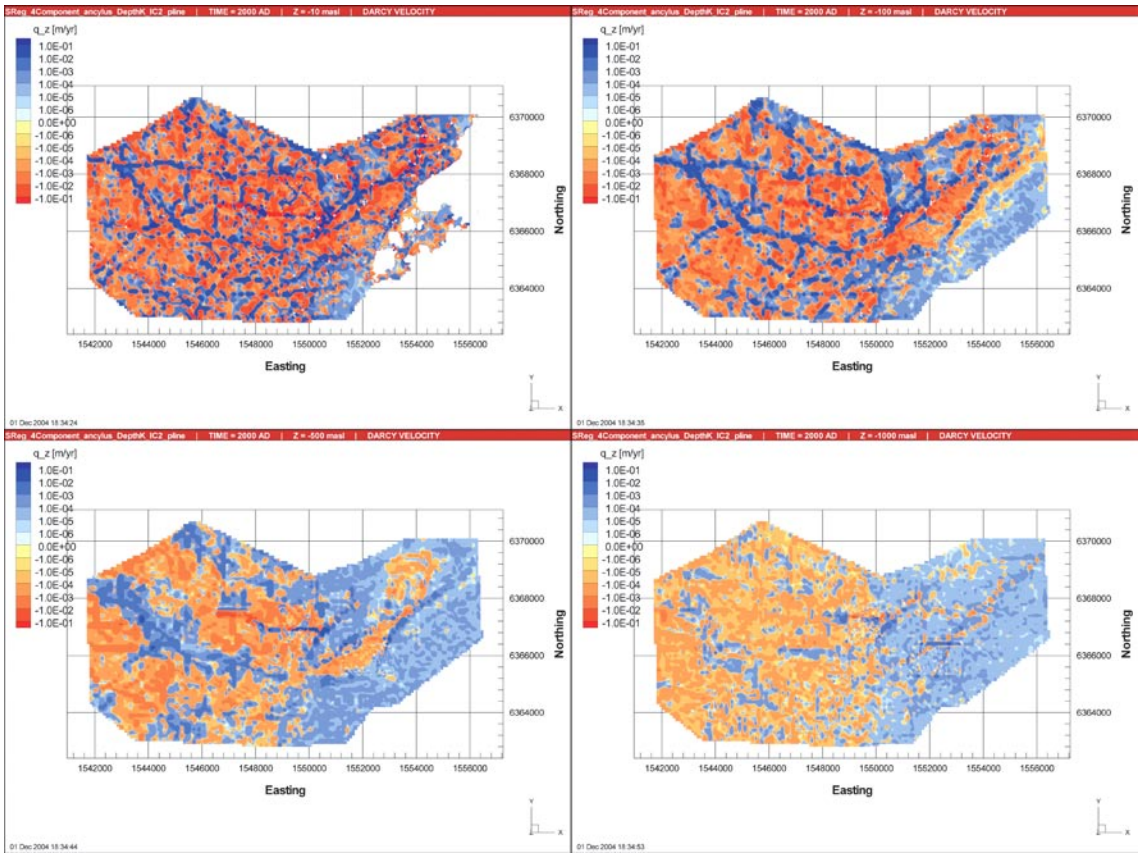

Figure 9-51. *Present-day distribution of the vertical Darcy velocity, q_z, in horizontal slices at elevations (from top to bottom) –10 m, –100 m, –500 m and –1,000 m, for a lower K at depth (SReg_4Component_DepthK_IC2).*

9.13 Increased hydraulic conductivity in top 100 m (SReg_4Component_K100m_IC2)

This case uses an increased hydraulic conductivity in the top 100 m.

9.13.1 Flow paths

In Figure 9-52 the distribution of the Log_{10}(F-quotient) at particles starting locations in the local-scale release area for the case with increased hydraulic conductivity in the top 100 m is presented. Figure 9-53 presents the F-quotient at particles exit locations in the local-scale area. Red colour indicates smaller F-quotient. The results are very similar to the Base Case considering both distribution of F-quotients and exit locations.

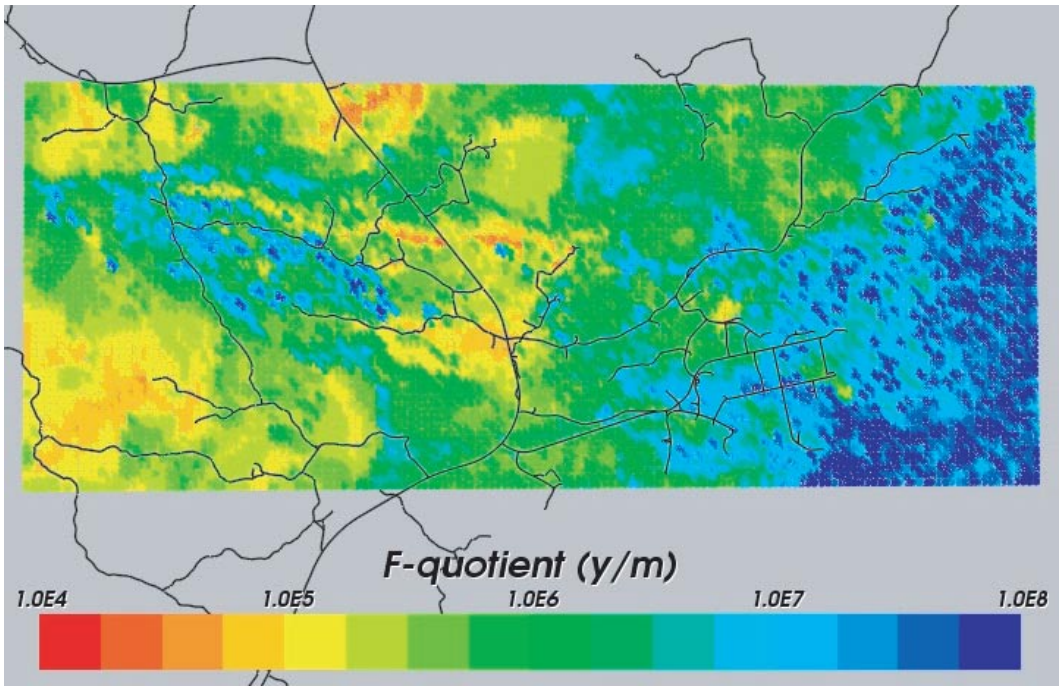

Figure 9-52. *Distribution of F-quotient (Log10) at particles starting locations in the local-scale release area for a higher K in top 100 m (SReg_4Component_K100m_ IC2). Roads are shown in black for context.*

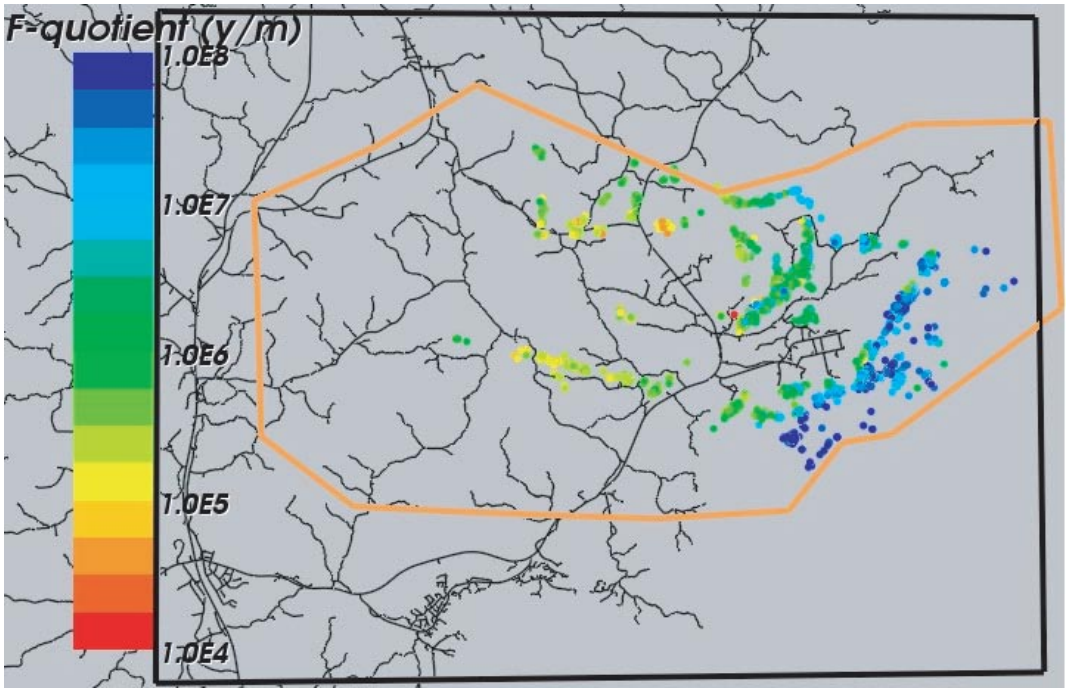

Figure 9-53. *Distribution of F-quotient (Log10) at particles exit locations in the local-scale release area for a higher K in top 100 m (SReg_4Component_K100m_ IC2). Roads are shown in black for context. The small-regional model domain is shown in orange, and the medium regional model domain is black.*

9.13.2 Regional distribution of reference waters

In this case the hydraulic conductivity was increased in the top 100 m. This had an impact on the top layers where more Rain 1960 water and Marine water now can be found on the expense of Glacial water that has been flushed out due to the higher velocities in the upper parts of the rock. Below –100 m there are no significant changes compared to the Base Case (see Figure 9-54).

9.13.3 Recharge and discharge rates

In Figure 9-55 the vertical Darcy velocity distribution under present-day flow conditions is presented in horizontal slices. The magnitude of the vertical Darcy velocity is slightly higher in the top 100 m in this case compared to the Base Case even if the differences are small. Apart from that, the flow appears generally the same as for the Base Case.

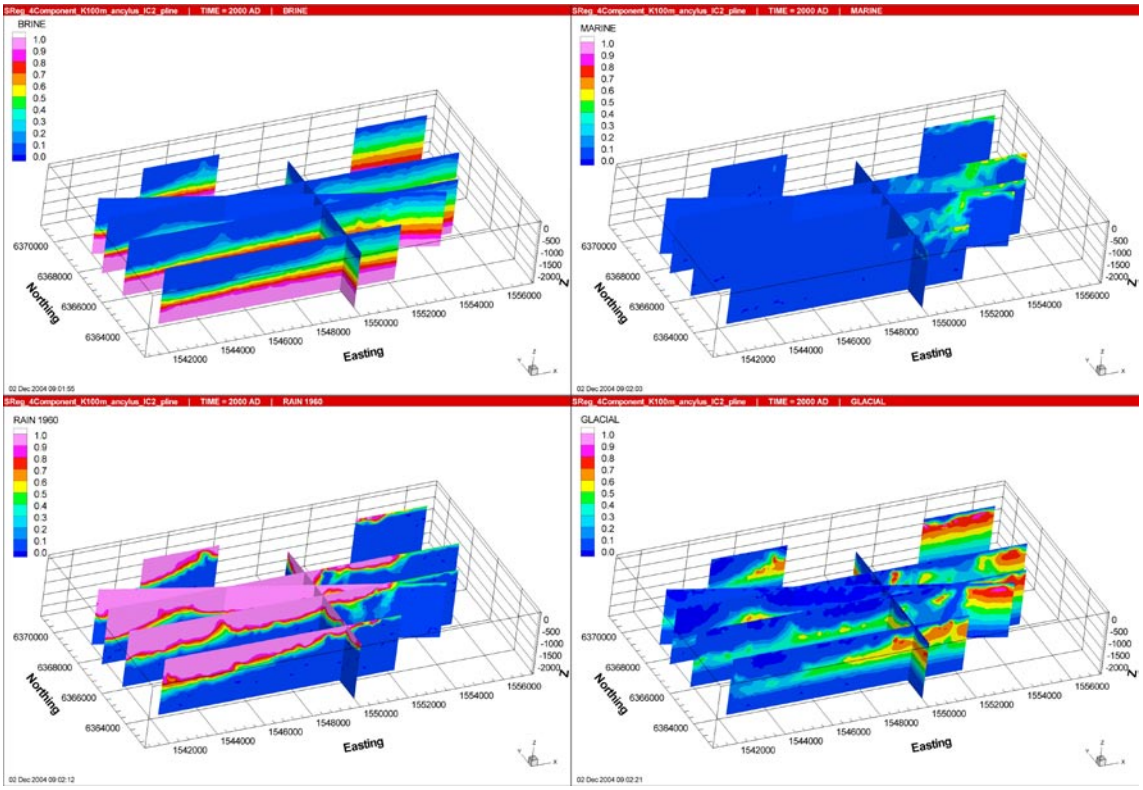

Figure 9-54. *Present-day distribution of the reference waters Brine (top left), Marine water (top right), Rain 1960 (bottom left) and Glacial water (bottom right) in vertical slices, for a higher K in top 100 m (SReg_4Component_K100m_ IC2).*

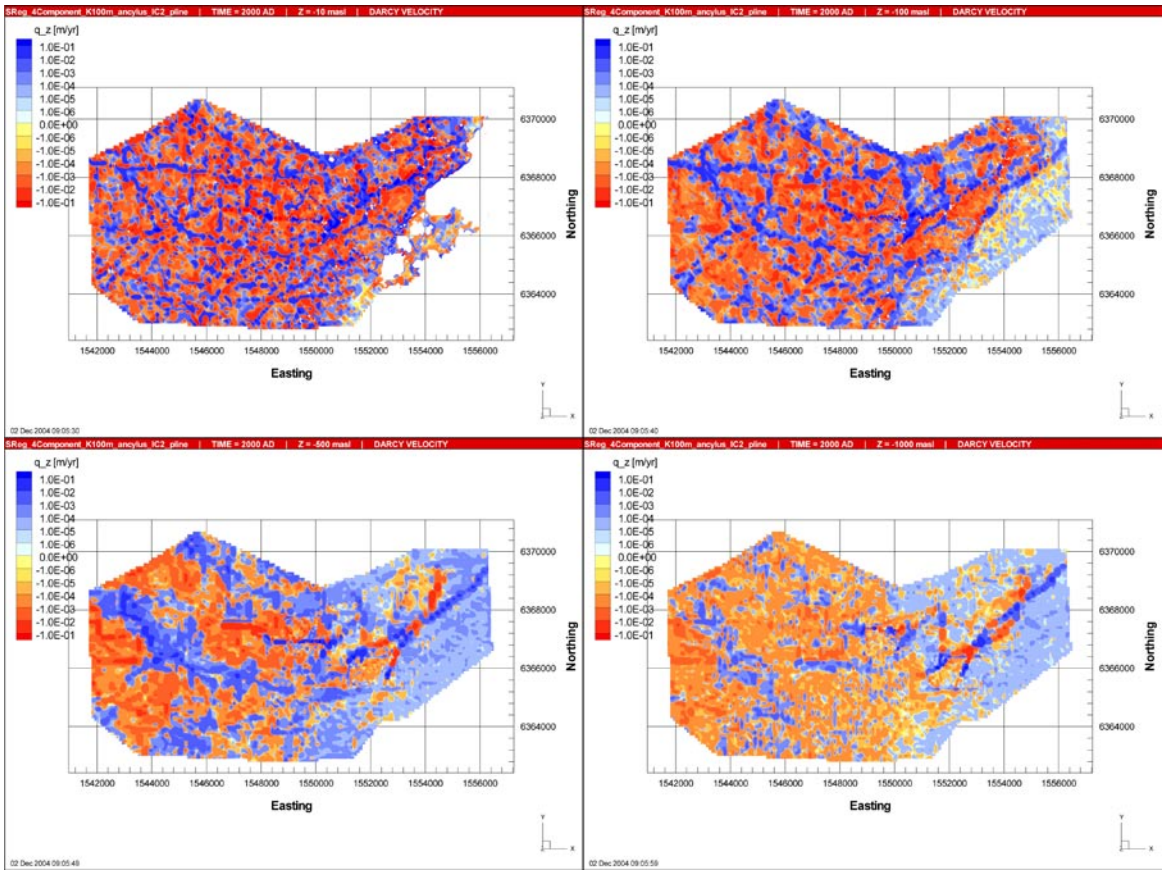

Figure 9-55. *Present-day distribution of the vertical Darcy velocity, q_z, in horizontal slices at elevations (from top to bottom) –10 m, –100 m, –500 m and –1,000 m, for a lower K at depth (SReg_4Component_DepthK_ IC2).*

9.14 Conclusions

Generally the sensitivity study shows that the model is not very sensitive to the changes considered. The distributions of the four reference waters and the vertical Darcy velocity are affected little in the different cases compared to the Base Case.

There are however a few parameters that clearly have significant effect on the results:

- Using a more shallow initial condition (IC1) where there is a linear transition between full Glacial at –500 and full Brine at –1,000 m. Because the Brine is present higher up in the rock from the start it is also found there to a higher degree at present-day compared to the Base Case.
- Uncorrelated transmissivity gives less slightly less mixing of the reference waters since it corresponds to a lower hydraulic conductivity on the 100 m block scale. The differences in the current borehole hydro-geochemistry predictions are not sufficient to rule out this case though.
- Decreasing K with depth. Even a small decrease in K (a factor 5) significantly changes the flow distribution. Due to the decrease in Darcy velocities, the Brine now stays deeper in model and the flow is shallower.

It shouldn't be concluded that the model is insensitive to all parameters. Rather we have found that quite specific reference water initial and boundary conditions are needed to achieve match, so there is little point retaining variants as alternatives if they do not calibrate. In terms of the hydraulic conductivity, the sensitivity is small to the variants considered, but then these have all been conditioned on the hydraulic data at the borehole, so it just confirms that the DFN properties reflect the site. Most parameters did not need to be changed from the initial values specified in the Task Description. An exception was the kinemeatic porosity of the HCD that needed to be modified significantly from the initial guess, increased by factor 10 from the HCD definition.

The variants considered for the HCD model just removed shorter or lower confidence zones. This produced little effect. However, this result may just be a consequence that all low confidence zones are assigned a median hydraulic conductivity that is not sufficient to have a great impact on regional groundwater flow. The model would probably become much more sensitive to the HCD model if the hydraulic properties of DZs were sampled stochastically from a distribution, but of course this would require many realisations.

The transport pathway studies suggest discharge areas are strongly linked to the HCD structures including the eastern end of ZSMEW007A in the centre of the local-scale area, ZSMEW004A in the south around the shore, and ZSMEW013A just north of Simpevarp. The F-quotient for most of the local-scale area is of order 10^6 yr/m, with lower values (10^4 to 10^5 yr/m) around the zone ZSMNE040A.

10 Discussion and general conclusions

10.1 Summary of main conclusions and feedback to other disciplines

From the Hydro-DFN study:

- A new methodology has been developed for integrating the PFL and PSS hydraulic data with the geological fracture interpretation to produce a conditioned Hydro-DFN model and to quantify the uncertainties to various assumptions. This methodology uses flow simulations in DFN models to calibrate several alternative relationships between fracture transmissivity and length.
- It is possible to calibrate several possible models for fracture transmissivity, although the direct correlation between transmissivity and length is perhaps easier to match to the borehole flow data.
- The GeoDFN model as delivered had several ambiguities that were hard to understand and hence required additional work to reproduce a DFN model that reflected the fracture statistics seen in the boreholes. These include: the threshold for splitting the sub-vertical and sub-horizontal sets; how the borehole and outcrop data has been combined; the basis for choosing the length distribution, especially for the sub-horizontal set; whether the length distributions chosen are continuous with the HCD model; how the Terzaghi correction has been implemented for calculating corrected fracture intensities.
- Using the PSS data to further calibrate the Hydro-DFN model beyond just the PFL anomaly actually helped narrow some uncertainties. This is primarily because it has a lower detection limit, so it was possible to eliminate some possibilities such as there being many small conductive fractures with transmissivities around 10^{-9} m^2/s that may effect the background flow and transport properties such as flow-wetted surface. The additional calibration helped narrow the range of uncertainties in the both $P32_c$ for open connected fractures and the transmissivity distribution.
- For a 100 m block the median Log (K_{eff}) is –8.2 for the correlated case, –8.9 for the uncorrelated case and –8.6 for the semi-correlated case.
- The correlated model gives greater heterogeneity of the hydraulic conductivity, but also a greater spatial correlation between blocks associated with large stochastic deformation zones.
- There is localised horizontal anisotropy within a block for all cases due to the discrete nature of the DFN. The median horizontal anisotropy Khmax/Khmin is about 2–3. For the uncorrelated model there is no regional trend to the anisotropy. Whereas for the correlated and semi-correlated case there is a clear trend toward higher Khmax in the direction with strike about 90°–130°. This is consistent with the orientations of PFL flow anomalies seen in KSH01A and KSH02. The fact that the direction of flow in the correlated case is more consistent with the PFL anomaly data compared to the uncorrelated case may add credence to the existence of a correlation between transmissivity and length. There is a regional anisotropy between the horizontal and vertical hydraulic conductivity with median ratio Khmax/Kz of about 2.5 to 3.
- Fracture porosity has a median of Log (phi) = –4.8 for a 100 m block. For the correlated case it does not have a strong dependence on L_{min}, but does for the uncorrelated case.

- Little bias is introduced whether the models is based on the PSS data from KLX01 or the combined PFL/PSS data from the Simpevarp boreholes KSH01A, KSH2 and KSH03A. The median hydraulic conductivities are very similar, but there is less variability for the KLX01 case, i.e. it is more homogeneous.
- The block-scale properties based on the Darcy Tools Team (DT) and CONNECTFLOW Team (CF) are consistent in terms of median value and variability, although the DT properties are more isotropic.

From the regional flow modelling and calibration against hydro-geochemistry:

- The minimum domain size is the Small-regional domain ~14 km (E-W) by 7 km (N-S) for reference water calculation for site areas. This is larger than model domain suggested by sensitivity analysis of groundwater pathways by the DarcyTools Team in the Version S1.1 modelling. It is thought this is due to the much greater emphasis of the sub-horizontal fracture set in the Version S1.2 Hydro-DFN giving rise to longer horizontal flow paths.
- Glacial water injected under high pressures down to about 700 m–1.5 km during early post-glacial period.
- Large Glacial water composition in early freshwater in the Baltic Lake, Yoldia Sea and Ancylus Lake periods.
- A variant with a specified potential infiltration has been investigated. For the base case parameters this gave almost identical results to the case where the watertable is specified to be at ground surface suggesting this is a reasonable approximation or this area of low topographic height.
- The Hydro-DFN properties give block-scale hydraulic conductivities of the correct order of magnitude to predict hydro-geochemistry.
- Smaller, low confidence zones have limited effect on regional-scale flows, but do affect hydro-geochemistry local to individual boreholes.
- This suggests one can use hydro-geochemistry to confirm extent and properties of individual zones locally.
- Reducing hydraulic conductivity at depth may give a better hydro-geochemistry match, but the average hydraulic conductivity from the Hydro-DFN needs to be conserved. However, quite moderate changes have an impact, so the depth decrease should only be a factor < 10.
- Calibrating the HSD properties requires a flux boundary condition to be considered.
- Generally the sensitivity study shows that the model is not very sensitive to the changes considered. The distributions of the four reference waters and the vertical Darcy velocity are affected little in the different cases compared to the Base Case.
- The only cases that appeared sensitive were: Using a more shallow initial condition for Brine; an uncorrelated transmissivity; having a gradual reduction in hydraulic conductivity with depth.
- The seeming lack of sensitivity is partly a result of the conditioning of the models against both hydraulic and hydro-geochemical information that appears to give a range of parameter uncertainties that do not impact the regional flow results significantly.
- The variants considered for the HCD model just removed shorter or lower confidence zones. This produced little effect. However, this result may just be a consequence that all low confidence zones are assigned a median hydraulic conductivity that is not sufficient to have a great impact on regional groundwater flow. The model would probably become much more sensitive to the HCD model if the hydraulic properties of DZs were sampled stochastically from a distribution, but of course this would require many realizations.

- Also the HCD model contained more DZs in the local-scale area presumably due to higher confidence data. This gives a misleading impression of the geology. A more spatial consistent HCD model should be constructed or stochastic DZs should be added away from the site areas to a give a more consistent and realistic HCD model.
- The use of data for tritium does indeed have the potential to help constrain and check a groundwater flow model. However, in order for the data to provide useful information, it is necessary to have a fair number of good quality measurements down a number of boreholes. The measurements need to have low detection levels, and small errors relative to the expected levels (of order a few TU). Care needs to be taken to ensure uncontaminated samples. Measurements need to be taken down to depths of as much as a kilometre or more, particularly in the vicinity of transmissive features. A sensitivity analysis on the flow-wetted surface suggests that a lower value of $a_r = 0.5$ m^2/m^3 may give an improved match than the value used in the Base Case (2.0 m^2/m^3).

A series of transport calculations were performed for each of the varaints considered to provide guidance for the Preliminary Safety Evaluation (PSE). These results are reported in Appendix B as plots and tables of statistics. Based on these results the following conclusions are drawn.

- The transport pathway studies suggest discharge areas are strongly linked to the HCD structures including the eastern end of ZSMEW007A in the centre of the local-scale area, ZSMEW004A in the south around the shore, and ZSMEW013A just north of Simpevarp. The F-quotient for most of the local-scale area is of order 10^6 yr/m, with lower values (10^4 to 10^5 yr/m) around the zone ZSMNE040A.
- The Simpevarp and Laxemar release areas show quite different statistics. The medians of both t_w and F are about one order of magnitude higher for the Simpevarp release area than for Laxemar release area. Correspondingly the median of q_c is about one order of magnitude lower in Simpevarp. This indicates the effects of differences in the local structural model (i.e. stochastic and deterministic fracture zones); and the positions relative to the regional hydrogeology with Laxemar being largely freshwater at 500 m depth, and Simpevarp having reduced flows due to the presence of salinity at 500 m depth.
- The variations in the performance measures between the variants considered is generally low, around 10%. This perhaps should not be a surprise since all the cases considered have been calibrated against the same hydraulic data in the case of the Hydro-DFN variants, and against the same hydro-geochemistry data in the case of regional flow and solute transport.

10.2 Conclusions and recommendations for further investigations and simulations

10.2.1 Recommendations for further simulations

Important issues that should be addressed in future studies include:

- Performing more detailed DFN flow simulations of the PSS tests to consider the transient response and flow geometry more explicitly.
- Modelling the transport of the major ions explicitly rather than interpreted mixing fractions and calibrating these against the measured ion concentrations from the boreholes. This will quantify the uncertainties associated with calibrating the model against the raw hydro-geochemistry data as opposed to the interpreted M3 mixing fractions.

- Only the Oxygen and hydrogen stable-isotope ratios have been used in this study since they can reasonably be assumed to be conservative. Tritium and Carbon-14 should also be considered as additional tracer as they may indicate flows on different time-scales, although radioactive decay and rock interactions would have to be represented
- A number of issues relating to the HCD model are outstanding. Firstly, the geometric properties (dips and thickness), and hydraulic properties (transmissivities) should be sampled stochastically. Secondly, there should be a more consistent spatial distribution of DZs to avoid the problem of having more DZs in the site area simply because of higher detection confidence. Away from the site area, stochastic DZs should be generated to supplement the regional HCD model.
- Simulations with a flux based boundary condition should be used to calibrate the near surface hydrology and quantify the uncertainty to the top surface flow boundary condition. This is non-trivial for a transient situation with land-rise and marine transgressions on the regional-scale since the areas of recharge and discharge will evolve.

10.2.2 Recommendations for further investigations

This study has suggested some issues on which to focus further acquisition of site data:

- The PSS data helped reduce uncertainty in the intensity of flowing features and the low end of the transmissivity distribution. This may be particularly useful for understanding flows on the canister-scale in safety assessment calculations.
- The hydro-geochemistry data in the Simpevarp sub-area shows indicates each reference water type is present above 600–700 m elevation, and hence this depth of data samples is probably adequate in the near coastal area. However, in the Laxemar sub-area the mixing zone is deeper and probably requires data down to 1 km to capture the reference water mixing and hence aid the calibration of groundwater models.
- The models of the reference water transport suggest some pockets of Glacial inland and Marine near the coast. This motivates an integration of the borehole location selection and the groundwater modelling to confirm some of model predictions.
- The groundwater model calibration has suggested that groundwater chemistry in the fracture system should be similar to that in the matrix. This is useful information since it suggests groundwater infiltrates a network of small but connected fractures that give access to significant matrix diffusion, and hence potential retardation of radionuclides in the host rock. Experiments would be useful to verify this finding.

References

1 **SKB, 2001.** Site Investigations. Investigation methods and general execution programme, SKB TR-01-29. Svensk Kärnbränslehantering AB.

2 **SKB, 2000.** Geoscientific programme for investigation and evaluation of sites for the deep repository. SKB report TR-00-20. Svensk Kärnbränslehantering AB.

3 **Andersson J, 2003.** Site descriptive modelling – strategy for integrated evaluation. SKB R-03-05. Svensk Kärnbränslehantering AB.

4 **Winberg A, 2004.** Preliminary site description: Simpevarp area – version 1.1, SKB R-04-25. Svensk Kärnbränslehantering AB.

5 **Hartley L J, Holton D, 2003.** CONNECTFLOW (Release 2.0) Technical Summary Document. SERCO/ERRA-C/TSD02V1.

6 **Hartley L J, Hoch A R, Cliffe K A C, Jackson C P, Holton D, 2003.** NAMMU (Release 7.2) Technical Summary Document. SERCO/ERRA-NM/TSD02V1.

7 **Hartley L J, Holton D, Hoch A R, 2003.** NAPSAC (Release 4.4) Technical Summary Document. SERCO/ERRA-N/TSD02V1.

8 **La Pointe P R, Wallmann P, Follin S, 1995.** Estimation of effective block conductivities based on discrete network analyses using data from the Äspö Site, Tech. Rep. TR 95-15. Svensk Kärnbränslehantering AB.

9 **Jackson C P, Hoch A R, Todman S, 2000.** Self-consistency of a heterogeneous continuum porous medium representation of a fractured medium. WATER RESOURCES RESEARCH, Vol. 36, No. 1, p 189–202.

10 **Marsic N, Hartley L, Jackson P, Poole M, Morvik A, 2001.** Development of hydrogeological modelling tools based on NAMMU, SKB R-01-49 (2001). Svensk Kärnbränslehantering AB.

11 **Hoch A R, Jackson C P, 2004.** Rock-matrix Diffusion in Transport of Salinity. Implementation in CONNECTFLOW. SKB R-04-78. Svensk Kärnbränslehantering AB.

12 **Carrera J, Sanchez-Vila X, Benet I, Medina A, Galarza G, Guimera J, 1998.** On Matrix Diffusion: Formulations, Solution Methods and Quantitative Effects, Hydrogeology Journal, 6, 1, p 178–190, (1998).

13 **Hartley L, Holton D, Hunter F, 2004.** Hydro-DFN modelling using CONNECTFLOW for Pre-1.2 data, SKB report PIR-04-18, (2004). Svensk Kärnbränslehantering AB.

14 **Darcel C, Davy P, Bour O, De Dreuzy J-R, 2004.** Alternative DFN model based on initial site investigations at Simpevarp, SKB R-04-76. Svensk Kärnbränslehantering AB.

15 **Dershowitz W, Winberg A, Hermanson J, Byegård J, Tullborg E-L, Andersson P, Mazurek M, 2003.** Äspö Hard Rock Laboratory. Äspö Task Force on modelling of groundwater flow and transport of solutes – Task 6C – A semi-synthetic model of block scale conductive structures at the Äspö HRL. SKB IPR-03-13. Svensk Kärnbränslehantering AB.

16 **Rhén I, 2004.** Personal communication, September (2004).

17 **Laaksoharju M et al. 2004.** Hydrogeochemical evaluation of the Simpevarp area, model version 1.2, SKB R-04-74, (2004). Svensk Kärnbränslehantering AB.

18 **Laaksoharju M et al. 2004.** Hydrogeochemical evaluation of the Simpevarp area, model version 1.1. SKB R-04-16 (2004). Svensk Kärnbränslehantering AB.

19 **Adams J J, Bachu S, 2002.** Equations of state for basin geofluids: algorithm review and intercomparison for brines, (2002), Geofluids, 2, 257–271.

20 **Kestin J, Khalifa H E, Correia R J, 1981.** Tables of dynamic and kinematic viscosity of aqueous NaCl solutions in the temperature range 20–150°C and the pressure range 0.1–35 MPa, (1981), J.Phys. Chem. Ref. Data Vol 10, No 1.

21 **Hartley L, Worth D, Gylling B, Marsic N, Holmen J, 2004.** Preliminary site description: Groundwater flow simulations. Simpevarp area (version 1.1) modelled with CONNECTFLOW. SKB R-04-63. Svensk Kärnbränslehantering AB.

22 **HCDs for Äspö HRL, 1997.** SKB report TR-97-06 (1997).

23 **Knutsson G, Morfeldt C-O, 2002.** Grundvatten, teori & tillämpning, AB Svensk Byggtjänst, Stockholm (2002). (In Swedish).

24 **Carlsson L, Gustafson G, 1997.** Provpumpning som geohydrologisk undersökningsmetodik (ver 2.1), Chalmers Tekniska Högskola, Geologiska institutionen, Publ C62. (In Swedish).

Appendix A

Glossary of abbreviations

BGNE – background north-east fracture set
BGNS – background north-south fracture set
BGNW – background north-west fracture set
BGHZ – background horizontal fracture set
DFN – discrete fracture network
DZ – deformation zone
DT – DarcyTools
EPM – equivalent porous medium
GWF – groundwater flow
HCD – hydraulic conductor domains
HRD – hydraulic rock domains
HSD – hydraulic surface domains
IC – initial condition
IFZ – implicit fracture zone
K – hydraulic conductivity
KAV – cored borehole at Ävrö
KAS – cored borehole at Äspö
KLX – cored borehole at Laxemar
KSH – cored borehole at Simpevarp
M3 – mixing and mass-balance modelling
P10 – linear fracture intensity: number of fractures per metre along a borehole
P21 – area fracture intensity: total fracture lengths per square metre of outcrop
P32 – volumetric fracture intensity: total fracture surface area per cubic metre of rock
PFL – Posiva flow-log
PSE – preliminary safety evaluation
PSS – Pipe-string system
TDS – total dissolved solids
TU – tritium units

Appendix B

Description of transport properties of the present-day flow paths

B.1 Methodology

The general approach to characterising transport properties is to track particles advected by the present-day flow-field and to record the initial Darcy-velocity (canister flux), travel time and F-quotient (See Section 2.1.6). The particles are released within a rectangle corresponding to the local-scale, Simpevarp or Laxemar release area s at –500 m elevation and with a spacing of 50 m. Statistics are given as percentiles and the first four moments (Mean, Variance, Skewness and Kurtosis) to measure the shape of the distributions rather just assume they are symmetric Gaussian.

B.2 Base case (SReg_4Component_IC2)

In Figure B-1 to Figure B-6 the statistical results for the Base Case are shown as scatter plots and histograms for the four calculated performance measures travel time (tw), canister flux (qc, Darcy velocity), F-quotient (F) and path length (L). The results presented in Figure B-1 and Figure B-4 are based on the ensemble of particles released within the local-scale release area. In Figure B-2 and Figure B-5 the results are based on particles released

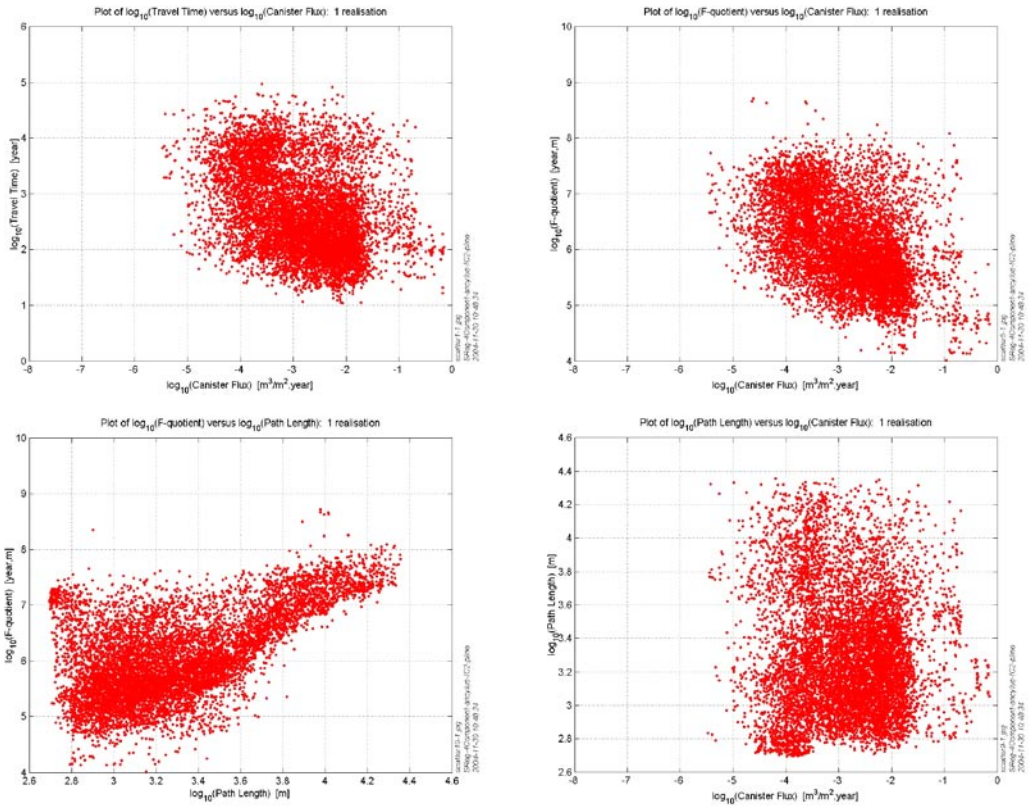

Figure B-1. *Scatter plots with different combinations of the calculated performance measures (t_w, q_c, F and L). Statistics shown for the ensemble of particles released in the local-scale release area for the Base Case (SReg_4Component_ IC2).*

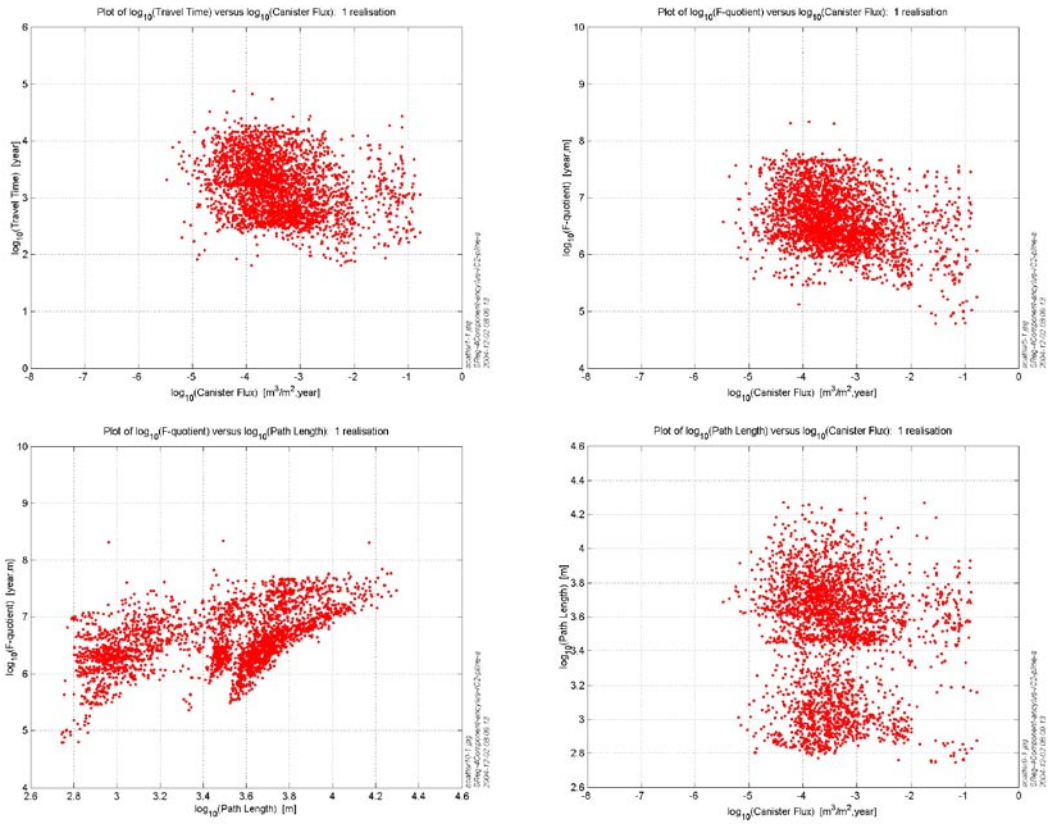

Figure B-2. *Scatter plots with different combinations of the calculated performance measures (t_w, q_c, F and L). Statistics shown for the Base Case (SReg_4Component_ IC2) for particles released within the Simpevarp release area.*

within the Simpevarp release area only. In Figure B-3 and Figure B-6 the results are based on particles released within the Laxemar release area only. The results demonstrate a slight bi-modal behaviour due to some particles starting in or near a fracture zone. The behaviour is more pronounced when separating the data from the two areas Simpevarp and Laxemar. Now, the two areas show quite different statistics indicating differences in the structural model, i.e. stochastic and deterministic fracture zones.

The statistical summaries are presented in Table B-1 to Table B-3, where the statistics are calculated for numbers in $\log_{10}$ space. The results presented are based on the ensemble of particles released in the local-scale release area. To quantify the differences between Laxemar and Simpevarp statistics were also calculated for the two sites separately. The performance measure statistics are presented in Table B-2 and Table B-3 for the two sites individually. The medians of both t_w and F are about one order of magnitude higher for the Simpevarp release area than for Laxemar release area. Correspondingly the median of q_c is about one order of magnitude lower in Simpevarp.

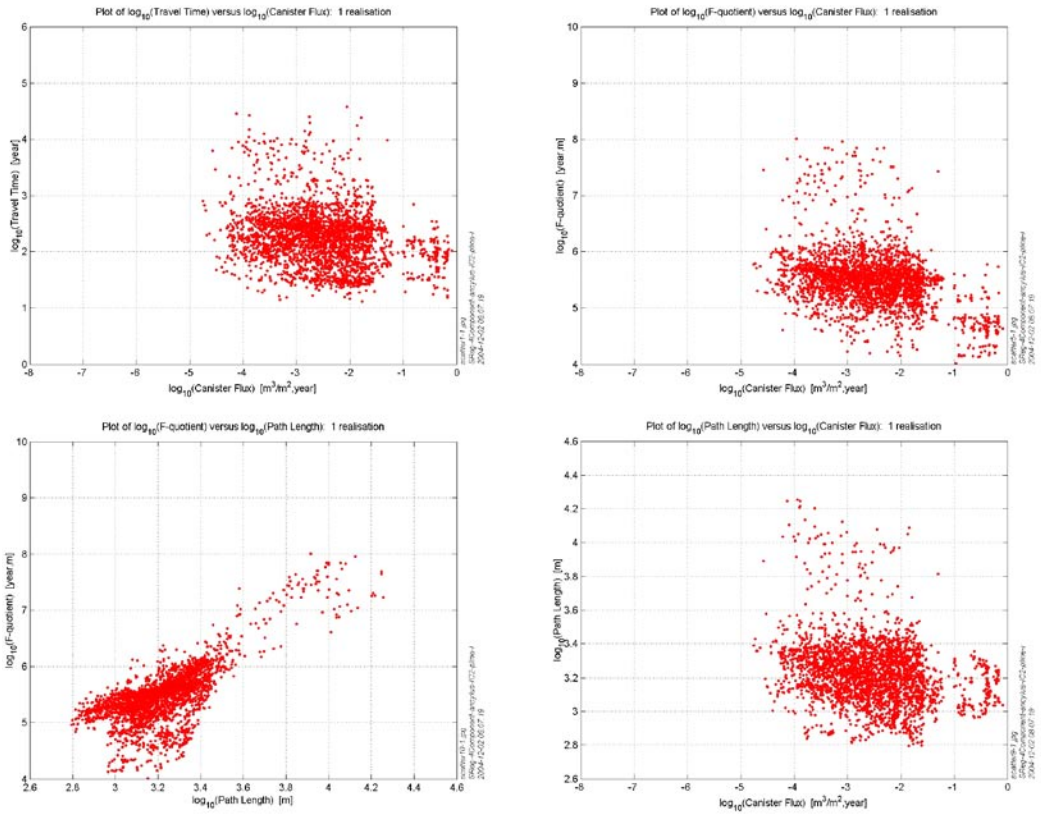

Figure B-3. *Scatter plots with different combinations of the calculated performance measures (t_w, q_c, F and L). Statistics shown for the Base Case (SReg_4Component_ IC2) for particles released within the Laxemar release area.*

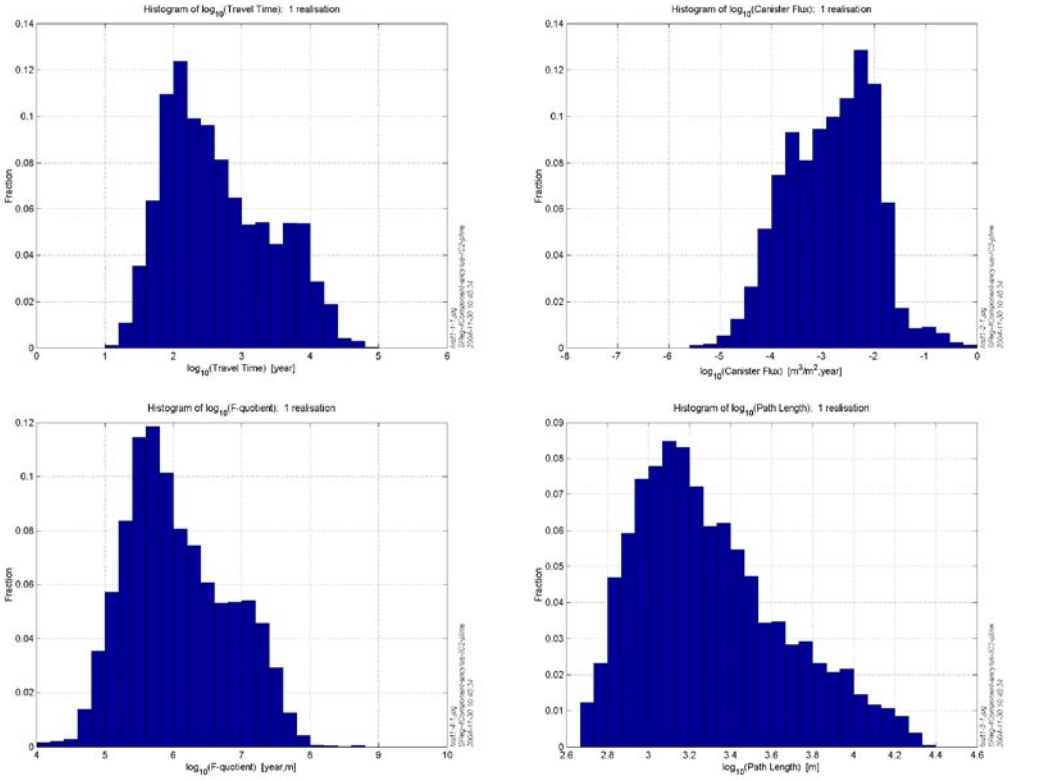

Figure B-4. *Histograms of the calculated performance measures (t_w, q_c, F and L). Statistics shown for the ensemble of particles released in the local-scale release area for the Base Case (SReg_4Component_ IC2).*

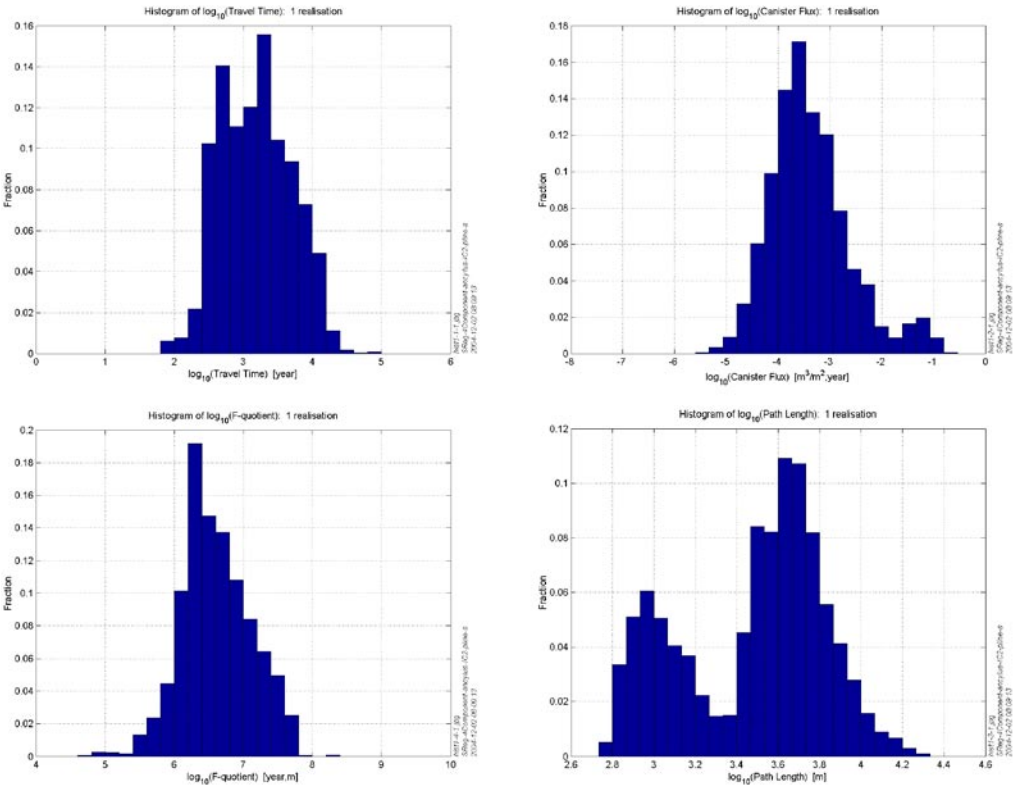

Figure B-5. *Histograms of the calculated performance measures (t_w, q_c, F and L). Statistics shown for the Base Case (SReg_4Component_ IC2) for particles released within the Simpevarp release area.*

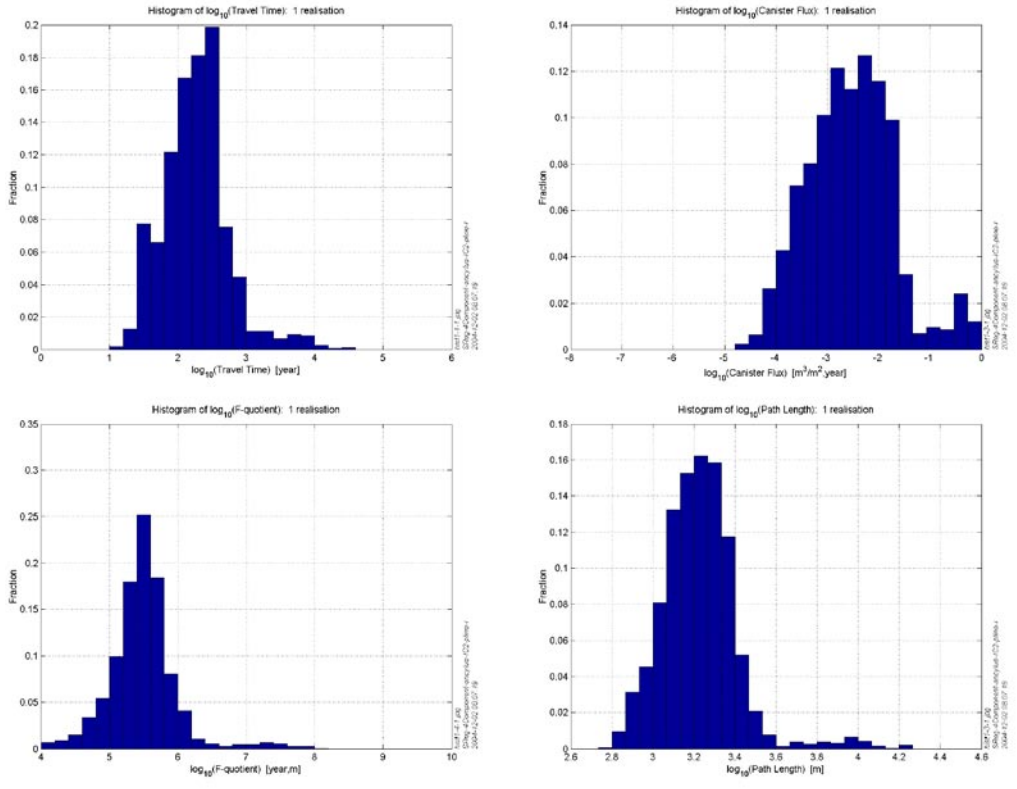

Figure B-6. *Histograms of the calculated performance measures (t_w, q_c, F and L). Statistics shown for the Base Case (SReg_4Component_IC2) for the particles released within the Laxemar release area.*

Table B-1. Statistical summary of the calculated performance measures (t_w, q_c, F and L) for the ensemble of particles released in the local-scale release area for the Base Case (SReg_4Component_ IC2).

Statistical entity	$Log_{10}(t_w)$	$Log_{10}(q_c)$	$Log_{10}(F)$	$Log_{10}(L)$
Mean	2.662	–2.864	6.061	3.303
Median	2.518	–2.807	5.939	3.235
5th percentile	1.616	–4.258	4.973	2.821
25th percentile	2.044	–3.533	5.503	3.028
75th percentile	3.249	–2.199	6.612	3.518
95th percentile	4.034	–1.649	7.390	3.999
Std dev	0.768	0.861	0.752	0.358
Variance	0.589	0.741	0.566	0.128
Skewness	0.470	–0.065	0.352	0.665
Kurtosis	–0.728	–0.372	–0.575	–0.232
Min value	1.042	–5.477	3.809	2.695
Max value	4.971	–0.153	8.708	4.356
Fraction OK	0.937	1.000	0.937	0.937

Table B-2. Statistical summary of the calculated performance measures (t_w, q_c, F and L) for the Simpevarp release area for the Base Case (SReg_4Component_IC2).

Statistical entity	$Log_{10}(t_w)$	$Log_{10}(q_c)$	$Log_{10}(F)$	$Log_{10}(L)$
Mean	3.182	–3.390	6.606	3.477
Median	3.179	–3.498	6.553	3.572
5th percentile	2.466	–4.527	5.814	2.883
25th percentile	2.755	–3.910	6.275	3.148
75th percentile	3.561	–2.999	6.946	3.728
95th percentile	4.040	–1.703	7.488	3.965
Std dev	0.508	0.792	0.504	0.348
Variance	0.258	0.626	0.254	0.121
Skewness	0.150	0.759	0.066	–0.372
Kurtosis	–0.651	0.855	0.011	–0.926
Min value	1.806	–5.476	4.788	2.746
Max value	4.871	–0.775	8.337	4.295
Fraction OK	0.824	1.000	0.824	0.824

Table B-3. Statistical summary of the calculated performance measures (t_w, q_c, F and L) for the Laxemar release area for the Base Case (SReg_4Component_ IC2).

Statistical entity	$Log_{10}(t_w)$	$Log_{10}(q_c)$	$Log_{10}(F)$	$Log_{10}(L)$
Mean	2.261	–2.552	5.489	3.227
Median	2.257	–2.589	5.495	3.222
5th percentile	1.497	–3.889	4.717	2.952
25th percentile	1.964	–3.140	5.244	3.111
75th percentile	2.497	–2.016	5.680	3.325
95th percentile	3.049	–0.919	6.154	3.486
Std dev	0.484	0.855	0.501	0.189
Variance	0.235	0.730	0.251	0.036
Skewness	0.826	0.357	1.059	1.338
Kurtosis	2.084	0.232	4.720	4.760
Min value	1.121	–4.755	3.699	2.794
Max value	4.583	–0.094	8.011	4.255
Fraction OK	0.986	1.000	0.986	0.986

B.3 Larger regional model (LReg_4Component_IC2)

In Figure B-7 and Figure B-8 the statistical results for the Larger regional model are shown as scatter plots and histograms for the four calculated performance measures travel time (t_w), canister flux (q_c, Darcy velocity), F-quotient (F) and path length (L). The results are based on the ensemble of particles released within the local-scale release area. Comparing the median value and the variance to the Base Case shows that the results are very similar between the cases.

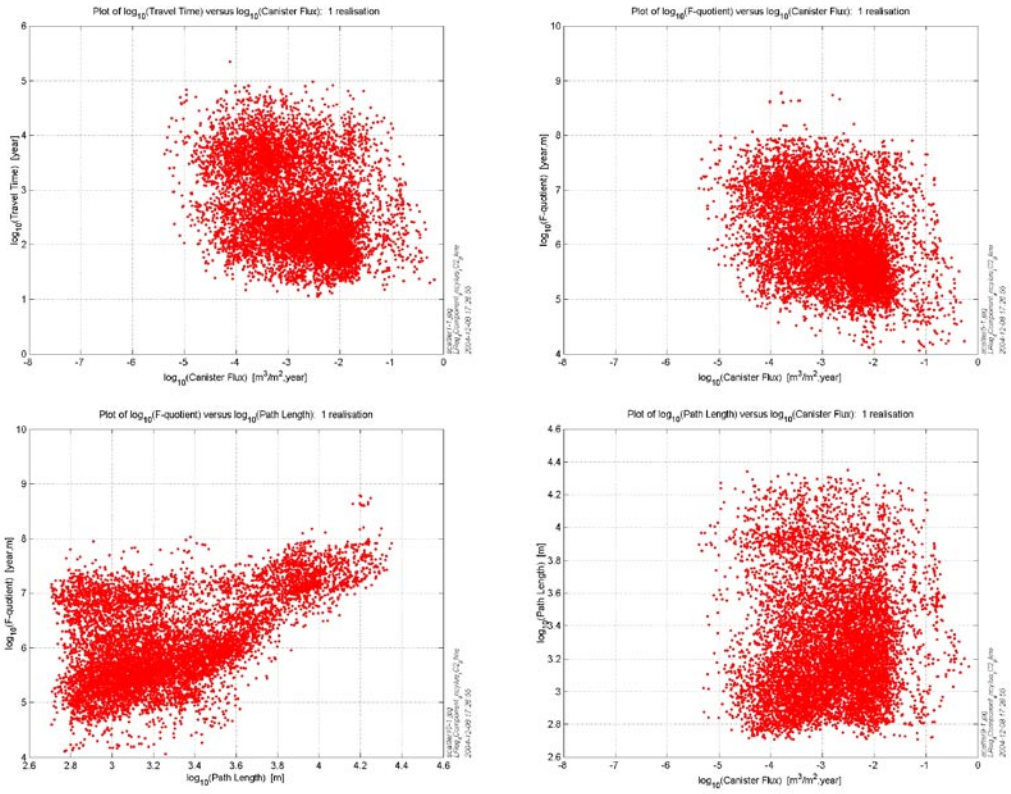

Figure B-7. *Scatter plots with different combinations of the calculated performance measures (t_w, q_c, F and L) for the ensemble of particles released in the local-scale release area for Base Case in larger regional model domain (LReg_4Component_IC2).*

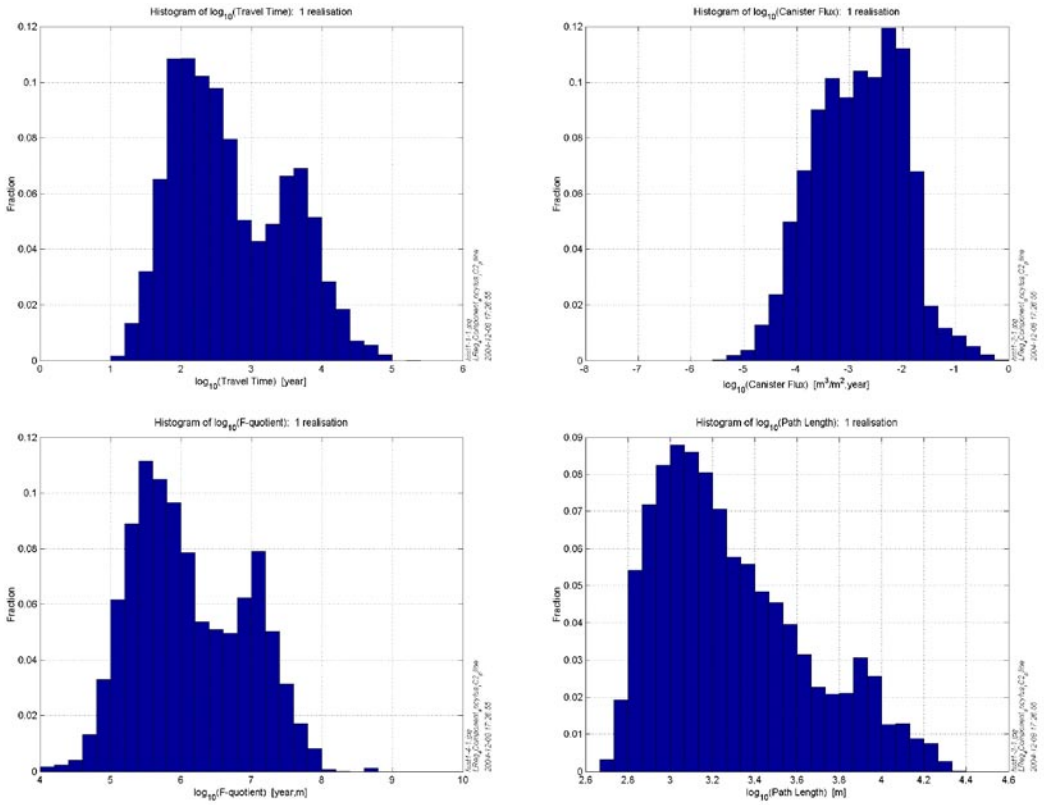

Figure B-8. *Histograms of the calculated performance measures (t_w, q_c, F and L) for the ensemble of particles released in the local-scale release area for Base Case in larger regional model domain T (LReg_4Component_IC2).*

Table B-4. Statistical summary of the calculated performance measures (t_w, q_c, F and L) for the ensemble of particles released in the local-scale release area for Base Case in larger regional model domain (LReg_4Component_IC2).

Statistical entity	$Log_{10}(t_w)$	$Log_{10}(q_c)$	$Log_{10}(F)$	$Log_{10}(L)$
Mean	2.702	–2.834	6.108	3.293
Median	2.537	–2.800	5.961	3.212
5th percentile	1.615	–4.218	4.981	2.836
25th percentile	2.044	–3.469	5.491	3.015
75th percentile	3.395	–2.178	6.800	3.513
95th percentile	4.072	–1.621	7.440	3.982
Std dev	0.799	0.842	0.797	0.356
Variance	0.638	0.708	0.635	0.127
Skewness	0.419	–0.080	0.299	0.730
Kurtosis	–0.802	–0.441	–0.769	–0.263
Min value	1.050	–5.386	3.878	2.708
Max value	5.353	–0.179	8.782	4.350
Fraction OK	0.973	1.000	0.973	0.973

B.4 Base Case Realisation 2 (SReg_4Component2_IC2)

In Figure B-9 and Figure B-10 the statistical results for Realisation 2 of the Base Case are shown as scatter plots and histograms for the four calculated performance measures travel time (t_w), canister flux (q_c, Darcy velocity), F-quotient (F) and path length (L). The results are based on the ensemble of particles released within the local-scale release area. Comparing the median value and the variance to the Base Case shows that the results are only differing by less than 10%, see Table B-5.

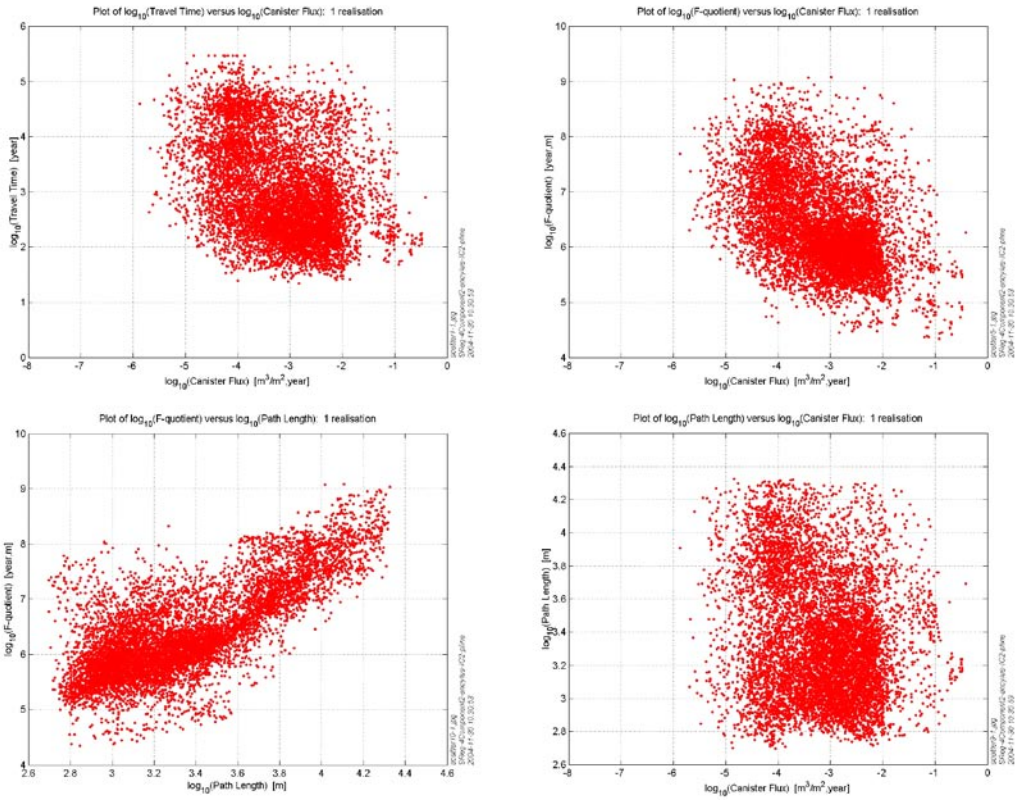

Figure B-9. *Scatter plots with different combinations of the calculated performance measures (tw, qc, F and L) for the ensemble of particles released in the local-scale release area for Base Case Realisation 2 (SReg_4Component2_ IC2).*

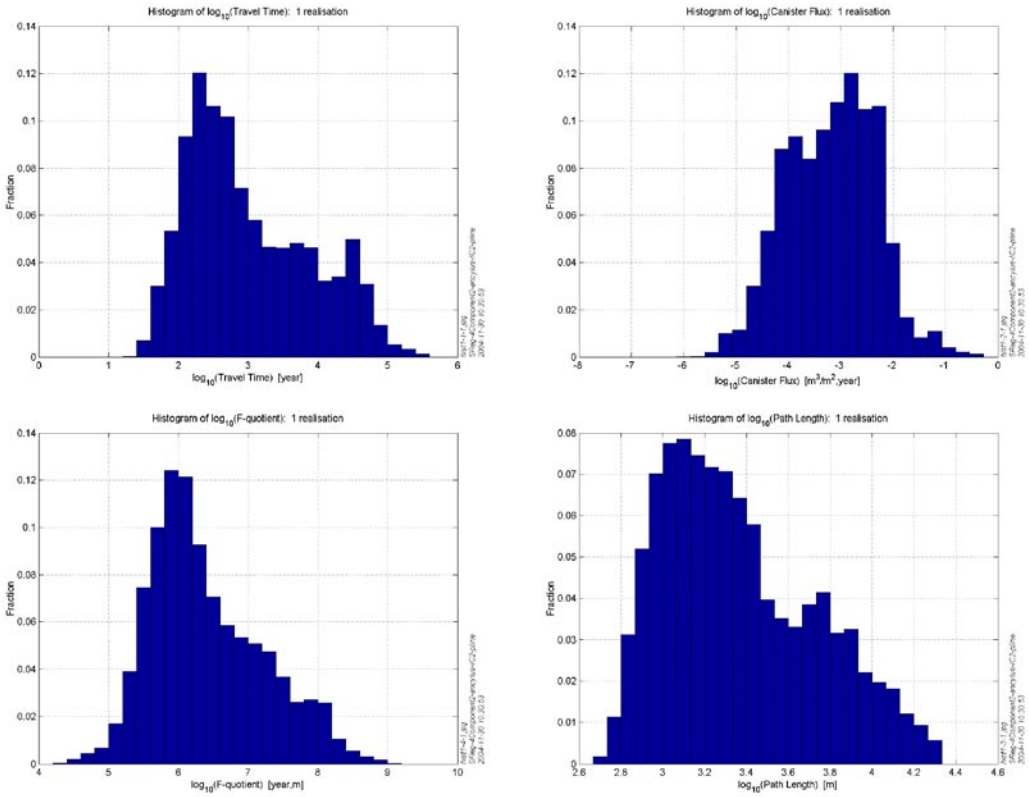

Figure B-10. *Histograms of the calculated performance measures (tw, qc, F and L) for the ensemble of particles released in the local-scale release area for Base Case Realisation 2 (SReg_4Component2_ IC2).*

Table B-5. Statistical summary of the calculated performance measures (t_w, q_c, F and L) for the ensemble of particles released in the local-scale release area for Base Case Realisation 2 (SReg_4Component2_IC2).

Statistical entity	$Log_{10}(t_w)$	$Log_{10}(q_c)$	$Log_{10}(F)$	$Log_{10}(L)$
Mean	3.005	–3.193	6.400	3.363
Median	2.772	–3.151	6.221	3.295
5th percentile	1.859	–4.562	5.312	2.877
25th percentile	2.307	–3.872	5.809	3.072
75th percentile	3.657	–2.538	6.944	3.631
95th percentile	4.618	–1.926	7.975	4.048
Std dev	0.880	0.862	0.814	0.364
Variance	0.774	0.743	0.662	0.132
Skewness	0.585	–0.006	0.593	0.554
Kurtosis	–0.658	–0.351	–0.188	–0.576
Min value	1.343	–5.872	4.338	2.698
Max value	5.473	–0.413	9.082	4.326
Fraction OK	0.920	1.000	0.920	0.920

B.5 Base Case Realisation 3 (SReg_4Component3_IC2)

In Figure B-11 and Figure B-12 the statistical results for Realisation 3 of the Base Case are shown as scatter plots and histograms for the four calculated performance measures travel time (t_w), canister flux (q_c, Darcy velocity), F-quotient (F) and path length (L). The results are based on the ensemble of particles released within the local scale area. Again, comparing the median value and the variance to the Base Case shows that the results are differing by about 10%, see Table B-6.

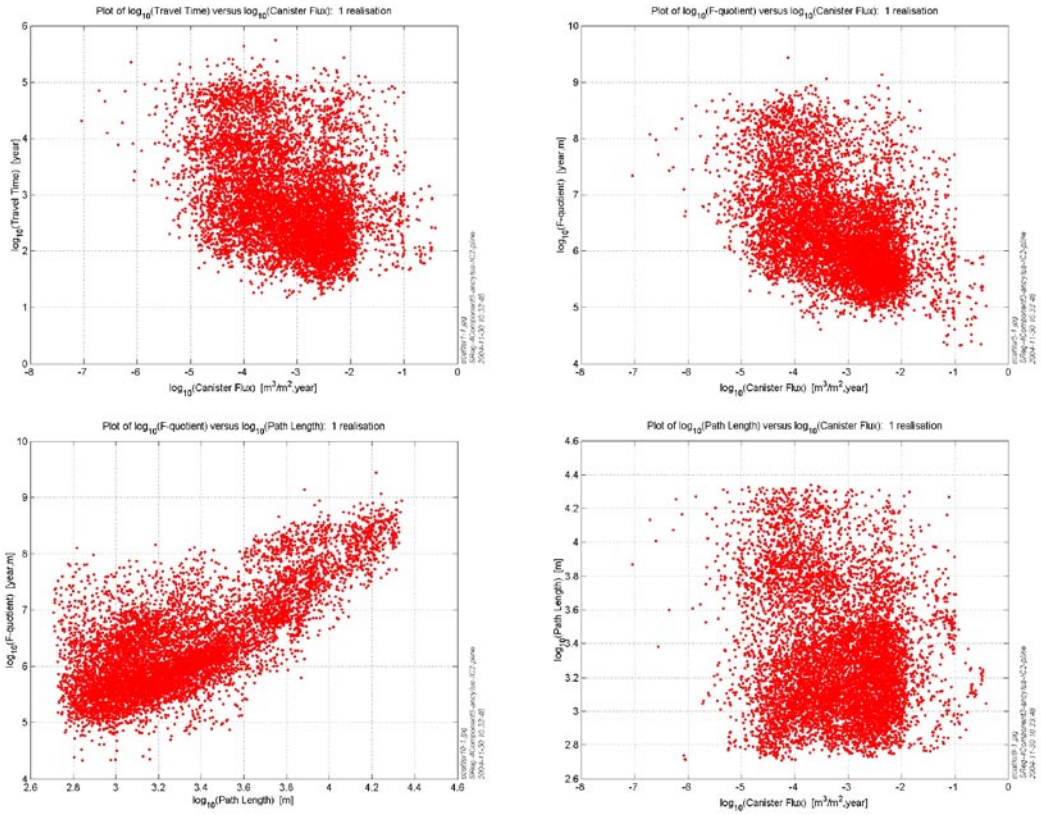

Figure B-11. *Scatter plots with different combinations of the calculated performance measures (t_w, q_c, F and L) for the ensemble of particles released in the local-scale release area for Base Case Realisation 3 (SReg_4Component3_ IC2).*

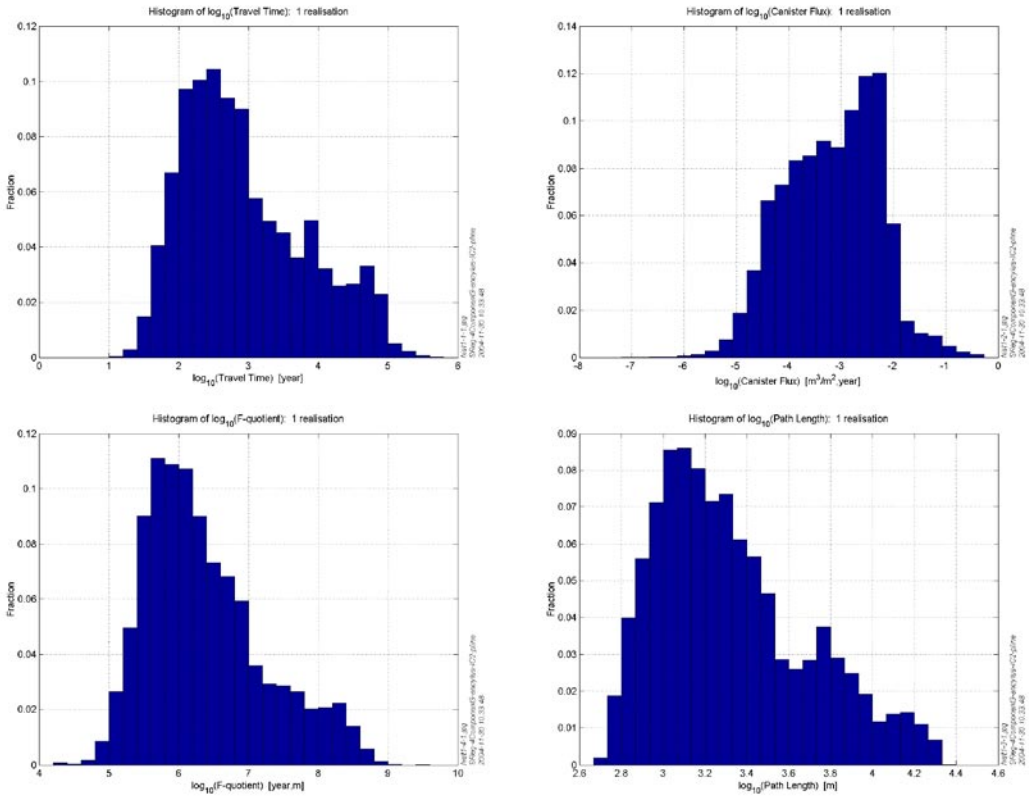

Figure B-12. *Histograms of the calculated performance measures (t_w, q_c, F and L) for the ensemble of particles released in the local-scale release area for Base Case Realisation 3 (SReg_4Component3_ IC2).*

Table B-6. Statistical summary of the calculated performance measures (t_w, q_c, F and L) for the ensemble of particles released in the local-scale release area for Base Case Realisation 3 (SReg_4Component3_ IC2).

Statistical entity	$Log_{10}(t_w)$	$Log_{10}(q_c)$	$Log_{10}(F)$	$Log_{10}(L)$
Mean	2.939	–3.205	6.367	3.327
Median	2.760	–3.149	6.189	3.257
5th percentile	1.770	–4.668	5.253	2.851
25th percentile	2.260	–3.914	5.728	3.050
75th percentile	3.518	–2.485	6.839	3.536
95th percentile	4.689	–1.935	8.129	4.044
Std dev	0.886	0.913	0.851	0.361
Variance	0.785	0.833	0.723	0.130
Skewness	0.628	–0.120	0.758	0.710
Kurtosis	–0.463	–0.412	–0.001	–0.237
Min value	1.162	–7.043	4.324	2.709
Max value	5.743	–0.419	9.438	4.338
Fraction OK	0.929	1.000	0.929	0.929

B.6 Hydro-DFN based on DarcyTools (SReg_4Component_DT_ IC2)

In Figure B-13 and Figure B-14 the statistical results for the case using a HydroDFN based on DarcyTools are shown as scatter plots and histograms for the four calculated performance measures travel time (t_w), canister flux (q_c, Darcy velocity), F-quotient (F) and path length (L). The results are based on the ensemble of particles released within the local scale area. Compared to the Base Case, the differences for the median value and the variance are very small, see Table B-7.

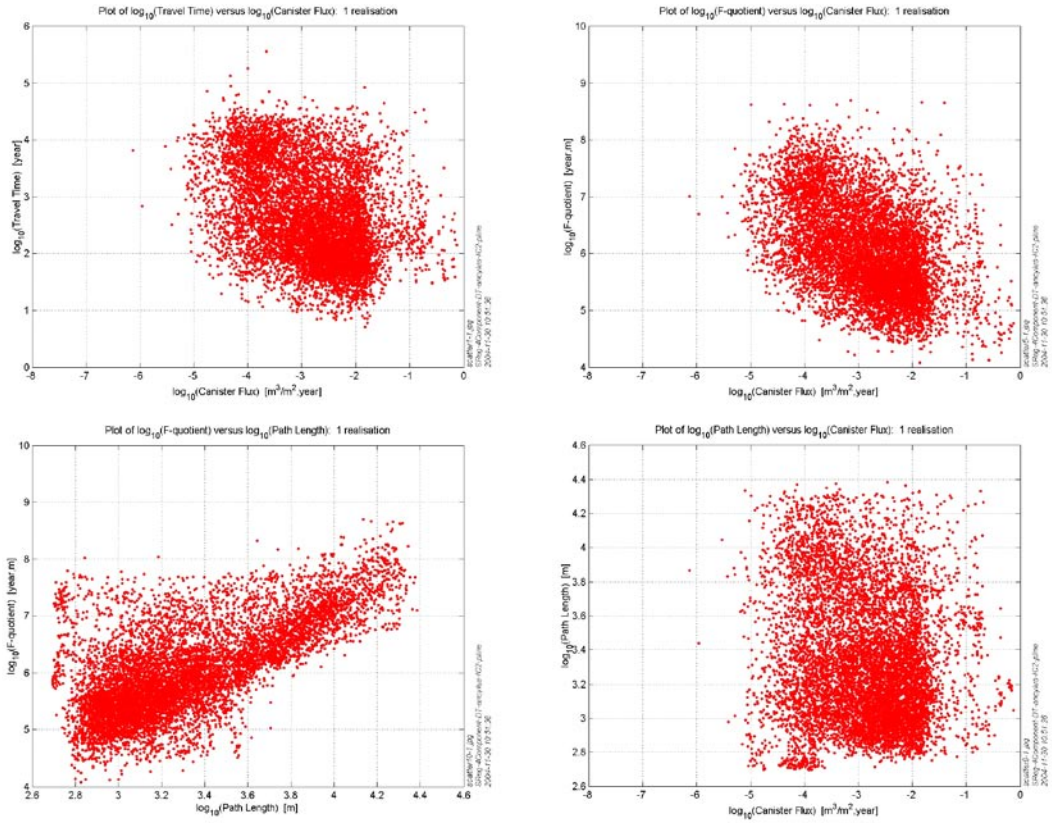

Figure B-13. *Scatter plots with different combinations of the calculated performance measures (t_w, q_c, F and L) for the ensemble of particles released in the local-scale release area for DT DFN (SReg_4Component_DT_ IC2).*

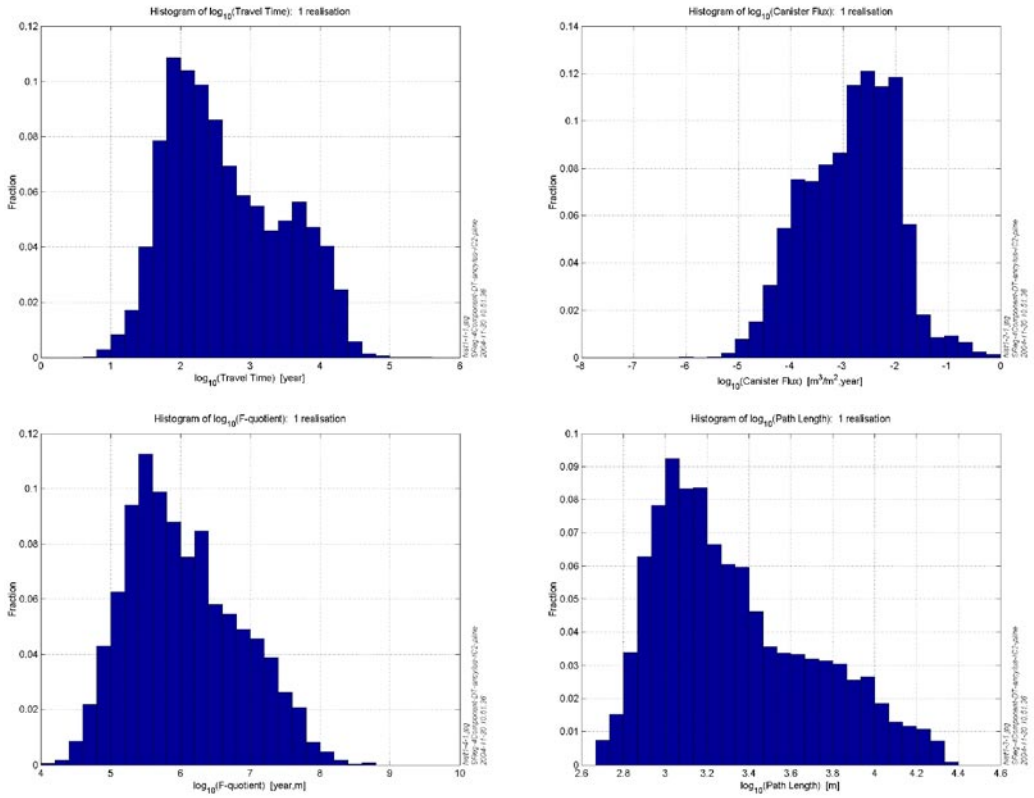

Figure B-14. *Histograms of the calculated performance measures (t_w, q_c, F and L) for the ensemble of particles released in the local-scale release area for DT DFN (SReg_4Component_ DT_ IC2).*

Table B-7. Statistical summary of the calculated performance measures (t_w, q_c, F and L) for the ensemble of particles released in the local-scale release area for DT DFN (SReg_4Component_DT_ IC2).

Statistical entity	$Log_{10}(t_w)$	$Log_{10}(q_c)$	$Log_{10}(F)$	$Log_{10}(L)$
Mean	2.649	–2.877	6.042	3.330
Median	2.486	–2.790	5.923	3.244
5th percentile	1.533	–4.323	4.904	2.858
25th percentile	1.989	–3.540	5.431	3.038
75th percentile	3.300	–2.217	6.602	3.584
95th percentile	4.097	–1.632	7.473	4.041
Std dev	0.823	0.875	0.800	0.372
Variance	0.678	0.765	0.639	0.138
Skewness	0.390	–0.121	0.424	0.673
Kurtosis	–0.800	–0.324	–0.468	–0.417
Min value	0.706	–6.129	4.080	2.696
Max value	5.557	–0.126	8.694	4.384
Fraction OK	0.934	1.000	0.934	0.934

B.7 Uncorrelated transmisisvity distribution (SReg_4Component_UnCorr_ IC2)

In Figure B-15 and Figure B-16 the statistical results for the case using a HydroDFN with an uncorrelated transmissivity distribution are shown as scatter plots and histograms for the four calculated performance measures travel time (t_w), canister flux (q_c, Darcy velocity), F-quotient (F) and path length (L). The results are based on the ensemble of particles released within the local scale area. Compared to the Base Case, the travel time is slightly longer, Darcy velocity smaller and F-quotient higher by about 10%, see Table B-8.

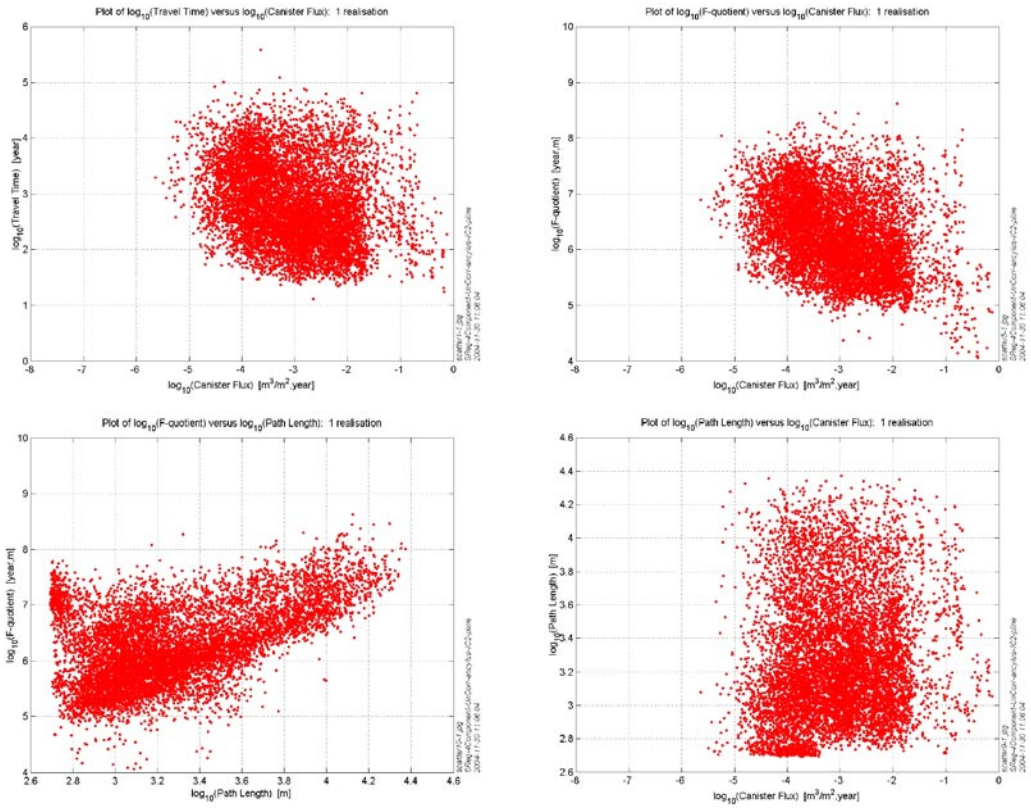

Figure B-15. *Scatter plots with different combinations of the calculated performance measures (t_w, q_c, F and L) for the ensemble of particles released in the local-scale release area for uncorrelated T (SReg_4Component_UnCorr_ IC2).*

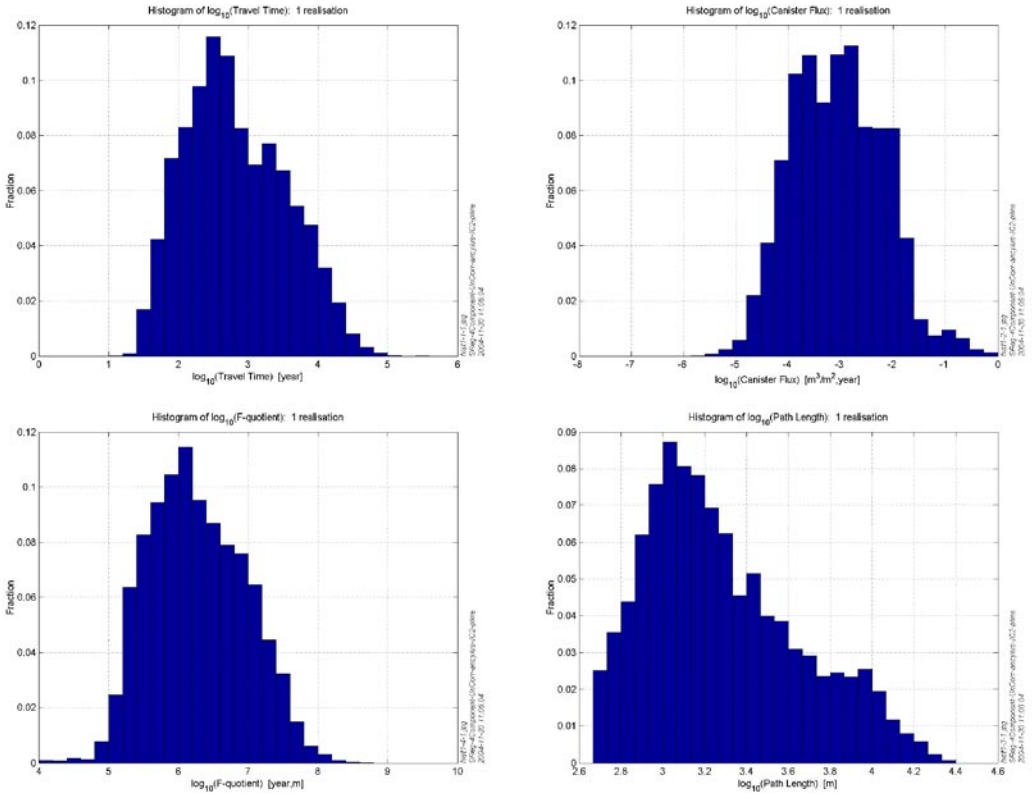

Figure B-16. *Histograms of the calculated performance measures (t_w, q_c, F and L) for the ensemble of particles released in the local-scale release area for uncorrelated T (SReg_4Component_UnCorr_ IC2).*

Table B-8. Statistical summary of the calculated performance measures (t_w, q_c, F and L) for the ensemble of particles released in the local-scale release area for uncorrelated T (SReg_4Component_UnCorr_ IC2).

Statistical entity	$Log_{10}(t_w)$	$Log_{10}(q_c)$	$Log_{10}(F)$	$Log_{10}(L)$
Mean	2.822	–3.052	6.268	3.286
Median	2.726	–3.075	6.208	3.212
5th percentile	1.759	–4.399	5.255	2.778
25th percentile	2.273	–3.727	5.745	3.006
75th percentile	3.353	–2.404	6.778	3.517
95th percentile	4.078	–1.694	7.443	3.996
Std dev	0.716	0.874	0.685	0.367
Variance	0.513	0.764	0.469	0.135
Skewness	0.336	0.233	0.211	0.629
Kurtosis	–0.625	–0.280	–0.491	–0.380
Min value	1.117	–5.642	3.872	2.693
Max value	5.577	–0.126	8.619	4.373
Fraction OK	0.966	1.000	0.966	0.966

B.8 Semi-correlated transmisisvity distribution (SReg_4Component_Semi_ IC2)

In Figure B-17 and Figure B-18 the statistical results for the case using a HydroDFN with a semi-correlated transmissivity distribution are shown as scatter plots and histograms for the four calculated performance measures travel time (t_w), canister flux (q_c, Darcy velocity), F-quotient (F) and path length (L). The results are based on the ensemble of particles released within the local scale area. Compared to the Base Case, the differences for the median value and the variance are very small, see Table B-9.

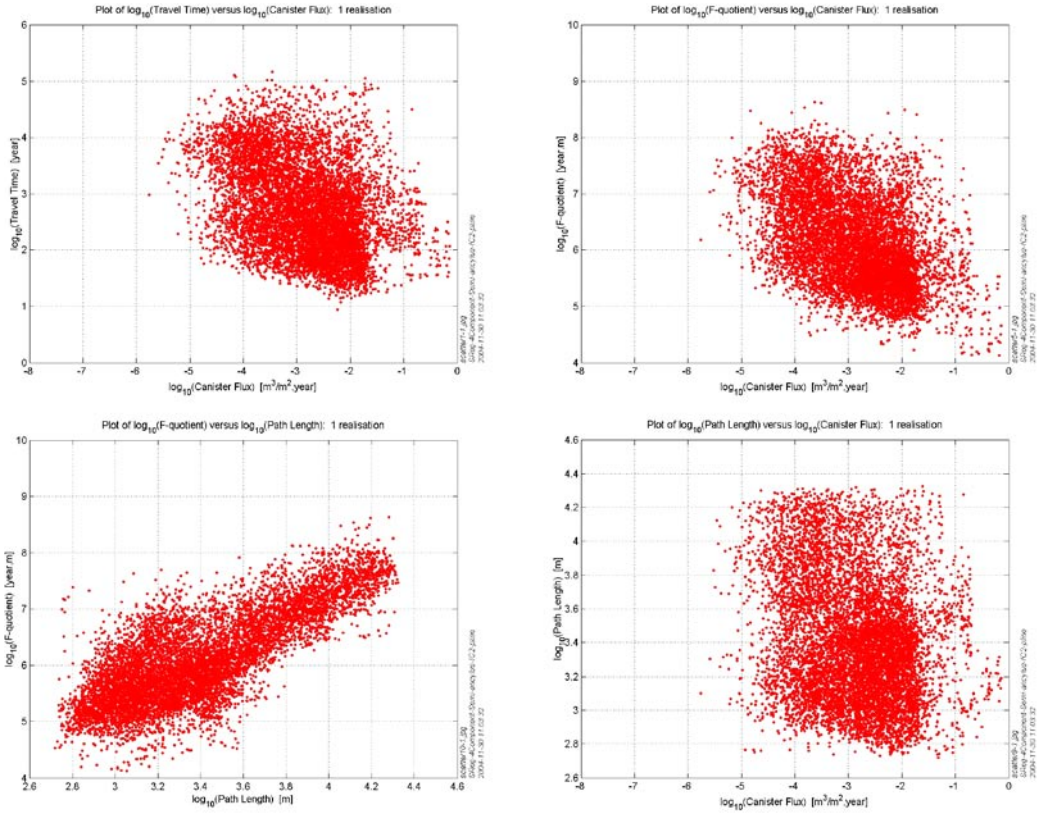

Figure B-17. *Scatter plots with different combinations of the calculated performance measures (t_w, q_c, F and L) for the ensemble of particles released in the local-scale release area for semi-correlated T (SReg_4Component_Semi_ IC2).*

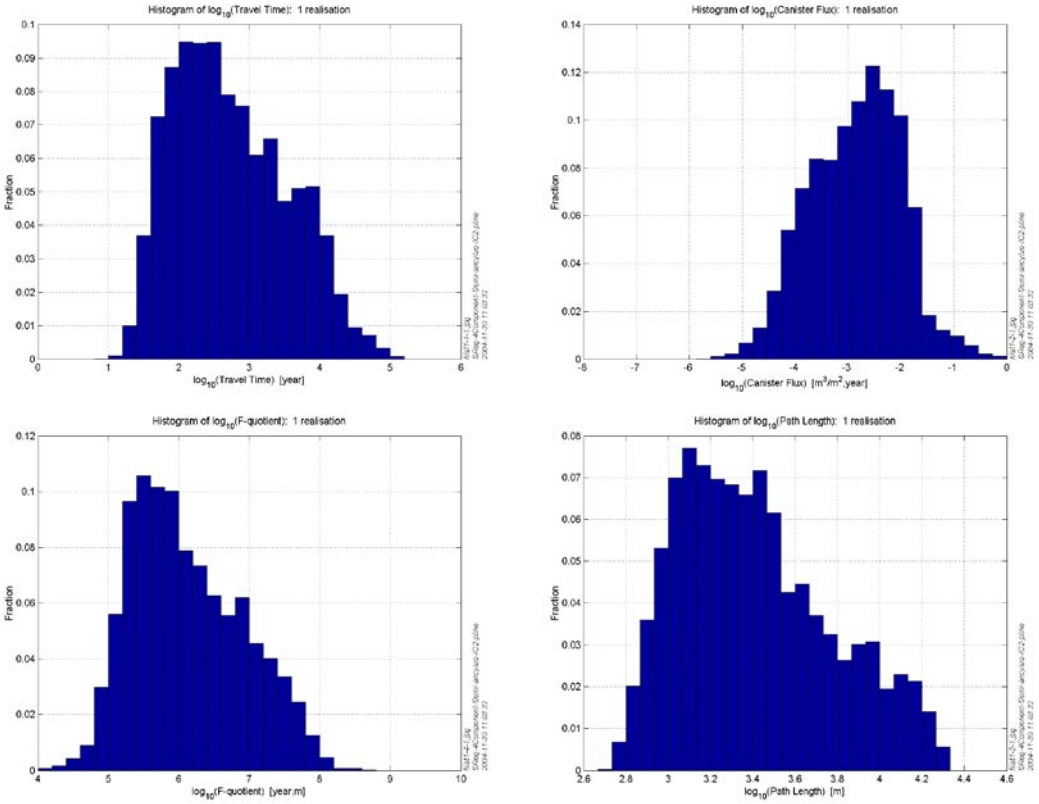

Figure B-18. *Histograms of the calculated performance measures (t_w, q_c, F and L) for the ensemble of particles released in the local-scale release area for semi-correlated T (SReg_4Component_Semi_ IC2).*

Table B-9. Statistical summary of the calculated performance measures (t_w, q_c, F and L) for the ensemble of particles released in the local-scale release area for semi-correlated T (SReg_4Component_Semi_ IC2).

Statistical entity	$Log_{10}(t_w)$	$Log_{10}(q_c)$	$Log_{10}(F)$	$Log_{10}(L)$
Mean	2.738	–2.871	6.121	3.411
Median	2.620	–2.805	5.988	3.361
5th percentile	1.609	–4.293	5.027	2.911
25th percentile	2.090	–3.529	5.503	3.122
75th percentile	3.321	–2.220	6.708	3.650
95th percentile	4.138	–1.622	7.561	4.110
Std dev	0.803	0.867	0.789	0.362
Variance	0.645	0.751	0.622	0.131
Skewness	0.404	–0.083	0.408	0.505
Kurtosis	–0.681	–0.331	–0.593	–0.583
Min value	0.947	–5.758	4.126	2.719
Max value	5.171	–0.139	8.630	4.325
Fraction OK	0.955	1.000	0.955	0.955

B.9 HCD Case 2 (SReg_4Component_IFZ2_IC2)

In HCD Case 2 only high confidence of existence HCDs and those with Length Class 2 and 3 (L > 1,500 m) are modelled. In Figure B-19 and Figure B-20 the statistical results for the variant using HCD Case 2 are shown as scatter plots and histograms for the four calculated performance measures travel time (t_w), canister flux (q_c, Darcy velocity), F-quotient (F) and path length (L). The results are based on the ensemble of particles released within the local scale area. Compared to the Base Case, the differences for the median value and the variance are very small, see Table B-10.

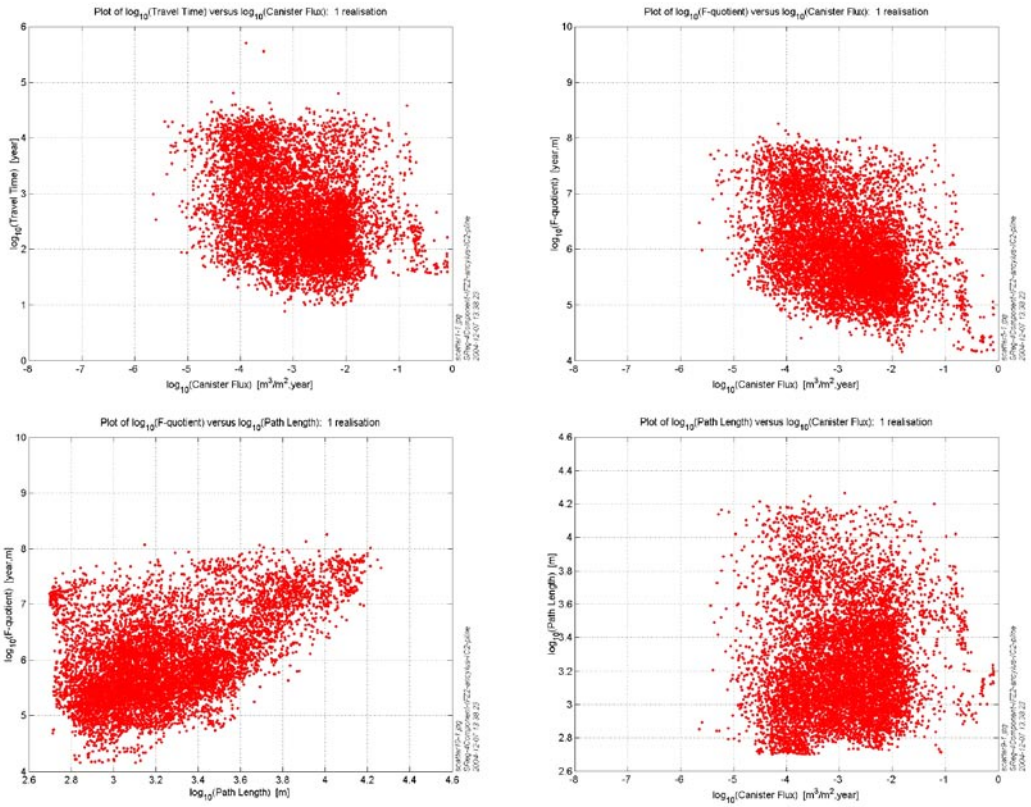

Figure B-19. *Scatter plots with different combinations of the calculated performance measures (t_w, q_c, F and L) for the ensemble of particles released in the local-scale release area for HCD Case 2 (SReg_4Component_IFZ2 _IC2).*

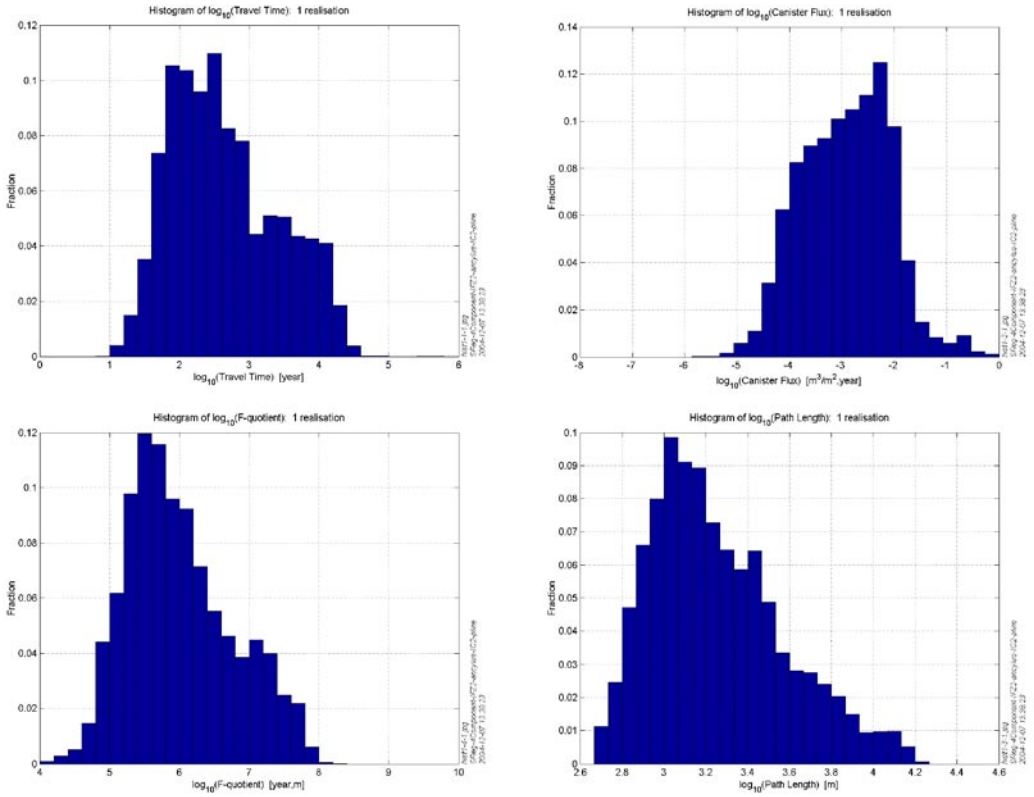

Figure B-20. *Histograms of the calculated performance measures (t_w, q_c, F and L) for the ensemble of particles released in the local-scale release area for HCD Case 2 (SReg_4Component_IFZ2_ IC2).*

Table B-10. Statistical summary of the calculated performance measures (t_w, q_c, F and L) for the ensemble of particles released in the local-scale release area for HCD Case 2 (SReg_4Component_IFZ3_ IC2).

Statistical entity	$Log_{10}(t_w)$	$Log_{10}(q_c)$	$Log_{10}(F)$	$Log_{10}(L)$
Mean	2.644	–2.930	6.004	3.252
Median	2.515	–2.895	5.875	3.194
5th percentile	1.587	–4.275	4.937	2.822
25th percentile	2.032	–3.592	5.442	3.015
75th percentile	3.215	–2.284	6.502	3.448
95th percentile	4.064	–1.695	7.416	3.866
Std dev	0.769	0.851	0.760	0.317
Variance	0.592	0.724	0.577	0.100
Skewness	0.442	0.066	0.472	0.682
Kurtosis	–0.669	–0.235	–0.471	–0.065
Min value	0.892	–5.646	4.157	2.699
Max value	5.705	–0.091	8.254	4.265
Fraction OK	0.960	1.000	0.960	0.960

B.10 HCD Case 3 (SReg_4Component_IFZ3_IC2)

In HCD Case 3 only high confidence of existence HCDs and those with Length Class 3 (L > 3,000 m) are modelled. In Figure B-21 and Figure B-22 the statistical results for the variant using HCD Case 3 are shown as scatter plots and histograms for the four calculated performance measures travel time (t_w), canister flux (q_c, Darcy velocity), F-quotient (F) and path length (L). The results are based on the ensemble of particles released within the local scale area. Compared to the Base Case, the differences for the median value and the variance are very small, see Table B-11.

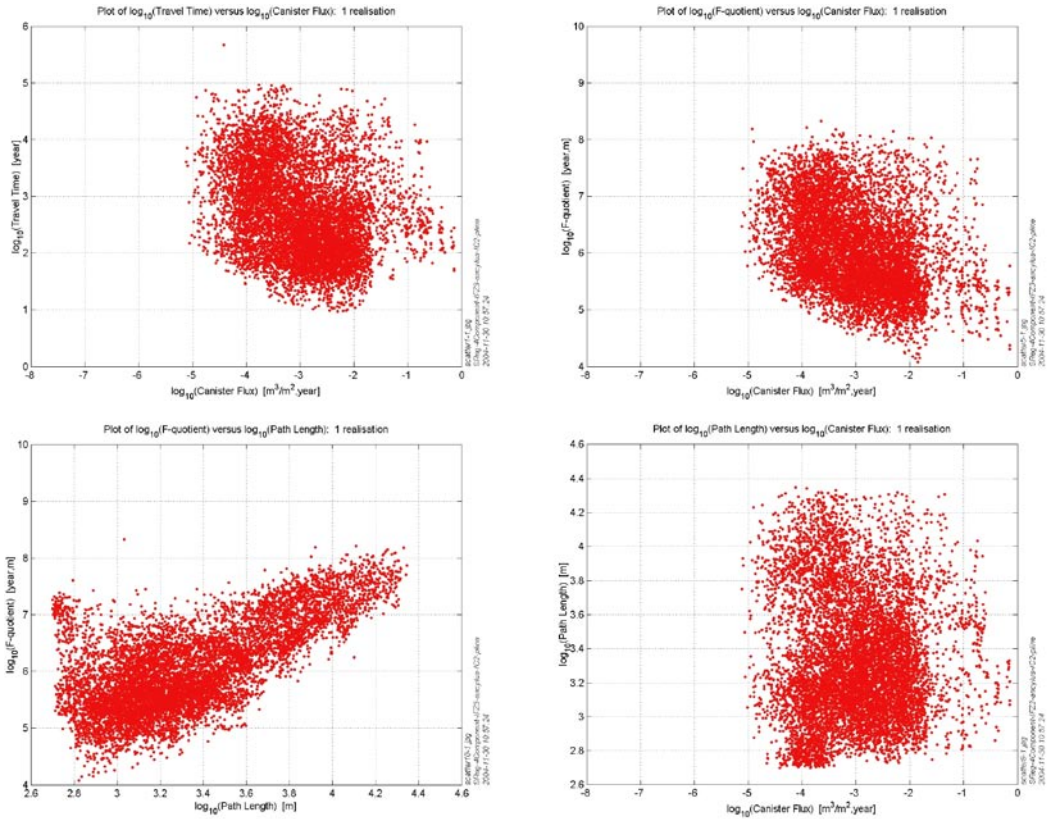

Figure B-21. *Scatter plots with different combinations of the calculated performance measures (t_w, q_c, F and L) for the ensemble of particles released in the local-scale release area for HCD Case 3 (SReg_4Component_IFZ3 _IC2).*

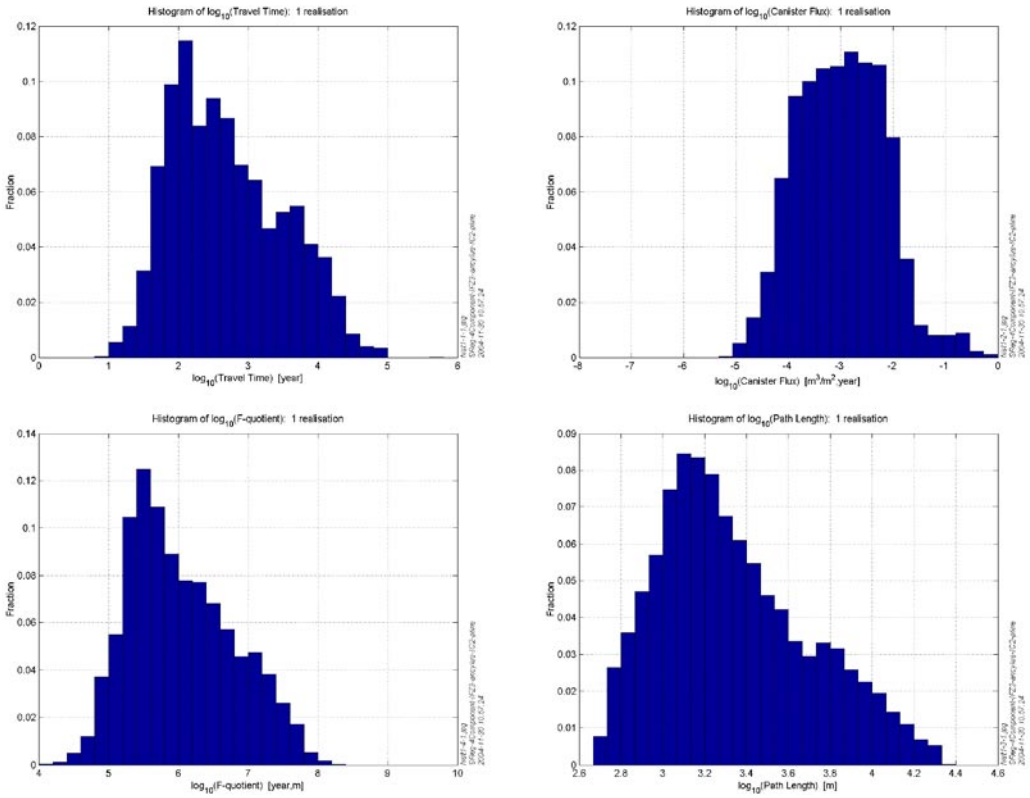

Figure B-22. *Histograms of the calculated performance measures (t_w, q_c, F and L) for the ensemble of particles released in the local-scale release area for HCD Case 3 (SReg_4Component_IFZ3_ IC2).*

Table B-11. Statistical summary of the calculated performance measures (t_w, q_c, F and L) for the ensemble of particles released in the local-scale release area for HCD Case 3 (SReg_4Component_IFZ3_ IC2).

Statistical entity	$Log_{10}(t_w)$	$Log_{10}(q_c)$	$Log_{10}(F)$	$Log_{10}(L)$
Mean	2.700	–2.994	6.038	3.338
Median	2.578	–2.996	5.909	3.270
5th percentile	1.606	–4.281	4.976	2.833
25th percentile	2.059	–3.632	5.462	3.068
75th percentile	3.286	–2.378	6.563	3.572
95th percentile	4.126	–1.711	7.404	4.027
Std dev	0.799	0.837	0.750	0.360
Variance	0.638	0.701	0.562	0.130
Skewness	0.434	0.231	0.424	0.565
Kurtosis	–0.634	–0.195	–0.569	–0.416
Min value	0.970	–5.117	4.076	2.699
Max value	5.671	–0.140	8.329	4.346
Fraction OK	0.956	1.000	0.956	0.956

B.11 Reduced hydraulic conductivity at depth (SReg_4Component_DepthK_IC2)

This case uses a hydraulic conductivity that reduces linearly with depth. In Figure B-23 and Figure B-24 the statistical results for the variant with a depth dependent K-field are shown as scatter plots and histograms for the four calculated performance measures travel time (t_w), canister flux (q_c, Darcy velocity), F-quotient (F) and path length (L). The results are based on the ensemble of particles released within the local scale area. Compared to the Base Case, the differences for the median value and the variance are very small, see Table B-12.

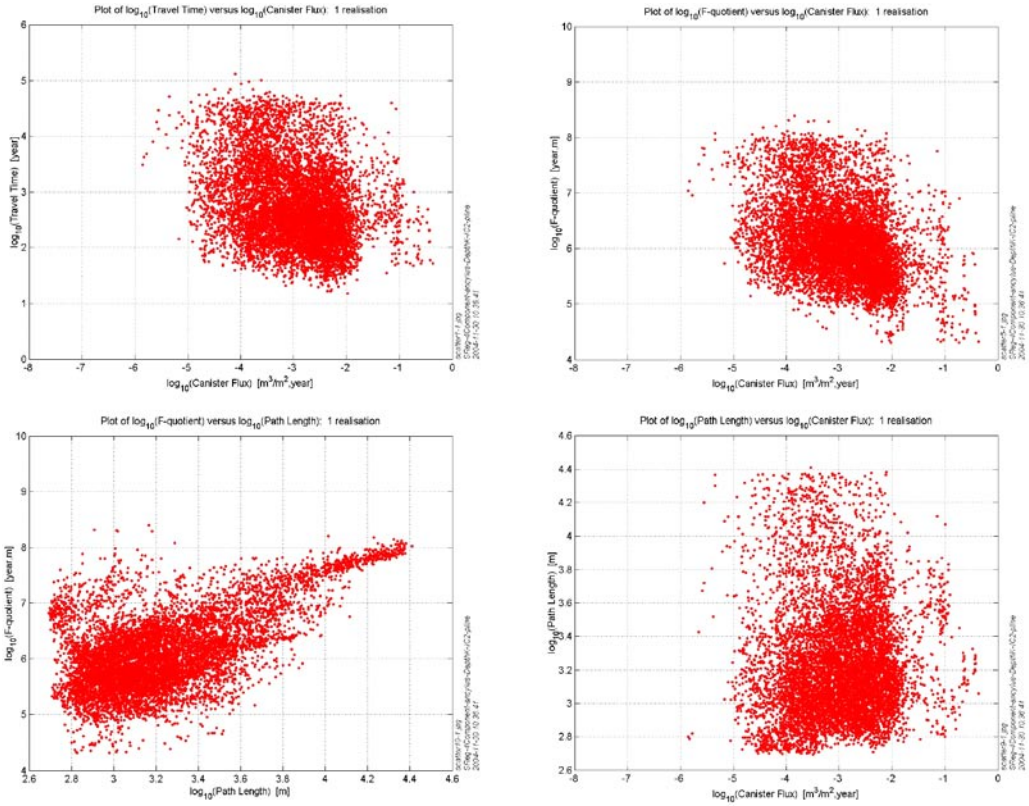

Figure B-23. *Scatter plots with different combinations of the calculated performance measures (t_w, q_c, F and L) for the ensemble of particles released in the local-scale release area for a lower K at depth (SReg_4Component_DepthK_IC2).*

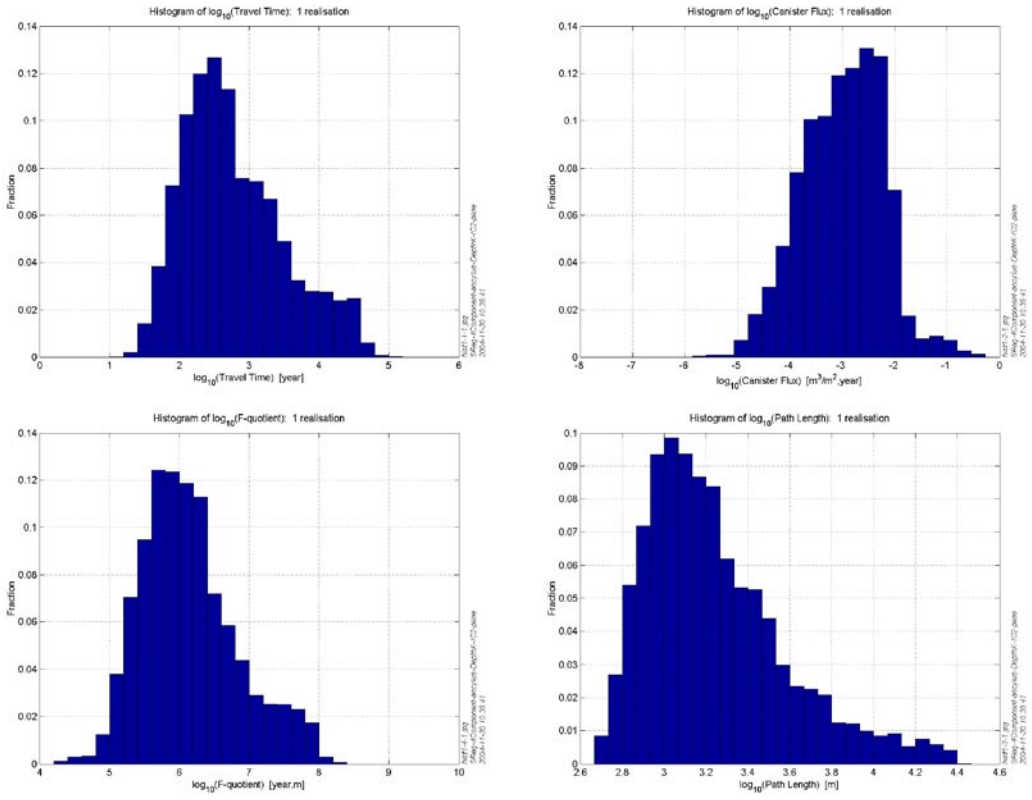

Figure B-24. *Histograms of the calculated performance measures (t_w, q_c, F and L) for the ensemble of particles released in the local-scale release area for a lower K at depth (SReg_4Component_ DepthK_IC2).*

Table B-12. Statistical summary of the calculated performance measures (t_w, q_c, F and L) for the ensemble of particles released in the local-scale release area for a lower K at depth (SReg_4Component_ DepthK_IC2).

Statistical entity	$Log_{10}(t_w)$	$Log_{10}(q_c)$	$Log_{10}(F)$	$Log_{10}(L)$
Mean	2.774	–3.026	6.138	3.243
Median	2.632	–2.975	6.047	3.174
5th percentile	1.783	–4.379	5.165	2.823
25th percentile	2.234	–3.595	5.643	2.997
75th percentile	3.224	–2.432	6.520	3.421
95th percentile	4.240	–1.924	7.551	3.934
Std dev	0.728	0.792	0.695	0.336
Variance	0.530	0.627	0.483	0.113
Skewness	0.641	–0.111	0.588	1.017
Kurtosis	–0.191	–0.037	0.041	0.808
Min value	1.184	–5.859	4.303	2.694
Max value	5.121	–0.366	8.395	4.410
Fraction OK	0.920	1.000	0.920	0.920

B.12 Increased hydraulic conductivity in top 100 m (SReg_4Component_K100m_IC2)

This case uses an increased hydraulic conductivity in the top 100 m. In Figure B-25 and Figure B-26 the statistical results for the variant with a depth dependent K-field are shown as scatter plots and histograms for the four calculated performance measures travel time (t_w), canister flux (q_c, Darcy velocity), F-quotient (F) and path length (L). The results are based on the ensemble of particles released within the local scale area. Compared to the Base Case, the differences for the median value and the variance are very small, see Table B-13.

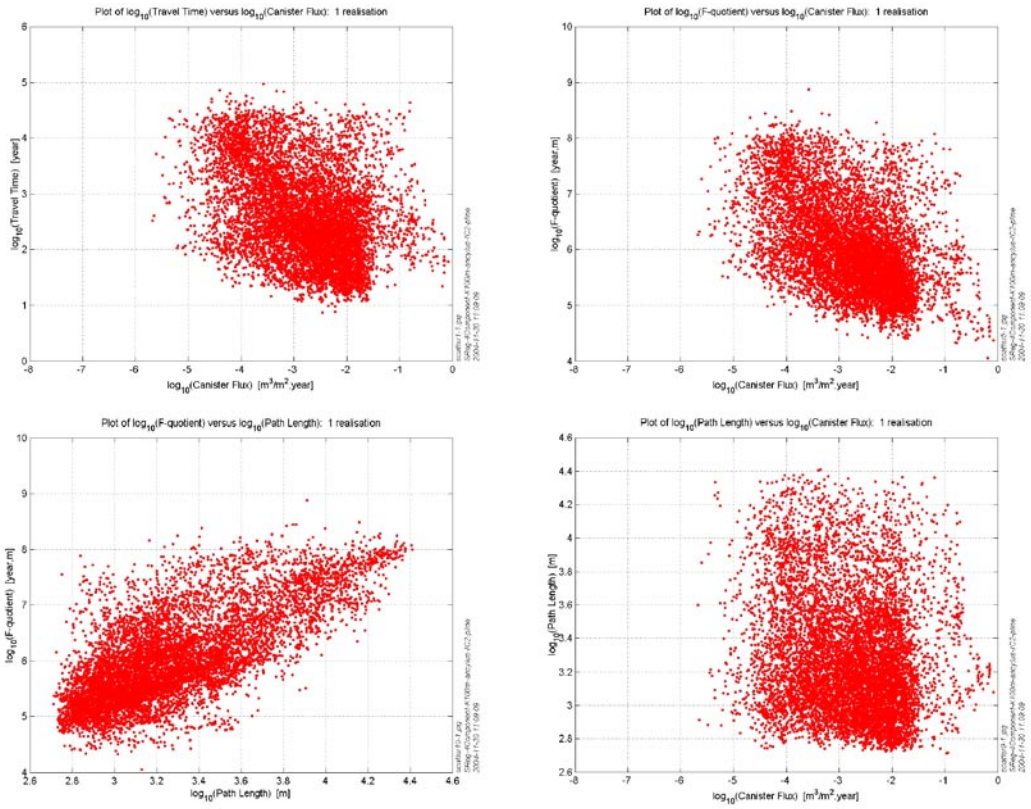

Figure B-25. *Scatter plots with different combinations of the calculated performance measures (t_w, q_c, F and L) for the ensemble of particles released in the local-scale release area for a higher K in top 100 m (SReg_4Component_K100m_ IC2).*

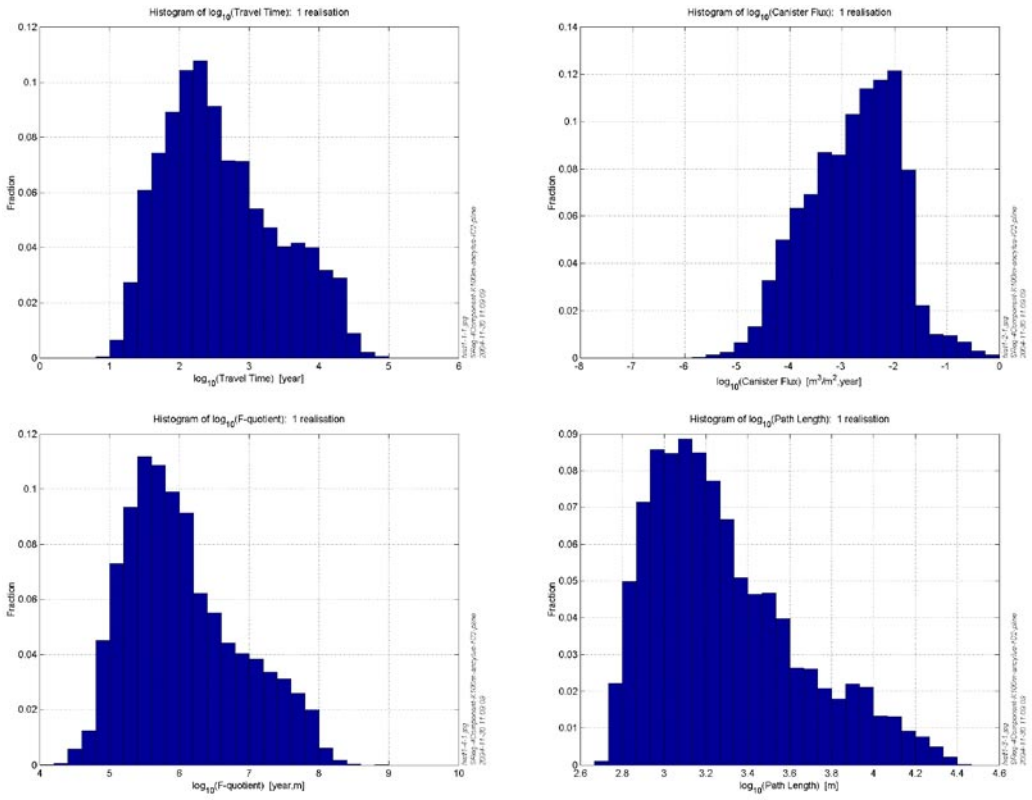

Figure B-26. *Histograms of the calculated performance measures (t_w, q_c, F and L) for the ensemble of particles released in the local-scale release area for a higher K in top 100 m (SReg_4Component_K100m_ IC2).*

Table B-13. Statistical summary of the calculated performance measures (t_w, q_c, F and L) for the ensemble of particles released in the local-scale release area for a higher K in top 100 m (SReg_4Component_K100m_ IC2).

Statistical entity	$Log_{10}(t_w)$	$Log_{10}(q_c)$	$Log_{10}(F)$	$Log_{10}(L)$
Mean	2.606	–2.804	6.052	3.288
Median	2.463	–2.711	5.897	3.209
5th percentile	1.459	–4.315	4.950	2.840
25th percentile	1.981	–3.445	5.440	3.015
75th percentile	3.170	–2.125	6.567	3.496
95th percentile	4.133	–1.572	7.639	4.001
Std dev	0.817	0.888	0.814	0.354
Variance	0.668	0.789	0.663	0.126
Skewness	0.473	–0.196	0.596	0.829
Kurtosis	–0.631	–0.316	–0.392	0.029
Min value	0.869	–5.680	4.052	2.712
Max value	4.969	–0.084	8.877	4.410
Fraction OK	0.958	1.000	0.958	0.958

B.13 Conclusions

The results demonstrate a slight bi-modal behaviour due to some particles starting in or near a fracture zone. The behaviour is more pronounced when separating the data from the two site-release areas Simpevarp and Laxemar. Also, the two areas show quite different statistics. The medians of both t_w and F are about one order of magnitude higher for the Simpevarp release area than for Laxemar release area. Correspondingly the median of q_c is about one order of magnitude lower in Simpevarp. This indicates the effects of differences in the local structural model (i.e. stochastic and deterministic fracture zones); and the positions relative to the regional hydrogeology with Laxemar being largely freshwater at 500 m depth, and Simpevarp having reduced flows due to the presence of salinity at 500 m depth.

The variations in the performance measures between the variants considered is generally low, around 10%. This perhaps should not be a surprise since all the cases considered have been calibrated against the same hydraulic data in the case of the Hydro-DFN variants, and against the same hydro-geochemistry data in the case of regional flow and solute transport. One variant that has not been considered here that may have a large effect would be to sample the HCD hydraulic properties in stochastic way rather than using global median values.